

AD-A189 295

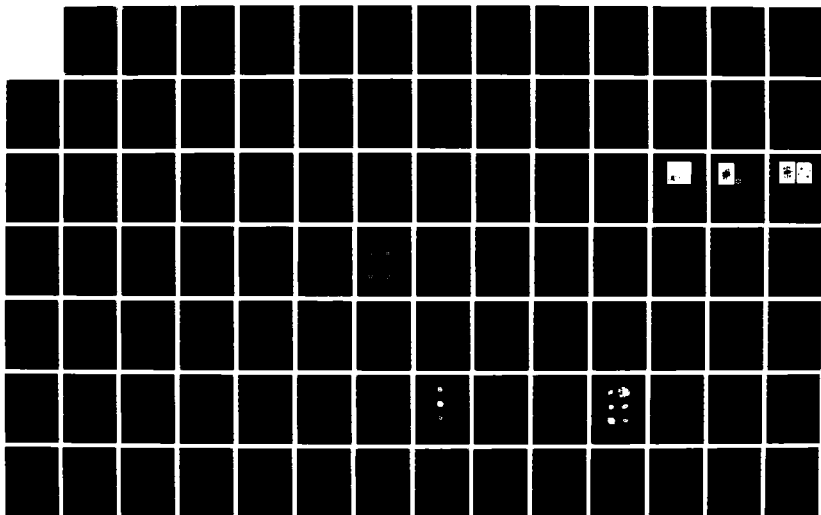
INVESTIGATIONS OF HIGH RESOLUTION IMAGING THROUGH THE
EARTH'S ATMOSPHERE. (U) STEWARD OBSERVATORY TUCSON ARIZ
E K HEGE 15 MAR 87 AFGL-TR-87-0097 F19628-84-K-0035

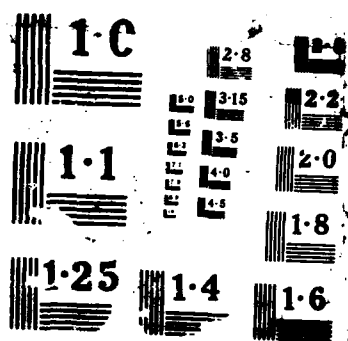
1/4

UNCLASSIFIED

F/G 28/6

NL





12

AFGL-TR-87-0097

**Investigations of High Resolution Imaging
Through the Earth's Atmosphere
Using Speckle Interferometry**

E. Keith Hege

University of Arizona
Steward Observatory
Tucson, Arizona 85721

DTIC
SELECTED
SEP 04 1987
C&D

15 March 1987

Final Report
1 August 1984 - 31 July 1986

Approved for public release; distribution unlimited

AIR FORCE GEOPHYSICS LABORATORY
AIR FORCE SYSTEMS COMMAND
UNITED STATES AIR FORCE
HANSCOM AIR FORCE BASE, MASSACHUSETTS 01731

AD-A189 295

Unclassified

SECURITY CLASSIFICATION OF THIS PAGE

REPORT DOCUMENTATION PAGE

1a. REPORT SECURITY CLASSIFICATION Unclassified		1b. RESTRICTIVE MARKINGS	
2a. SECURITY CLASSIFICATION AUTHORITY		3. DISTRIBUTION/AVAILABILITY OF REPORT Approved for public release; distribution unlimited	
2b. DECLASSIFICATION/DOWNGRADING SCHEDULE			
4. PERFORMING ORGANIZATION REPORT NUMBER(S)		5. MONITORING ORGANIZATION REPORT NUMBER(S) AFGL-TR-87-0097	
6a. NAME OF PERFORMING ORGANIZATION University of Arizona	6b. OFFICE SYMBOL (If applicable)	7a. NAME OF MONITORING ORGANIZATION Air Force Geophysics Laboratory	
6c. ADDRESS (City, State and ZIP Code) Steward Observatory Tucson, Arizona 85721		7b. ADDRESS (City, State and ZIP Code) Hanscom Air Force Base Massachusetts 01731	
8a. NAME OF FUNDING/SPONSORING ORGANIZATION	8b. OFFICE SYMBOL (If applicable)	9. PROCUREMENT INSTRUMENT IDENTIFICATION NUMBER F19628-84-K-0035	
8c. ADDRESS (City, State and ZIP Code)		10. SOURCE OF FUNDING NOS.	
		PROGRAM ELEMENT NO. 611027	PROJECT NO. 2311
11. TITLE (Include Security Classification) Investigations of High Resolution Imaging		12. PERSONAL AUTHOR(S) E. Keith Hege	
13a. TYPE OF REPORT Final Report	13b. TIME COVERED FROM 8/1/84 TO 7/31/86	14. DATE OF REPORT (Yr., Mo., Day) 1987 March 15	15. PAGE COUNT 354
16. SUPPLEMENTARY NOTATION			
17. COSATI CODES		18. SUBJECT TERMS (Continue on reverse if necessary and identify by block number)	
FIELD	GROUP	SUB. GR.	Speckle Interferometry, Diffraction Limited Imaging ←
19. ABSTRACT (Continue on reverse if necessary and identify by block number) Speckle Interferometry can now be used to produce images with spatial resolution of order 100x sharper than that normally permitted by the Earth's atmosphere. During this two year program of technique development we achieved high resolution imaging capability (wavelength dependent; 60 nrad at 410 nm) and approached that resolution in imaging a geosynchronous communications satellite utilizing the Multiple Mirror Telescope (MMT) and the Fienup method. We continued the pattern of parallel programs established in our previous AFGL work: E. K. Hege, P. A. Strittmatter and N. J. Woolf, "Investigations of High Resolution Imaging Through the Earth's Atmosphere Using Speckle Interferometry," AFGL Report AFGL-TR-84-0116, 1984. Specific to this contract work, in our first year we completed a fully co-phased optical beam-combiner for implementation of the full 6.9m aperture imaging capability of the MMT. During our second year we met our final objective, by producing a 100 nrad resolution image			
20. DISTRIBUTION/AVAILABILITY OF ABSTRACT UNCLASSIFIED/UNLIMITED <input checked="" type="checkbox"/> SAME AS RPT. <input type="checkbox"/> DTIC USERS <input type="checkbox"/>		21. ABSTRACT SECURITY CLASSIFICATION Unclassified	
22a. NAME OF RESPONSIBLE INDIVIDUAL Richard R. Radick		22b. TELEPHONE NUMBER (Include Area Code) (505)434-1390	22c. OFFICE SYMBOL AFGL/PHS

Continuation of Block 11;

Through the Earth's Atmosphere Using Speckle Interferometry

Continuation of Block 19;

of the geosynchronous Earth satellite FLTSATCOM1. We have proposed designs for systems to accomplish in real-time the data integrations necessary for Fienup and Knox-Thompson image reconstructions.

Throughout the interval we continued work on algorithm development and seeing calibration. Our most notable achievement was applications of seeing calibration techniques and refinements of the shift-and-add method applied successfully in our scientific program of studies of red supergiants. Also, we used the Knox-Thompson algorithm to produce the first scientifically useful images of the surface of an asteroid: analysis of a sequence of images of Vesta resolved ambiguous interpretations of previous studies based on surface-integrated measures alone.

(Keyboards)



Accession for	
NTIS ORNL	<input checked="" type="checkbox"/>
DTIC EIS	<input type="checkbox"/>
Unpublished	<input type="checkbox"/>
Justified	
By	
Date	
Approved	
Date	
A-1	

TABLE OF CONTENTS

1. Introduction	1
2. All Proposed Objectives are Met	1
2.1 The MMT Interferometer is Completed	1
2.2 An Image Reconstruction Program is Successful	3
2.3 A Geosynchronous Satellite is Imaged and Measured	3
2.4 Real-time Data Processing is Proposed	6
3. A Productive Scientific Program is Published	6
3.1 Atmospheric Calibrations	6
3.2 Red Supergiant Images	7
3.3 Asteroid Shapes and Images	7
4. Conclusions	8
5. Acknowledgments	8
6. Publications	9
6.1 Citations (Alphabetic by Author)	9
6.2 Abstracts	12

TABLE OF CONTENTS

APPENDIX:

The Use of the MMT for Interferometric Imaging	31
Diameter and Limb-Darkening Measures for Alpha Orionis	46
Seeing Calibration of Optical Astronomical Speckle Interferometric Data	54
Multi-Wavelength Images of α Orionis	62
Isoplanicity Measurements for Calibration of Speckle Holography Amplitudes	84
Images From Astronomical Speckle Data: Weighted Shift-and-Add Analysis	91
Self-Calibrating Shift-and-Add Technique for Speckle Imaging	99
Toward Solving the Lost Photon Problem in Image Intensifiers	112
A Proximity-Focused Image Intensifier for Astronomy	118
Speckle Interferometry of Asteroids. I. 433 Eros	134
Speckle Interferometry of Asteroids. II. 532 Herculina	154
Speckle Interferometry of Asteroids. III. 511 Davida and its Photometry	163
Speckle Interferometry of Asteroids. IV. Reconstructed Images of 4 Vesta	176
Statistical Analysis of the Weighted Shift and Add Image Reconstruction Technique	210
Two-Dimensional Images of Alpha Orionis	215
The H α Chromosphere of Alpha Orionis	227
Differential Speckle Imaging With the Cophased Multiple Mirror Telescope	236
Images of the Envelope of Alpha Orionis	254
Multiple Mirror Telescope as a Phased Array Telescope	256
Real-Time Signal Processing Requirements for Diffraction Limited Optical Imaging	268
High-Speed Digital Signal Processing for Speckle Interferometry	278
Diffraction Limited Image of a Geosynchronous Object Using the Multiple Mirror Telescope and Fienup Phase Reconstruction	286

The Noise Bias Problem in Optical Speckle Imaging
Experience With a Real Detector

293

The H-Alpha Envelope of Aopha Ori

Phased Array Imaging With the Multiple Mirror Telescope

Real-Time Amplitude and Phase Integration for Diffraction
Limited Imaging Discrete Photon Case

Co-Phasing and Co-Aligning the Multiple Mirror Telescope

A Real-Time Photoelectron Event-Detecting Video System

Astronomical Imaging by Filtered Weighted-Shift-and-Add
Technique

Detection of the Lensing Galaxy in PG 1115+08¹

Use of Matched Filtering to Identify Speckle Locations

1. Introduction

Speckle Interferometry can now be used to produce images with spatial resolution of order 100x sharper than that normally permitted by the Earth's atmosphere. In this work we achieved high resolution imaging capability (wavelength dependent: 60 nrad at 410 nm) and approached that resolution in imaging a geosynchronous communications satellite utilizing the Multiple Mirror Telescope (MMT) and the Fienup method. This report is in the form of an annotated review of the fully published results of that work.

In section 2 we summarize the accomplishment of all of the proposed technical objectives: i) construction of a fully co-phased optical beam-combiner for implementation of the 6.9m aperture imaging capability of the MMT, ii) implementation of image reconstruction methodology, iii) a 100 nrad resolution image of the geosynchronous Earth satellite FLTSATCOM1, and iv) designs for systems to accomplish in real-time the data integrations necessary for Fienup and Knox-Thompson image reconstructions.

In section 3 we summarize the accomplishment of the proposed scientific objectives: i) seeing calibration, ii) applications of seeing calibration techniques and refinements of the shift-and-add method in studies of red supergiants, and iii) use of the Knox-Thompson algorithm to produce the first scientifically useful images of the surface of the asteroid 4 Vesta.

Conclusions and acknowledgments follow in sections 4 and 5. The abstracts of the publications from this research effort are contained in section 6.

2. All Proposed Objectives are Met

2.1 The MMT Interferometer is Completed

The starting point for this work was the successful cophasing of the MMT described in detail by Hege, Beckers, Strittmatter and McCarthy (1985). In a related publication, Beckers and Hege (1984), described other possible MMT type aperture configurations and an internal cophasing/coalignment system for MMT type telescopes was proposed.

The first successful imaging experiments utilized the technique of differential speckle imaging (developed in a parallel NSF funded effort). The technique, summarized by Hebden, Hege, and Beckers, (1985), yielded the first MMT diffraction-limited images of the surface structure of Alpha Orionis. This work was further reported, together with engineering performance details in two other technical reports by Hebden, Hege and Beckers (1986a,b).

The successful operation of the fully implemented co-phasing and co-alignment systems, which complete the MMT for interferometric imaging applications, was reported by Janes and Montgomery (1987) who also provide further engineering performance details. The present configuration of the MMT for coaligned, cophased speckle imaging is shown in figure 1.

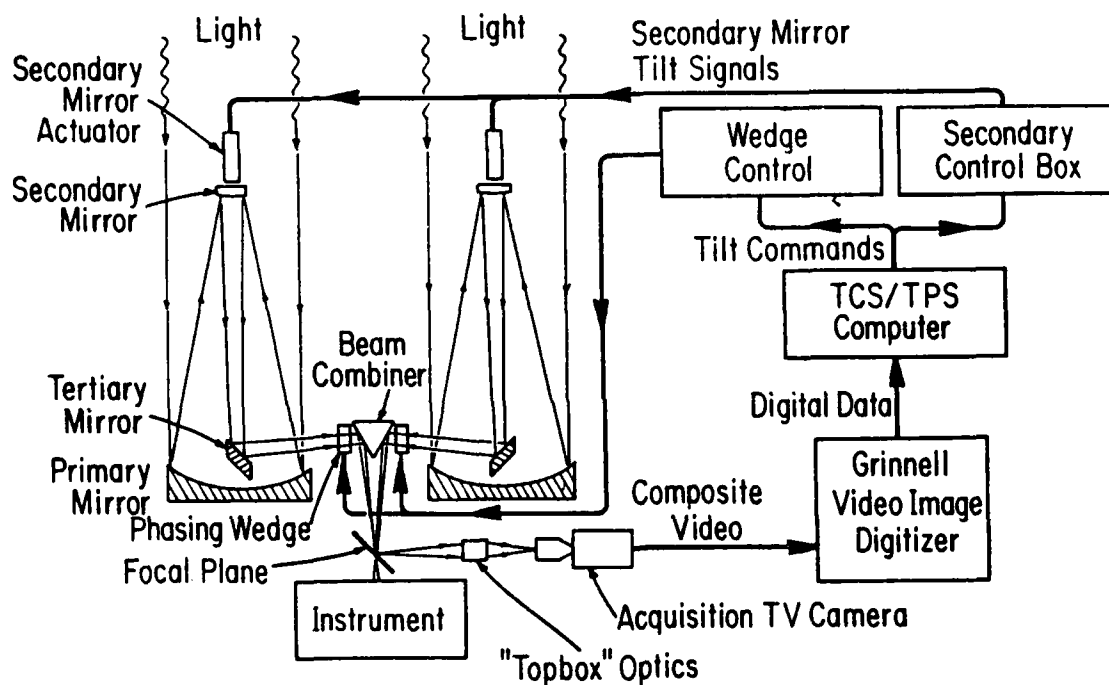


Figure 1. The coaligned, cophased Multiple Mirror Telescope.

Since the differential speckle interferometry program, developed concurrently with this project, was supported entirely with National Science Foundation funds, it is not further reviewed here.

2.2 An Image Reconstruction Program is Successful

During the course of this project Christou, Hege, Freeman and Ribak (1985,1986a,b) implemented a variation of the shift-and-add method, incorporating weighting and deconvolution, which produces very accurately diffraction limited images, self-calibrated for seeing effects without reference to a second measurement of a point source. This method was demonstrated to be particularly applicable to bright objects with simple structure (a single bright feature). Ribak, Hege and Christou (1985) and Ribak (1986) proposed and demonstrated an extension of that weighted-shift-and-add method utilizing a matched-filter technique to accomodate structures with more than a single bright feature.

Code for both weighted-shift-and-add with deconvolution of seeing effects (WSA/D), as well as the matched-filter variation thereof which also extends its applicability to faint objects, is now implemented as Fortran77 processes on the Steward Observatory Data General MV10000 computing system. These are adaptable for implementation on supercomputers. Hege and Christou (1986) reviewed signal processing requirements for diffraction limited optical imaging.

In related work Christou, Hege, Freeman and Ribak (1985) demonstrated the dynamic range and fidelity of images from astronomical speckle data using weighted shift-and-add analysis. Freeman, Ribak, Christou and Hege (1985) gave a statistical analysis of the weighted shift-and-add image reconstruction technique.

An implementation of the conventional shift-and-add method, modified to shift on image centroids rather than the brightest feature, was used successfully by Shaklan and Hege (1986) for a low-resolution, but photon-noise limited, detection of the lensing galaxy in the triple QSO PG1115+08.

2.3 A Geosynchronous Satellite is Imaged and Measured

Hege and Eckart (1987) described the acquisition and calibration of a diffraction limited image of FLTSATCOM1 using the MMT and Fienup phase reconstruction methods. That work was also reported, together with a summary of recent MMT performance and further imaging results on Alpha Orionis, by Hege, McCarthy, Hebden and Christou (1987).

FLTSATCOM1 was observed at elevation 50° , azimuth 160° from Mt. Hopkins on 4 Nov 85 UT. The observations were made using the coherently cophased MMT (Hege *et al.* 1985). Four 20 minute segments of video data were recorded with a 10 nm bandpass centered at 550 nm using the Steward Observatory/AFGL speckle camera. The image intensifier system was operated at full gain so that individual photoelectron events could easily be localized in the video raster, using the off-line digital video data

capture system. The telescope cophasing system was operated in open-loop mode: a reference star was used to cophase the telescope, by visual inspection of the fringe visibility as seen in the real-time video display, before each 20 minute observation of the satellite. The open-loop predictions (Hebden *et al* 1986b) were used to keep the telescope cophased as it was offset from the reference star to the satellite position.

The FLTSATCOM1 data has yielded an image of sufficient quality to obtain measures of overall dimensions, shape and orientation with precision commensurate with the 3 m (projected at geosynchronous range) MMT beam, Figure 2. A signal-to-noise ratio of approximately 6 was obtained with Fienup's method of phase reconstruction from the integrated autocorrelation function of 20 minutes of integrated data, calibrated by use of a model of the seeing (without reference to a point source).

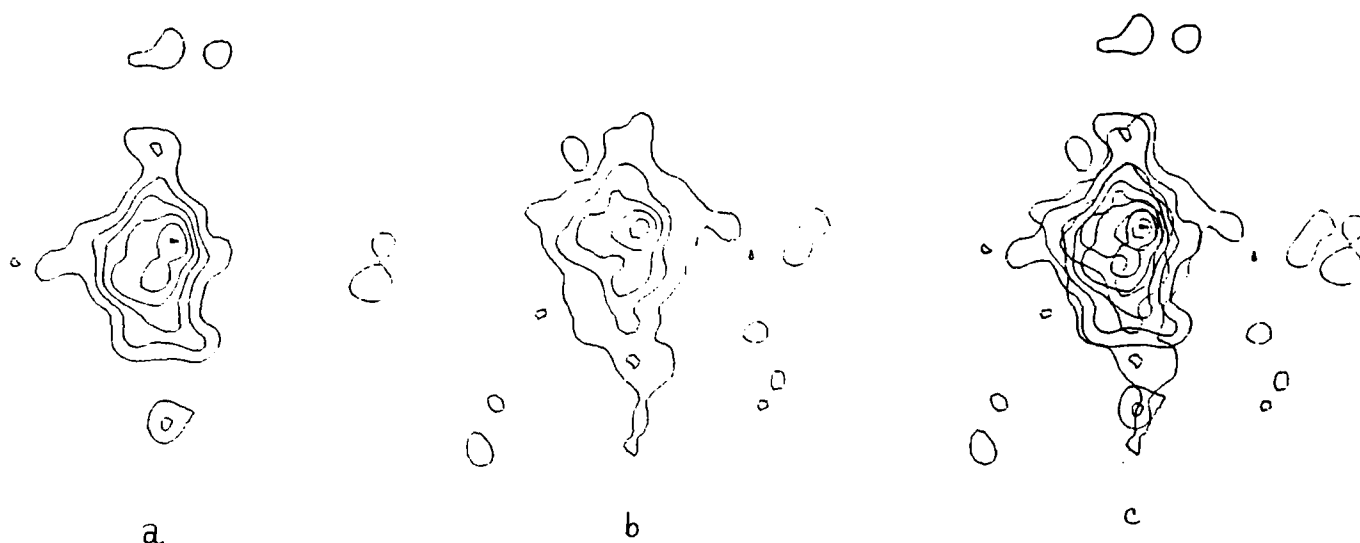


Figure 2. MMT Images of FLTSATCOM1. a) First half of data. b) Second half of data. c) Contour plots superimposed. Contours are at 1,2,...6 times the rms noise in the image plane exterior to the resolved object outline. Fienup reconstructions are ambiguous by 180° rotation. The second image was rotated to give best contour matching compared to the first image.

The reference star was always selected to provide an optimum match to the satellites 50° elevation (usually within $2-3^\circ$) and as close in azimuth as possible (usually within $20-30^\circ$). These large angular distances between object and cophasing reference were consequent to the requirement for a source bright enough for visual analysis of the fringes (5th magnitude or brighter).

Experience showed that the open-loop phasing model worked well for elevation differences as large as 10° and was essentially independent of azimuth variations. The large angles (and times) between object and reference observations made the point source observations of little use in detailed seeing calibrations, however.

The autocorrelation function analysis, self-correction for seeing, and Fienup image reconstruction are being published in detail by Hege and Eckart (1987). Our estimate of the image size is taken from the 2 sigma contours of the images shown in Fig. 2. The estimate of precision corresponds to the mean contour spacing at the 2 sigma contour. The computed beam size at the object is 3 m. We define the Signal-to-noise ratio = $SNR = \text{Brightest Feature} / \text{Background Noise}$. This measurement gives convincing precision, judged from the degree of reproducibility of the contours compared to the telescope's diffraction limited beam size plotted at the same scale. The reduction of the first data segment compares favorably with the reduction of the last segment.

Major Axis: $13.0 \pm 2.3m$
 Minor Axis: $7.4 \pm 2.3m$
 Position Angle: 3.5°
 SNR: 6

The position angle is with respect to the elevation great circle defined by the telescope, FLTSATCOM1 and Zenith.

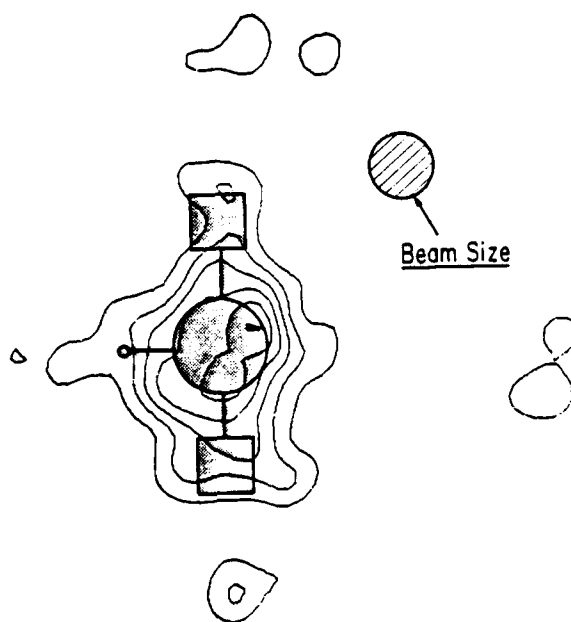


Figure 3. Schematic outline of FLTSATCOM1 compared to our first reconstructed MMT image. The circle gives the diffraction limited MMT beam size (= 3 m at geosynchronous range).

We made no attempt to calibrate image amplitudes or to obtain quantitative estimates of the relative albedos of the identifiable components of our images. There is qualitative evidence i) that the central component is brighter than the extended features, ii) for asymmetry corresponding to the unresolvable component offset from the main object, iii) that, due to the solar phase angle, there appear to be strong brightness variations across the central object, and iv) that the extended components do not reflect equally. Figure 3 compares out first image contour plot to a schematic representation of FLTSATCOM1.

2.4 Real-time Data Processing is Proposed

We have implemented the digital video photon-detection (photon image coordinates) system proposed in the previous work by Macklin, Hege and Strittmatter (1982), and in this effort Hege and Vokac (1986) published a new proposal for real-time Knox-Thompson integration. The Full-FFT implementation proposed by Hege, Cocke, Strittmatter and Worden (1983) in the previous work could realize the full dynamic range from the brightest- to the faintest-possible applications; a more economical complex autocorrelator which can realize the necessary integrations for faint objects (photon image coordinate data only) is the design result of this work.

The continuing development of high-performance image intensifiers reported by Cromwell, Funk, Frank, Strittmatter, Allen, Hege and Marien (1985), leading to a proposal for a proximity focused image intensifier for astronomy, is crucial to the successful implementation of future high-resolution imaging over the full isoplanatic patch permitted by the Earth's atmosphere.

Cromwell (1986) has also made progress toward solving the lost photon problem in image intensifiers, which is crucial in achieving good performance at the photon-starved faint object limit.

3. A Productive Scientific Program is Published

In the course of developing and validating the methods successfully applied to achieve the primary goal of imaging artificial Earth satellites using the full resolving power of the MMT, other scientific investigations were conducted.

3.1 Atmospheric Calibrations

Christou, Cheng, Hege and Roddier (1985) accomplished a seeing calibration of the image centroids of optical astronomical speckle interferometric data against rotationally sheared pupil

plane interferometry obtained concurrently. This led to methods for binning the data according to a measure of the instantaneous seeing in order to calibrate speckle interferometry under conditions of variable seeing. In Christou and Hege (1986) isoplanicity measurements for calibration of speckle holography amplitudes were reported.

The complications of noise bias and seeing calibrations for speckle interferometry of faint object (photon Poisson statistics limited) were studied by Hege, Eckart and Christou (1986).

3.2 Red Supergiant Images

In addition to the technique validation results noted above in discussing the MMT performance, scientifically interesting results were reported in the archival literature. Hebden, Christou, Cheng, Hege, Strittmatter, Beckers and Murphy (1986) presented a sequence of two dimensional images of Alpha Orionis obtained by various methods and with various telescopes. Cheng, Hege, Hubbard, Goldberg, Strittmatter and Cocke (1986) reported the first direct, albeit noisy, limb-darkening measures, as well as direct evidence of a constant (wavelength independent) photospheric diameter, for Alpha Orionis. In our latest work, Hebden, Eckart and Hege (1987), well-resolved images of the H-alpha chromosphere of Alpha Orionis, as well as of the limb-darkened photosphere, are shown. The original 4m telescope observations taken early in the previous segment of this continuing AFGL study have only now been fully and completely analyzed with the WSA/D method by Christou, Hebden and Hege (1987), yielding the first set of multi-wavelength images of Alpha Orionis.

The Alpha Orionis work was also reported at international conferences by Hege, Hebden and Christou (1986) and by Hebden, Hege and Eckart (1987).

3.3 Asteroid Shapes and Images

Power spectrum modelling was used by Drummond, Cocke, Hege, Strittmatter and Lambert (1985) to obtain the figure and pole orientation of 433 Eros. That work also yielded the formalism for greatly enhanced techniques for analyzing the object shape and orientation information content of integrated photometric observations. That technique was further applied by Drummond, Hege and Freeman (1985) to 532 Herculina, yielding the first direct evidence for surface structure on an asteroid (hinted by significant deviations in the details of the model fits in the previous work on Eros). The Drummond and Hege (1986) work on 511 Davida showed still more evidence for surface structure (albedo) variation.

In a detector evaluation experiment in collaboration with the Harvard University speckle interferometry group, and using

the Knox-Thompson imaging method, Drummond, Eckart and Hege, (1987) successfully reconstructed images of 4 Vesta. This work is particularly significant because the set of dark and bright features inferred from that imagery unambiguously shows Vesta's period to be 5 hr. This resolved a longstanding 5 or 10 hr rotational period ambiguity in the possible interpretations of lightcurve data alone. Furthermore, that set of features not only correctly predicts the lightcurve observed at that opposition, but it also successfully predicts lightcurves measured at other oppositions. A surprising result is that the lightcurve minimum occurs at a maximum of the projected area of Vesta's figure due to the effect of dark surface features.

4. Conclusions

The objectives of this work, i) to demonstrate the use of the Multiple Mirror Telescope for diffraction limited imaging, ii) to apply appropriate techniques to yield an image at that resolution of an Earth orbiting satellite, and iii) to design a system capable of the real-time image integrations necessary for imaging of deep-space objects, have been achieved. Also iv) a scientific observing program was conducted simultaneously in a parallel effort, the productivity of which was enhanced by this AFGL supported program.

5. Acknowledgments

The coinvestigators in this project were Drs. Peter A. Strittmatter and Neville J. Woolf. This was a Steward Observatory team effort comprising contributions both from visitors:

Dr. Julian Christou, Ph.D. degree research, New Mexico State University

Dr. Vernon Easterling, Wabash College

Dr. Erez Ribak, Weizmann Fellowship, Tel Aviv University

Dr. Andreas Eckart, Max-Planck Institut fur Astronomie

and from these University of Arizona personnel:

Dr. Jeremy Hebden, Imaging Program

Mr. Jonathan Freeman, Graduate Student: Imaging Program

Dr. Jack Drummond, Scientific Program (Asteroids)

Dr. Donald McCarthy, MMT Interferometer Development

Dr. Jacques Beckers, MMT Interferometry Development

The following Undergraduate Research Assistants:

Stuart Shaklan, Anthony Szumilo, Nicolas Stroble,
and Ronald Watkins

The Steward Observatory Technical Division Staff

The Multiple Mirror Telescope Observatory Staff

6. Publications

This section contains a comprehensive listing of all of the publications resulting from work supported in any part by this AFGL contract. These items have been reviewed briefly in the main text. Section 6.1 is an alphabetical listing of the citations and section 6.2 contains the abstracts, in the order of the alphabetic citations, for quick reference. A companion appendix contains complete reprints, or preprints, as available at the time of this report.

6.1 Citations (Alphabetic by Author)

1. J. M. Beckers and E. K. Hege, "The Use of the MMT for Interferometric Imaging," In Proc. IAU Colloq. #79, Very Large Telescopes, Their Instrumentation and Programs, p279, 1984.
2. A.Y.S. Cheng, E. K. Hege, E. N. Hubbard, L. Goldberg, P. A. Strittmatter and W. J. Cocke, "Diameter and Limb-Darkening Measure for Alpha Orionis," Astrophys. J. **309**, 737, 1986.
3. J. C. Christou, A. Y. S Cheng, E. K. Hege and C. Roddier, "Seeing Calibration of Optical Astronomical Speckle Interferometric Data," Astron. J. **90**, 2644, 1985.
4. J. C. Christou, J. C. Hebden and E. K. Hege, "Multi-wavelength Images of Alpha Orionis," Astrophys. J. (Submitted) 1987.
5. J. C. Christou and E. K. Hege, "Isoplanicity Measurements for Calibration of Speckle Holography Amplitudes," Optics Commun **58**, 4, 1986.
6. J. C. Christou, E. K. Hege, J. D. Freeman and E. Ribak, "Images from Astronomical Speckle Data: Weighted Shift-and-Add Analysis," Proc. SPIE **556**, 255, 1985.
7. J. Christou, K. Hege, J. Freeman and E. Ribak, "A Self-Calibrating Shift-and-Add Technique for Speckle Imaging," J. Opt. Soc. Am. A **3**, 204, 1986a.

8. J. C. Christou, E. Ribak, E. K. Hege, and J. D. Freeman, "Images from Astronomical Speckle Data by Weighted Shift-and-Add," Optical Engng. **25**, 724, 1986b.
9. R. H. Cromwell, "Toward Solving the Lost Photon Problem in Image Intensifiers," Proc. SPIE **627**, 610, 1987.
10. R. H. Cromwell, P. A. Strittmatter, R. G. Allen, E. K. Hege, H. Köhr, K.-H. Marien, H. W. Funk and K. Frank, "A Proximity Focused Image Intensifier for Astronomy," Adv. in Electron. and Electron Phys. **64A**, 77, 1985.
11. J. D. Drummond, W. J. Cocke, E. K. Hege, P. A. Strittmatter and J. V. Lambert, "Speckle Interferometry of Asteroids. I. 433 Eros," Icarus **61**, 132, 1985.
12. J. D. Drummond, E. K. Hege, W. J. Cocke, J. Freeman, J. C. Christou and R. P. Binzel, "Speckle Interferometry of Asteroids. II. 532 Herculina," Icarus **61**, 232, 1985.
13. J. D. Drummond and E. K. Hege, "Speckle Interferometry of Asteroids III. 511 Davida," Icarus **67**, 251, 1986.
14. J. D. Drummond, A. Eckart and E. K. Hege, "Speckle Interferometry of Asteroids. IV. Reconstructed Images of 4 Vesta," Icarus (Submitted) 1987.
15. J. D. Freeman, E. Ribak, J. C. Christou and E. K. Hege, "Statistical Analysis of the Weighted Shift-and-Add Image Reconstruction Technique," Proc. SPIE **556**, 279, 1985.
16. J. C. Hebden, J. C. Christou, A. Y. S. Cheng, E. K. Hege, P. A. Strittmatter, J. M. Beckers and H. P. Murphy, "Two Dimensional Images of Alpha Orionis," Astrophys. J. **309**, 745, 1986.
17. J.C. Hebden, A. Eckart and E.K. Hege, "The H-alpha Chromosphere of Alpha Orionis," Astrophys. J. **314**, 690, 1987.
18. J. C. Hebden, E. K. Hege, and J. M. Beckers, "Differential Speckle Imaging with the Cophased Multiple Mirror Telescope," Proc. SPIE **556**, 284, 1985.
19. J. C. Hebden, E. K. Hege and J. M. Beckers, "Differential Speckle Imaging with the Cophased Multiple Mirror Telescope," Optical Engng. **25**, 712, 1986a.
20. J.C. Hebden, E.K. Hege and J.M. Beckers, "Use of the Coherent MMT for Diffraction Limited Imaging," Proc. SPIE **628**, 42, 1986b.
21. J.C. Hebden, E.K. Hege and A. Eckart, "Images of the Envelope of Alpha Orionis," In Proc. IAU Symposium #122 Circumstellar Matter (Heidelberg 1986). ed. I. Appenzeller and C. Jordan (D. Riedel, Dordrecht), p , 1987.

22. E. K. Hege, J. M. Beckers, P. A. Strittmatter and D. W. McCarthy, "The Multiple Mirror Telescope as a Phased Array Telescope," Appl. Opt. **24**, 2565, 1985.
23. E. K. Hege and J. C. Christou, "Real-time Signal Processing Requirements for Diffraction Limited Optical Imaging," In Proc. Conf. on Use of Supercomputers in Astronomy, ed. T. Cornwell and J. Dickey, 1986.
24. E. K. Hege, W. J. Cocke, P. A. Strittmatter, S. P. Worden and W. C. Booth, "High-Speed Digital Signal Processing for Speckle Interferometry," Proc. SPIE **445**, 469, 1983.
25. E. K. Hege and A. Eckart, "Diffraction Limited Image of Geosynchronous Object using the Multiple Mirror Telescope and Fienup Phase Reconstruction," Appl. Opt. (Submitted) 1987.
26. E. K. Hege, A. Eckart and J.C. Christou, "The Noise Bias Problem in Optical Speckle Imaging: Experience with a Real Detector," Proc. SPIE **627**, 772, 1986.
27. E.K. Hege, J. C. Hebden and J. C. Christou, "The H-Alpha Envelope of Alpha Orionis," In Cool Stars, Stellar Systems, and the Sun, Lecture Notes in Physics, Vol. 9, p 414, 1986. (Proc. 4th Cambridge Workshop, Santa Fe, 1985 October) ed. M. Zeilik and D.M. Gibson (Springer-Verlag, Berlin/Heidelberg).
28. E. K. Hege, D. W. McCarthy, J. C. Hebden and J. C. Christou, "Phased Array Imaging with the Multiple Mirror Telescope," In Interferometric Imaging in Astronomy, ESO/NOAO Workshop, Oracle, Arizona, January 1987, ed J. Goad, p105, 1987.
29. E. K. Hege and P. R. Vokac, "Real-time Amplitude and Phase Integration for Diffraction-Limited Imaging: Discrete Photon Case," Proc. SPIE **627**, 780, 1986.
30. C. C. Janes and J. W. Montgomery, "Co-Phasing and Co-Aligning the Multiple Mirror Telescope," Proc. SPIE **748**, Paper 04, 1987.
31. R. H. Macklin, E. K. Hege and P. A. Strittmatter, "A Real-Time Photoelectron Event-Detecting Video System," Proc. SPIE **359**, 135, 1982.
32. E. Ribak, "Astronomical Imaging by Filtered Weighted-shift-and-add Technique," J. Opt. Soc. Am. A **3**, 2069, 1986.
33. E. Ribak, E. K. Hege and J. C. Christou, "Use of Matched Filtering to Identify Speckle Locations," Proc. SPIE **556**, 196, 1985.
34. S. B. Shaklan and E. K. Hege, "Detection of the Lensing Galaxy in PG1115+08," Astrophys. J. **303**, 605, 1986.

THE USE OF THE MMT FOR INTERFEROMETRIC IMAGING

Jacques M. Beckers
National Optical Astronomy Observatories *
Tucson, AZ 85726

E. Keith Hege
University of Arizona
Tucson, AZ 85721

ABSTRACT

We describe recent progress with interferometric imaging using the Multiple Mirror Telescope (MMT). All six telescopes can now be phased over a wide field of view simultaneously resulting in a (u, v) plane coverage corresponding to that of a 686 cm aperture telescope. We describe the open-loop phasing control of the MMT for gravitational changes and we describe a concept of an internal cophasing/coalignment system for MMT type telescopes.

Proceedings of the IAU Colloquium No. 79: "Very Large Telescopes, their Instrumentation and Programs", Garching, April 9-12, 1984.

THE ASTROPHYSICAL JOURNAL, 309:737-744, 1986 October 15
© 1986 The American Astronomical Society. All rights reserved. Printed in U.S.A.

The U.S. Government is authorized to reproduce and sell this report. Permission for further reproduction by others must be obtained from the copyright owner.

DIAMETER AND LIMB-DARKENING MEASURES FOR ALPHA ORIONIS

A. Y. S. CHENG, E. K. HEGE,¹ E. N. HUBBARD,¹ L. GOLDBERG,² P. A. STRITTMATTER,¹ AND W. J. COCKE
Steward Observatory, University of Arizona, Tucson
Received 1985 September 12; accepted 1986 April 17

ABSTRACT

Previously reported speckle interferometric measurements of the angular diameter of α Ori are widely scattered and apparently inconsistent. Stellar atmosphere models predict a stellar disk to be limb-darkened differently for different spectral features, and that less limb-darkening will be observed at longer wavelengths. Upon careful analysis of calibrated speckle observations obtained at various wavelengths with the KPNO 4 m telescope, we find a single diameter parameter to be inadequate to explain all of the features of our measurements. There is evidence for a central stellar component of $42.1(\pm 1.1)$ mas diameter with extended structure surrounding it. Limb-darkening effects are suggested by attempts to fit cosine model image profiles to the data which yield limb-darkening coefficients ranging from ~ 0.9 in TiO absorption bands to ~ 0.4 in Ca II absorption lines. These fits have significant residuals at large radii suggesting a faint envelope extending from 1 to $5 R_*$, although calibration errors cannot be ruled out entirely. There is a suggestion of wavelength dependence in single-parameter diameter measures with a linear coefficient of $\sim -6(\pm 1) \times 10^{-3}$ mas nm^{-1} . Possible model-dependent biases in these results are discussed.

Subject headings: interferometry - stars: diameters - stars: individual - stars: supergiants

SEEING CALIBRATION OF OPTICAL ASTRONOMICAL SPECKLE INTERFEROMETRIC DATA

JULIAN C. CHRISTOU,^{a)} ANDREW Y. S. CHENG, E. KEITH HEGE^{b)}
Steward Observatory, University of Arizona, Tucson, Arizona 85721

CLAUDE RODDIER^{c)}
Optical Sciences Center, Tucson, Arizona 85726
Received 31 May 1985

ABSTRACT

In this paper we show the effect of different seeing conditions, as parametrized by the atmospheric coherence scale r_0 , upon standard Labeyrie (1970) analysis for independent observations of both a resolved object and its point-source calibrator. Atmosphere-dependent effects are shown by using both models and data. We show how to sort the data into like-seeing bins in order to produce a calibrated-image power-spectrum estimate. We also justify using a stronger weighting of intermediate spatial frequencies in the image power-spectrum estimator when fitting physical parameters constrained by image models to characterize the object. The use of data-editing techniques to eliminate bad specklegrams, thus improving the image power-spectrum estimate, is also discussed.

Multi-wavelength Images Of α Orionis

Julian C. Christou

Advanced Development Program

*National Optical Astronomy Observatories**

Jeremy C. Hebden, E. Keith Hege[†]

Steward Observatory, University of Arizona

submitted to: The Astrophysical Journal

March 16, 1987

Abstract

We have used a recently developed high-spatial resolution imaging technique, known as Weighted Shift-and-add, to obtain diffraction-limited images of the red supergiant α Orionis at the resolution of the KPNO Mayall 4 m telescope. Images were obtained at six different bandpasses and the measured disk diameters agree to within a few % of the values obtained from the previously published power spectrum and autocorrelation analysis of the same data set. From the major and minor axes of models fit to the intensity profiles, we obtain asymmetry measures of both the disk and envelope components of $4(\pm 2)\%$ and $37(\pm 13)\%$ respectively. In addition we have searched for the proposed nearby companion but our data shows no direct evidence of it suggesting an upper limit to the magnitude difference of 4.5.

Subject headings: interferometry · stars: diameters · stars: individual · stars: supergiants

ISOPLANICITY MEASUREMENTS FOR CALIBRATION OF SPECKLE HOLOGRAPHY AMPLITUDES

Julian C. CHRISTOU¹ and E. Keith HEGE

Steward Observatory, University of Arizona, Tucson, AZ 85721, USA

Received 23 December 1985

We show how the technique of astronomical speckle holography is dependent upon the degree of isoplanicity between the object and the discrete point source. A well calibrated measurement of the degree of correlation between two quasi-instantaneous simultaneous point source speckle patterns (separation = $2.6''$) are presented to illustrate this non-isoplanatic effect as a function of the spatial frequency. This two-dimensional measurement is in qualitative agreement with previously computed models and shows a high degree of correlation at seeing dominated frequencies with a severe attenuation (but not total loss of correlation) for frequencies approaching the diffraction limit. We show how such measurements may be used to reweight (calibrate) the Fourier amplitude of a speckle holographic image observed under similar seeing conditions in order to compensate for the non-isoplanatic degradation at high spatial frequencies.

Images From Astronomical Speckle Data: Weighted Shift-and-Add Analysis

J.C.Christou^{**}, E.K.Hege⁺, J.D.Freeman & E.Ribak

Steward Observatory, University Of Arizona, Tucson, Az 85721

SPIE
San Diego, 1985
p 255

Abstract

We have applied a variant of the Shift-and-Add algorithm originally developed by Lynds, Worden & Harvey to astronomical speckle interferometric data. A set of impulses corresponding in location and magnitude to the local maxima in each specklegram is generated and used to obtain an average speckle by means of a Wiener-type filter deconvolution procedure. This technique yields diffraction limited images which appear to be self calibrating for seeing effects. Realistic point spread functions have been obtained for a number of telescopes at different wavelengths and results are also presented for the resolved red supergiant Alpha Orionis. The limiting signal-to-noise of the technique as indicated by the results presented here suggests a dynamic range of ~ 6 stellar magnitudes with no evidence of residual seeing effects.

The U.S. Government is authorized to reproduce and sell this report.
Permission for further reproduction by others must be obtained from
the copyright owner.

Reprinted from *Journal of the Optical Society of America A*, Vol. 3, page 204, February 1986.
Copyright © 1986 by the Optical Society of America and reprinted by permission of the copyright owner.

Self-calibrating shift-and-add technique for speckle imaging

Julian C. Christou,⁺ E. Keith Hege,[†] Jonathan D. Freeman, and Erez Ribak

Steward Observatory, University of Arizona, Tucson, Arizona 85721

Received June 3, 1985, accepted September 24, 1985

An image-reconstruction technique for astronomical speckle interferometric data is described. This variant of the shift-and-add algorithm originally developed by Lynds *et al.* [*Astrophys. J.* 207, 174 (1976)] utilizes a weighted impulse distribution of speckle positions to extract an average speckle for a data set. This is done by means of a weighted deconvolution procedure, similar in form to a Wiener filter, which deconvolves the specklegram by the impulse distribution. Results show that this method appears to be self-calibrating for seeing effects. It yields point-spread functions, for observations of an unresolved star, that compare quantitatively with computed Airy patterns for both simple apertures and the fully phased multiple mirror telescope array. Images of the resolved object Alpha Orionis show evidence of an extended stellar envelope.

Images from astronomical speckle data: weighted shift-and-add analysis

J. C. Christou
E. Ribak
E. K. Hege
J. D. Freeman
Steward Observatory
University of Arizona
Tucson, Arizona 85721

Abstract. We have applied a variant of the shift-and-add algorithm originally developed by Lynds, Worden, and Harvey [Astrophys. J. 207, 174 (1976)] to astronomical speckle interferometric data. A set of impulses corresponding in locations and magnitudes to the local maxima in each specklegram is generated and used to obtain an average speckle by means of a Wiener-type filter deconvolution procedure. This technique yields diffraction-limited images that appear to be self-calibrating for seeing effects. Realistic point spread functions have been obtained for a number of telescopes at different wavelengths, and results are also presented for the resolved red supergiant Alpha Orionis. The limiting signal-to-noise ratio of the technique as indicated by the results presented here suggests a dynamic range of ≈ 6 stellar magnitudes, with no evidence of residual seeing effects. A matched filter technique is demonstrated for use in locating the speckles of complicated objects or for objects dominated by photon noise.

Subject terms: speckle; speckle imaging; shift-and-add; seeing calibration; astronomy.

Optical Engineering 25(6), 724-730 (June 1986).

SPIE, March 1986

Toward solving the lost photon problem in image intensifiers

R. H. Cromwell

Steward Observatory, University of Arizona
Tucson, Arizona 85721

Abstract

A summary is given of measurements of the photoelectron counting efficiency of a variety of image intensifiers manufactured by several different manufacturers. With one exception, the counting efficiency is disappointingly low. Typically only slightly over half of the photoelectrons from the first photocathode produce a detectable signal on the output phosphor screen in most diode-type intensifiers. For microchannel plate intensifiers, the counting efficiency is even less. Results are given of experiments intended to produce diode-type intensifiers having improved counting efficiency. Improvements have been achieved through refinements in the manufacturing steps of the phosphor screen, the tube component identified as responsible for the lost photoelectron pulses in diode-type tubes. The best tubes so far have counting efficiencies of 70%, which represent an improvement by a factor of about 1.4.

A Proximity-Focused Image Intensifier for Astronomy

R. H. CROMWELL, P. A. STRITTMATTER, R. G. ALLEN, E. K. HEGE, H. KÜHR,
and K.-H. MARIEN†

Steward Observatory, The University of Arizona, Tucson, Arizona, U.S.A.

and

H. W. FUNK and K. FRANK

Proxitronic-Funk GmbH & Co. KG, Weiterstadt/Darmstadt, Federal Republic of Germany

INTRODUCTION

Image intensifiers are currently the primary detector for ground-based optical astronomy. They are used with photographic emulsions and with various electronic readout systems, as in the Wampler-Robinson scanner (image dissector),¹ the Boksenberg IPCS (Plumbicon),² and the Sheckman³ and the Steward Observatory⁴ scanners (Reticon). The image intensifier offers the advantages of reasonably high quantum efficiency, essentially noise-free amplification to very high gain values and suitability for rapid readout. Although the CCD offers significantly better detective quantum efficiency in certain applications, especially for medium to high signal-to-noise ratio observations at wavelengths above 4000–4500 Å, there are nonetheless a number of astronomical problems for which the image intensifier is likely to remain superior. These include any problems in which it is necessary to read out rapidly, as for example in speckle interferometry, polarimetry, and high-resolution photon-counting centroided spectroscopy. It also seems likely that, in the UV spectral range ($\lambda < 4000$ Å) the DQE of image intensifiers will remain competitive with that of CCDs for some time to come.

At Steward Observatory we have tested a variety of image intensifiers that are commercially available or under development. Tables I and II list the major design types we have examined, and give a summary of our test results, some of which have been reported elsewhere.^{5–11}

† Visitor from the Max-Planck-Institute für Astronomie, Heidelberg, Federal Republic of Germany

Speckle Interferometry of Asteroids

I. 433 Eros

J. D. DRUMMOND, W. J. COCKE, E. K. HEGE, AND P. A. STRITTMATTER

Steward Observatory, University of Arizona, Tucson, Arizona 85721

AND

J. V. LAMBERT

Department of Astronomy, New Mexico State University, Las Cruces, New Mexico 88003

Received May 4, 1984; revised September 11, 1984

Analytic expressions for the semimajor and semiminor axes and an orientation angle of the ellipse projected by a triaxial ellipsoid (an asteroid) and of the ellipse segment cast by a terminator across the ellipsoid as functions of the dimensions and pole of the body and the astero-centric position of the Earth and Sun are derived. Applying these formulae to observations of the Earth-approaching asteroid 433 Eros obtained with the speckle interferometry system of Steward Observatory on December 17-18, 1981, and January 17-18, 1982, the following dimensions are derived: $(40.5 \pm 3.1 \text{ km}) \times (14.5 \pm 2.3 \text{ km}) \times (14.1 \pm 2.4 \text{ km})$. Eros' north pole is found to lie within 14° of $RA = 0^h 16^m$ Dec. $= +43^\circ$ (ecliptic longitude 23° , latitude $+37^\circ$). Other than knowing the rotation period of Eros, these results are completely independent of any other data, and in the main confirm the results obtained in the 1974-1975 apparition by other methods. These dimensions, together with a light curve from December 18, 1981, lead to a geometric albedo of 0.156 ± 0.010 . A series of two-dimensional power spectra and autocorrelation functions of the resolved asteroid clearly show it spinning in space. © 1985 Academic Press, Inc.

The U.S. Government is authorized to reproduce and sell this report.
Permission for further reproduction by others must be obtained from
the copyright owner.

Speckle Interferometry of Asteroids

II. 532 Herculina

J. D. DRUMMOND, E. K. HEGE, W. J. COCKE, J. D. FREEMAN,
AND J. C. CHRISTOU¹

Steward Observatory, University of Arizona, Tucson, Arizona 85721

AND R. P. BINZEL

Department of Astronomy, University of Texas, Austin, Texas 78712

Received May 21, 1984; revised October 5, 1984

Speckle interferometry of 532 Herculina performed on January 17 and 18, 1982, yields triaxial ellipsoid dimensions of $(263 \pm 14) \times (218 \pm 12) \times (215 \pm 12) \text{ km}$, and a north pole for the asteroid within 7° of $RA = 7^h 47^m$ and $DEC = -39^\circ$ (ecliptic coordinates $\lambda = 132^\circ$ $\beta = -59^\circ$). In addition, a "spot" some 75% brighter than the rest of the asteroid is inferred from both speckle observations and Herculina's lightcurve history. This bright complex, centered at astero-centric latitude -35° , longitude 145° - 165° , extends over a diameter of 55° (115 km) of the asteroid's surface. No evidence for a satellite is found from the speckle observations, which leads to an upper limit of 50 km for the diameter of any satellite with an albedo the same as or higher than Herculina. © 1985 Academic Press, Inc.

Speckle Interferometry of Asteroids

III. 511 Davida and Its Photometry

J. D. DRUMMOND AND E. K. HEGE

Steward Observatory, University of Arizona, Tucson, Arizona 85721

Received May 23, 1985; revised March 24, 1986

511 Davida was observed with the technique of speckle interferometry at Steward Observatory's 2.3-m telescope on May 3, 1982. Assuming Davida to be a featureless triaxial ellipsoid, based on five 7-min observations its triaxial ellipsoid dimensions and standard deviations were found to be $(465 \pm 90) \times (358 \pm 58) \times (258 \pm 356)$ km. This shape is close to an equilibrium figure (a gravitationally shaped "rubble pile") suggesting a density of 1.4 ± 0.4 g/cm³. Simultaneously with the triaxial solution for the size and shape of Davida, we found its north rotational pole to lie within 29° of RA = 19^h08^m, Dec = +15° ($\lambda = 291^\circ$, $\beta = +37^\circ$). If Davida is assumed to be a prolate biaxial ellipsoid, then its dimensions were found to be $(512 \pm 100) \times (334 \pm 39)$ km, with a north pole within 16° of RA = 10^h52^m, Dec = +16° ($\lambda = 322^\circ$, $\beta = +32^\circ$). We derive and apply to Davida a new simultaneous amplitude-magnitude (SAM)-aspect method, finding, from photometric data only, axial ratios of $a/b = 1.25 \pm .02$, $b/c = 1.14 \pm .03$, and a rotational pole within 4° of $\lambda = 307^\circ$, $\beta = +32^\circ$. We also derive a (weighted) linearized form of the amplitude-aspect relation to obtain axial ratios and a pole. However, amplitudes must be known to better than .01 if the b/c or a/c ratios are desired to better than 10%. Combining the speckle and SAM results, we find for the Gehrels and Tedesco phase function a geometric albedo of $.033 \pm .009$ and for the Lumme and Bowell function $.041 \pm .011$, for a unified model of $437 \times 350 \times 307$ km. Differences between the photometric and speckle axial ratios and poles are probably due to the effects of albedo structure over the asteroid; details on individual lightcurves support this conclusion. © 1986 Academic Press, Inc.

The U.S. Government is authorized to reproduce and sell this report. Permission for further reproduction by others must be obtained from the copyright owner.

Speckle Interferometry of Asteroids.

IV. Reconstructed Images of 4 Vesta

J. Drummond, A. Eckart, and E.K. Hege

Steward Observatory, University of Arizona, Tucson, Arizona 85721

Abstract

The first glimpses of an asteroid's surface have been obtained from images of 4 Vesta reconstructed from speckle interferometric observations made on November 16 and 17, 1983, using Steward Observatory's 2.3m telescope coupled with Harvard's PAPA camera. From power spectrum analysis of the ten images Vesta is found to have a 'normal' triaxial ellipsoid shape of $584(\pm 16) \times 531(\pm 11) \times 467(\pm 12)$ km. Its rotational pole lies within 4° of R.A. = $21^h 00^m$, Dec. = $+41^\circ$ (Ecliptic long. = 336° , lat. = $+55^\circ$). Our observations definitely support a 5hr 20.5min rotational period, and do not fit one twice as long.

Reconstructed images reveal dark and bright patterns, reminiscent of the Moon, which can be followed across the disk as the asteroid rotates. By placing circular 'spots' with diameters of 135km ($=0.11$ arcsec, the effective resolution) over three dark and three bright features, and assigning albedos (relative to the surrounding material) of 0 to the dark spots and 2 to the bright spots (except one with an albedo of 1.2), we are nearly able to match its visible lightcurve. It only requires an additional bright spot deep in Vesta's southern hemisphere, an area not visible during our observations, to provide a near perfect match to all low solar phase angle lightcurves ever obtained of this asteroid. At phase angles greater than about 10° the observed amplitude becomes greater by up to 0.02 mag. The dark areas so dominate one face of Vesta that a minimum in the lightcurve occurs when the maximum cross-sectional area is visible. Its lightcurve is determined primarily by albedo structure rather than shape, leading to one maximum and one minimum per rotation instead of the expected two of each associated with its triaxial ellipsoid shape.

SPDF
San Diego, '85

Statistical Analysis of the Weighted Shift and Add Image Reconstruction Technique

J.D. Freeman, E. Ribak, J.C. Christou^{**}, E.K. Hege⁺

Steward Observatory, University of Arizona, Tucson, Az 85721

Abstract

The Weighted Shift-and-Add algorithm (WSA) is an image reconstruction technique whereby diffraction limited images of astronomical objects are obtained from speckle interferometric data.

This paper attempts to put the understanding of WSA on a firm mathematical basis by a statistical analysis of the algorithm. The approach follows that of the Hunt, Fright, and Bates study carried out for the Simple Shift-and-Add algorithm. The expected WSA profile is found to be linearly dependent on the square modulus complex coherence function of a speckle pattern. The last section of this paper contains a discussion of how the statistical analysis compares to the results obtained with our new Weighted Shift-and-Add procedures using cross-correlation (WSA/XC) and deconvolution (WSA/WD).

THE ASTROPHYSICAL JOURNAL, 309:745-754, 1986 October 15
© 1986 The American Astronomical Society. All rights reserved. Printed in U.S.A.

The U.S. Government is authorized to reproduce and sell this report.
Permission for further reproduction by others must be obtained from
the copyright owner.

TWO-DIMENSIONAL IMAGES OF ALPHA ORIONIS¹

J. C. HEBDEN, J. C. CHRISTOU,² A. Y. S. CHENG, E. K. HEGE,³ AND P. A. STRITTMATTER³

Steward Observatory, University of Arizona, Tucson

J. M. BECKERS³
NOAO, Tucson

AND

H. P. MURPHY
NRAO, Socorro, New Mexico

Received 1985 November 1; accepted 1986 April 7

ABSTRACT

Between 1981 February and 1983 December a series of speckle interferometric observations were made of the M-type supergiant α Orionis in an attempt to produce two-dimensional images of the star at the H α line. The telescopes employed include the Steward Observatory 2.3 m and NOAO 4 m telescopes at Kitt Peak and the fully phased six-mirror Multiple Mirror Telescope. Two types of data reduction techniques were used: (1) shift-and-add methods applied to conventional speckle interferometric observations, and (2) differential speckle interferometry. Data analysis included the application of the CLEAN algorithm to calibrate the images produced by the shift-and-add technique with data reduced similarly for a point source. The images produced are encouragingly consistent in suggesting asymmetric atmospheric structure; possible evolution of that structure over the three-year period of observations is noted.

Subject headings: interferometry — stars: individual

THE ASTROPHYSICAL JOURNAL, 314:690-698, 1987 March 15
© 1987 The American Astronomical Society. All rights reserved. Printed in U.S.A.

THE H α CHROMOSPHERE OF ALPHA ORIONIS¹

JEREMY C. HEBDEN, ANDREAS ECKART, AND E. K. HEGE

Steward Observatory, University of Arizona

Received 1986 May 5; accepted 1986 June 27

ABSTRACT

Images have been obtained of the H α chromospheric envelope of α Ori at the diffraction-limited resolution of the cophased Multiple Mirror Telescope. A phaseless image reconstruction was applied to speckle interferometric data obtained at continuum wavelengths, and the result was used to produce images of the highly extended H α region from results achieved using the differential imaging technique. Two such images are presented which were obtained from observations made almost 2 yr apart. Significant, and highly isotropic emission out to several stellar radii is exhibited. A very large optical depth in H α is indicated. A simple mathematical expression for the radially averaged profile of the images is derived empirically.

Subject headings: interferometry — stars: chromospheres — stars: individual

Differential speckle imaging with the
 cophased Multiple Mirror Telescope

J.C. Hebden, E.K. Hege
 Steward Observatory, University of Arizona, Tucson, Az 85721

and J.M. Beckers
 NOAO, 950 N. Cherry Ave., Tucson, Az 85726.

Abstract

A new technique known as Differential Speckle Interferometry has been applied to data obtained using the fully-phased six-mirror aperture of the Multiple Mirror Telescope. By observing stellar objects at two distinct wavebands simultaneously, differences in the object resulting from the different wavelengths can be derived. Observations were made of the supergiant star Alpha Orionis in order to investigate the Hydrogen-alpha emission from the surrounding envelope. The data reduction process consists of a frame-by-frame weighted deconvolution procedure. This process involves an inherent Wiener-type filtering which must be removed in order to preserve high spatial frequency information. Results for Alpha Orionis and for the unresolved source Gamma Orionis are presented.

Differential speckle imaging with the cophased Multiple Mirror Telescope

J. C. Hebden
 E. K. Hege
 Steward Observatory
 University of Arizona
 Tucson, Arizona 85721

Jacques M. Beckers
 National Optical Astronomy Observatories
 950 N. Cherry Ave.
 Tucson, Arizona 85726

Abstract. Differential speckle interferometry has been applied to data obtained using the fully phased six-mirror aperture of the Multiple Mirror Telescope. Wavelength-dependent differences in the appearance of a stellar object are derived from simultaneous observations at two distinct wavebands. The supergiant star Alpha Orionis was observed this way to investigate its appearance in hydrogen-alpha emission. Data reduction consists of a frame-by-frame weighted deconvolution. An inherent Wiener-type filtering must be removed in order to preserve high spatial frequency information. Results for Alpha Orionis are compared to similar results for the unresolved source Gamma Orionis.

Subject terms: speckle; differential speckle interferometry; astronomy; Multiple Mirror Telescope; phased-array optical imaging.

Optical Engineering 25(6), 712-715 (June 1986).

Use of the Coherent MMT for Diffraction Limited Imaging

J.C. Hebden, E.K. Hege
 Steward Observatory, University of Arizona, Tucson, Az 85721

and J.M. Beckers
 NOAO, 950 N. Cherry Ave., Tucson, Az 85726

Abstract

All six MMT telescopes can now be optically cophased simultaneously over a wide field of view yielding coherent coverage of the complete Fourier transform plane corresponding to that of a pupil-masked telescope of 6.86m aperture. Open-loop phasing control compensates for flexure-induced path-length changes due to variable gravitational loading as a function of elevation. The system has been used to produce diffraction limited images and differential images of Alpha Orionis using narrow-band (1.2Å) filters centered both on Hydrogen-alpha and on a similar bandpass out of the absorption line. Corresponding wide (100Å) and narrow-band images of Gamma and Epsilon Orionis show the expected result for unresolved sources at the diffraction limited resolution of the fully-phased MMT.

Proc. IAU Symposium #122

"Circumstellar Matter"

ed. I. Appenzeller and C. Jordan

(Heidelberg, 1986)

D. Riedel

IMAGES OF THE ENVELOPE OF ALPHA ORIONIS

Jeremy C. Hebden, E. Keith Hege, and Andreas Eckart
Steward Observatory
University of Arizona
Tucson
AZ 85721, USA

ABSTRACT. Two images have been obtained, from observations made almost two years apart, of the H-alpha chromospheric envelope of Alpha Orionis at the diffraction limited resolution of the co-phased Multiple Mirror Telescope. Significant emission out to a distance of several stellar radii above the photosphere is observed.

The U.S. Government is authorized to reproduce and sell this report.
Permission for further reproduction by others must be obtained from
the copyright owner.

Reprinted from Applied Optics, Vol. 24, page 2565, August 15, 1985
Copyright © 1985 by the Optical Society of America and reprinted by permission of the copyright owner.

Multiple mirror telescope as a phased array telescope

E. Keith Hege, J. M. Beckers, P. A. Strittmatter, and D. W. McCarthy

By adjusting the optical path lengths of its individual beams, it is possible to make the multiple mirror telescope (MMT) into a phased array with a 6.86-m base line. A coherent phased focus can be achieved with tilted focal planes if the tilt angle is chosen so that the internal phase differences exactly compensate the external phase differences. This amounts to a slight change in configuration so that the beams are brought together at $f/8.39$ rather than the originally designed $f/9$. We summarize experiments which have used the MMT subapertures as a phased array and as a coherent phased telescope and present a simple analysis of the tilted focal plane geometry for coherent observation. The phased operation of the MMT is important not only for obtaining high angular resolution but also for obtaining the higher detection sensitivity which results from the better discrimination against the sky emission background for IR diffraction-limited images. Full-aperture (six-beam) diffraction-limited results for the unresolved source Gamma Orionis, the well-known close binary Capella, and the resolved red supergiant Betelgeuse (including a diffraction-limited differential speckle image of the latter) are presented as preliminary demonstration of the potential capabilities of this configuration.

REAL-TIME SIGNAL PROCESSING REQUIREMENTS FOR DIFFRACTION LIMITED OPTICAL IMAGING

E. Keith Hege^{1,2} and Julian C. Christou
Steward Observatory
University of Arizona

Abstract

Diffraction limited optical images can now be produced using large ground-based astronomical telescopes. This is quite new, with convincing validation being achieved only in the past year. The computational requirements necessary to implement this capability for routine observations already challenge the capacity of present superminicomputers. Extension to larger telescopes will require supercomputer support from the beginning.

HIGH-SPEED DIGITAL SIGNAL PROCESSING FOR SPECKLE INTERFEROMETRY

E. K. Hege, W. J. Cocke, P. A. Strittmatter, S. P. Worden

Steward Observatory
Tucson, AZ 85721

William C. Booth

Signal Processing Systems
Waltham, MA 02154

Abstract

Speckle Interferometry has now been shown capable of yielding diffraction limited information on objects as faint as visual magnitude 16. Research in progress at Steward Observatory is aimed at improving (a) the resolution, (by using the Multiple Mirror Telescope with its 6.9 meter baseline), (b) the accuracy of the derived results (by implementing better recording devices and reduction algorithms), and (c) the efficiency and speed with which the information can be provided (by means of high-speed digital signal-processing hardware).

The instrumentation proposed here will improve spatial resolution at visible wavelengths to approximately 15 milliarc-seconds (75×10^{-9} radians, the best possible for any existing telescope), reduce detector induced image distortion to less than 1% and increase the throughput to essentially real-time complex Fourier transform amplitude and phase integrations at the telescope.

DIFFRACTION LIMITED IMAGE OF A GEOSYNCHRONOUS OBJECT
USING THE MULTIPLE MIRROR TELESCOPE AND FIENUP PHASE RECONSTRUCTION

E. Keith Hege and Andreas Eckart⁺
University of Arizona, Steward Observatory, Tucson, Arizona 85721

Submitted to Applied Optics

Abstract

The geosynchronous communications satellite FLTSATCOM1 has been resolved at the diffraction limit of the Multiple Mirror Telescope* (MMT). At 550nm the resolution corresponds to a beam size of approximately three meters at the object. Image amplitudes were obtained using speckle interferometry and image phases were reconstructed using Fienup's method. Two integrations of 20 minutes each in the 10nm bandpass, centered at 550nm, yielded images from which the size of the object could be determined to a precision of 75% of the beam size: Major axis = 13.0(+2.3)m; minor axis = 7.4(+2.3)m. Although noisy (brightest feature/rms background noise = 6), the images show evidence of structural features of the object.

THE NOISE BIAS PROBLEM IN OPTICAL SPECKLE IMAGING
Experience with a Real Detector

E. K. Hege, A. Eckart and J. C. Christou

Steward Observatory, University of Arizona
Tucson, AZ 85721

Abstract

We have obtained diffraction limited images for bright objects using various large astronomical telescopes, including the MMT, but the results have not been convincing for fainter objects. All speckle interferometric techniques utilizing image power spectrum or autocorrelation methods to obtain calibrated image amplitudes are subject to noise bias induced by the Poisson statistics of photon detection. This noise bias, independent of image frequency for ideal detectors with delta-function like point spread functions, must be removed to obtain calibrated image amplitudes. The noise bias characteristic of our intensified TV detector, both as a raster event localizer (faint object mode) and as a conventional image amplitude detector (bright object mode), is not only image frequency dependent but signal rate and signal distribution dependent as well. This precludes signal independent calibration of the characteristic bias functions and sets limits on object faintness for successful image recovery. Implications for detector development are noted.

THE H-ALPHA ENVELOPE OF ALPHA ORI

E. K. Hege, J. C. Hebden and J. C. Christou
Steward Observatory
Tucson, AZ 85721 USA

We use weighted shift-and-add with deconvolution (WSA/WD) to produce well-calibrated images of Alpha Orionis using data from the KPNO¹ 4m and the Steward 2.3m telescopes. Differential speckle interferometry (DSI) images have also been produced with data from the 2.3m and the Multiple Mirror Telescope² (MMT). We find evidence for a Northwest-to-Southeast elongated circumstellar envelope, extending to >4 stellar radii, around a limb-darkened 42 millisecond of arc (mas) stellar disk. Azimuthally averaged radial intensity profiles are in qualitative agreement with those predicted by Hartmann and Avrett, although significant quantitative differences suggesting non-uniform outflow are seen. MMT diffraction limited images of Alpha Orionis, observed in a narrow band centered on H-alpha, show measurable, resolved surface structure within the stellar disk. Our images do not show clear evidence for secondary companions.

Phased Array Imaging with the Multiple Mirror Telescope

E. Keith Hege
Donald W. McCarthy, Jr.
Jeremy C. Hebden
Julian C. Christou*
*Steward Observatory
University Of Arizona
Tucson AZ 85721*

Introduction

The 6.86m Multiple Mirror Telescope (MMT) has been operated as a co-phased optical array since 1983 [1]. We have used it to obtain seeing calibrated diffraction-limited images of the point source γ Orionis and the resolved red supergiant α Orionis. The point source images validate the imaging performance of the system as a function of wavelength (4100 - 8500 Å) and of coherence length (6 μ m to 3.6mm). We have measured a stable point spread function (PSF) with an FWHM of 75 nanoradians or 15 milli-arcseconds (mas) which matches the theoretical prediction. Images of α Orionis have been obtained both in the chromospheric H_α emission and in the adjacent line-blanketed "continuum" with $\lambda^2/\Delta\lambda = 3.6$ mm. In addition, we have also obtained images of a geosynchronous communications satellite in a broader bandpass ($\lambda = 5500$ Å with $\lambda^2/\Delta\lambda = 30\mu$ m). The resolution of both of these images is consistent with the observed PSF's.

REAL-TIME AMPLITUDE AND PHASE INTEGRATION FOR DIFFRACTION LIMITED IMAGING
Discrete Photon Case

E. Keith Hege
Steward Observatory, University of Arizona
Tucson, AZ 85721

Peter R. Vokac
Digital Television Imagery
Tucson, AZ 85741

Abstract

Both video raster detectors and newly developed 2-D photoelectron event locators are now employed to collect data at large astronomical telescopes for diffraction limited optical imaging by a number of speckle interferometric techniques. The Knox-Thompson algorithm is among the best understood of these techniques. The image amplitude and phase integrations required for its implementation can be accomplished directly in event-coordinate space (in the extreme photon-limited case) more efficiently than in the more conventional Fourier transform space. We describe hardware to accomplish the integrations required for Knox-Thompson image reconstruction in real-time at the telescope, thus alleviating the principal data processing bottleneck in the present applications of diffraction limited astronomical imaging. Parallel digital recording of the photon coordinate lists permits subsequent off-line re-analysis of the data by other methods if desired. The basic system consists of hardware to localize discrete photoelectron responses in a CCD TV raster and for accumulation of the complex autocorrelogram. A generalization of the system can integrate triple correlations.

Co-Phasing and Co-Aligning the Multiple Mirror Telescope

C. C. Janes and J. W. Montgomery

Multiple Mirror Telescope Observatory,
Smithsonian Institution / University of Arizona
Tucson, Arizona 85721-0465

Abstract

The Multiple Mirror Telescope is an array of six 1.8 m diameter folded Cassegrain telescopes used to achieve the collecting area equivalent to that of a telescope with a single 4.5 m primary mirror. For most applications, the six images are co-aligned in such a way that overlapping images appear to result from a single telescope. Another application requires that the wavefronts from all six telescopes be co-phased within 1 micron, concurrent with co-alignment. This paper describes the successful operation of the co-alignment and co-phasing capabilities, the control system and devices used in the applications, and test results to date.

A real-time photoelectron event-detecting video system

R. H. Macklin, E. K. Hege and P. A. Strittmatter

Steward Observatory, Tucson, AZ 85721

Abstract

We describe a system for localization of photoelectron events utilizing an intensified Plumbicon camera and a Grinnell video digitizer. The Grinnell digitizer, arithmetic unit and memory are used to produce a real-time video difference between current pixel value and previous pixel value thereby suppressing multiple detection of the same event. A master clock provides synchronization with the camera in operation at 60 Hz in 240 lines/field, repeat field mode. Our event-localization scheme provides double-buffered line-address and event-amplitude for up to 32 events along a 512 pixel video line. A software algorithm allows localization of multiple detections of the same event, and provides a unique address interpolated with 1/2 line resolution by the host minicomputer in a 480 x 512 format.

The U.S. Government is authorized to reproduce and sell this report.
Permission for further reproduction by others must be obtained from
the copyright owner.

Astronomical imaging by filtered weighted-shift-and-add technique

Erez Ribak

Jet Propulsion Laboratory-NASA, Mail Stop 169-314, California Institute of Technology, 4800 Oak Grove Drive,
Pasadena, California 91109

Received January 23, 1986; accepted July 28, 1986

The weighted-shift-and-add speckle imaging technique is analyzed using simple assumptions. The end product is shown to be a convolution of the object with a typical point-spread function (psf) that is similar in shape to the telescope psf and depends marginally on the speckle psf. A filter can be applied to each data frame before locating the maxima, either to identify the speckle locations (matched filter) or to estimate the instantaneous atmospheric psf (Wiener filter). Preliminary results show the power of the technique when applied to photon-limited data and to extended objects.

SPICE Aug
San Diego, '85

Use of matched filtering to identify speckle locations.*

E. Ribak, E. K. Hege** and J. C. Christou†

Steward Observatory, University of Arizona
Tucson, Arizona 85721

Abstract

In many cases the speckle maxima required for the our realization of the Shift-and-Add method¹ are not well defined. This is due mainly to Poisson noise, inherent in the detection process, which obliterates the shape of faint speckles. The problem is aggravated for extended objects with local peaks, such as binary stars. As a remedy, we use a filter that smoothes out each speckle and at the same time defines its location.

The best filter should be very close to the mean speckle itself: a matched filter. The initial guess for this filter is a bell function, slightly wider than the expected mean speckle. This initial guess is used to locate filtered speckle maxima which are then used to produce a better mean speckle estimate by shift-and add. The procedure is iterated until the mean speckle converges.

We find that the iterative speckle estimate is not the optimum matched filter. The most suitable filter must suppress the variable background created by coalescing speckles in a large speckle cloud as well as smooth the single-photon event noise. Thus we combine the mean speckle with a band-pass filter into a matched filter. Local speckle maxima are thus enhanced, whereas single photons are discriminated against by using a comparison low-pass filtered frame, since they do not contain much power. The combined process, speckle identification and weighted-shift-and-add, can be carried out in the image plane or in the Fourier plane. We have experimented in both domains.

THE ASTROPHYSICAL JOURNAL, 303 605-613, 1986 April 15
© 1986 The American Astronomical Society. All rights reserved. Printed in U.S.A.

The U.S. Government is authorized to reproduce and sell this report.
Permission for further reproduction by others must be obtained from
the copyright owner.

DETECTION OF THE LENSING GALAXY IN PG 1115+08¹

STUART B. SHAKLAN AND E. K. HEGE

Steward Observatory, University of Arizona
Received 1985 June 24; accepted 1985 October 3

ABSTRACT

We have fitted models to good-seeing (0".6) postguided observations of the triple quasar PG 1115+08 in blue and red light. The four components (A, A', B, and C) all have similar point spread functions in the blue fit. There are no significant blue residuals after subtraction of the model from the image. The fits to components A, A', and C in the red image are consistent, but that of the B component suggests that there is an excess red flux from an area between all four components. The residuals show that this flux has a peak magnitude of 19.8 ± 0.3 mag in the R band and a $V-R$ color of at least 2.7 ± 0.5 mag. The position of this flux excess is consistent with that of the lensing galaxy in models of gravitational imaging.

Subject headings: gravitation — quasars

Appendix to:

AFGL-TR-87-0097

Investigations of High Resolution Imaging
Through the Earth's Atmosphere Using
Speckle Interferometry

E. Keith Hege

University of Arizona
Steward Observatory
Tucson, Arizona 85721

19 May 1987

Publications of Work Supported by
AFGL Contract #F19628-84-K-0035

Approved for public release; distribution unlimited

AIR FORCE GEOPHYSICS LABORATORY
AIR FORCE SYSTEMS COMMAND
UNITED STATES AIR FORCE
HANSCOM AIR FORCE BASE, MASSACHUSETTS 01731

THE USE OF THE MMT FOR INTERFEROMETRIC IMAGING

Jacques M. Beckers
National Optical Astronomy Observatories *
Tucson, AZ 85726

E. Keith Hege
University of Arizona
Tucson, AZ 85721

ABSTRACT

We describe recent progress with interferometric imaging using the Multiple Mirror Telescope (MMT). All six telescopes can now be phased over a wide field of view simultaneously resulting in a (u, v) plane coverage corresponding to that of a 686 cm aperture telescope. We describe the open-loop phasing control of the MMT for gravitational changes and we describe a concept of an internal cophasing/coalignment system for MMT type telescopes.

Introduction

In previous publications ^{1, 2} we described the use of the Multiple Mirror Telescope (MMT) for interferometry in

*Operated by the Association of Universities for Research in Astronomy, Inc., under contract with the National Science Foundation.

Proceedings of the IAU Colloquium No. 79: "Very Large Telescopes, their Instrumentation and Programs", Garching, April 9-12, 1984.

the visible, infrared and sub-millimeter regions of the electromagnetic spectrum. This paper is an update of those papers describing the progress made since then in using the MMT as a phased array in visible wavelengths.

Fully Phased Operations of all Six MMT Telescopes

We recently completed the construction of a phasable beam combiner for the MMT, consisting of six pairs of identical BK7 glass wedges, one in each of the six MMT telescopes (mode C, in the sketch shown in figure 3, in paper 1). The wedges have an angle of 10° . Each pair of wedges acts effectively as a parallel glass plate whose thickness can be varied by translating one of the wedges thus changing the pathlength of the telescope. The motion of the wedges is controlled by a stepper motor which is interfaced with a computer. Each step of the motor corresponds to a $0.18\mu\text{m}$ pathlength change and the total range of pathlength adjustment is about 3mm. The pathlengths of each of the telescopes were initially made equal to $\pm 0.5\text{mm}$ by adjusting the height of the tertiary mirrors so that the adjustment range of the wedge pairs suffices.

The combination of the six beams was done in the so called wide field mode described in paper 2. In it, the pathlength equality between a star and the image plane of the MMT is maintained when moving the object star off axis at least over an amount equal to the isoplanatic path. This wide field condition is achieved by matching the exit and entrance pupils of an interferometric array as shown in

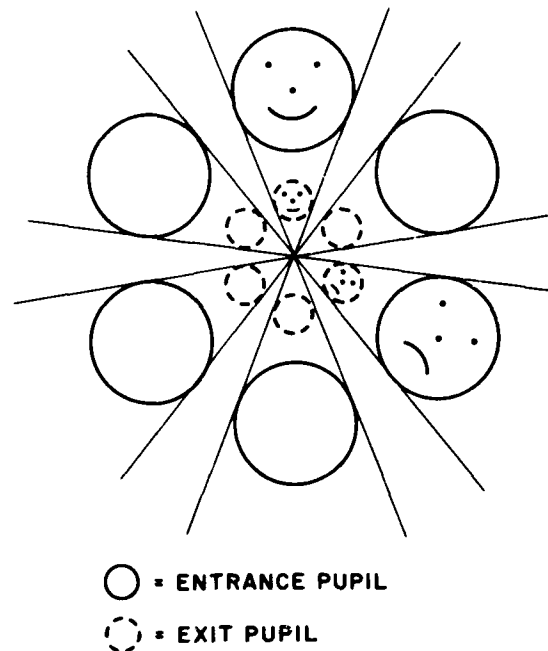


Figure 1: For wide field interferometry, the entrance and exit pupils should be identical except for a linear scaling factor. Identity is also required for structure within the pupils.

the cartoon drawing in figure 1. It means that when the diameters of the individual entrance and exit pupils are matched, the distance between the pupils are also matched. Also (as shown by the faces in figure 1), the internal structure of the pupils must be preserved.

We phase the six telescopes with the use of a speckle camera³. One of the telescopes is used as a reference. The other 5 telescopes are then phased to the reference telescope, one by one, by searching for the interference fringes in the combined telescope star images, and by centering the white light fringe on the star image. This process takes about 5 minutes after which all six images are combined to give the combined interferometric/speckle



Figure 2: Speckle image of an unresolved star using the HMT as a fully phased array.

image. Figure 2 shows the combined image for an unresolved star. In the center of the image the complex fringe/speckle image is, as expected, showing speckles corresponding in size to the 686 cm telescope aperture. The speckles are, however, clearly of a different character than those of a single aperture telescope because of the predicted preferred spatial frequencies. At the edge of the image where due to seeing, telescope aberrations and image misalignments the six images do not overlap, the full speckle patterns disappear. Figure 3 shows the 2D power spectrum for the unresolved star β Tau. The location of the peaks corresponds to those predicted from the (u, v) plane coverage of the six element polygon array (figure 4). The variable amplitudes of the peaks are due to a variety of instrumental effects including image misalign-

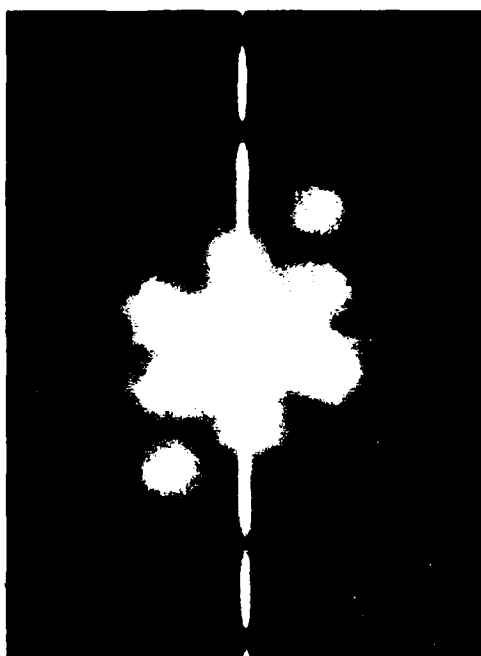


Figure 3: Two dimensional power spectrum of β Tau.

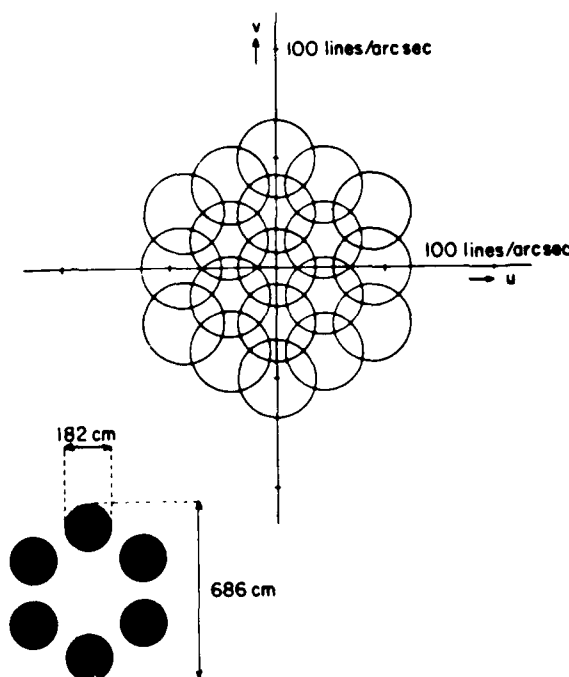


Figure 4: Predicted (u, v) plane coverage of MMT

ments, telescope aberrations, imperfect phasing and the absence of a correction for the off-axis polarization/retardation effects in the six telescopes. Figure 5 shows the 2D power spectrum for the binary star Capella which at 750nm now shows a full 1.5 cycles of the power spectrum fringe resulting of the binary nature. Because of changing phasing conditions between the observations the ratio of the Capella and β Tau power spectrum (figure 6) show many artifacts (including detector "hot spots"), which makes it dangerous to infer reality for other sets of fringes visible in the ratio spectrum.

These changing phasing and coalignment conditions make it very difficult to do quantitative analysis of the phased

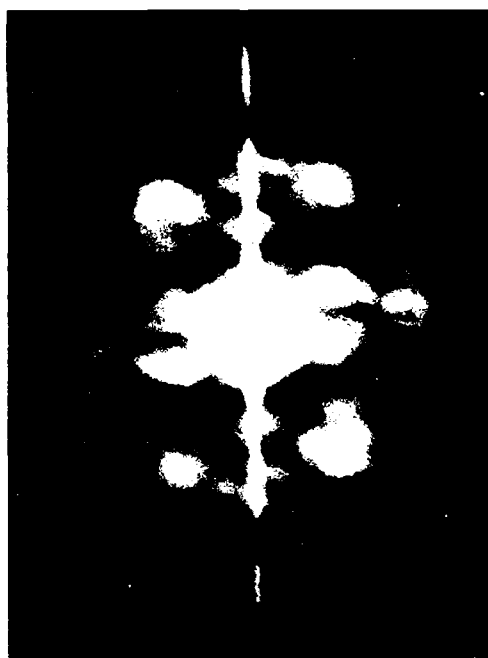


Figure 5: Power spectrum of Capella

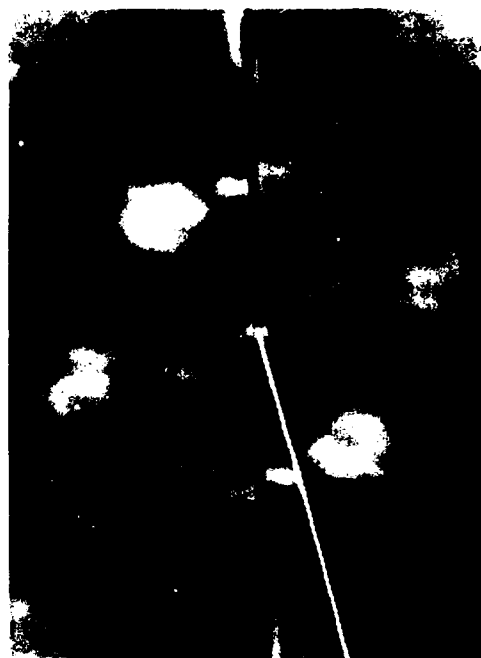


Figure 6: Ratio of Capella and β Tau power spectra

MMT images. We have, therefore, undertaken a development program aimed at maintaining phasing and coalignment of the MMT images. This program includes attempts to correct open-loop for elevation and temperature effects, and plans to construct an internal laser coalignment/cophasing system for the MMT. We will describe these efforts below.

OPEN-LOOP COPHASING

Most of the variation in the telescope pathlengths results from the gravitational flexure of the telescope structure. We measured the variation of pathlength as a function of the elevation pointing of the MMT on a number of occasions. Figure 7 shows the relative variation in the pathlength for each telescope as made on two nights about one month apart,

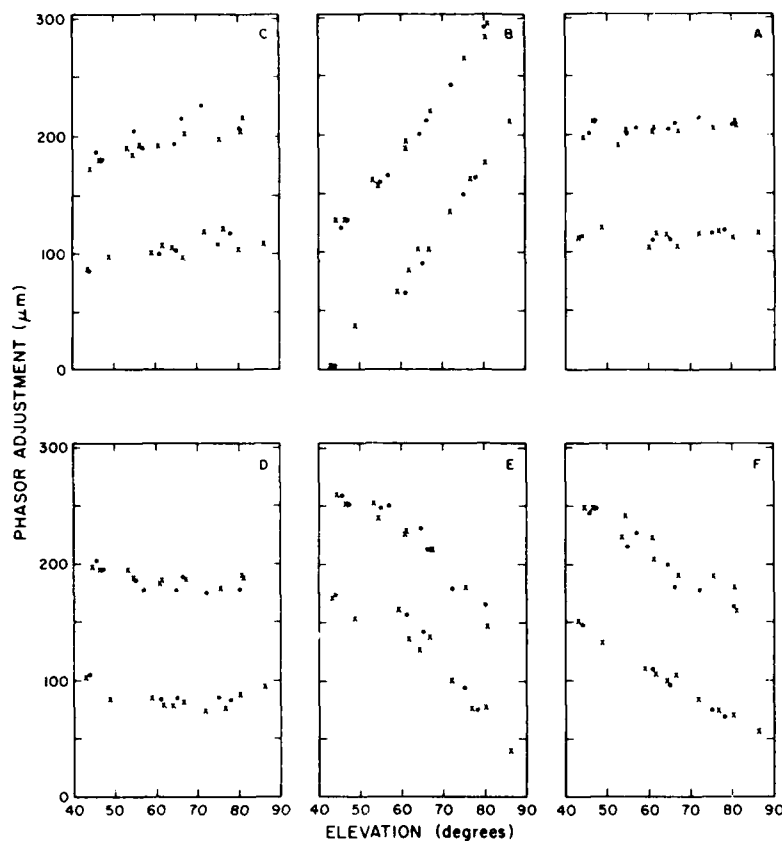


Figure 7: Pathlength variation in each of the six MMT Telescopes for two different observing runs. Increasing values correspond to increasing pathlength.

on January 21 and February 13, 1984. The 5 measurements of pathlength difference were adjusted so that the average pathlength was kept constant as one changed elevation. That condition resulted in the six data sets (one for each telescope) shown in figure 7. From this data, one concludes that (i) the systematic changes are very repeatable between the two data set. Between the dates of the two sets, a number of adjustments were made on the MMT like replacing the tertiary, secondary and beam-combiner optics. The repeatability is therefore remarkable. Also the pathlength difference between telescopes B and E

repeats quite closely the difference between those telescopes measured over half a year before and shown in paper 2 (figure 10), (ii) the hysteresis between up and downward motions is small. The largest amount (for telescope B) is $5\mu\text{m}$ and (iii) the residual scatter of the observations amounts to $\sim 20\mu\text{m}$ peak to peak. That is substantially more than the measurement errors ($\pm 2\text{--}3\mu\text{m}$) and is at least, to some extent, due to thermal changes in the optics support structure.² The curves shown in figure 7 have been fitted with a second degree polynomial and the wedge position is now open-loop computer controlled to remove the systematic elevation variation.

It should be pointed out that in an array telescope like the MMT, the pointing of the individual telescopes and the phasing of these telescopes are highly interactive. If pointing errors caused by imperfect mount pointing (typically 0.5-1 arc sec) are corrected by tilting the secondary mirrors, the phasing of the telescopes is destroyed (1 arc sec causing as much as a $25\mu\text{m}$ pathlength difference). It is therefore important not to do so at the MMT, and to point the telescope as a whole using its elevation and azimuth axis. It is equally important to define an algorithm for the differential pointing corrections by the secondary mirrors needed to correct for co-pointing errors between the MMT telescopes. For phasing experiments the algorithm adopted keeps the average position of the six telescope images, in both elevation and azimuth direction, stays the same.

As described in paper 2, we suspect that the residual $20\mu\text{m}$ PTP variations are due to thermal changes in the MMT optics support structure (OSS), one degree thermal change across the structure causing a $\sim 65\mu\text{m}$ change in the differential pathlength. A plan to measure the OSS temperatures and to correct open-loop for their change, remains to be implemented. When implemented, it should improve the cophasing. Until implemented, we cannot evaluate the residual variations.

DESCRIPTION OF AN INTERNAL COALIGNMENT/COPHASING SYSTEM

Ultimately, it is desirable to couple the individual telescopes in MMT configuration systems with a system internal to the MMT, since the open-loop correction systems are not perfect and since coalignment and cophasing on nearby stars will not always be possible. We describe in this section an internal laser coalignment/cophasing system (LC^2S) which is aimed at doing simultaneously both internal coalignment and cophasing. As pointed out in the previous section, the coalignment and cophasing of an MMT type telescope are closely related so that an LC^2S system which does both is highly desirable.

A diagram of the LC^2S system is shown in figure 8. It is based on a similar system described by Butts, et al.⁵ Figure 8^a shows the front view of the 4 mirror MMT concept under discussion for the U.S. National New Technology Telescope (NNTT). The dark bars between adjacent

telescopes are the LC^2S bridges which will coalign and cophase telescopes A to B to C and to D. The fourth bridge between D and A is redundant and can be used as a check and as a spare, in case any of the other bridges fail. A similar scheme with 5 or 6 bridges could be used for the present six mirror MMT. Figure 8^b shows the cross section Q through the telescope. It shows how a multiwavelength Argon laser is projected out of the telescope to infinity. Figure 8^c shows cross section P through the

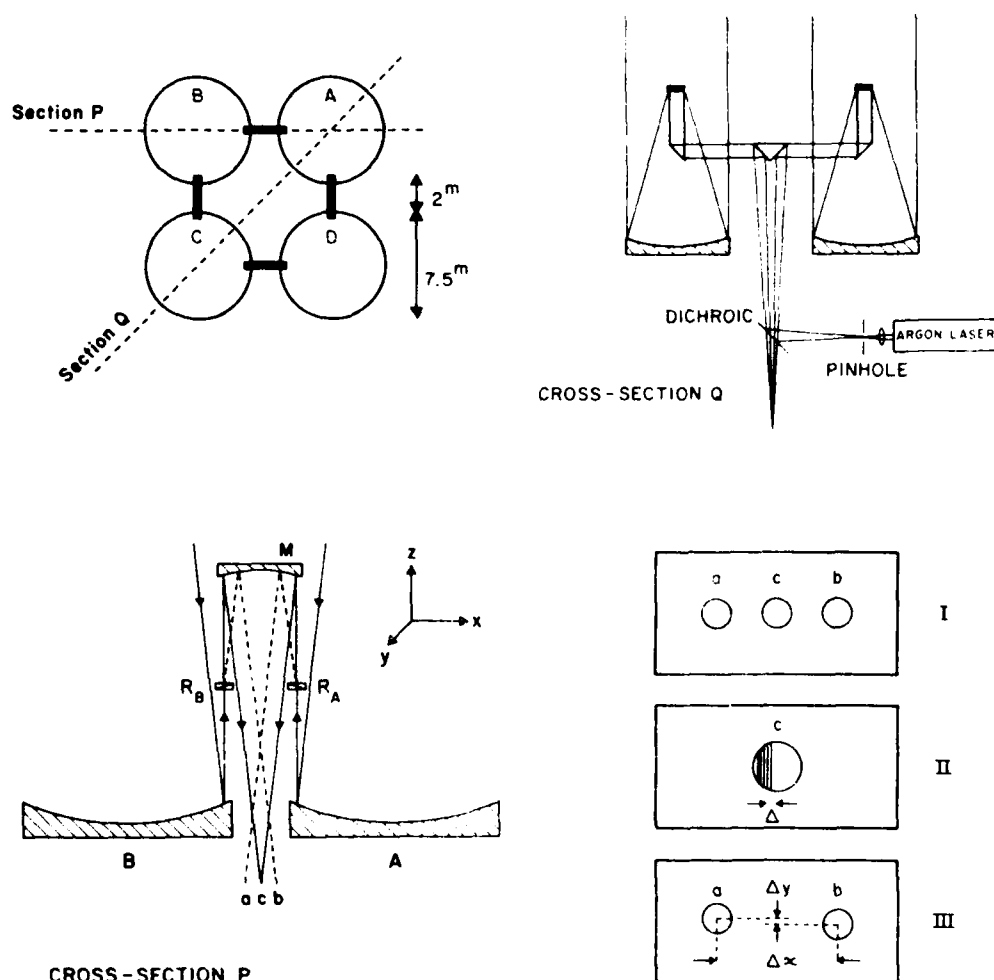


Figure 8: Diagram of the laser coalignment/cophasing system for the NTT-MMT concept. 8^a, Upper right = 8^b, etc.

telescopes A and B and through the bridge connecting them. The Argon laser beams at the facing edges of telescopes A and B are intercepted by an inverted telescope M which focuses the laser beam at image c. Two Rochon prisms R_A and R_B split the incoming laser beam in orthogonal linear polarizations. The image c results from the combined undeviated beams whereas the deviated beams from telescopes A and B form two separate images a and b respectively. In figure 8^d the three images are shown on a single detector (I) or on two separate detectors (II and III). Image II shows the location of the quasi whitelight fringe with respect to the laser source image. The displacement Δ between the whitelight fringe and the center of the image c result from a phasing error and can be used as an error signal to adjust the phase of the telescope with respect to telescope A by means of any of the phase adjustment arrangement described in paper (2). Image III shows the displacements (Δx , Δy) of images a and b. These displacements can be used to coalign telescopes A and B, for example by tilts of their secondary mirrors. Tilts and displacements of the inverse telescope M will displace images a, b and c but will keep the values for Δ , Δx and Δy quite undisturbed. In paper (4) the sensitivity of the LC²S scheme to misalignments of the inverse telescope M were discussed. The most critical misalignment is a defocusing of the telescope M which will cause Δx to change resulting in a misalignment of the optics. It is important to maintain and/or measure the distance M - c with high precision. The second most critical misalignment is a tilt

of M around the y axis which result in a change in Δ .

This LC^2S scheme at the moment is untested, as is a similar scheme by N. Woolf which uses a flat mirror for M . The Δ , Δx and Δy values will of course be subject to variations due to atmospheric seeing inside the telescope, as was the case for the so called laser collignment system which was part of the original MMT design. To reduce the effects of seeing, one should measure these quantities every 0.1 second and then average them digitally until the desired coalignment/cophasing precision is reached. An estimate for reasonable internal seeing conditions ⁴ results in a RMS coalignment and cophasing error of 0.01 arc second and $0.14\mu m$ for an integration time of 30 seconds which is much less than any image motion and phasing errors introduced by the atmosphere in front of the telescope.

NON-REDUNDANT MMT ARRAYS

The present MMT and the proposed MMT concept for the NNTT have a highly redundant aperture configuration from the point of view of interferometry. If one sets as a goal the filling of the maximum area in the (u, v) plane with a polygonal array of telescopes, one would do substantially better with an odd number of telescopes. With 3, 4, 5, 6, 7, 8, 9 and 10 sided polygons, one has 3, 4, 10, 9, 21, 16, 36 and 25 non-redundant baselines respectively. Figures 9, 10, 11 and 12 show the (u, v) plane coverage with an optimized array of 3, 4, 5 and 6 telescopes, optimized in the sense that gaps in the (u, v) plane coverage are just

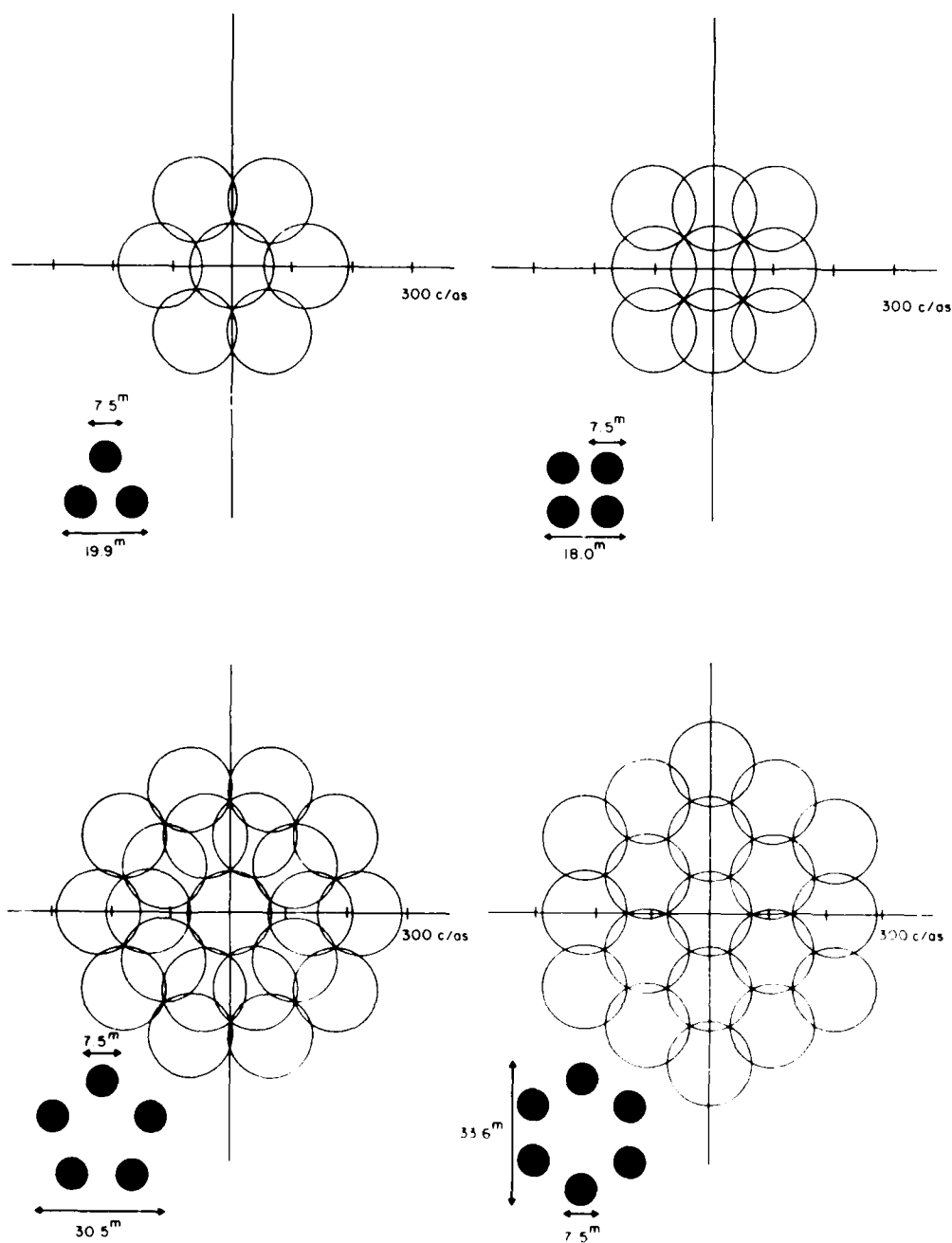


Figure 9: Coverage of the (u, v) plane for 3, 4, 5, and 6 sided polygonal MMT arrays.

avoided. The (u, v) plane coverage for the $(2n-1)$ telescope is about the same as that for the $2n$ telescope because of the absence of the redundancy in the former. Structural considerations appear to lead to a preference for even numbered polygons like the MMT and the NNTT-MMT so that the odd numbered non-redundant polygon MMT may be more a curiosity than a realistic proposal.

CONCLUSION

The MMT has shown itself to be a very powerful interferometric device. When long coherence lengths (small $\Delta\lambda$) are used the MMT, as it is now with the open-loop flexure correction, is very good as a coherent array. For broad bandwidth applications in the visible region of the spectrum, the residual 10-20 μ m variations in pathlength are unacceptable. A more refined open-loop control system may not be adequate to cure that and it appears that an optical closed loop control system like the LC²S will be needed.

ACKNOWLEDGEMENTS

The MMT interferometry project owes much to the support of the Steward Observatory shops, especially R. Young, and to the help of the engineering and operations staff of the Multiple Mirror Telescope Observatory. This work was supported by NSF grants AST 8113212 and AST 8201092 and USAF Contract F19628-82-K-0025.

REFERENCES

- (1) Beckers, J.M.; Hege E.K.; Low, F.J.; McCarthy, D.W. and Strittmatter, P.A.: "The Use of the Multiple Mirror Telescope as a Phased Array", SPIE Proceedings 440, 136, 1983.
- (2) Beckers, J.M.; Hege, E.K. and Strittmatter, P.A.: "Optical Interferometry with the MMT", SPIE Proceedings 444, 85, 1983.
- (3) Beckers, J.M.; Hege, E.K.; Murphy, H.P.: "The Differential Speckle Interferometer", SPIE Proceedings 445, 462, 1984.
- (4) Beckers, J.M. and Shu, K.L.: "Tolerancing and Limiting Accuracies and Precisions of a NNTT-MMT Coalignment/Cophasing System." NOAO-Advanced Development Program R&D Note 84-2.
- (5) Butts, R.R.; Cusumano, S.J.; Fender, J.S. and DeHainaut, C.R.: "A concept for a Phased Array Laser Transmitter", SPIE Proceedings Nr. 440, 118, 1983.

DISCUSSION

J.E. Noordam: Redundant spacings in the aperture plane are a very powerful calibration-tool in radio aperture synthesis. Since it is possible in optical interferometry to disentangle their contributions and then use them for this same purpose, one should not eliminate them by building non-redundant arrays.

J. Beckers: You are of course correct. Phase closure techniques have not yet been used in optical astronomy. If and when they come about, redundancy may indeed be of help.

DIAMETER AND LIMB-DARKENING MEASURES FOR ALPHA ORIONIS

A. Y. S. CHENG, E. K. HEGE,¹ E. N. HUBBARD,¹ L. GOLDBERG,² P. A. STRILLMEIER,¹ AND W. J. COCKE¹

Steward Observatory, University of Arizona, Tucson

Received 1985 September 12; accepted 1986 April 17

ABSTRACT

Previously reported speckle interferometric measurements of the angular diameter of α Ori are widely scattered and apparently inconsistent. Stellar atmosphere models predict a stellar disk to be limb-darkened differently for different spectral features, and that less limb-darkening will be observed at longer wavelengths. Upon careful analysis of calibrated speckle observations obtained at various wavelengths with the KPNO 4 m telescope, we find a single diameter parameter to be inadequate to explain all of the features of our measurements. There is evidence for a central stellar component of $42.1 (\pm 1.1)$ mas diameter with extended structure surrounding it. Limb-darkening effects are suggested by attempts to fit cosine model image profiles to the data, which yield limb-darkening coefficients ranging from ~ 0.9 in TiO absorption bands to ~ 0.4 in Ca II absorption lines. These fits have significant residuals at large radii suggesting a faint envelope extending from 1 to $5 R_*$, although calibration errors cannot be ruled out entirely. There is a suggestion of wavelength dependence in single-parameter diameter measures with a linear coefficient of $\sim -6 (\pm 1) \times 10^{-3}$ mas nm⁻¹. Possible model-dependent biases in these results are discussed.

Subject headings: interferometry — stars: diameters — stars: individual — stars: supergiants

1. INTRODUCTION

Alpha Orionis is an M2 Iab, SRc late-type supergiant star with mass loss rate $\sim 10^{-6} M_\odot \text{ yr}^{-1}$. High-resolution speckle interferometric observations have the potential capability of measuring the photospheric sizes, the inner mass flow sizes, and the extended mass flow geometries for a number of late-type supergiant stars of known mass loss rates. Yet there is a large variation in the values reported for the angular diameter of α Ori obtained by speckle interferometry.

We find evidence that such scatter in angular diameter measures can be resolved by using an appropriate stellar model: a limb-darkened stellar disk with a wavelength-dependent limb-darkening coefficient surrounded by a faint observing bandpass-dependent envelope extending from 1 to 5 stellar radii.

In this paper, only the photospheric radius, derived from azimuthally averaged radial profiles, is discussed in detail. We have been particularly careful about seeing calibrations, as discussed by Christou *et al.* (1985).

Other non-spherically symmetric details of α Ori, which we have previously reported (Goldberg *et al.* 1981) and which have been confirmed by others (Roddier and Roddier 1983, 1985), are being studied further. Evidence of the detection of faint extended chromospheric structures is presented in Hebdén *et al.* (1986).

Previously, somewhat larger angular diameters have been inferred by speckle interferometry than by photometric techniques (see, e.g., Tsuji 1976). Such discrepancies may be accounted for with very careful analysis of any measurement biases implicit in the previous work, including the effects of a larger scale circumstellar shell. We find a consistently smaller diameter and offer a possible explanation for the wide varia-

tions in the generally larger diameters previously reported by speckle interferometry results. Any remaining discrepancy in interferometric and photometric angular sizes can only be resolved by refined modeling of the temperature structure of the star, including dust shell effects (see, e.g., Tsuji 1978), and with improved knowledge of the distance.

II. OBSERVATIONS

Alpha Orionis was observed with unusually good seeing at the KPNO 4 m telescope (pupil masked to 3.8 m) on 1981 February 2 and 3, using the Steward Observatory intensified video speckle camera (Hege *et al.* 1982). The seeing on the first night was $\sim 0.5''$ and less than $1''$ on the second night. Various bandpasses were used to observe both α and γ Ori (the object and the calibration star respectively). The recently discovered (Papaliolos, Nisenson, and Ebstein 1985) faint secondary of γ Ori was outside our field of view.

Video specklegrams for each bandpass were recorded for ~ 10 – 15 minutes on the object and ~ 5 minutes on the calibration star. The specklegrams were recorded with 15 ms exposures at the rate of 7.5 Hz (every fourth video frame). At this shutter frequency the afterglow of the image intensifier has sufficiently decayed between exposures that it can be removed by means of video subtraction of consecutive frames during data digitization. The 15 ms exposure time is short enough to freeze the turbulence in Earth's atmosphere, so that the specklegrams retain image details up to the full diffraction limit of the telescope.

The video specklegrams were digitized 8 bits deep in a 128×128 pixel array with a Grinnell digital television system, yielding a detector image scale of $7.22 \text{ mas pixel}^{-1}$ and written on tape using the Steward Observatory minicomputer system.

It has been shown theoretically that the point-spread function calibration in speckle interferometric analysis is very sensitive to the seeing, characterized by Fried's parameter r_0 . We adopted a new and more careful reduction procedure to calibrate the seeing and instrumental point-spread function (Christou *et al.* 1985). That reduction procedure includes spe-

¹ Visiting Astronomer, Kitt Peak National Observatory, National Optical Astronomy Observatories, which is operated by the Association of Universities for Research in Astronomy, Inc., under contract to the National Science Foundation.

² Also Kitt Peak National Observatory.

cific measures (1) to edit the data, (2) to remove known systematic detector-induced artifacts, and (3) to bin the specklegrams according to instantaneous seeing. The good seeing data give a better signal-to-noise ratio. For example, 100 frames of good seeing data and 1000 frames of moderate seeing data give similar signal-to-noise ratios in the final results.

The image power spectra (PSs) of the digitized specklegrams, edited, corrected, and binned, were accumulated using the NOAO CDC Cyber 720/170 and the fast Fourier transform algorithm. The PSs were then written onto tape and transported back to the Steward Observatory computing facilities for analysis.

The detector-colored photon noise bias (see Hege *et al.* 1982) was deconvolved from each binned, summed PS by dividing by a two-dimensional anamorphic Gaussian fit to the data at spatial frequencies larger than the diffraction limit cutoff frequency and subtracting 1.0 to remove the bias.

The effects of seeing and of the combined instrumental and telescope optical transfer functions were calibrated by dividing the debiased PS of the object (α Ori) by that of a point source (γ Ori) of comparable seeing (i.e., corresponding bins of same r_0) to give clean, deconvolved PSs of the object. Autocorrelation functions (ACFs) were obtained as Fourier transforms of these calibrated, debiased power spectra.

III. MODEL-DEPENDENT RESULTS

We have analyzed our data both in the image ACF and in the image PS domains. The models used in each case are subject to biases, but the biases are weighted differently in the two domains.

We first assumed that, at the resolution of the 4 m telescope, limb-darkening effects might be negligible. Thus we modeled ACF data with a uniform disk autocorrelation function constrained by the data in a least-squares fit. This produced the results shown as the filled circles in Figure 1 and reported in the first two columns of Table 1. The scatter in these results is typical of the scatter seen in the results of other observers, as summarized in Table 2.

We next attempted to make the model more complex by

TABLE 1

SUMMARY OF α ORIONIS AUTOCORRELATION FUNCTION ANALYSIS

λ (Å)	D_m (mas)	R_m (3)	B/A (4)	Figure of Bias (B/A) R_m (5)	D_m (mas)
(1)	(2)	(3)	(4)	(5)	(6)
3700	52 ± 6	—	—	—	47.0
4100	51 ± 2	0.79	10.9	0.86	41.8
5200	50 ± 1	0.072	10.5	0.76	42.0
5500	48 ± 1	— ^a	—	—	—
6500	58 ± 1	0.202	7.8	1.57	41.4
6563	44 ± 1	0.141	1.4	0.20	42.3
8500	46 ± 1	0.122	1.6	0.20	43.9
8542	43 ± 1	0.202	1.7	0.34	40.2
Mean	47.3 ± 3.5	—	—	—	42.1 ± 1.1

^a Too noisy to measure.

^b Experiment inadvertently omitted 5500 Å.

introducing a limb-darkening parameter in an attempt to find an internally consistent interpretation of these puzzling results.

The calibrated image PS data were analyzed directly by fitting power spectra of model images to the azimuthally averaged observed radial PS profiles to extract (model-dependent estimates of) two physical parameters, the radius R_m and the limb-darkening coefficient U . A typical averaged radial PS profile, together with a typical model fit, is shown in Figure 2.

The model image PS was computed for a limb-darkened stellar disk image intensity profile $I(r; R_m, U)$:

$$I(r; R_m, U) = I_0[(1 - U) + U \cos(\pi r / 2R_m)] \quad \text{for } r \leq R_m, \\ = 0 \quad \text{for } r > R_m,$$

with R_m being the model radius of the star and U being the limb-darkening coefficient. We computed normalized intensity profiles, setting $I_0 = 1$. A uniform disk corresponds to $U = 0$. For a spherically symmetric disk, the corresponding model PS $P(r; R_m, U)$ is given by

$$P(r; R_m, U) = 4\pi^2 \left| \int_0^r dr' r' I(r'; R_m, U) J_0(2\pi r r') \right|^2.$$

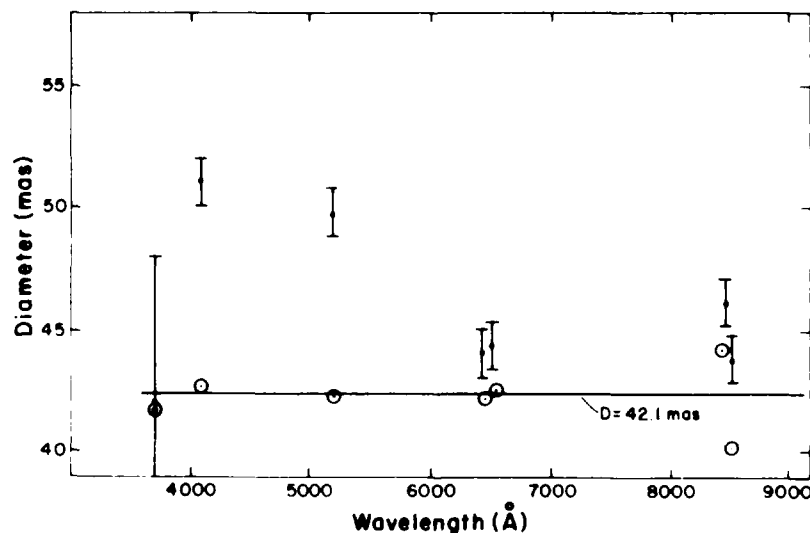


FIG. 1. Best-fit autocorrelation diameter measures (filled circles) for the various observing bandpasses. A linear regression analysis shows a strong correlation with a measure of the bias induced by the soft image wings and the model fit diameter value. Using the empirical linear regression to predict the unbiased diameter (open circles) as a function of the measured diameter yields the wavelength-independent result $D_0 = 42.1 \pm 1.1$ mas.

TABLE 2
PREVIOUS MEASURED DIAMETER OF α ORIONIS

Wavelength (Å)	U^a	Diameter (mas)	Reference
5750	...	34 to 47	Pease 1931
5000 \pm 125	...	< 50	Giazari <i>et al.</i> 1972
4220	...	69 \pm 5	Bonneau and Labeyrie 1973
4880	...	67 \pm 5	
5700	...	55 \pm 5	
7190	...	52 \pm 5	
10400	...	< 50	
4213 \pm 34	...	62 \pm 17	Currie <i>et al.</i> 1974
5025 \pm 35	...	47 \pm 6	
5823 \pm 46	...	57 \pm 9	
5992 \pm 15	...	57 \pm 6	
6336 \pm 16	...	44 \pm 13	
5100 \pm 50	0	49 \pm 1	Lynds <i>et al.</i> 1976
	1	74 \pm 1	
5180 \pm 50	0	53 \pm 1	
	1	79 \pm 1	
5100 \pm 50	0.6	66 \pm 6	McDonnell and Bates 1976
5300 \pm 80	...	35 \pm 10 ^b	Ricort <i>et al.</i> 1981
		100 \pm 40 ^c	
6000 \pm 50	0	45 \pm 1	Welter and Worden 1980
	0.5	50 \pm 2	
	1	62 \pm 2	
6500 \pm 50	0	45 \pm 2	
	0.5	49 \pm 2	
	1	61 \pm 3	
7000 \pm 50	0	42 \pm 1	
	0.5	45 \pm 1	
	1	55 \pm 2	
7400 \pm 50	0	30 \pm 4	
	0.5	32 \pm 4	
	1	39 \pm 4	
5350 \pm 90	...	37 \pm 3	Rodder and Rodder 1983
4050 \pm 75	...	45 \pm 2	Balega <i>et al.</i> 1982
7100 \pm 25	...	54 \pm 3	
7150 \pm 10	...	67 \pm 4	
5750 \pm 42	...	62 \pm 1.5	
5870 \pm 8	...	62 \pm 1.5	
7520 \pm 8	...	50 \pm 2	
7730 \pm 42	...	62 \pm 1	

^a Value omitted if not stated in reference.

^b Core.

^c Halo.

where $J_0(2\pi r v)$ is the zeroth order Bessel function of the first kind and v is the spatial frequency. For a uniform disk, namely $U = 0$, $P(r; R_m, 0)$ reduces to

$$P(r; R_m, 0) = [J_1(2\pi r v) / r]^2,$$

with J_1 being the first-order Bessel function of the first kind. The computed model PS and its first partial derivatives, $\partial P(r; R_m, U) / \partial R_m$ and $\partial P(r; R_m, U) / \partial U$ (computed as first differences) were tabulated for use in an iterative nonlinear least-squares fitting procedure (patterned after Jeffreys 1980, 1981). Since aperture effects were removed by the point source calibration, this function should model the PS data up to the cut-off frequency of the telescope for the corresponding observing bandpass.

The observed PSs $P_0(r)$ were then fitted by the linear combination

$$P_0(r) = 4P(r; R_m, U) + B,$$

where A and B are constant parameters. A allows the scaled model to be scaled to the data, and B was introduced to required to model the excess power consistently observed at the highest spatial frequencies. The ratio $B/(A + B)$ represents "unresolved power" in this model: the star may have surface features unresolved at the telescope diffraction limit.

Figure 3 displays two different models which are indistinguishable, over the spatial domain investigated and the statistical precision achieved, with regard to their simulated PS typical radial profile. This illustrates the ambiguity in the models given the marginal capability of the 3.8 m aperture to resolve this star: we could not simultaneously fit both parameters R_m and U uniquely to any single observed PS profile. Therefore, we fixed the limb-darkening parameter U and fitted the data by only the three parameters R_m , A , and B . The limb-darkening parameter U was then varied between 0 and 1, $A/U = 0.1$, and different R_m , A , and B values are obtained for each of the corresponding three-parameter fits. The results, together with the statistics from those fits, are listed in Table 3. The unresolved power and rms error of the fits for $U = 0$ are typical for all values of U ; they were useful as discrimination of goodness of fit.

The results in Table 3 are shown in Figure 4. The effect of the wide scattering of the inferred radius for each spectral bandpass and for a fixed limb-darkening coefficient. This figure also shows the extremes of how different limb-darkening models give different measured radii for our data sets. Interpreted this way, the ensemble of fits suggests a physical key to selecting a most appropriate model from the ensemble of possible models.

The limb darkening is expected to be a function of wavelength. An interpretation of these results, which we have depicted graphically in Figure 4, is possible if we require a single fixed physical stellar radius. Our choice (still model-dependent) is represented by the horizontal line, $R_m = 32.5$ mas, in Figure 4. If we assume that the cosine limb-darkening coefficient U can be no greater than 1, nor less than 0, our measurements and model actually set upper and lower limits of the physical diameter of α Ori (the dot-dash lines in Fig. 4). When a radius is fixed for the star, the limb-darkening coefficients for each of the spectral bandpasses can be predicted from the intersections of the radius and the fitted curves. Possible values are tabulated in Table 4. Alternatively, if limb-darkening coefficients are known from other sources (e.g., model atmosphere calculations), then the radius of the star is measured.

The limb-darkening coefficients for an M2 supergiant star have been computed by Tsuji (1976) to be $\sim 0.9-1.0$ for TiO bands, and $0.4-0.7$ for CN and CO bands which are generated in deeper layers of the stellar atmosphere. In our measurements, the bands at 6500 Å \pm 20 Å, 5500 Å \pm 100 Å, and 5200 Å \pm 100 Å fall into strong TiO bands, and they are highly limb-darkened with U at $\sim 0.9-1$. This yields the model radius $R_m = 32.5$ mas, based on Figure 4.

Extremes for the limb-darkening coefficients are tabulated in Table 4. The values inferred are due to the combined result of all of the spectral features included within the particular observing bandpass. In late-type supergiant stars, numerous features are usually present in 3-20 Å bandpasses.

Unfortunately, this value for R_m predicts $D_{\text{core}} = 65$ mas, larger than any of the values found by the ACE analysis of the same data sets. Uniform disk models, as shown in Figure 2, are expected to give the largest possible estimates for R_m . Section

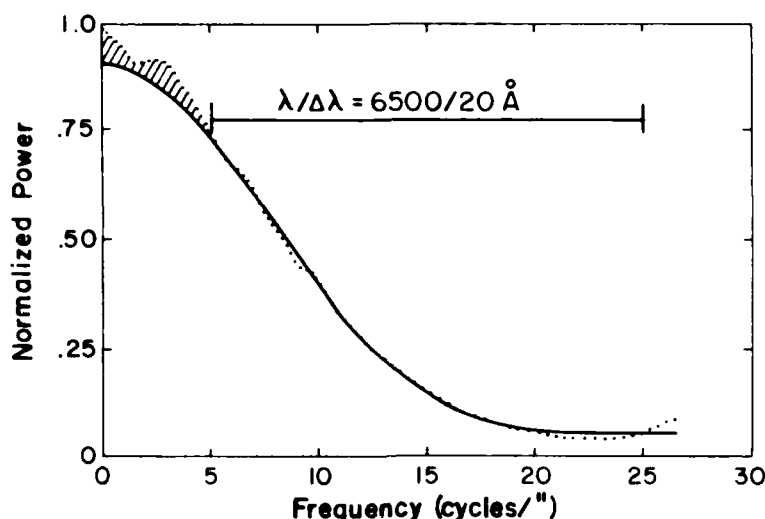


FIG. 2. Typical normalized radial averaged data and model PS. The dotted line is from data at $6500 \text{ Å} \pm 20 \text{ Å}$, and the solid line is for a best fit to the data of a selected model. The shaded region is due either to seeing calibration error or to large extended structures (or both). The horizontal bar shows the region used for model fitting.

IV discusses our efforts to understand these model-dependent discrepancies.

IV. INTERPRETATION OF RESULTS

We consistently use the notation R_m (D_m) to denote model-dependent estimates of the stellar radius (diameter). These estimates are model-dependent because α Ori is probably a more complex object than can be described by the simple model used. There is strong empirical evidence for model-inadequacy bias in the results obtained by both our modeling procedures.

Evidence from several other sources (e.g., Ricort *et al.* 1981, Roddier and Roddier 1983; Tsuji 1979, White 1980, and references therein) also suggests that α Ori is surrounded by a faint envelope detectable in optical bandpasses out to 5 stellar radii.

Least-squares fitting procedures minimize residuals by adjusting the available parameters. Fitting models with no parameters to describe such extensions will yield biased parameters.

The PS analysis showed the inability of models fitted to data at the 3.8 m resolution of the telescope to distinguish between a soft-edged, limb-darkened object and a hard-edged object of smaller radius. The PS model profile is a good fit to the data at radii corresponding to the PS fitting domain (indicated in Fig. 2), but it seriously overestimates the diameter of the object. Similarly, experiments in the image ACF domain emphasize the high-frequency response produced by the stellar core. Models of both, however, will be biased by additional signal at intermediate to lower image frequencies.

The series of models fit in the image ACF domain also

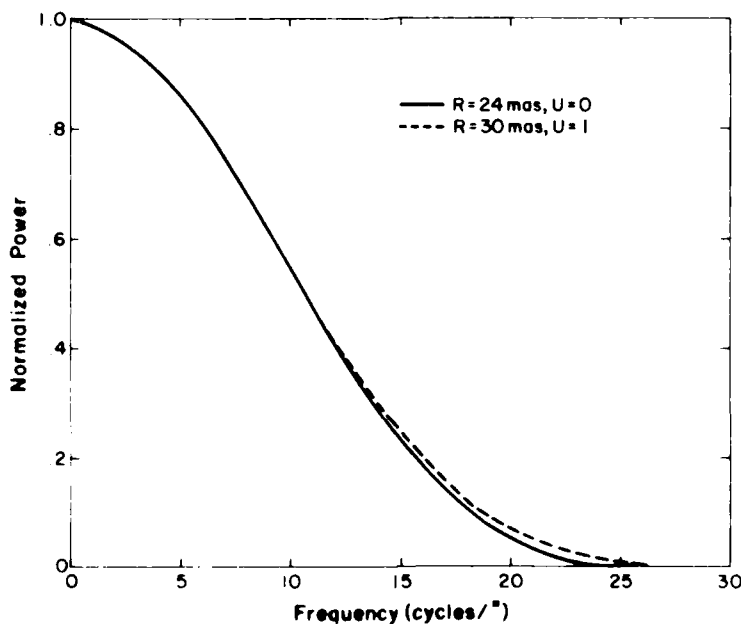


FIG. 3. Two typical model PSs. The solid line is for $R = 24 \text{ mas}$ and $U = 0$, and the dashed line is for 30 mas and $U = 1$.

TABLE 3
SUMMARY OF MODELS FITTED TO α ORIONIS IMAGE FLUORESCENCE

LIMB-DARKENING COEFFICIENT U	Wavelength (Å)						
	8542 ^a	8500 ^b	6563 ^c	6400	5500	5200	4100
Radius (mas)							
0.0	31.2 ± 0.7	28.9 ± 0.4	28.4 ± 0.2	26.6 ± 0.1	26.6 ± 0.1	26.6 ± 0.1	26.6 ± 0.1
0.1	31.5 ± 0.7	29.1 ± 0.4	28.8 ± 0.2	26.8 ± 0.1	27.2 ± 0.1	28.2 ± 0.2	28.2 ± 0.2
0.2	31.8 ± 0.7	29.4 ± 0.4	29.1 ± 0.2	27.2 ± 0.1	27.8 ± 0.1	29.2 ± 0.2	29.2 ± 0.2
0.3	32.1 ± 0.7	29.8 ± 0.4	29.4 ± 0.2	27.5 ± 0.1	27.9 ± 0.2	29.5 ± 0.2	29.5 ± 0.2
0.4	32.6 ± 0.7	30.2 ± 0.4	29.9 ± 0.2	27.9 ± 0.1	28.3 ± 0.2	29.8 ± 0.2	29.8 ± 0.2
0.5	33.3 ± 0.8	30.7 ± 0.4	30.5 ± 0.2	28.1 ± 0.1	28.8 ± 0.2	29.8 ± 0.2	29.8 ± 0.2
0.6	33.9 ± 0.8	31.5 ± 0.4	31.1 ± 0.2	29.1 ± 0.1	29.4 ± 0.2	29.8 ± 0.2	29.8 ± 0.2
0.7	34.7 ± 0.8	32.2 ± 0.4	32.0 ± 0.2	29.8 ± 0.1	29.2 ± 0.2	29.8 ± 0.2	29.8 ± 0.2
0.8	35.8 ± 0.8	33.2 ± 0.4	33.0 ± 0.2	30.7 ± 0.1	30.1 ± 0.2	29.8 ± 0.2	29.8 ± 0.2
0.9	37.2 ± 0.9	34.6 ± 0.5	34.4 ± 0.2	32.0 ± 0.1	32.4 ± 0.3	29.8 ± 0.2	29.8 ± 0.2
1.0	39.2 ± 0.9	36.4 ± 0.5	36.2 ± 0.2	33.7 ± 0.1	34.5 ± 0.3	29.8 ± 0.2	29.8 ± 0.2
Unresolved Power							
0.0	0.274 ± 0.008	0.201 ± 0.006	0.101 ± 0.003	0.064 ± 0.002	0.050 ± 0.001	0.040 ± 0.001	0.040 ± 0.001
Standard Error (rms) in the Fit							
0.0	0.103	0.050	0.042	0.017	0.011	0.008	0.008

^a Bandpass 3 Å.

^b Bandpass 100 Å.

Bandpass 20 Å.

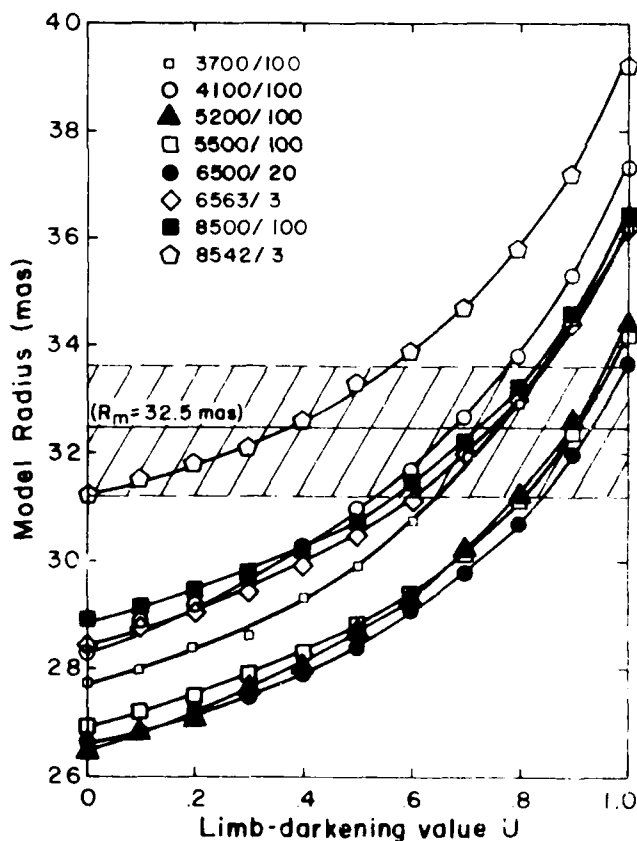


FIG. 4. Best-fit PS models vs. limb-darkening parameter U for each observing bandpass. The shaded region defines the range of model radii values, $R_m = 32.5 \pm 0.7$ mas, permitted by the sets of fits to the data. The uncertainty is that allowed by $0 < U < 1$.

showed bias effects. We were able to establish a "figure of bias" for the ACLE results which yields a more consistent result for the uniform disk stellar diameter. With ACLEs showed (1) soft edges (as compared to uniform disk profiles) and (2) a nonzero residual to rather large extents. The case for the 6563 20 Å bandpass, shown in Figure 5, is typical. These "extensions" (whether real or systematic, induce a bias to any value of D_* inferred by least-squares fits to such data. Since both effects cause the ACLE model fits to give overestimates for D_* , we constructed the "figure of bias" as $F = (B - 4)R_m$, where $B - 4$ is the relative magnitude of the positive extended residual and R_m is the radius of the background residual as indicated (highly statistically significant). (See Fig. 5). These experimental results are summarized in columns (3)–(5) of Table 1.

Regardless of whether this background is real or a seeing residual, it causes a bias in the estimate of D_* . A simple linear regression was used to calibrate the effect of F . This is equivalent to the assumption used to draw a circle in Figure 6, namely that the star has a single well-defined physical radius. The assumption of a fixed stellar radius is not unrealistic for this analysis, since scale heights, even for this supergiant, are expected to be small (~ 1 mas) compared to the precision of the measurements themselves. We expect the star disk to be the same size viewed through a green or a red filter.

A linear regression (slope and intercept) indicates that the figure of bias F varies directly with D_* and is zero at $D_* = 43.5$ mas. Using the results of this regression to predict the unbiased value for the stellar diameter D_* produces a single value, $D_* = 43.1 \pm 1.1$ mas, which is all the data for the precision of the individual measures. These unbiased estimates are given in column (6) of Table 1 and are plotted as the open circles in Figure 1.

The alternate assumption that the star disk can be represented by a fixed stellar radius is consistent with the same linear

TABLE 4
PS MODEL LIMB-DARKENING COEFFICIENTS OF α ORIONIS

R_m (mas)	WAVELENGTH (\AA)							
	8543 ^a	8500 ^b	6563 ^a	6500 ^c	5500 ^b	5200 ^b	4100 ^b	3700 ^b
Lower limit 31.2	0.00	0.56	0.61	0.84	0.81	0.80	0.53	0.6
Mean 32.5	0.38	0.73	0.74	0.93	0.90	0.89	0.68	0.7
Upper limit 33.7	0.55	0.84	0.86	1.00	0.98	0.96	0.80	0.8

^a Bandpass 3 \AA .

^b Bandpass 100 \AA .

^c Bandpass 20 \AA .

least-squares sense, diameter variations with a $\Delta D/\Delta\lambda = -6(\pm 1) \times 10^{-3}$ mas nm⁻¹ wavelength dependence.

Although empirical, our method for determining the bias in ACF diameter measures yields an estimate of the model-dependent bias determined from analysis of the data itself (by linear regression). It invokes no further physical models of the stellar structure. The linear regression is of course itself a model adding two further degrees of freedom in the interpretation of the data. The data statistics do not permit us to categorically assert that the stellar envelope extends to the large radii (to $R_{\text{sty}} = 0.72$) seen in some of the ACFs. These residuals may still be due to poor seeing calibrations. The fact that the residuals are always positive suggests a stellar effect. Furthermore, we conclude that the soft edges are real. This has been modeled, at least in first approximation, by the limb-darkening measures discussed above.

This begs the issue of bias in the limb-darkening measures. At the resolution of the 3.8 m aperture used, it is a subtle effect

at best. As shown in Figure 4, we do sense an edge-softening effect. Our values of U can be little more than qualitative indicators, but it is significant that they appear to vary in qualitative agreement with astrophysical predictions (e.g., Tsuji 1976). We believe the net effect of our ACF bias analysis is to rescale the values of the PS radius estimates (ordinate of Fig. 4), so that the line representing the common $R_m = 32.5$ mas falls at an unbiased value $R_* = 21$ mas, the physical radius of the star. This conjecture was tested by attempting other fits with successively higher low-frequency limits to the model-fitting range (shown in Fig. 2). This should have reduced the sensitivity of the model to low-frequency image extensions. As expected, the fits did yield smaller R_m values but could not be made to move them all the way to overlap the values obtained from the ACF fits. This inconclusive result is apparently a consequence of the inadequacy of a 3.8 m aperture for these measurements.

Most of the previous results, Table 2, lie above our smaller unbiased result. We suggest the reason is that most of those results are biased by the presence of a real, possibly time-variable, circumstellar shell and by wavelength-dependent limb-darkening. We believe that the scatter in the measures represents real attributes of the star, but that failure to adequately model them yields overestimates of the stellar diameter.

V. CONCLUSIONS

The scatter of past speckle interferometric angular diameter measures for α Ori appears to indicate that the models used to extract the results were inevitably inadequate to account for all the complexity of the star contained in the data. A simple stellar disk intensity profile, namely a limb-darkened disk with variable coefficients for different spectral features and with a single, physical radius, is an improved, but still biased, model of our data. When adjusted appropriately for the bias induced by circumstellar features (real or seeing residual), the scatter in our results is accommodated. This leads to a reasonable explanation for the wide scatter in other observed data as well. Our measured angular diameter, $D_* = 42.1 \pm 1.1$ mas, independent of wavelength, is consistent with all previous measurements if the measures of previous workers are subject to limb-darkening effects and similar model-dependent biases induced by a possibly variable (Hebden *et al.* 1986) extended stellar envelope.

There is a good deal of evidence that the apparent extensions, between 1 and $5R_*$, which bias simple speckle interferometry diameter measures, are physical attributes of α Ori and not systematics of the speckle interferometric process, and further that they are wavelength-dependent. Roddier and Roddier (1983, 1985), for example, find a 37 mas angular diam-

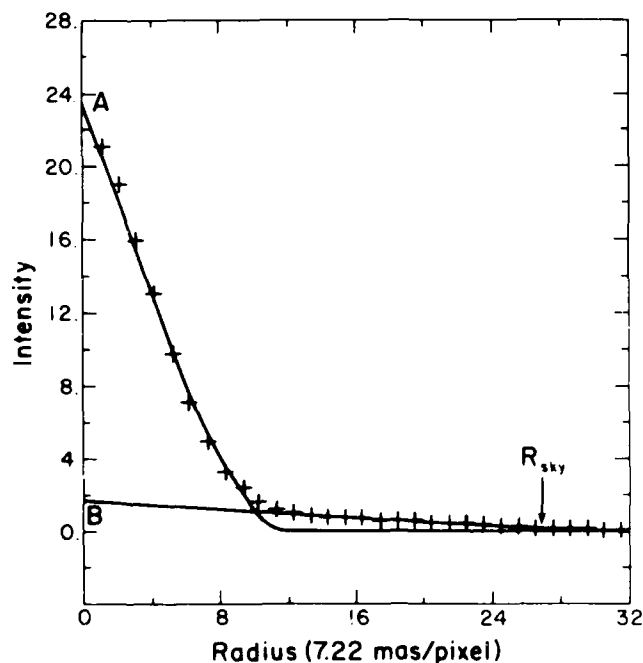


FIG. 5—The ACF corresponding to the same 26500 20 \AA data as in Fig. 2 (pluses). A uniform disk model fitted to the data shows large, positive residuals beyond the apparent stellar limb. A straight line fit through the most poorly modeled data points, as shown, was used to estimate B and R_{sty} (Table 1, cols. [3]–[4]) for computing the "figure of bias" (Table 1, col. [5]), as discussed in the text.

eter stellar disk embedded in an envelope of 80 mas diameter at $\lambda = 5348 \text{ \AA}$, consistent with earlier measures by Ricort *et al.* (1981). Karovska *et al.* (1986) suggest the further complication of faint companions.

It is not clear whether the Roddiers' $D_{\text{eff}} = 37 \text{ mas}$ result includes limb-darkening effects; if it does not, then that measurement is consistent with our limb-darkened measures. Theoretical predictions (e.g., Hartmann and Avrett 1984) suggest extended structures. White (1980) summarized the wavelength dependence of various measures of α Ori, obtained from a number of techniques, indicating evidence for larger diameters at shorter wavelengths, qualitatively similar to our ACF measures shown in Table 1 and Figure 1. White (1980) also notes that circumstellar emissions would bias occultation diameters to larger values, a suggestion similar to the one we have invoked here. Based on estimates of the effects of such bias, White concludes that the best estimate for the limb-darkened photospheric diameter is 43 mas, a value quite consistent with our 1981 data by this analysis.

Our measured limb-darkening values are also consistent with those predicted from model atmosphere calculations. Refined model atmosphere calculations of the particular limb-darkening coefficients for our observed spectral bands are required, in order to evaluate more precisely the exact radius of α Ori. If speckle interferometry is to be a direct probe of the atmosphere of resolvable late-type supergiant stars, very careful choice of spectral regions for observation, as well as more sophisticated models for the interpretation of measurements, are required.

The effective temperature of α Ori remains an open question (see review in Tsuji 1978). Tsuji's limb-darkened angular diameter of $41 \pm 3 \text{ mas}$, corresponding to $3900 \pm 150 \text{ K}$, spans both our observed 42 mas value and the 43 mas inferred by White

(1980). A lower effective temperature favors formation of silicate dust in its circumstellar envelope, which has been observed in the past (see, e.g., Woolf and Ney 1969).

The further study of theoretical model atmospheres of late-type supergiant stars, their circumstellar envelopes, and related mass loss mechanisms will benefit greatly from future higher resolution measures obtainable (Hege *et al.* 1985) using the MMT. Computed profiles showing the added advantage due to the higher MMT resolution are given in Figure 6. We anticipate that details of temperature calculations can be refined using better limb-darkening measures.

There remains the possibility not only that the measurement of the radius of α Ori by speckle interferometry is subject to methodological bias, but also that the stellar diameter may indeed be variable with time. Because of the uncertainty in what was actually measured, plotting diameters determined by speckle interferometry as a function of the phase of its 5.8 yr period (as in White 1980) is inconclusive. Variability of diameter is certainly an interesting possibility and deserves careful monitoring in a systematic and unbiased way. White (1980) suggests diameter variations on the order of $\pm 15\%$, based strongly on a review therein of Pease's earlier (1931) Michelson's interferometer observations.

It appears that there are features on the surface of α Ori, which remain unresolved at the diffraction limit of even the largest telescopes (Goldberg *et al.* 1981; Hebden *et al.* 1986). If these features are variable, this would have also biased Pease's fringe visibility estimates of diameter to systematically lower values, as the high spatial frequency component (as seen, for example, in Fig. 1) would cause the fringe visibility to persist to larger shears in proportion to its relative energy. Thus the question becomes, Is α Ori a diameter variable as well as a surface activity variable?

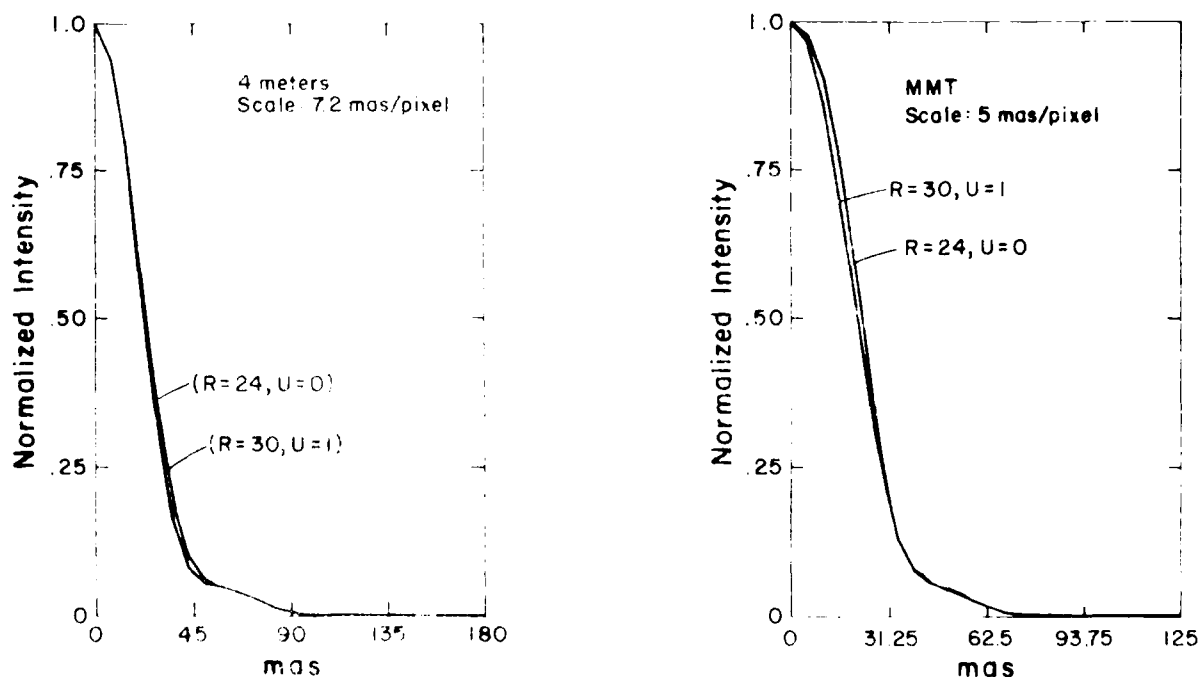


Fig. 6. Comparison of limb-darkening profiles for α Ori using the 38 m KPNO aperture (left) and 6.8 m MMT aperture (right). Results for $U = 0$ and $U = 1$ are shown; the curves are calculated using the limb-darkening spread function. Differences in profile shape due to limb darkening will be more readily detectable using the MMT.

All this argues the need for a systematic set of measures, done in a self-consistent way, with the highest resolution possible, which is currently that obtainable with the MMT.

This work was supported in part by the National Science Foundation (grants AST-8113212 and AST-8201092 and access to the CDC Cyber 720/170 at NOAO) and the US Air Force (AFGL contract F19628-82-K-0025 and AFOSR grant

82-0020). We also acknowledge the contributions of A. Szumilo for support and revisions to the data reduction software, and, together with S. Shaklan, for part of the data digitization. We particularly thank the NOAO staff for help with these extensive data reductions, and the support staff at Kitt Peak who made the installation and use of our visitor instrument at the 4 m telescope a successful delight. We also thank Dr. N. J. Woolf for many interesting and helpful discussions and suggestions.

REFERENCES

- Balega, Y., Blazit, A., Bonneau, D., Koechlin, L., Foy, R., and Labeyrie, A. 1982, *Astr. Ap.*, **115**, 253.
 Bonneau, D., and Lebeyrie, A. 1973, *Ap. J. (Letters)*, **181**, L1.
 Christou, J. C., Cheng, A. Y. S., Hege, E. K., and Roddier, C. 1985, *A.J.*, **90**, 2644.
 Currie, D. G., Knapp, S. L., and Liewer, K. M. 1974, *Ap. J.*, **187**, 131.
 Gezari, D. Y., Labeyrie, A., and Stachnik, R. V. 1972, *Ap. J. (Letters)*, **173**, L1.
 Goldberg, L., Hege, E. K., Hubbard, E. N., Strittmatter, P. A., and Cocke, W. J. 1981, in *Second Cambridge Workshop on Cool Stars, Stellar Systems, and the Sun*, ed. M. S. Giampapa and L. Golub (*SAO Spec. Rept.*, No. 392), Vol. 1, p. 131.
 Hartmann, L., and Avrett, E. H. 1984, *Ap. J.*, **284**, 238.
 Hebdén, J. C., Christou, J. C., Cheng, A. Y. S., Hege, E. K., Beckers, J. M., and Murphy, H. P. 1986, *Ap. J.*, **309**, 745.
 Hege, E. K., Beckers, J. M., Strittmatter, P. A., and McCarthy, P. W. 1985, *Appl. Optics*, **24**, 2565.
 Hege, E. K., Hubbard, E. N., Strittmatter, P. A., and Cocke, W. J. 1982, *Optica Acta*, **29**, 701.
 Jacoby, G. H., Hunter, D. A., and Christian, C. A. 1984, *Ap. J. Suppl.*, **65**, 257.
 Jeffreys, W. H. 1980, *A.J.*, **85**, 177.
 ———, 1981, *A.J.*, **86**, 149.
 Karovska, M., Nisenson, P., Noyes, P., and Stachnik, R. 1986, in *Lecture Notes in Physics*, Vol. 193, *Cool Stars, Stellar Systems, and the Sun* (Proc. 4th Cambridge Workshop, Santa Fe, 1985 October), ed. M. Zeilik and D. M. Gibson (Berlin Heidelberg: Springer-Verlag), in press.
 Lynds, C. R., Worden, S. P., and Harvey, J. W. 1976, *Ap. J.*, **207**, 174.
 McDonnell, M. J., and Bates, R. H. T. 1976, *Ap. J.*, **208**, 443.
 Papaliolios, C., Nisenson, P., and Ebstein, S. 1985, *Appl. Optics*, **24**, 287.
 Pease, F. G. 1931, *Ergebnisse Exacter Naturwissenschaft*, **10**, 84.
 Ricort, G., Aime, C., Vernin, J., and Kadiri, S. 1981, *Astr. Ap.*, **99**, 232.
 Roddier, C., and Roddier, F. 1983, *Ap. J. (Letters)*, **270**, L23.
 Roddier, F., and Roddier, C. 1985, *Ap. J. (Letters)*, **295**, L21.
 Tsuji, T. 1976, *Pub. Astr. Soc. Japan*, **28**, 567.
 ———, 1978, *Pub. Astr. Soc. Japan*, **30**, 435.
 ———, 1979, *Pub. Astr. Soc. Japan*, **31**, 43.
 Welter, G. L., and Worden, S. P. 1980, *Ap. J.*, **242**, 673.
 White, N. M. 1980, *Ap. J.*, **242**, 646.
 Woolf, N. J., and Ney, E. D. 1959, *Ap. J. (Letters)*, **155**, L181.

A. Y. S. CHENG, W. J. COCKE, E. K. HEGE, and P. A. STRITTMATTER: Steward Observatory, University of Arizona, Tucson, AZ 85721

L. GOLDBERG: Kitt Peak National Observatory, Tucson, AZ 85719

E. N. HUBBARD: Titan Systems, 9191 Center Drive, San Diego, CA 92122

SEEING CALIBRATION OF OPTICAL ASTRONOMICAL SPECKLE INTERFEROMETRIC DATA

JULIAN C. CHRISTOU,^{a)} ANDREW Y. S. CHENG, E. KEITH HEGE^{b)}

Steward Observatory, University of Arizona, Tucson, Arizona 85721

CLAUDE RODDIER^{c)}

Optical Sciences Center, Tucson, Arizona 85726

Received 31 May 1985

ABSTRACT

In this paper we show the effect of different seeing conditions, as parametrized by the atmospheric coherence scale r_0 , upon standard Labeyrie (1970) analysis for independent observations of both a resolved object and its point-source calibrator. Atmosphere-dependent effects are shown by using both models and data. We show how to sort the data into like-seeing bins in order to produce a calibrated-image power-spectrum estimate. We also justify using a stronger weighting of intermediate spatial frequencies in the image power-spectrum estimator when fitting physical parameters constrained by image models to characterize the object. The use of data-editing techniques to eliminate bad specklegrams, thus improving the image power-spectrum estimate, is also discussed.

I. INTRODUCTION

An intensified video camera with digital readout has been used at Steward Observatory since 1979 (Hubbard *et al.* 1979) to obtain high-angular-resolution information about a number of astronomical objects (Hege *et al.* 1981, 1982a,b; Drummond *et al.* 1985a,b; Cheng *et al.* 1985; Hege *et al.* 1985). The standard reduction process for speckle interferometry (SI) is that first proposed by Labeyrie (1970) and involves computing the *unbiased* power spectrum for data sets of both a resolved object and an unresolved point source. A seeing-compensated image power-spectrum estimator of the resolved object is obtained by taking the quotient of the two. A full description of this process is given by Hege *et al.* (1982a) and is further discussed in Sec. II.

If the time-dependent statistics of the atmosphere are different between the resolved object and the unresolved object, then this power-spectrum estimator quotient is not properly calibrated for the variable seeing effects. Because of this, an image power-spectrum estimator, computed as a simple quotient as above, will contain spurious power, which can lead to misinterpretation of the final results. This problem has been previously discussed by Aime *et al.* (1978) for application to speckle measurements of the solar granulation and by Mariotti *et al.* (1983) for application to infrared speckle imaging. We have studied this problem using both normal and log-normal models for the statistics of the complex wave front after passing through the turbulent atmosphere. A procedure has been implemented which (i) locates and omits "bad" specklegrams from a data set and (ii) sorts the good specklegrams into bins of like seeing as determined from the second-order moment of the speckle cloud.

The final power spectrum estimators are then computed by using data from the same seeing bins for each object. The results produced for the resolved red supergiant Alpha Orionis by this improvement to the reduction procedure are

reported in another paper (Cheng *et al.* 1985), whereas this paper concentrates upon the theory and technique of seeing calibration.

II. EXPERIMENTAL DETERMINATION OF THE OBJECT POWER SPECTRUM

An individual specklegram is conventionally represented as a convolution of the object distribution $O(r)$ with the instantaneous point-spread function of the telescope-atmosphere combination $s(r)$, i.e.,

$$i(r) = o(r) * s(r), \quad (1)$$

where $*$ denotes convolution and r implies a two-dimensional spatial domain. The time-averaged power spectrum can be written as

$$PS = \langle |I(f)|^2 \rangle = |O(f)|^2 \langle |S(f)|^2 \rangle, \quad (2)$$

where $I(f)$ is the Fourier transform of $i(r)$, etc. in the corresponding two-dimensional spatial frequency domain f . In Labeyrie's theory of SI (Labeyrie 1970), the measured power spectrum for the resolved object is deconvolved by dividing it by the power spectrum of an unresolved object taken under similar seeing conditions as implied by Roddier (1981). The power spectrum of the unresolved object should give the speckle transfer function (STF), $\langle |S(f)|^2 \rangle = PS_\delta$, so that the desired object power spectrum can be recovered by the following relation

$$|O(f)|^2 = PS/PS_\delta. \quad (3)$$

The measured power spectra in equation (2) also include noise-bias terms due to photon statistics, which must be removed before the quotient (3) is computed (Hege *et al.* 1982a).

III. MODELING THE SPECKLE TRANSFER FUNCTION

Equation (2) represents the time-averaged power spectrum of a set of specklegrams as the product of the object power spectrum with the time-averaged STF given also by equation (2) for an unresolved (point) source. The quality of the measurement of the STF determines the ability of SI to obtain diffraction-limited information in the presence of the turbulent atmosphere. This function contains terms representing both the telescope and atmosphere transfer functions and has been well studied, with excellent descriptions of its

^{a)} Visiting Astronomer from Department of Astronomy, New Mexico State University, Las Cruces, NM 88003.

^{b)} Visiting Astronomer, Kitt Peak National Observatory, National Optical Astronomy Observatories, operated by the Association of Universities for Research in Astronomy, Inc., under contract to the National Science Foundation.

^{c)} On leave from UER de Mathematiques, Universite de Provence, Marseille, France; also visiting Astronomer at NOAO-ADP Division.

derivation given by Korff (1973), Fried (1979), and Roddier (1981). They show that the STF has no simple analytical expression when log-normal statistics are used, but that it can be represented approximately by a two-component model for the normal statistics case. The first component is for spatial frequencies up to the atmospheric cutoff $f_0 = r_0/\lambda$ and the second for frequencies lying between f_0 and the telescope diffraction limit $f_c = D/\lambda$, where λ is the wavelength of observation, r_0 is the coherence length of the atmosphere as defined by Fried (1966), and D is the diameter of the telescope aperture. Fried (1979) has shown that this two-component model is a valid approximation, especially for large values of the ratio of D/r_0 (notably large telescopes or poor seeing).

The low-frequency ($0 < f < f_0$) component is approximated by the transfer function of a long exposure with the wave front tilt removed, as for a rapid guided image, i.e.,

$$\langle |S(f)|^2 \rangle_{LF} = |T(f)|^2 \exp \{ -6.88(\lambda f/r_0)^{5/3} [1 - (\lambda f/D)^{1/3}] \}, \quad (4)$$

where $T(f)$ is the telescope transfer function given by the autocorrelation of the aperture. The high-frequency ($f_0 < f < f_c$) component is approximated by the relation

$$\langle |S(f)|^2 \rangle_{HF} = 0.435(r_0/D)^2 T(f). \quad (5)$$

The above approximations describe a STF dependent upon three parameters. Two of these, D and λ , can be controlled by the observer, but the third, r_0 , is determined from the random nature of the seeing. It is therefore important to consider the effect of varying r_0 upon the STF. Figure 1(a) shows the STF, as computed using equations (4) and (5), for a range of values of r_0 from 10 to 35 cm for a telescope of aperture $D = 4$ m and an observing bandpass centered at $\lambda = 650$ nm. Figure 1(b) shows the same thing, but computed-

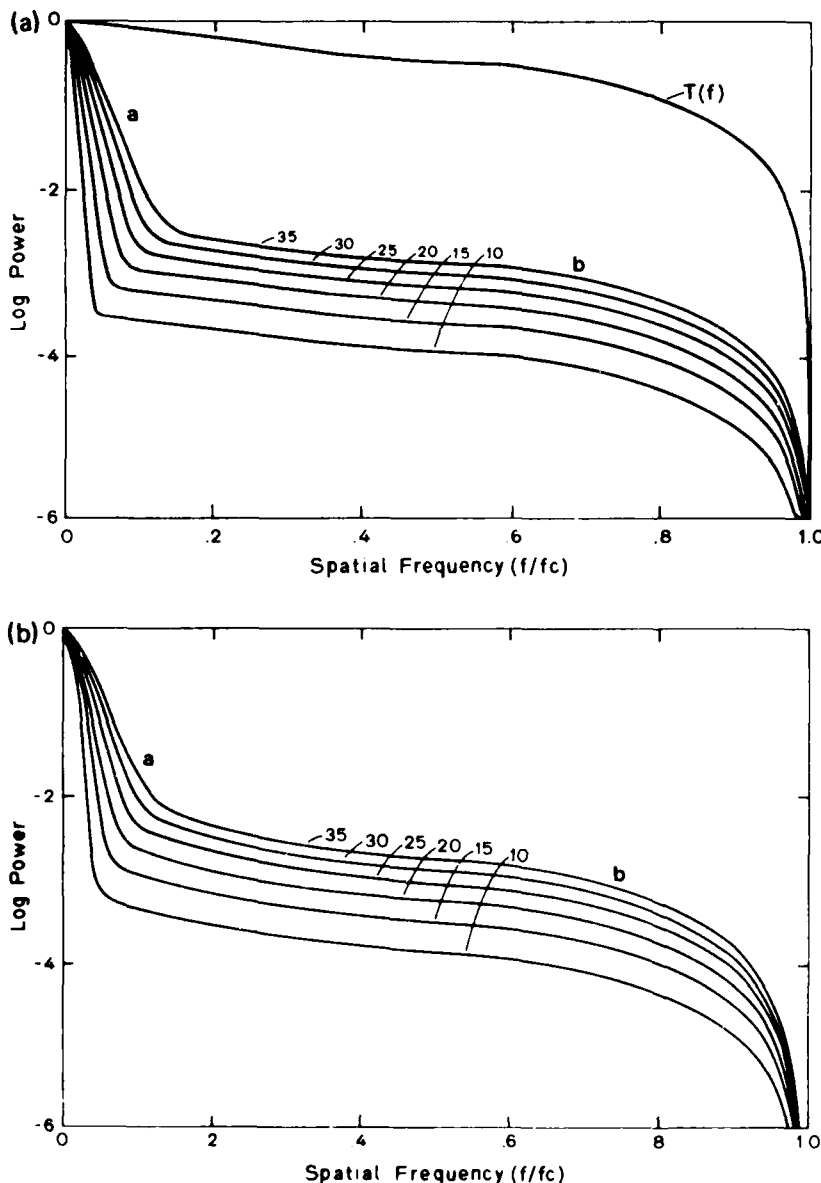


FIG. 1. (a) Models of the speckle transfer function using the two components as described in the text. "a" is the seeing-dominated component and "b" is the high-frequency term, which allows information recovery to the diffraction limit. The parameters were chosen for an obscured aperture corresponding to the 4 m and for r_0 equal to 10, 15, 20, 25, 30, and 35 cm. The telescope transfer function $T(f)$ is also shown for $D = 3.8$ m with an obscuration ratio of 0.3. (b) STF models for the same range of r_0 with the log-normal statistical model.

ed using the log-normal model. It can be seen in both sets of plots that as r_o decreases in value then both the width of the low-frequency component and the amplitude of the high-frequency component decrease. The telescope transfer function $T(f)$ is also shown. Comparison of Figs. 1(a) and 1(b) shows that as r_o increases the difference between the two models also increases, especially over the intermediate frequency range. However, the normal model is shown to be a good approximation when the ratio D/r_o is large.

The object power-spectrum estimator (3) can be rewritten as

$$PS_o = |O(f)|^2 PS'_o / PS_\delta, \quad (6)$$

where PS'_o represents the STF for the object data set and PS_δ is the STF of the point source. If the seeing is the same for both objects, then $PS'_o = PS_\delta$ and PS_o is in fact a good estimate of the object power spectrum. However, for different seeing conditions the power spectrum will be contaminated by the term PS'_o / PS_δ . In order to study the effect of this contamination we computed quotients of the STF at different values of r_o . This effect is seen in Fig. 2, which shows the quotients for different values of r_o relative to two different "worst cases" of 10 cm [Fig. 2(a)] and 39 cm [Fig. 2(b)], respectively, as computed using the normal model. For the latter case when $D/r_o \sim 10$ the quotients are also shown computed for the log-normal model [Fig. 2(c)]. Figures 2(b) and 2(c) agree very well at spatial frequencies $> 0.3f_c$. At lower spatial frequencies, however, the log-normal model has a greater range over which the differences in seeing affect the slope of the quotient. The frequency of greatest difference is at a lower frequency in the log-normal model than in the other. These figures demonstrate the seeing statistics dominated domain at the lowest spatial frequencies ($f < f_o$) modeled by (4). Over the seeing-dominated region of the quotient there is a sharp increase in excess power as the seeing degrades. For higher spatial frequencies, where the telescope transfer function dominates, the excess power is frequency independent and goes as the square of the ratio of the two different r_o 's. The greater the relative difference in r_o , the more pronounced are those effects and the more sensitive the quotient becomes to the differences in seeing. It can also be seen that the worse the seeing the larger the quotient becomes for the same absolute difference in r_o , although the width of the low-frequency spike is reduced commensurate with the larger seeing disk. The effect of an inadequate seeing calibration is therefore to multiply the object power spectrum by a function resembling those shown in the two panels of Fig. 2. For the case of the point source having poorer seeing, the energy at frequencies in the seeing domain will be increased and significant spurious unresolved energy will be introduced. A correct deconvolution therefore requires that observations of the resolved and unresolved objects with similar seeing statistics be accumulated before attempting the calibration given by (3).

IV. DATA SELECTION

The arguments of the preceding section imply a requirement that the data be binned according to the seeing. Besides being affected by the seeing, the specklegrams are also contaminated by a variety of processes after detection, due to the nature of the detector and signal-processing hardware. We have implemented a data-editing algorithm which inspects every specklegram to identify and exclude any bad frames, including those (i) where the speckles are saturated such that

they become "clipped," (ii) which contain anomalously low signal due to a shutter malfunction or to passing clouds and (iii) which contain only part of the speckle cloud due to guiding errors within the detector field of view (typically 0.5–5 arcsec).

For high-precision work, we have also found it useful to correct for calibratable systematic detector-induced artifacts including (i) geometric (pincushion) distortion, (ii) detector vignetting and flatfield response, and (iii) signal-dependent video pedestal ("black level") due to the video-cassette recorder response characteristics. When seeing conditions and choice of detector image scales are such that the specklegram at the instrumental focal plane is larger than the detector field of view, additional apodizing to force the data smoothly and continuously to zero at its boundaries is also necessary.

Our specklegrams are digitized into 128×128 arrays of 8-bit pixels. The saturated specklegrams are located as those which have the greatest number of pixels with values > 250 . The limit is chosen by visual inspection of a sample of the specklegrams. The low-power frames are simply found by summing all the power within a specklegram and comparing to some threshold. The poorly guided frames are located by computing the first-order moment of the specklegram to obtain the frame centroid. If this lies outside a certain range, then the frame is omitted.

The second-order moments about the centroid of the well-guided specklegrams are also computed, giving the dispersion of power within the frame, and thus the size of the speckle cloud. This size parameter is then used to sort the data according to the instantaneous seeing. In order to relate this size parameter σ to an estimate of the seeing as defined by the Fried parameter r_o , we assume the speckle cloud to obey (in first approximation) a Gaussian distribution, i.e.,

$$i(r) = A \exp[-(r^2/2\sigma^2)]. \quad (7)$$

The Fourier transform of (7) is

$$I(f) = \sqrt{2\pi} A \exp[-2(\sigma\pi f)^2], \quad (8)$$

where the exponent can be compared to the form $\exp[-(f/f_1)^2]$ such that

$$f_1 = 1/\sqrt{2}\pi\sigma. \quad (9)$$

Seeing theory (Woollf 1982) predicts that the seeing disk has no analytic expression but is the *Fourier transform* of a function of the form $\exp[-(f/f_1)^{5/3}]$ [cf. equation (4)]. The difference between this and a Gaussian is nonnegligible but small, with the Gaussian having greater amplitude at low frequencies and falling far below at higher frequencies. The rms difference between the two functions is approximately 2% of the peak amplitude. Thus the Gaussian represents a good first-order approximation. Since $f_1 = r_o/2.1\lambda$ (Woollf 1982) we obtain the r_o estimator

$$r_o \sim \lambda/2\sigma. \quad (10)$$

Theoretically, it is not strictly possible to interpret the measurement of r_o as being an estimate of r_o because the latter is defined only for a long-exposure image. Equation (10) is, however, an expedient estimate of the equivalent aperture size for which the speckle cloud represents the instantaneous angular resolution of the atmosphere.

V. EXPERIMENTS

We have analyzed specklegrams for the resolved supergiant Alpha Orionis (object) and an unresolved star Gamma

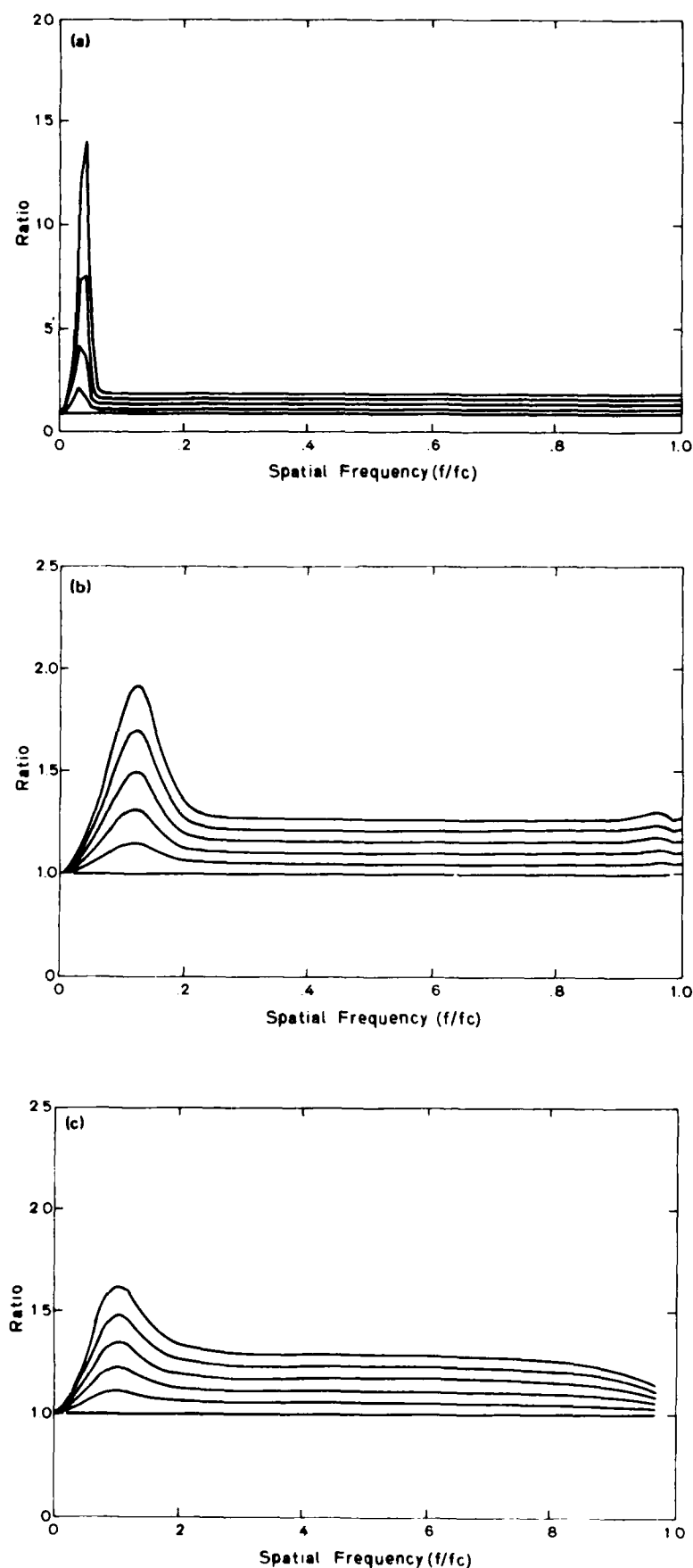


FIG. 2. Quotients of the speckle transfer function for different values of r_o chosen so that the denominator has poorer seeing. (a) (using the normal model) represents quotients for r_o values of 14, 13, 12, 11, and 10 cm with the STF at $r_o = 10$ cm, (b) represents the quotients at $r_o = 44, 43, 42, 41, 40$, and 39 cm with $r_o = 39$ cm for the normal model, and (c) same as (b) but for the log-normal model.

Orionis (comparison) taken 2 and 3 February 1981 with the 4 m Mayall telescope (with an effective aperture of 3.8 m) operated at Kitt Peak National Observatory, National Optical Astronomy Observatories (NOAO). Observations at a number of different wavelengths with integration times of approximately 10 min for the program object and 5 min for the comparison were made. The data were acquired with the Steward Observatory speckle camera and recorded onto 3/4" U-Matic videotape using the system described by Hege *et al.* (1982a). The video specklegrams were digitized later using the Grinnell and EDS Point 4 systems at Steward Observatory and the data reduction was accomplished using the Cyber 720/172 at NOAO.

Before the power spectra were computed we ran the data through a selection algorithm to flag the good and bad frames and to tag the good ones according to the seeing estimate r_s . We found that the selection algorithm could throw out as much as 70% of the data, mostly because of saturated speckles (there was considerable variable high cirrus), indicating the need for careful monitoring of the detector gain while observations are in progress. Seeing bins of width $r_s = 1.5$ cm were chosen.

The power-spectrum reduction routines then computed average power spectra for the data in each of the seeing bins. The interpretation and analysis of this successful reduction of the Alpha Orionis power spectra, yielding the first ever set of stellar limb-darkening measures, is discussed by Cheng *et al.* (1985).

The mean values of the seeing estimates for three data sets of Alpha and Gamma Orionis are presented in Table I. This also gives the mean measurements of the speckle cloud size indicating the spectacular subarcsecond seeing for this observing run. (It *can* happen at Kitt Peak). The seeing estimates r_s are also shown corrected for zenith angle z and computed for the standard wavelength of 500 nm using the relation

$$r_o \approx \lambda^{6/5} \cos^{3/5} z. \quad (11)$$

Figure 3 shows histograms for the distribution of the instantaneous seeing estimates r_s for all six data sets. For the 650 nm data set the seeing distribution for the two is very similar, with mean values of approximately 42 cm for each. The 854.2 nm data set, however, represents the other extreme, where the tails of the two distributions barely overlap. At 656.3 nm there is more of an overlap but the mean of the two distributions are separated by more than 4 cm. Based on the model calculations, these plots manifestly demonstrate the need for seeing-dependent calibrations.

TABLE I. Measured seeing parameters

Object	Wavelength (nm)	Speckle cloud size (2 σ in arc sec)	Seeing parameters (cm)		Zenith angle (z°)
			r_s	500 nm, r_o	
Gamma Orionis	650	0.17	42.8	41	31
	656.3	0.13	33.0	27.8	34
	854.2	0.43	43.7	14.5	34
Alpha Orionis	650	0.17	43.0	41.5	37
	656.3	0.16	37.5	30.0	35
	854.3	0.46	46.0	18.1	26

The shapes of these histograms differ somewhat from each other, but all appear superficially to resemble a normal distribution. However, it is important to note that both tails of the distribution have been clipped due to the data-selection algorithm. The exclusion of the saturated data sets affects the high r_s tail because for good seeing there is a greater average power per speckle and therefore a greater probability of saturation. The low r_s tail is effected by the exclusion of specklegrams whose effective width was equivalent to the frame size, thus making it difficult to obtain an estimate of r_s .

The data presented here were not taken with the usual obvious observing disciplines and techniques which the models imply. This in part explains the differences in the seeing distribution between Alpha and Gamma Orionis. The objects are not close in the sky and no attempt was made to chop back and forth between them to minimize the differences of the seeing statistics.

We have since begun an observing technique similar to that used for photometry. Two comparisons are observed bracketing the program object, and for bright objects the integration times are kept short (≈ 2 min), whereas they are longer for fainter objects (≈ 10 min) in order to increase the photon SNR. This allows for a greater probability of similar seeing, but r_s has been observed to vary substantially within a 5–10 min interval. Thus the specific observing program must optimize the competing opposite tendencies, a not unusual physical circumstance.

Figure 4 illustrates the nature of such variable seeing. This shows the variation of r_s , as estimated for 1 s data bins, as a function of time. The data set was of one of the components of ϵ^2 Lyrae taken with the Steward Observatory 2.3 m at Kitt Peak. The seeing estimate varies from ~ 11 to ~ 17 cm with a ~ 14 cm mean value. There is ~ 90 s period in the variability of the seeing, indicating that even with such short integration times it would be possible to have quite different mean seeing values. Hence there is still a need for the seeing calibration of the speckle data.

The effects of seeing stability have not yet been thoroughly investigated, and the statistics of the variation of r_s as a function of time, as well as the effects of atmosphere correlation time variability, are beyond the scope of this paper, although they are currently under investigation.

The curves presented in Fig. 2 show the model-predicted appearances of the SFF quotients at different values of r_o . Figure 5 shows observations of the same effects using the data for Gamma Orionis at $\lambda = 650$ nm. The quotients are computed with respect to the worst seeing (smallest r_s) case. Qualitatively, the models (Fig. 2) and the data are very similar, showing two components, a constant bias at high spatial frequencies, and a sharp excess in the seeing-dominated domain. The quantitative differences can be explained as being due in part to values of r_s not having been properly calibrated to r_o and also to errors caused by the fitting and removal of the photon-noise bias and detector transfer function. The curve for $r_s = 39$ cm was computed by splitting the data set into two halves and taking the quotient of the two debiased power spectra. This gives a measure of the inherent noise in these quotients. The amplitudes of the low-frequency spikes of the seeing-dominated component are similar; however, the models predict a greater discrepancy than observed for the high-frequency component. The qualitative behavior of the curves is the same in that the closer the two values of r_s the nearer unity is the frequency-independent component

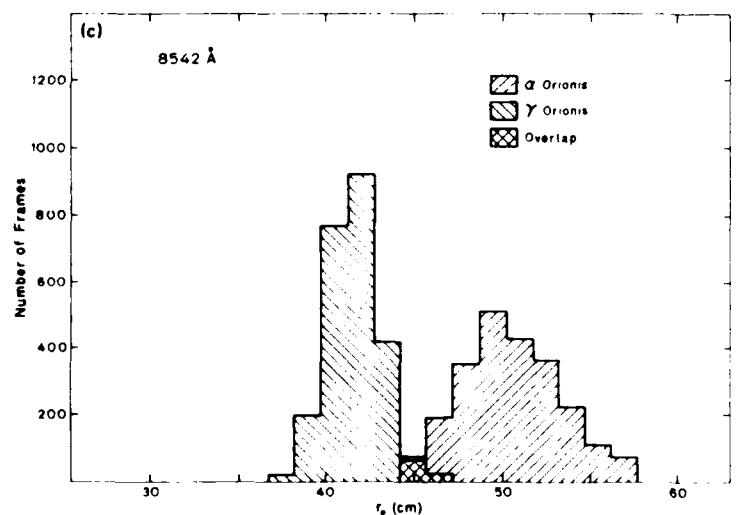
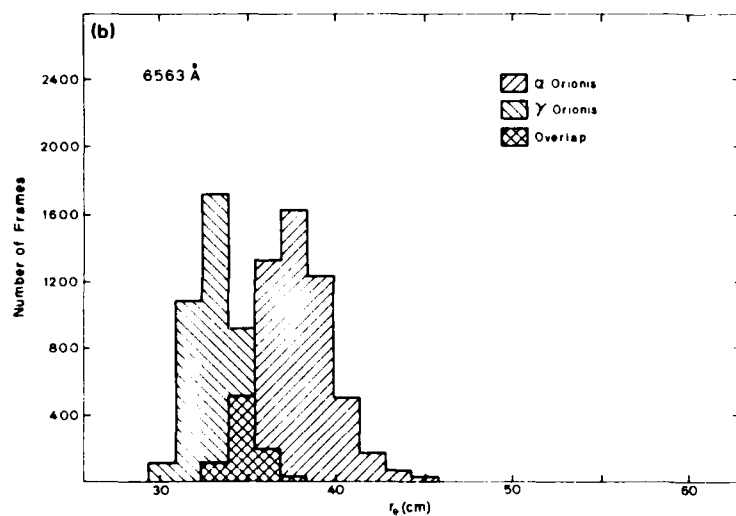
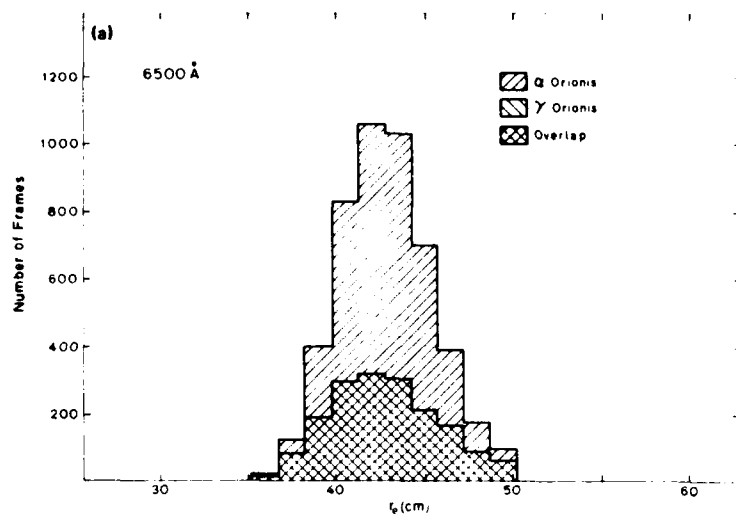


FIG. 3. Histograms of the estimate of the seeing r_s for three different data sets of Alpha and Gamma Orionis. (a) is at 650 nm, (b) is at 656.3 nm, and (c) is at 854.2 nm.

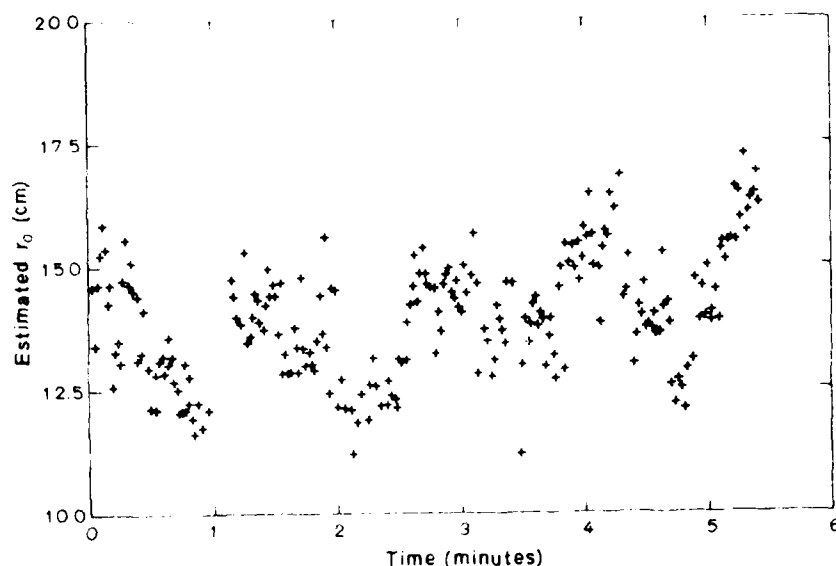


FIG. 4. Variation of r_o for 1 s bins as function of time showing periodic variability of the seeing.

($f_o < f < f_c$). For frequencies below but near f_c , the effects of signal statistics and small number divisions dominate.

Because of the binning of the power spectra, the number of frames in each bin is less than the total, thus decreasing the apparent signal-to-noise ratio (SNR) for each of the binned power spectra compared to the usual ensemble summed power spectrum, especially at the tail ends of the distribution of r_o . The number of speckles in a speckle cloud depends upon the ratio $(D/r_o)^2$. For good seeing (large r_o) there are fewer speckles with more power per speckle than for poorer seeing. Thus the SNR per specklegram is greater for the better seeing. The curves of the STF in Fig. 1 support this: the higher frequencies carry relatively greater power for larger r_o . However, in the data set there are only a few specklegrams with the very best seeing. Thus the data from the two tails of the seeing distribution should not be weighted equally in combining the bin-calibrated power-spectrum estimators. Of course, the SNR of the final power spectrum is deter-

mined by the number of specklegrams in each of the corresponding bins for the object and the point source. In practice, each of the bins yields an independent reduction for the object power spectrum and the final power spectrum will be a weighted average with the weighting proportional to the number of observations in each bin and proportional to r_o^2 corresponding to the bin. The first weight is suggested by Poisson statistics (assuming the same number of photons in each observation) and the second by the seeing model.

VI. CONCLUSIONS

We have presented models and data to show the importance of a detailed seeing calibration of speckle data sets reduced by the standard SI power-spectrum analysis. Both the models and the data show the same effect: that for the case of poor or no calibration the resultant object power spectrum will be contaminated in different, and unpredicta-

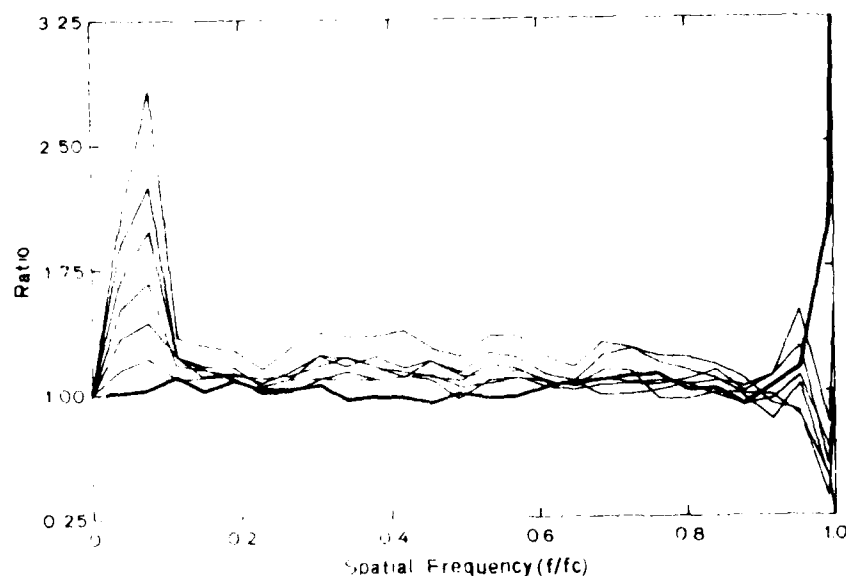


FIG. 5. Measured quotients of the speckle transfer function for Gamma Orionis at 650 nm. Note that the SNR is given by splitting bin 1 into two parts and taking the quotient. Because the SNR is fairly small (≈ 8), especially at the highest frequencies, the quotients overlap, making it difficult to distinguish them from each other. The bold line is the ratio of the two halves of the $r_o = 39$ cm data set.

ble, ways at the low frequencies ($0 < f < f_c$) and at the highest frequencies ($f < f_c$). We suggest that for all such analyses the possible differences in seeing between the object and the point source must be taken into account. In this, we support the conclusions of Mariotti *et al.* (1983), who considered similar problems for infrared speckle data.

It is reassuring, however, for the work reported in Drummond *et al.* (1985a,b) and Cheng *et al.* (1985) that this same model analysis predicts that the shape of such a power-spectrum estimate, if not its frequency-independent bias, is largely unaffected by these seeing effects. In these reductions, the parametrization of the physical model was accomplished by fits to the intermediate spatial-frequency range, avoiding the seeing-dominated region, of the power-spectrum estimates. In both of these studies the physical models produced a measurable amount of unresolvable power. For Drummond's asteroid work this could be interpreted as being due to unresolvable surface structure, and for Cheng's analysis the binning evidence also indicates that the unresolved power was real. The $r_c = 39$ cm curve in Fig. 5, having a mean value of ~ 1 , implies that the Poisson noise bias (Hege *et al.* 1982a) is consistent up to $0.9f_c$ and therefore does not lead to an extra bias in the object power spectrum.

Our new (albeit more computationally intensive than ever!) SI reduction procedures sort the data sets of both the object and point source into seeing bins to obtain a set of seeing-weighted, deconvolved power spectra. In order to do this sorting we have developed a technique to obtain an expedient estimate of the instantaneous value of the atmospheric coherence length r_c from the second-order moment of the speckle cloud. We have also implemented editing schemes to ignore bad specklegrams which can also contaminate the final results and to correct for detector systematics which can distort them. The importance of this refined analysis is

apparent, especially when considering subsequent processing, including various schemes of image reconstruction that use the Fourier modulus such as Fienup (1978), Knox-Thompson (1974), and Phase-Unwrapping (Cocke 1979), or which invoke model-fitting procedures to constrain physical image parameters.

There is a need for chopping between the point-source calibrators and the resolved object in order to minimize the seeing differences. Binning of the data sets for seeing calibration is still required because the variations in r_c can be greater than the integration time. We believe that, even with improved observing and data-acquisition protocol, the accuracy of power-spectra analysis is significantly improved by careful processing of the data to take into account the seeing variations and bad specklegrams within the data set and worth the additional computation overhead.

This work was supported in part by the NSF (Grants Nos. AST-8113212 and AST-8201092 and access to the Cyber 720/172 at NOAO), AFGL (Contract No. F19628-82-K-0025) and the AFOSR (Contract No. 82-0020). We also acknowledge the contributions of A. Szumilo for support and revisions to the data-reduction software, and, together with J. Freeman and S. Shaklan, for many long hours of tedious data digitization and computer babysitting. We also thank P. A. Strittmatter, N. J. Woolf, and F. Roddier for many useful discussions and advice.

We particularly thank the NOAO staff and visitors for enduring any inconveniences caused by these extensive data reductions, and the support staff at Kitt Peak who made the installation and use of our visitor instrument at the 4 m telescope a successful delight.

REFERENCES

- Aime, C., Ricort, G., Roddier, C., and Lago, G. (1978). *J. Opt. Soc. Am.* **68**, 1063.
- Cheng, A. Y. S., Strittmatter, P. A., Hege, E. K., Hubbard, E. N., Goldberg, L., and Cocke, W. J. (1985). In preparation.
- Cocke, W. J. (1980). *SPIE Proc.* **231**, 99.
- Drummond, J. D., Cocke, W. J., Hege, E. K., Strittmatter, P. A., and Lambert, J. V. (1985a). *Icarus* **61**, 132.
- Drummond, J. D., Hege, E. K., Cocke, W. J., Freeman, J. D., Christou, J. C., and Binzel, R. P. (1985b). *Icarus* **61**, 232.
- Fienup, J. R. (1978). *Opt. Lett.* **3**, 27.
- Fried, D. L. (1966). *J. Opt. Soc. Am.* **56**, 1372.
- Fried, D. L. (1979). *Opt. Acta* **26**, 597.
- Hege, E. K., Hubbard, E. N., Strittmatter, P. A., and Worden, S. P. (1981). *Astrophys. J. Lett.* **248**, L1.
- Hege, E. K., Hubbard, E. N., Strittmatter, P. A., and Cocke, W. J. (1982a). *Opt. Acta* **29**, 701.
- Hege, E. K., Hubbard, E. N., Drummond, J. D., Strittmatter, P. A., Worden, S. P., and Lauer, T. (1982b). *Icarus* **50**, 72.
- Hege, E. K., Beckers, J. M., Strittmatter, P. A., and McCarthy, D. W. (1985). *Appl. Opt.* **24**, 2565.
- Hubbard, E. N., Hege, E. K., Reed, M. A., Strittmatter, P. A., and Worden, S. P. (1979). *Astron. J.* **84**, 1437.
- Knox, K. T., and Thompson, B. J. (1974). *Astrophys. J. Lett.* **193**, L45.
- Korff, D. (1973). *J. Opt. Soc. Am.* **63**, 971.
- Labeyrie, A. (1970). *Astron. Astrophys.* **6**, 85.
- Mariotti, J. M., Chelli, A., Foy, R., Lena, P., Sibelle, F., and Tchountonov, G. (1983). *Astron. Astrophys.* **120**, 237.
- Roddier, F. (1981). *Prog. Opt.* **19**, 281.
- Woolf, N. J. (1982). *Annu. Rev. Astron. Astrophys.* **20**, 367.

Multi-wavelength Images Of α Orionis

Julian C. Christou

*Advanced Development Program
National Optical Astronomy Observatories**

Jeremy C. Hebden, E. Keith Hege[†]

Steward Observatory, University of Arizona

submitted to: The Astrophysical Journal

March 16, 1987

Abstract

We have used a recently developed high-spatial resolution imaging technique, known as Weighted Shift-and-add, to obtain diffraction-limited images of the red supergiant α Orionis at the resolution of the KPNO Mayall 4 m telescope. Images were obtained at six different bandpasses and the measured disk diameters agree to within a few % of the values obtained from the previously published power spectrum and autocorrelation analysis of the same data set. From the major and minor axes of models fit to the intensity profiles, we obtain asymmetry measures of both the disk and envelope components of $4(\pm 2)\%$ and $37(\pm 13)\%$ respectively. In addition we have searched for the proposed nearby companion but our data shows no direct evidence of it suggesting an upper limit to the magnitude difference of 4.5.

Subject headings: interferometry - stars: diameters - stars: individual - stars: supergiants

*operated by the Association of Universities for Research in Astronomy, Inc., under contract with the National Science Foundation

[†]Visiting Astronomer, Kitt Peak National Observatory, operated by the Association of Universities for Research in Astronomy, Inc., under contract with the National Science Foundation.

Contents

1	Introduction	4
2	Imaging Technique	5
3	Data Reduction	5
4	Results	7
4.1	γ Orionis	7
4.2	α Orionis	7
4.2.1	One-Dimensional Analysis	10
4.2.2	Images	13
4.2.3	Discussion of image structure	13
4.3	Multiplicity of α Orionis	17
5	Summary	19
6	Acknowledgements	20

List of Figures

1	Azimuthally averaged radial profiles of the WSA images of γ Orionis compared to model Airy patterns.	8
2	Azimuthally averaged radial profiles of α Orionis compared to those of γ Orionis.	9
3	(a) dirty beam, (b) dirty map and (c) clean map of α Orionis at $\lambda 6500$. (10% contour intervals).	11
4	Radial profiles of the Gaussian fit to the disk of α Orionis (solid lines) compared to limb darkened models $\mu = 0, 1$, (dashed lines): $R_* = 21$ mas.	12
5	CLEANed images of α Orionis. (a) $\lambda 5200$, (b) $\lambda 5500$, (c) $\lambda 6500$, (d) $\lambda 6563$, (e) $\lambda 8500$ and (f) $\lambda 8542$	14
6	Azimuthally averaged radial profile of the $\lambda 6563$ CLEANed WSA image compared to the clean beam (dashed line) and the Hartmann-Avrett model.	16
7	Combined positive residuals to the 2D Gaussian fit to the CLEANed α Orionis images. The \bullet represents the predicted position of the secondary. See text for discussion.	19

1 Introduction

The M2 Iab supergiant α Orionis has been one of the most frequently studied stars in high-spatial resolution astronomy. Since the first experiments by Michelson and Pease (1920) many measurements of its diameter have been made. These results have been comprehensively summarized by White (1980) and Cheng *et al.* (1986). They show a surprisingly large scatter and suggest a far from straightforward wavelength dependence. White (1980) suggested that the star has a blue halo, transparent at long wavelengths, to explain the observed diameter variations. A possible variance of the diameter with time has also been tentatively proposed. Conversely Cheng *et al.* (1986) conclude that their results, obtained at the Mayall 4 m, can be made consistent with a single photospheric diameter if limb darkening is taken into account for all wavelengths. Their results also suggest evidence for a faint circumstellar envelope possibly extending to about $5R_*$, although seeing calibration difficulties made this inconclusive. More recently Roddier *et al.* (1986) have concluded that the star is surrounded by a dust envelope which shows evidence for time evolution. Hebden *et al.* (1987) give conclusive evidence for the emission envelope extending to at least $4.5 R_*$ in H_α .

In this paper we present a series of diffraction-limited images of α Orionis obtained at the KPNO Mayall 4 m telescope. The images were produced using the weighted shift-and-add algorithm (WSA) recently developed at Steward Observatory (Christou *et al.* 1986a, 1986b). Both broad band (20 - 100 Å, line blanketed continuum) and narrow band (2.8 Å, spanning chromospheric emission lines) data were analyzed. Using this same data Cheng *et al.* (1986) estimated a stellar diameter of 42.1 ± 1.1 milli-arcseconds (mas) and a preliminary image at $\lambda 6500$, using the Knox-Thompson imaging technique was published by Hege *et al.* (1982). However, in both analyses, seeing calibration was made using observations of a point source, γ Orionis, and as they freely admit, errors in such calibrations may not be negligible although great care was taken to reduce data sets of similar seeing statistics. By comparison the WSA algorithm is essentially self-calibrating for seeing and the corresponding point source measurements have been used to verify the technique as well as give a measure of the telescope/detector point spread function. The primary aim of the work presented in this paper has been to determine, as unambiguously as possible, the photospheric diameter of α Orionis and to investigate any possible correlation among the size, limb-darkening of the stellar disk and the observational wavelength. This has been investigated from the reconstructed images and not from power spectrum or autocorrelation visibilities. Furthermore, estimates have been made of the luminosity ratio between the disk and the envelope by using a two-component Gaussian model for each image. The envelope appears to be clearly associated with the supergiant star and not to be a seeing calibration difficulty as the WSA images of γ Orionis do not show such an effect. Finally, we have derived from our data a lower limit for the magnitude difference between the supergiant and the nearby companion recently proposed by Karovska *et al.* (1986).

2 Imaging Technique

The WSA image reconstruction technique (Christou *et al.* 1986a, 1986b) is a variant of the shift-and-add algorithm initially developed by Lynds *et al.* (1976). It utilizes a weighted distribution of speckle positions to deconvolve an average speckle from a typical speckle cloud by means of a weighted deconvolution procedure. It has been shown to produce seeing self-calibrated point spread functions (PSF's) for both single and multiple aperture systems with point source data. Furthermore these PSF's agree, to within a few percent, with the theoretical Airy patterns at different wavelengths. The limiting signal-to-noise (SNR) of the technique suggests that the current detection system is capable of a dynamic range of ~ 6 magnitudes, with no evidence for residual seeing effects for a point source. The technique appears to be limited by the accuracy of the detection of the loci and amplitudes of the speckle maxima (see Christou *et al.* 1987). These are used to generate the deconvolution key, therefore limiting it to bright object data, for which atmospheric noise and not photon noise is the dominant image characteristic. It is also limited in its application to either point sources or objects which are barely resolved although recent improvements using an iterative matched filter analysis (Ribak 1986) suggest that it can be applied both to extended objects and in the photon noise dominated domain.

Because α Orionis has a small angular size, diameter ~ 42 mas, it is only barely resolvable at the resolution of a 3.8 m aperture especially at the longer wavelengths. For example at 5000 Å the telescope's theoretical resolution is ~ 27 mas and at 8500 Å is ~ 46 mas. Thus, we can use the WSA technique as the speckles of this bright object will be barely larger than point source speckles allowing the speckle maxima to be easily located and measured.

3 Data Reduction

Both α Orionis and its point source calibrator, γ Orionis, were observed with the KPNO 4 m Mayall telescope (pupil masked to 3.8 m) on 1981 February 2 and 3, using the Steward Observatory intensified video speckle camera (Hege *et al.* 1982). The seeing was exceptionally good, $\sim 0.5''$ on the first night and $\leq 1''$ on the second night. The objects were both observed at bandpasses of 5200/100 Å, 5500/100 Å, 6500/20 Å, 6563/3 Å, 8500/100 Å and 8542/3 Å. Data obtained at bandpasses of 3700/100 Å and 4100/100 Å were not used because they did not meet the photon noise criterion discussed above, and it was beyond the scope of this work to fully implement Ribak's (1986) matched filtered methodology.

The specklegrams were recorded with 15 ms exposures at a rate of 7.5 Hz onto videotape and were subsequently digitized 8 bits deep, using a Grinnell digital television system, into 128×128 pixel arrays yielding a detector image scale of 7.22 milli-arcseconds (mas) per pixel. This pixel scale was determined by use of a calibration mask and confirmed by the well determined parameters of the orbit of

α Aurigae. The spatial distortion due to the pincushion of the image intensifier was uncorrected because no geometric calibration grid was available. However, we have found that the distortion over a few pixels is minimal compared to the field and as the WSA technique relies on the accurate centroiding of the speckles, their relative locations are not as important. The spatial distortion over the size of the individual speckles is considered to be negligible as they are only a few pixels in size.

We did find it necessary, however, to remove the signal-dependent pedestal on each video frame. This pedestal is due to the automatic gain control of the video cassette recorder and has the effect of introducing a sloping black-level to the specklegram (see Christou 1985). We also edited the data to remove specklegrams which contained either saturated speckles or which contained only part of a speckle cloud. The WSA technique was then applied to all twelve data sets. We have found that a weighted ensemble deconvolution procedure yields significantly better results (in terms of SNR) than one which deconvolves each individual specklegram. Thus we accumulate the average cross-spectrum of the specklegram with the impulse distribution and the average power spectrum of the impulse distribution. Inverse Fourier transforming the quotient of these yields the resultant image. This process is described in more detail by Christou *et al.* (1986b).

The next stage of the reduction consists of 'despiking' each of the resultant images. Because the measured speckle distribution is obtained from the local maxima in the individual specklegrams, the cross-spectrum between the specklegram and this impulse distribution will contain a photon noise bias term due to the correlation of Poisson noise. This bias is, in turn, multiplied by the detector transfer function and both are removed by fitting a Gaussian to the signal beyond the telescope cut-off limit, $f_c = D/\lambda$, of the Fourier modulus (Hege *et al.* 1982; Christou *et al.* 1986b). An error in the fitting of the detector bias transforms to either an overestimate or underestimate in the image at the center two pixels.

Although the WSA reconstructed image is insensitive to seeing changes and also self-calibrating for seeing, it carries artifacts due to the detector, e.g. nonlinear effects of the video system, as well as non-uniformity of the combined optical PSF. These problems have been discussed in a previous paper (Hebden *et al.* 1986). In order to produce images free of these effects we have used a technique which has been successfully applied in the past to radio interferometric images. This is the CLEAN algorithm developed by Högbom (1974) which uses the point source image as a deconvolution key for the object image. In the CLEAN notation the point source image is referred to as the "dirty beam" and the object image as the "dirty map". CLEAN is an iterative process which locates the global maxima in the dirty map and subtracts, at these locations, the dirty beam whose peak intensity is set at a percentage of the maximum of the dirty map. This process is then repeated on the residual so that a set of impulses (δ functions) of varying intensities is built up. Thus the dirty map may be considered to be the weighted sum of dirty beams at the location of these impulses plus the final residual. Typically the intensity in the final residual is equal to the expected noise level. A "clean map" is then obtained by

convolving the array of impulses with a "clean beam", commonly obtained by fitting a Gaussian to the central component of the dirty beam. Therefore, the clean map is restored to the same resolution as the dirty map but with systematics removed.

We applied the CLEAN algorithm to all six pairs of data in order to minimize the problem of interpreting a system artifact as a physical property of the star. The effectiveness of this technique on visible high spatial resolution data has been shown by Hebden *et al.* (1986).

4 Results

4.1 γ Orionis

Azimuthally averaged radial profiles of the γ Orionis reconstructed images (dirty beams) at all six bandpasses are shown in Figure 1 compared to the corresponding theoretical profiles (Airy patterns). As can be seen the FWHM in *all* cases matches the computed Airy pattern. The $\lambda 6500$ and $\lambda 8500$ results show the best agreement with the model Airy patterns and the first minimum is clearly seen. The differences between the observed point spread functions and the models (easily distinguished because they show the minimum) can be due to a number of factors. Firstly, we have found that a slight defocussing of the system can fill in the minimum thereby reducing the contrast of the first ring. Secondly, overcorrection of the noise-bias will affect the peak amplitude therefore emphasizing the low power structure and thirdly, the effective wavelengths of the filters are compromised, especially at the longer wavelengths, because of the roll-off of the image tube response. Taking these into account we see the data match the models to within a few percent with no evidence for significant ($\geq 1-2\%$) seeing residuals.

4.2 α Orionis

Figure 2 shows the azimuthally averaged radial profiles of α Orionis (dirty map) compared to those of γ Orionis (dirty beam) at the corresponding bandpasses. In all six cases it can be seen that the former is easily resolved (beam size ~ 28 mas at $\lambda 5200$) although at the longer wavelengths the degree of resolution is less showing the first Airy ring in the resolved object image (beam size ~ 46 mas at $\lambda 8500$). The beam size at these wavelengths corresponds to measured values of the size of the unresolved stellar disk.

The dirty maps were CLEANed as discussed in the previous section by using the corresponding γ Orionis images as the dirty beams. We applied a two dimensional Gaussian least squares fit to the central lobes of the dirty beams to obtain the clean beams. The effect of the CLEANing is easily seen in Figure 3 which shows the reconstructed $\lambda 6500$ α Orionis image (dirty map), the corresponding clean map and dirty beam. A lumpy first Airy ring is seen in both the dirty beam and the dirty map. However, the clean map shows no evidence of this structure illustrating the

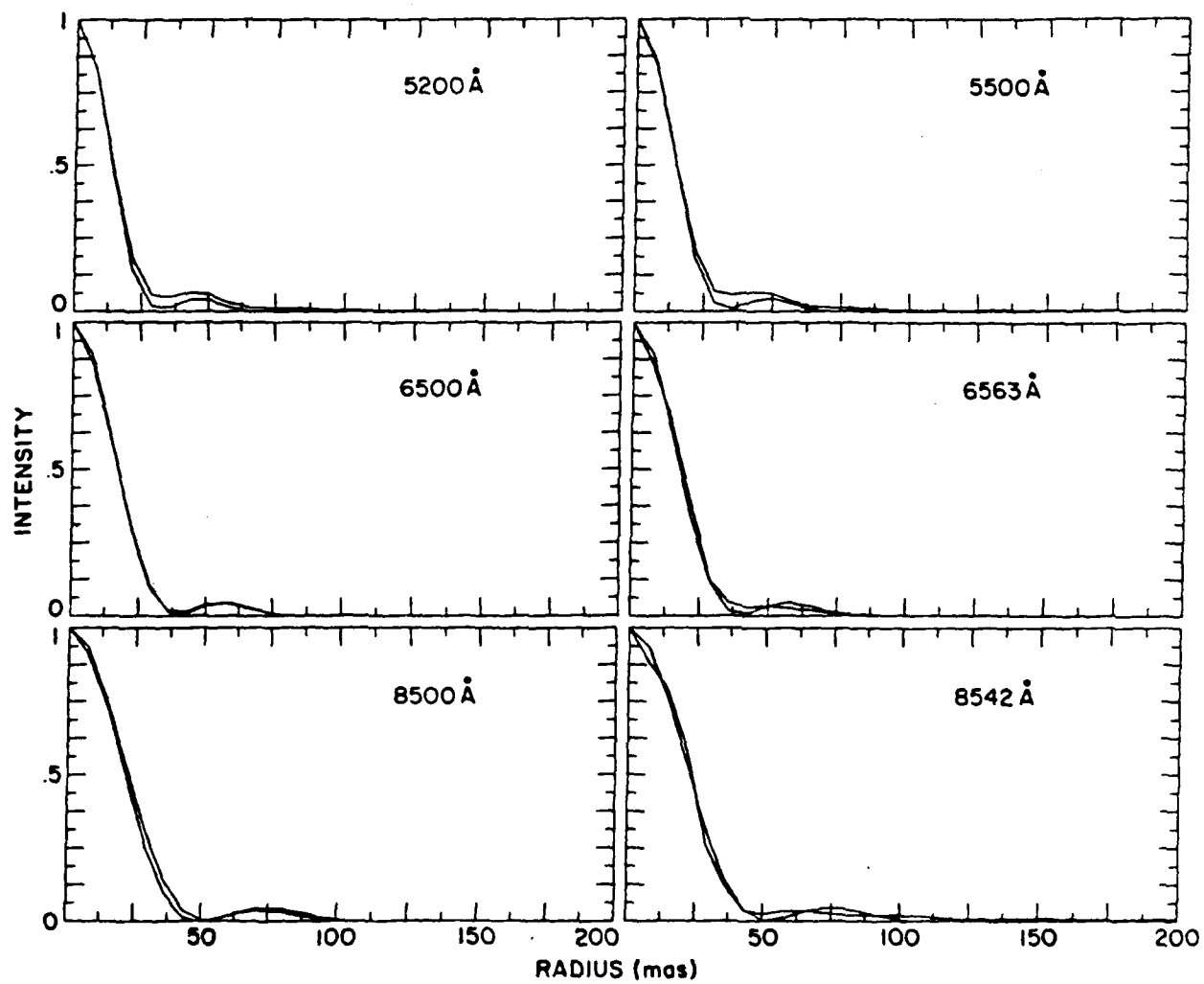


Figure 1: Azimuthally averaged radial profiles of the WSA images of γ Orionis compared to model Airy patterns.

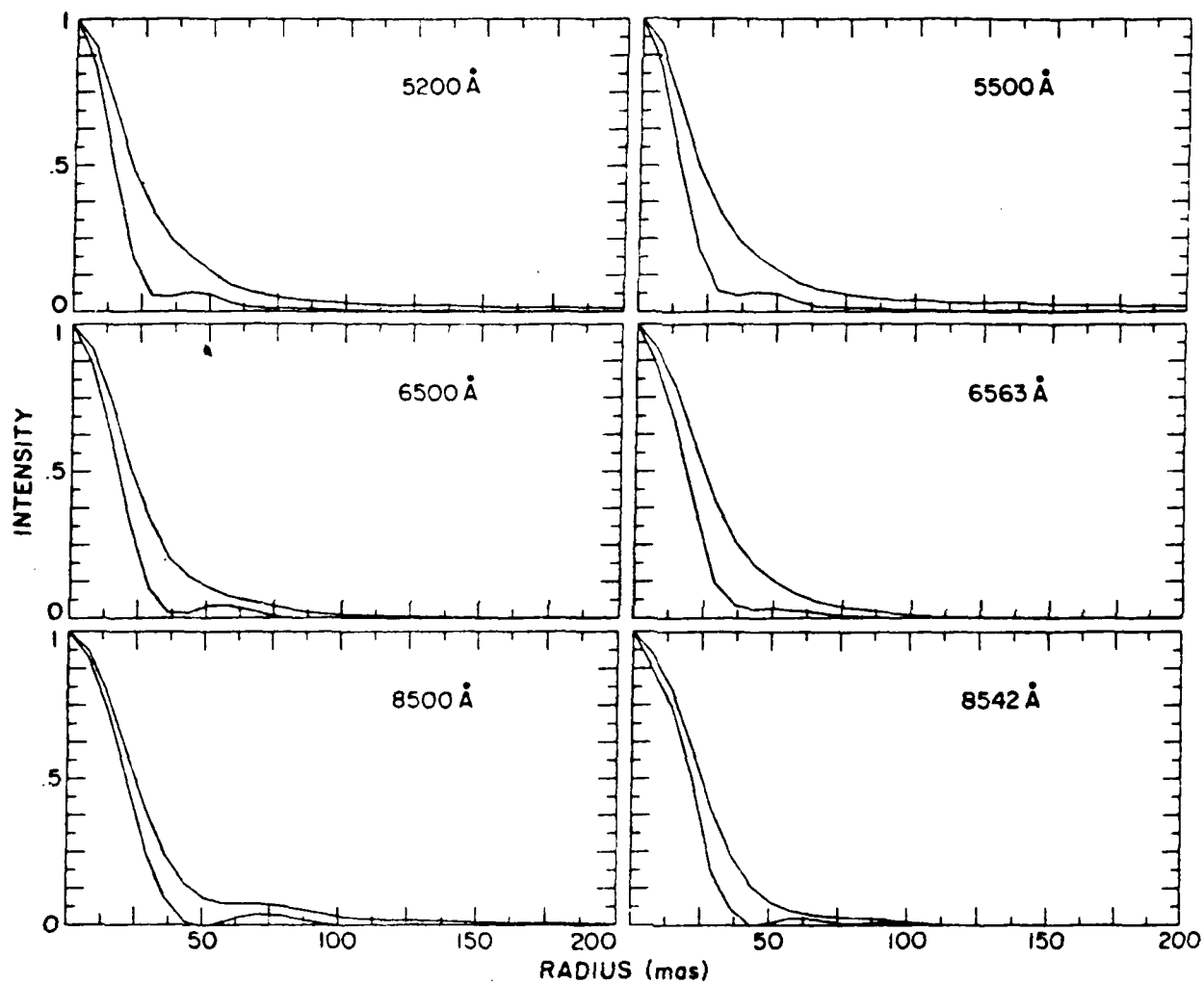


Figure 2: Azimuthally averaged radial profiles of α Orionis compared to those of γ Orionis.

Table 1: Radius estimates of α Orionis by Gaussian deconvolution. The standard errors were $\sim 1\%$.

Bandpass (\AA)	Radius σ_* (mas)
5200/100	20.5
5500/100	19.6
6500/20	19.4
6563/3	21.0
8500/100	18.4
8542/3	19.8
Mean	19.8 ± 0.7

successful application of the deconvolution procedure. Similar results were obtained for the other bandpasses.

4.2.1 One-Dimensional Analysis

Initial estimates of the size of the star were made by fitting a pair of two-dimensional Gaussians to the CLEANed images. We used a non-linear least squares analysis with one Gaussian representing the disk component and the other the extended envelope structure surrounding the disk. We computed the mean width σ_* of the disk Gaussian and compared it to that of the CLEAN beam at each bandpass to obtain the results in Table 1. Here we have assumed that the stellar disk can be represented by a Gaussian of width σ_* which is computed by the relation $\sigma_*^2 = \sigma_{\alpha O r_1}^2 - \sigma_{\gamma O r_1}^2$ where the latter are the widths of the Gaussian fit to the disk component of the clean map and clean beam respectively. A mean value of σ_* for the six bandpasses was found to be 19.8 ± 0.7 mas which compares well with the value of 21.1 ± 1.1 obtained by Cheng *et al.* (1986). In order to investigate this correlation further we compared the azimuthally averaged radial profiles of disk Gaussians with a 21 mas limb darkened model convolved with the corresponding clean beams. Figure 4 shows the Gaussian fit (solid line) compared to the models (dashed lines) for no limb darkening and total limb darkening.

Investigation of these profiles shows that, at the higher resolutions (shorter wavelengths), there are significant, consistent departures from the Gaussian models for radii where the profile is less than 50% of the peak. For the bandpasses $\lambda 5200$, $\lambda 5500$ and $\lambda 6500$ the amount of excess power diminishes as the resolution decreases. At $\lambda 8500$, where the stellar diameter is less than the beam size, this excess power has disappeared entirely and the profile agrees well with the model Gaussian. For the two narrow bandpass observations, $\lambda 6563$ and $\lambda 8542$, there appears to be evidence for even more extended structure. Note that in the continuum, $\lambda 6500$, the inner region of the disk compares well to a 21 mas radius uniform disk. However, the H_α profile is larger than the model at *all* radii showing that α Orionis is larger in the

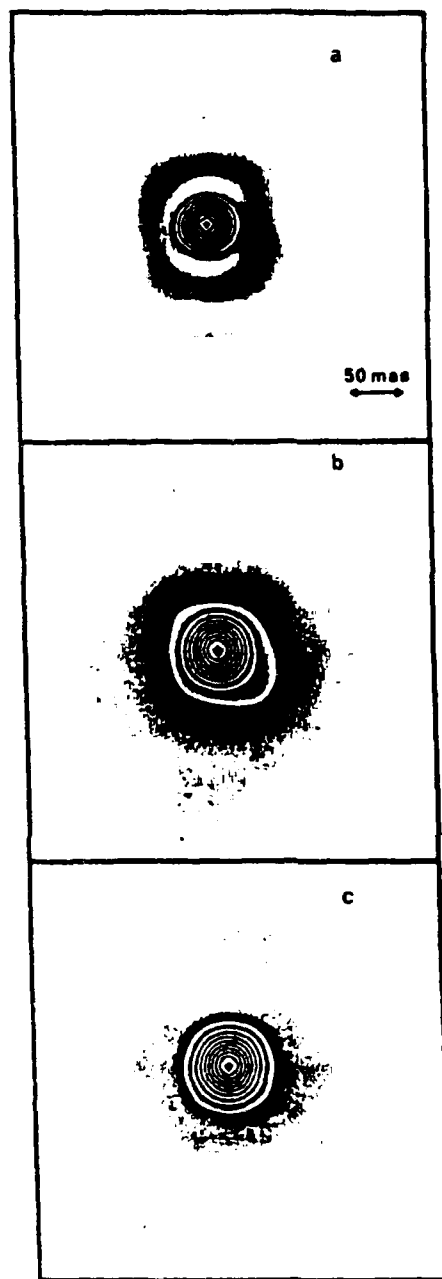


Figure 3: (a) dirty beam, (b) dirty map and (c) clean map of α Orionis at $\lambda 6500$. (10% contour intervals).

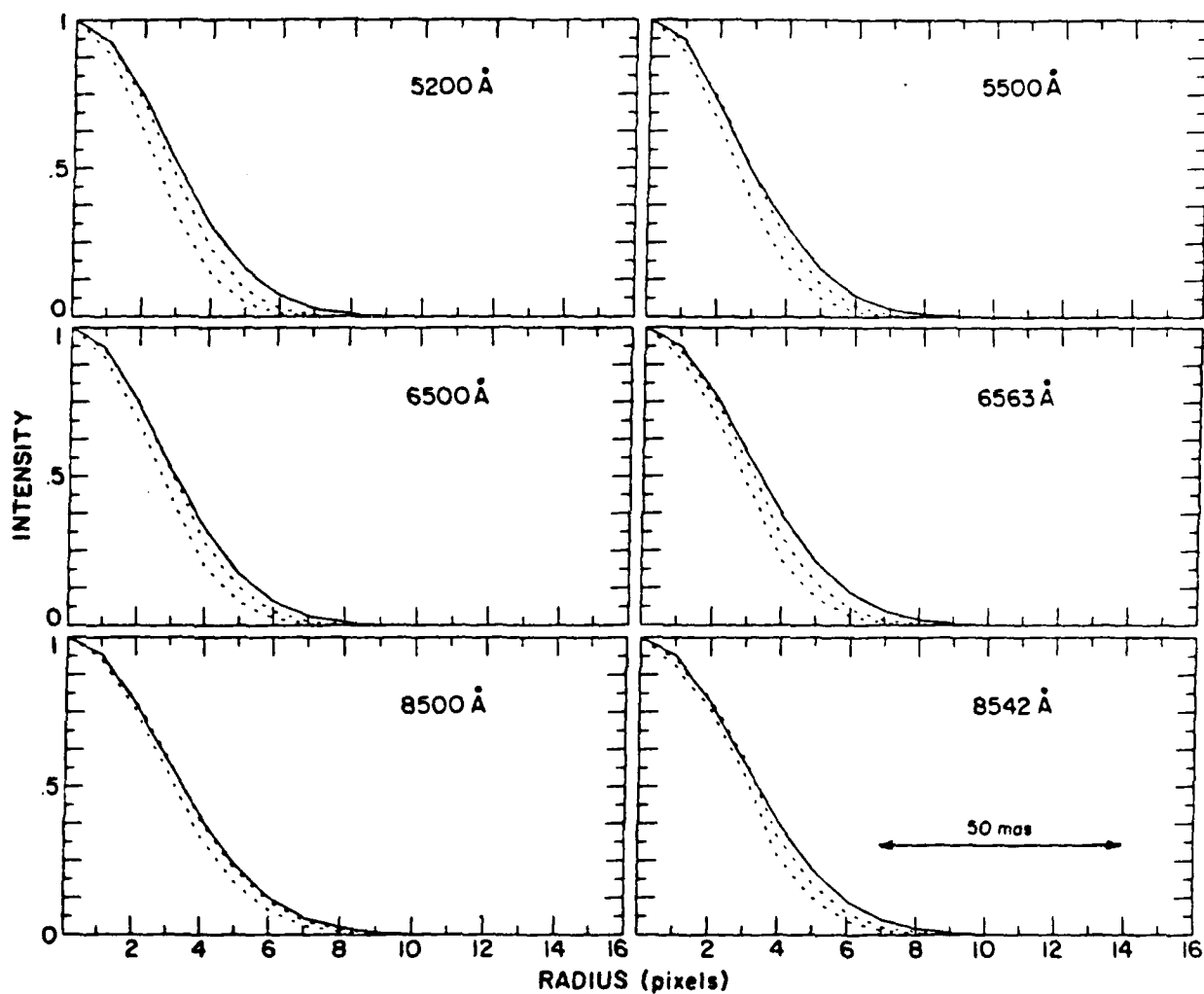


Figure 4: Radial profiles of the Gaussian fit to the disk of α Orionis (solid lines) compared to limb darkened models $\mu = 0, 1$, (dashed lines): $R_* = 21$ mas.

Table 2: Ratio of the flux and amplitude of the envelope : disk for all six bandpasses.

Bandpass (\AA)	Flux Ratio	Amplitude Ratio
5200/100	0.9	1.7 %
5500/100	2.0	3.0 %
6500/20	0.4	2.6 %
6563/3	0.4	6.6 %
8500/100	0.9	4.3 %
8542/3	6.2	6.5 %

chromospheric line than in the continuum. This measurement compares well with the recent results of Hebden *et al.* (1987) who have used differential speckle interferometry to map the stellar disk in H_α and have found it to be significantly larger than in the nearby continuum. The $\lambda 8542$ profile shows extended structure at the larger radii (*cf.* the $\lambda 8500$ profile), the central part of the disk being unresolved. Thus, in the two chromospheric lines the stellar disk is larger suggesting the presence of an extended atmosphere compared to the nearest continuum wavelengths.

4.2.2 Images

Figure 5 shows the reconstructed clean maps at all six bandpasses. As expected from the profiles in Figure 2, there is evidence for extended structure to radii $> 2R_*$ in the continuum images. The SNR of the dirty beams would imply that this structure is real, at least to $\sim 1\%$ of the peak. In order to quantify this extended structure we used the two-component, two-dimensional Gaussian to represent the disk and the "envelope". Table 2 gives the flux and amplitude ratios of envelope Gaussian to the disk Gaussian. The three images at $\lambda 5200$, $\lambda 5500$ and $\lambda 8500$ show the strongest extended structure. Because of the decreased resolution, we expect the ratio of the disk to envelope area to increase as the wavelength increases. In general, this is what we observe. However, both the $\lambda 5500$ and $\lambda 8500$ images show greater power in the envelope than the nearby bandpasses. It may be possible, in spite of the results for γ Orionis, that the observed extended structures in all the images are seeing residuals due to incorrect determination of the speckle maxima. But the γ Orionis profiles illustrate the success of the WSA technique to produce level zero-mean backgrounds. Thus we believe that extended low power structure in the α Orionis images is real. Investigation of the images shows structure to this envelope extending out to $\sim 4 R_*$, a distance commensurate with the H_α envelope observed by Hebden *et al.* (1987).

4.2.3 Discussion of image structure

Our reconstructed images of α Orionis show that the star has a complicated structure. Cool stars with extended atmospheres are likely to have photospheres whose

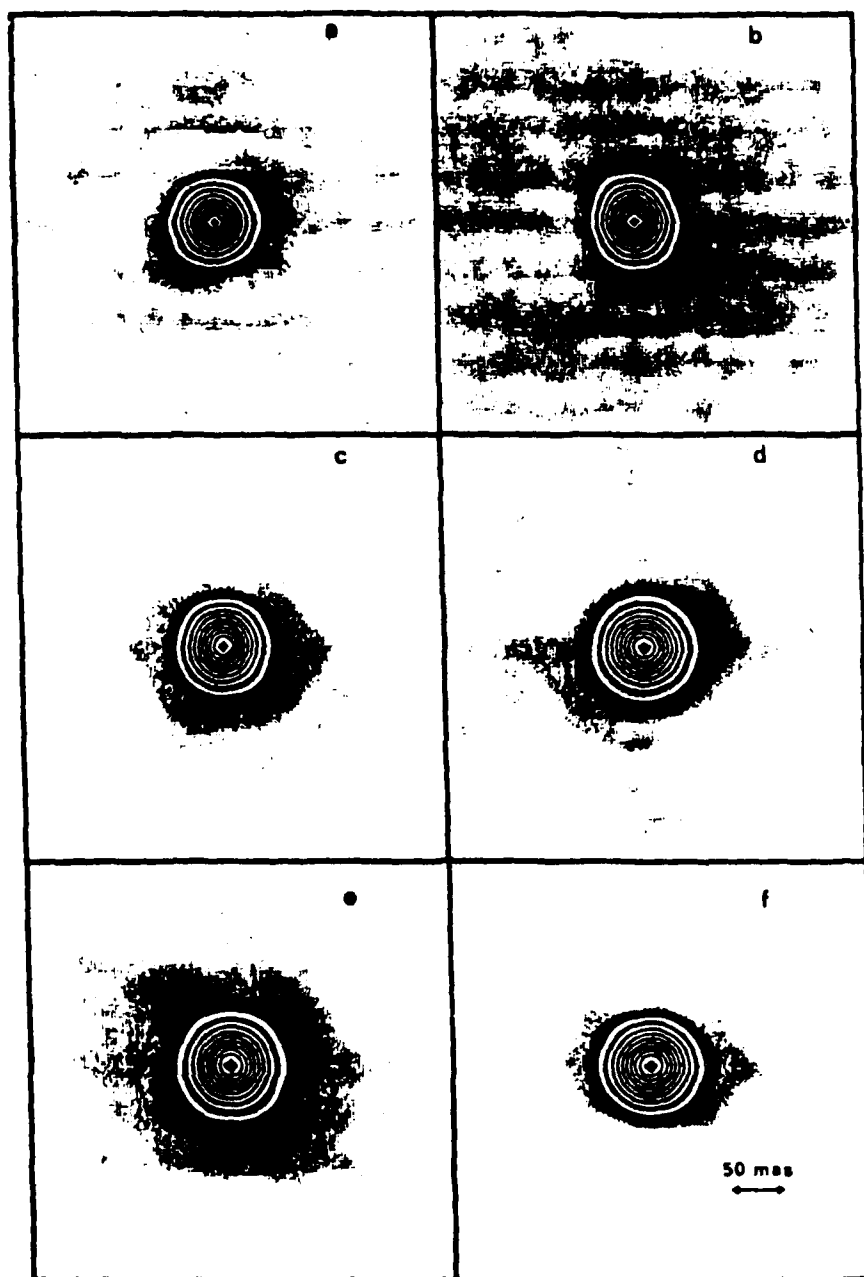


Figure 5: CLEANed images of α Orionis. (a) $\lambda 5200$, (b) $\lambda 5500$, (c) $\lambda 6500$, (d) $\lambda 6563$, (e) $\lambda 8500$ and (f) $\lambda 8542$.

diameters are dependent on wavelength because of variations in the opacity of the surrounding medium. Ridgway *et al.* (1980) predict a 3% difference in the apparent diameter of K and M giants at visible and near infrared wavelengths (smaller in the near infrared), and suggest that this variation could be significantly larger for supergiants. From Table 1 it can be seen that the apparent size of the disk decreases towards longer wavelengths for the continuum measurements. At $\lambda 8500$ the disk diameter is $\sim 6\%$ smaller than that of at $\lambda 5500$ thus qualitatively agreeing with Ridgway *et al.* (1987). A linear regression analysis to these observed angular diameters yielded a linear coefficient of $\sim -6(\pm 1) \times 10^{-3} \text{ mas(nm)}^{-1}$ agreeing well with a similar fit to autocorrelation diameters in Cheng *et al.* (1986). Welter and Worden (1980) also noted a smaller red diameter although not specifically at the same bandpasses used for this work.

The two component Gaussian modelling of our CLEANed reconstructed images, summarized in Tables 1 and 2, also yields asymmetry measures for both the disk and the envelope components. The disk component, with $19.8(\pm 0.7)$ mas average radius, shows a $4(\pm 2)\%$ major axis elongation at an angle of $193(\pm 20)^\circ$. The weaker envelope component, with correspondingly larger uncertainty in the fit, shows a $37(\pm 13)\%$ major axis elongation at $95(\pm 14)^\circ$ and evidence for significant flux to $\sim 130(\pm 70)$ mas. The standard error in the fit of this two component model, to a radius of $0.''360$ (50 pixels), is 0.5% rms of the peak image intensity. The position angle of the elongated disk image component is strikingly consistent with the position angle of the image extension seen at $\sim 202^\circ \text{ (mod } 180^\circ)$ by Roddier and Roddier (1983) only 2.5 months earlier. These image asymmetry angles are somewhat different from those reported by Goldberg *et al.* (1981) and Hege *et al.* (1984). The earlier values, 208° for the disk and $\sim 165^\circ$ for the envelope, were based on a single Knox-Thompson (see Hege *et al.* 1982) reconstruction for the $\lambda 6500$ data and are consistent with the ensemble variance for the six bandpasses reported here. Our analysis of the disk image component continues to be consistent with the earlier assertions in Goldberg *et al.* (1981) and Hebden *et al.* (1986) in that it suggests evidence for possible large scale convection effects in the form of a "hot spot" on the stellar surface near the stellar limb.

Radial velocity measurements in the core and wings of the H_α line of α Orionis by Weymann (1962) and Goldberg (1979) suggest that the star possesses a chromosphere detached from the photosphere. The recent H_α images of α Orionis by Hebden *et al.* (1987) have shown that the extended H_α atmosphere has a remarkably Gaussian-like profile, and extends out to a radius of at least $4.5 R_\odot$. This extent agrees well with the theoretical model chromosphere developed by Hartmann and Avrett (1984). The blue shifted core of the line suggests that it is formed in an expanding region, although Hartmann and Avrett (1984) conclude that the atmosphere is predominantly "quasi-static", whereby only a fraction of ejected matter is accelerated to escape velocity. The presence of an extended chromosphere around α Orionis has also been confirmed by radio observations. Altenhoff *et al.* (1979) suggest that radiation at $< 20 \text{ GHz}$ is consistent with a

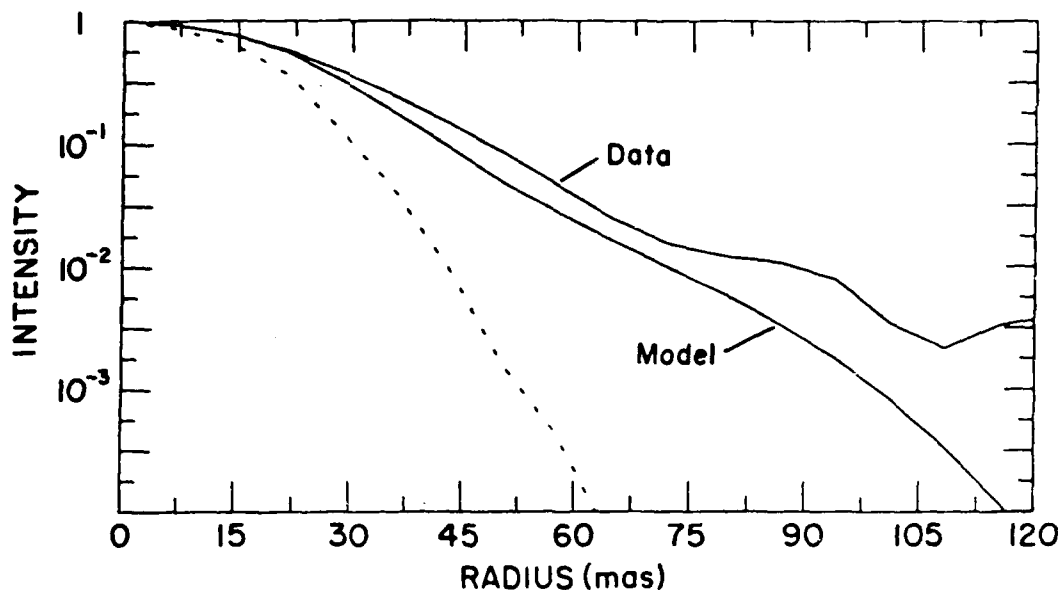


Figure 6: Azimuthally averaged radial profile of the $\lambda 6563$ CLEANed WSA image compared to the clean beam (dashed line) and the Hartmann-Avrett model.

photosphere/chromosphere transition region extending to $\sim 2 - 3 R_{\odot}$. Similarly, Newell and Hjeltning (1982) have concluded that radio emission between 1 - 100 GHz is due to a warm chromosphere-like region extending from 1 - 4 R_{\odot} .

Figure 6 shows the azimuthally averaged radial profile of the clean map at H_{α} compared to both the clean beam (dashed line) and the model predicted by Hartmann and Avrett (1984). Their model was interpolated for the 2.8 Å bandpass used at an image scale of $7.22 \text{ mas(pixel)}^{-1}$ and assuming a disk radius of 21 mas. The model and data match out to $\sim R_{\odot}$ but at greater radii we measure excess intensity. The model assumes a flux of Alfvén waves sufficient to drive an outflow of $10^{-6} M_{\odot}(\text{year})^{-1}$ and used electron density data obtained from radio measurements. Hebden *et al.* (1987) have recently compared the same model, suitably modified for a 1.2 Å effective bandwidth, with profiles obtained from DSI images obtained at the Multiple Mirror Telescope (MMT). They also show that the model does not predict sufficient emission. We see an inflection in the data curve corresponding to $\sim 3 - 4 R_{\odot}$ which may be evidence for increased outflow of material at an earlier epoch. Roddier *et al.* (1986) have suggested that material is ejected in bursts which would then agree with our interpretation and therefore would signify a variability in mass outflow (Goldberg 1984).

Inspection of the azimuthally averaged radial profiles of the CLEANed images (Figure 4) shows that the Cheng *et al.* (1986) model of a limb darkened uniform disk of $R_{\odot} = 21 \text{ mas}$ agrees with the continuum images. We are unable to accurately determine the degree of limb darkening because of insufficient resolution. This difficulty of jointly estimating the radius and limb darkening from speckle

interferometric measurements has been recently discussed by Kuz'menkov (1986). At the shorter bandpasses, i.e. greater resolution, the profiles show an extended atmosphere at $\sim 2R_*$ which appears to be optically thick within the chromospheric lines ($H_\alpha - \lambda 6563$ and $\text{CaII} - \lambda 8542$), increasing the apparent size of the stellar disk. This is commensurate with an extended chromosphere lying in the range of $1 - 4 R_*$. It is obvious from these images that in order to study the photospheric and chromospheric structure of this and other stars, much greater resolution is needed, i.e. > 2 resolution elements across the disk! Even at the resolution of the fully phased MMT (equivalent to a 6.86 m pupil) there are only < 3 resolution elements across the disk at $\lambda 5500$, and therefore even less at longer wavelengths. The Hubble Space Telescope, by comparison, only has one resolution element across the disk at $\lambda 5500$. Thus with our existing large aperture instruments, the investigation of structure on stellar surfaces is still severely limited.

Prior observations of α Orionis have produced overwhelming evidence for the existence of a circumstellar envelope, extending out to several stellar radii. Ricort *et al.* (1981) interpret their results, observed at $\lambda 5300/160$, as being consistent with a 35 mas disk embedded in a 100 mas diameter envelope whose luminosity is a few percent of the disk. In addition, Roddier and Roddier (1985) and Roddier *et al.* (1986) suggest that their measurements indicate the existence of dust condensation close to the stellar disk as well as evidence for its evolution. Draine (1981) also supports the view that dust condensation as close as $1.8 R_*$ to the disk is possible. Furthermore, the presence of a dust shell close to the star has been suggested as the primary cause of the discrepancy between photometric and interferometric photospheric diameters (Tsuji 1978; White 1980). However, infrared measurements by a number of investigators (McCarthy *et al.* 1977; Sutton *et al.* 1984; Bloemhof *et al.* 1984) show that most of the $10 \mu\text{m}$ emission does not originate close to the star. Our images show the presence of an extended low power envelope at all continuum wavelengths out to a distance of $\sim 4 R_*$ corresponding to the previous measurements.

4.3 Multiplicity of α Orionis

Recently, Karovska *et al.* (1986) and Roddier *et al.* (1986) have postulated the existence of two companions to α Orionis. The first is at an angular separation of $0.''4 - 0.''5$ and is outside of our field of view. The second, however, lies at a distance of $\sim 0.''06$ and should therefore be visible in our data, especially as its magnitude difference is estimated to be ~ 3.4 at $\lambda 6563$ and ~ 3.0 at $\lambda 6568$. We firstly investigated the power spectra of the entire data sets to look for fringes. None were found however. This is not too surprising as this magnitude difference is stretching the dynamic range capability of the simple power spectral analysis. We then looked for evidence of this secondary in the WSA images. Based on remarks by Bates (1984), our WSA method is expected to produce the highest signal-to-noise results possible as it is a first-order interferometric process. Specifically, WSA is not subject to de-

panion being outside our detector window. Obviously, α Orionis is an extremely complicated object and further study is needed to resolve some of the important questions concerning the nature of such highly evolved objects. The development of increased performance, spatial distortion free detectors and new image recovery algorithms on large apertures (≥ 8 m) should go a long way to improve the quality of the information determined by interferometric techniques. Since it is possible to obtain diffraction-limited images, the question of interpreting the information they carry is now more important. Obviously, better SNR images would make this interpretation easier and greater resolution would solve some of the ambiguities. The use of the MMT as a phased array (Hege *et al.* 1985; Hebden *et al.* 1987) has shown that significant astrophysical information can be obtained but there is still a long way to go if we wish to extend these techniques to fainter, and possibly more interesting, objects.

6 Acknowledgements

This work was supported in part by the National Science Foundation (grants AST-8201092 and AST-8312976) and by the United States Air Force (AFOSR grant 82-0020 and AFGL contracts F19628-82-K-0025 and F19628-84-K-0035). We also wish to thank Dr. Hartmann and Dr. Avrett for providing us with their theoretical models and Dr. Andreas Eckart for implementation of the CLEAN algorithm. In addition we acknowledge the assistance of the NOAO support staff at Kitt Peak for the installation of our visitor instrument at the Mayall telescope. All computer reductions were made on the Steward Observatory Data General MV10000 (supported by the NSF grant AST 8412206), and we wish to thank the computer support staff for their help and other users for their patience during the extensive reduction time. We also wish to express our thanks (especially EKH) to Dr. Leo Goldberg for encouraging us to initiate this investigation in 1981 and for his many helpful suggestions along the way towards these succesful image reconstructions.

References

- [1] Altenhoff, W.J., Oster, L., and Wendker, H.J., (1979), *Astron. Astrophys.*, **73**, L21.
- [2] Balega Yu.Yu., and Balega I.I., (1985), *Sov. Astron. Lett.*, **11**, 47. translated from *Pis'ma Astron. Zh.*, **11**, 112.
- [3] Bates, R.H.T., "Astronomical Speckle Imaging", in *Indirect Imaging* ed. J.A.Roberts, (1984), Cambridge Univ. Press, 91.
- [4] Bloemhof, E.E., Townes, C.H., and Vanderwyck, A.H.B., (1984), *Astrophys. J.*, **276**, L21.
- [5] Cheng A.Y.S., Hege, E.K., Hubbard, E.N., Goldberg, L., Strittmatter, P.A., and Cocke, W.J., (1986), *Astrophys. J.*, **309**, 737.
- [6] Christou, J.C., (1985). Dissertation. New Mexico State University.
- [7] Christou, J.C., Hege, E.K., Freeman, J.D., and Ribak, E., (1986a), *J. Opt. Soc. Am. A*, **3**, 204.
- [8] Christou, J.C., Ribak, E., Hege, E.K., and Freeman, J.D., (1986b), *Opt. Eng.*, **25**, 724.
- [9] Christou, J.C., Freeman, J.D., and Hege, E.K., (1987), in *Proc. ESO/NOAO Workshop on High Angular Resolution Imaging from the Ground Using Interferometric Techniques*, ed. J. Goad, Oracle, Az., Jan 12 - 15.
- [10] Draine, B., (1981), in *Physical Processes in Red Giants*, ed. I.Iben and A.Rezini (Dordrecht:Reidel).
- [11] Goldberg, L., (1979), *Quart. J. Roy. Astron. Soc.*, **20**, 361.
- [12] Goldberg, L., (1984), *Pub. Astron. Soc. Pac.*, **96**, 366.
- [13] Goldberg, L., Hege, E.K., Hubbard, E.N., Strittmatter, P.A.S., and Cocke, W.J., (1981), in *Second Cambridge Workshop on Cool Stars, Stellar Systems, and the Sun*, ed. M.S. Giampapa and L. Golub (SAO Spec. Rept., No. 392), **1**, 131.
- [14] Hartmann, L., and Avrett, E.H., (1984), *Astrophys. J.*, **284**, 238.
- [15] Hebden, J.C., Christou, J.C., Cheng, A.Y.S., Hege, E.K., Strittmatter, P.A., Beckers, J.M., and Murphy, H.P., (1986), *Astrophys. J.*, **309**, 745.
- [16] Hebden, J.C., Eckart, A., and Hege, E.K., (1987), *Astrophys. J.*, 314 in press.

- [17] Hege, E.K., Hubbard, E.N., Strittmatter, P.A., and Cocke, W.J., (1982), *Optica Acta*, **29**, 701.
- [18] Hege, E.K., Strittmatter, P.A., and Woolf, N.J., (1984), Air Force Geophysics Laboratory report AFGL-TR-84-0116.
- [19] Hege, E.K., Beckers, J.M., Strittmatter, P.A., and McCarthy, D.W., (1985), *Appl. Optics*, **24**, 2565.
- [20] Högbom, J.A., (1974), *Astron. Astrophys. Suppl.*, **15**, 417.
- [21] Karovska, M., Nisenson, P., and Noyes, R., (1986), *Astrophys. J.*, **308**, 260.
- [22] Kuz'menkov, S.G., (1986), *Sov. Astron.*, in press.
- [23] Lynds, C.R., Worden, S.P., and Harvey, J.W., (1976), *Astrophys. J.*, **207**, 174.
- [24] McCarthy, D.W., Low, F.J., Howell, R., (1977), *Astrophys. J.*, **214**, L85.
- [25] Michelson, A.A., and Pease, F.G., (1920), *Astrophys. J.*, **51**, 257.
- [26] Newell, R.T., and Hjellming, R.M., (1982), *Astrophys. J.*, **263**, L85.
- [27] Ribak, E., (1986), *J. Opt. Soc. Am. A*, **3**, 2069-2076.
- [28] Ricort, G., Aime, C., Vernin, J., and Kadiri, S., (1981), *Astron. Astrophys.*, **99**, 232.
- [29] Ridgway, S.T., Joyce, R.R., White, N.M., and Wing, R.F., (1980), *Astrophys. J.*, **235**, 126.
- [30] Roddier, F., and Roddier, C., (1983), *Astrophys. J.*, **270**, L23.
- [31] Roddier, F., and Roddier, C., (1985), *Astrophys. J.*, **295**, L21.
- [32] Roddier, F., Roddier, C., Petrov, R., Martin, F., Ricort, G., and Aime, C., (1986), *Astrophys. J.*, **305**, L77.
- [33] Sutton, E.C., Storey, J.W.V., Betz, A.L., Townes, C.H., and Spears, D.L., (1977), *Astrophys. J.*, **217**, L97.
- [34] Tsuji, T., (1978), *Pub. Astron. Soc. Japan*, **30**, 435.
- [35] Welter, G.L., and Worden, S.P., (1980), *Astrophys. J.*, **242**, 673.
- [36] Weymann, R., (1962), *Astrophys. J.*, **136**, 844.
- [37] White, N.M., (1980), *Astrophys. J.*, **242**, 646.

ISOPLANICITY MEASUREMENTS FOR CALIBRATION OF SPECKLE HOLOGRAPHY AMPLITUDES

Julian C. CHRISTOU¹ and E. Keith HEGE

Steward Observatory, University of Arizona, Tucson, AZ 85721, USA

Received 23 December 1985

We show how the technique of astronomical speckle holography is dependent upon the degree of isoplanicity between the object and the discrete point source. A well calibrated measurement of the degree of correlation between two quasi-instantaneous simultaneous point source speckle patterns (separation $\approx 2.6''$) are presented to illustrate this non-isoplanatic effect as a function of the spatial frequency. This two-dimensional measurement is in quantitative agreement with previously computed models and shows a high degree of correlation at seeing dominated frequencies with a severe attenuation (but not total loss of correlation) for frequencies approaching the diffraction limit. We show how such measurements may be used to reweight (calibrate) the Fourier amplitude of a speckle holographic image observed under similar seeing conditions in order to compensate for the non-isoplanatic degradation at high spatial frequencies.

1. Introduction

The high spatial resolution techniques of speckle holography [1] (SH) and adaptive optics [2] (AO) make use of measurements of the short-exposure point spread function (PSF) of the atmosphere to recover diffraction limited images. The short-exposure PSF, with exposure times of less than 30 ms, serves as a measure of the wavefront distortion introduced by the random turbulence of the atmosphere. In AO the wavefront in one direction (i.e. the resolved object) may be corrected by sensing the wavefront in a slightly different direction (i.e. a point source). In SH the resolved object specklegram is deconvolved by a simultaneously acquired point source specklegram to obtain the short-exposure estimate of its diffraction limited image. If the wavefront distortion is identical for both objects then either of the above techniques will yield a perfect diffraction limited image in the absence of statistical and systematic noise. However, the assumption that the PSF is space invariant (isoplanatic) is not valid for wide field imaging (typically $>5''$) because the two light paths pass

through different perturbations in the atmosphere.

Thus there is likely to be a requirement for calibration of the SH or AO images to compensate for non-isoplanatic effects. In section 3 we show that the SH image is degraded by the isoplanatic parameter

The region over which the PSF is spatially invariant is described as the *isoplanatic patch*. Determination of the size of this region (of isoplanicity) is therefore a useful measure of the spatial limitations of both AO and SH. This problem has been addressed by a number of theoretical investigations [3–8] and measurements of isoplanicity have been reported by a number of investigators [9–15] for both speckle interferometry and adaptive optics. The variously defined values obtained range from $\sim 1''$ to $5''$ or even larger for regions of partial isoplanicity [12]. In the following section it is shown that the size of the isoplanatic patch is dependent upon the highest spatial frequency measured.

2. The isoplanatic parameter

A calibration of the degree of isoplanicity at a given separation can be obtained by comparing the simultaneous specklegrams of the unresolved compo-

¹Visiting Astronomer from Department of Astronomy, New Mexico State University, Las Cruces, NM 88003, USA.

nents of a close binary star. These specklegrams are a measurement of the combined short-exposure PSF's of the atmosphere and the telescope. The Fourier transform of the PSF (transfer function) is given by the autocorrelation of the aperture, i.e.

$$P(f) \approx \int_{-\infty}^{\infty} dr U(r) U^*(r + \lambda f) W(r) W(r + \lambda f) \quad (1)$$

where r defines the pupil plane, f the spatial frequency plane, $U(r)$ the complex wavefront and $W(r)$ the pupil transmittance (i.e. = 1 inside the pupil and 0 elsewhere). A comparison of the two PSF's is best made by computing the ensemble averaged cross-spectrum between them, i.e.

$$XS(f) = \langle P_1(f) P_2^*(f) \rangle, \quad (2)$$

where $P_1(f)$ and $P_2(f)$ are the Fourier transforms of the combined telescope-atmosphere PSF's for objects 1 and 2, * denotes complex conjugate and $\langle \dots \rangle$ represents the ensemble average. If $P_1(f) = P_2(f)$ then (2) reduces to a measurement of the speckle transfer function (STF). The ratio of (2) to the STF therefore characterizes the effects of non-isoplanaticity as a function of the spatial frequency f . We define this ratio as the spatial frequency dependent *isoplanatic parameter*, $T(f)$ given by

$$T(f) = \langle P_1(f) P_2^*(f) \rangle / \langle |P(f)|^2 \rangle, \quad (3)$$

where $\langle |P(f)|^2 \rangle = \langle |P_1(f)|^2 \rangle = \langle |P_2(f)|^2 \rangle$ assumes that both components are observed with similar seeing as indeed they should be for simultaneous measurements. Both the cross-spectrum and the STF are normalized to unity at the dc point ($f = 0$). $T(f)$ describes the effects of non-isoplanaticity on the fringe modulation of the power spectra of binary stars [9,10] and also represents the frequency dependent correlation coefficient between the two PSF's for either AO or SH. Roddier [16] defines both the cross-spectrum and power spectrum as

$$\langle P_1(f) P_2^*(f) \rangle \approx \int df' M_{12}(f, f') A(f, f'),$$

and

$$\langle |P(f)|^2 \rangle \approx \int df' M(f, f') A(f, f'), \quad (4)$$

where $M(f, f')$ and $M_{12}(f, f')$ are fourth order moments over the perturbed complex wavefronts. These represent the atmospheric contribution, i.e.

$$M_{12}(f, f')$$

$$= \langle U_1(r) U_1^*(r + \lambda f) U_2^*(r + \lambda f') U_2(r + \lambda f + \lambda f') \rangle,$$

and

$$M(f, f') = \langle U(r) U^*(r + \lambda f) U^*(r + \lambda f') U(r + \lambda f + \lambda f') \rangle. \quad (5)$$

$A(f, f')$ is a telescope dependent term consisting of a four pupil overlap integral which allows for the recovery of the high spatial frequencies up to the diffraction limit, i.e.

$$A(f, f') = \int dr W(r) W(r + \lambda f) W(r + \lambda f') W(r + \lambda f + \lambda f'). \quad (6)$$

Thus the isoplanatic parameter, $T(f)$, is not in general independent of the telescope transfer function because of the integral over $A(f, f')$. If the complex wavefront is assumed to obey gaussian statistics then the telescope transfer function drops out for the highest and lowest spatial frequencies: the approximations to the STF contain multiplicative terms corresponding to the telescope MTF and its modulus squared (see Roddier [16]).

For complete isoplanaticity, i.e. $P_1(f) = P_2(f) = P(f)$, the isoplanatic parameter (3) will be unity for all spatial frequencies. There will be complete non-isoplanaticity when the two PSF's do not correlate so that $T(f)$ will be zero at all spatial frequencies greater than $f > 0$. Partial isoplanaticity is therefore defined for $0 < T(f) < 1$.

Models of (3) for different separation angles, θ , have shown [10] that it is a center symmetric but non isotropic function. The component orthogonal to the separation vector has greater correlation than the parallel component.

3. Astronomical speckle holography

Speckle holography uses a discrete unresolved object within the same (partially isoplanatic) field as the object of interest. For example two important astrophysical systems worthy of synoptic imaging studies at the resolution of the multiple mirror telescope are Alpha Scorpii and Alpha Herculis. Both of these have unresolved companions ~ 3 s of arc from a resolved primary making them good astrophysical candidates

for SH. It is therefore relevant and important to understand the details of speckle holographic imaging.

A short exposure image of the point source acts as a deconvolution key for the nearby resolved object. Weigelt has successfully used this technique to obtain the correct separation and orientation of close unresolved binary stars and star cluster systems [17].

Using the isoplanatic imaging equation, the short exposure image of the resolved object, $o(r)$, can be written as

$$i(r) = o(r) * p(r), \quad (7)$$

where $*$ denotes convolution and $p(r)$ is the combined telescope-atmosphere PSF. For an unresolved source the short exposure image is the PSF so that a simultaneous measurement of the PSF allows for the object recovery by inverting (7). This unresolved source has to be "nearby" the object so that the seeing conditions are similar. The limit of the separation between the point source and object for which SH can be used depends upon how well the non-isoplanatic effects can be calibrated for by the frequency dependent quantitative measure (3).

A weighted deconvolution technique is required to recover the object distribution in eq. (7) because of the problems associated with small number and zero divides in each of the complex quotients of an inversion by linear deconvolution. Experiments with differential speckle interferometry [18] have shown that when the weighting is the power spectrum of the PSF, then the deconvolution reduces to a single complex quotient for the complete data set which is intrinsically Wiener filtered by the time average of the noise biased power spectrum. Denoting the Fourier transforms of the terms in eq. (7) by uppercase notation then a signal averaged estimate of the object transform, $O'(f)$, obtained by linear deconvolution is expressed as

$$O'(f) = \sum_n I_n(f) / P_n(f), \quad (8)$$

where the subscript defines the n th specklegram and the sum is over all specklegrams. The estimate obtained using a power spectrum weighted deconvolution gives

$$O'(f) = \sum_n I_n(f) P_n^*(f) / \sum_n |P_n(f)|^2. \quad (9)$$

Eq. (9) represents the speckle holographic image for the isoplanatic case. However, as the discrete point source is generally no closer to the object than a few seconds of arc ($\sim 3''$) then the effects of non-isoplanaticity have to be considered. Letting the PSF for the object be given as $P_1(f)$ and for the reference as $P_2(f)$ then (9) becomes

$$O'(f) = O(f) P_1(f) P_2^*(f) / \langle |P_2(f)|^2 \rangle. \quad (10)$$

If the seeing is the same then the speckle transfer functions will be identical so that $|P_1(f)|^2 = |P_2(f)|^2$. For the case of complete isoplanaticity, when the short exposure transfer functions are identical, the estimate of the object transform reduces to the object. However for the non-isoplanatic case (10) the object estimate transform is weighted by the isoplanatic parameter (3). Therefore in order to fully recover the diffraction limited object it is necessary to multiply its Fourier transform (10) by the inverse of the isoplanatic parameter (3) as measured for the same separation under similar (if not, ideally, identical) seeing conditions.

The need for frequency dependent reweighting of speckle holographic amplitudes is not unlike the requirement for reweighting the simple Labeyrie speckle image amplitudes as we have discussed previously [19]. In this case we need a nearby simple binary star with *unresolved* components instead of a single point source. We suspect that similar binning techniques [19] to accumulate the variable statistics due to variable seeing will also be appropriate.

4. Measurements of $T(f)$

To investigate the non-isoplanatic effects as discussed above we observed the binary star Epsilon [2] Lyrae whose separation of $\sim 2.6''$ compares with those of the two components of Alpha Scorpii and Alpha Herculis. The data was taken with the Steward Observatory (SO) 2.3 m telescope at Kitt Peak and the SO speckle camera [20] at a wavelength of 550 nm for two different bandpasses of 10 nm and 30 nm. A 5 ms shutter was used. The data were recorded on to 3/4" U-Matic videotape and subsequently digitized

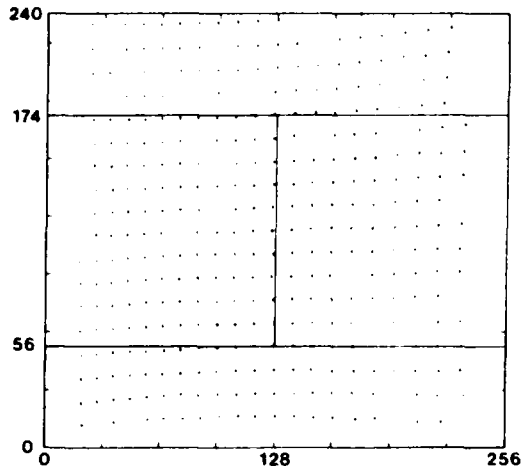


Fig. 1. A digitized regular grid showing the effects of the geometric distortion. The removal of this intensified video detector distortion, frame-by-frame, is a necessary step in an isoplanicity calibration. The left and right fields (see text) are also shown.

into specklegrams of 256 by 128 pickels with an image scale of 20 ms of arc (msa)/pixel which over-samples the 50 msa diffraction limit. The orientation of the two, nearly equal magnitude, components was almost E-W so that pixels 0-127 (left field) along the x dimension contained the W component and pixels 128-255 (right field) contained the E component.

The first stage of the reduction process comprised of data editing [19] to remove the saturated, low-power and poorly guided specklegrams. Those specklegrams where the W component overlapped the right field and vice-versa were also edited out. The next stage of the processing consisted of removing any detector non-isoplanicity. Each specklegram was re-mapped to remove the geometric distortion imposed by the electrostatic image tube and, to a lesser degree, the television camera (fig. 1). This was done by means of a bilinear interpolation procedure using a set of regular grid points, shown in fig. 1, as observed with the intensified video detector. The figure also illustrates the 256 X 128 pixel digitization window.

Estimates of the mean seeing r_o and the instantaneous seeing r_e for both data sets were computed from the width of the speckle clouds [19]. Fig. 2a shows the instantaneous seeing (binned into intervals

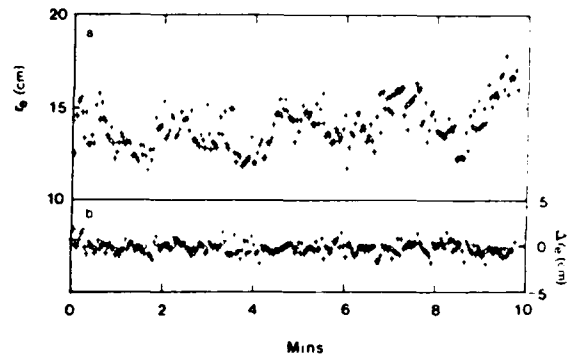


Fig. 2. (a) Measurements of the instantaneous seeing for the LHS component of the 550/30 nm data set. (b) Difference in estimation of the instantaneous seeing for the 550/30 nm data set. The RMS difference is 0.33 cm. Results for 550/10 nm were similar.

~ 1 s) for the W component of the 550/30 nm data set. The difference of r_e between the two components is shown in fig. 2b. The measurements for the other data set were very similar. The mean values of r_e , (and therefore r_o), agree to 1% for the two components of each data set. Thus, the assumption of similar STF's for both components is valid. Furthermore, the variation of the instantaneous seeing is identical for each component indicating the expected strong degree of isoplanicity at spatial frequencies corresponding to the seeing limit $f_o = r_o/\lambda$.

The ensemble average cross-spectrum and power spectra for each component were computed and corrected for the statistical Poisson noise bias [20]. This correction also removed the effects of the detector transfer function. The measured power spectrum $PS_m(f)$ can be written as

$$PS_m(f) = \{PS_o(f) + N\}D(f), \quad (11)$$

where $PS_o(f)$ is the object power spectrum, N the frequency independent noise bias due to Poisson statistics and $D(f)$ the detector transfer function. The oversampling of the diffraction limit allows the factor $ND(f)$ to be measured beyond the cut-off frequency. Experiments [20] have shown that this can be fit with a gaussian to interpolate to the lower frequencies. This was done and the fit was divided out i.e.

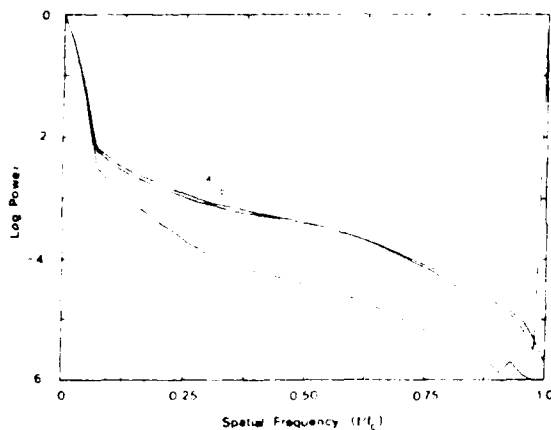


Fig. 3. Averaged radial profiles of the power spectra (a) and (b) and the cross-spectrum (c) for a bandpass of 550/30 nm. The 550, 10 nm were quantitatively similar.

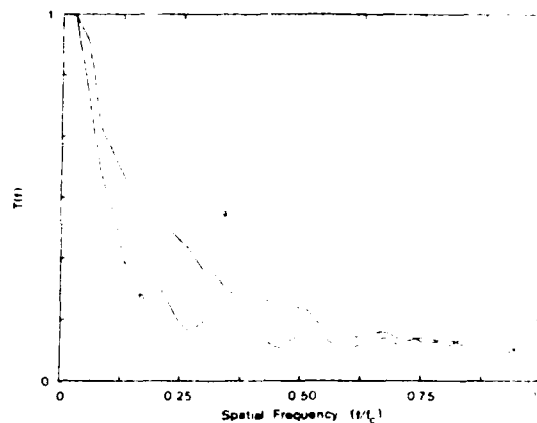


Fig. 4. Orthogonal (a) and parallel (b) components of the isoplanatic parameter for 550/30 nm.

$$PS_m(f)/ND(f) = PS_o(f)/N + 1. \quad (12)$$

The object power spectrum was then recovered by subtracting unity, the factor N being inconsequential because of later normalization.

Fig. 3 shows azimuthally averaged radial profiles of the final power spectra and cross spectrum for the 550/30 nm data set. Similar results were obtained for the other data set. At the low spatial frequencies corresponding to the seeing limit ($f < f_o$) the cross-spectrum agrees well with the power spectra but at higher frequencies it is attenuated in a similar manner to that predicted by Roddier et al. [6]. Generally for $f > 0.9 f_c$, where f_c is the telescope cut off frequency, the accuracy of the debiased power spectra and cross-spectrum is reduced because of uncertainties in calibrating the detector transfer functions.

Figs. 4 and 5 show profiles through the isoplanatic parameter $T(f)$ both (a) orthogonal and (b) parallel to the separation vector for the two data sets. There is almost complete correlation over the seeing dominated low frequencies (cf. the difference in the instantaneous seeing shown in fig. 2b). For higher frequencies, however, the correlation falls off fairly rapidly reaching a threshold value of ~ 0.1 for both data sets. There is a greater correlation for the orthogonal cuts than for the parallel cuts as predicted by earlier

models [10]. Although poorer signal to noise (due to fewer photons), the narrower bandpass tends, as predicted, to give a slightly better high frequency response, especially in the midrange spatial frequencies.

The isoplanatic parameter (3) shows the variation of isoplanicity as a function of the spatial frequency. A quantitative cut-off frequency limited measure of isoplanicity can be obtained by taking the two dimensional integral over f of $T(f)$. We define this as the

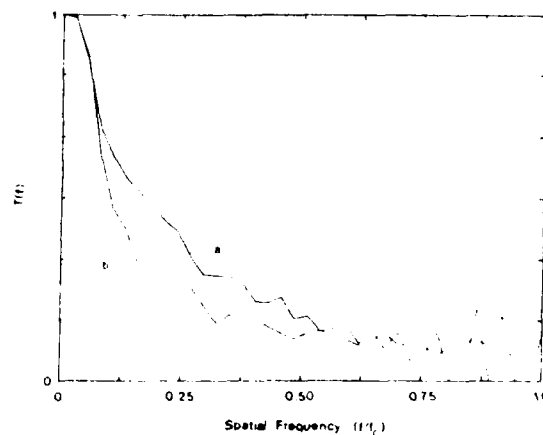


Fig. 5. Same as fig. 4 but for 550/10 nm. It shows enhanced midrange response compared to 550/30 nm.

degree of isoplanicity, $\gamma(f_c)$. It is equivalent to the peak amplitude of the cross-correlation as used by Lohmann and Weigelt [9]. For these two data sets $\gamma(f_c = 20.3 \text{ cycles/second-of-arc})$ was found to be $\sim 13\%$ of its value for complete isoplanicity ($T(f) = 1 \forall f$).

5. Discussion

The isoplanatic parameters $T(f)$ for the two data sets, which were taken under similar seeing conditions ($r_0 = 12 \text{ cm}$ and 14 cm), were found to be very similar to each other. Their shape is qualitatively similar to previous model predictions [10] which showed that the isoplanatic parameter would have significant correlation at the seeing dominated frequencies and would tend to level off to a constant value almost to the diffraction limit. Recent measurements by Ebsenberger and Weigelt [15] also show similar behavior. The asymmetry of $T(f)$, as shown by the quotient of the parallel to orthogonal components, is also predicted by the models.

For the separation, seeing conditions, and telescope used there is evidence that there is measurable correlation in the PSF's nearly to the diffraction limit. Thus, for SH observations, it should be possible to correct the Fourier amplitude of the final image to compensate for the high frequency attenuation when a pair of point sources of similar separation are observed un-

der nearly the same seeing conditions with the same instrumentation.

The limitations of this amplitude reweighting need to be investigated to as large a separation as possible in order to study the spatial frequency limits of the SH process and also to see if models of the isoplanatic parameter can be used when there is not a suitable measurement for the calibration.

We emphasize that as defined the degree of isoplanicity, $\gamma(f_c)$, is a function of the highest spatial frequency measured. Fig. 6 shows the normalized integral over the isoplanatic parameter as a function of f_c , the upper limit of integration. As expected $\gamma(f_c)$ is larger at lower resolution so that comparisons of the degree of isoplanicity can only be valid for measures at the same resolution (regardless of telescope aperture). The almost zero high frequency slope in fig. 6 predicts a significant degree of isoplanicity out to much higher spatial frequencies further emphasizing the need for measurements with larger apertures such as the cophased 6.8 meter MMT as well as over a range of angular separations ($\leq 1'$).

If speckle holography is to be used to obtain accurate diffraction limited images then a thorough study of these effects of non-isoplanatism is necessary. Such a study should investigate the variations of the isoplanatic parameter with respect to the spatial and temporal effects of seeing (r_0 and τ_0 respectively), separation and zenith angle.

Acknowledgement

This work has been supported in part by the U.S. Air Force under AFGL contract F19628-82-0025 and AFOSR grant 82-0020.

References

- [1] R.H.T. Bates, P. Gough and P.J. Napier, *Astron. Astrophys.* 22 (1973) 319.
- [2] N.J. Woolf, *Proc IAU Colloq.* 79, Garching, 1984.
- [3] D. Korff, G. Dryden and R.P. Leavitt, *J. Opt. Soc. Am.* 65 (1975) 1321.
- [4] C.P. Wang, *Optics Comm.* 14 (1975) 200.
- [5] D.L. Fried, *Proc. SPIE* 75 (1976) 20.
- [6] J.H. Shapiro, *J. Opt. Soc. Am.* 66 (1976) 469.
- [7] D.L. Fried, *Optica Acta* 26 (1979) 597.

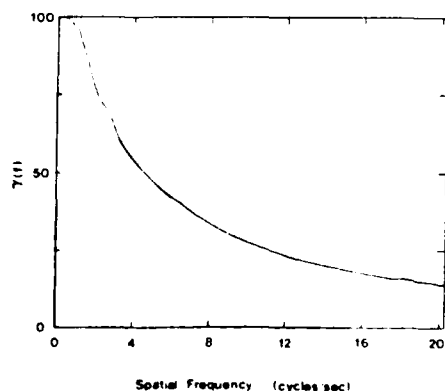


Fig. 6. Frequency dependence of the degree of isoplanicity, γ , for the bandpass 550/30 nm.

- [8] F. Roddier, J.M. Gill and J. Verdon, *J. Optics (Paris)* 13 (1982) 63.
- [9] P. Nisenson and R.V. Stachnik, *J. Opt. Soc. Am.* 68 (1978) 169.
- [10] A.M. Schneidman and D.P. Kato, *J. Opt. Soc. Am.* 68 (1978) 338.
- [11] A.W. Lohmann and G.P. Weigelt, *Optik* 53 (1979) 167.
- [12] G.P. Weigelt, *Optica Acta* 26 (1979) 1351.
- [13] S. Pollaine, A. Buffington and S.F. Crawford, *J. Opt. Soc. Am.* 69 (1979) 84.
- [14] F.N. Hubbard, F.K. Hege, M.A. Reed, P.A. Strittmatter and N.J. Woolf, *Astron. J.* 84 (1979) 1437.
- [15] J. Ebersberger and G. Weigelt, *Optica Acta* (1985).
- [16] F. Roddier, in: *Progress in optics*, ed. E. Wolf (North-Holland, Amsterdam, 1981) p. 320-324.
- [17] G. Weigelt, G. Baer, J. Ebersberger, T. Fleischmann, K.-H. Hofman and R. Ladebeck, *Proc. SPIE* 556 (1985) 238.
- [18] J.C. Hebdon, E.K. Hege and J.M. Beckers, *Proc. SPIE* 556 (1985) 284.
- [19] J.C. Christou, A.Y.S. Cheng, F.K. Hege and C. Roddier, *Astron. J.* (1985).
- [20] F.K. Hege, F.N. Hubbard, P.A. Strittmatter and W.J. Cocke, *Optica Acta* 29 (1982) 701.

Images From Astronomical Speckle Data: Weighted Shift-and-Add Analysis*

J.C.Christou**, E.K.Hege+, J.D.Freeman & E.Ribak

Steward Observatory, University Of Arizona, Tucson, Az 85721

Abstract

We have applied a variant of the Shift-and-Add algorithm originally developed by Lynds, Worden & Harvey to astronomical speckle interferometric data. A set of impulses corresponding in location and magnitude to the local maxima in each specklegram is generated and used to obtain an average speckle by means of a Wiener-type filter deconvolution procedure. This technique yields diffraction limited images which appear to be self calibrating for seeing effects. Realistic point spread functions have been obtained for a number of telescopes at different wavelengths and results are also presented for the resolved red supergiant Alpha Orionis. The limiting signal-to-noise of the technique as indicated by the results presented here suggests a dynamic range of ~ 6 stellar magnitudes with no evidence of residual seeing effects.

Introduction

The Shift-and-Add techniques of image reconstruction were first suggested by Bates & Cady¹ and Lynds, Worden & Harvey². These techniques make use of the observation that an individual speckle is a highly distorted version of the diffraction limited image. Thus the average over the speckles yields an estimate of the true image. For the Bates & Cady approach (hereafter referred to as SAA) the brightest pixel in a specklegram is located and the specklegram is shifted to place this pixel at the frame center where it is co-added with other shifted specklegrams to give the SAA image. This result consists of the estimate of the diffraction limited image superimposed upon a seeing dependent background which is produced from the co-adding of the remainder of the specklegrams. For the Lynds, Worden & Harvey analysis (referred to as LWH) the final result is obtained by using the brighter speckles (typically $\sim 10\%$) in the specklegram. An impulse distribution consisting of unit amplitude delta functions is obtained from the specklegram. This is then cross-correlated with the specklegram which has the effect of shifting each of the bright speckles to the frame center and superimposing. The final image, like that of SAA, consists of an estimate of the true image superimposed upon the seeing produced background.

Both the SAA and LWH techniques yield results which are seeing dependent. Thus the extraction of the diffraction limited image is dependent upon the seeing conditions. When the object size is close to the size of the seeing disk, or has extended low power surrounding a brighter center, the presence of the background makes it difficult to extract the complete image. A technique which is self calibrating for the seeing is therefore preferable.

Weighted Shift-and-Add technique

The technique which we use is derived from that of LWH. Instead of using just the brightest speckles we generate an impulse distribution from all the local maxima in the specklegram above a background noise level. The impulses are each weighted by the amplitude of the corresponding local maxima. For a noise free case, a specklegram can be considered to be the convolution of the diffraction limited image with an infinite set of weighted delta functions representing the random amplitudes and phases of the perturbations of the incoming complex wavefront due to the refractive index variations (caused by turbulence) in the atmosphere.

* Observations reported here were obtained at Kitt Peak National Observatory** and at the Multiple Mirror Telescope Observatory, a joint facility of the University of Arizona and the Smithsonian Institution.

** Visiting Astronomer from Department Of Astronomy, New Mexico State University, Las Cruces, NM88003.

+ Visiting Astronomer, Kitt Peak National Observatory**.

++ Kitt Peak National Observatory is a division of the National Optical Astronomy Observatories, operated by the Association of Universities for Research in Astronomy, Inc., under contract to the National Science Foundation.

We assume that the specklegram, $i(r)$, can be approximated as

$$i(r) \approx o_d(r) * \text{imp}(r) \quad (1)$$

where $\text{imp}(r)$ is the (finite) set of weighted delta functions obtained as described above and $o_d(r)$ is the diffraction limited image which is given by the convolution of the object distribution $o(r)$ with the telescope point spread function $p(r)$. r defines the two dimensional image space and $*$ is used to denote convolution.

If (1) is assumed to be a reasonable representation of a specklegram, then an estimate of the diffraction limited image can be obtained by inverting the equation when the impulse distribution is known. However, a simple deconvolution, which is a complex quotient in Fourier space, suffers from problems caused by zero or small number divisions. Thus we have implemented a weighted deconvolution procedure which, because of the effects of noise bias is similar in form to that of Wiener filtering. Denoting the Fourier transform by the upper case, i.e. $\text{FT}\{i(r)\} = I(f)$, the complex quotient can be written as

$$o_d(f) = \frac{\sum_n [I_n(f) / \text{Imp}_n(f)] W_n(f)}{\sum_n W_n(f)} \quad (2)$$

where f is the spatial frequency domain corresponding to r , n identifies the n 'th specklegram and $W_n(f)$ is its weighting function. This weighting function was chosen to be the power spectrum of the impulse distribution, i.e. $W_n(f) = |\text{Imp}_n(f)|^2$. Substituting this into (2) then gives

$$o_d(f) = \frac{\sum_n I_n(f) \text{Imp}_n^*(f)}{\sum_n |\text{Imp}_n(f)|^2} \quad (3)$$

where $*$ denotes the complex conjugate. The numerator is now the cross-spectrum between the specklegram and the impulse distribution. There is only one complex division which is performed after accumulating the sums in the numerator and the denominator. The latter contains a bias term and is non-zero at all spatial frequencies thus removing the effects of the zero and small number divisions, and acting, in effect, as a Wiener filter.

The Fourier transform of the numerator is the cross-correlation of the specklegram with the impulse distribution and therefore represents a slightly modified LWH image which we call the Weighted Shift-and-Add with cross-correlation (WSA/XC) image. Thus our final result is the weighted deconvolution of the WSA/XC image with the averaged power spectrum of the impulses. It is this term which removes (or minimizes) the seeing background usually found in SAA and LWH images. Because of this process we label this technique as WSA/WD where WD stands for the Weighted Deconvolution.

Measurements

When applied to real data the local maxima in each specklegram do not necessarily represent the positions and amplitudes of the noise-free speckles. In fact, each specklegram is contaminated by Poisson noise so that the images produced by the Shift-and-Add techniques contain a photon 'spike' at the image center. Before interpreting the final result it is therefore important to remove this spike. In the Fourier plane the spike transforms into a noise bias which is colored by the detector response (detector transfer function) and has non-zero power beyond the telescope diffraction limit³. We have found that when this function is fit with a Gaussian (which is a good first order approximation) and divided out, the result gives a Poisson noise bias free image. If the speckles are relatively small (i.e. a few pixels in width) then the Poisson noise will have little effect upon locating the speckle position because the photon event, spread over a splotch of diameter ~ 2 pixels with our detector³, acts as a low pass filter. It has been previously noted⁴ that a Shift-and-Add image is object dependent and is the convolution of the diffraction limited image with an object dependent point spread function for the reduction process. This latter term reflects the accuracy with which the speckle maxima can be located. For low-contrast objects much larger than the detector response, the uncertainty in the locations of the speckle maxima due to the additive Poisson noise blurs the final image. Thus the Poisson noise can affect the

Shift-and-Add images in two ways, (i) by adding a (detector colored) noise spike to the image amplitude and (ii) by blurring the final image due to the errors in the detection of the speckle maxima. For the results presented here, the objects have been chosen to be relatively small (or diffraction limited) with a FWHM ~ 2 to 3 times the detector response. Thus the blurring due to uncertainty in the location of the speckles is minimal.

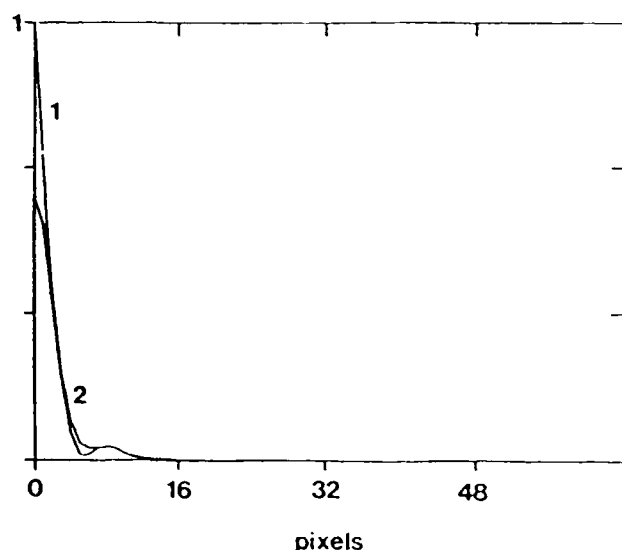


Figure 1: Azimuthally averaged radial profiles for Gamma Orionis (1) with & (2) without the photon spike.

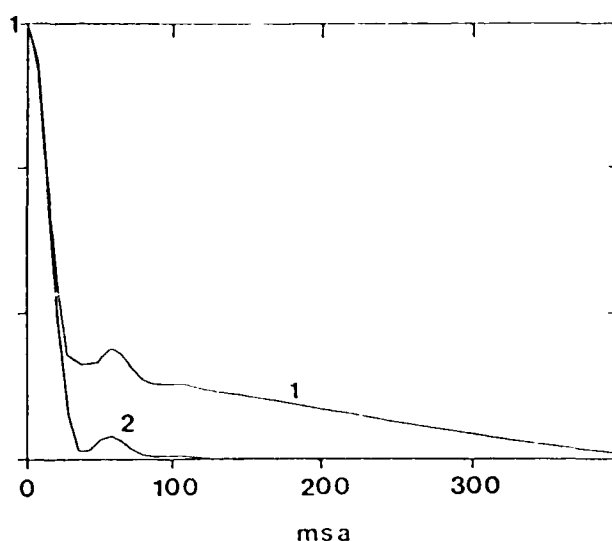


Figure 2: Azimuthally averaged radial profiles for Gamma Orionis (1) WSA/XC & (2) WSA/WD both 'spike' corrected.

We have reduced a number of sets of data of the unresolved star Gamma Orionis and the resolved supergiant Alpha Orionis. This data was taken with the KPNO 4m telescope on February 2 1981. Figure 1 shows the azimuthally averaged radial profiles of the WSA/WD image of Gamma Orionis, at a wavelength of 650nm and a bandpass of 2nm, both with and without the photon spike. As can be seen the image is approximately twice the width of the photon spike thus minimizing the object dependency discussed above. This oversampling of the diffraction limit is in fact required in order to separate the resolved signal and the noise bias as two distinct components. Figure 2 shows the final WSA/WD and WSA/XC images. Note that the seeing produced background, which is clearly visible in the WSA/XC image, is reduced to a flat zero background in the WSA/WD image.

It is important for any image reconstruction or image recovery algorithm that a realistic point spread function be produced when an unresolved object is observed. Figures 3(a)-(c) show the azimuthally averaged WSA/WD radial profiles for Gamma Orionis compared to the computed telescope point spread functions (using a 3.8m aperture with an obscuration ratio of .3). Three different bandpasses were analyzed (a) 650/2 nm, (b) 656.3/.3 nm and (c) 850/10 nm. As can be seen there is good agreement between the models and the images especially for (a) and (c). The width of the central maxima and positions and amplitudes of the secondary maxima compare favorably. The narrow band interference filter used for (b) appears to produce a blurring (defocusing) by comparison to the other data sets.

Figures 3(d)-(f) compare the azimuthally averaged radial profiles for Gamma Orionis with the resolved star Alpha Orionis for the same three bandpasses, (d) 650/2 nm, (e) 656.3/.3 nm and (f) 850/10 nm. For (d) and (e) Alpha Orionis is clearly resolved compared to the measured point spread function. For (f) the disk of the star can be seen to be just resolved and the secondary maximum is becoming visible. At 850 nm the diffraction limit of a 3.8 m aperture corresponds to 46 milli-seconds of arc (msa) whereas the value for the diameter of Alpha Orionis, obtained from extensive analysis of conventional autocorrelation function and power spectrum reductions³, is approximately 42 msa⁵. This profile shows the presence of an extended envelope around the star out to a radius of 300 msa which has also been implied from several other measurements, using a number of related techniques, including differential speckle interferometry⁶.

A data set of Gamma Orionis taken with the fully phased Multiple Mirror Telescope⁷ at a bandpass of 656.30/.13 nm has also been reduced with this technique. Figure 4 shows

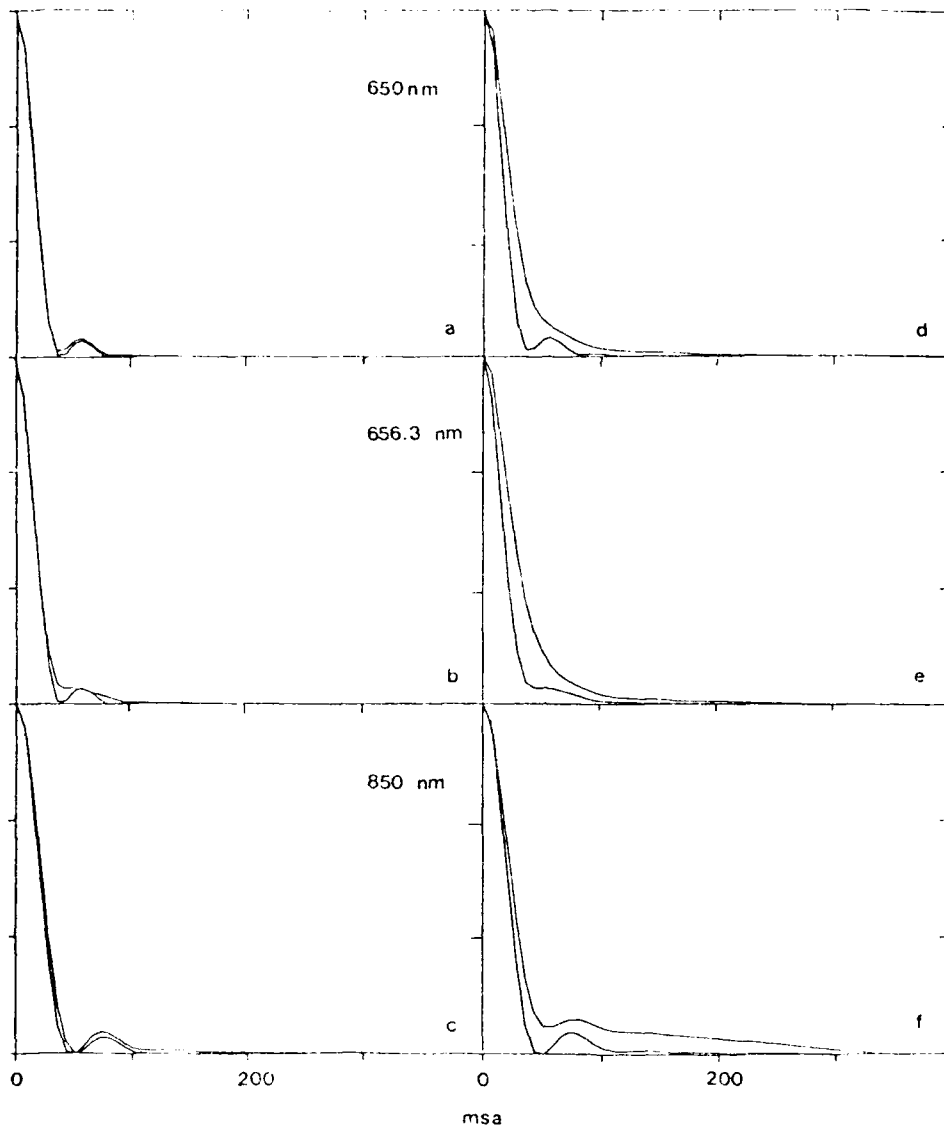


Figure 3: Azimuthally averaged radial profiles of Gamma Orionis (a)–(c) with 3.8m Airy pattern, (d)–(f) with the resolved star Alpha Orionis for the three wavelengths shown.

the final image. The FWHM of the central lobe is consistent with that of an Airy disk for a 6.9 m aperture at the same wavelength (120msa). The six-fold symmetry of the point spread function is seen but its non-uniform appearance indicates imperfect phasing.

Signal-to-noise measurement:

In order to evaluate the ability of the present method to detect faint features, we have performed a series of measurements of the background level in the gamma-ray image relates to the number of frames used for the reconstruction. The results for images of Gamma Orionis at 650 keV are shown in Figure 1. The number of frames used is 4, 8, 16, 32, 64, 128, 256, 512, 1024, 2048, 4096, 8192, 16384, 32768, 65536, 131072, 262144, 524288, 1048576, 2097152, 4194304, 8388608, 16777216, 33554432, 67108864, 134217728, 268435456, 536870912, 1073741824, 2147483648, 4294967296, 8589934592, 17179869184, 34359738368, 68719476736, 137438953472, 274877906944, 549755813888, 1099511627776, 2199023255552, 4398046511104, 8796093022208, 17592186044416, 35184372088832, 70368744177664, 140737488355328, 281474976710656, 562949953421312, 1125899906842624, 2251799813685248, 4503599627370496, 9007199254740992, 18014398509481984, 36028797018963968, 72057594037927936, 144115188075855872, 288230376151711744, 576460752303423488, 1152921504606846976, 2305843009213693952, 4611686018427387904, 9223372036854775808, 18446744073709551616, 36893488147419103232, 73786976294838206464, 147573952589676412928, 295147905179352825856, 590295810358705651712, 1180591620717411303424, 2361183241434822606848, 4722366482869645213696, 9444732965739290427392, 18889465931478580854784, 37778931862957161709568, 75557863725914323419136, 151115727451828646838272, 302231454903657293676544, 604462909807314587353088, 1208925819614629174706176, 2417851639229258349412352, 4835703278458516698824704, 9671406556917033397649408, 19342813113834066795298816, 38685626227668133590597632, 77371252455336267181195264, 154742504910672534362390528, 309485009821345068724781056, 618970019642690137449562112, 1237940039285380274899124224, 2475880078570760549798248448, 4951760157141521099596496896, 9903520314283042199192993792, 19807040628566084398385987584, 39614081257132168796771975168, 79228162514264337593543950336, 158456325028528675187087900672, 316912650057057350374175801344, 633825300114114700748351602688, 1267650600228229401496703205376, 2535301200456458802993406410752, 5070602400912917605986812821504, 10141204801825835211973625643008, 20282409603651670423947251286016, 40564819207303340847894502572032, 81129638414606681695789005144064, 162259276829213363391578010288128, 324518553658426726783156020576256, 649037107316853453566312041152512, 1298074214633706907132624082305024, 2596148429267413814265248164610048, 5192296858534827628530496329220096, 10384593717069655257060992658440192, 20769187434139310514121985316880384, 41538374868278621028243970633760768, 83076749736557242056487941267521536, 166153499473114484112975882535043072, 332306998946228968225951765070086144, 664613997892457936451903530140172288, 1329227995784915872903807060280344576, 2658455991569831745807614120560689152, 5316911983139663491615228241121378304, 10633823966279326983230456482242756608, 21267647932558653966460912964485513216, 42535295865117307932921825928971026432, 85070591730234615865843651857942052864, 170141183460469231731687303715884105728, 340282366920938463463374607431768211456, 680564733841876926926749214863536422912, 1361129467683753853853498429727072845824, 2722258935367507707706996859454145691648, 5444517870735015415413993718908291383296, 10889035741470030830827987437816582766592, 21778071482940061661655974875633165533184, 43556142965880123323311949751266331066368, 87112285931760246646623899502532662132736, 174224571863520493293247799005065324265472, 348449143727040986586495598010130648530944, 696898287454081973172991196020261297061888, 1393796574908163946345982392040522594123776, 2787593149816327892691964784081045188247552, 5575186299632655785383929568162090376495104, 11150372599265311570767859136324180752990208, 22300745198530623141535718272648361505980416, 44601490397061246283071436545296723011960832, 89202980794122492566142873090593446023921664, 178405961588244985132285746181186892047843328, 356811923176489970264571492362373784095686656, 713623846352979940529142984724747568191373312, 1427247692705959881058285969449495136382746624, 2854495385411919762116571938898990272765493248, 5708990770823839524233143877797980545530986496, 11417981541647679048466287755595961091061972992, 22835963083295358096932575511191922182123945984, 45671926166590716193865151022383844364247891968,

AD-A189 295

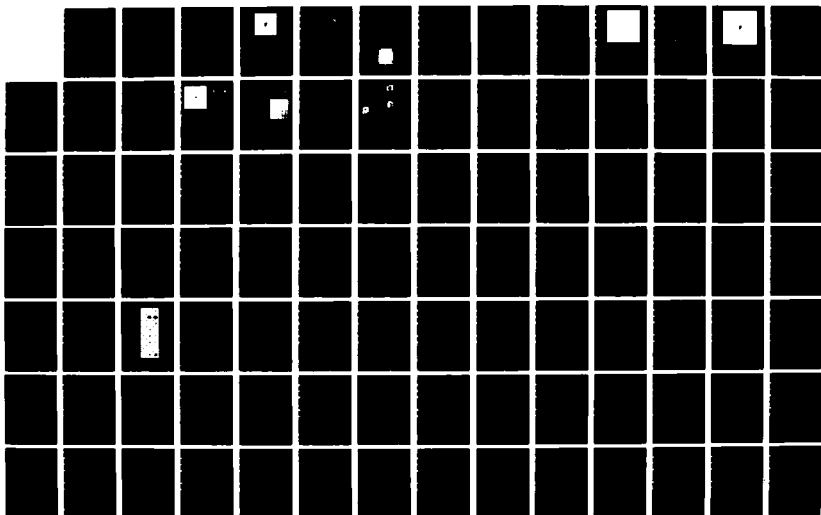
INVESTIGATIONS OF HIGH RESOLUTION IMAGING THROUGH THE
EARTH'S ATMOSPHERE (U) STEWARD OBSERVATORY TUCSON ARIZ
E K HEGE 15 MAR 87 AFGL-TR-87-0097 F19628-84-K-0035

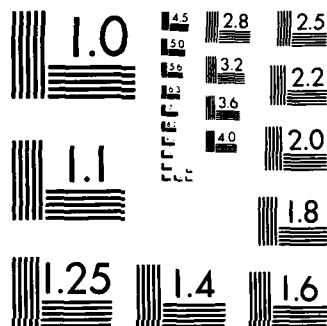
2/4

UNCLASSIFIED

F/G 20/6

NL





MICROCOPY RESOLUTION TEST CHART
NATIONAL BUREAU OF STANDARDS-1963-A

Shift-and-Add images in two ways, (i) by adding a (detector colored) noise spike to the image amplitude and (ii) by blurring the final image due to the errors in the detection of the speckle maxima. For the results presented here, the objects have been chosen to be relatively small (or diffraction limited) with a FWHM ~ 2 to 3 times the detector response. Thus the blurring due to uncertainty in the location of the speckles is minimal.

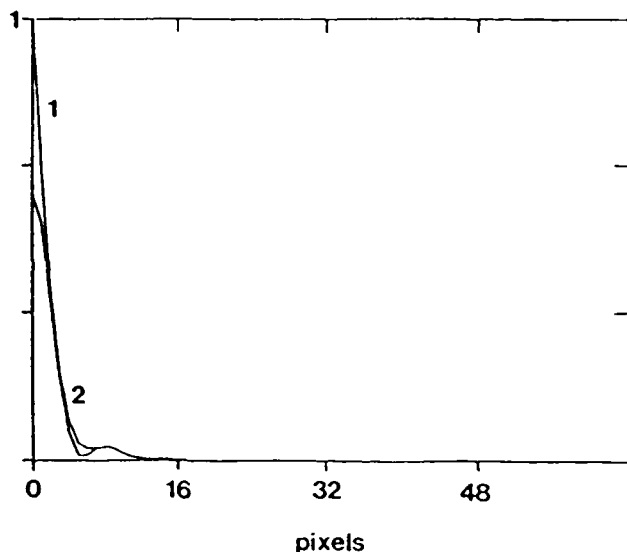


Figure 1: Azimuthally averaged radial profiles for Gamma Orionis (1) with & (2) without the photon spike.

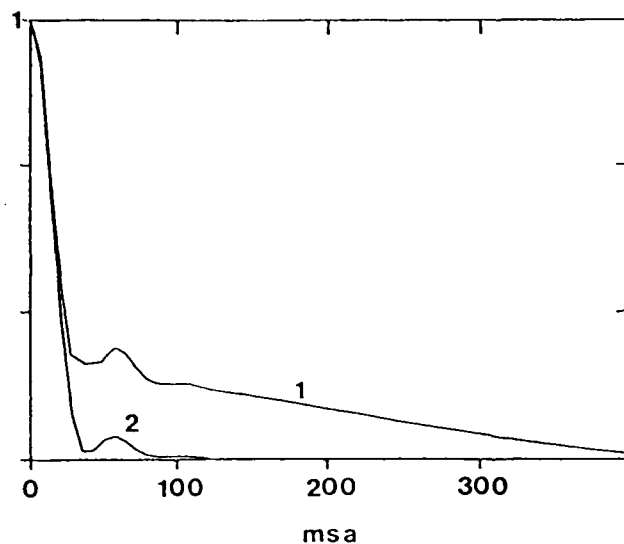


Figure 2: Azimuthally averaged radial profiles for Gamma Orionis (1) WSA/XC & (2) WSA/WD both 'spike' corrected.

We have reduced a number of sets of data of the unresolved star Gamma Orionis and the resolved supergiant Alpha Orionis. This data was taken with the KPNO 4m telescope on February 2 1981. Figure 1 shows the azimuthally averaged radial profiles of the WSA/WD image of Gamma Orionis, at a wavelength of 650nm and a bandpass of 2nm, both with and without the photon spike. As can be seen the image is approximately twice the width of the photon spike thus minimizing the object dependency discussed above. This oversampling of the diffraction limit is in fact required in order to separate the resolved signal and the noise bias as two distinct components. Figure 2 shows the final WSA/WD and WSA/XC images. Note that the seeing produced background, which is clearly visible in the WSA/XC image, is reduced to a flat zero background in the WSA/WD image.

It is important for any image reconstruction or image recovery algorithm that a realistic point spread function be produced when an unresolved object is observed. Figures 3(a)-(c) show the azimuthally averaged WSA/WD radial profiles for Gamma Orionis compared to the computed telescope point spread functions (using a 3.8m aperture with an obscuration ratio of .3). Three different bandpasses were analyzed (a) 650/2 nm, (b) 656.3/.3 nm and (c) 850/10 nm. As can be seen there is good agreement between the models and the images especially for (a) and (c). The width of the central maxima and positions and amplitudes of the secondary maxima compare favorably. The narrow band interference filter used for (b) appears to produce a blurring (defocusing) by comparison to the other data sets.

Figures 3(d)-(f) compare the azimuthally averaged radial profiles for Gamma Orionis with the resolved star Alpha Orionis for the same three bandpasses, (d) 650/2 nm, (e) 656.3/.3 nm and (f) 850/10 nm. For (d) and (e) Alpha Orionis is clearly resolved compared to the measured point spread function. For (f) the disk of the star can be seen to be just resolved and the secondary maximum is becoming visible. At 850 nm the diffraction limit of a 3.8 m aperture corresponds to 46 milli-seconds of arc (msa) whereas the value for the diameter of Alpha Orionis, obtained from extensive analysis of conventional autocorrelation function and power spectrum reductions³, is approximately 42 msa⁵. This profile shows the presence of an extended envelope around the star out to a radius of 300 msa which has also been implied from several other measurements, using a number of related techniques, including differential speckle interferometry⁶.

A data set of Gamma Orionis taken with the fully phased Multiple Mirror Telescope⁷ at a bandpass of 656.30/.13 nm has also been reduced with this technique. Figure 4 shows

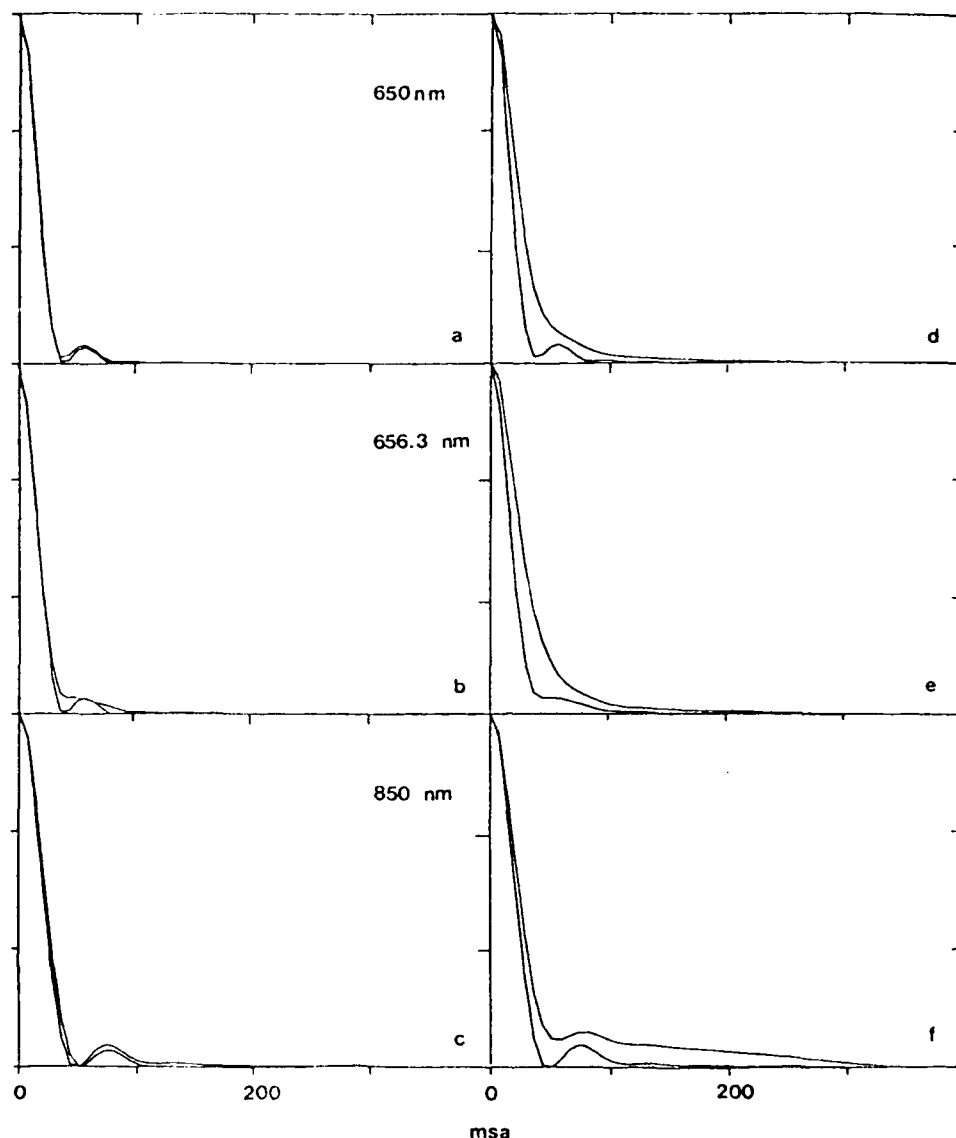


Figure 3: Azimuthally averaged radial profiles of Gamma Orionis (a)-(c) with 3.8m Airy pattern, (d)-(f) with the resolved star Alpha Orionis for the three wavelengths shown.

the final image. The FWHM of the central lobe is consistent with that of an Airy disk for a 6.9 m aperture at the same wavelength (~ 20 msa). The six-fold symmetry of the point spread function is seen but its non-uniform appearance indicates imperfect phasing.

Signal-to-Noise measurements

In order to evaluate the ability of this technique to recover low power information we have performed a series of measurements to show how the background of the WSA/WD image relates to the number of frames processed. Figures 5(a)-(e) show contour plots of images of Gamma Orionis at 650/2 nm for (a) 4, (b) 16, (c) 64, (d) 256 and (e) 1024 frames respectively. There are 25 contour levels at 2% intervals starting from a minimum of 1% to a maximum at the half power point. Each image is comprised of 128 x 128 pixels with an image scale of 7.22 msa/pixel. For only four frames the central maximum is clearly visible and the first Airy ring is beginning to appear above the noise. The background is flat but noisy to a 5% level. As the number of frames is quadrupled the noise level decreases by the expected factor of 2. The final image of 1024 frames, 5(e), shows no background at the 1% level for radii greater than the second Airy ring (~ 30 pixels). The first ring is now clearly complete but lumpy. All our observations show this same effect and we conclude this to be caused by aberrations within our own optical system. A somewhat noisy second Airy ring is also visible. The vertical stripes at the 1% level are caused by clocks related to the video and digitization process.

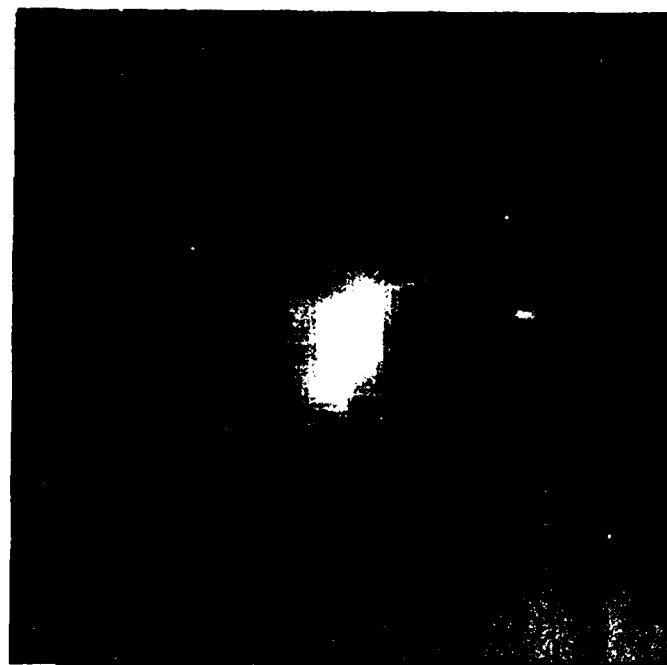


Figure 4: WSA/WO image of Gamma Orionis showing the point spread function of the Large Space Telescope.

The RMS noise for pixels greater than the second Airy ring (1.47 pixels ≈ 2.07 arc) was computed for images comprising of 2, 4, 8, 16, 32, 64, 128, 256, 512, 1024 and 1638 frames. These values are shown plotted on a log-log scale in figure 5(f). There is a linear relationship (on a log scale) between the RMS noise and the number of frames, N , up to 128 frames. A power law of -1.5 plotted through these points shows the expected square root behavior. However, for larger numbers of frames this behavior begins to flatten out showing the limitations imposed on the data due to the instrumentation, e.g., the clock systematics seen in 5(e). We define a S/N measurement as the quotient of this RMS noise to the image maximum. When measured as S/N it is found that this saturation level has a value of ~ 233 indicating a limiting dynamic range for this data set at the wavelengths. A recently discovered secondary of is outside our field of view.

Effects of seeing on WSA/WO images

The results presented in the previous sections show that the WSA/WO image had a better seeing and at the 13 level unlike the SAA and LWH images. This implies that the seeing is corrected for seeing at this level. In order to investigate any residual seeing effect we re-reduced the same 4n data set of Gamma Orionis but this time the specklegrams were selected for different seeing bins⁹. This was done by computing the width of each speckle cloud by means of the second order moment about the centroid to give an instantaneous estimate of the Fried seeing parameter r_0 , which we designate as r_{ij} . Table 1 shows the histogram of the seeing estimate for the data set after elimination of low power and poorly guided specklegrams. The data was sorted into seeing bins of 1/2 arc incremental width. This histogram also shows the (fortunately) fixed seeing during this observing run.

The RMS difference between the images for each seeing bin compared to the best seeing bin, in this case $r_0 = 34-40$ arc, was computed. For all cases it was found that the RMS difference was less than 1% of the maximum of the central peak suggesting that all observations were limited by the instrumental system and not by the seeing. There was a tendency for the difference to get larger when the seeing difference increased but this was at the WSA level and is not considered to be significant because of the diff. systematic noise in the images. A similar investigation for the Alpha Ori. data shows RMS differences of 4.1% over a 1/2 arc range of r_0 .

Contour plots of 60-frame reductions of Gamma Orionis for the 26-30 arc bin and 30-35 arc bin are shown in figures 5(a) and 5(b) respectively. The contour levels are the same as for figures 5(a)-(c). The latter seeing shows a brighter peak at the 13 level but

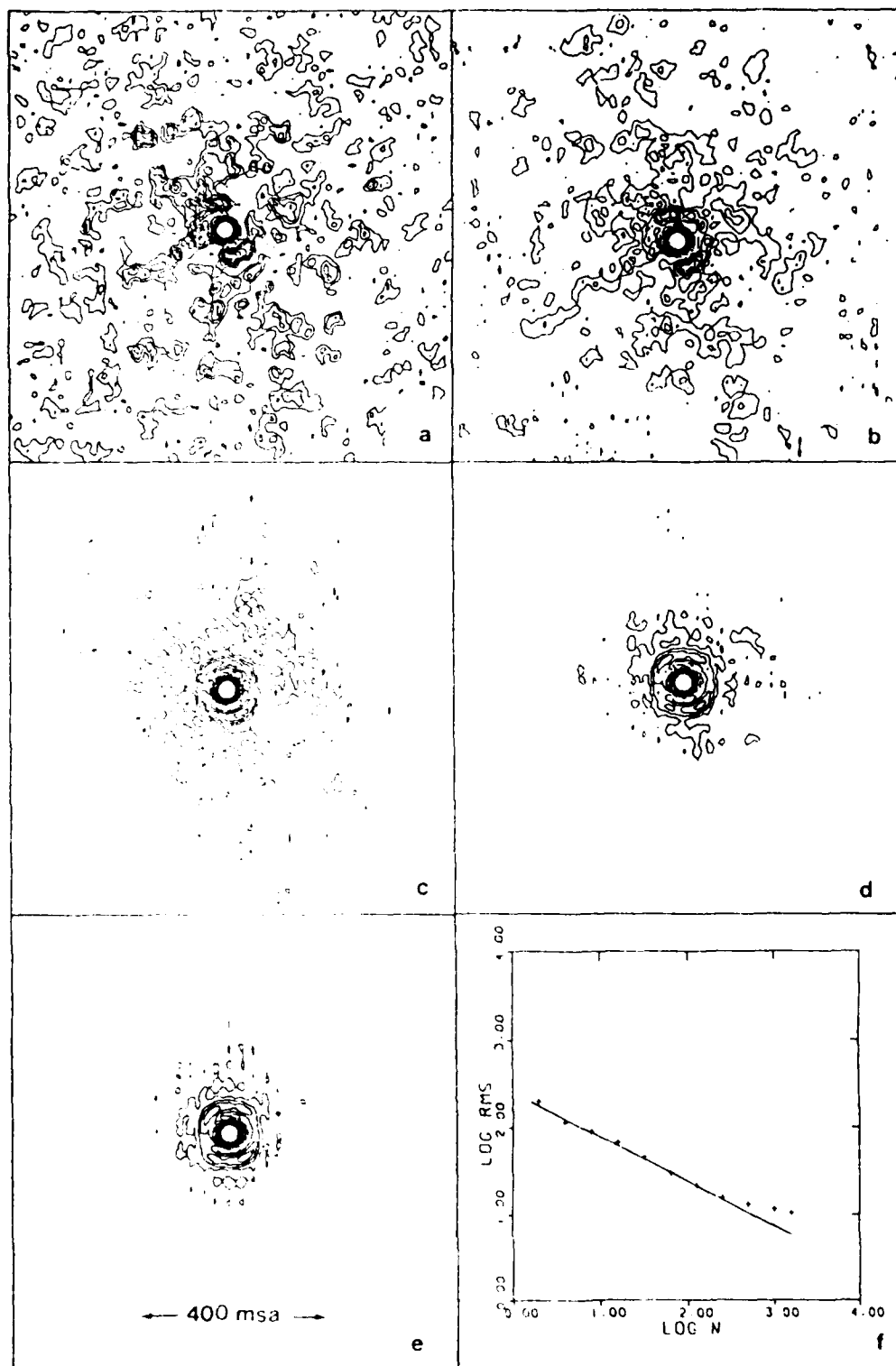


Figure 5: WSA/WD images of Gamma Orionis for (a) 4 (b) 16 (c) 64 (d) 256 & (e) 1024 frames. (f) RMS noise for radii 30 pixels vs. number of frames. The solid line is a power law of -1.5 .

from the 3% contour up the two images are practically identical. Figure 6(c) shows the spatial uniformity of the difference between these two images. The RMS value of this difference is 7.5% with the extremes approaching 1%. As can be seen this difference is

essentially constant with a slight increase for radii < 30 pixels (< 210 mas). The greatest discrepancies are found at the image center. These result from an artifact of the video tape recorder undershoot downline of a bright pixel. The better seeing data has brighter speckles and therefore will tend to have more of an undershoot which shows up as the 1% difference level near the center of the figure.

Seeing Estimate r_e (cm)	No. Of Frames
24 - 25	5
26 - 27	195
28 - 29	486
30 - 31	435
32 - 33	331
34 - 35	83
36 - 37	2

Table 1. Histogram of the Instantaneous Seeing Estimate r_e for the 2 Feb 1981 4m Gamma Orionis data.

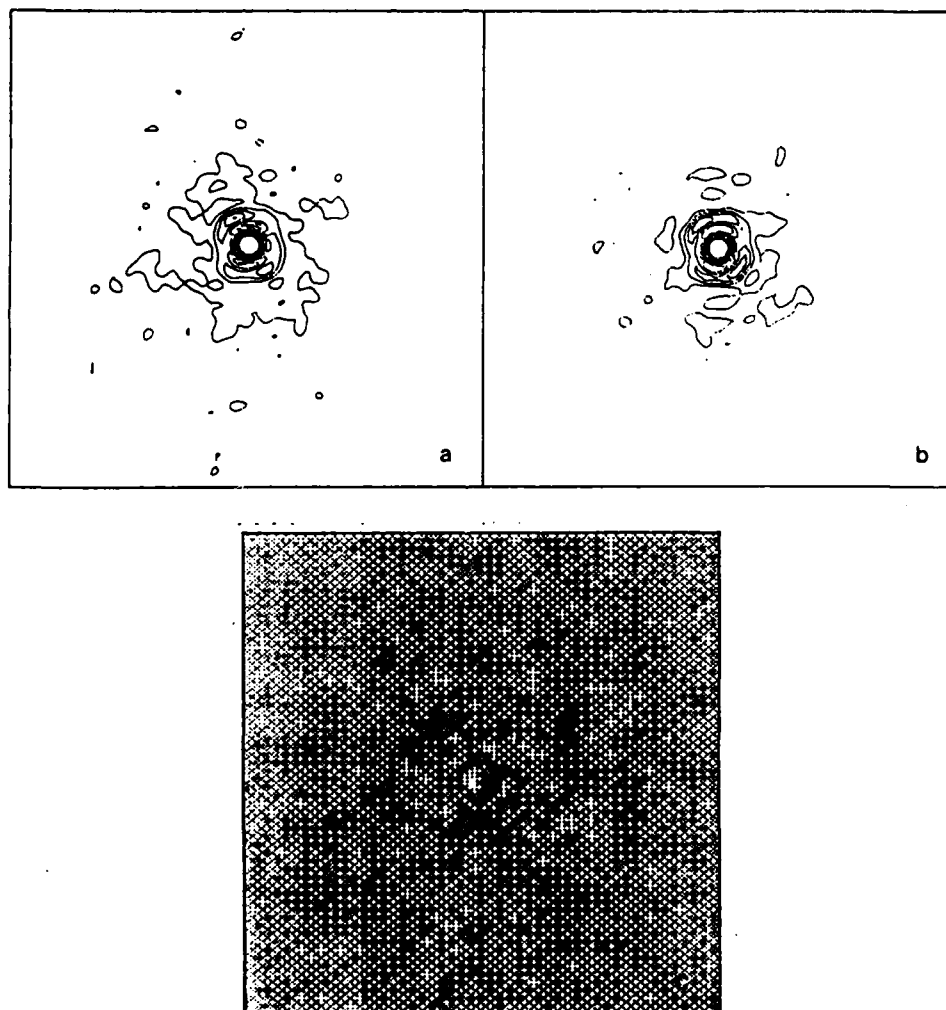


Figure 6: WSA/WD images of Gamma Orionis for 80 frames with $r_e =$ (a) 26-28cm & (b) 34-36cm. (c) is the difference between these two (i.e. (a)-(b)).

Conclusions

We have presented a version of the Shift-and-Add algorithm, for use with astronomical speckle interferometric data, and have demonstrated its ability to produce diffraction limited images which appear to be self calibrating for seeing effects with a dynamic range of up to 6 magnitudes. For the case when the FWHM of the object is a few times greater than the detector point spread function we have been able to obtain realistic telescope point spread functions for an obscured single mirror (i.e. the KPNO 4m) and a phased optical array (6.9m MMT). A resolvable stellar disk has been measured for Alpha Orionis. Preliminary measurements of this disk are in good agreement with power spectral determinations for the same data set and also for other data^{5,6}.

There are, however, limitations to the direct use of this algorithm and Shift-and-Add algorithms in general. The first is the difficulty of detecting the correct speckle maxima. As discussed earlier the detection of a local maximum can easily be affected by the presence of Poisson noise in the specklegram and can produce a blurred image⁴ when the object, and therefore its speckles, is significantly wider than the detector response. The second limitation is the difficulty of recovering a diffraction limited image of an object with multiple maxima where no one maximum dominates. The simplest example of this is a binary star with two unresolved components. In this case these algorithms produce 'ghosts', because of the duplicity of the speckles, tending to mimic autocorrelation functions when the two components have comparable brightnesses. In order to apply Shift-and-Add to such objects so as to be able to produce the correct impulse distributions and therefore diffraction limited images, an improved technique of finding the speckle locations must be applied. One such technique involves the use of matched filters and is discussed in a companion paper¹⁰.

The data presented here are for bright objects where the speckles are easily identifiable. However for faint objects, where there are only a few photons per speckle, the local maximum finding algorithm is no longer valid. The use of matched filter analysis¹⁰ should help identify speckles in the photon limited domain and thus extend this imaging technique to much fainter objects ($m_v > 8$) such as galactic nuclei and QSO's as well as asteroids and other faint solar system objects.

The underlying assumption of all Shift-and-Add techniques is that speckles are highly distorted diffraction limited images. For objects much smaller than the seeing disk this can be considered a reasonable approximation as illustrated by the results presented here. This approximation, however, is empirical and further statistical analysis about the formation of specklegrams is needed to validate this assumption. A statistical analysis of the WSA technique is discussed by Freeman et al.¹¹ in a companion paper.

Acknowledgements

This work was supported in part by the National Science Foundation (grants AST-8201092 and AST-8312976). One of us (E.Ribak) is supported by a Weizmann Fellowship.

References

1. Bates, R.H.T. & F.W.Cady, 'Towards True Imaging by Wideband Speckle Interferometry', Opt.Commun., 32, 368, 1980.
2. Lynds, C.R., S.P.Worden & J.W.Harvey, 'Digital Image Reconstruction Applied to Alpha Orionis', Astrophys.J., 207, 174, 1976.
3. Hege, E.K., E.N.Hubbard, P.A.Strittmatter & W.J.Cocke, 'The Steward Observatory Speckle Interferometry System', Optica Acta, 29, 701, 1982.
4. McDonnell, M.J. & R.H.T.Bates, 'Digital Restoration of an image of Betelgeuse', Astrophys.J., 208, 443, 1976.
5. Cheng, A.Y.S., E.K.Hege, E.N.Hubbard, L.Goldberg, P.A.Strittmatter & W.J.Cocke, 'Diameter and Limb Darkening Measures for Alpha Orionis', in preparation, 1985.
6. Hebden, J.C., J.C.Christou, A.Y.S.Cheng, E.K.Hege, P.A.Strittmatter & J.M.Beckers, 'Two Dimensional Imaging of Alpha Orionis', in preparation, 1985.
7. Hege, E.K., J.M.Beckers, P.A.Strittmatter & D.W.McCarthy, 'The Multiple Mirror Telescope as a Phased Array Telescope', Appl.Opt., 24, 1985.
8. Papaliolios, C., P.Nisenson & S.Ebstein, 'Speckle Imaging with the PAPA Detector', Appl.Opt., 24, 287, 1985.
9. Christou, J.C., A.Y.S.Cheng, E.K.Hege & C.Roddier, 'Seeing Calibration of Optical Astronomical Speckle Interferometric Data', Submitted to Astron.J., 1985.
10. Ribak, E., E.K.Hege & J.C.Christou, 'The Use Of Matched Filters to Identify Speckle Locations', Proc. SPIE, 556-27, 1985.
11. Freeman, J.D., E.Ribak, J.C.Christou & E.K.Hege, 'Statistical Analysis of the Weighted Shift-and-Add Image Reconstruction Technique', Proc. SPIE, 556-40, 1985.

Self-calibrating shift-and-add technique for speckle imaging

Julian C. Christou,* E. Keith Hege,† Jonathan D. Freeman, and Erez Ribak

Steward Observatory, University of Arizona, Tucson, Arizona 85721

Received June 3, 1985; accepted September 24, 1985

An image-reconstruction technique for astronomical speckle interferometric data is described. This variant of the shift-and-add algorithm originally developed by Lynds *et al.* [*Astrophys. J.* **207**, 174 (1976)] utilizes a weighted impulse distribution of speckle positions to extract an average speckle for a data set. This is done by means of a weighted deconvolution procedure, similar in form to a Weiner filter, which deconvolves the specklegram by the impulse distribution. Results show that this method appears to be self-calibrating for seeing effects. It yields point-spread functions, for observations of an unresolved star, that compare quantitatively with computed Airy patterns for both simple apertures and the fully phased multiple mirror telescope array. Images of the resolved object Alpha Orionis show evidence of an extended stellar envelope.

INTRODUCTION

Since its introduction by Labeyrie,¹ speckle interferometry has been used to obtain diffraction-limited information about astronomical objects. In its original form the technique yielded the object distribution power spectrum estimate of a series of short-exposure (~60-msec) images (specklegrams). This power spectrum estimate only contains information about the modulus of the Fourier transform of the object distribution and, without the phases of the Fourier transform, cannot be used to reconstruct the object. A number of techniques have been developed to reconstruct these phases and therefore the object by invoking the fact that for measured data sets a unique phase solution exists.²⁻⁴ These techniques, however, rely on no input phase information. Furthermore, the effects of measured noise on the numerical efficiency of the phase-retrieval algorithms, on which these techniques are based, are not as yet fully understood. A number of other imaging techniques exist that recover the phases from the original specklegrams. Among those are the shift-and-add algorithms^{5,6} and the Knox-Thompson⁷ approach. Comprehensive reviews of speckle imaging techniques can be found in work by Bates⁸ and Dainty.⁹

The preferred imaging techniques are those that use the phase information available in the specklegrams. One such set of methods make use of the intuitive interpretation of a speckle as being a highly distorted version of the diffraction-limited image. Variations of this form of analysis were proposed by Lynds *et al.*³ and Bates and Cady,⁶ and a theoretical study by Hunt *et al.*¹⁰ has shown that diffraction-limited information is preserved. The latter method, known as shift-and-add (SAA) has been further developed by Baguolo.^{11,12} SAA is accomplished by first locating the brightest pixel in each specklegram and then shifting the specklegram to place this pixel at the center of image space. The final image is obtained by averaging over a set of shifted specklegrams. The result is a diffraction-limited image sitting on top of a seeing-produced background, which is produced by averaging over the remaining speckles of the speck-

legram. Thus the SAA image is dependent on the seeing conditions and contains a seeing-dependent bias (background). The Lynds, Worden, and Harvey (LWH) technique utilizes those speckles whose intensities lie above some threshold (typically the brightest 10%) and uses them to generate an impulse distribution of delta functions having unit amplitude at the speckle positions. The LWH image is built up by cross correlating the specklegram with the impulse distribution to shift these brightest speckles to the center of image space. The final result is obtained by averaging over the whole data set. Like the SAA image, the LWH image also comprises two components, the diffraction-limited image on top of a broader seeing background. For both methods the extraction of the diffraction-limited image is dependent on the seeing conditions, and this is made more difficult when the size of the object approaches that of the seeing disk.

METHOD

The technique that we have used is derived from that of LWH but utilizes *all* speckles in the specklegram above a background noise level. The specklegram $i(\mathbf{r})$ is assumed to be approximated by a convolution of the object $o(\mathbf{r})$ with the telescope point-spread function $a(\mathbf{r})$ all convolved with a set of weighted delta functions (impulse distribution), $\text{Imp}(\mathbf{r})$, corresponding to the amplitudes and positions of the speckles, i.e.,

$$i(\mathbf{r}) = [o(\mathbf{r}) * a(\mathbf{r})] * \text{Imp}(\mathbf{r}), \quad (1)$$

where $*$ denotes convolution and \mathbf{r} represents the image domain. This simple model takes into account that the specklegram is formed by random phase shifts in the complex wave front due to refractive-index variations in the atmosphere. Thus a specklegram can be considered to be a set of highly distorted diffraction limited images within a region defined by the seeing disk. Therefore, if this assumption is true, the diffraction-limited image can be obtained by deconvolving the specklegram by the impulse distribution.

The impulse distribution can be obtained by locating all the speckle maxima and setting the amplitudes of the delta functions equal to that of the corresponding speckle amplitudes. Thus, when the specklegram Eq. (1) is deconvolved by the impulse distribution, the result is, to a first approximation, the diffraction-limited image of the object. In this analysis we used the local maxima in the specklegrams to define the amplitude and position of the impulses.

To avoid the problems inherent in regular deconvolution techniques, i.e., division by zero or small numbers in the complex quotient, we have implemented a weighted deconvolution procedure similar in form to a Wiener filter. Denoting the Fourier transform by uppercase letters, then the complex quotient can be written as

$$FT\{o(\mathbf{r})^*a(\mathbf{r})\} = \frac{\sum_n [I_n(\mathbf{f})/\text{Imp}_n(\mathbf{f})] W_n(\mathbf{f})}{\sum_n W_n(\mathbf{f})}, \quad (2)$$

where \mathbf{f} is the spatial frequency domain corresponding to \mathbf{r} , n identifies the n th specklegram, and $W_n(\mathbf{f})$ its weighting.

In order to minimize the number of complex divisions and to obtain a function that is always nonzero we chose the weighting function to be the power spectrum of the impulse distribution, i.e., $W_n(\mathbf{f}) = |\text{Imp}_n(\mathbf{f})|^2$. The numerator in Eq. (2) then becomes the cross spectrum between the specklegram and the impulse distribution, thus reducing the number of complex quotients to one, that of the ensemble average (sum) of the cross spectra and the impulse power spectra, so that Eq. (2) can be rewritten as

$$FT\{o(\mathbf{r})^*a(\mathbf{r})\} = \frac{\sum_n I_n(\mathbf{f}) \text{Imp}_n^*(\mathbf{f})}{\sum_n |\text{Imp}_n(\mathbf{f})|^2}. \quad (3)$$

The averaged impulse-distribution power spectrum contains a bias term due to Poisson statistics and is therefore nonzero at all frequencies. Because we use a weighted impulse distribution and a weighted deconvolution technique we call this analysis weighted shift-and-add/weighted deconvolution (WSA/WD).

It is interesting to note that the numerator of Eq. (3) is the Fourier transform of the cross correlation of the specklegram with the weighted impulse distribution and therefore is a minor modification to the LWH technique, which we denote by WSA/XC.

RESULTS

The WSA images, as well as the images from other SAA techniques, contain a photon spike at the center owing to the photon noise in the specklegrams. This can be removed by a correction applied in the Fourier plane. At the same time, the effects of the detector transfer function can also be removed. Hege *et al.*¹³ have reported that the detector response is a sharp Gaussian. In the spatial frequency domain this becomes a broad Gaussian, which is a multiplicative term because of the convolution of the detector response with the signal. A Gaussian is fitted to frequencies beyond the telescope cutoff ($f > D/\lambda$), where D is the diameter of the

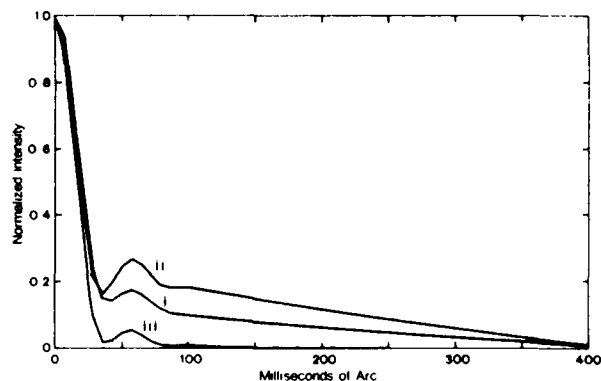


Fig. 1. Radial average profiles for Gamma Orionis: (i) SAA, (ii) WSA/XC, and (iii) WSA/WD at $\lambda = 650.0/0.2$ nm using the KPNO 4-m telescope.

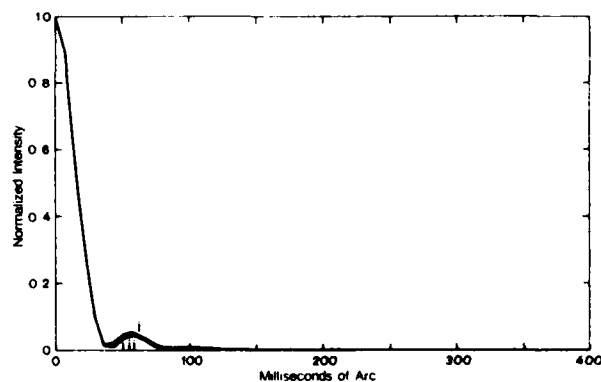


Fig. 2. Radial averaged profiles for (i) WSA/WD Gamma Orionis and (ii) Airy pattern of 3.8-m aperture with a 1:3 central obscuration at $\lambda = 650.0/0.2$ nm.

aperture and λ is the observing wavelength. This Gaussian is divided out, and the remaining bias of unity is subtracted. This effectively removes the photon-noise biased-induced photon spike from these images.

Figure 1 shows the radial averaged profiles for the SAA, WSA/XC, and WSA/WD images for the point-source Gamma Orionis observed at the Kitt Peak National Observatory (KPNO) 4-m Mayall telescope with a bandpass of 2.0 nm centered on 650.0 nm using the Steward Observatory (SO) speckle camera.¹³ Comparison of these profiles clearly shows the seeing-produced background in both the SAA and WSA/XC reductions to be substantially reduced to the flat background shown in the WSA/WD profile. Figure 2 compares the same WSA/WD result to that of an Airy profile for a 3.8-m aperture with a central obscuration ratio of 1:3, which is the case for the Mayall telescope. These two profiles compare very favorably: the width of the central lobe and the position and amplitude of the first Airy ring agree to within a few percent. Figure 3 shows the theoretical Airy pattern and the reconstructed Airy pattern image from which the radial-averaged profiles were computed. The rms difference between these two images is $\sim 0.2\%$ that of the peak for radii greater than the first Airy ring (the region where the seeing is dominant in the SAA and WSA/XC images). The effects of a nonuniform Airy pattern give an rms difference of $\sim 1.9\%$ for radii within the first Airy ring.

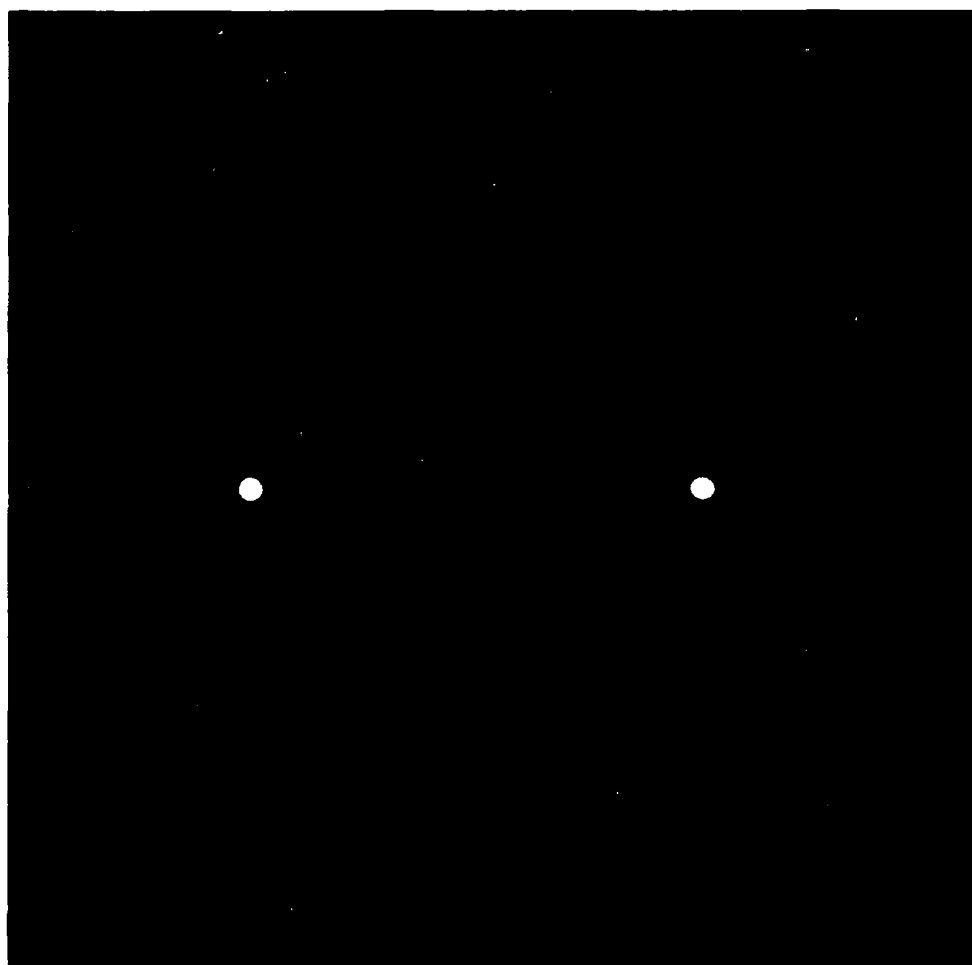


Fig. 3. (Left) Theoretical and (right) measured Airy patterns of the KPNO 4-m telescope. (See Fig. 2 for parameters.) Scale, 7.2 msa/pixel.

WSA/WD radial profiles for the extended object Alpha Orionis and the unresolved point sources Gamma and Epsilon Orionis, taken with the SO 2.3-m telescope, are shown in Fig. 4. The observing bandpass of 0.3 nm was centered on 854.2 nm. The point-source observations of Gamma and Epsilon Orionis bracketed the measurements of Alpha Orionis. They give similar profiles, the difference indicating a residual sensitivity of the technique to differences in the data sets. At $\lambda = 850$ nm the diffraction limit of the 2.3 m is 76 milliseconds of arc (msa) so that the ~ 42 -msa disk of Alpha Orionis¹⁴ remains unresolved, as is seen in the figure. The Alpha Orionis profile shows an extension, most probably due to the presence of a circumstellar gaseous envelope, up to a radius of ~ 300 msa. This measurement is commensurate with power-spectrum analysis of a 4-m data set at the same wavelength as reported by Goldberg *et al.*¹⁵ A circumstellar envelope has also been detected with a rotation shearing interferometer¹⁶ at an observing wavelength of 535 nm.

Reconstructed images of both Alpha Orionis and Gamma Orionis are shown in Fig. 5. These observations were taken with the KPNO telescope with bandpasses of 656.3/0.3 nm and 650.0/2.0 nm. The Gamma Orionis images show a lumpy Airy ring at a NE SW position angle [Figs. 5b and 5e]. By comparison with the point source, Alpha Orionis is clearly resolved by this larger telescope (Figs. 5a and 5d).

and the images also show structure at the same position angle as the lumpy Airy ring.

In order to remove the effects of the lumpy point-spread function (PSF) from these Alpha Orionis images, we used the CLEAN¹⁷ algorithm. CLEAN has been successfully applied in the past to radio interferometric observations in order to remove artifacts and systematics due to the interfer-

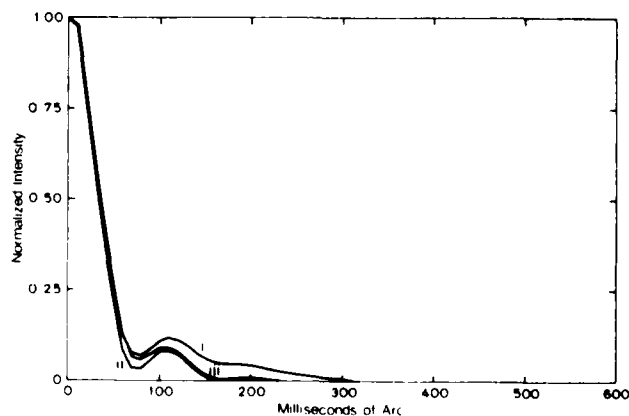


Fig. 4. WSA/WD radial averaged profiles of (i) Alpha Orionis, (ii) Epsilon Orionis, and (iii) Gamma Orionis taken with the Steward Observatory 2.3-m telescope at $\lambda = 854.2 \pm 0.3$ nm.

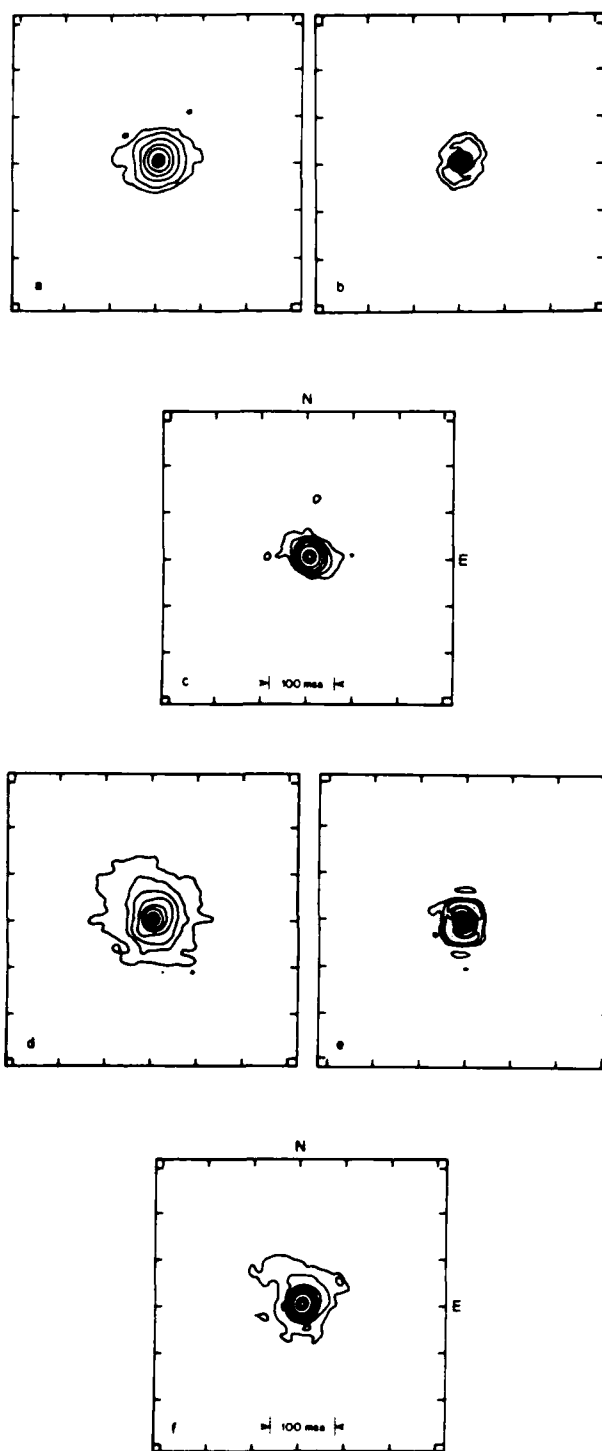


Fig. 5. Reconstructed images of Alpha and Gamma Orionis. a, WSA/WD Alpha Orionis ($\lambda = 656.3/0.3$ nm); b, WSA/WD Gamma Orionis ($\lambda = 656.3/0.3$ nm); c, a cleaned by b as described in text; d-f, as before but at $\lambda = 650.0/2.0$ nm. All observations at KPNO 4-m telescope.

ometer beam. It is an iterative process that locates the brightest pixel in the dirty map (resolved object image), and at this location it subtracts the dirty beam (point-source image), which is set to be a factor (loop gain, G) of the current peak in the dirty map. The process is repeated on

the residual. The algorithm generates an array of delta functions of varying intensities in such a way that the dirty map can be considered to be the weighted sum of the dirty beam at the delta-function locations plus the final residual. The iterations stop either when the intensity of the final residual is at the image noise level or when a certain number of negative delta functions is reached. The clean map is generated by convolving the delta-function array with a clean beam, which is usually obtained by fitting a Gaussian to the central component of the dirty beam. The quality of the final clean map depends on both the value of G and the number of iterations.

The cleaned images of Alpha Orionis are shown in Figs. 5c and 5f. The loop gain was set at 70%, and 50 iterations were used. These images show the removal of the lumpy Airy ring and indicate a nonuniform structure of the stellar envelope.

The use of CLEAN is further demonstrated in the next figure. A data set of Alpha Orionis and Epsilon Orionis taken with the SO 2.3-m telescope at a wavelength of 650 nm was reduced using the WSA/XC algorithm. These images are shown in Figs. 6a and 6b, respectively. They still include the photon spike, but the seeing background was removed by approximating it by a Gaussian and then subtracting. Both of these images contain, in addition to the noise spike, a video artifact due to the nonlinear response of the TV camera. This undershoot is produced by the video cassette recorder electronics after scanning across a bright speckle. The Epsilon Orionis image was used as a dirty beam to CLEAN the Alpha Orionis image (Fig. 6c) as described above. The loop gain was also set to 70% for 50 iterations. This clean image shows the removal of the undershoot artifact and also shows the presence of a probable stellar envelope with a position angle similar to that seen in the 4-m data set. The astrophysical interpretation of these

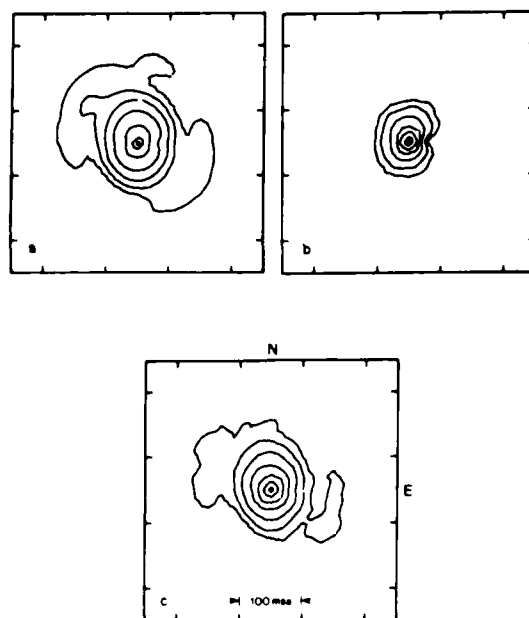


Fig. 6. Reconstructed images of Alpha and Gamma Orionis. a, WSA/XC Alpha Orionis; b, WSA/XC Gamma Orionis; c, a cleaned by b as described in text. Observations at SO 2.3-m telescope at $\lambda = 650.0/2.0$ nm.

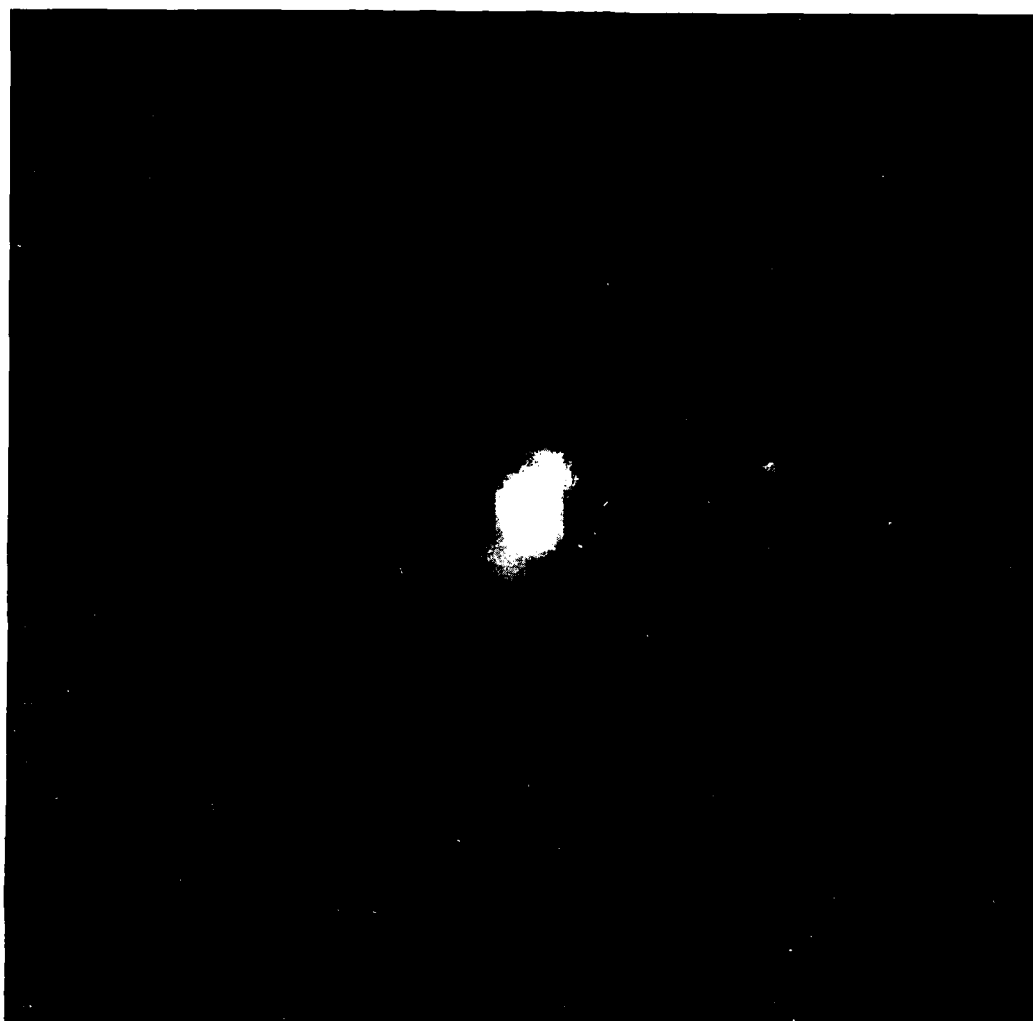


Fig. 7. WSA WD image of Gamma Orionis taken with the fully phased MMT at $\lambda = 656.3/0.3$ nm. The artifacts are a result of the apodizing window caused by the video digitizer. This is the MMT PSF. Scale, 5 msa/pixel.

and other Alpha Orionis images is currently in preparation for publication elsewhere.¹⁷

Finally, Fig. 7 shows the PSF of the fully phased multiple mirror telescope (MMT) at a bandpass of 0.3 nm centered on 656.3 nm, using Gamma Orionis as an unresolvable source. The FWHM of the central lobe ~ 20 msa, which is consistent with that of an Airy pattern for a 6.9 m aperture at the same wavelength. The sidelobes show the sixfold symmetry expected, but nonuniform amplitudes indicate imperfect phasing. The computed response published by Angel¹⁸ can be compared favorably with this result. The potential utility of the MMT as a phased array high-resolution imaging telescope is discussed further by Hogg *et al*.¹⁹

DISCUSSION

The WSA technique appears to produce realistic PSFs for three telescopes: the SOFAR, the KPNO 4 m, and the fully phased MMT. The results for the extended object, Gamma Orionis, are consistent with the results of the WSA technique for the point source case. The disk images of Gamma Orionis are consistent with the other measures of the resolution of the telescope, but the comparison with

other SAA analyses is its apparent seeing self-calibration, which produces a flat background (i.e., no residual seeing bias), thus permitting realistic interpretation of extended low-power structure such as stellar envelopes. This self-calibration is due to the selection of all speckles and the weighting of the impulses so that there is no residual when a speckle is deconvolved by its corresponding impulse. The use of the CLEAN algorithm allows the systematics of the telescope PSF (and even serious video artifacts) to be removed when an unresolved point source (dirty beam) is observed.

Throughout this analysis it has been assumed that both the resolved and the unresolved objects produce object independent WSA WD images. However, it was previously noted that SAA images are object dependent owing to the convolution of the diffraction limited object with an object-dependent PSF.¹⁴ The latter term can arise for a number of reasons. The presence of Poisson noise in the data may affect the accuracy with which the speckle maxima are located. This will be especially true for low-contrast extended objects, and the net effect is a blurring of the final image. For the case of a binary star each speckle will have two maxima that lead to the presence of ghosts in the final image. The data presented in this paper consist of single maximum

high-contrast speckles and appear not to suffer from the effect of the object-dependent point-spread function. A new method of locating the speckle positions is needed for the cases of multiple-peaked objects and in the presence of strong Poisson noise. A matched-filter approach has been applied and is reported elsewhere.²² It is hoped that this will also allow extension of the WSA/WD analysis to the faint object (photon-limited) domain, e.g., quasi-stellar objects and galactic nuclei.

The results presented here represent a preliminary analysis of a much larger data base, which is currently being studied for astrophysical content.¹⁸

ACKNOWLEDGMENTS

We wish to thank Andreas Eckart for the application of the CLEAN algorithm. We would also like to thank R. H. T. Bates for many useful discussions, which enabled us to understand the properties of SAA images.

The research of E. Ribak is supported by a Weizmann Fellowship. This work was supported in part by Air Force Geophysics Laboratory contract F19628-82-0025, U.S. Air Force Office of Scientific Research grant 82-0020, and National Science Foundation grants AST-8201092 and AST-8312976.

Observations reported here were obtained at the Multiple Mirror Telescope Observatory, a joint facility of the University of Arizona and the Smithsonian Institution, and at Kitt Peak National Observatory.

Kitt Peak National Observatory is a division of the National Optical Astronomy Observatories, operated by the Association of Universities for Research in Astronomy, Inc., under contract to the National Science Foundation.

* Visiting Astronomer from Department of Astronomy, New Mexico State University, Las Cruces, New Mexico 88003.

† Visiting Astronomer at Kitt Peak National Observatory.

REFERENCES

1. A. Labeyrie, "Attainment of diffraction limited resolution in large telescopes by Fourier analyzing speckle patterns in a star image," *Astron. Astrophys.* **6**, 85 (1970).
2. J. R. Fienup, "Phase retrieval algorithms: a comparison," *Appl. Opt.* **21**, 2758 (1982).
3. R. H. T. Bates and W. R. Fright, "Composite two-dimensional

- phase restoration procedure," *J. Opt. Soc. Am.* **73**, 358 (1983).
- "Reconstructing images from their Fourier intensities," in *Advances in Computer Vision and Image Processing*, T. S. Huang, ed. (JAI, Greenwich, Conn., 1984, vol. 1, Chap. 5).
4. S. F. Gull and G. J. Daniell, "Image reconstruction from incomplete and noisy data," *Nature* **272**, 686 (1978).
5. C. R. Lynds, S. P. Worden, and J. W. Harvey, "Digital image reconstruction applied to Alpha Orionis," *Astrophys. J.* **207**, 174 (1976).
6. R. H. T. Bates and F. W. Cady, "Towards true imaging by wideband speckle interferometry," *Opt. Commun.* **32**, 365 (1980).
7. K. T. Knox and B. J. Thompson, "Recovery of images from atmospherically degraded short-exposure photographs," *Astrophys. J.* **193**, L45 (1974).
8. R. H. T. Bates, "Astronomical speckle imaging," *Phys. Rep.* **90**, 203 (1982).
9. J. C. Dainty, "Stellar speckle interferometry," in *Laser Speckle and Related Phenomena*, Vol. 9 of Topics in Applied Physics (Springer-Verlag, Berlin, 1984), Chap. 7.
10. B. R. Hunt, W. R. Fright, and R. H. T. Bates, "Analysis of the shift-and-add method for imaging through turbulent media," *J. Opt. Soc. Am.* **73**, 456 (1983).
11. W. G. Bagnuolo, "The application of Bates' algorithm to binary stars," *Mon. Not. R. Astron. Soc.* **200**, 1113 (1982).
12. W. G. Bagnuolo, "Image restoration by the shift-and-add algorithm," *Opt. Lett.* **10**, 200 (1985).
13. E. K. Hege, E. N. Hubbard, P. A. Strittmatter, and W. J. Cocke, "The Steward Observatory speckle interferometry system," *Opt. Acta* **29**, 701 (1982).
14. A. Y. S. Cheng, P. A. Strittmatter, E. K. Hege, E. N. Hubbard, L. Goldberg, and W. J. Cocke, "Diameter and limb-darkening measures for Alpha Orionis," submitted to *Astrophys. J.*
15. L. Goldberg, E. K. Hege, E. N. Hubbard, P. A. Strittmatter, and W. J. Cocke, "Speckle interferometry of Alpha Orionis: preliminary results," in *Second Cambridge Workshop on Cool Stars, Stellar Systems and the Sun*, M. S. Giampapa and L. Golub, eds., SAO Special Report 392 (Smithsonian Astrophysical Observatory, Cambridge, Mass., 1982), Vol. 1, p. 131.
16. C. Roddier and F. Roddier, "High angular resolution observations of Alpha Orionis with a rotation shearing interferometer," *Astrophys. J.* **270**, L23 (1985).
17. J. A. Högbom, "Aperture synthesis with a non-regular distribution of interferometer baselines," *Astron. Astrophys. Suppl.* **15**, 417 (1974).
18. J. C. Hebdén, J. C. Christou, A. Y. S. Cheng, E. K. Hege, P. A. Strittmatter, J. M. Beckers, and H. P. Murphy, "Two dimensional images of Alpha Orionis," submitted to *Astrophys. J.*
19. R. P. Angel, "Very large ground-based telescopes for optical and IR astronomy," *Nature* **295**, 651 (1982).
20. E. K. Hege, J. M. Beckers, P. A. Strittmatter, and D. W. McCarthy, "The multiple mirror telescope as a phased array telescope," *Appl. Opt.* **24**, 2565 (1985).
21. M. J. McDonnell and R. H. T. Bates, "Digital restoration of an image of Betelgeuse," *Astrophys. J.* **208**, 443 (1976).
22. E. Ribak, E. K. Hege, and J. C. Christou, "The use of matched filters to identify speckle locations," *Proc. Soc. Photo-Opt. Instrum. Eng.* **556**, 196 (1985).

Images from astronomical speckle data: weighted shift-and-add analysis

J. C. Christou

E. Ribak

E. K. Hege

J. D. Freeman

Steward Observatory
University of Arizona
Tucson, Arizona 85721

Abstract. We have applied a variant of the shift-and-add algorithm originally developed by Lynds, Worden, and Harvey [Astrophys. J. 207, 174 (1976)] to astronomical speckle interferometric data. A set of impulses corresponding in locations and magnitudes to the local maxima in each specklegram is generated and used to obtain an average speckle by means of a Wiener-type filter deconvolution procedure. This technique yields diffraction-limited images that appear to be self-calibrating for seeing effects. Realistic point spread functions have been obtained for a number of telescopes at different wavelengths, and results are also presented for the resolved red supergiant Alpha Orionis. The limiting signal-to-noise ratio of the technique as indicated by the results presented here suggests a dynamic range of ≈ 6 stellar magnitudes, with no evidence of residual seeing effects. A matched filter technique is demonstrated for use in locating the speckles of complicated objects or for objects dominated by photon noise.

Subject terms: speckle; speckle imaging; shift-and-add; seeing calibration; astronomy.

Optical Engineering 25(6), 724-730 (June 1986).

CONTENTS

1. Introduction
2. Weighted shift-and-add technique
3. Measurements
4. Signal-to-noise measurements
5. Effects of seeing on WSA/WD images
6. Locating speckles using a matched filter technique
7. Conclusions
8. Acknowledgments
9. References

1. INTRODUCTION

The shift-and-add techniques of image reconstruction were first suggested by Bates and Cady¹ and Lynds, Worden, and Harvey.² These techniques make use of the observation that an individual speckle is a highly distorted version of the diffraction-limited image. Thus, the average over the speckles yields an estimate of the true image. For the Bates and Cady approach (hereafter referred to as SAA), the brightest

pixel in a specklegram is located, and the specklegram is shifted to place this pixel at the frame center, where it is co-added with other shifted specklegrams to give the SAA image. This result consists of the estimate of the diffraction-limited image superimposed upon a seeing-dependent background produced from co-adding the remainder of the specklegrams. For the Lynds, Worden, and Harvey analysis (referred to as LWH), the final result is obtained by using the brighter speckles (typically $\sim 10\%$) in the specklegram. An impulse distribution consisting of unit amplitude delta functions is obtained from the local maxima representing these brighter speckles. This is then cross-correlated with the specklegram, which has the effect of shifting each of the bright speckles to the frame center and superimposing them. The final image, like that of the SAA technique, consists of an estimate of the true image superimposed upon the seeing-produced background.

Both the SAA and LWH techniques yield results that are seeing dependent. Thus, the extraction of the diffraction-limited image is dependent upon the seeing conditions. When the object size is close to the size of the seeing disk or has extended low power surrounding a brighter center, the presence of the background makes it difficult to extract the complete image. A technique that is self-calibrating for the seeing is therefore preferable.

Invited Paper ST-110 received Nov. 5, 1985; revised manuscript received Jan. 28, 1986; accepted for publication March 27, 1986; received by Managing Editor March 31, 1986. This paper is a revision of Paper 556-36 which was presented at the SPIE International Conference on Speckle, Aug. 20-23, 1985, San Diego, Calif. The paper presented there appears (unrefereed) in SPIE Proceedings Vol. 556.

© 1986 Society of Photo-Optical Instrumentation Engineers.

The technique we use was discussed in an earlier paper.³ The present paper emphasizes the signal-to-noise measurements, the effects of seeing variability, and the implementation of a matched filter analysis to locate the speckles for objects that have more than one local maximum (which otherwise would be multiply detected). The matched filter approach may also be used for objects where the speckle location is poorly determined due to the availability of only a few photons per speckle.

2. WEIGHTED SHIFT-AND-ADD TECHNIQUE

The weighted shift-and-add technique is a logical extension to that of LWH, but instead of using just the brightest speckles, we generate an impulse distribution from *all* of the local maxima in the specklegram above a background noise level. Each impulse is weighted by the amplitude of the corresponding local maximum. For a noise-free case, a specklegram can be considered to be the convolution of the diffraction-limited image with an infinite set of weighted delta functions representing the random amplitudes and phases of the perturbations of the incoming complex wavefront due to the refractive index variations (caused by turbulence) in the atmosphere.

We assume that the specklegram $u(r)$ can be approximated as

$$u(r) \approx o_d(r) \otimes \text{imp}(r), \quad (1)$$

where $\text{imp}(r)$ is the (finite) set of weighted delta functions obtained as described above, $o_d(r)$ is the diffraction-limited image given by the convolution of the object distribution $o(r)$ with the telescope point spread function $p(r)$, r defines the two-dimensional image space, and \otimes denotes convolution.

If Eq. (1) is assumed to be a reasonable representation of a specklegram, then an estimate of the diffraction-limited image can be obtained by inverting the equation when the impulse distribution is known. However, a simple deconvolution, which is a complex quotient in Fourier space, suffers from problems caused by zero or small number divisions. Thus, we have implemented a weighted deconvolution procedure that, because of the effects of noise bias, is similar in form to that of Wiener filtering. Denoting the Fourier transform by the upper case, i.e., $\text{FT}[i(r)] = I(f)$, the complex quotient can be written as

$$O_d(f) = \frac{\sum_n [I_n(f) \text{Imp}_n^*(f)] W_n(f)}{\sum_n W_n(f)}, \quad (2)$$

where f is the spatial frequency domain corresponding to r , n identifies the n th specklegram, and $W_n(f)$ is its weighting function. This weighting function was chosen to be the power spectrum of the impulse distribution, i.e., $W_n(f) = \text{Imp}_n(f)^2$. Substituting this into Eq. (2) then gives

$$O_d(f) = \frac{\sum_n I_n(f) \text{Imp}_n^*(f)}{\sum_n \text{Imp}_n(f)^2}, \quad (3)$$

where $*$ denotes the complex conjugate. The numerator is now the cross spectrum between the specklegram and the impulse distribution. There is only one complex division,

performed after accumulating the sums in the numerator and the denominator. The latter contains a bias term due to Poisson statistics⁴ and is nonzero at all spatial frequencies, thus removing the effects of the zero and small number divisions and acting, in effect, as a Wiener filter.

The Fourier transform of the numerator is the cross-correlation of the specklegram with the impulse distribution and therefore represents a slightly modified LWH image, which we call the weighted shift-and-add with cross-correlation (WSA/XC) image. Thus, our final result is the weighted deconvolution of the WSA/XC image with the averaged power spectrum of the impulses. It is this weighting term that removes (or minimizes) the seeing background usually found in SAA and LWH images. Because of this process, we label this technique WSA/WD, where WD stands for the weighted deconvolution.

3. MEASUREMENTS

When applied to real data, the local maxima in each specklegram do not necessarily represent the positions and amplitudes of the noise-free speckles. In fact, each specklegram is contaminated by Poisson noise so that the images produced by the shift-and-add techniques contain a photon "spike" at the image center. Before interpreting the final result, it is therefore important to remove this spike. In the Fourier plane the spike transforms into a noise bias that is colored by the detector response (detector transfer function) and has nonzero power beyond the telescope diffraction limit.⁵ This estimate of the object transform can be written as

$$O_d(f) = [O_d(f) - N]D(f), \quad (4)$$

where $O_d(f)$ is the bias-free object transform, N is the frequency-independent noise bias, and $D(f)$ is the detector transfer function. The bias-free result is obtained by first fitting a Gaussian (which is a good first-order approximation⁵) to the factor $D(f)N$ for frequencies greater than the diffraction limit and then dividing, followed by the subtraction of unity at all frequencies. The result is the required bias-free object transform divided by the frequency-independent factor N . If the speckles are relatively small (i.e., a few pixels wide), then the Poisson noise will have little effect upon locating the speckle position because the photon event, spread over a splotch of diameter ~ 2 pixels with our detector,⁵ acts as a low-pass filter. It has been previously noted⁶ that a shift-and-add image is object dependent and is the convolution of the diffraction-limited image with an object-dependent point spread function for the reduction process. This latter term reflects the accuracy with which the speckle maxima can be located. For low contrast objects much larger than the detector response, the uncertainty in the locations of the speckle maxima due to the additive Poisson noise blurs the final image. Thus, the Poisson noise can affect the shift-and-add images in two ways, (1) by adding a (detector-colored) noise spike to the image amplitude and (2) by blurring the final image due to the errors in the detection of the speckle maxima. For the results presented here, the objects have been chosen to be relatively small (or diffraction limited) with a FWHM on the order of two to three times the detector response. Thus, the blurring due to uncertainty in the location of the speckles is minimal.

We have reduced a number of sets of data of the unresolved star Gamma Orionis and the resolved supergiant Alpha

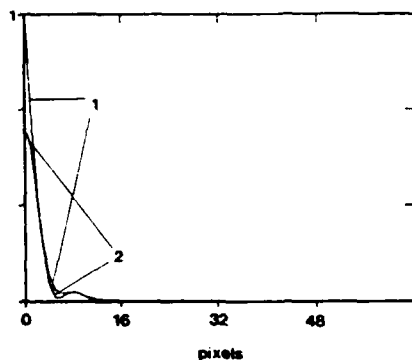


Fig. 1. Azimuthally averaged WSA/WD radial profiles of Gamma Orionis (1) with and (2) without the photon spike.

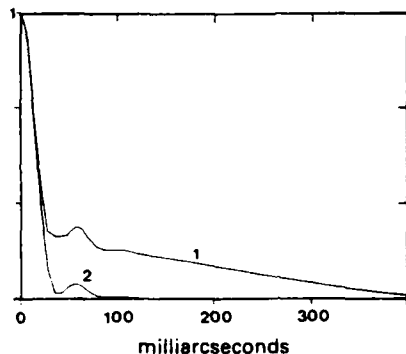


Fig. 2. Azimuthally averaged radial profiles of Gamma Orionis, (1) WSA/XC and (2) WSA/WD, both spike corrected.

Orionis. These data were taken with the Kitt Peak National Observatory (KPNO) 4 m telescope on Feb. 2, 1981. Figure 1 shows the azimuthally averaged radial profiles of the WSA/WD image of Gamma Orionis at a wavelength of 650 nm and a bandpass of 2 nm both with and without the photon spike. As can be seen, the image is approximately twice the width of the photon spike, thus minimizing the object dependency discussed above. This oversampling of the diffraction limit is in fact required in order to separate the resolved signal and the noise bias as two distinct components. Figure 2 shows the final WSA/WD and WSA/XC images. Note that the seeing-produced background, which is clearly visible in the WSA/XC image, is reduced to a flat zero background in the WSA/WD image.

It is important for any image reconstruction or image recovery algorithm that a realistic point spread function be produced when an unresolved object is observed. Figures 3(a) through 3(c) show the azimuthally averaged WSA/WD radial profiles for Gamma Orionis compared to the computed telescope point spread functions (using a 3.8 m aperture with an obscuration ratio of 0.3). Three different bandpasses were analyzed: (a) 650/2 nm, (b) 656.3/0.3 nm, and (c) 850/10 nm. As can be seen, there is good agreement between the models and the images, especially for (a) and (c). The widths of the central maxima and positions and amplitudes of the secondary maxima compare favorably. The narrowband interference filter used for (b) appears to produce a blurring (defocusing) by comparison to the other data sets.

Figures 3(d) through 3(f) compare the azimuthally averaged

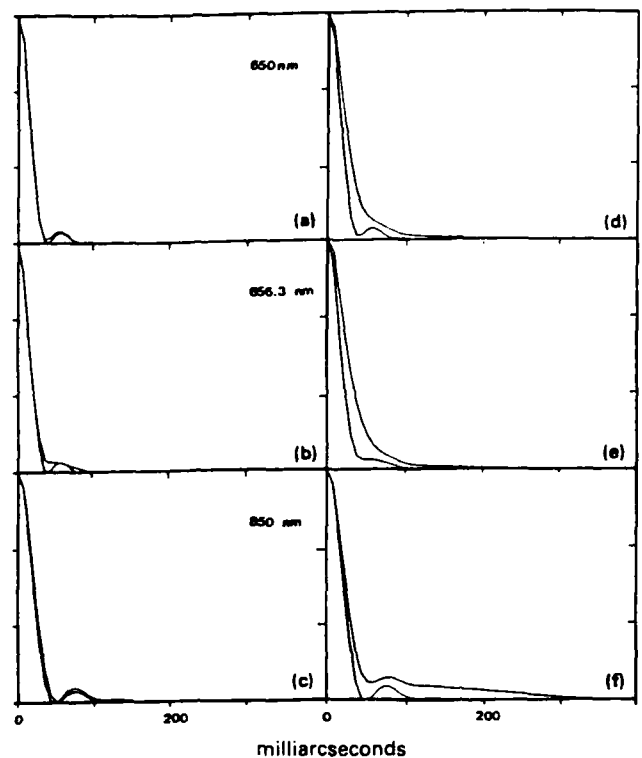


Fig. 3. Azimuthally averaged WSA/WD radial profiles of the unresolved star Gamma Orionis compared with (a) - (c) 3.8 m Airy patterns and (d) - (f) the resolved star Alpha Orionis for three wavelengths.

radial profiles for Gamma Orionis with the resolved star Alpha Orionis for the same three bandpasses: (d) 650/2 nm, (e) 656.3/0.3 nm, and (f) 850/10 nm. For (d) and (e) Alpha Orionis is clearly resolved compared to the measured point spread function. For (f) the disk of the star can be seen to be just resolved, and the secondary maximum is becoming visible. At 850 nm the diffraction limit of a 3.8 m aperture corresponds to 46 milliarcsec, whereas the value for the diameter of Alpha Orionis, obtained from extensive analysis of conventional autocorrelation function and power spectrum reductions,⁵ is approximately 42 milliarcsec.⁷ This profile shows the presence of an extended envelope around the star out to a radius of 300 milliarcsec, which has also been implied from several other measurements using a number of related techniques including differential speckle interferometry.⁸

A data set of Gamma Orionis specklegrams taken with the fully phased Multiple Mirror Telescope (MMT)⁹ at a bandpass of 656.30/0.13 nm has also been reduced with this technique. Figure 4 shows the final image. The FWHM of the central lobe is consistent with that of an Airy disk for a 6.9 m aperture at the same wavelength (~20 milliarcsec). The sixfold symmetry of the point spread function is seen, but its nonuniform appearance indicates imperfect phasing.⁹

4. SIGNAL-TO-NOISE MEASUREMENTS

To evaluate the ability of this technique to recover low power information, we performed a series of measurements to show how the background of the WSA/WD image relates to the number of specklegrams processed. Figures 5(a) through 5(e)



Fig. 4. WSA/WD image of Gamma Orionis showing the point spread function of the fully phased Multiple Mirror Telescope.

show contour plots of images of Gamma Orionis at 650/2 nm for (a) 4, (b) 16, (c) 64, (d) 256, and (e) 1024 specklegrams. There are 25 contour levels at 2% intervals starting from a minimum of 1% to a maximum at the half-power point. Each image is composed of 128×128 pixels with an image scale of 7.22 milliarcsec/pixel. For only four specklegrams the central maximum is clearly visible, and the first Airy ring is beginning to appear above the noise. The background is flat but noisy to a 5% level. As the number of specklegrams is quadrupled, the noise level decreases by the expected factor of 2. The final image of 1024 specklegrams, Fig. 5(e), shows no background at the 1% level for radii greater than the second Airy ring (~ 30 pixels). The first ring is now clearly complete but lumpy. All of our observations show this same effect, and we conclude this to be caused by aberrations within our own optical system. A somewhat noisy second Airy ring is also visible. The vertical stripes at the 1% level are caused by clocks related to the video and digitization process.

The rms noise for pixels greater than the second Airy ring (> 30 pixels ≈ 200 milliarcsec) was computed for images composed of 2, 4, 8, 16, 32, 64, 128, 256, 512, 1024, and 1616 specklegrams. These values are shown plotted on a log-log scale in Fig. 5(f). There is a linear relationship (on a log scale) between the rms noise and the number of specklegrams N up to 256 specklegrams. A power law of -0.5 plotted through these points shows the expected square root behavior. However, for larger numbers of specklegrams this behavior begins to flatten out, showing the limitations imposed on the data due to the instrumentation, e.g., the clock systematics seen in Fig. 5(e). We define a S/N measurement as the quotient of this rms noise to the image maximum. This S/N saturation level has a value of ~ 200 , indicating a limiting dynamic range for this data set of ~ 6 magnitudes.

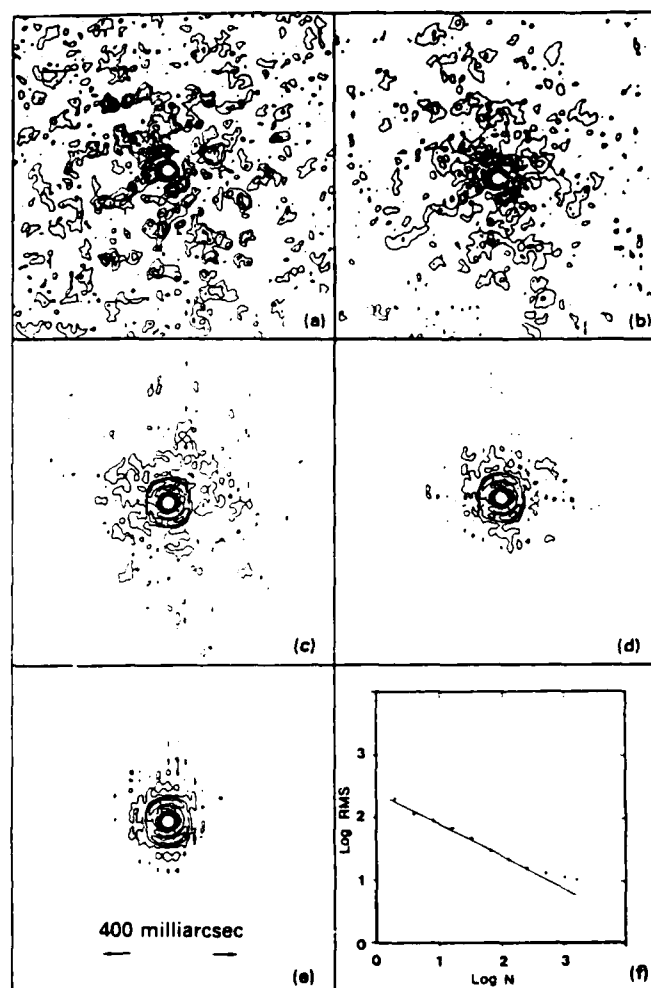


Fig. 5. WSA/WD images of Gamma Orionis for (a) 4, (b) 16, (c) 64, (d) 256, and (e) 1024 specklegrams. (f) rms noise for radii > 30 pixels vs number of specklegrams. The solid line is a power law of -0.5 .

A recently discovered¹⁰ secondary of Gamma Orionis is outside our field of view.

5. EFFECTS OF SEEING ON WSA/WD IMAGES

The results presented in the previous sections show that the WSA/WD image has a flat background at the 1% level, unlike the SAA and LWH images. This implies that the image is corrected for seeing at this level. To investigate any residual seeing effect we rereduced the same 4 m data set of Gamma Orionis, but this time the specklegrams were selected for different seeing bins.¹¹ This was done by computing the width of each speckle cloud by means of the second-order moment about the centroid to give an instantaneous estimate of the Fried seeing parameter r_0 , which we designate as r_e . Table I shows the histogram of the seeing estimate for the data set after low power and poorly guided specklegrams have been eliminated. The data were sorted into seeing bins of 2 cm incremental width. This histogram also shows the (fortunately) good seeing during this observing run.

The rms difference between the images for each seeing bin compared to the best seeing bin, in this case $r_e = 34$ to 35 cm, was computed. For all cases it was found that the rms differ-

TABLE I. Histogram of the instantaneous Seeing Estimate r_s for the Feb. 2, 1981, 4 m Gamma Orionis Data

Seeing estimate r_s (cm)	No. of frames
24 - 25	5
26 - 27	195
28 - 29	486
30 - 31	435
32 - 33	331
34 - 35	83
36 - 37	2

ence was less than 1% of the maximum of the central peak, suggesting that all observations were limited by the instrumental system and not by the seeing. There was a tendency for the difference to get larger when the seeing difference increased, but this was at the 0.05% level and is not considered to be significant because of the 0.5% systematic noise in the images. A similar investigation for the Alpha Orionis images also showed rms differences of <1% over a 10 cm range of r_s .

Contour plots of 80-specklegram reductions of Gamma Orionis for the 26 to 28 cm bin and the 34 to 36 cm bin are shown in Figs. 6(a) and 6(b), respectively. The contour levels are the same as for Figs. 5(a) through 5(e). The better seeing shows a tighter peak at the 1% level, but from the 3% contour up, the two images are practically identical. Figure 6(c) shows the spatial uniformity of the difference between these two images. The rms value of this difference is $\sim 0.5\%$, with the extremes approaching 1%. As can be seen, this difference is essentially constant, with a slight increase for radii <30 pixels (<210 milliarcsec). The greatest discrepancies are found at the image center. These result from an artifact of the videotape recorder undershoot downline of a bright pixel. The better seeing data have brighter speckles and therefore will tend to have more of an undershoot, which shows up as the 1% difference level near the center of the figure

6. LOCATING SPECKLES USING A MATCHED FILTER TECHNIQUE

The results presented in the earlier sections were for relatively simple objects. The specklegrams for both Alpha Orionis and Gamma Orionis have many photons and have single maximum speckles that are only a few pixels in width. Thus, the maxima in specklegrams are relatively easy to locate. However, such objects are not the only ones of interest, and the ability to extend this imaging technique to more complicated and fainter object distributions is desirable. The simplest example of a more complicated object is the binary star Alpha Auriga (Capella), which has two components of nearly equal magnitude. The speckles for Capella show two maxima, corresponding to each of the components. When standard SAA techniques are applied, the local-maximum-finding algorithm locates both maxima and shifts on these, thereby producing "ghosts" in the final image. These ghosts may be avoided by using a matched filter speckle-finding algorithm that locates only a single speckle maximum, thereby producing a more realistic image. The matched filter approach may be used since the required a priori knowledge of the object can be

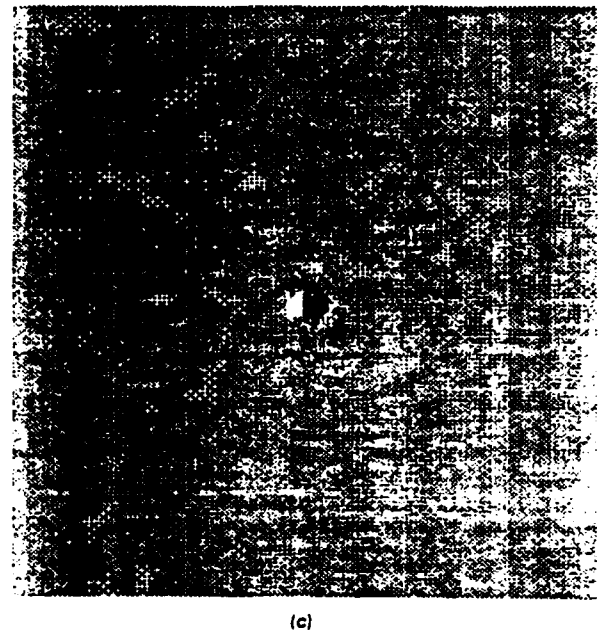
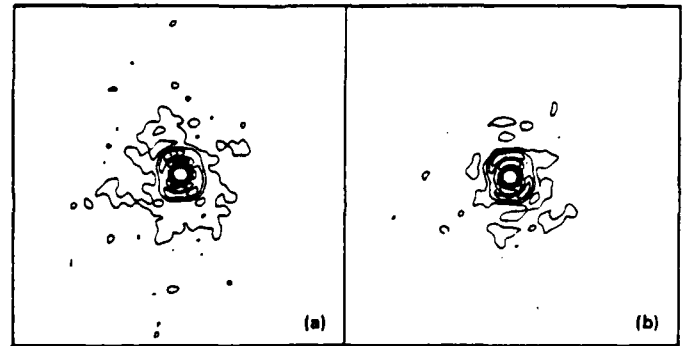


Fig. 6. WSA/WD images of Gamma Orionis for 80 specklegrams with (a) $r_s = 26$ to 28 cm and (b) $r_s = 34$ to 36 cm. (c) Difference between (a) and (b).

obtained from the results of standard power spectrum/autocorrelation analysis. A Gaussian slightly wider than the object may also be used as an initial estimate for the matched filter.

The initial estimate of the matched filter, however obtained, is correlated with the specklegram to obtain a filtered specklegram. The peaks of this filtered specklegram should represent the speckle locations, since these represent the positions of greatest correlation of the filter with the specklegram. However, due to the range of intensities of the speckles within a specklegram, there is a problem in determining which peaks of the filtered specklegram represent the speckles and which are partial correlations or noise. A highly smoothed specklegram obtained by convolving with a low-pass filter is used as a threshold criterion to distinguish true speckle locations from noise and ghost locations. A speckle location is defined when the peaks in the matched filtered specklegram have a greater amplitude than do the corresponding locations in the smoothed specklegram. Thus, a matched filter impulse distribution is obtained, and the WSA/WD analysis described above is used to obtain the image. The technique can be further improved by iteration. By using the result from approximately 1000 detected speckles to update the matched

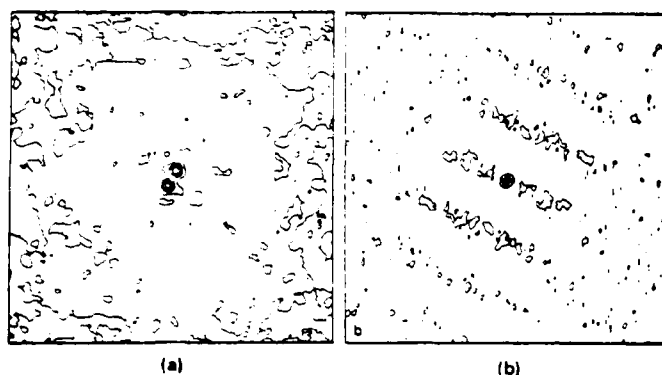


Fig. 7. WSA/WD with matched filter reductions for Capella. (a) Final image showing the two strong components. (b) Impulse power spectrum showing residue fringes, indicating that not all speckles were located with a single maximum.

filter estimate, a very crude initial estimate of the filter was shown to converge to the mean speckle. A more detailed discussion of this matched filter analysis is given by Ribak et al.¹²

Figure 7 shows the results of the matched filter WSA/WD as applied to approximately 1000 specklegrams of Capella. The data were obtained with the KPNO 4 m telescope during the same observing run as for the Alpha Orionis and Gamma Orionis data. The observing bandpass was 10 nm centered on 550 nm. Figure 7(a) shows the final result, easily revealing a double-peaked object. Although there is some evidence of ghosting at the 20% level, this represents a dramatic improvement over the screened shift-and-add method proposed by Bagnuolo,¹³ which was applied to this same data set. The power spectrum of the impulse distribution in Fig. 7(b) shows residue fringes at a 0.5% level of the peak due to the occasional double peak detection of some of the speckles. The final result yields an intensity ratio for the two components of approximately 90%, which is commensurate with other results.¹⁴

There are some deficiencies with the current implementation of the matched filter algorithm. The first is that for extended objects, too few low power speckles are found so that the impulse distribution does not completely sample the speckle cloud (and therefore the seeing). The second is for double (multiple) peaked objects, e.g., Capella, where some double-peaked speckles are located. The algorithm is currently undergoing modification to remedy these drawbacks.

7. CONCLUSIONS

We have presented a study of the performance of a weighted shift-and-add algorithm with seeing deconvolution for use with astronomical speckle interferometric data and have demonstrated its ability to produce diffraction-limited images. It appears to be self-calibrating for seeing effects with a dynamic range of up to 6 magnitudes (subject to present digitizer systematics) when applied to a data set of Gamma Orionis. For the case when the FWHM of the object is a few times greater than the detector point spread function, we have been able to obtain realistic telescope point spread functions for an obscured single mirror (i.e., the KPNO 4 m) and a phased optical array (6.9 m MMT). A resolvable stellar disk has been measured for Alpha Orionis. Preliminary measurements of

this disk are in good agreement with power spectral determinations for the same data set and also for other data.^{7,8} Application of a matched filter speckle-locating algorithm has successfully recovered an image for the binary star Capella that avoids the strong ghosts typically found in SAA reductions.¹³

Limitations to the direct use of this algorithm, and shift-and-add algorithms in general, exist. The first is the difficulty of detecting the correct speckle maxima. As discussed earlier, the detection of a local maximum can be easily affected by the presence of Poisson noise in the specklegram and can produce a blurred image⁶ when the object, and therefore its speckles, is significantly wider than the detector response. The second limitation is the difficulty of recovering a diffraction-limited image of an object with multiple maxima where no one maximum dominates. The simplest example of this is a binary star with two unresolved components. These algorithms produce ghosts because of the duplicity of the speckles, tending to mimic autocorrelation functions when the two components have comparable brightnesses. We have demonstrated that a matched filter approach yields improved speckle locations and also reduces the problems associated with the locations of peaks dominated by Poisson noise.

Although the data presented here are for bright objects where the speckles are easily identifiable, we have evidence that our matched filter analysis¹² helps identify speckles in the photon-limited domain, where a simple local-maximum-finding algorithm is inadequate. This extends this imaging technique to much fainter objects ($m_v > 8$) such as galactic nuclei and quasi-stellar objects as well as asteroids and other faint solar system objects.

The underlying assumption of all shift-and-add techniques is that speckles are highly distorted diffraction-limited images. For objects much smaller than the seeing disk this can be considered a reasonable approximation, as illustrated by the results presented here. This approximation, however, is empirical, and further statistical analysis about the formation of specklegrams is needed to validate this assumption. A preliminary statistical analysis of the WSA technique is discussed by Freeman et al.¹⁵

8. ACKNOWLEDGMENTS

This work was supported in part by the National Science Foundation (grants AST-8201092 and AST-8312976). One author, E. Ribak, is supported by a Weizmann Fellowship. J. C. Christou is a visiting astronomer from New Mexico State University, and E. K. Hege was a visiting astronomer at Kitt Peak National Observatory, a division of the National Optical Astronomy Observatories operated by the Association of Universities for Research in Astronomy Inc., under contract to the National Science Foundation. The Multiple Mirror Telescope is a joint facility of the University of Arizona and the Smithsonian Institution.

9. REFERENCES

1. R. H. T. Bates and F. W. Cady, "Towards true imaging by wideband speckle interferometry," *Opt. Commun.* 32, 365-369 (1980).
2. C. R. Lynds, S. P. Worden, and J. W. Harvey, "Digital image reconstruction applied to Alpha Orionis," *Astrophys. J.* 207, 174 (1976).
3. J. C. Christou, E. K. Hege, J. D. Freeman, and E. Ribak, "Self-calibrating shift-and-add technique for speckle imaging," *J. Opt. Soc. Am. A* 3, 204-209 (1986).
4. J. W. Goodman and J. F. Belsher, "Fundamental limitations in linear invariant restoration of atmospherically degraded images," in *Imaging Through the Atmosphere*, J. C. Wyant, ed., *Proc. SPIE* 75, 141-154 (1976).

5. E. K. Hege, E. N. Hubbard, P. A. Strittmatter, and W. J. Cocke, "The Steward Observatory speckle interferometry system," *Opt. Acta* 29, 701 (1982).
6. M. J. McDonnell and R. H. T. Bates, "Digital image restoration of an image of Betelgeuse," *Astrophys. J.* 208, 443 (1976).
7. A. Y. S. Cheng, E. K. Hege, E. N. Hubbard, L. Goldberg, P. A. Strittmatter, and W. J. Cocke, "Diameter and limb-darkening measures for Alpha Orionis," *Astrophys. J.*, in press (1986).
8. J. C. Hebden, J. C. Christou, A. Y. S. Cheng, E. K. Hege, P. A. Strittmatter, and J. M. Beckers, "Two-dimensional images of Alpha Orionis," *Astrophys. J.*, in press (1986).
9. E. K. Hege, J. M. Beckers, P. A. Strittmatter, and D. W. McCarthy, "The Multiple Mirror Telescope as a phased array telescope," *Appl. Opt.* 24, 2565 (1985).
10. C. Papaliolios, P. Nisenson, and S. Ebstein, "Speckle imaging with the PAPA detector," *Appl. Opt.* 24, 287-292 (1985).
11. J. C. Christou, A. Y. S. Cheng, E. K. Hege, and C. Roddier, "Seeing calibration of optical astronomical speckle interferometric data," *Astron. J.* 90, 2644 (1985).
12. E. Ribak, E. K. Hege, and J. C. Christou, "Use of matched filtering to identify speckle locations," in *Int. Conf. on Speckle*, H. H. Arsenault, ed., Proc. SPIE 556, 196-201 (1985).
13. W. G. Bagnuolo, "The application of Bates' algorithm to binary stars," *Mon. Not. R. Astron. Soc.* 200, 1113-1122 (1982).
14. W. G. Bagnuolo and H. A. McAllister, "The true nodal quadrant of Capella," *Publ. Astron. Soc. Pac.* 95, 992-995 (1983).
15. J. D. Freeman, E. Ribak, J. C. Christou, and E. K. Hege, "Statistical analysis of the weighted shift and add image reconstruction technique," in *Int. Conf. on Speckle*, H. H. Arsenault, ed., Proc. SPIE 556, 279-283 (1985).



Julian C. Christou was born in Wales in 1954. He holds a B.Sc. degree in physics and astronomy from the University of London, an M.S. degree in physics from Southern Illinois University at Carbondale, and an M.S. degree in astronomy from New Mexico State University, where he recently completed his Ph.D. degree. He is currently a visiting astronomer at Steward Observatory. His research interests involve imaging techniques as applied to stellar speckle interferometry

with application to supergiant stellar disks and envelopes, as well as the study of atmospheric seeing.



Erez Ribak was born in Israel in 1950. He got his first and second degrees in physics from the Technion in Haifa and his third degree in physics and astronomy from Tel Aviv University. His thesis involved building a real-time shearing interferometer for astronomical measurements. He is currently a Weizmann fellow at Steward Observatory. His research interests involve astronomical interferometry, and optical and digital processing of data.

E. K. Hege: Biography and photograph appear following the paper "Differential speckle imaging with the cophased Multiple Mirror Telescope" in this issue.



Jonathan D. Freeman was born in Buffalo, New York, in 1959. He received his B.S. in physics from the University of Arizona in 1981 and is currently pursuing an advanced degree in applied mathematics there. While employed at Steward Observatory, he assisted with the implementation and statistical analysis of new imaging techniques. He is currently the holder of an internship at Kitt Peak National Observatory, where he is working on an application of the speckle masking algorithm.

Toward solving the lost photon problem in image intensifiers

R. H. Cromwell

Steward Observatory, University of Arizona
Tucson, Arizona 85721Abstract

A summary is given of measurements of the photoelectron counting efficiency of a variety of image intensifiers manufactured by several different manufacturers. With one exception, the counting efficiency is disappointingly low. Typically only slightly over half of the photoelectrons from the first photocathode produce a detectable signal on the output phosphor screen in most diode-type intensifiers. For microchannel plate intensifiers, the counting efficiency is even less. Results are given of experiments intended to produce diode-type intensifiers having improved counting efficiency. Improvements have been achieved through refinements in the manufacturing steps of the phosphor screen, the tube component identified as responsible for the lost photoelectron pulses in diode-type tubes. The best tubes so far have counting efficiencies of 70%, which represent an improvement by a factor of about 1.4.

Introduction

We have discovered in the past few years that many of the image intensifier systems used as primary detectors in astronomical instruments fail to record nearly half of the photoelectrons released from their photocathodes.^{1,2,3} The reason for this is that many first stage photoelectrons released in an image intensifier simply fail to produce any measurable light pulse whatsoever when they strike the first phosphor screen.³ The following is a summary of our measurements of the "photoelectron counting efficiency" of a number of high quality image intensifiers used in low light level astronomical applications. We also summarize our progress toward solving the "lost photon problem", or low photoelectron counting efficiency, that exists in most image intensifiers. This work is being carried out jointly with the manufacturer Proxitronic in an ongoing collaboration with Steward Observatory to develop a proximity focused image intensifier for astronomy.

Counting efficiency of several intensifiers

Table 1 summarizes our measurements of the photoelectron counting efficiency, or simply "counting efficiency", of a number of image intensifiers. The various measurement techniques have been described elsewhere.^{1,2} Most of the results, and all of the results listed as "new" in Table 1, have been obtained using the Steward Observatory analog intensified Reticon system operated in a pulse counting mode to determine the pulse height distribution and counting efficiency. The pulse height distributions (PHDs) measured for several of the intensifiers are shown in Figures 1, 2 and 3. The counting efficiencies given in Table 1 and the figures are slightly revised from values given in earlier publications, and are more accurate owing to recalibration of test apparatus.

With the single notable exception of the Varo electrostatically focused diode (serial no. 15777), all other tubes listed in Table 1 have a disappointingly low counting efficiency. Indeed, all of the candidates for application as a primary astronomical detector in the blue and uv spectral region have counting efficiencies in the range of only 50 to 64%. These include the magnetically focused tubes manufactured by EMI, ITT and RCA, and the standard production proximity focused tubes manufactured by Proxitronic. As will be discussed later, some of the Proxitronic tubes with experimental P-20 phosphor screens are showing improved counting efficiency.

The 90% counting efficiency and superior PHD shown in Figure 1 for the Varo tube no. 15777 is fairly representative of at least five different samples of Varo tubes. Two 40 mm tubes have been measured by us and three 25 mm tubes have been measured by Latham.^{4,5} The Varo tube no. 28542 is the first Varo electrostatic tube we have found that exhibits a rather low counting efficiency (61%).

The very low counting efficiency (about 33%) measured for all three microchannel plate intensifier tubes listed in Table 1 illustrates the reason why at Steward Observatory we have never chosen to use such a tube as a first stage intensifier in an instrument package. However, very recently other researchers have reported higher counting efficiency figures for devices where microchannel plates were used as a first stage amplifier (an experimental resistive anode array detector manufactured by Instrument Technology, Ltd.⁶ and the MAMA detector of Timothy's⁷). Subsequent discussions have not led to an explanation of the

discrepancy between these measurements and our own. To understand this important discrepancy, it would be very useful to repeat measurements of the microchannel plate devices in question in our laboratory using our standard test procedure.

Improving the phosphor screens

A "diode-type" intensifier usually consists of a single photocathode and a single phosphor screen anode, with no intervening gain structure, such as a microchannel plate. (A variant of a diode-type intensifier is a "cascade" intensifier, where the phosphor of one diode is sandwiched to the photocathode of the next, forming a multistage diode-type intensifier.) To study the problem of low counting efficiency in diode-type intensifiers, a number of experimental proximity focused diode image tubes have been constructed by Proxitronic. Each sample contains a phosphor screen that has been made utilizing specific variances from the standard screen manufacturing process. Each sample was then tested for its PHD, counting efficiency and its overall gain. Results are beginning to be encouraging, although there have been several surprises along the way.

Coarse grain screens

The standard Proxitronic tubes we have investigated most thoroughly in the past are made with P-20 phosphor screens deposited by a sedimentation technique. The phosphor powder is supplied by Riedel de Haen (the same phosphor used by Varo), and normally fine grain particles are selected by columnar separation. By examining images recorded with a scanning electron microscope, we find that the grains are typically 0.5 to 3 microns in diameter, with an average size of 1 micron. It has been reported by Giakoumakis et al. and others that larger diameter phosphor grains are more efficient, and we therefore reasoned that larger grains might possibly also show higher counting efficiency of single electrons. Samples of tubes were made with coarse grain screens by utilizing the larger grains that settle out first from the phosphor sedimentation solution. The grain diameters in these screens range from 1 to 4 microns, with an average of 1.5 microns.

Our first tests of coarse grain tubes showed that there was indeed a substantial improvement in the overall light output, or "gain", from such tubes, but that the counting efficiency was, in fact, degraded (see tube C in Figures 2 and 4). (A description of how we measure gain in an intensifier is given in reference 1.) Thus, photoelectron pulses from the screen were bigger in amplitude, but, for a given number of electrons incident on the screen, the number of output pulses was reduced. We shall see below, that when the screens are not subjected to electron scrubbing, then there is no longer an improvement in gain in the coarse grain screens (for example, compare tubes E and G in Figure 4, each tube having a 2X thickness, non-scrubbed screen). Moreover, the coarse grain screens continue to have lower counting efficiency (Figure 3). We conclude from these tests that there isn't really an inherently higher efficiency (ie, light output) in the coarser grains, but rather that the coarser grains are simply less degraded in efficiency than finer grains when both are subjected to too much electron scrubbing. From the point of view of counting efficiency, there appears to be no advantage, but instead a disadvantage, in coarser grains.

Screens having no electron scrubbing

A variety of arguments have led us to suspect that there simply exist completely deadened, or insensitive, phosphor grains in the screen, and that these dead grains are responsible for the lost photoelectron pulses. Because the deadened grains may be preferentially located on the impinging-electron side of the screen, adjacent to the aluminum coating over the phosphor, their presence would go largely undetected during the manufacturing process.³ In normal production, an effort is made to rid the screens of any contamination by scrubbing the screens with 10 kV electrons before the screens are placed in the final intensifier. The current density during this process is much higher than the screens normally experience in an operating intensifier. Thus, the scrubbing process appeared to be a possible cause of dead grains. Samples of tubes were produced with screens receiving no electron scrubbing to test this hypothesis (for example, tubes D, E, F and G).

By studying the results illustrated in Figure 4 (plus the results of several more tubes not shown), we conclude that the gain is not affected very much by electron scrubbing when the screens are comprised of larger grains, but that the gain is significantly reduced by electron scrubbing in finer grain screens. In general, when the screens are not scrubbed, both the fine grain and coarse grain screens have comparable, high gain.

There is no clear evidence that electron scrubbing has an adverse effect on counting efficiency. For example, neither the counting efficiency nor the shape of the PHD curve of the non-scrubbed tube D was measurably improved over the standard tube A. The pulses are brighter in tube D compared to A, commensurate with the higher gain, but the counting

efficiencies are virtually identical. (Note: Figures 2 and 3 don't reveal the fact that the pulses are brighter in D than in A because of the way in which the data have been normalized in these figures. The normalization has been done to facilitate comparison of the relative shapes of the various PHDs.) Nevertheless, it is true that the only tubes to show marked improvement in counting efficiency contain screens that were not electron scrubbed (the 2x thick samples E, F and G, discussed below). Clearly more study needs to be carried out before the effects of electron scrubbing are fully understood.

Thicker screen layers

In the standard production tubes the thickness of the phosphor sedimentation layer is selected to produce a highly uniform, nearly grainless, output light from the phosphor screen. The layer is kept as thin as possible to maintain high resolving power. Typically, the screens have an area density of around 0.7 mg/cm^2 . Inspection of the screens with a high power optical microscope reveals that there exist voids, which are areas completely free of phosphor particles, in the screen layer. Clearly, any electron that falls in such a void will create no output pulse from the screen. Thus, experimental screens were made of 2X and 4X the standard thickness in an attempt to reduce the area of voids. In the 2X screens, no electron scrubbing was employed in order to achieve the highest possible gain. One sample was also baked out at a lower temperature (300°C) than normal (425°C) to investigate the possibility of dead, or reduced sensitivity grains due to the high bakeout temperature.

Results of tests of the intensifiers with 2X thicker screens are immediately encouraging, as is evident in the figures (tubes E, F and G). Not only are the gains very high, but for the first time we see a significant improvement in the PHD and counting efficiency. The tube F with the screen baked out at a lower temperature shows even more improvement in gain, but shows no significant difference in counting efficiency from the otherwise identical tube E. Thus, it appears as though a lower bakeout temperature simply improves the light output from the screen, but apparently does not revive any suspected dead grains, an effect that closely parallels the effect of electron scrubbing.

The results of tests of the 4X thicker screen tubes H and I are somewhat confusing. Although the phosphors received standard electron scrubbing (by mistake), our earlier results suggest that the only effect this would have is to reduce the gain of the tubes. Based upon a reasonable set of extrapolations of the results of the earlier tubes, we had expected that the 4X tubes would have gains at least somewhat higher than the standard tube A (they don't), would most likely have sharper PHDs than the 2X tubes E and F (they don't), and would certainly have higher counting efficiencies than the 2X tubes E and F (they don't even come close). Clearly there needs to be more investigation into these very recent results.

More interesting recent results

A decaying phosphor

A repeat of the gain and counting efficiency measurements of tube F some 15 months after the original measurements reveal that the phosphor screen of this tube has decayed significantly. The gain has decreased by a factor 0.90 and the counting efficiency has dropped by a factor 0.76. These two results may appear discrepant at first, but are in fact commensurate when the change in the PHD shape is taken into account: The recent PHD of the tube has relatively substantially fewer small amplitude pulses whereas the number of the largest amplitude pulses remain unchanged. (In Figure 2 this is best represented if the PHD of F' is simply moved to the right by a scaling factor until the large amplitude portion of the curves F and F' are superposed. To maintain the proper relationship, the vertical height of F' must simultaneously be divided by the same scaling factor.) The active decay of this phosphor's counting efficiency is likely to be a very important clue as to the cause of lost counts. Just as a check of our laboratory technique, a repeat was also run of the PHD and counting efficiency of the Varo 15777 tube, originally measured over two years earlier. The results of the new measurements were indistinguishable from the original set. This gives us added confidence that the Varo tube 15777 is stable, and so is our measurement technique.

A low counting efficiency Varo tube

The results shown for the Varo tube 28441 are highly interesting. First, the counting efficiency of this tube is surprisingly low compared to all earlier measurements of other Varo samples. Second, its PHD shape is in fact sharper (ie narrower FWHM and fewer small amplitude pulses) than tube 15777, in spite of the fact that its counting efficiency is lower. This is contrary to our earlier findings that a sharper PHD is correlated with a higher counting efficiency. Is this Varo tube exhibiting the same kind of phosphor decay as we see in the standard tube F? Or is this simply an example of a Varo phosphor that

is too thin and therefore full of voids? Again, there are some interesting new clues here.

Concluding remarks

Image intensifiers will continue to play a vital role in photon counting and low light level applications in astronomy and other fields where detectors are starved for light. Prevention of the loss of nearly half of the photoelectrons from an intensifier photocathode will considerably improve the signal-to-noise performance of future intensified detectors. Many who rely upon such detectors for their research are impatiently waiting for a solution to the lost photon problem.

We are very encouraged to have produced counting efficiencies in recent experimental intensifiers that approach a factor of 1.4 improvement, but can be satisfied only when such a factor is routinely and stably exceeded.

Acknowledgements

The proximity tube development program and much of the research reported in this paper have been supported by NSF Grant AST 8201002.

References

1. Cromwell, R. H., Strittmatter, P. A., Allen, R. G., Hege, E. K., Kuhr, H., Marien, K. H., Funk, H. W. and Frank, K., 1985, "A Proximity Focused Image Intensifier for Astronomy", Adv.E.E.P., 64A, 77-92.
2. Allen, R. G., Cromwell, R. H., Liebert, J. W., Macklin, R. H. and Stockman, H. S., 1983, "The Steward Observatory Intensified Photon-Counting Reticon System", Proc. S.P.I.E., 445, 168-175.
3. Cromwell, R. H., 1984, "The Lost Photon Problem in Image Intensifiers", Bul. A.A.S. 16, No.4, 904 (abstract). Steward Observatory Preprint No. 565, (full paper).
4. Latham, D. W., 1982, "Spectroscopy With Photon-Counting Reticons", Proc. IAU-Colloquium 67.
5. Latham, D. W., 1985, private communication.
6. Cromwell, R. H., unpublished tests of the Steward Observatory image tube laboratory.
7. Giakoumakis, G. E., Nomicos, C. D. and Euthymiou, P. C., 1980, "Absolute Efficiency of Zn:CdS:Ag Screens Excited by an Electron Beam", J. Appl. Phys. 51.
8. Powell, J. R. and Lyons, A., 1985, private communication.
9. Timothy, J. G., 1985, private communication.

TABLE 1 - Photoelectron counting efficiency of several image intensifiers

Intensifier		C. Eff.		Comments	References
Manufacturer	Model	Type (1)	(%)		
Varo	8605	ESF diode	90	Serial No. 15777, see text	1, 2, 3
Varo	8605	ESF diode	61	Serial No. 28542, see text	new
RCA	C33011	MF 2-stg cascade	60		2
ITT	F4089	MF diode	55		2
EMI	9916 FO	MF 2-stg cascade	64		new
EMI	9914 FO	MF 3-stg cascade	58		new
ITT	F4111	PF MCP	33		2
ITT	F4150	PF dual MCP	35		6
Varo	3603	ESF MCP	30		6
Proxitronic (2)	BV2502	PF diode			
A	(3861)		56	Standard phosphor	1, 2, 3
B	(8137)		53	Standard phosphor	new
C	(5822)		42	Coarse grain	3, new
D	(7919)		55	Non scrubbed (N.S.)	new
E	(8553)		70	N.S., 2X Thk.	3, new
F	(8558)		67	N.S., 2X Thk., 300° Bake	3, new
F'	(8558)		51	Same as Tube F, only measurements made 15 months later	new
G	(8555)		60	N.S., 2X Thk., Coarse grain	new
H	(9307)		50	4X Thk.	new
I	(11830)		59	4X Thk.	new

(1) ESF, MF and PF designate electrostatically, magnetically and proximity focused, respectively.

MCP designates microchannel plate.

(2) Listed for each Proxitronic tube is an identification letter (A-I) of the respective tube used in Figures 2, 3 and 4, and the serial number of each tube (in parenthesis).

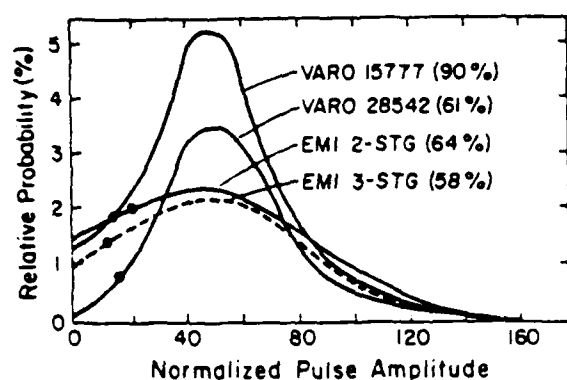


Figure 1 Pulse height distribution of several image tubes. The photoelectron counting efficiency of each tube appears in parentheses. All measured curves have been normalized in Figures 1, 2, and 3 for comparison purposes so that each mean pulse amplitude is 50. Pulses with amplitudes smaller than those indicated by the heavy dot of each curve were too small to be accurately counted above the noise in the measurement technique, and their relative probability of occurrence has been estimated by extrapolation of the measured data.

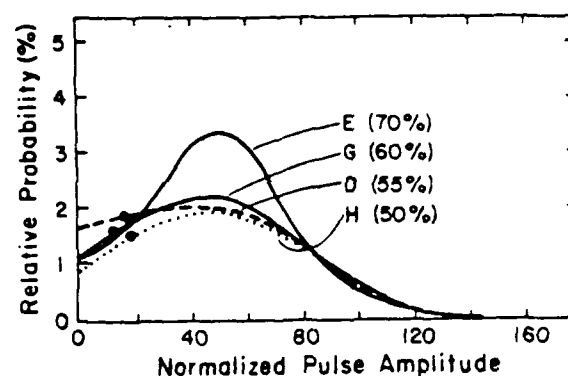


Figure 3 Same as Figure 1. Tubes are identified in Table 1.

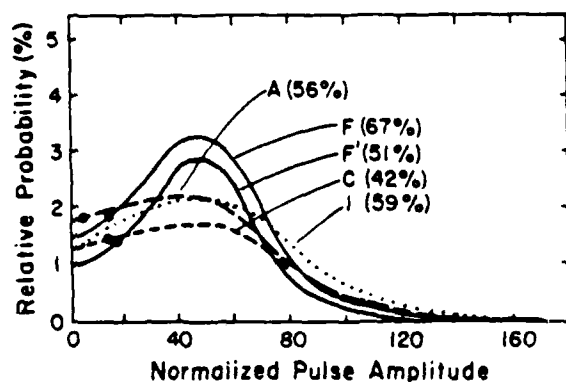


Figure 2 Same as Figure 1. Tubes are identified in Table 1.

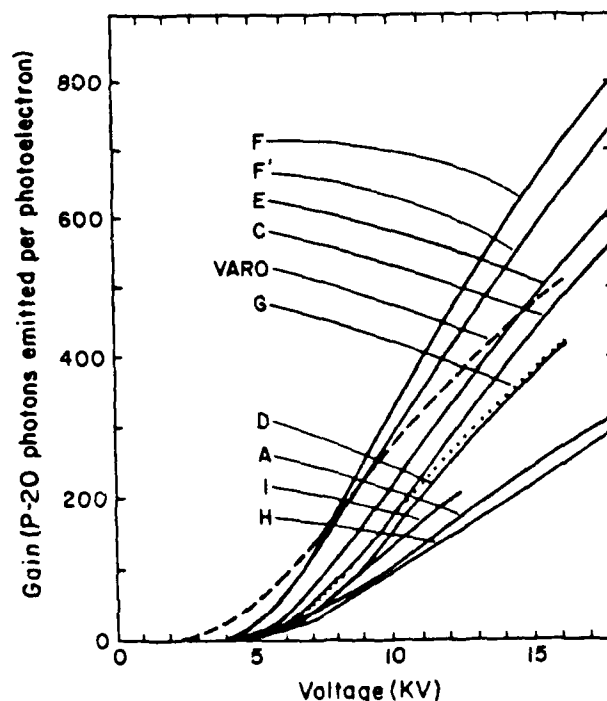


Figure 4 Gain vs. voltage for a number of Proxitronic image tubes having experimental and standard P-20 phosphors (identified in Table 1). Also shown is the Varo image tube number 28542.

The U.S. Government is authorized to reproduce and sell this report.
Permission for further reproduction by others must be obtained from
the copyright owner.

A Proximity-Focused Image Intensifier for Astronomy

R. H. CROMWELL, P. A. STRITTMATTER, R. G. ALLEN, E. K. HEGE, H. KUHR,
and K.-H. MARIEN[†]

Steward Observatory, The University of Arizona, Tucson, Arizona, U.S.A.

and

H. W. FUNK and K. FRANK

Proxitronic-Funk GmbH & Co. KG, Weiterstadt/Darmstadt, Federal Republic of Germany

INTRODUCTION

Image intensifiers are currently the primary detector for ground-based optical astronomy. They are used with photographic emulsions and with various electronic readout systems, as in the Wampler-Robinson scanner (image dissector),¹ the Boksenberg IPCS (Plumbicon),² and the Shectman³ and the Steward Observatory⁴ scanners (Reticon). The image intensifier offers the advantages of reasonably high quantum efficiency, essentially noise-free amplification to very high gain values and suitability for rapid readout. Although the CCD offers significantly better detective quantum efficiency in certain applications, especially for medium to high signal-to-noise ratio observations at wavelengths above 4000–4500 Å, there are nonetheless a number of astronomical problems for which the image intensifier is likely to remain superior. These include any problems in which it is necessary to read out rapidly, as for example in speckle interferometry, polarimetry, and high-resolution photon-counting centroided spectroscopy. It also seems likely that, in the UV spectral range ($\lambda < 4000$ Å) the DQE of image intensifiers will remain competitive with that of CCDs for some time to come.

At Steward Observatory we have tested a variety of image intensifiers that are commercially available or under development. Tables I and II list the major design types we have examined, and give a summary of our test results, some of which have been reported elsewhere.^{5–11}

[†] Visitor from the Max-Planck-Institute für Astronomie, Heidelberg, Federal Republic of Germany.

TABLE I
Performance characteristics of image intensifiers

Tube type (manufacturer)	Field diameter (mm)	Overall voltage (kV)	Gain (photons per photoelectron)	Pulse height distribution	Resolution ^a (lp mm ⁻¹)		Geometrical distortion (%)	Signal-induced background	
					Center	Edge		Analog (%)	Ion/electron ratio
Gen I electrostatic 1-stage (Varo)	25, 40	15	4×10^2	Poissonian	76	25	5	2	EST $< 5 \times 10^{-4}$
Gen I electrostatic 4-stage (Varo)	25, 40	60 ^b	3×10^2	Poissonian (cf. 4-stage) (see Fig. 7)	23	15	27	4	EST $< 5 \times 10^{-4}$
Flat field electrostatic 1-stage (Varo, Variam)	17	15	4×10^2	Poissonian ^c	50	15	6	2	—
Magnetic 1-stage (ITT)	40	15	3×10^2	Poissonian ^d	85	75	1.5	13	EST $< 1 \times 10^{-3}$
Magnetic 2-stage cascade (RCA)	36	20	2×10^4	Poissonian ^e	45	22	2	22	—
Magnetic 4-stage cascade (EMI)	46	45	9×10^4	— ^f	25	—	2	47	—
Proximity micro channel plate (ITT)	18	6	2×10^4	Exponential ^g	16	16	0	10	—
Electrostatic micro channel plate (Nitec)	25	8	$\sim 3 \times 10^4$	Exponential ^h	23	—	~ 6	—	—

^a Line spread FWHM may be found by taking the reciprocal of the resolution given in lp mm⁻¹.

^b Each stage operated at 15 kV. Overall voltage of 4-stage may be kept well below 60 kV by use of fiber optic boules to drop voltages between stages.

^c Pulse height distribution not measured, but is assumed to be Poissonian based on measurement of similar phosphor tubes.

^d Pulse height distribution discussed in Ref. 15.

^e Pulse height distribution not measured. Might be somewhat broader than other cascaded tube we've measured due to blackened, lower-gain phosphors of EMI tube.

^f Pulse height distribution not directly measured, but estimated to be qualitatively similar to ITT MCP based on visual inspection of output phosphor.

TABLE II

Manufacturer of proximity diode	Separation (mm)	Overall voltage (kV)	Phosphor black layer	Signal-induced background	
				Analog (%)	Ion/electron ratio
ITT	1.27	6	No	35	—
ITT	1.27	6	No	21	—
ITT	1.27	6	No	32	—
ITT	2.2	10	Yes	14	1.4×10^{-3}
Proxitronic	1.5	9	Yes	5	—
Proxitronic	2.5	9	Yes	4	—
Proxitronic	2.5	15	Yes	11	3.3×10^{-4}
Proxitronic	2.5	15	Yes	—	1.4×10^{-4}
Proxitronic	2.5	9	Yes	5	—
(P-11 phosphor)		15		9	—
Proxitronic	3.5	9	Yes	3	—
		15		7	—
		21		13	—

Experience in the last 3 years with proximity-focused intensifiers indicates to us that these tubes have reached a sufficient degree of development that they can, with modest further development, provide high-quality solutions to a wide range of astronomical problems. Therefore, Steward Observatory has undertaken a joint project with Proxitronic-Funk, the manufacturer of the most promising proximity tubes, to optimize the tube performance for astronomical applications. The present paper summarizes our experience with proximity tubes and gives a progress report on our development program.

TUBE CONFIGURATION

Figure 1 illustrates the major components of the Proxitronic tube structure. The input window can be made of fiber optic, glass, or quartz. The active diameter of the diode is 25 mm. The photocathode is normally a multialkali S-20 or S-25, although more recently, bialkali photocathodes have also been fabricated. The screen is made of a sedimentation layer of fine-grained phosphor, usually P-20, on which is deposited a reflective aluminum layer on the side facing the photocathode. The latter suppresses light feedback from the phosphor toward the photocathode and increases phosphor brightness on the output side. There is an additional layer of black aluminum on the reflective aluminum to prevent light that is

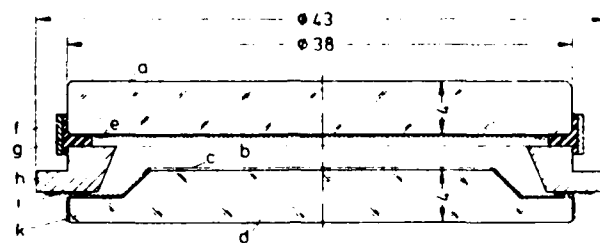


FIG. 1. Proximity-focused image intensifier. a, Entrance window; b, photocathode; c, screen; d, output window; e, contact ring; f, indium containment ring; g, indium seal; h, distance ring; i, contact ring; k, screen contact.

transmitted by the photocathode from being reflected. The output window can be of glass or fiber optic.

The separation between photocathode and phosphor is determined by the thickness of the "distance ring" in Fig. 1. Presently, tubes are manufactured with a separation of 1.5, 2.5, or 3.5 mm. Each tube is intended to operate at an electric field strength of up to 6 kV mm^{-1} , and therefore at maximum voltages of 9, 15, or 21 kV, respectively. At such high field strengths, a sharp edge on nearly any surface, or a discontinuity in the field near the wall of the distance ring, becomes a troublesome source of field emission. To control these problems, extreme cleanliness has been required during each manufacturing step. Electrical discharges from the wall were controlled only after developing a bulk conductive glass for the material in the distance rings. In the manufacturing process, screens with output windows that are connected to their conductive distance rings and entrance windows carrying a photocathode are separately stored in sealed glass containers. These two components are put into a vacuum chamber along with a third element, the indium mount, and are combined to complete the diode.

Particularly desirable features of the finished proximity diode include (1) complete freedom from distortion, (2) uniform light output, (3) uniform resolution from center to edge, (4) small size, (5) flat input and output windows, and (6) insensitivity to strong external electric or magnetic fields.

PHOTOCATHODE RESPONSE

Measurements of photocathode response are made by uniformly illuminating a 2.3-cm-diameter area of the photocathode with a distant lamp and by directly measuring the resulting photocurrent with an electrometer. A

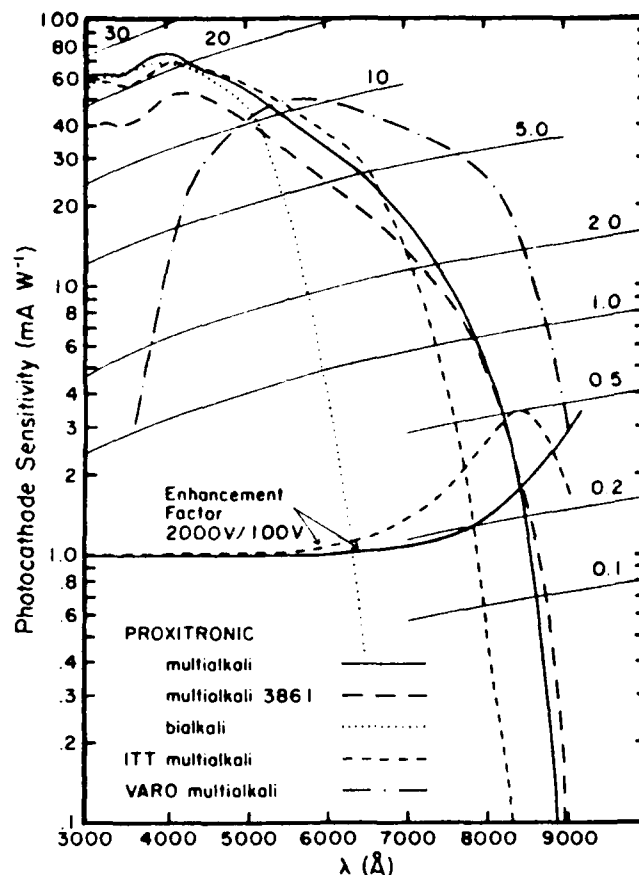


FIG. 2. Spectral sensitivity of several photocathodes, enhancement factor of two. Curves of constant quantum efficiency are shown.

series of 100-Å bandwidth filters are used to define several spectral regions throughout the wavelength interval 3000 to 9000 Å. The absolute calibration of the lamp is maintained to better than $\pm 5\%$ by use of several reference image tube photocathodes which have been calibrated against a National Bureau of Standards detector.¹²

Our goal in the proximity tubes is to have the highest possible photocathode response in the "blue" spectral region from 3000 to 5000 Å. In Fig. 2 we show the spectral response of four quartz-windowed proximity tubes of recent manufacture and of one Varo electrostatically focused tube. Each curve represents an attempt to provide a photocathode having

a good blue response. The Varo tube illustrates the disadvantage of using a fiber optic input window and a relatively thick multialkali photocathode for the blue spectral region. This tube is the first stage in a four-stage detector package ("Big Red") that has been, and continues to be, a major observatory detector for the spectral region above 5000 Å. It is particularly useful for speckle interferometry.

Two multialkali photocathodes in Fig. 2, one from ITT and one from Proxitronic, plus the Proxitronic bialkali photocathode represent three of the very best blue response photocathodes we have measured in any intensifier in the past 10 years. Unfortunately, all of these three tubes were found unsuitable for astronomy because of some other shortcoming, which illustrates the practical difficulty in obtaining truly first-rate blue tubes. Proxitronic has been successful recently in producing consistently high-response bialkali photocathodes, and this looks very encouraging. The somewhat lower blue response photocathode (Proxitronic multialkali 3861) is contained in an excellent diode overall, one that looks very promising for astronomy. We expect to see more diodes like this in the future with higher blue response.

Shown for two of the photocathodes in Fig. 2 is the "enhancement factor," the ratio of the photocathode response measured with 100 V across the diode (the plotted response curves) to that measured with 2000 V across the diode. Some additional enhancement in the photocathode response is expected when the tubes are operated at their full rated voltage. The enhanced response, due to a high field strength at the surface of the photocathode, is something we only became aware of in the proximity type intensifiers where the field strengths are typically 20 to 100 times higher than in other types. The enhancement factor is only significantly greater than unity in the long wavelength tail of the response curve, where the quantum efficiency is less than 2%. We have observed an analogous effect in the bialkali photocathodes as well.

RESOLUTION

The measured limiting resolution, R_M , in lp mm⁻¹ for a proximity-focused diode is a convolution of three components according to the equation

$$1/R_M^2 = 1/R_{PC}^2 + 1/R_{PHOS}^2 + 1/R_{FO}^2$$

where R_{PC} is the inherent resolution of the photocathode and its proximity-focused image, and R_{PHOS} and R_{FO} are the resolutions of the phosphor screen and the fiber optic faceplate, respectively. Furthermore, it follows

from the parabolic trajectories of the proximity-focused photoelectrons that

$$R_{PC}(\lambda) = [C(\lambda)V^{1/2}]/d$$

where V is the applied voltage across the diode, d is the separation between photocathode and screen, and $C(\lambda)$ is a parameter that is dependent upon the tangential velocity of the emitted photoelectrons (and hence is a function of the wavelength of incident light). There is nowhere near as strong a dependence of resolution on wavelength in magnetically or electrostatically focused intensifiers, nor have we detected a significant effect.

Figure 3 shows the measured resolution versus wavelength for five proximity intensifiers. The values plotted are the "dynamic resolution," measured by scanning a Baum resolution test pattern¹³ back and forth in order to smooth out the discrete nature of the fiber optic output faceplate and to smooth the grain noise in the phosphor. Typically, if the test pattern is not scanned but is kept stationary, the resolution measured in the intensifiers is 10–20% lower.

An interesting way of studying the resolution of proximity tubes is to express the measured values as a "photocathode inherent resolution," which is a model prediction calculated by taking into account the known fiber optic and phosphor resolutions in each tube and, through the above

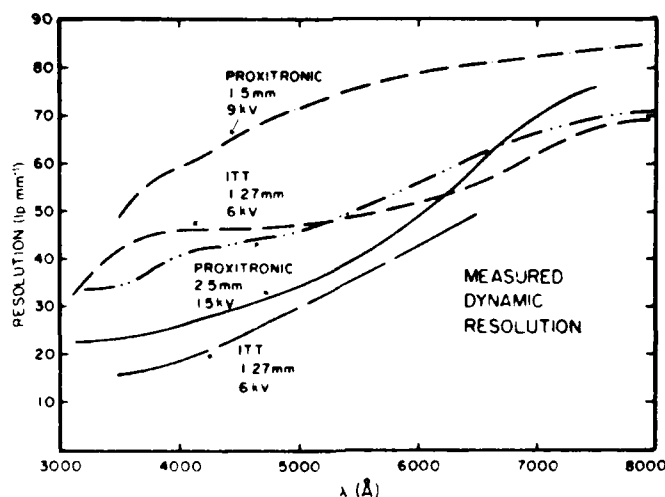


FIG. 3. Resolution of five proximity tubes. Solid curves are for bialkali photocathodes, dashed curves for multialkali.

equations, predicting the resolution each tube would have if the phosphor and fiber optic resolutions were infinitely high and if a standard voltage and separation were applied to each tube. This has been done for 10 multialkali and 2 bialkali tubes, and the results are shown in Fig. 4. The dynamic value of R_{FO} for all tubes was assumed to be the same, and is 167 lp mm^{-1} for fibers having $6\text{-}\mu\text{m}$ spacing. The dynamic value of R_{PHOS} for the ITT tubes was determined to be 125 lp mm^{-1} and for the Proxitronic tubes 180 lp mm^{-1} .

The data for all the multialkali photocathode tubes fall within a band in Fig. 4. The width of the band is created no doubt in part due to true differences in resolution from one photocathode to the next, but also due to the inaccuracies in the assigned values of R_M , R_{FO} , and R_{PHOS} . Presumably, the two bialkali tubes plotted in this figure roughly define a similar band that describes bialkali photocathodes. The data in both Figs. 3 and 4 illustrate that, somewhat surprisingly, multialkali photocathodes have inherently superior resolution to bialkali photocathodes in the blue spectral region. This was observed for proximity tubes from three manufacturers, ITT, Proxitronic, and Galileo. The one bialkali photocathode which created sufficient signal at 7500 \AA to provide a measurable image showed a resolution comparable to the multialkali photocathodes. This would be expected based on the very low emission energy of photoelectrons emit-

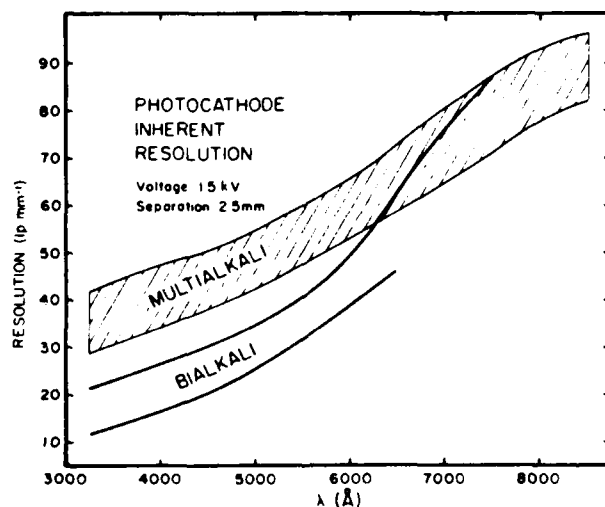


FIG. 4. Photocathode inherent resolution of 10 multialkali and two bialkali proximity tubes.

ted by light at the extreme long wavelength threshold of the photocathode.

The resolution goal we have set for a single-stage astronomical tube is 30–40 lp mm⁻¹ in the blue spectral region. This value is commensurate with that of a multistage, high-gain intensifier system (cf. Table I), with which the proximity tube will ultimately be combined, and is competitive with many current detectors. Figures 3 and 4 show that tubes with multi-alkali photocathodes (and with concurrent satisfactory gains, as we shall see later) can meet this goal, whereas tubes with bi-alkali photocathodes presently have difficulty. We expect some improvement in the future with different spacings and higher gain phosphors.

GAIN

The electron gain of a fiber optically coupled pair of intensifiers is determined by measuring directly the two respective dc photocurrents in the first- and second-stage tubes. When the electron gain of the coupled pair measured in this way and the quantum efficiency of the second stage are known, the photon gain (or simply, "gain") of the first tube may be expressed as the number of photons emitted by its phosphor per photoelectron. The results measured for gain as a function of voltage are shown in Fig. 5 for several proximity tubes and for a Varo electrostatic tube. Each curve is an average of two or more samples of the respective class of tube shown. The "dead voltage," or the amount of energy lost by the electrons in penetrating the bright aluminum layer (plus the black alumi-

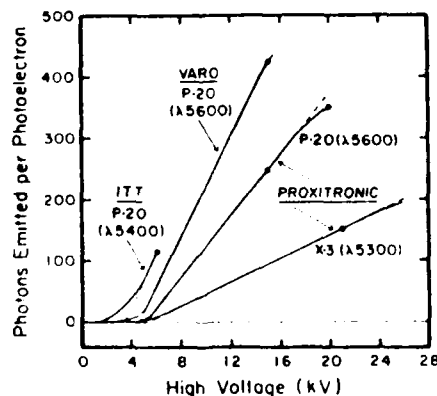


FIG. 5. Gain vs voltage for several intensifiers. Effective wavelength of phosphor emission is shown in parenthesis.

num layer in the Proxitronic tubes), is indicated by the intercept on the abscissa with extrapolation of the straight line portion of the curves. The maximum operating voltages, and therefore maximum gains, of the respective tube(s) represented in each curve are indicated by heavy dots. The efficiencies of the various phosphors may be compared by measuring the straight line slope of each curve. We are now evaluating a Proxitronic tube having a higher efficiency P-20 phosphor (using larger phosphor grains). In spite of the low efficiency and gain of the X-3 phosphor, it remains of interest because its time response is roughly 10^4 times faster than that of a P-20 phosphor.

In an analog detector, the gain of an intensifier must be high enough for the noise in the final recorded image to be dominated by the statistical fluctuations produced by the original photoelectrons released from the first photocathode. When this is the case, the DQE of the detector system is the same as the photocathode quantum efficiency. Stated another way, the counting efficiency of the primary photoelectrons is 100%. Because of a variety of noise sources in most image detectors used to record intensifier outputs (CCDs, linear diode arrays, photographic emulsions, etc.) the gain of a single-stage intensifier is seldom high enough to fulfill this condition. One way of obtaining sufficient gain is through the use of one or more "gain stage" intensifiers using fiber optic coupling between stages. An example of these concepts is the "Big Red" four-stage Varo system with an analog Reticon readout where a DQE of about 90% of the first cathode is achieved.⁴

PULSE HEIGHT DISTRIBUTION

Another requirement for achieving a system DQE equal to the photocathode quantum efficiency is that the intensifier have a good pulse height distribution (PHD). The ideal PHD would be nearly gaussian with few events producing very large or very small signals.

Theoretically, the first stage gain must be high enough that the statistical fluctuations in the number of second stage photoelectrons do not significantly degrade the PHD. In our practical experience, we have found that the gains of intensifiers must be substantially higher than would be predicted on this simple basis because of the inherently broad PHD of a phosphor output intensifier. Indeed, at low gains, the phosphor PHD is quasi-exponential and, even at high gains, more Poissonian than gaussian. This is shown in Figs. 7 and 8.

Figure 6 illustrates the method of measurement of PHDs. Through use of the front shutter, the image of a slit creates a 100-msec burst of a known number of photoelectrons from the first photocathode. The intensified

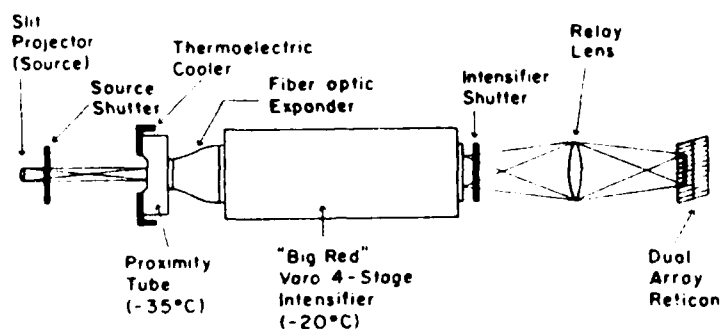


FIG. 6. Experimental apparatus for measuring PHD.

image falls entirely within the area of one of the dual arrays of the Reticon. Dark emission is simultaneously sampled by the adjacent array. The intensifier shutter is opened slightly ahead of the source shutter and remains open for 600 msec to integrate the light from the photoelectron pulses. The resulting video from one such frame gives a highly resolved, high dynamic range record of individual photoelectron pulses.⁴ The total signal from each pulse is integrated over typically three to five diodes via computer, and a PHD, expressed as the probability that a photoelectron pulse will be a given size, is formed of all detected pulses from several hundred frames of data. A PHD of the dark emission in the adjacent array is subtracted from the pulsed lamp PHD, leaving a PHD of the photoemitted electrons only.

The final PHD for "Big Red" alone is given in Fig. 7, which shows the measured data (somewhat noisy), a smoothed representation of same (solid curve), and an estimate of the true relationship (dashed curve) toward the very small-pulse size end of the measured data which otherwise contain a systematic measurement error. Final PHDs for Proxitronic intensifiers operated at three different high voltages are shown in Fig. 8. The abscissa is calibrated in terms of the number of secondary electrons released from Big Red's photocathode by dividing the measured pulse size by the mean pulse size of Big Red alone (Fig. 7).

COUNTING EFFICIENCY

The counting efficiency of an intensifier system operated in the pulse counting mode is the probability that a primary photoelectron will create a detectable pulse at the final output phosphor that is counted one time and

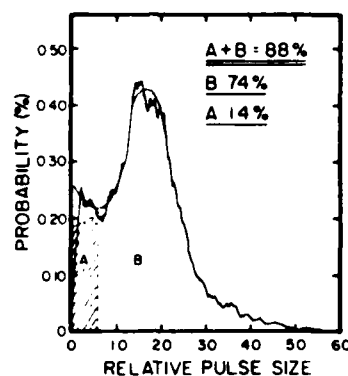


FIG. 7. PHD of Big Red intensifier system. Counting efficiency is $A + B$.

one time only. This probability is equal to the area of the PHD curve. For Big Red alone, the counting efficiency is 88%. This is the sum of the accurately measured area "B" of the PHD in Fig. 7 plus the estimated portion "A." This value is in excellent agreement with our past analog measurements of Varo tubes,⁴ and the pulse-counting measurements of Latham.¹⁴

For the Proxitronic tubes in Fig. 8, the counting efficiencies are disappointingly low, remaining at roughly 50% once the gain is sufficiently above a threshold, which occurs at an operating voltage of 15 kV or so. We are presently investigating the cause of the low counting efficiency. Two magnetically focused intensifiers, one manufactured by RCA and one by ITT, exhibit similar low counting efficiencies (55%).¹⁵ Because neither of these utilizes blackened layers over their phosphors, we do not feel that the black aluminum layer in the Proxitronic tubes is likely to be the cause of the lost electron pulses. Indeed, we suspect the loss is caused by a deadening of phosphor grains during the screen manufacturing process. The uniquely and consistently high counting efficiency measured in Varo tubes, which have screens manufactured in a "dry brushed" process which is significantly different to that of all others we have measured, encourages us that we will discover the exact cause.

A primary motivation in our developing the proximity focused diode for astronomy rather than a microchannel intensifier is because of the exponential PHD and poor (about 33%) counting efficiency we measure for the latter devices.¹⁵ While the present proximity diodes are indeed better, a major goal is to improve them still more.

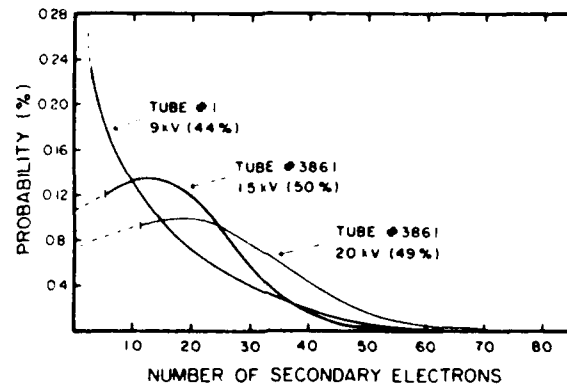


FIG. 8. PHD of proxitronic proximity tubes. Counting efficiency is given in parenthesis.

SIGNAL-INDUCED BACKGROUND

Measurements of the signal-induced background (SIB) are made by measuring the analog output signal in a region of the tube where an opaque mask has been placed over the photocathode window. The photocathode is uniformly illuminated with light of wavelength 4250 Å. The mask is 1.2 mm wide and extends across the full diameter of the field. The output is measured through a 0.8 mm diameter aperture. Results are expressed as a percentage of the output signal (with SIB removed) from an adjacent unmasked area.

SIB measurements are summarized in Table II. The importance of using a blackened layer on the screens of proximity tubes is clearly demonstrated. Indeed, the ITT tubes without a blackened layer exhibited severe SIB. Our attempts to measure the counting efficiency in one such tube were so overwhelmed by SIB that no meaningful value was determined.⁴ Comparison can be made of the SIB in magnetic and electrostatic tubes using Table I and Refs. 6 and 7 (the most meaningful comparison being between single stages).

Also given in Table II (and Table I) is the number of bright ion events created per photoelectron under conditions of uniform full-field illumination. The one ITT proximity tube having a black-layer phosphor (which clearly lowered the overall SIB) emitted one ion for every 700 electrons, severely reducing the signal-to-noise ratio of images. An important difference between the ion SIB in proximity tubes compared to magnetic tubes and especially electrostatic tubes is that the ions remain spatially much closer to the original image element in the signal that causes them.

FIELD EMISSION

We have observed field emission in nearly every proximity tube we have examined when operated at their maximum rated voltages. Considerable effort has gone into eliminating field emission in the Proxitronic tubes during the past few years, and the effort has paid off. A few recent samples of tubes have been operated at their full 6 kV mm^{-1} field strengths while showing no bright emitting points within the active field nor any such points located beyond the active edge. (The latter are revealed by creating an enhanced electron and ion dark emission that falls off with increasing distance from the "beyond-the-edge" source.)

DARK EMISSION

Figure 9 shows the dependence of dark emission on temperature and voltage for a Proxitronic tube with a multialkali photocathode and a separation of 2.5 mm. The curves shown are felt to be representative of other

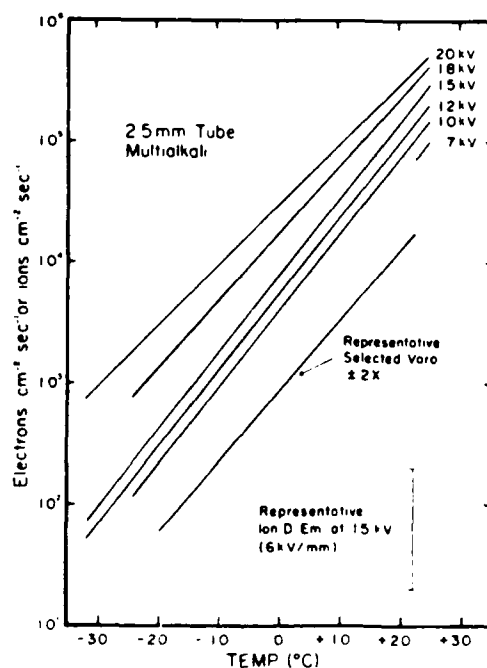


FIG. 9 Dark emission vs temperature and voltage of proximity tube and of Varo electrostatic tube.

Proxitronic and ITT proximity tubes we have examined at comparable field strengths, although our other measurements are not as accurate. The data are for one of the few Proxitronic tubes (No. 3861) that is completely free of field emission, so that the true dark emission of the photocathode could be accurately measured. (There may be evidence via the cooled 18 and 20 kV data that some very weak field emission exists at these two elevated voltages.) The data were obtained by comparing the phosphor output brightness measured by a photomultiplier tube while the photocathode was alternately in complete darkness and then uniformly illuminated such that a known photoelectron flux left the photocathode. A similar measurement is shown of a Varo tube for comparison.

Although dark emission is roughly 10 times higher in a proximity tube than in other tubes, it can be reduced to levels of interest in astronomy by cooling to -30°C , and can probably be further reduced by cooling still more. Our preliminary measurements of a bialkali photocathode at $+20$ and -35°C indicate that the dark emission is at least 10 times lower than that of the multialkali.

A representative range of ion dark emission at room temperature measured in ITT and Proxitronic tubes is indicated in Fig. 9. For Proxitronic tube No. 3861, the lowest value applies, and the temperature dependence follows the same slope as shown for the electron dark emission.

UNIFORMITY OF RESPONSE

Scans of proximity tubes (both ITT and Proxitronic) show them to be uniform in response throughout their field to typically $\pm 2\%$. Fiber optic bundle pattern, phosphor granularity, and mottle structure are so consistently equal or superior to the best tubes we have measured previously* that we no longer quantify them.

SUMMARY

Progress in the development of a proximity intensifier for astronomy is very encouraging. A few samples have now been produced that exhibit good blue response, resolution, gain, dark emission (when cooled), and freedom from field emission. Manufacturing yield of such samples is still low. In the next year we expect to see improved yield and performance through continued refinements. An important next step is to discover and eliminate the cause of lost counting efficiency, observed in several diode intensifiers.

ACKNOWLEDGMENTS

Funding is provided by the National Science Foundation to Steward Observatory for laboratory analysis and scientific input toward the development of a proximity tube for astronomy. Proxitronic-Funk is manufacturing the tubes as their contribution to the development program. We would like to thank Drs. J. B. Oke of Hale Observatories, H. W. Epps of the University of California at Los Angeles Astronomy Department, and H. R. Butcher of the Kitt Peak National Observatory for loaning samples of ITT proximity tubes to Steward Observatory for analysis, and Drs. D. W. Latham and J. C. Geary of the Smithsonian Astrophysical Observatory for first bringing to the attention of Steward Observatory the Proxitronic-Funk intensifiers and for loaning early samples to Steward Observatory. We very much appreciate the discussions of phosphor screen manufacture with Mr. G. Stowe of Varo.

REFERENCES

1. McNall, J., Robinson, L. and Wampler, E. J., *In* "Astronomical Use of Television-Type Image Sensors," NASA SP-256, p. 117 (1970).
2. Boksenberg, A. and Burgess, D. E., *In* "Adv. E.E.P." Vol. 33B, p. 835 (1972).
3. Sheckman, S. A., *Year Book—Carnegie Inst. Washington* **80**, 586 (1981).
4. Hege, E. K., Cromwell, R. H. and Woolf, N. J., *In* "Adv. E.E.P." Vol. 52, p. 397 (1979).
5. Cromwell, R. H., Optical Sciences Center Technical Report No. 38 (1969).
6. Cromwell, R. H. and Dyvig, R. R., *In* "Adv. E.E.P." Vol. 33B, p. 677 (1972).
7. Cromwell, R. H. and Dyvig, R. R., Optical Sciences Center Technical Report No. 81 (1973).
8. Cromwell, R. H. and Smith, G. H., *Proc. S.P.I.E.* **42**, 155 (1973).
9. Cromwell, R. H. and Angel, J. R. P., *In* "Adv. E.E.P." Vol. 52, p. 183 (1979).
10. Angel, J. R. P., Cromwell, R. H. and Magner, J., *In* "Adv. E.E.P." Vol. 52, p. 347 (1979).
11. Craine, E. R. and Cromwell, R. H., *In* "Adv. E.E.P." Vol. 52, p. 339 (1979).
12. Lind, M. A., Zalewski, E. F. and Fowler, J. B., *NBS Tech. Note (U.S.)* **950** (1977).
13. Baum, W. A., *In* "Adv. E.E.P." Vol. 16, p. 391 (1962).
14. Latham, D. W., *Proc. of the IAU-Colloquium* **67** (1982).
15. Allen, R. G., Cromwell, R. H., Liebert, J. W., Macklin, R. H. and Stockman, H. S., *Proc. S.P.I.E.* **445**, 168 (1984).

Speckle Interferometry of Asteroids

I. 433 Eros

J. D. DRUMMOND, W. J. COCKE, E. K. HEGE, AND P. A. STRITTMATTER

Steward Observatory, University of Arizona, Tucson, Arizona 85721

AND

J. V. LAMBERT

Department of Astronomy, New Mexico State University, Las Cruces, New Mexico 88003

Received May 4, 1984; revised September 11, 1984

Analytic expressions for the semimajor and semiminor axes and an orientation angle of the ellipse projected by a triaxial ellipsoid (an asteroid) and of the ellipse segment cast by a terminator across the ellipsoid as functions of the dimensions and pole of the body and the astero-centric position of the Earth and Sun are derived. Applying these formulae to observations of the Earth-approaching asteroid 433 Eros obtained with the speckle interferometry system of Steward Observatory on December 17-18, 1981, and January 17-18, 1982, the following dimensions are derived: $(40.5 \pm 3.1 \text{ km}) \times (14.5 \pm 2.3 \text{ km}) \times (14.1 \pm 2.4 \text{ km})$. Eros' north pole is found to lie within 14° of $RA = 0^h 16^m$ Dec. $= +43^\circ$ (ecliptic longitude 23° , latitude $+37^\circ$). Other than knowing the rotation period of Eros, these results are completely independent of any other data, and in the main confirm the results obtained in the 1974-1975 apparition by other methods. These dimensions, together with a lightcurve from December 18, 1981, lead to a geometric albedo of 0.156 ± 0.010 . A series of two-dimensional power spectra and autocorrelation functions of the resolved asteroid clearly show it spinning in space. © 1985 Academic Press, Inc.

I. INTRODUCTION

While speckle interferometric observations of asteroids have been made in the past (Worden, 1979; Hege *et al.*, 1980a, b; Bowell *et al.*, 1981), they have been used mainly to demonstrate the high angular resolution capability of the technique. [For an introduction into astronomical speckle interferometry we recommend Dainty (1975), Worden (1979), and Hege *et al.* (1982a).] To obtain the most information from this powerful direct method, an asteroid needs to be followed throughout its rotational cycle. By assuming that the asteroid can be modeled as a rotating triaxial ellipsoid, we show in Section II that the changing semimajor axis, semiminor axis, and orientation of the projected ellipse theoretically lead not only to the three axial dimensions of the

asteroid but to the location of its spin axis as well. We also include the case of a non-zero solar phase angle and take into account the terminator cast across the projected ellipse. These analytic expressions for obtaining the dimensions and pole of an asteroid as functions of quantities observable with speckle interferometry can also be used to interpret an entire photometric lightcurve not just the extrema or amplitude, if it is assumed that a lightcurve is generated by the visible illuminated portion of the projected ellipse.

With the speckle interferometry system at Steward Observatory (Hege *et al.*, 1982a), we have begun a program to observe asteroids of various taxonomic classes to provide a check of the assumptions and results obtained by radar, radiometry, photometry, polarimetry, etc., and to

132

0019-1035/85 \$3.00

Copyright © 1985 by Academic Press, Inc.
All rights of reproduction in any form reserved.

The U.S. Government is authorized to reproduce and sell this report. Permission for further reproduction by others must be obtained from the copyright owner.

provide calibration asteroids for these methods. To demonstrate the ability of speckle interferometry to obtain useful results, we begin our program by applying our speckle technique to 433 Eros, since the various methods used to observe it in 1974–1975 have converged to well-agreed-upon dimensions and pole, summarized by Zellner (1976). Our observations of Eros with speckle interferometry in 1981–1982 and the subsequent analysis are presented in Section III, and in Section IV we display a spectacular series of power spectra and autocorrelation functions clearly showing Eros spinning in space.

In several cases, asteroids have been implicated as having satellites from speckle interferometric observations (Hege *et al.*, 1980b; Bowell *et al.*, 1981). If a satellite can be detected with speckle interferometry, then the proof of its existence will be in the ability of the technique to follow the satellite in its orbit about the asteroid, which will also lead to a determination of the mass of the system. Hege *et al.* (1982b) summarize speckle interferometric observations of such a system as represented by Pluto and Charon. We have in hand or have scheduled observations of several of the suspected binary asteroids, but Eros gives no indication of having a satellite by speckle observations.

II. THE FUNDAMENTAL EQUATIONS

A. Derivations

In matrix form, the equation for a point on the surface of a triaxial ellipsoid (asteroid) can be written as

$$\begin{aligned}\bar{\mathbf{x}}'\mathbf{T}'\mathbf{x}' - 1 \\ &= (x'y'z') \begin{pmatrix} 1/a^2 & & \\ & 1/b^2 & \\ & & 1/c^2 \end{pmatrix} \begin{pmatrix} x' \\ y' \\ z' \end{pmatrix}^{-1} \\ &= (x'/a)^2 + (y'/b)^2 \\ &\quad + (z'/c)^2 - 1 = 0. \quad (1)\end{aligned}$$

Let $a \geq b \geq c$ be the principal axial radii, c being the rotational axis. The projection

of the ellipsoid onto the plane of the Earth's sky is an ellipse of the form $\bar{\mathbf{y}}\mathbf{Q}\mathbf{y}$, where \mathbf{y} is a two dimensional vector and \mathbf{Q} is a 2×2 matrix. In an arbitrary coordinate system the equation for the ellipsoid is

$$\bar{\mathbf{x}}\mathbf{T}\mathbf{x} - 1 = 0. \quad (2)$$

Let $\mathbf{x}' = \mathbf{R}\mathbf{x}$, where the transformation between coordinate systems \mathbf{x}' and \mathbf{x} is given by the rotation matrix \mathbf{R} . Then from (1) and (2)

$$\bar{\mathbf{x}}\mathbf{T}\mathbf{x} = \bar{\mathbf{x}}'\mathbf{T}'\mathbf{x}' = \bar{\mathbf{x}}\hat{\mathbf{R}}\mathbf{T}'\mathbf{R}\mathbf{x} \quad (3)$$

which implies that $\mathbf{T} = \hat{\mathbf{R}}\mathbf{T}'\mathbf{R}$.

Writing (2) explicitly

$$\begin{aligned}\bar{\mathbf{x}}\mathbf{T}\mathbf{x} - 1 &= \sum_{ij} T_{ij}x_i x_j - 1 \\ &= T_{11}x^2 + 2T_{12}xy + T_{22}y^2 + 2T_{13}xz \\ &\quad + T_{33}z^2 + 2T_{23}yz - 1 = 0.\end{aligned}$$

Or, gathering terms in x

$$\begin{aligned}T_{11}x^2 + 2(T_{12}y + T_{13}z)x \\ + (T_{22}y^2 + 2T_{23}yz + T_{33}z^2 - 1) = 0. \quad (4)\end{aligned}$$

If we orient ourselves so that the yz plane is the plane of the sky and x lies along our line of sight to a triaxial ellipsoid asteroid, then for a point on the edge of the apparent ellipse not only must x satisfy (4), but since for a given y and z there is only one x which corresponds to the edge, the roots of (4) must be real and equal. Thus the discriminant of (4) must vanish:

$$\begin{aligned}4(T_{12}y + T_{13}z)^2 \\ - 4T_{11}(T_{22}y^2 + 2T_{23}yz + T_{33}z^2 - 1) = 0\end{aligned}$$

or gathering terms in y and z and multiplying by $-1/4T_{11}$

$$\begin{aligned}[1/T_{11}]\{ &(T_{11}T_{22} - T_{12}^2)y^2 \\ &+ 2(T_{11}T_{23} - T_{12}T_{13})yz \\ &+ (T_{11}T_{33} - T_{13}^2)z^2\} - 1 = 0. \quad (5)\end{aligned}$$

Now this equation is in itself quadratic and diagonalizable and can be expressed as

$$\bar{\mathbf{y}}\mathbf{Q}\mathbf{y} - 1 = 0, \quad (6)$$

where $\bar{\mathbf{y}} = (y, z)$ and

$$\mathbf{Q} = \frac{1}{T_{11}} \begin{pmatrix} T_{11}T_{22} - T_{12}^2 & T_{11}T_{23} - T_{12}T_{13} \\ T_{11}T_{23} - T_{12}T_{13} & T_{11}T_{33} - T_{12}^2 \end{pmatrix}.$$

Since (5) is the general equation for an ellipse in the yz plane of the sky, the presence of the cross term in yz indicates that the semimajor (semiminor) axis of the apparent ellipse makes an angle γ with the $y(z)$ axis, where γ is given by

$$\tan 2\gamma = 2Q_{12}/(Q_{11} - Q_{22}). \quad (7)$$

To relate the matrix \mathbf{Q} to the semiaxes of the apparent ellipse we need to find the eigenvalues q of \mathbf{Q} , where

$$\mathbf{Q}\mathbf{y} = q\mathbf{y}.$$

The equation we need to solve then is

$$|\mathbf{Q} - q\mathbf{I}| = 0 = \begin{vmatrix} Q_{11} - q & Q_{12} \\ Q_{12} & Q_{22} - q \end{vmatrix}$$

or

$$q^2 - (Q_{11} + Q_{22})q + (Q_{11}Q_{22} - Q_{12}^2) = 0.$$

From the quadratic formula

$$q = \frac{(Q_{11} + Q_{22}) \pm [(Q_{11} + Q_{22})^2 - 4(Q_{11}Q_{22} - Q_{12}^2)]^{1/2}}{2} \quad (8)$$

and q is related to the semimajor and semiminor axes α and β by

$$q^2 = \begin{pmatrix} 1/\beta^2 \\ 1/\alpha^2 \end{pmatrix}.$$

Now in defining our coordinate system let us choose the y axis as coincident to the asteroid's largest axis (a) at the instant in the rotation when a lies unprojected in the plane of the Earth's sky perpendicular to our line of sight. This allows us to use Euler angles as defined and illustrated by Goldstein (1950). Thus the Euler angle θ is the angle between our z axis in the plane of the sky and z' , the asteroid's spin axis. The Euler angle ϕ is the angle between the line of sight to the asteroid and the line of nodes (which lies in the plane of the Earth's sky), and by our chosen coordinate system is a

constant $\pi/2$. The third Euler angle, ψ , is the rotational phase angle defined as the angle between x' (along which a lies) and the line of nodes; ψ is 0 when the longest body axis is perpendicular to our line of sight and occurs at maximum projected area. The transformation (3) leads to the symmetric T matrix, where

$$T_{11} = \frac{\cos^2\theta \sin^2\psi}{a^2} + \frac{\cos^2\theta \cos^2\psi}{b^2} + \frac{\sin^2\theta}{c^2}$$

$$T_{12} = T_{21} = -\frac{\cos\theta \sin\psi \cos\psi}{a^2} + \frac{\cos\theta \sin\psi \cos\psi}{b^2}$$

$$T_{13} = T_{31} = -\frac{\cos\theta \sin\theta \sin^2\psi}{a^2} - \frac{\cos\theta \sin\theta \cos^2\psi}{b^2} + \frac{\sin\theta \cos\theta}{c^2}$$

$$T_{22} = \frac{\cos^2\psi}{a^2} + \frac{\sin^2\psi}{b^2}$$

$$T_{23} = T_{32} = \frac{\sin\theta \sin\psi \cos\psi}{a^2} - \frac{\sin\theta \sin\psi \cos\psi}{b^2}$$

$$T_{33} = \frac{\sin^2\theta \sin^2\psi}{a^2} + \frac{\sin^2\theta \cos^2\psi}{b^2} + \frac{\cos^2\theta}{c^2}.$$

After simplification (8) can be written

$$q^2 = \frac{-B \pm \sqrt{B^2 - 4AC}}{2A} \quad (9)$$

where

$$A = a^2b^2c^2T_{11} = b^2c^2 \cos^2\theta \sin^2\psi + a^2c^2 \cos^2\theta \cos^2\psi + a^2b^2 \sin^2\theta$$

$$-B = a^2b^2c^2T_{11}(Q_{11} + Q_{22}) = a^2(\sin^2\theta \sin^2\psi + \cos^2\psi) + b^2(\sin^2\theta \cos^2\psi + \sin^2\psi) + c^2 \cos^2\theta$$

$$C = a^2b^2c^2T_{11}(Q_{11}Q_{22} - Q_{12}^2) = 1.$$

Therefore, the semimajor and semiminor axes of the ellipse projected by a triaxial ellipsoid are

$$\alpha = (q^+)^{-1/2} = \left[\frac{2A}{-B - \sqrt{B^2 - 4AC}} \right]^{1/2}$$

$$\beta = (q^-)^{-1/2} = \left[\frac{2A}{-B + \sqrt{B^2 - 4AC}} \right]^{1/2}$$

and γ makes an angle with the y axis

$$\gamma = \frac{1}{2} \tan^{-1} \left[\frac{2 \sin \theta \cos \psi \sin \psi (b^2 - a^2)}{a^2(\sin^2 \theta \sin^2 \psi - \cos^2 \psi) + b^2(\sin^2 \theta \cos^2 \psi - \sin^2 \psi) + c^2 \cos^2 \theta} \right] \quad (10)$$

from (7).

Note that (9) is expressed as a quadratic solution which has some well-known properties. For instance, since the product of the roots of a quadratic equation are

$$q^+ q^- = C/A,$$

we can easily express the projected area of the triaxial ellipsoid as

$$\begin{aligned} \pi \alpha \beta &= \pi (q^+ q^-)^{-1/2} = (A/C)^{1/2} = A^{1/2} \\ &= abc T_{11}^{1/2} \quad \text{since } C = 1. \end{aligned}$$

Over a few rotations of the asteroid, we can regard θ as constant and $\phi = \pi/2$. Therefore we can find α , β , and γ as functions of only ψ , the rotational angle. If the latitude of the sub-Earth point is high enough, the projected ellipse will rotate smoothly through 360° . If, however, the latitude is low the ellipse will appear to reverse directions. Taking the derivative of γ with respect to ψ we can see that when the sub-Earth point lies in the body's northern hemisphere ($\theta > 0$), γ will increase monotonically, or decrease monotonically if in the southern hemisphere ($\theta < 0$), provided that $\cos^2 \theta < (a^2 - b^2)/(a^2 - c^2)$. If $\cos^2 \theta > (a^2 - b^2)/(a^2 - c^2)$ the projected ellipse will reverse directions when

$$\cos^2 \psi = \{ [\sec^2 \theta (a^2 - b^2)/(a^2 - c^2)] - 1 \} / \{ [(a^2 - b^2)/(a^2 - c^2)] - 2 \}.$$

Another consideration is that there is a twofold ambiguity in the determination of θ . The rotational axis can make either an angle θ or $180^\circ - \theta$ with the plane of the sky, both corresponding to the same latitude in the same hemisphere for the sub-

Earth point. The northern or southern hemisphere can easily be determined by the sense of rotation: if the apparent ellipse rotates through the y axis (through the maximum α) in a counterclockwise (north-east-south-west) direction, the sub-Earth point lies in the northern hemisphere, and vice versa. However, without some other piece of information, such as would be conveyed by a terminator, it is not possible to resolve the θ ambiguity.

We now have the equations relating the body dimensions and rotational pole direction to the observed size, shape, and orientation of the ellipses projected by a rotating triaxial ellipsoid. Using a nonlinear least squares technique we can solve for the six unknown parameters a , b , c , θ , and the zero points ψ_0 and γ_0 , from measurements of the observables α , β , and γ as a function of time (or ψ) for a known rotational period. Thus far we have assumed, however, that we see the projected ellipse at full illumination, i.e., at a solar phase angle of 0 . Particularly at large phase angles we must take the terminator into consideration. We will now outline the derivation for the size, shape, and orientation of the terminator ellipse segment as a function of the same parameters, with the added information of the known position of the Sun, but this time from a vector analysis approach rather than from the use of matrix transformations. The answers should converge for a solar phase angle of 0 .

We first note that in body-centered coordinates, where a point on the surface of triaxial ellipsoid is given by (1)

$$f(x', y', z') = (x'/a)^2 + (y'/b)^2 + (z'/c)^2 = 1, \quad (11)$$

the unit vector to the Earth is given by $\mathbf{E} = (i, j, k)$ where

$$\begin{aligned} i &= -\cos \theta \sin \psi \\ j &= -\cos \theta \cos \psi \\ k &= \sin \theta \end{aligned} \quad (12)$$

and the unit vector to the Sun is given by $\mathbf{S} = (l, m, n)$ where

$$\begin{aligned} l &= -\cos \theta_{\odot} \sin \psi_{\odot} \\ m &= -\cos \theta_{\odot} \cos \psi_{\odot} \\ n &= \sin \theta_{\odot}. \end{aligned} \quad (13)$$

The body centered celestial coordinates of the Earth and Sun are θ, ψ , and $\theta_{\odot}, \psi_{\odot}$, where the θ 's are latitudes of the sub-Earth and sub-Sun points and the ψ 's are related to the longitudes of these points (L , measured in a right-handed coordinate system from the a axis) by $\psi = -(L + 90^\circ)$.

Since the outward normal for a point on the surface of an ellipsoid described by f (Eq. (1)) is given by ∇f , and since the terminator is the locus of points whose outward normals are perpendicular to the direction to the Sun (\mathbf{S}), the terminator equation is $\mathbf{S} \cdot \nabla f = 0$, which leads to

$$\begin{aligned} -x'_T \cos \theta_{\odot} \sin \psi_{\odot}/a^2 \\ - y'_T \cos \theta_{\odot} \cos \psi_{\odot}/b^2 \\ + z'_T \sin \theta_{\odot}/c^2 = 0 \end{aligned} \quad (14)$$

where from (1)

$$(x'_T/a)^2 + (y'_T/b)^2 + (z'_T/c)^2 = 1. \quad (15)$$

As before we rotate the yz plane of the Earth's sky so that the z axis coincides with the projection of the body's rotational axis. The obliquity, ρ , is the angle required to rotate about the line of sight to the asteroid (the x axis) until the spin axis is in the xz plane. If the Earth and Sun define the original xy plane, then ρ is also the angle between the position angle of the Sun (centered on the asteroid) and the y axis, measured counterclockwise (N-E-S-W) from the Sun (see Appendix I). We then get

x'_T, y'_T , and z'_T in terms of the new coordinates x, y, z

$$x'_T = -x \cos \theta \sin \psi + y \cos \psi + z \sin \theta \sin \psi$$

$$y'_T = -x \cos \theta \cos \psi - y \sin \psi + z \sin \theta \cos \psi \quad (16)$$

$$z'_T = x \sin \theta + z \cos \theta.$$

and substituting into (14) and recombining, we obtain

$$\begin{aligned} x(l/a^2 + jm/b^2 + kn/c^2) \\ + y(l \cos \psi/a^2 - m \sin \psi/b^2) \\ + z(l \sin \theta \sin \psi/a^2 \\ + m \sin \theta \cos \psi/b^2 \\ + n \cos \theta/c^2) = 0. \end{aligned} \quad (17)$$

Next we solve (17) for x , substitute this back into (16), and use x'_T, y'_T, z'_T in terms of only y and z in (14). This yields an expression for the terminator as seen projected onto the Earth's plane of sky, which we transform into an ellipse as we did in the solar phase = 0 case, except that the discriminant of (4) does not vanish, and therefore (4) must be solved fully.

It is advantageous to express the unit vector to the Sun in terms of known constraints, e.g., $\mathbf{E} \cdot \mathbf{S} = \cos \omega$, where ω is the known solar phase angle:

$$\begin{aligned} l &= -\cos \theta_{\odot} \sin \psi_{\odot} \\ &= -[\cos \omega \cos \theta \sin \psi \\ &\quad + \sin \omega (\sin \rho \sin \theta \sin \psi \\ &\quad - \cos \rho \cos \psi)] \end{aligned}$$

$$\begin{aligned} m &= -\cos \theta_{\odot} \cos \psi_{\odot} \\ &= -[\cos \omega \cos \theta \cos \psi \\ &\quad + \sin \omega (\cos \rho \sin \psi \\ &\quad + \sin \theta \sin \rho \cos \psi)] \end{aligned}$$

$$\begin{aligned} n &= \sin \theta_{\odot} = \cos \omega \sin \theta \\ &\quad - \sin \omega \cos \theta \sin \rho. \end{aligned} \quad (18)$$

We finally get after solving (4) and (8) for the terminator as seen by the Earth, and simplifying, an expression analogous to (9)

$$q_T^2 = \frac{-B_T \pm \sqrt{B_T^2 - 4A_T C_T}}{2A_T}$$

where $A_T = b^2 c^2 i l + a^2 c^2 j m + a^2 b^2 k n$

$$C_T = b^2 c^2 l^2 + a^2 c^2 m^2 + a^2 b^2 n^2$$

$$-B_T = -BC_T - a^2 b^2 c^2 \sin^2 \omega$$

and the expression analogous to (10)

$$\gamma_T = \frac{1}{2} \tan^{-1} \left[\frac{\sin \theta \sin 2\psi(a^2 - b^2) + \sin^2 \omega \sin 2\rho a^2 b^2 c^2 / C_T}{[\cos 2\psi(a^2 - b^2) + (a^2 i^2 + b^2 j^2 + c^2 k^2) - c^2 - \sin^2 \omega \cos 2\rho a^2 b^2 c^2 / C_T]} \right]$$

B. Implications for Lightcurves

Since the cusps are points that lie on the edge of both the projected ellipse and the terminator ellipse, since the terminator ellipse is internally tangent to the projected ellipse, and since a line connecting the cusps passes through the common center of both ellipses, it can be shown that the illuminated visible area (A_i) of a smooth ellipsoid seen at some phase angle is given by

$$A_i = (\pi\alpha\beta + \pi\alpha_T\beta_T)/2$$

$$= \pi/2[A^{1/2} + A_T/C_T^{1/2}] \quad (19)$$

and the area in shadow is

$$A_s = \pi/2[A^{1/2} - A_T/C_T^{1/2}]. \quad (20)$$

The area in shadow is larger than the illuminated area when $A_T < 0$ (and therefore β_T is negative). Derivations of the lightcurve equations for a geometrically scattering triaxial ellipsoid are given by Barucci and Fulchignoni (1982) and by Ostro and Connelly (1984). The latter authors correct some of the equations of the former and note that the area in shadow can be larger or smaller than the illuminated area depending, respectively, on whether or not "the plane of the terminator intersects the solar phase angle."

Equations (19) and (20) lead to some interesting considerations with regard to information gathered from photometry. Assuming that a lightcurve is generated by only the changing illuminated area as a function of rotation, then (19) is our analytic expression for a lightcurve. In reality, (19) may only be proportional rather than equal to the observed intensity as a function of time, but the proportionality factors

should be expressible as functions of not only ω , the solar phase angle (the usual phase function), but also of the obliquity ρ and the aspect ($90^\circ - \theta$). In fact, any attempt to deduce microscopic or macroscopic properties of asteroids should include the geometrical effect that a terminator has on the amount of area in shadow. The usual phase function does not completely describe the behavior or the brightness of an asteroid over time. Especially at larger phase angles, completely different lightcurves or extrema of brightness can result from a different θ or ρ at the same ω (Dunlap, 1971; Surdej and Surdej, 1978; Barucci *et al.*, 1982).

The three methods of rotational pole determination, the lightcurve amplitude/aspect relation, the brightness/aspect relation (Zappalà *et al.* 1983; Zappalà and Knežević 1984), and photometric astrometry (Taylor, 1979; Taylor and Tedesco, 1983), are all affected by improper consideration of the area in shadow bounded by the terminator and the dark limb. The amplitude and brightness of lightcurves should be judged taking the location of the terminator into effect. Photometric astrometry, which relies on a comparison of extremal timings over long intervals, will lead to spurious results if the terminator is not considered, because the epoch of maximum and minimum light shift with respect to the maximum and minimum projected total area as a function of ω and θ and ρ . Taylor and Tedesco (1983) are aware of this and restrict lightcurve comparisons to observations made at the same ecliptic longitude and solar phase angle, which eliminates the dependence of lightcurve shifts with respect

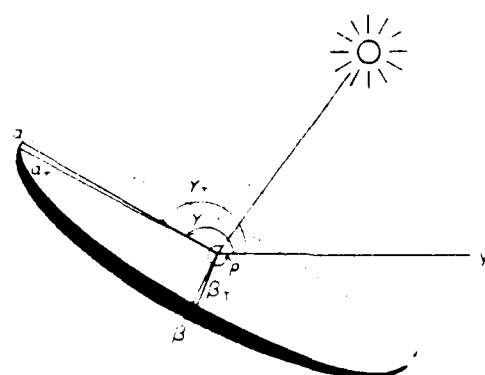


FIG. 1. The ellipse projected by a triaxial ellipsoid. $\alpha, \beta, (\alpha_T, \beta_T)$ are the semimajor and semiminor axes of the projected body (terminator) ellipse, and $\gamma(\gamma_T)$ is the position angle of $\alpha(\alpha_T)$ measured from x in the xy plane of the Earth's sky. The x axis lies along the line of sight to the asteroid. The obliquity p is defined in Appendix I.

to θ and ω , but not to ρ . We define an amplitude of a predicted lightcurve as the maximum illuminated area divided by the minimum over a rotation, a phase lag as the epoch of maximum illuminated area minus the epoch of maximum total projected area, and list these quantities in the results of each model fit for Eros in Section III.

C. Summary

Recapitulating, with reference to Fig. 1, to Appendices I and II, and to the unit vectors (12) and (18), the semiaxes of the el-

lipse of the body seen in projection for solar phase angle $\omega = 0$ are (from Eq. (9) *et seq.*)

$$(\alpha^*)^2, (\beta^*)^2 = \frac{2A}{-B \pm \sqrt{B^2 - 4AC}}, \quad (21)$$

where superscript signs specify the corresponding eigenvalues and

$$\begin{aligned} A &= (bci)^2 = (acj)^2 + (abk)^2 \\ -B &= a^2(1 - i^2) + b^2(1 - j^2) \\ &\quad + c^2(1 - k^2) \\ C &= 1, \end{aligned}$$

and

$$\tan 2\gamma = \frac{[\sin \theta \sin 2\psi(a^2 - b^2)]}{\{\cos 2\psi(a^2 - b^2) + [(ai)^2 + (bj)^2 + (ck)^2] - c^2\}}. \quad (22)$$

We note that γ reverses direction if

$$\cos^2 \theta > \frac{a^2 - b^2}{a^2 - c^2}.$$

For solar phase angle $\omega \neq 0$ the semiaxes of the ellipse due to the terminator (subscript T) are

$$(\alpha_T)^2, (\beta_T)^2 = \frac{2A_T}{-B_T \pm \sqrt{B_T^2 - 4A_T^2 C_T}}, \quad (23)$$

where the sign convention for the roots is as for Eq. (21) and

$$A_T = (bci)^2 + (acj)^2 + (abk)^2$$

$$C_T = (bci)^2 + (acm)^2 + (abn)^2$$

$$-B_T = C_T(-B) - a^2 b^2 c^2 \sin^2 \omega, \text{ and}$$

$$\tan 2\gamma_T = \frac{[\sin \theta \sin 2\psi(a^2 - b^2) + \sin^2 \omega \sin 2\rho a^2 b^2 c^2 / C_T]}{\{\cos 2\psi(a^2 - b^2) + [(ai)^2 + (bj)^2 + (ck)^2] - c^2 - \sin^2 \omega \cos 2\rho a^2 b^2 c^2 / C_T\}}. \quad (24)$$

Note that as the solar phase angle goes to 0, $C_T \rightarrow A$, $A_T \rightarrow A$, $B_T \rightarrow AB$, and, thus, $\alpha_T, \beta_T \rightarrow \alpha, \beta$, and $\gamma_T \rightarrow \gamma$. The illuminated area is given by (19) and the area in shadow by (20).

III. 433 EROS

A. Speckle Interferometry

To inaugurate our speckle interferometry studies of minor planets, treated as smooth,

featureless, geometrically scattering tri-axial ellipsoids, rotating about their shortest (c) axis, we chose the asteroid 433 Eros since it is perhaps the best studied asteroid of all, with well-agreed-upon rotational pole coordinates and axial dimensions. With a 300-Å-wide filter at 5500 Å, we made seven 10-min observations of Eros over the two consecutive nights of December 17 and 18, 1981, and again over January 17 and 18, 1982, using the 2.3-m telescope and speckle camera and equipment (Hege *et al.*, 1982a) of Steward Observatory. Each Eros observation was preceded and followed by a similar observation of a nearby ($<1^\circ$) star. The unbiased two-dimensional speckle image power spectrum of Eros was divided (deconvolved) by the unbiased power spectrum of the stars observed before and after to remove the modulation transfer function of the telescope and the seeing (Hege *et al.*, 1982a). The adopted parameters of the projected ellipse for each observation are the averages of four independent measurements of α , β , and γ ; each deconvolution (one with a star observed before and one with a star observed after Eros) was examined over two regions (one at high spatial frequencies and one at low frequencies). The semimajor axis, semiminor axis, and relative position angle of the long axis were determined by finding the best fit to the power spectrum of a uniformly bright ellipse.

We assume that the measured ellipse will be well approximated by an ellipse that is a

TABLE I
LEAST-SQUARES RESULTS FOR EROS DECEMBER
17-18, 1981: BIAXIAL CASE $\omega = 40^\circ$

	2a	2b	θ	ϕ_0	ρ
2a = 38.9 \pm 2.5 km	2.5 km				
2b = 14.0 \pm 1.9 km	0.11	1.9 km			
$\theta = -75^\circ \pm 26^\circ$	0.66	-0.02	26°		
$\phi_0 = -7^\circ \pm 106^\circ$	-0.05	0.14	-0.19	106°	
$\rho = 69^\circ \pm 105^\circ$	0.06	-0.14	0.20	-1.00	105°

Note: Pole (1950): RA = 48° DEC = +48° ($\pm 31^\circ$). Phase lag of maximum = 64°, minimum = 66°. Amplitude: 1.094. Standard error of fit: 4.8 km.

TABLE II
LEAST-SQUARES RESULTS FOR 433 EROS JANUARY
17-18, 1982: BIAXIAL CASE $\omega = 52^\circ$

	2a	2b	θ	ϕ_0	ρ
2a = 43.8 \pm 4.3 km	4.3 km				
2b = 14.6 \pm 3.0 km	0.08	3.0 km			
$\theta = -58^\circ \pm 12^\circ$	0.51	0.15	12°		
$\phi_0 = 48^\circ \pm 14^\circ$	0.09	0.56	0.24	14°	
$\rho = -59^\circ \pm 14^\circ$	-0.08	-0.54	0.25	0.94	14°

Note: Pole (1950): RA = 5° DEC = 37° ($\pm 10^\circ$). Phase lag of maximum = 4°, minimum = 2°. Amplitude: 1.369. Standard error of fit: 7.9 km.

mean between the ellipse due to the terminator and the projected ellipse. To form this mean we calculate the ellipse that has the same area and the same ratios of moments as does the visible illuminated part of the asteroid as found with the equations derived in Section II. Assuming uniform illumination, a y moment, z moment and cross moment can be calculated for the illuminated figure as

$$\int y^2 dy dz, \quad \int z^2 dy dz, \quad \int yz dy dz,$$

respectively. We include a "photometric constraint" by requiring that the mean ellipse have the same area as does the visible illuminated portion of the asteroid, in addition to having the same ratio of y , z , and yz moments. We then compare these calculated mean ellipses to our observations using sets of measured α , β , and γ , as functions of rotational phase, by means of a nonlinear least-squares program adapted from Jefferys (1980). To put the dimensionless γ on equal footing in the least-squares program with α and β we weight each γ by $(\alpha^2 - \beta^2)^{1/2}$. This makes sense because the more eccentric the ellipse, the easier it is to determine its position angle, and the greater the weight assigned to γ .

Table I lists the results of a five-parameter (biaxial) fit for the December 1981 run, while Tables II and III list the biaxial and triaxial results for January 1982. Biaxial fits yield the diameters 2a and 2b ($c = b$), the astero-centric sublatitudes of the Earth, θ , a

TABLE III
LEAST-SQUARES RESULTS FOR 433 EROS JANUARY 17-18, 1982: TRIAXIAL CASE $\omega = 52$

	2a	2b	2c	θ	ψ_0	ρ
2a = 46.7 ± 4.5 km	4.5 km					
2b = 18.8 ± 3.7 km	0.21	3.7 km				
2c = 13.3 ± 13.3 km	0.01	-0.17	13.3 km			
$\theta = -51^\circ \pm 9^\circ$	0.56	0.03	0.35	9°		
$\psi_0 = 30^\circ \pm 15^\circ$	0.08	0.50	-0.01	-0.01	15°	
$\rho = -43^\circ \pm 15^\circ$	-0.08	-0.49	-0.00	-0.02	-0.94	15°

Note. Pole (1950) RA = 356° DEC = $+46^\circ$; ($\pm 10^\circ$). Phase lag of maximum: -8° ; minimum: -4° . Amplitude: 1.365. Standard error of fit: 8.3 km.

rotational zero point, ψ_0 , and the obliquity, ρ . Triaxial fits also yield c , but near a polar aspect c is so foreshortened that it becomes indeterminate and only a biaxial fit becomes possible. This was the case in December and a triaxial solution could not be found.

The θ , $180^\circ - \theta$ ambiguity exists only for a solar phase angle of 0. In theory, the effect of the terminator should resolve the ambiguity, but in practice the difference may not always be significant enough to provide a solution. For every model, we examined fits for both counterparts of the θ ambiguity, but near a polar aspect only one global minimum in the χ^2 hyperspace is to be expected since the ambiguity disappears when $\theta = \pm 90^\circ$. Thus, between the two solutions for January, the one most closely matched to the single December solution is chosen.

In each table are listed the results and the 1σ (standard deviation) errors determined from the fit. The full correlation matrix, where the diagonal elements are these same formal errors and the off-diagonal elements are the normalized correlation coefficients, is given in each table as well. The 1950 celestial coordinates of the pole derived from θ , ρ , the position of the asteroid, and the position of the Sun are then given, followed by the phase lags and lightcurve amplitudes as previously defined, with the phase lag for maximum listed first. Finally, the value of the standard error (in kilometers) from the fit is listed, i.e.

$$SE = \left[\frac{\text{residuals}^2}{N - n} \right]^{1/2} \quad (25)$$

where $N = 21$ equations of condition, $n = 5$ or 6 parameters, and the residuals are between the measured and predicted α , β , and $(\alpha^2 - \beta^2)^{1/2}\gamma$. To mitigate, to some extent, the model dependence of our final determination of the dimensions and pole of Eros, we first form weighted averages of the parameters from Tables II and III for January using $c = b$ from biaxial fits, and using the $1/\sigma^2$ as weights. Then we find weighted averages between January and December.

The determination of the error in the location of the pole depends only on the errors of θ and ρ . The area of uncertainty on the sky surrounding each pole is wedge shaped, but we quote the radius of a circle with the same area for convenience. When finding the weighted pole between two determinations (for example, between the December and January poles), we weight each according to the area of error and locate the pole between the two.

Our best estimate of the dimensions and pole are given in Table IV, along with a consensus model from Zellner (1976), who used photometric, polarimetric, spectroscopic, radiometric, radar, and occultation results from the 1974-1975 apparition of Eros to synthesize a coherent model. His pole is based on the results of Millis *et al.* (1976) and Scaltriti and Zappalà (1976), who used an amplitude/aspect relationship to

TABLE IV
COMPARISON OF RESULTS FOR 433 EROS

Dimensions		
Speckle interferometry (this paper)		
$2a = 40.5 \pm 3.1$ km	Pole (1950) RA	-4°
$2b = 14.5 \pm 2.3$ km		$+14^\circ$
$2c = 14.1 \pm 2.4$ km		DEC = $+43^\circ$
Consensus model (Zellner, 1976)		
$2a = 36 \pm 1$ km	Pole (1950) RA	$-10 \pm 2^\circ$
$2b = 15 \pm 1$ km		DEC = $+16 \pm 2^\circ$
$2c = 13 \pm 1$ km		
Radar (Jurgens and Goldstein, 1976)		
$2a = 37.2 \pm 0.3$ km	Assumed Pole	
$2b = 15.7 \pm 0.3$ km		
$2c$ assumed = 14 km		
Radiometry (Lebofsky and Rieke, 1979)		
$2a = 39.3 \pm 2.0$ km	Assumed Pole	
$2b = 16.1 \pm 0.8$ km		
$2c$ assumed = $2b$		
Pole Coordinates		
	1950 Ecliptic	
	Longitude	Latitude
This paper	$23^\circ (\pm 14^\circ)$	$+37^\circ$
Scaltrini and Zappala (1976)	$17^\circ \pm 1^\circ$	$+10^\circ \pm 4^\circ$
Millis <i>et al.</i> (1976)	$15.4^\circ \pm 2.2^\circ$	$+9.3^\circ \pm 3.8^\circ$
Dunlap (1976)	$16^\circ \pm 3^\circ$	$+12^\circ \pm 1^\circ$
Lumme <i>et al.</i> (1981)	15°	$+20^\circ$
Taylor (1984) from 1974-1975	$18^\circ (\pm 2.0^\circ)$	$+7^\circ$
from 1981-1982	$21^\circ (\pm 3.3^\circ)$	$+13^\circ$

find a pole, and of Dunlap (1976), who used photometric astrometry. Table IV also shows the results of the radar study of Eros by Jurgens and Goldstein (1976), who assumed a c axis diameter of 14 km and from Dunlap's pole a sublatitude of 20° (although according to our calculations with Dunlap's pole it should have been 6°). A detailed thermal modeling of Eros was compared to radiometric observations by Lebofsky and Rieke (1979), who assumed $b = c$ and Zellner's pole; their results are also shown in Table IV. The ecliptic coordinates of Eros' pole as determined since Vesely's (1971) summary of the subject complete Table IV. Taylor (1984) has used photometric astrometry for the 1974-1975 apparition of Eros, and independently for the 1981-1982 lightcurves to find the poles listed in Table IV.

Figure 2 shows our weighted model (solid line) prediction and the measured major axes (upper symbols) and minor axes (lower) points for the December (solar phase angle = 40°) run. The upper dashed

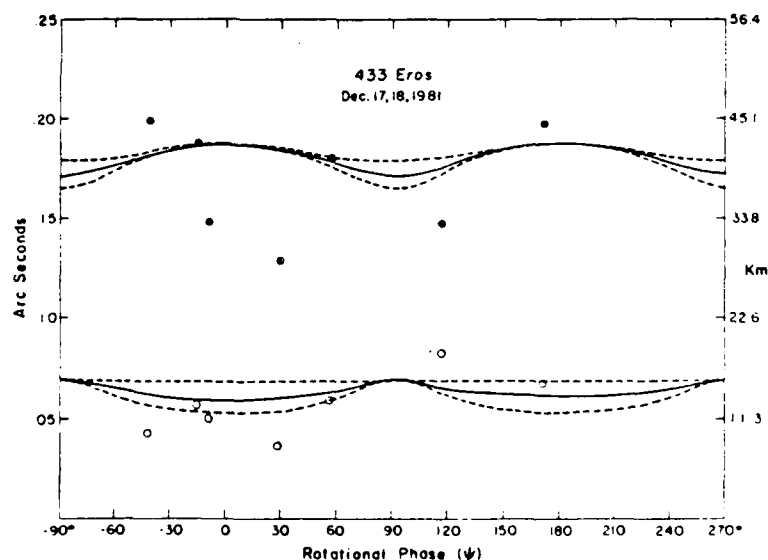


FIG. 2. Major diameter (upper part of figure) and minor diameter of 433 Eros as a function of rotational phase over Dec. 17-18, 1981. The measured diameters are shown as dots (solid for major and open for minor diameters), the solid lines are the predicted measured diameters using our results from Table IV, the dashed line above each solid line is the predicted projected body diameter, and the dashed line below is the predicted terminator diameter.

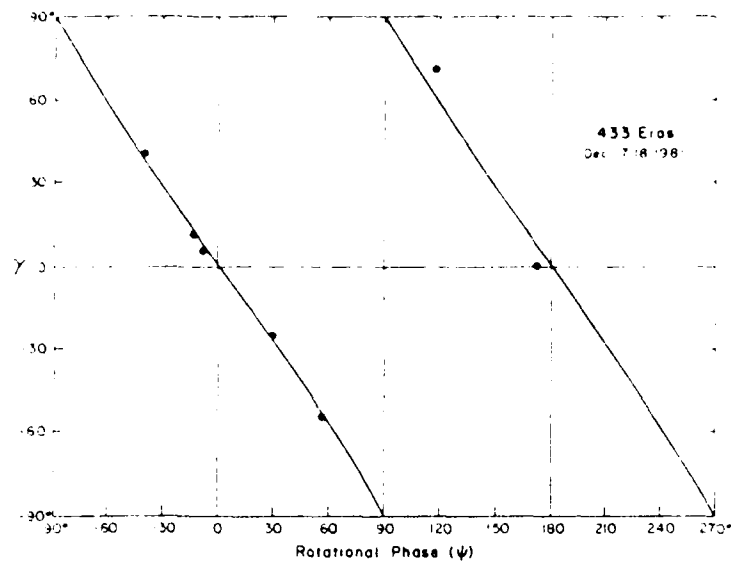


FIG. 3. γ as a function of rotational phase over Dec. 17-18, 1981. Measured γ 's are dots; the solid line is the predicted position angle of the illuminated ellipse using our parameters in Table IV. The position angle of the projected ellipse and the terminator fall within the width of the solid line. The negative slope indicates that the sub-Earth point lies in the asteroid's southern hemisphere.

line through each set of points is due to the projected body ellipse while the lower dashed line is due to the terminator ellipse; the actual model fit always falls between the two. Figure 3 shows the fit to γ . Figures 4 and 5 are for the January (52°) run, but this time the nonlinear, least-squares program tended to values of 0 for the minor

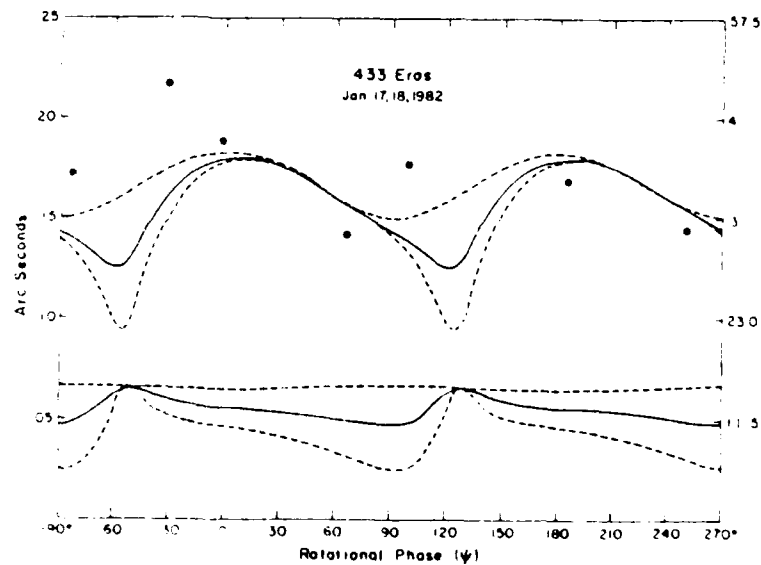


FIG. 4. Same as Fig. 2, but for Jan. 17-18, 1982. Because the minor diameter was apparently unresolved, we do not plot the measured minor diameters. The nominal resolution limit of the 2.3-m telescope is 0.05.

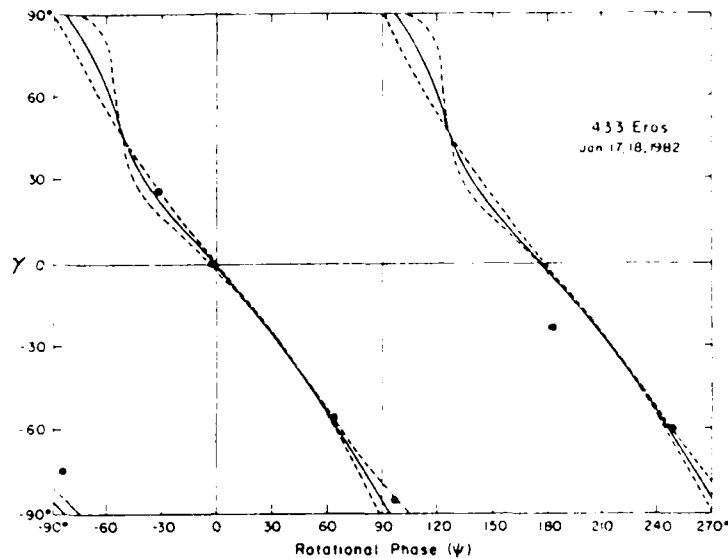


FIG. 5. Same as Fig. 3, but for Jan. 17–18, 1982. The dashed line through (0,0) is the position angle of the projected ellipse. The other dashed line is the position angle of the terminator.

axes, implying that the short dimension of the projected body ellipse, made even smaller by the terminator, was 0, i.e., was not resolved. We, therefore, set the "measured" minor axes equal to $0''.05$ ($=11.5$ km), the nominal resolution limit of the 2.3-m telescope, but did not use the β residuals in finding SE, set $N = 14$ instead of 21 in Eq. (25), and did not plot measured β 's in Fig. 4. While the scatter is rather large for α and β (with some systematic trend evident in the residuals for January), it is small for the γ curve. This is to be expected since the viewing geometries during these runs is rather polar, with latitudes of the sub-Earth point being -74° in December and -57° in January. Such situations create little change in α or β and a nearly linear change in γ as a function of rotational phase. It is immediately obvious that the Earth lies in the asteroid's southern hemisphere because for our coordinate system a $\theta < 0$ yields a negative slope for the γ curve, and for $\theta > 0$, a positive slope, as a function of ψ . The sense of rotation is undoubtedly the easiest piece of information to obtain from speckle interferometry, whereas neither photomet-

ric astrometry nor radiometry (Matson, 1971; Morrison, 1977) can determine this in less than several months.

Figures 6 and 7 illustrate the lightcurve for December and January generated by (19), again with the upper dashed line representing the area of the projected ellipse, the lower dashed line that of the terminator ellipse, and the solid line that of the total illuminated area.

B. Eros' Lightcurve and Albedo

On December 18, 1981, D. Tholen obtained the lightcurve of Eros shown in Fig. 8 with the 154-cm telescope at the Catalina station of the University of Arizona. A minimum of $B = 10.96$ occurred at 4.517 UT and a maximum of 10.59 at 5.955 UT. With a rotational period of 5.2703 hr from Tedesco (1979), which is the mean of the sidereal periods determined by Millis *et al.* (1976) and Dunlap (1976) during the 1974–1975 apparition, we note that the difference between the maximum and minimum is 1.438 hr or 98° in rotational phase. A comparison of Tholen's lightcurve characteristics with one predicted from Zellner's

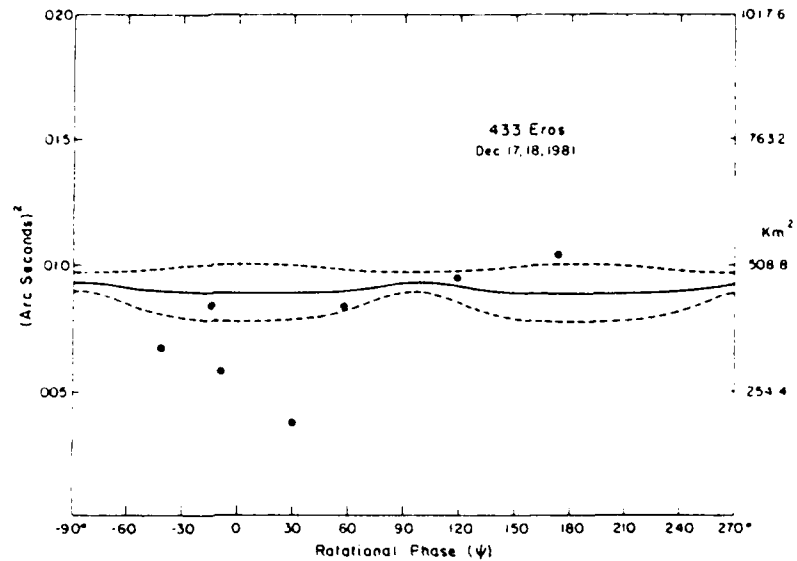


FIG. 6. Predicted "lightcurve" of Eros for Dec. 17-18, 1981. Assuming that the lightcurve is generated by the illuminated area, the upper dashed line is the predicted area of the projected body ellipse, the lower dashed line is the area of the terminator ellipse, and the solid line is the illuminated area, all from our model for Eros given in Table IV. The dots in the figure are the products of our measured α and β .

model, one from the December fit, and one from our weighted model (Fig. 6) is listed in Table V. (Note that the ordinate of Fig. 6 is area, which if assumed proportional to in-

tensity, leads to the superimposed lightcurve in Fig. 8.)

Specification of the positions of the Sun, the asteroid, and the asteroid's pole does

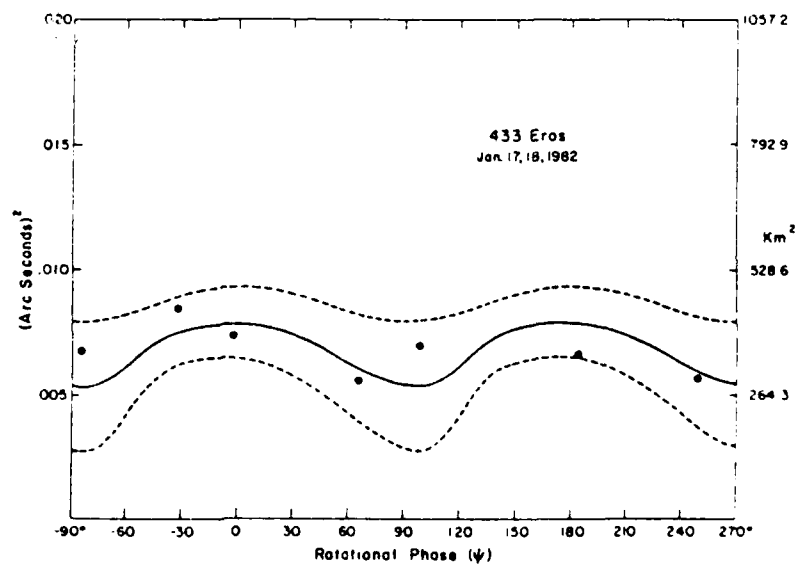


FIG. 7. Same as Fig. 6, but for Jan. 17-18, 1982.

TABLE V
COMPARISON OF OBSERVED AND THEORETICAL LIGHTCURVE CHARACTERISTICS

	Tholen	Zellner	Dec. fit only	Dec. + Jan. model
Rotational phase difference max - min	98°	100°	88°	112°
Rotational phase difference of max from Tholen's max	0	-24°	-33°	-36°
Rotational phase difference of min from Tholen's min	0	-22°	-43°	-22°
Amplitude in mag	0.37	0.23	0.10	0.07

not lead to predictions of the times of extrema unless an epoch and period are also known. In other words, even if the pole is known it is not possible to predict the lightcurve for a given night without a time reference. Therefore, in order to compare the observed lightcurve to the predicted ones we proceed as follows. With the position of the pole it is possible to predict the position angle of maximum elongation (the location of the y axis). Then it is merely a matter of noting the time that the rotating ellipse at-

tains this position angle, which establishes rotational phase zero. For high sub-Earth latitudes, γ varies nearly directly with ψ , as can be seen by the slope of nearly -1 for the γ curve in Fig. 3 and the cross correlation of -1 for ψ_0 and ρ in Table I. Thus the sum of ψ_0 and ρ is nearly a constant, and if ρ is known then ψ_0 can be obtained from the measured value of the constant. From Table I the value for the constant is 62° , from the adopted pole ρ is -98° , and ψ_0 , then, is -20° relative to the time of our first mea-

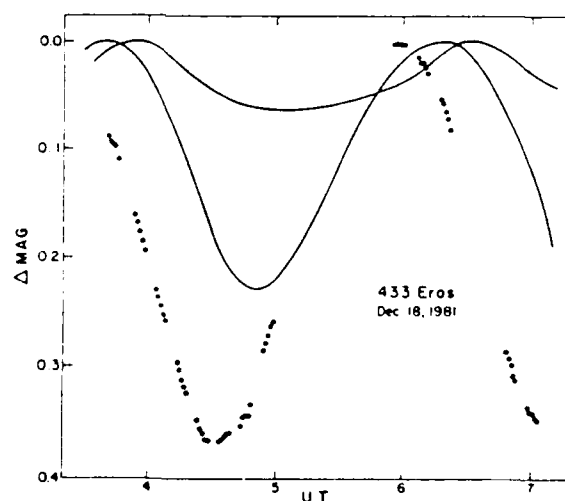


FIG. 8. Lightcurve of Eros obtained by D. Tholen with the 154-cm telescope at the Catalina station of the University of Arizona. Solid dots constitute the lightcurve measured by Tholen, the shallow curve represents the lightcurve predicted from our model, assuming that intensity is proportional to illuminated area as discussed in the text, and the deeper curve is the lightcurve from the consensus model with the same assumption. The maximum for Tholen's lightcurve is $B = 10.59$ and the minimum is $B = 10.96$.

surement point (the fourth point in Fig. 6). Using the same constant, but ρ as predicted from Zellner's pole, we can also make a predicted lightcurve for Zellner's model, all of which leads to Table V and Fig. 8.

At first it might appear that the agreement between the observed and theoretical lightcurves is poor. However, since both Dunlap (1976) and Millis *et al.* (1976) found that lightcurve amplitudes from models must be scaled up, especially at larger solar phase angles, in order to match Eros' observed amplitudes, the amplitude discrepancies are not worrisome to our results for the size and shape of the asteroid. In addition, it should be recalled that our predicted "lightcurves" are only the total projected area in illumination and do not include any particular scattering law, although at lower solar phase angles ($<20^\circ$), assuming that the intensity is proportional to the illuminated area is tantamount to assuming Lommel-Seeliger scattering. In fact, the poor phase and amplitude match between the observed and predicted lightcurves could result from any one or combination of the following: high sub-Earth latitudes produce low-amplitude lightcurves containing relatively little phase information, making it difficult to establish a zero phase point accurately; no scattering laws are included; and Eros may depart from a smooth triaxial ellipsoid. Indeed, Jurgens and Goldstein (1976) noted that not only was Eros rough on the scale of 3.5 and 12.6 cm, as well as 70 cm (Campbell *et al.*, 1976), but that the projected axis of rotation did not equally divide the projected area, as would be the case for an ellipsoid. For these reasons we place little importance in the phase discrepancies, attributing them to the microscopic properties of Eros. The gross features (size, shape, and pole) are well established by speckle interferometry.

Using the phase coefficient of 0.024 mag/deg, the reddening of 0.001 mag/deg, and the $B - V$ of 0.88 for Eros from Zellner (1976), together with the maximum B of 10.59 from Tholen's lightcurve and our de-

termination of the illuminated area at lightcurve maximum, we find a $V_0(1,0)$ (magnitude at maximum light corrected to unit distance and zero solar phase angle) of 10.85 and a geometric albedo of 0.156 ± 0.010 . This $V_0(1,0)$ is somewhat fainter than Zellner's 10.78 ± 0.04 from the 1974-1975 apparition of Eros, which was 0.5 mag brighter than that found in earlier apparitions. The error in our albedo covers the extreme range induced by assigning maximum or minimum illuminated area, from the December results or from the combined January/December model, to the observed maximum in Tholen's lightcurve. The albedo stands between Zellner's 0.19 ± 0.01 and Lebofsky and Rieke's (1979) radiometric determination of 0.125 ± 0.025 .

IV. A VISUAL COMPARISON

Figure 9 is a summary of the actual speckle data for the 17-18 December 1981 observations after processing to correct for atmospheric seeing effects. The principal result of this analysis is the set of debiased seeing-corrected power spectra [see Hege *et al.* (1982a,b) for further details of speckle data reductions] shown in the center row. On the left is the result for an unresolved star showing energy, nearly uniformly, to the diffraction limit of the measurement. The next seven frames show results for Eros at different lightcurve phases. These are characteristically different from the result for an unresolved star in two ways: the energy falls off more rapidly than the diffraction-limited result (i.e., the object is resolved) and it does not fall off uniformly (the object is more highly resolved—longer—in a particular direction). Unfortunately, instrumental effects are also present, notably vertically (N-S), and especially near the center (at lowest spatial frequencies). Nevertheless, the two significant attributes of these data sets, those showing the object to be resolved and elongated, are sufficient to support the further analysis described in this paper.

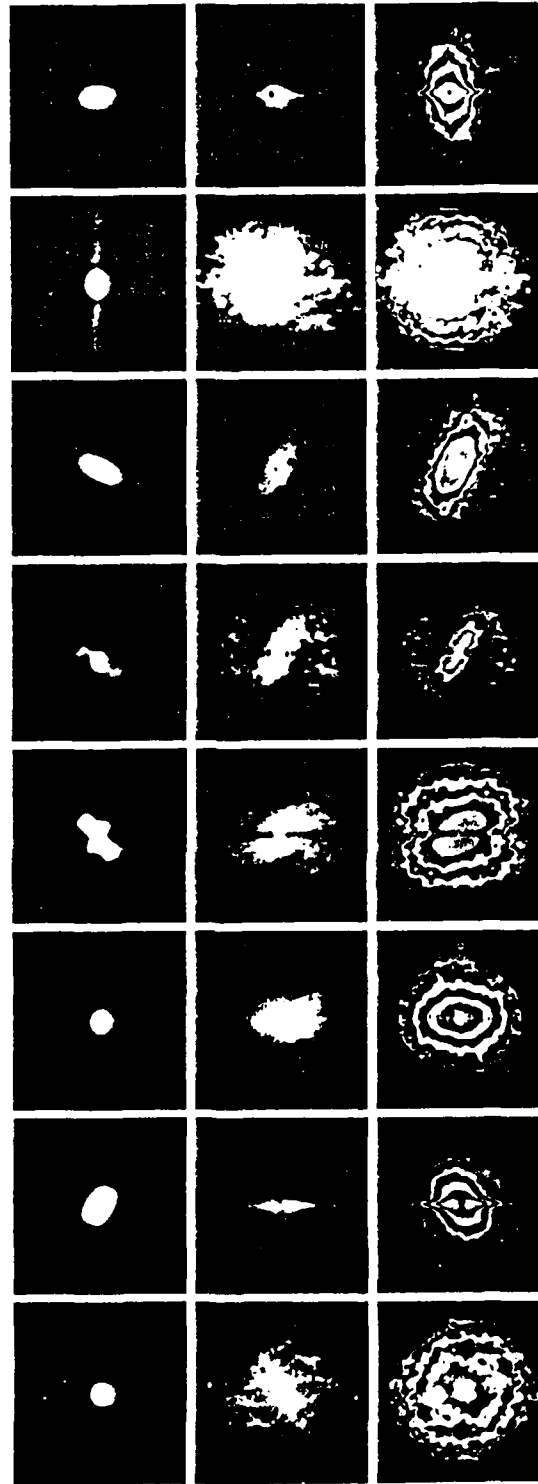


FIG. 9. The actual data for the Dec. run. The first frame in each row is an unresolvable source (a star). The remaining frames in the top row are the seven autocorrelation functions of Eros, those in the middle row are the two-dimensional power spectra for the same Eros points, and those in the bottom row are these same power spectra but with contours of intensity. The order of the frames is not in the same sequence as in Fig. 2, but can be matched to the following sequence of points in Fig. 2: 5, 6, 1, 2, 3, 7, 4. Measurements yielding α , β , and γ were made in power spectrum space (the middle row). Data from the central region, and along the vertical axis, of the power spectrum were excluded from our least-squares analysis in order to avoid fitting instrumental artifacts at those frequencies.

In order to help the reader better visualize these attributes, intensity contours (shown as brighter regions) are superimposed on the power spectra in the bottom row. The intensity is maximum at (or near) the center. Each energy contour is a factor of 2 less than its neighbor toward the center. Typically five contours are visible indicating a signal-to-noise of about $2^5 = 32$. Although not exactly elliptical, the generally *oblong* character of these contours is easily noted. Our first least-squares parameterization fits elliptical contours to each of these energy distributions in order to extract three characteristic primary parameters, the semimajor and semiminor axes, and the position angle for each observation. This set of α , β , and γ values is analyzed using a second least-squares procedure to determine the actual body parameters and pole as previously described.

The top row of frames is the same set of data, presented as autocorrelation functions (Fourier transforms of the power spectra in the middle row). These are more directly comparable to the actual diffrac-

tion-limited telescopic images in that they preserve both the ratio of length to width and the orientation of the object itself. The stellar (unresolved) autocorrelation shows a strong, symmetric Airy minimum and a faint (if asymmetric) first Airy maximum surrounding a central diffraction disk. The results for the asteroid all show, to a greater or lesser degree, evidence for an elongated object at a characteristic position angle. The instrumental artifacts, seen vertically in the power spectra, are now (by the properties of the Fourier transform) seen horizontally and mainly at larger distances in these autocorrelation functions. We have made no attempt in this work to analyze the significance of the obvious departures from simple elliptical shape (e.g., particularly in the third and fourth Eros frames) which are caused in part by details on the surface of the asteroid. We have limited this analysis, as noted above, to considerations *only* of overall shape (length and width of projected image) and orientation (position angle).

Figures 10 and 11 are side-by-side comparisons of our measured ellipses superim-

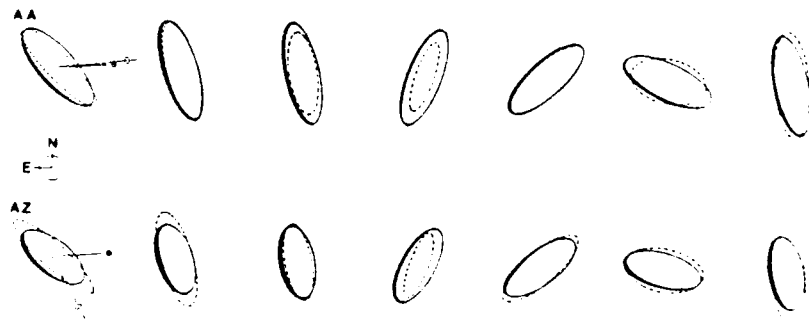


FIG. 10. Comparison of predicted projected ellipses and measured ellipses for Dec. 17-18, 1981. Our adopted solution for the dimensions and pole of Eros (Table IV) results in the upper series (AA) of projected ellipses (solid line figures). The dashed ellipses are our measured ellipses at the same rotational phase. The lower series (AZ) are the projected ellipses from the consensus solution (Table IV), and again superimposed are our measured ellipses at the same rotational phase. From our solution the sub-Earth latitude during this run was -74° and the sub-Sun latitude was -34° . The difference between the sub-Earth and sub-Sun longitudes was $+6^\circ$. For the consensus model the sub-Earth latitude was -58° , the sub-Sun latitude was -30° , and the difference between the longitudes was $+43^\circ$. The solar phase angle was 40° , Eros' position was 1^h44^m , and $+46^\circ$ and its distance from the Earth was 0.311 AU. On the 0.05 diameter circle, which corresponds to the minimum resolution disk of the 2.3-m telescope, north and east are indicated. On the first ellipse of each series, the direction to the Sun and to Eros' north pole are shown according to each solution.



FIG. 11. Comparison of predicted projected ellipses and measured ellipses for Jan. 17-18, 1982. As in Fig. 10, the upper series (BB) of solid line ellipses are from our solutions, and the lower series (BZ) are from the consensus solution. The sub-Earth latitude from our model during the Jan. run was -57° , the sub-Sun latitude was -11° , and the difference between the sub-Earth and sub-Sun longitudes was -32° . For the consensus model the sub-Earth latitude was -56° , the sub-Sun latitude was -4° , and the difference between longitudes was $+6^\circ$. The solar phase angle was 52° . Eros' position was $2^h57^m, +32^\circ$ and its distance from the Earth was 0.317.

posed on our model and on the consensus model of Eros for December 1981 and January 1982, respectively. Presented in this manner the agreement between the two models is indeed convincing. Judging from the agreement between earlier works and the current speckle interferometric efforts for Eros, it appears that speckle is capable of obtaining the same information for asteroids as several other methods in concert, but in only one or two nights, provided the rotational period is known.

APPENDIX I

In an attempt to avoid any possible confusion of the term obliquity as used in this paper and as used by Dunlap (1971) and Barucci and Fulchignoni (1982), or Taylor (1979), we present Fig. 12, which shows the position of the Sun projected onto the plane of the Earth's sky, centered on the asteroid, for each possible quadrant. The z axis is the projection of the asteroid's spin axis and the y axis is the line of nodes (the intersection of the asteroid's equator and the plane of the Earth's sky). Both Dunlap and Taylor define obliquity as a positive quantity, the former restraining the obliquity to lie between 0 and $\pi/2$ and the latter between 0 and π . We define obliquity as a position angle with the normal convention that the

angle measured in a counterclockwise direction (N-E-S-W) is positive and varies between 0 and 2π .

Define three position vectors in the asteroid's coordinate system (Section IIA), one for the Earth, one for the Sun, and one for the line of nodes:

$$\mathbf{E} = (i, j, k)$$

$$\mathbf{S} = (l, m, n)$$

$$\hat{\mathbf{Y}} = (\cos \psi, -\sin \psi, 0).$$

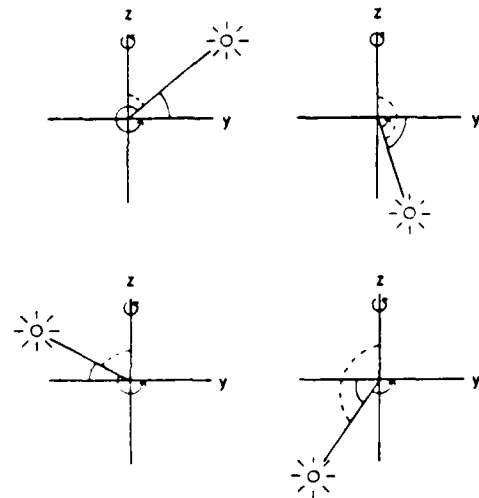


FIG. 12. Obliquity as defined by Dunlap (1971), —; by Taylor (1979), ---; and this paper (Appendix I), →.

The cosine of the solar phase angle, ω , is given by $\mathbf{E} \cdot \mathbf{S}$. Our obliquity, ρ , measured from the projection of \mathbf{S} onto the plane of the Earth's sky to \mathbf{v} , can be found from

$$\cos \rho = \hat{\mathbf{Y}} \cdot \mathbf{S} / \sin \omega \\ = (l \cos \psi - m \sin \psi) / \sin \omega$$

$$\sin \rho = \hat{\mathbf{Y}} \cdot \mathbf{E} \times \mathbf{S} / \sin \omega \\ = (k \cos \omega - n) / (\sin \omega \cos \theta).$$

APPENDIX II: NOMENCLATURE

A, B, C	terms used in quadratic formula for projected ellipse		
A_i	illuminated area of projected ellipse, bounded by terminator and bright limb		
A_s	area of projected ellipse in shadow, bounded by terminator and dark limb		
A_T, B_T, C_T	terms used in quadratic formula for terminator ellipse	π	3.1416 . . .
$a \geq b \geq c$	semidiameters of triaxial ellipsoid rotating about c	ρ	obliquity (see Appendix I)
$\mathbf{E} = (i, j, k)$	position vector of Earth in astero-centric coordinates [see Eq. (12)]	ϕ	the Euler angle between the line of sight and the line of nodes; by our selected coordinate system this angle is a constant $\pi/2$
L	astero-centric longitude measured positive in a right-handed coordinate system, from the longest body axis (a); $L = -(\psi + 90^\circ)$	$\psi (\psi_O)$	the Euler angle equivalent to the rotational phase angle measured from the line of nodes, with $\psi = 0$ when the longest body axis (a) is perpendicular to the line of sight and lies unprojected in the plane of the sky; $\psi = -(L + 90^\circ)$, $\psi_O = -(L_O + 90^\circ)$
$\mathbf{S} = (l, m, n)$	position vector of Sun in astero-centric coordinates [see Eq. (18)]	ω	solar phase angle, the angle between the Sun and Earth as seen by the asteroid; $\mathbf{E} \cdot \mathbf{S} = \cos \omega$
$\hat{\mathbf{Y}}$	position vector of line of nodes: the intersection of the asteroid's equatorial plane and the plane of the Earth's sky		
x, y, z	astero-centric rectangular coordinates with the x axis pointed toward the Earth, and the y axis coincident with the line of nodes		
x', y', z'	astero-centric rectangular coordinates rotating with		
	the asteroid, with a, b, c lying along $x', y',$ and z		
	semidiameters of ellipse projected by ellipsoid	$\alpha \geq \beta$	
	semidiameters of terminator ellipse	$\alpha_T \geq \beta_T$	
	position angle measured in the plane of the sky, between the y axis and α	γ	
	position angle measured in the plane of the sky, between the y axis and α_T	γ_T	
	astero-centric latitude of sub-Earth (sub-Sun) point, or equivalently the Euler angle between the asteroid's rotation axis and the Earth's (Sun's) sky plane	$\theta (\theta_O)$	

ACKNOWLEDGMENTS

We are grateful to D. Tholen for obtaining the light-curve of Eros on our behalf and for providing ephemerides for our asteroid observations. J. Freeman digitized the data, and unbiased and deconvolved the power spectra. His diligent efforts were essential to the science garnered from the observations and are greatly appreciated. This work was supported in part

by NASA Grant NAGW-224, by AFGL Contract F19628-82-K-0025, and by AFOSR Grant 82-0020.

REFERENCES

- BARUCCI, M. A., R. CASACCHIA, M. FULCHIGNONI, R. BURCHI, A. D. PAOLOANTONIO, C. GIULIANI, L. MILANO, F. SCALTRITI, AND V. ZAPPALÀ (1982). Laboratory simulation of photometric light curves of the asteroids. *Moon Planet* **27**, 387-395.
- BARUCCI, M. A., AND M. FULCHIGNONI (1982). The dependence of asteroid lightcurves on the orientation parameters and the shapes of asteroids. *Moon Planet* **27**, 47-57.
- BOWELL, E., B. L. MORGAN, K. LUMME, J. C. DAINTY, H. A. VINE, AND M. POUTANEN (1981). Speckle interferometric observations of Ceres, Vesta, Hebe, and Victoria. *Bull. Amer. Astron. Soc.* **13**, 719.
- CAMPBELL, D. B., G. H. PETTENGILL, AND I. I. SHAPIRO (1976). 70-cm radar observations of 433 Eros. *Icarus* **28**, 17-20.
- DAINTY, J. C. (1975). Stellar speckle interferometry. In *Laser Speckle and Related Phenomena* (J. C. Dainty, Ed.), pp. 255-279. Springer-Verlag, Berlin.
- DUNLAP, J. L. (1971). Laboratory work on the shapes of asteroids. In *Physical Studies of Minor Planets* (T. Gehrels, Ed.), pp. 147-154. Univ. of Arizona Press, Tucson.
- DUNLAP, J. L. (1976). Lightcurves and the axis of rotation of 433 Eros. *Icarus* **28**, 69-78.
- GOLDSTEIN, H. (1950). *Classical Mechanics*. Addison-Wesley, Reading, Mass.
- HEGE, E. K., W. J. COCKE, E. HUBBARD, M. GESHAM, P. A. STRITTMATTER, R. RADICK, AND S. P. WORDEN (1980a). Speckle interferometric observations of Pallas. *Bull. Amer. Astron. Soc.* **12**, 509.
- HEGE, E. K., W. J. COCKE, E. N. HUBBARD, J. CHRISTOU, AND R. RADICK (1980b). Possible secondaries of asteroids found by speckle interferometry. *Bull. Amer. Astron. Soc.* **12**, 662.
- HEGE, E. K., E. N. HUBBARD, P. A. STRITTMATTER, AND W. J. COCKE (1982a). The Steward Observatory speckle interferometry system. *Optica Acta* **29**, 701-715.
- HEGE, E. K., E. N. HUBBARD, J. D. DRUMMOND, P. A. STRITTMATTER, AND S. P. WORDEN (1982b). Speckle interferometric observations of Pluto and Charon. *Icarus* **50**, 72-81.
- JEFFERYS, W. H. (1980). On the method of least squares. *Astron. J.* **85**, 177-181.
- JURGENSEN, R. F., AND R. M. GOLDSTEIN (1976). Radar observations at 3.5 and 12.5 cm wavelength of asteroid 433 Eros. *Icarus* **28**, 1-15.
- LEROFSKY, L. A., AND G. H. RIEKE (1979). Thermal properties of 433 Eros. *Icarus* **40**, 297-308.
- LUMME, K., M. POUTANEN, AND E. BOWELL (1981). Photometric determinations of asteroid shapes and spin axial directions. *Bull. Amer. Astron. Soc.* **13**, 719.
- MATSON, D. L. (1971). Infrared observations of asteroids. In *Physical Studies of Minor Planets* (T. Gehrels, Ed.), pp. 45-50. NASA SP-267, Washington, D.C.
- MILLIS, R. L., E. BOWELL, AND D. T. THOMPSON (1976). UBV photometry of asteroid 433 Eros. *Icarus* **28**, 53-67.
- MORRISON, D. (1977). Asteroid sizes and albedos. *Icarus* **31**, 185-220.
- OSTRO, S. J., AND R. CONNELLY (1984). Convex profiles from asteroid lightcurves. *Icarus* **57**, 443-463.
- SCALTRITI, F., AND V. ZAPPALÀ (1976). Photometric lightcurves and pole determination of 433 Eros. *Icarus* **28**, 29-31.
- SURDEJ, A., AND J. SURDEJ (1978). Asteroid lightcurves simulated by the rotation of a three-axes ellipsoidal model. *Astron. Astrophys.* **66**, 31-36.
- TAYLOR, R. C. (1979). Pole orientations of asteroids. In *Asteroids* (T. Gehrels, Ed.), pp. 480-493. Univ. of Arizona Press, Tucson.
- TAYLOR, R. C. (1984). The pole orientation of asteroid 433 Eros by applying photometric astrometry. Submitted for publication.
- TAYLOR, R. C., AND E. F. TEDESCO (1983). Pole orientation of asteroid 44 Nysa via photometric astrometry, including a discussion of the method's application and its limitations. *Icarus* **54**, 13-22.
- TEDESCO, E. F. (1979). Lightcurve parameters of asteroids. In *Asteroids* (T. Gehrels, Ed.), pp. 1098-1107. Univ. of Arizona Press, Tucson.
- VESELY, C. D. (1971). Summary on orientations of rotation axes. In *Physical Studies of Minor Planets* (T. Gehrels, Ed.), pp. 133-140. NASA SP-267, Washington, D.C.
- WORDEN, S. P. (1979). Interferometric determinations of asteroid diameters. In *Asteroids* (T. Gehrels, Ed.), pp. 119-131. Univ. of Arizona Press, Tucson.
- ZAPPALÀ, V., AND Z. KNEŽEVIĆ (1984). Rotation axes of asteroids: Results for 14 objects. *Icarus* **59**, 436-455.
- ZAPPALÀ, V., M. DI MARTINO, P. FARINELLA, AND P. PAOLICCHI (1983). An analytical method for the determination of the rotational direction of asteroids. In *Asteroids, Meteors, and Comets* (C.-I. Lagerkvist and H. Rickman, Eds.), pp. 73-76. Astronomiska Observatoriet, Uppsala, Sweden.
- ZELLNER, B. (1976). Physical properties of asteroid 433 Eros. *Icarus* **28**, 149-153.

Speckle Interferometry of Asteroids

II. 532 Herculina

J. D. DRUMMOND, E. K. HEGE, W. J. COCKE, J. D. FREEMAN,
 AND J. C. CHRISTOU¹

Steward Observatory, University of Arizona, Tucson, Arizona 85721

AND R. P. BINZEL

Department of Astronomy, University of Texas, Austin, Texas 78712

Received May 21, 1984; revised October 5, 1984

Speckle interferometry of 532 Herculina performed on January 17 and 18, 1982, yields triaxial ellipsoid dimensions of $(263 \pm 14) \times (218 \pm 12) \times (215 \pm 12)$ km, and a north pole for the asteroid within 7° of RA = $7^h 47^m$ and DEC = $+39^\circ$ (ecliptic coordinates $\lambda = 132^\circ$, $\beta = -59^\circ$). In addition, a "spot" some 75% brighter than the rest of the asteroid is inferred from both speckle observations and Herculina's lightcurve history. This bright complex, centered at astero-centric latitude $+35^\circ$, longitude 145° – 165° , extends over a diameter of 55° (115 km) of the asteroid's surface. No evidence for a satellite is found from the speckle observations, which leads to an upper limit of 50 km for the diameter of any satellite with an albedo the same as or higher than Herculina. © 1985 Academic Press, Inc.

INTRODUCTION

Assuming that an asteroid is a smooth triaxial ellipsoid rotating about its shortest axis, the resolved asteroid will project onto the plane of the Earth's sky as an ellipse. Even at low to moderate solar phase angles ($<45^\circ$), the illuminated portion of an asteroid can still be approximated by an ellipse. At low solar phase angles, a smooth, airless dark body tends to suffer little or no limb darkening (French and Veverka, 1983). Even for objects similar in albedo to Herculina, French and Veverka (1983) found that what limb darkening may exist is nearly (but not totally) reduced by macroscopic surface roughness. Thus, treating an asteroid as a smooth triaxial ellipsoid uniformly bright from the terminator to the opposite limb appears to be a useful approximation and is indeed what is traditionally used (e.g., Ostro and Connelly, 1984). As the asteroid rotates it presents a series of ellipses

that change in size, shape, and orientation. There is a transformation from each ellipse to actual body parameters that involve six variables, three dimensions and three (Euler) angles. The asteroid's axial dimensions and the direction of its spin axis, including the sense of rotation, can then be found from a least-squares analysis of this ellipse series. The derivation of the relevant equations was given by Drummond *et al.* (1985, Paper I) and applied to speckle interferometric observations of 433 Eros. In the present paper we use the same technique to study 532 Herculina.

THE DATA AND RESULTS

Four observations of Herculina were made on January 17, 1982, and another four on January 18, at the 2.3-m telescope of Steward Observatory, using the equipment as described by Hege *et al.* (1982). Each observation was a 10-min videotape of Herculina taken at 30 Hz. Each 10-min observation was later Fourier transformed, and the power spectra were coadded. In order to remove the modulation transfer function

¹ Visiting Astronomer from Department of Astronomy, New Mexico State University, Las Cruces, N.M.

of the telescope and the seeing (Hege *et al.*, 1982), the unbiased two-dimensional speckle image power spectrum accumulated from each 10-min observation was divided (deconvolved) by the two-dimensional power spectrum of a star observed immediately before and again by the power spectrum of a different star observed immediately after Herculina. Each deconvolved power spectrum of Herculina was then fit over two regions of spatial frequencies to the power spectrum of a uniformly bright ellipse. The major axis, minor axis, and position angle of the major axis for the asteroid's elliptical power spectrum were taken as the average of two measurements from both of the deconvolved power spectra. The average standard deviation from the mean of the four measurements of each Herculina observation ranged between 0".002 and 0".018 for the long axis dimension, between 0".003 and 0".043 for the short axis dimension, and between 1 and 6° for the position angle. Image scale and absolute orientation were calibrated with a mask placed over the secondary mirror at the end of the run. The diffraction limit of the 2.3-m telescope is 0".05 at 5500 Å and the scale was 0".01 per pixel.

On a "poor" night seeing may not be a statistically stationary process during observations of the first nearby standard, the asteroid, and the second nearby standard. However, since the observation of the asteroid is always sandwiched between the two standards, and the results are the average between the two deconvolutions, any trend in the seeing should be compensated. Furthermore, even if a change in seeing is not entirely compensated, the remaining "error" will simply be manifest as noise on the measurements when all observations are fit simultaneously, resulting, perhaps, in increased errors for the final parameters. (See below.)

Table I gives pertinent data regarding the observing circumstances for Herculina, which moved less than one-third of 1° between the first observation on the first night

TABLE I

ASPECT DATA FOR SPECKLE OBSERVATIONS

DATE	RA (1950)	DEC
January 17 and 18, 1982	8 ^h 58 ^m	+25°41'
Distance from Earth 1.495 AU	Distance from Sun 2.459 AU	
Solar phase angle 6°	Position angle of Sun, centered on Herculina 74°	

and the last observation on the second night. Because the solar phase angle was only 6°, the terminator was virtually coincident with one edge of the projected ellipse.

Three independent quantities are measured for each of the eight observations of the projected ellipse: a major axis dimension α , a minor axis dimension β , and a position angle γ of the long axis. Altogether, then, there are 24 equations of condition to solve for six unknown parameters. However, as discussed later, four measurements were not used in the analysis, leaving 20 equations of condition. A nonlinear least-squares (Jeffreys, 1980) routine was used to solve for the dimensions of the three axes a , b , c , the latitude of the sub-Earth point θ , a zero point for the rotational phase ψ_0 (corresponding to maximum light), and the obliquity ρ (as defined in Paper I). With θ , ρ , and the position of Herculina, we calculate the location of the pole directly. The error in the position of the pole arises from the error in θ and ρ , and corresponds to the radius of a circle with the same area as the area enclosed by the various poles calculated by varying θ and ρ by their errors. Table II lists the least-squares solution for each of the parameters and presents the matrix of normalized correlation coefficients for the full six-parameter fit. Table III lists the same for a five-parameter fit, where b is assumed equal to c (the prolate spheroid biaxial case), and Table IV shows the information for the biaxial fit using all the points, including the four discrepant ones. A triaxial solution could not be found

TABLE II

TRIAXIAL SOLUTION AND CORRELATION MATRIX
(WITHOUT FOUR LOWEST ψ 'S)

$a = 261 \pm 14$ km	$\psi_0 = 35 \pm 13$
$b = 222 \pm 16$ km	$\theta = 29 \pm 23$
$c = 213 \pm 18$ km	$\rho = 30 \pm 8$
Standard error of fit = 0.019 = 21 km	
RA	Pole (1950)
7°59'	33
	+14
13°39'	+77

	a	b	c	ψ_0	θ	ρ
a	—					
b	0.60	—				
c	0.33	0.35	—			
ψ_0	0.12	0.11	0.15	—		
θ	0.63	0.80	0.79	-0.14	—	
ρ	0.08	0.07	0.09	0.90	0.07	—

in the latter case if these four points were included in the analysis. Table V gives our adopted weighted (by the inverse errors squared) solution between Tables II and III. For each case the standard error of fit is listed and both poles for the θ , $\pi - \theta$ ambiguity (see Paper I) are given. However, based on the available published light-curves (next section), the first listed pole is the correct one. From occultation (Bowell *et al.*, 1978), radiometric (Morrison and Le-

TABLE III

BIAXIAL SOLUTION AND CORRELATION MATRIX
(WITHOUT FOUR LOWEST ψ 'S)

$a = 265 \pm 15$ km	$\psi_0 = -38 \pm 9^\circ$
$b = c = 216 \pm 10$ km	$\theta = 23 \pm 5^\circ$
	$\rho = 32 \pm 7$
Standard error of fit = 0.018 = 20 km	
RA	Pole (1950)
7°42'	39
+6	
15°22'	+75

	a	b	ψ_0	θ	ρ
a	—				
b	0.35	—			
ψ_0	0.01	0.04	—		
θ	0.13	0.04	0.02	—	
ρ	0.01	0.03	0.87	0.01	—

TABLE IV

BIAXIAL SOLUTION AND CORRELATION MATRIX
(INCLUDING FOUR LOWEST ψ 'S)

a	278 ± 17 km	ψ_0	-37 ± 9
b	$c = 181 \pm 11$ km	θ	24 ± 6
		ρ	32 ± 7
Standard error of fit = $0.030 = 33$ km			
RA	Pole (1950)	DEC	
$7^{\circ}45'$		38°	
	± 7		
$15^{\circ}14'$		$+76$	

	a	b	ψ_0	θ	ρ
a	—				
b	-0.22	—			
ψ_0	-0.03	0.01	—		
θ	0.21	0.04	0.01	—	
ρ	0.02	0.005	0.82	-0.05	—

bofsky, 1979), and polarization (Bowell *et al.*, 1979) results, the diameter of Herculina has been found to be 217, 219, and 220 km, respectively. No published pole has been noted in the literature.

Figure 1 shows our measured major axis (diamonds) and minor axis (filled circles; open circles are not used in the analysis) plotted against rotational phase ψ . The upper line is the predicted major axis dimension from Table V, while the lower curve is the predicted minor axis. Figure 2 shows the predicted position angle (γ) of the major axis as a function of rotational phase. At rotational phase $\psi = 0$, maximum light occurs, the long body dimension a is perpendicular to our line of sight, and γ is zero.

TABLE V

ADOPTED SOLUTION (WEIGHTED MEAN OF
TABLES II AND III)

$a = 263 \pm 14$ km
$b = 218 \pm 12$ km
$c = 215 \pm 12$ km
$\psi_0 = -37 \pm 10$
$\theta = 23 \pm 7$
$\rho = 31 \pm 7$
RA
7°47'
+7
Pole (1950)
39

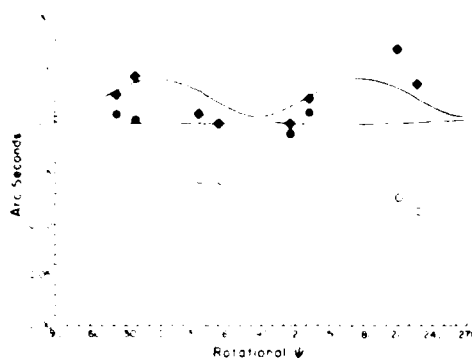


FIG. 1. Major (diamonds) and minor (circles) axis dimensions (0.01 = 10.84 km) plotted against rotational phase over Jan 17 and 18, 1982. Because of the effect of the bright spot on measuring the minor axes, open circles were not used in finding the solution. The upper (lower) line is the predicted major (minor) axis dimension from our adopted weighted solution (Table V).

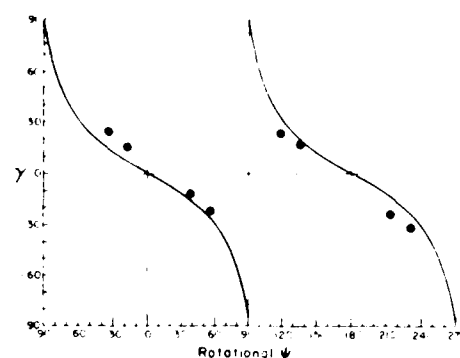


FIG. 2. The position angle (γ) of the major axis plotted as a function of rotational phase over Jan 17 and 18, 1982. At $\psi = \gamma = 0$, maximum light would occur, and Herculina's longest axis would lie in the plane of the Earth's sky perpendicular to our line of sight. The line is the position angle predicted from the results listed in Table V and is superimposed on our measured γ 's, the solid dots.

HERCULINA'S LIGHTCURVES

Including the 1982 apparition, lightcurves have been obtained at four oppositions (Table VI): in 1954 (Groeneveld and Kuiper), in 1963 (Chang and Chang), in 1978 (Harris and Young, 1979), and in 1982 (independently by M. Di Martino (1984, private

communication) by Cunningham (1983) and by R. P. Binzel—see Table VII and below). The four oppositions are summarized in Table VI. For all but the 1978 opposition, Herculina displayed one maximum and one minimum in ~ 9 hr, implying an 18-hr rotational period. However, in 1978, Harris and Young found two (and perhaps even three)

TABLE VI

SUMMARY OF PREVIOUS LIGHTCURVES

DATE	RA (1950)	DEC	Solar phase angle	Amplitude (mag)	Sub-Earth ^a latitude	Comments
Jan 2, 1954 ^b	6 ^h 07 ^m	+12°30'	4.5	0.08	-29°	
Jan 19-22, 1963 ^c	4 24	+11 47	17	0.18	-21	
Jun 25, 1978 ^d	14 52	+2 08	20	0.15	+14	Second min. 0.12 mag. lower than primary max.
Mar 20-25, 1982 ^e	8 21	+32 46	21.5	0.15	-18	

^a Based on pole location of 7°47', -39°.

^b Groeneveld and Kuiper (1954).

^c Chang and Chang (1963).

^d Harris and Young (1979). Lightcurves were obtained from May 29 through August 1 by Harris and Young at Table Mountain and by E. Bowell and L. Martin at Lowell. All lightcurves are quite similar, and the Jun 25 aspect data are chosen as representative of the middle of the period.

^e R. P. B. (this paper). M. Di Martino (1984, personal communication) obtained a similar 0.15-magnitude amplitude lightcurve for Jan 29-31, 1982, as did Cunningham (1983) for Feb 26-Mar 29, 1982, but with a slightly higher amplitude of 0.18 magnitude.

TABLE VII
ASPECT DATA FOR 1982 LIGHT CURVE

DATE (0 ^h UT)	RA (1950)	DEC	Earth distance (AU)	Sun distance (AU)	Phase angle	Ecliptic	
						Long	Lat
1982 Mar 20	8 ^h 21 ^m	32°45'	1.710	2.374	21.2	120	13
Mar 21	21	32°46'	1.719	2.373	21.4	120	13
Mar 22	21	32°46'	1.729	2.372	21.7	120	13
Mar 25	22	32°46'	1.757	2.368	22.3	120	13

maxima and minima in 9 hr, and convincingly demonstrated that a 9.406 hr period was correct.

Figure 3 shows the lightcurve constructed from four nights of data obtained by R.P.B. in March 1982, assuming a 9.406-hr period. A two-channel photometer was used on the 0.91-m telescope at McDonald Observatory. The second channel of the photometer which is described in Nather (1973) was offset to a nearby star to monitor the photometric constancy of the night. The observations were made differentially with respect to a second nearby comparison star SAO 060790, spectral Type F5. All observations were made using an uncooled RCA 8850 photomultiplier tube and a standard B filter (Schott 385 and BG 12) and were transformed to the Johnson B system using solar-type standards from Landolt (1973). The small $\delta B - V$ between all of the objects allowed second-order color terms to be ignored in the reduction.

Each measurement is the average of at

least 100 sec of integration time on the asteroid and on the comparison star. Differential extinction was accounted for in the reduction using nightly determined extinction coefficients. The resulting error for each of the observations is less than 0.01 magnitude.

The observing circumstances for each of the four nights are presented in Table VII. Phase angle and distance corrections were applied in order to place the observations from the four nights on the vertical scale. No correction for light time was applied.

A SPOT ON HERCULINA

In Fig. 1 it is obvious that the lowest four β measurements are unreasonably low and should be excluded from a fit of a uniform smooth ellipsoid model. If they are not excluded, Table IV suggests a maximum light-curve amplitude of nearly 0.5 magnitude—unrealistically large. In order to assess the effect of what a dark spot would have on the power spectrum of an asteroid, we cal-

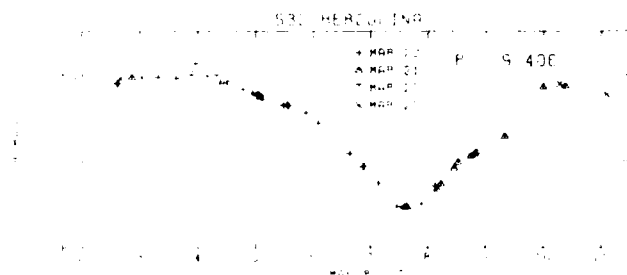


FIG. 3. The lightcurve of 532 Herculina as measured with a B filter at the 0.91-m telescope at McDonald Observatory. (See text.)

culated the two-dimensional power spectrum of an ellipse with a dark or bright spot at various locations. It turned out that the biggest effect is caused by a *bright* spot. In fact, the easiest way to cause an underestimate of the size of the *minor* axis in image space (from measurements made in power spectrum space) is to place a bright spot at the end of the *major* axis.

After several such numerical experiments we were able to locate a bright spot on Herculina that not only qualitatively explains the speckle interferometric measurements, but to a large extent explains the lightcurves observed. A spot with the following characteristics is suggested:

Asterocentric latitude	-35°
Asterocentric longitude	145°
(measured in a right-handed system from the longest axis in the equatorial plane)	
Diameter	$55^\circ = 115 \text{ km}$
Albedo relative to non-spot surface	1.75

When such a spot is located on the limb, midway between the major and minor axes, it causes us to severely underestimate the minor axis (the first two low β 's in Fig. 1) and slightly underestimate the major axis. When the spot is on the tip of the major axis it not only causes an underestimation of β , but also causes a small overestimation of α (as in the second set of low β 's). When the spot is near the center of the ellipse, it has the least effect (the two measurements at $\psi \approx 125^\circ$). Moreover, when the latitude of the sub-Earth point lies in Herculina's southern hemisphere (as in 1954, 1963, and 1982), the bright spot "fills in" one of the lightcurve minima, and when the sub-Earth latitude is in the northern hemisphere (1978), two minima should be seen. Harris and Young (1979) correctly interpreted the lightcurve data by concluding that "the pole orientation of 532 Herculina is such that the two aspects (1963 and 1978) were both at midlatitudes but opposite hemispheres

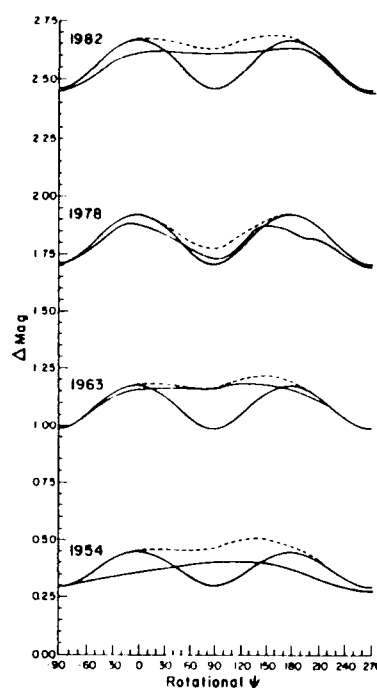


FIG. 4. Theoretical lightcurves for four oppositions. Using the model from Table V, lightcurves for the four epochs considered in Table VI are shown as sinusoidal solid lines. The dashed line is the lightcurve with the contribution from the bright spot included. Note how the spot raises one of the minima to the level of the maxima in three of four cases. The 1978 lightcurve was the only one obtained when the sub-Earth point was in the asteroid's northern hemisphere (the spot is at latitude -35°). We urge the reader to compare these lightcurve shapes with the actual ones from the references listed in Table VI, but for convenience we have sketched in the observed (lower amplitude) lightcurves.

from one another." This is essentially what we find from our speckle observations.

We were able to reproduce the shape of the observed lightcurves listed in Table VI quite well by placing the spot at longitude 165° instead of 145° , a difference that is allowed by the simplistic approach (a single, uniform, circular spot). Figure 4 shows the lightcurves generated with this spot, and we urge comparison to the observed ones. Our computer-generated lightcurves include the visible illuminated area of the asteroid, plus the contribution of the illuminated area of the spot (75% brighter than

the rest of the asteroid), and takes into account foreshortening of the spot. It is also necessary to include a Lambertian term for the spot in order to even remotely match the observed lightcurves, i.e., the foreshortened illuminated area of the spot was multiplied by the cosine of the angle between the asteroid's radius vector to the spot and the astero-centric position of the Sun. Although the shapes of the lightcurves agree well, the computer-generated lightcurves are an average of 0.08 magnitude greater than those observed. But again this may be due to our simplistic approach to what is undoubtedly a complex albedo structure, especially in the southern hemisphere of Herculina. If the spot and the solar phase angle are ignored in our calculated lightcurve, then the discrepancy is reduced to 0.04 magnitude. A 0.08-magnitude amplitude discrepancy is also less than the range in amplitudes calculated by varying the dimensions of Herculina by the errors in Table V.

AN AMPLITUDE/ASPECT CHECK

As a check of the consistency of our estimates for the dimensions and pole of Herculina, we performed a simple amplitude/aspect analysis. Using the dimensions from Table V of $263 \times 218 \times 215$, ignoring the effect of the solar phase angle, and disregarding the spot, the amplitude can be expressed as the ratio of maximum to minimum projected area and is a function of aspect ($90^\circ - \theta$) only. For amplitudes (A) converted to a linear scale, the sub-Earth latitude (θ) can be found from

$$\tan^2 \theta = c^2(A^2 b^2 - a^2) / [a^2 b^2 (1 - A^2)],$$

where a , b , and c are the triaxial diameters. From observed amplitudes (Table VI) and our dimensions, we convert each lightcurve amplitude to a θ . We then plot the position of the asteroid on the celestial sphere and draw a circle around it of radius $90^\circ - \theta$. Ideally, since the pole must lie somewhere on each circle, all the circles should intersect at the location of the pole. Figure 5

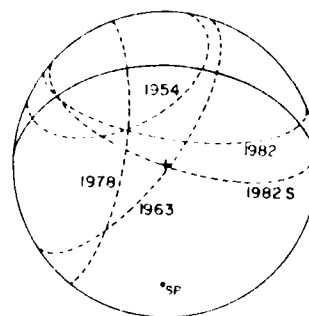


FIG. 5. A graphical representation of the amplitude/aspect analysis for Herculina. On the celestial sphere (note the south celestial pole and the solid equator), tipped so that our pole at $7^h47^m, -39^\circ$, is directly beneath us (the plus), each curve (derived from the amplitudes in Table VI and the dimensions in Table V) is drawn centered on the position of the asteroid at the time of the observations. The 1982S curve comes from our own speckle observation. Note the intersection of the 1963 curve with our pole, and the intersection of the 1954, 1978, and 1982 curves some 20° away at $6^h48^m, -24^\circ$.

shows four circles from the four lightcurves of Table VI, as well as the circle from our own speckle observations.

In fact, the speckle results not only give a circle but indicate where on the circle the pole lies. We have tipped the celestial sphere so that the location of this pole at $7^h47^m, -39^\circ$, lies at the center (a plus). The circle from the 1963 lightcurve intersects the speckle (1982S) curve at precisely this point, while the three other lightcurves intersect at $6^h48^m, -24^\circ$, a difference of 20° . We feel this is good agreement and adds confidence to our results for Herculina.

A SATELLITE?

The possibility of a satellite orbiting Herculina was suggested by a secondary event observed during a stellar occultation in 1978 (Bowell *et al.*, 1978; Van Flandern *et al.*, 1979). However, no indications of a satellite could be found at any rotational phase from our speckle observations (i.e., no interference fringes were seen in the power spectra). According to the diameter and orbital radius of the hypothetical satellite

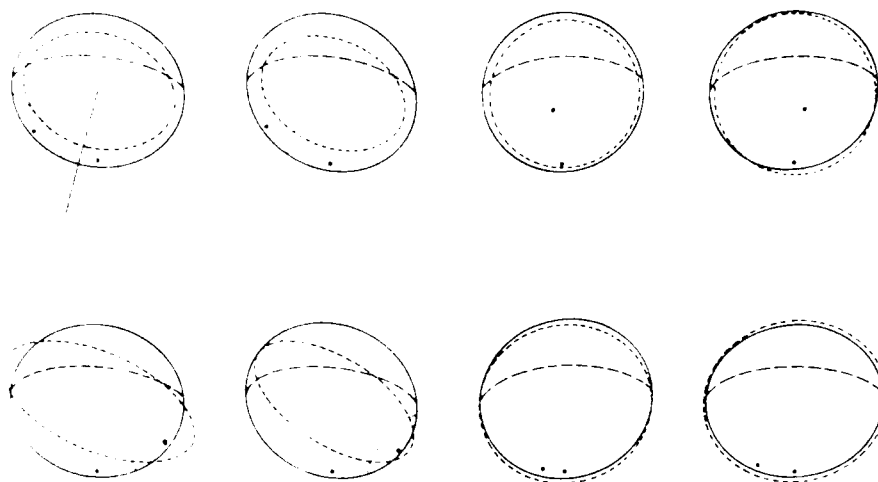


FIG. 6. 532 Herculina on Jan 17 and 18, 1982. North is indicated on the first "frame." Each frame shows Herculina's south pole and equator, the ellipse (dashed) as measured by speckle interferometry, and the location of the bright spot (dotted) with its center denoted by a large dot. In the last two frames the bright spot is on the other side of the asteroid. The spot is slightly larger than the resolution disc of 0.05 for the 2.3-m telescope. The order of the frames in this figure is chronological. The last two frames here correspond to the first two in Figs. 1 and 2, the first frame here is point 3 in the earlier figures, frame 2 is point 4, etc.

(50- and 1000-km separation), it should have been continuously within our 2.5 field of view. We can therefore set an upper limit for the diameter of an object with the same albedo as Herculina at $0''.05 = 50$ km, and for a satellite with an albedo 75% brighter, corresponding to the albedo of the bright spot, an upper limit of 40 km. Our observations, then, lead to the conclusion that if a satellite exists for Herculina, it is probably smaller than previously suggested.

SUMMARY

By modeling Herculina as a triaxial ellipsoid with a large bright spot in its southern hemisphere, we have been able to explain its lightcurves and its speckle interferometric observations. Figure 6 summarizes our results by combining the information from Figs. 1 and 2. At the rotational phase of each speckle measurement, the predicted projected ellipse from the ellipsoid in Table V is shown (solid line ellipse), as well as the measured ellipse (dashed), the bright spot (dotted) and its center, and the asteroid's

south pole and equator. In the last two frames the bright spot is not visible but its center is shown on the other side of the asteroid. Note the correlation between the location of the bright spot and, in particular, the size of the minor axis of the measured ellipse; the greatest effect occurs when the spot is on the limb.

We predict that if colorimetry or polarimetry had been performed during any of the lightcurves from Table VI, except 1978, there would have been variation with rotation because of the spot. By the same token we predict one maximum and minimum during one rotational cycle and variations in color and polarization over the rotational cycle when the sub-Earth point lies in the southern hemisphere of Herculina. This will occur around the November 1985 opposition when θ will be -25° . During the July 1988 opposition, since the sub-Earth point will lie in Herculina's northern hemisphere ($+23^\circ$), two maxima and two minima will be seen, and little if any color or polarization variation with rotation will be seen.

In 1987 and 1989, the latitudes will be $+7^\circ$ and -8° , respectively, and the situation will be intermediate.

ACKNOWLEDGMENTS

This work was supported by NASA Contract NAGW-224, AFGI Contract F19628-82-K-0025, and AFOSR Grant 82-0020. The observations by R. P. Binzel were supported by NASA Grant NGR 44-012-152.

REFERENCES

- BOWELL, E., J. McMAHON, K. HORNE, M. F. A'HEARN, D. W. DUNHAM, W. PESHOLLOW, G. F. TAYLOR, L. H. WASSERMAN, AND N. M. WHITE (1978). A possible satellite of Herculina (abstract). *Bull. Amer. Astron. Soc.* **10**, 594.
- BOWELL, E., T. GEHRELS, AND B. ZELLNER (1979). Magnitudes, colors, types, and adopted diameters of the asteroids. In *Asteroids* (T. Gehrels, Ed.) pp. 1108-1129. Univ. of Arizona Press, Tucson.
- CHANG, Y. C., AND C. CHANG (1963). Photometric observations of variable asteroids. II. *Acta Astron. Sin.* **11**, 139-149.
- CUNNINGHAM, C. (1983). Photoelectric photometry of asteroid 532 Herculina. *Minor Planet Bull.* **10**, 4-5.
- DRUMMOND, J. D., W. J. COCKE, F. K. HUGL, P. A. STRITTMATTER, AND J. V. LAMBERT (1985). Speckle interferometry of asteroids. I. 433 Eros. *Icarus* **61**, 132-151.
- FRENCH, L. M., AND J. VEVERKA (1983). Limb darkening of meteorites and asteroids. *Icarus* **54**, 38-47.
- GROENEVELD, L., AND G. P. KUIPER (1954). Photometric studies of asteroids II. *Astrophys. J.* **120**, 529-546.
- HARRIS, A. W., AND J. YOUNG (1979). Photoelectric lightcurves of asteroids 42 Isis, 45 Eugenia, 56 Melete, 103 Hera, 532 Herculina and 558 Carmen. *Icarus* **38**, 100-105.
- HUGL, F. K., E. N. HUBBARD, P. A. STRITTMATTER, AND W. J. COCKE (1982). The Steward Observatory speckle interferometry system. *Opt. Acta* **29**, 701-715.
- JEFFREYS, W. H. (1980). On the method of least squares. *Astron. J.* **85**, 177-181.
- LANDOLT, A. U. (1979). UVV photoelectric sequences in celestial equatorial Selected Areas 92-115. *Astron. J.* **78**, 959-981.
- MORRISON, D., AND L. A. LEROFSKY (1979). Asteroid radiometry. In *Asteroids* (T. Gehrels, Ed.) pp. 184-205. Univ. of Arizona Press, Tucson.
- NATHIER, R. E. (1973). High speed photometry. *Vistas Astron.* **15**, 91-111.
- OSTRO, S. J., AND R. CONNELLY (1984). Convex profiles from asteroid lightcurves. *Icarus* **57**, 443-463.
- VAN FLANDERN, T. C., E. F. TEDISCO, AND R. P. BINZEL (1979). Satellites of asteroids. In *Asteroids* (T. Gehrels, Ed.) pp. 443-465. Univ. of Arizona Press, Tucson.

Speckle Interferometry of Asteroids

III. 511 Davida and Its Photometry

J. D. DRUMMOND AND E. K. HEGE

Steward Observatory, University of Arizona, Tucson, Arizona 85721

Received May 23, 1985; revised March 24, 1986

511 Davida was observed with the technique of speckle interferometry at Steward Observatory's 2.3-m telescope on May 3, 1982. Assuming Davida to be a featureless triaxial ellipsoid, based on five 7-min observations its triaxial ellipsoid dimensions and standard deviations were found to be $(465 \pm 90) \times (358 \pm 58) \times (258 \pm 356)$ km. This shape is close to an equilibrium figure (a gravitationally shaped "rubble pile") suggesting a density of 1.4 ± 0.4 g/cm³. Simultaneously with the triaxial solution for the size and shape of Davida, we found its north rotational pole to lie within 29° of RA = 1908°, Dec = +15° ($\lambda = 291^\circ$, $\beta = +37^\circ$). If Davida is assumed to be a prolate biaxial ellipsoid, then its dimensions were found to be $(512 \pm 100) \times (334 \pm 39)$ km, with a north pole within 16° of RA = 10°52', Dec = +16° ($\lambda = 322^\circ$, $\beta = +32^\circ$). We derive and apply to Davida a new simultaneous amplitude-magnitude (SAM)-aspect method, finding, from photometric data only, axial ratios of $a/b = 1.25 \pm .02$, $b/c = 1.14 \pm .03$, and a rotational pole within 4° of $\lambda = 307^\circ$, $\beta = +32^\circ$. We also derive a (weighted) linearized form of the amplitude-aspect relation to obtain axial ratios and a pole. However, amplitudes must be known to better than .01 if the b/c or a/c ratios are desired to better than 10%. Combining the speckle and SAM results, we find for the Gehrels and Tedesco phase function a geometric albedo of $.033 \pm .009$ and for the Lumme and Bowell function $.041 \pm .011$, for a unified model of $437 \times 350 \times 307$ km. Differences between the photometric and speckle axial ratios and poles are probably due to the effects of albedo structure over the asteroid; details on individual lightcurves support this conclusion. © 1986 Academic Press, Inc.

INTRODUCTION

In order to find its triaxial dimensions and the direction of its angular momentum vector (its spin axis) we have obtained five speckle interferometric observations of the sixth largest (Zellner, 1979) minor planet, 511 Davida. Zappala and Knezevic (1986) have applied the amplitude-magnitude-aspect relationship (Zappala *et al.*, 1983; Zappala and Knezevic, 1984) to lightcurves of Davida extending back to 1952. We, too, derive and apply a new simultaneous amplitude-magnitude-aspect, and a weighted amplitude-aspect, method to the extensive photometric data of Davida. These methods lead to an independent photometric determination of the location of Davida's spin axis and its axial ratios, whereas speckle interferometry, being a high angular resolution technique, follows the chang-

ing size, shape, and orientation of the projection of the asteroid to derive its pole and dimensions.

For image modeling and photometric purposes, an asteroid is assumed to be a triaxial ellipsoid rotating about its shortest axis ($a \geq b \geq c$), smooth (no large craters, mountains, etc.), featureless (no albedo variations), and uniformly bright (scatters geometrically). Such an ellipsoidal model asteroid projects as an apparent ellipse of uniform brightness on the plane of the Earth's sky. The two-dimensional image autocorrelation function of a uniformly bright ellipse has the same shape and orientation (but twice the size) as the ellipse itself. The corresponding image power spectrum also has the same elliptical shape, but appears rotated 90° because of the reciprocal relation between image extent and spatial frequency. The projected figure of the

real asteroid on the plane of the Earth's sky is thus characterized by the fit of an elliptical model to the observed image autocorrelation function or image power spectrum data. This yields the observed major axis dimension (α), minor axis dimension (β), and position angle of the major axis (γ) for a particular time in the asteroid's rotational cycle. The equations relating the observed elliptical parameters (α , β , γ) for a series of rotational phase angles ψ to the three axes dimensions and pole direction of the triaxial ellipsoid are given by Drummond *et al.* (1985a). Thus, a nonlinear least-squares routine is applied to a series of (α , β , γ) and yields simultaneously six parameters: the three axes dimensions, two Euler angles (θ , the sub-Earth point latitude, and ψ_0 , the zero point in the rotational cycle), and the obliquity (ρ , the projected angle between the asteroid's north pole and the ecliptic north pole; see Appendix I of Drummond *et al.*, 1985a).

OBSERVATIONS AND RESULTS

On May 3, 1982, with the 2.3-m telescope of Steward Observatory and the speckle camera and equipment described by Hege *et al.* (1982), five 7-min speckle observations of Davida were made, each observation being preceded by an observation of one nearby star, and followed by another

TABLE I

ASPECT DATA FOR SPECKLE OBSERVATIONS

Date	RA	Dec	Ecliptic	
3 May 1982	15 ^h 56 ^m	2 ^h 08 ^m	Long	Lat
			23°	+18°
Solar phase angle	Distance		Distance	
6.3	from Earth		from Sun	
	2.655 AU		3.604 AU	
Midtimes of observations (UT)				
9.99				
10.29				
10.57				
10.88				
11.16				

TABLE II

TRIAxIAL SOLUTION

		Pole 1	
a	465 ± 90 km	RA	19 ^h 08 ^m Dec. +15°
b	358 ± 58 km	Ecliptic long	291° Lat. +17°
c	258 ± 356 km		
ψ_0	10 ± 34	Pole 2	
θ	40 ± 50	RA	12 ^h 40 ^m Dec. +18°
ρ	285 ± 17	Long	196° Lat. +12°
ρ_1	105 ± 17	The error radius around each pole solution is 29°	

Normalized correlation matrix

	a	b	c	ψ_0	θ	ρ
a	1					
b	03	1				
c	30	66	1			
ψ_0	44	40	20	1		
θ	51	70	95	02	1	
ρ	17	47	4	72	30	1

observation of a second star. The coadded power spectra of Davida for each 7 min were divided by the power spectra of the flanking stars in order to remove the telescope modulation transfer function and the seeing (Hege *et al.*, 1982; Drummond *et al.*, 1985a, 1985b). The aspect data for Davida on May 3, 1982, is given in Table I.

Table II gives the six-parameter fit to the 15 equations of condition (five α 's, five β 's, and five γ 's) and the normalized correlation matrix. As for most nonlinear least-squares routines, our program (adopted from Jefferys, 1980, 1981) linearizes about the residuals. The errors for the parameters can then be computed directly during the solution of the equations of condition. For 433 Eros (Drummond *et al.*, 1985a) and 532 Herculina (Drummond *et al.*, 1985b), the errors so computed appear to be reasonable. However, for Davida they are unreasonably large, especially for the smallest dimension, c , because at certain orientations of the asteroid, the residual space (or χ^2 hyperspace) is quite convoluted and even discontinuous. As explained by Drummond *et al.* (1985a), at certain configurations, when $\cos^2\theta > (a^2 - b^2)/(a^2 - c^2)$, the projection of the asteroid will appear to reverse directions as the asteroid rotates. Near this configuration a small change in any of the six

parameters during the iterations will result in a large change in the predicted position angles, and thus in the residuals. In other words, the derivatives of the parameters with respect to the observables can approach infinity at certain points in the rotation. The errors computed in such a situation may not be realistic. For instance, the minimum in the χ^2 hyperspace results in the solution that appears in Table II, but the formal error for c of ± 356 km implies that our data allow c to be negative.

Table III gives the five-parameter solution and correlation matrix for the prolate spheroid case ($b = c$). Since the projected figure of a biaxial ellipsoid can never reverse direction of rotation, the χ^2 hyperspace is not warped, and there are no problems finding the solutions or computing the errors. The standard errors of fit for the triaxial (106 km) and biaxial (100 km) solutions do not allow a clear choice between the two.

In Fig. 1, we show the measured α 's (upper filled circles) and β 's (lower open circles), as a function of rotational phase for our triaxial solution. The upper line is the predicted α from the solution in Table II, and the lower line is the predicted β . Figure 2 shows the measured (circles) and predicted (line) γ 's. To illustrate the problem

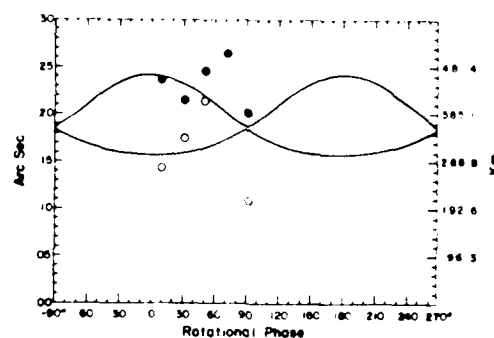


FIG. 1. Measured major (α) and minor (β) axis dimensions (solid and open dots, respectively) for the triaxial solution of Table II as a function of rotational phase for 511 Davida on May 3, 1982. The upper line is the least-squares fit to the major axis dimensions and the lower line is the simultaneous fit to the minor axis dimensions. Maximum area (maximum light) occurs at rotational phase 0° and 180° .

caused by the weird shape of the residual space, Fig. 3 results from using the solution of Table II, but changing the latitude of the sub-Earth point, θ , by 1° from -39.6 to -40.6 . In Fig. 2, $\cos^2\theta > (a^2 - b^2)/(a^2 - c^2)$ and the condition for rotation reversal of the projected ellipse is satisfied. In Fig. 3, $\cos^2\theta < (a^2 - b^2)/(a^2 - c^2)$ and the ellipse does not reverse directions. Figures 4 and 5

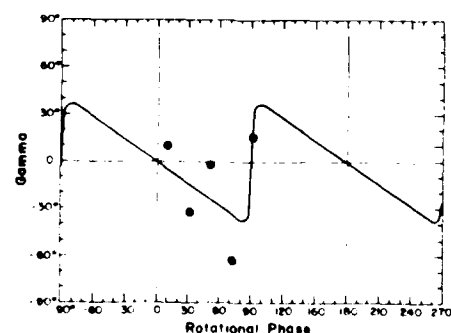


FIG. 2. Measured relative position angles (dots) of the major axis and the simultaneous (along with the data in Fig. 1) least-squares fit to the measured position angles (γ) for the triaxial solution of Table II as a function of rotation on May 3, 1982. At rotational phase 0° and 180° , maximum area is reached, and a is perpendicular to our line of sight, lying unforeshortened in the plane of the Earth's sky. Note that the position angle reverses direction near minimum light at rotational phases -90° and 90° .

TABLE III
BIAXIAL SOLUTION

a	512 ± 100 km	Pole 1
$b = c$	334 ± 39 km	RA = $20^\circ 56'$, Dec = $+16^\circ$
ψ	-24 ± 14	Ecliptic long = 322° , Lat = $+32^\circ$
θ	-14 ± 13	
ρ	290 ± 17	Pole 2
ρ	110 ± 17	RA = $10^\circ 52'$, Dec = -17°
		Long = 171° , Lat = -23°

The error radius around each pole solution is 16.

Normalized correlation matrix

	a	b	ψ	θ	ρ
a	1.00				
b	0.22	1.00			
ψ	0.40	0.04	1.00		
θ	0.05	0.16	0.15	1.00	
ρ	0.19	0.10	0.61	0.54	1.00

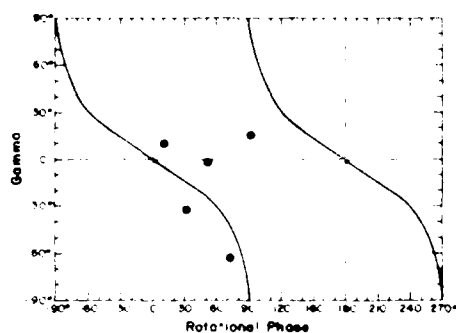


FIG. 3. Same as Fig. 2, but the latitude of the sub-Earth point (θ) has been changed by one degree. Unlike in Fig. 2, for this aspect the asteroid would not appear to reverse directions during rotation. The one degree change in θ results in a large change to the structure of the residuals (see text).

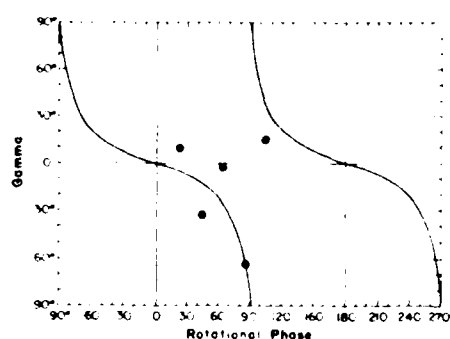


FIG. 5. Same as Fig. 2, but for the biaxial solution of Table III.

show the same information as in Figs. 1 and 2, but for the biaxial solution in Table III.

DAVIDA AS A RUBBLE PILE

A particular subset of triaxial ellipsoid figures is allowed if a body is in hydrostatic as well as gravitational equilibrium. The shape of such objects is maintained by gravity only since they have no internal strength (Chandrasekhar, 1969; Weidenschilling, 1981). If an asteroid suffers a catastrophic collision, it is possible that reaccumulation could occur among the ejecta with relative velocities less than the escape velocity of the largest remnant (Zappalà *et al.*, 1984). If such rubble piles behaved like perfect fluids (Davis *et al.*, 1979), they would form a par-

ticular triaxial ellipsoid equilibrium figure that is a function only of its angular momentum.

Within the errors, our determination of the triaxial shape of Davida suggests the possibility that it could be such an equilibrium figure, and since we know its volume and rotation period, it is possible to find its mean density as was suggested by Farinella *et al.* (1981). Following their lead, we note that for the equilibrium figure of $465 \times 377 \times 244$, which falls within the errors of our observations, and has the same long dimension and volume as the solution from Table II, a rotational period of 5.1297 hr (Zappalà and Knezevic, 1986) leads to a mean density of $1.4 \pm 0.4 \text{ g/cm}^3$. This density is rather low and could mean that there is substantial void space within the asteroid, or for that matter, may suggest that Davida is not a rubble pile after all. A prolate spheroid is not an equilibrium figure, and so we do not address the issue for the solution in Table III.

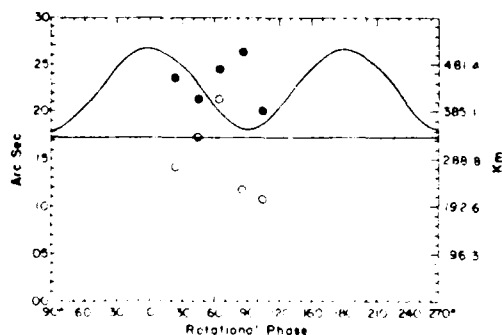


FIG. 4. Same as Fig. 1, but for the biaxial solution of Table III.

PHOTOMETRY

When the solar phase angle (ω) is less than substantial, there is a two-fold ambiguity in determining the pole direction from the changing size, shape, and orientation of the projected ellipses. However, this $\pi, \pi - \theta$ ambiguity (Drummond *et al.*, 1985a) which is manifest as a choice between two obliquities, and therefore two poles, can

TABLE IV
MAGNITUDES AND AMPLITUDES

Date	1950 Ecliptic		Solar phase angle (ω)	Max $V(1, \omega)$	Min $V(1, \omega)$	Amp	θ^a	Source ^b
	Long	Lat						
Jan 26, 1952	112°	+3°	5°0	6.55	6.61	.06	+52°	1
Apr 8, 1953	200	+22	6.6	6.72	6.97	.25	+2	1
Jan 26, 1958	147	+12	8.1	6.72	6.81	.09	+42	2
Dec 5, 1962	63	-17	6.9	—	—	.14	+31	3
Dec 30, 1968	100	-4	1.65	6.35	6.43	.08	+52	4
Mar 21, 1970	195	+22	7.8	6.82	7.07	.25	+6	4
Aug 7, 1972	304	-7	3.6	6.48	6.54	.06	-51	4
Oct 31, 1979	60	-20	10.7	6.86	7.04	.18	+30	5
Nov 12, 1979	59	-20	7.9	6.73	6.91	.18	+29	5
Dec 6, 1979	52	-18	10.0	6.83	7.00	.17	+22	5
Dec 17, 1979	51	-17	12.8	6.96	7.15	.19	+22	5
Jan 3, 1980	50	-14	17.2	7.13	7.31	.18	+18	5

^a Based on a pole at $\lambda = 307$, $\delta = +32$.

^b (1) Groeneveld and Kuiper (1954). (2) Gehrels and Owings (1962). (3) Chang and Chang (1963). Contrary to the .12 mag amplitude that the authors list for their lightcurve, we estimate an amplitude more like .14. (4) Vesely and Taylor (1985). The average between the Dec 29 and Dec 30 position, ω , V_0 , and amplitude is used. (5) Zappala and Knezevic (1986). Although the paper shows only a composite lightcurve, we have inspected the individual lightcurves, kindly provided by the authors, and listed the relevant parameters for each individual lightcurve.

easily be resolved by considering lightcurve data. We compare the observed lightcurve amplitudes in Table IV to our predicted amplitudes using the axial dimensions and pole 1 in Table II. The RMS deviation from the observed amplitudes is .05 mag, whereas with pole 2 it was found to be .14 mag. The choice between the two pole solutions is obvious.

Next we derive and apply yet another magnitude-amplitude-aspect relation. Several versions of the principle are currently used, e.g., Zappala's amplitude-magnitude (AM; Zappala *et al.*, 1983; Zappala and Knezevic, 1984), Tedesco and Taylor's (1985) magnitude-amplitude-shape-aspect (MASA), Pospieszalska-Surdej and Surdej's (1985) amplitude-aspect relationships, or Magnusson's (1985) combination. To distinguish our new technique we dub our method the simultaneous amplitude-magnitude (SAM) relation. Adopting the assumptions from the introduction of this paper, the square of the amplitude

(converted from magnitudes to a linear scale) of an asteroid's lightcurve is given as the ratio of maximum to minimum projected area squared:

$$R^2 = (A + B \cos^2 \theta) / (A + C \cos^2 \theta) \quad (1)$$

where $A = a^2 b^2$, $B = a^2 c^2 - a^2 b^2$, and $C = b^2 c^2 - a^2 b^2$. The latitude of the sub-Earth point, θ , comes from

$$\sin \theta = -[\cos(\lambda - \lambda_p) \cos \delta \cos \delta_p + \sin \delta \sin \delta_p],$$

where λ , δ and λ_p , δ_p are the known celestial or ecliptic coordinates of the asteroid and the unknown coordinates of the asteroid's pole, respectively.

Unlike photometric astrometry (Taylor, 1979; Taylor and Tedesco, 1983), which takes advantage of the movement of the sub-Earth point across lines of longitude on the asteroid to derive a pole direction, all amplitude-magnitude-aspect methods, which take advantage of the movement of

the sub-Earth point across lines of latitude on the asteroid, are model dependent in that they are a function not only of the location of the pole but of the axial ratios as well. With a nonlinear least-squares solution of Eq. (1) for ab , ac , bc , λ_p , and δ_p (or A , B , C , λ_p , and δ_p) one could find $a^2/b^2 = (A + B)/(A + C)$, $b^2/c^2 = A/(A + B)$, $a^2/c^2 = A/(A + C)$ and λ_p , δ_p . A separate solution of the numerator in (1), using $V_0(1,0)$ converted to intensity (the magnitude-aspect relation), would yield only $b^2/c^2 = A/(A + B)$ and a pole position, if the amplitudes are not available. Thus two separate determinations of b^2/c^2 and the pole are made with the amplitude-aspect [Eq. (1)] and the magnitude-aspect methods.

Another way of attacking the problem is to use a grid of possible poles and axial ratios to find the combination that minimizes the residuals between observed and predicted amplitudes and maximum intensities. Our new method, however, uses a linear least-squares technique to find the axial ratios from a grid of possible poles, thus eliminating the necessity of sampling a grid of axial ratios. First, if only amplitudes are considered, then by manipulating (1), we can form a linear amplitude-aspect relation

$$(R^2 - 1)^{-1} = k + l \tan^2 \theta \quad (2)$$

and solve for k and l for each trial pole, where $k = (A + C)/(B - C)$ and $l = A/(B - C)$, and thus $a^2/b^2 = (k + 1)/k$, $b^2/c^2 = l/(k + 1)$, and $a^2/c^2 = l/k$. The pole and the resulting k and l that minimize the residuals between "observed" and predicted $(R^2 - 1)^{-1}$ are chosen as the best solution. The drawbacks to this method are that it is a nonlinear relation between the observable quantity R and the independent variable θ , and that it must be weighted to compensate for the distortion of the assumed equal uncertainties in amplitudes when the amplitudes are transformed to $(R^2 - 1)^{-1}$. However, (2) is the simplest linear statement of the amplitude-aspect relation.

If both V_0 and an amplitude for a given epoch are provided, then it is possible to

convert the maximum and minimum light to intensities squared, X^2 and N^2 , respectively. Two linear combinations of these quantities yield two equations to solve for three unknowns. Adding and subtracting the numerator and denominator in (1) yields

$$X^2 + N^2 = K + L \cos^2 \theta \quad (3)$$

$$X^2 - N^2 = M \cos^2 \theta \quad (4)$$

A linear least-squares solution of these equations for each trial pole is made, and again the pole giving the lowest vector sum of the residuals in (3) and (4) is chosen. The corresponding K , L , and M give the axial ratios:

$$\frac{a^2}{b^2} = \frac{K + L + M}{K + L - M} = \frac{A + B}{A + C}$$

$$\frac{a^2}{c^2} = \frac{K}{K + L - M} = \frac{A}{A + C}$$

$$\frac{b^2}{c^2} = \frac{K}{K + L + M} = \frac{A}{A + B}$$

The advantage of this amplitude-magnitude-aspect method is that a linear least-squares estimate is made for the unknowns, which yield axial ratios for the pole giving the lowest residuals for all the available information simultaneously.

We now apply this new method (SAM) by selecting the 11 amplitudes in Table IV for Davida that have a corresponding V_0 . But first, we use all the $V(1, \omega)$'s in Table IV to construct the standard solar phase function plot of $V(1, \omega)$ vs ω , and show this as Fig. (6). For $\omega > 7^\circ$, we fit

$$V(1,0) + \beta \omega = V(1, \omega),$$

and for $\omega < 7^\circ$, we fit

$$V(1,0) + \beta(7^\circ) - .538 - .134\omega^{-14} + V(1, \omega),$$

in accordance with the opposition effect as formulated by Gehrels and Tedesco (1979), for which we find $V(1,0) = 6.40(\pm .04) + \omega(.043(\pm .004))$, with an RMS deviation from the solid line of .034 mag. If we choose the

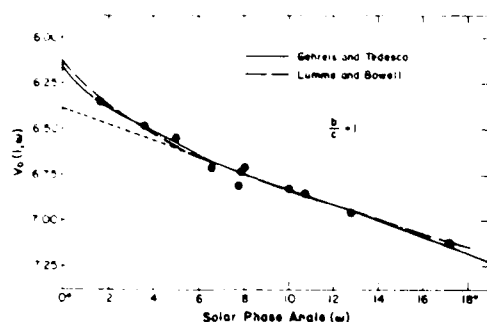


FIG. 6. Standard (b assumed equal to c) solar phase plot of V_0 (from Table IV) vs solar phase angle. The data from Table IV is plotted, and the results are given in Table VI under the speckle (bi) entry. A biaxial ($b = c$) ellipsoid model implies that no change in $V(1,0)$ occurs with a change in aspect.

Lumme and Bowell (1981a, 1981b; Bowell and Lumme, 1979) phase function description, we fit

$$10^{-4} V(1, \omega) = E + F\eta$$

where the magnitude at zero solar phase angle $m(0) = -2.5 \log E$, the multiple scattering parameter $Q = 1 + E/F$, and the independent variable $\eta = \sin \omega (1.124 + 1.407 \sin \omega - .758 \sin^2 \omega)$. For Davida we derive $m(0) = 6.13 (\pm .02)$ and $Q = 0.045 (\pm .055)$ with an RMS scatter of 0.033 mag. (Fig. 6). Both methods describe the data adequately.

Implicit in the standard phase plot (Fig. 6) is that $b/c = 1$, that the maximum area does not change with θ . But let us attribute the residuals in Fig. 6 to differences in θ at various oppositions, and convert each residual to an intensity. Then using the 11 residuals that have corresponding amplitudes in Table IV, we can derive 11 (X^2, N^2) pairs for input into the SAM method. The only data that is excluded is the 1962 amplitude for which a V_0 was not found. Next we construct a grid of pole positions at 1° intervals in both ecliptic longitude and latitude and solve for k and l for each pole. The solution which yields the lowest residuals in $1/(R^2 - 1)$ is chosen. With this pole and b/c ratio, we then convert each V_0 to the brightness as viewed from above the same astero-centric latitude, e.g., from over the

pole or above the equator, and correct these new magnitudes for solar phase angle effects by constructing another solar phase angle plot. We then repeat the process by converting the new residuals to (X^2, N^2) pairs for input into the SAM method, readjust the V_0 's with the new pole and b/c ratio, etc. Iterating between the solar phase angle fit and the SAM method until no change occurs in the parameters assures that the residuals are minimized with respect to both the solar phase angle and the aspect ($90^\circ - \theta$).

We find solutions for both our SAM method [Eqs. (3) and (4)], and for the amplitude-aspect relation as given by (2). Bevington (1969, p. 180) suggests that when a nonlinear equation is transformed to a linear equation, the equations of condition should be weighted. In our case, this means that (2) should be weighted by

$$\left[\frac{d(R^2 - 1)^{-1}}{dR} \right]^2 = \frac{(R^2 - 1)^4}{R^2}.$$

Table V gives the pole and axial ratios for the SAM and weighted amplitude-aspect (WAA) methods, along with the errors as found by a formal analysis of the propagation of the uncertainties in the coefficients K , L , and M , or k and l , generated from the linear least-squares routines. For instance the error in the a/c ratio using (2) is

$$\begin{aligned} \sigma_{a/c} &= \frac{\partial(a/c)}{\partial(a^2/c^2)} \sigma_{a^2/c^2} = \frac{\partial(l/k)^{1/2}}{\partial(l/k)} \sigma_{l/k} \\ &= .5(a/c)^{1/2} (k^2 \sigma_l^2 + l^2 \sigma_k^2)^{1/2}. \end{aligned}$$

The RMS error for the location of the pole arises from the differences between the θ 's calculated from the given pole and from inverting (2):

$$\begin{aligned} \theta &= \tan^{-1} \left[\frac{(R^2 - 1)^{-1} - k}{l} \right]^{1/2} \\ &= \tan^{-1} \left[\frac{c^2/b^2 - R^2 c^2/a^2}{R^2 - 1} \right]^{1/2}. \end{aligned}$$

The RMS amplitudes (converted back to magnitude from intensities) arise from com-

TABLE V
POLE AND AXIAL RATIO SOLUTIONS

	Ecliptic pole coordinates			Axial ratios			RMS AMP ($n = 12$)
	λ	δ	RMS error ($n = 12$)	a/b	a/c	b/c	
SAM (G&T)	307	+32	4	$1.25 \pm .02$	$1.41 \pm .06$	$1.13 \pm .03$.015
SAM (B&L)	308	+31	4	$1.25 \pm .02$	$1.43 \pm .04$	$1.15 \pm .02$.015
WAA	307	+31	4	$1.25 \pm .01$	$1.40 \pm .10$	$1.11 \pm .08$.016
Speckle (Tr)	291	+37	10	$1.30 \pm .33$	1.80 ± 2.51	1.39 ± 1.93	.050
Speckle (Br)	322	+32	28	$1.53 \pm .35$	$1.53 \pm .35$	$1.00 \pm .17$.200

paring the observed amplitudes to a rearranged (1)

$$R^2 = \frac{\frac{c^2}{b^2} \cos^2 \theta + \sin^2 \theta}{\frac{c^2}{a^2} \cos^2 \theta + \sin^2 \theta}$$

Rounding out Table V are the equivalent results from the method of speckle interferometry based on the May 3, 1982, observations. Note that the error for the speckle pole in Table V is determined from photometric data, whereas the uncertainties in Tables II and III derive from speckle observations.

In Table VI, we show the solar phase functions for each of the solutions in Table V, using both the Gehrels and Tedesco phase function and the Lumme and Bowell formulation. The observed $V(1, \omega, \theta)$'s were

corrected to the polar view $V(1, \omega, 90^\circ)$ using the appropriate b/c and pole. Figure 7 shows the G/T phase function for the SAM results and Fig. 8 shows the same for the L/B function. Figure 9 is an aspect-max-min plot for the G/T SAM solution, showing the change of brightness with θ for both maximum and minimum light, corrected to a solar phase angle of zero with the G/T function. Using the L/B phase function would result in virtually the same figure, but with the magnitudes scaled brighter by 0.27 mag.

Of the photometric solutions for the pole and axial ratios in Tables V and VI, we prefer the results from the simultaneous-amplitude-magnitude method because it uses both V_0 and amplitudes simultaneously and is a simple combination of linear equations. Contrary to what Pospieszalska-Surdej and Surdej (1985) conclude, we find that the am-

TABLE VI
PHASE FUNCTIONS

	Gehrels and Tedesco			Lumme and Bowell		
	$V(1, \omega, 90^\circ)$	Phase coefficient	RMS mag ($n = 11$)	$m(0)$	Q	RMS mag ($n = 11$)
SAM	$6.37 \pm .01$	$0.67 \pm .007$.018	$6.10 \pm .02$	$130 \pm .035$.022
WAA	$6.37 \pm .01$	$0.67 \pm .007$.018	$6.11 \pm .02$	$108 \pm .035$.022
Speckle (L)	$6.34 \pm .01$	$0.68 \pm .008$.055	$6.03 \pm .05$	$171 \pm .100$.058
Speckle (Br)	$6.37 \pm .01$	$0.65 \pm .004$.031	$6.13 \pm .02$	$045 \pm .055$.033

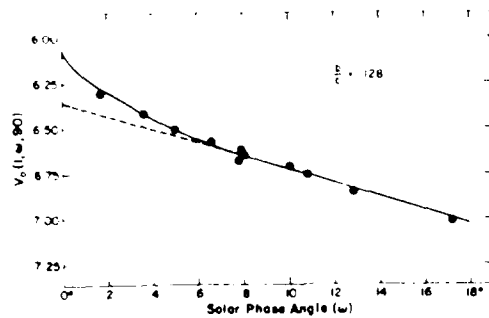


FIG. 7. Solar phase function for the simultaneous-amplitude-magnitude (SAM) aspect results given in Tables V and VI. Here the brightness $V(1, \omega, \theta)$ is corrected to $V(1, \omega, 90)$, the view from above the pole and the Gehrels and Tedesco phase function formulation is used.

plitude-aspect method is not to be preferred over the amplitude-magnitude-aspect method, because it requires that amplitudes be known to better than .01 mag. For example, in the present case, if we use the amplitudes predicted by the results from the WAA method in Table V, but rounded off to the nearest hundredth of a magnitude, and input these back into the WAA method, we do not get the results that we started with. The pole is found to be located at (310; +34) and $a/b = 1.25$, $a/c = 1.53$, and $b/c = 1.22$. However, if we round off the predicted amplitudes to the nearest thousandth of a magnitude, we do indeed obtain the results that generated the amplitudes in the first place.

Moreover, if we use 11 instead of 12 observations in the WAA method, eliminat-

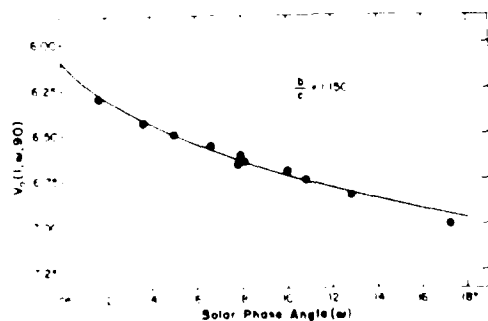


FIG. 8. Same as Fig. 7, but using the Lumme-Bowell phase function.

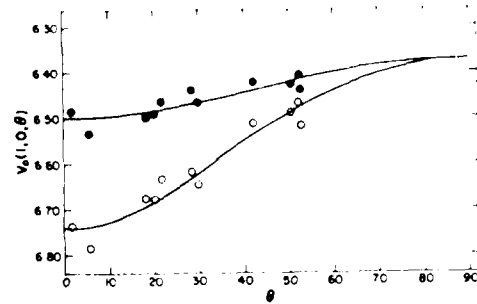


FIG. 9. A plot of $V(1, \theta, \omega = 0)_{max}$ and $V(1, \theta, \omega = 0)_{min}$ vs θ for the SAM method results, using the Gehrels and Tedesco phase function. If the Lumme and Bowell phase function were used, the same plot and curve would result, but the magnitude scale would have to be brighter by 0.27 mag.

ing only one of the five 1979 amplitudes, the results depend considerably on which of the five are not used. The pole for the five cases is fairly stable, ranging from (307; +30) to (309; +34), as is the a/b ratio, ranging from 1.25 to 1.26. However, a/c ranges from 1.37 to 1.55, and b/c from 1.09 to 1.23, depending on which of the 1979 amplitudes is not used. If we use only one amplitude from each opposition, choosing the 1979 amplitude observed at the smallest phase angle (7°9'), for the seven amplitudes we find a pole at (313; +33), $a/b = 1.27$, $a/c = 1.66$, and $b/c = 1.31$, with the WAA method. On the other hand, the SAM method reproduces the results in Table V to within one in the last digit for the pole and axial ratios, regardless of which of the 1979 observations are used or eliminated.

The conclusions from this analysis of photometric data, then, are that:

(1) The SAM method is more stable and reliable than the WAA method. It is only fortuitous that the WAA method with all 12 amplitudes from seven oppositions yields virtually the same results as the SAM method, since the answers, especially a/c and b/c , change considerably with the elimination of even one amplitude from the WAA analysis.

(2) Regardless of the method, the a/b ratio seems to be well determined.

(3) The location of the pole is also fairly well determined and is not very sensitive to the method.

(4) The a/c and b/c ratios vary dramatically with the location of the pole and the method of analysis, being most sensitive to the precision of the amplitudes in the WAA method.

COMBINING SPECKLE AND PHOTOMETRY

One of the most useful applications of speckle and photometric data is in the derivation of rather precise albedos, especially for dark objects where the polarization slope-albedo law saturates (Dollfus and Zellner, 1979). For each of the fits for Davida in Table VI, we find the figure requiring the least change (in an RMS sense) to the triaxial speckle dimensions to meet the axial ratios found from the photometry. These dimensions are listed in Table VII along with the uncertainties, where the latter are calculated as the vector sum of the uncertainty in the speckle dimension plus the difference between the speckle and photometric dimension. Also listed in the table are the visual albedos calculated with the $V(1,0,\theta = 90^\circ)$'s and $m(0)$'s of Table VI according to Eq. (3) of Dollfus and Zellner (1979), where the errors in the albedos follow from the propagation of the uncertainties in a , b , and $V(1,0,\theta = 90^\circ)$ or $m(0)$. Note that albedos and errors are given for the cross section viewed from above the pole, i.e., for πab . The albedos for the equatorial aspect (πac or πbc) would be the same but the associated uncertainty would be much

larger because of the error assigned to the speckle determination of c .

DISCUSSIONS AND COMPARISONS

In one night, speckle interferometric observations of Davida led to a triaxial ellipsoid solution or a biaxial solution for its figure, and a pair of possible rotational poles for each. A simple inspection of the light-curve amplitudes easily distinguishes which pole is correct for each solution. The pole for the triaxial solution lies within 29° of ($\lambda = 291^\circ$; $\beta = +37^\circ$), and for the biaxial solution, within 16° of ($322, +32$).

We devise a new simultaneous amplitude-magnitude (SAM)-aspect method that for Davida yields a pole within 4° of ($307; +32$). If only amplitudes are considered, then our version of a weighted amplitude-aspect (WAA) relation gives a pole within 4° of ($307; +31$). Zappala and Knezevic (1986) have determined with their amplitude-magnitude (AM)-aspect method that Davida's pole lies at ($303 \pm 4; +34 \pm 5$), or taking into account the effect of light scattering on their method, at ($302 \pm 6; +29 \pm 6$). The average of the two speckle pole locations from the triaxial and biaxial fits lies at ($306.5; +34.5$), in excellent agreement with all photometric methods. Chang and Chang (1963), from only four light-curves, found a pole at ($306; +34$) with an early version of the amplitude-aspect technique, superceding the one Gehrels and Owings (1962) found at ($122; +10$) from three lightcurves.

Although Taylor (Vesely and Taylor,

TABLE VII
DIMENSIONS AND ALBEDOS

	a	b	c	$p, (G&L)$	$p, (L\&B)$
Speckle (1)	458 ± 90	358 ± 58	258 ± 35	0.34 ± 0.09	0.41 ± 0.10
Speckle (3)	512 ± 100	333 ± 39	334 ± 39	0.28 ± 0.07	0.36 ± 0.08
SAM (G&L)	455 ± 97	349 ± 59	309 ± 54	0.33 ± 0.09	
SAM (L&B)	478 ± 94	371 ± 58	305 ± 38		0.41 ± 0.11
WAA	435 ± 48	347 ± 89	311 ± 36	0.33 ± 0.09	0.42 ± 0.12

1985) was not able to achieve totally satisfactory results with photometric astrometry of Davida, by considering only pairs of observations at the same ecliptic longitudes a pole within 22° of $(285; +45)$ was suggested, which is only 9° from the speckle triaxial pole. Perhaps the reason for the failure of the technique also explains the discrepancies between the speckle and photometrically determined axial ratios, namely the presence of albedo structure on Davida.

The geometric albedo derived by combining speckle and photometry results is quite insensitive to the method of determining the rotational pole and axial ratios, but does depend on the phase functions. For the Gehrels-Tedesco phase function, and the triaxial ellipsoid dimensions adjusted to the axial ratios found through photometry, the visual albedo is $p_v = .033 \pm .009$ and with the Lumme-Bowell law is $p_v = .041 \pm .011$. The radiometric diameter of Davida is listed as 323 km by Morrison and Zellner (1979) and 335 by Bowell *et al.* (1979). These diameters, obtained at unknown rotational phases and unknown aspects, would correspond to albedos between 0.034 and 0.048, and between 0.031 and 0.044, respectively, depending on whether the diameters refer to minimum light at an equatorial aspect, or to a polar view, with the SAM method and the GT phase function. For the Lumme and Bowell phase function, the two radiometric diameters would lead to albedos between 0.043 and 0.061, and between 0.040 and 0.057, respectively.

The triaxial ellipsoid fit to the speckle observations yields axial ratios of $a/b = 1.30 \pm .33$ and $b/c = 1.39 \pm 1.93$, and the biaxial ellipsoid fit gives $a/b = 1.53 \pm .35$ and $b/c = 1.00 \pm .17$. Zappala and Knezevic found $a/b = 1.26$ and $b/c = 1.18$ (or 1.19 and 1.13 with corrections for scattering). With the SAM method we find $a/b = 1.25 \pm .02$ and $b/c = 1.14 \pm .03$ (averaging the results from the Gehrels-Tedesco and the Lumme-Bowell phase functions). With the WAA method we find $a/b = 1.25 \pm .01$ and $b/c = 1.11 \pm .08$.

Since the amplitude is only a weak function a/c or b/c , for the WAA method the amplitudes must be known to better than .01 mag if accurate b/c or a/c ratios are to be found. The location of the pole is also affected by amplitude precision, but not as much as b/c or a/c . However, since the amplitude is a strong function of a/b , the a/b ratio is affected the least by the lack of precision in amplitudes. Pospieszalska-Surdej and Surdej offer a way not only to determine from lightcurves the appropriateness of applying ellipsoid geometry, but to increase the precision of the amplitude by using every point in the lightcurve. However, we feel that the SAM method is still to be preferred because it is a more stable, linear relation between the observable quantities (maximum and minimum brightness) and the pole and axial ratios.

The excellent agreement among the photometrically determined axial ratios is encouraging. It is obvious that the speckle triaxial a/b ratio of 1.30 is also in good agreement with the photometric consensus of 1.25, but the biaxial a/b of 1.53 is too strongly affected by the assumption of $b/c = 1$. However, the assumption of $b/c = 1$ leads to a better solar phase angle plot than the triaxial $b/c = 1.39$. With our preference for the SAM method, we offer as a unified model from photometry and speckle, and averaging the results for the GT and L/B phase functions, absolute dimensions for Davida of $437 \times 350 \times 307$ km, and a rotational pole at $(307; +32)$.

As we are learning from Herculina (Taylor *et al.*, 1986), albedo features have a much greater impact on our power spectra analysis of asteroid data than previously believed. Since it is not easy to predict or account for the effect of albedo markings on image power spectra, we are now attempting to make all measurements on reconstructed images, which would circumvent the influence of albedo spots on speckle interferometry observations. We also feel that albedo markings have a greater effect on photometry than previ-

ously suspected. It appears that Herculina's lightcurve is due almost entirely to albedo features rather than to the shape of the asteroid (Taylor *et al.*, 1986). The failure of photometric astrometry on Davida, coupled with the exaggerated axial ratios found from speckle power spectra analysis, imply significant albedo structure on Davida. This conclusion is further supported by the fact that the high-amplitude lightcurves of 1979, 1970, and especially 1953 all show considerable structure near one of the minima, and the low-amplitude lightcurves of 1952, 1968, and 1972 are quite irregular. According to a pole at $(307; +32)$, the speckle observations were made at a sublatitude of $\sim 26^\circ$, midway between the equatorial ($+2^\circ$) lightcurve of 1953 and the low-amplitude lightcurve of 1972 (-51°), both of which show strong indications of a nonuniform surface on Davida.

ACKNOWLEDGMENTS

We thank Eugene Perinot and Gary Schmidt for helpful discussions regarding the properties of least-squares fitting procedures. This work is supported under NASA Contract NAGW-224.

REFERENCES

- BEVINGTON, P. R. (1969). *Data Reduction and Error Analysis for the Physical Sciences*. McGraw-Hill, New York.
- BOWELL, E., T. GEHRELS, AND B. ZEILNER (1979). Magnitudes, colors, types, and adopted diameters of the asteroids. In *Asteroids* (T. Gehrels, Ed.), pp. 1108-1129. Univ. of Arizona Press, Tucson.
- BOWELL, E., AND K. LUMME (1979). Colorimetry and magnitudes of asteroids. In *Asteroids* (T. Gehrels, Ed.), pp. 132-159. Univ. of Arizona Press, Tucson.
- CHANDRASEKHAR, S. (1962). *Ellipsoidal Figures of Equilibrium*. Yale Univ. Press, New Haven, Conn., London.
- CHANG, Y.-C., AND C. GOSWAMI (1979). Photometric observations of variable asteroids. In *Astr. Soc. Am. Ser.* **11**, 139-149.
- DAVIS, D. R., L. K. CHEEMAN, R. GREENBERG, S. C. WEIDENSOHLT, AND A. W. HARRIS (1979). Collisional evolution of asteroids. Population, formation, and evolution. In *Asteroids* (T. Gehrels, Ed.), pp. 528-557. Univ. of Arizona Press, Tucson.
- DOUGLAS, A., AND R. TAYLOR (1979). The orbital photometry of asteroids. In *Asteroids* (T. Gehrels, Ed.), pp. 170-183. Univ. of Arizona Press, Tucson.
- DRUMMOND, J. D., W. J. COCKE, E. K. HEGE, P. A. SRIKUMAR, AND J. V. LAMBERT (1985a). Speckle interferometry of asteroids. I. 433 Eros. *Icarus* **61**, 132-151.
- DRUMMOND, J. D., E. K. HEGE, W. J. COCKE, J. D. FREEMAN, J. C. CHRISTOU, AND R. P. BINZEL (1985b). Speckle interferometry of asteroids. II. 532 Herculina. *Icarus* **61**, 232-240.
- PARINELLO, R., P. PAGLIUCHI, E. F. TEDI, AND V. ZAPPALÀ (1981). Triaxial equilibrium ellipsoids among the asteroids. *Icarus* **46**, 114-123.
- GEHRELS, T., AND D. OWINGS (1962). Photometric studies of asteroids. IX. Additional lightcurve. *Astrophys. J.* **135**, 906-914.
- GEHRELS, T., AND E. F. TEDI (1979). Minor planets and related objects. XXVIII. Asteroid magnitudes and phase relations. *Astron. J.* **84**, 1079-1088.
- GROENVELD, L., AND G. P. KUIPER (1954). Photometric studies of asteroids. I. *Astrophys. J.* **120**, 200-220.
- HEGE, E. K., E. N. HUBBARD, P. A. SRIKUMAR, AND W. J. COCKE (1982). The Steward Observatory speckle interferometry system. *Optica Acta* **29**, 701-715.
- JEFFERYS, W. H. (1980). On the method of least squares. *Astron. J.* **85**, 177-181.
- JEFFERYS, W. H. (1981). On the method of least squares. II. *Astron. J.* **86**, 149-155.
- LUMME, K., AND E. BOWELL (1981a). Radiative transfer in the surfaces of atmosphereless bodies. I. Theory. *Astron. J.* **86**, 1694-1704.
- LUMME, K., AND E. BOWELL (1981b). Radiative transfer in the surfaces of atmosphereless bodies. II. Interpretation of phase curves. *Astron. J.* **86**, 1705-1721.
- MAGNUSSEN, P. (1985). Distribution of spin axes and senses of rotation for large main belt asteroids. *Icarus*, in press.
- MORRISON, D., AND B. ZEILNER (1979). Polarimetry and radiometry of the asteroids. In *Asteroids* (T. Gehrels, Ed.), pp. 1080-1097. Univ. of Arizona Press, Tucson.
- POSPITZKA-SURDEJ, A., AND J. SURDEJ (1985). Determination of the pole orientation of an asteroid. The amplitude aspect relation revisited. *Astron. Astrophys.* **149**, 185-194.
- TAYLOR, R. C. (1979). Pole orientations of asteroids. In *Asteroids* (T. Gehrels, Ed.), pp. 480-493. Univ. of Arizona Press, Tucson.
- TAYLOR, R. C., P. V. BIRCH, J. DRUMMOND, J. SURDEJ, AND A. SURDEJ (1986). Asteroid 532 Herculina: Photoelectric Light Curves, the Pole Orientation from Photometric Astrometry, and a Unifying Model. Submitted for publication.
- TEDI, E. F., R. C. AND E. F. TEDI (1983). Pole orientation of asteroid 44 Nysa via photometric astrometry.

- try, including a discussion of the method's application and its limitations. *Icarus* **54**, 13-22.
- TEDESCO, E. F., AND R. C. TAYLOR (1985). Pole orientation of 16 Psyche by two independent methods. *Icarus* **61**, 241-251.
- VESELY, C. D., AND R. C. TAYLOR (1985). Photometric light curves of 21 asteroids. *Icarus* **64**, 37-52.
- WEIDENSCHILLING, S. J. (1981). How fast can an asteroid spin? *Icarus* **46**, 124-126.
- ZAPPALÀ, V., M. DIMARTINO, P. FARINELLA, AND P. PAOLICCHI (1983). An analytical method for the determination of the rotational directions of asteroids. In *Asteroids, Comets, Meteors* (C. I. Lagerkvist and H. Rickman, Eds.), pp. 73-76. Uppsala Universitet Repocentralen HSC, Uppsala.
- ZAPPALÀ, V., P. FARINELLA, Z. KNEZEVIC, AND P. PAOLICCHI (1984). Collisional origin of the asteroid families: Mass and velocity distributions. *Icarus* **59**, 261-285.
- ZAPPALÀ, V., AND Z. KNEZEVIC (1984). Rotation axes of asteroids: Results for 14 objects. *Icarus* **59**, 436-455.
- ZAPPALÀ, V., AND Z. KNEZEVIC (1986). Pole coordinates of the asteroid 511 Davida via the amplitude-magnitude method. *Icarus* **65**, 122-128.
- ZELLNER, B. (1979). Asteroid taxonomy and the distribution of the compositional types. In *Asteroids* (T. Gehrels, Ed.), pp. 783-806. Univ. of Arizona Press, Tucson.

Speckle Interferometry of Asteroids.

IV. Reconstructed Images of 4 Vesta

J. Drummond, A. Eckart, and E.K. Hege

Steward Observatory, University of Arizona, Tucson, Arizona 85721

Submitted to Icarus December , 1986

Running Title: A Mottled Vesta

Send correspondence and proofs to:

Jack Drummond
Steward Observatory
University of Arizona
Tucson, Arizona 85721

Abstract

The first glimpses of an asteroid's surface have been obtained from images of 4 Vesta reconstructed from speckle interferometric observations made on November 16 and 17, 1983, using Steward Observatory's 2.3m telescope coupled with Harvard's PAPA camera. From power spectrum analysis of the ten images Vesta is found to have a 'normal' triaxial ellipsoid shape of $584(\pm 16) \times 531(\pm 11) \times 467(\pm 12)$ km. Its rotational pole lies within 4° of R.A. = $21^h 00^m$, Dec. = $+41^\circ$ (Ecliptic long. = 336° , lat. = $+55^\circ$). Our observations definitely support a 5hr 20.5min rotational period, and do not fit one twice as long.

Reconstructed images reveal dark and bright patterns, reminiscent of the Moon, which can be followed across the disk as the asteroid rotates. By placing circular 'spots' with diameters of 135km ($=0.11$ arcsec, the effective resolution) over three dark and three bright features, and assigning albedos (relative to the surrounding material) of 0 to the dark spots and 2 to the bright spots (except one with an albedo of 1.2), we are nearly able to match its visible lightcurve. It only requires an additional bright spot deep in Vesta's southern hemisphere, an area not visible during our observations, to provide a near perfect match to all low solar phase angle lightcurves ever obtained of this asteroid. At phase angles greater than about 10° the observed amplitude becomes greater by up to 0.02 mag. The dark areas so dominate one face of Vesta that a minimum in the lightcurve occurs when the maximum cross-sectional area is visible. Its lightcurve is determined primarily by albedo structure rather than shape, leading to one maximum and one minimum per rotation instead of the expected two of each associated with its triaxial ellipsoid shape.

I. Introduction

The first images of an asteroid that show details on its surface have been reconstructed from speckle interferometric data obtained on November 16 and 17, 1983, with Steward Observatory's 2.3m telescope and a two dimensional photon counting camera (Papaliolios et al. 1985). These images show high contrast features which dominate the visible lightcurves. In the next section we give the results of our standard power spectrum analysis, finding the absolute dimensions and rotational pole of the triaxial ellipsoid figure that yields the observed changing size, shape, and orientation of the two dimensional ellipse projected by the ellipsoid. In Sec. III we give the detailed procedures that resulted in our successful image reconstructions. In Sec. IV we develop a model from our maps of Vesta that explain in good detail the observed lightcurves of this very interesting asteroid. Sec. V summarizes our results and compares them to others.

II. Power Spectrum Analysis

As in previous speckle interferometry work at Steward Observatory (Drummond et al. 1985a, 1985b; Drummond and Hege 1986) we assume that an asteroid can be treated as a uniformly bright triaxial ellipsoid that scatters geometrically, in which case the asteroid will project onto the plane of the sky as a two dimensional ellipse. The two dimensional power spectrum of the image at each rotational phase is measured for its semi-major (α) and semi-minor (β) axes dimensions, and for a position angle (γ) with respect to North. This series of α 's, β 's, and γ 's is fit to the relative rotational phases of each observation and yields from a non-linear least squares routine the asteroid's three axes dimensions, the astero-centric latitude of the sub-Earth point, the obliquity, and the zero point in the rotation.

Vesta was observed eight times on November 16, 1983, and twice on November 17. Aspect data for the observations is given in Table I. Each observation was a 5 min. videotape of the asteroid, and was preceded and followed by a similar observation of either SAO 094927 or SAO 094883. Vesta observations were generally fifteen minutes (16-17° in rotational phase) apart. A 30nm filter centered at 550nm was used, producing a data rate of 60 kHz for Vesta and the first star and 30 kHz for the second star. The data were digitized and binned into frames of 128x128 pixels

[illegible]

The least squares solutions for α 's, β 's, and γ 's were made with a rotational program written by J. A. M. Iqbal et al. (1985). The measured semimajor axis a is plotted in Fig. 1 as a function of time. The measured a is composed of two solid lines representing the variation of the projected asteroid (upper line) and the variation of the projected minor axis (lower line). The measured a and the model a are shown in Fig. 1 as closed circles and open circles, respectively. The solid line represents the measured a and the dashed line represents the model a . The measured a and the model a are shown in Fig. 1 as closed circles and open circles, respectively. The solid line represents the measured a and the dashed line represents the model a .

(indicated by tick marks to the left of the symbols) were folded back with the 5hr period and nearly fall on top of the first two points of the first night, not only in rotational phase (with either a 5 or 10 hr period) but in the measured parameters as well.

A prolate spheroid (biaxial ellipsoid: $a > b = c$) model was tried but the program diverged, giving no solution. An attempt was also made to fit the measured parameters against a 10hr 41min period, but the fitting program again diverged after a few iterations. Thus our observations indicate that Vesta is a 'normal' triaxial ellipsoid with a rotational period of 5hr and 20.5min, in spite of a lightcurve that only shows one maximum and minimum over this period.

III. Image Reconstructions

Images of Vesta were made with the amplitudes and phases obtained from the power spectra and Knox-Thompson cross spectra. For the present use the power spectra of Vesta and the calibration stars were normalized to a power of unity. Both quotients for each Vesta power spectrum indicated that both stars are good point sources at the given wavelength, resolution, and sensitivity of the measurements. Since the quotients were in all cases in excellent agreement at spatial frequencies larger than 11 pixels, we calibrated the Vesta data using the average power spectra of the adjacent star observations. With respect to the achieved signal to noise ratio the calibrated power spectra of Vesta did not appear to provide any significant information over the noise at greater than 30 pixels in power spectrum space (less than 0.18 arcsec in image space). This means that small hard-edged high-contrast features on Vesta did not produce strong signals in power spectrum space. Since the theoretical resolution limit of the 90-inch telescope at 550nm is 0.06 arcsec, and in order to suppress the noise smoothly on this highly resolved object we apodized the power spectra with a gaussian of full width at $1/e$ of 30 pixels (25 pixels full width at half power - FWHP) corresponding to a convolution in image space with a gaussian of 3.2 pixels FWHP. Therefore the effective beam width or resolution limit is 0.11 arcsec. The resulting power spectra are shown in Fig. 3a - 3j.

Due to residual misalignments of the photon masks (Papaliolios et al 1985), these deconvolved Vesta power spectra exhibited a small amount of artificial power at distinct locations along the axes. This power was removed by subtracting a gaus-

sian of comparable width and amplitude at the positions of the the corresponding spikes (Fig. 4a - 4j). The total amount of power contained in these artifacts appears to be different for the individual data sets and is about 1 % of the average total power and less than about 30 % to 40 % of the power contained in the first diffraction ring corresponding to the sharp edge of the asteroid. As seen by comparing Fig. 5a and Fig. 5b these corrections did not introduce any significant changes of the basic structural features observed.

In addition to the artifacts the calibrated power spectra suffered from seeing mismatches at the lowest spatial frequencies. The average of the 10 available power spectra on the other hand appeared to be free of these mismatches, consistent with the fact, that under- and over-estimates of the power spectra appeared equally frequent and therefore resulted in a correct average seeing calibration. Therefore in order to obtain a reasonable estimate of the power spectra at the lowest spatial frequencies we recapped them using the average power spectrum. Moreover the recapping procedure can be justified by the following points:

- 1) At the lowest spatial frequencies the actual shape of the power spectrum (provided it is smooth) cannot have any significant influence on the resulting images, since it contains information corresponding to structures larger than the known size of Vesta.

- 2) The power spectrum analysis (Sec. II) revealed that the actual cross-sectional of Vesta changed only by a small amount, so that the re-capping of the individual power spectra by the average power spectrum should not have a large influence on the resulting images.

- 3) Both points are supported by the comparison of the final images to those obtained after using a different approach to correct for the seeing mismatch. In this approach we iteratively transformed back and forth between power spectrum domain and autocorrelation domain, replacing negative values by zero in each domain and iteration. After a small number of iterations (10 to 20) this resulted (as required) in power spectra with increasing power towards lower frequencies in all cases. We decided not to obtain our final Vesta power spectra following this approach because - depending on the nature of the seeing mismatch - it resulted in amplitudes larger than unity, which is not to be expected in the case of a properly

seeing-calibrated power spectra normalized to unity. Nevertheless, Fig. 5 shows that both attempts to correct the seeing mismatch for the first Vesta image result in essentially the same map for the same data set.

In order to get a smooth transition between the recapping function PS_C and the Vesta power spectra PS_V , we combined them using a circular cosine-bell function:

$$C = \begin{cases} 1, & \text{if } r \leq r_{inner}; \\ 0.5 * (1 - \cos(\pi * (r - r_{inner}) / (r_{outer} - r_{inner}))), & \text{if } r_{inner} < r < r_{outer}; \\ 0, & \text{if } r \geq r_{outer}. \end{cases}$$

$$r = \sqrt{u^2 + v^2}.$$

The final improved power spectra PS_f were obtained via

$$PS_f = (1 - C) * PS_V + C * PS_C$$

using an outer radius of $r_{outer} = 9pix$ and an inner radius of $r_{inner} = 5pix$.

The (complex) phases of the individual Vesta data sets were obtained using the phase differences in u and v direction given by the Knox-Thompson cross spectra. Since the power spectra of Vesta suggested an almost circular symmetric appearance with only a small amount of structure, all phase differences were treated with equal weight. The phase at the DC point was set equal to zero and an initial estimate of the phases was obtained by integrating the phase difference vectors along two ways parallel to the u, v -axis and averaging both resulting vectors (Knox, 1976).

The phases were then subject to an iterative phase relaxation algorithm (Hardy et al. 1977), which was accomplished by spiraling around the DC point towards higher spatial frequencies, alternating between right and left directions. This algorithm uses the phases of the current iteration and the measured phase differences to calculate the phases for the next iteration. After 100 iterations the algorithm essentially converged and the deviations of the achieved phases from the expected hermitian symmetry were less than 0.1 radian. These small deviations were removed by averaging the phase vectors at locations (u, v) and $(-u, -v)$ in a way appropriate to the required hermitian symmetry.

The square root of the final power spectra were combined with these phases and Fourier transformed into image space. The resulting images exhibited on the

average 30 % negative power with negative amplitudes of less than 4 % of the maximum amplitudes in the images. To minimize the amount of negativity we next used a Fienup algorithm (Fienup 1978). Fig. 6 shows maps of the first Vesta observation obtained by direct inverse Fourier transformation, and using 50, 100, and 200 Fienup iterations. In all cases the significant structural features remain essentially unchanged. For the final Vesta maps we used 200 Fienup iterations. These maps contained only 10 % negative power having negative amplitudes of less than 2 % of the maximum.

Fig. 7 shows power spectra, phases, and Fienup images of the double star SAO 093840 used for the calibration of the image scale and orientation, and for the first Vesta observation. All the final maps of Vesta are shown in Fig. 8 and discussed further in the next section.

IV. The Images and a Model

The first images of any asteroid showing surface details are presented in the top row of Fig. 8. Since the two observations of Vesta from the second night are similar to, but noisier than, the first two observations of the first night, and were obtained at nearly the same rotational phases, only the eight images of November 15 are shown. From Sec. II we know the location of Vesta's North Pole and can therefore produce the second row of Fig. 8, where lines of astero-centric longitude and latitude at intervals of 30° are superimposed on the images of Vesta. The individual pixels visible in the top row are convolved (smoothed) down for the second and third rows. By consulting Fig. 1 the scale of the images can be determined. For instance, the asteroid ellipse for the first observation has a major axis dimension of 561km (0.46 arcsec) and a minor axis dimension of 470km (0.38 arcsec). The small plus in the middle of each image is the sub-Earth point at astero-centric latitude $+16^\circ$, the small off-center square is the sub-Sun point at latitude $+7.5^\circ$, and the terminator is perhaps visible along the limb opposite the sun. As the asteroid rotates, the sub-Earth point sweeps over lines of decreasing longitude. Thus the sub-Earth point is located at a longitude 9° greater than the sub-Sun point. The longitudes of the sub-Earth point for the eight images in Fig. 8 are 232, 216, 203, 185, 168, 151, 134, and 117° , where 0 and 180° longitudes correspond to the minimum cross-sectional area. The corresponding rotational phases are equal to 360° minus the longitudes. True

celestial North is 36° to the right (west) of the vertical, the direction of astero-centric North.

The third row of Fig. 8 shows 15% contour levels. Also, rings of diameter of 0.11 arcsec, the approximate effective minimum resolution (Sec. III), are drawn around features to be discussed next. Each image has been centered on the lowest 15% contour, since centering on say the brightest contour noticeably skews the entire asteroid so that the lowest flux levels on one edge of the asteroid fall outside the ellipses in the second row. This centering is also the way the eye tends to center the images. Once the images are centered, it is possible to identify and locate features with the longitude/latitude grid and follow them from one frame to the next. The coordinates and a description of each of the circled features A-F, appearing from right to left (in order of decreasing longitude), is now given:

A) 295; +15 A bright arm or peninsula is visible in the first image, only part of which falls under the circle in the bottom row. In the second frame this feature lies right on the limb, and in fact spills over the edge of the asteroid because of the smearing produced by the convolution discussed in Sec. III. It has rotated out of sight after the second frame.

B) 270; 0 The darkest area visible in the first frame is circled, but appears to be part of a much more extensive lunar maria-like (because of the darkness and large extent of the features) region that covers a great deal of the hemisphere. The dark region appears to encompass not only features B, C, and E, but obviously extends south of B as can be seen in the first frame. Feature B is last visible on the limb in the third frame.

C) 260; +20 The darkest area visible in the second frame is circled, and overlaps feature B. It is also part of the continuous dark region in this hemisphere. In the first frame part of feature C falls under the enhanced bright region that appears in all of the images (see below); in the fourth frame it is disappearing behind the limb.

D) 235; -20 A bright island in the middle of a dark sea clearly stands out in the third frame. This feature is also responsible for the extension of the enhanced bright central region toward the lower right in the first two frames before it becomes detached in the third.

E) 225; +7 The third of the dark areas dominates the third frame,

and contributes to the image of a tributary extending from B and C and flowing around D. To the south and towards lower longitudes the dark region continues, separating bright areas D and F.

F) 185;-5 From the second through the seventh frames a bright feature seems to distort the shape of the enhanced bright central region.

The enhanced bright central region, which in fact dominates the images, is caused by the occasional multiple detection of photons by the PAPA camera. The routines recently developed by the Harvard group to compensate for this problem were not available at the time this data was digitized. Thus it is necessary to 'look under and around' the variable bright central feature. Sometimes, it isn't until the features rotate from under this region that they become clearly visible.

To compare our triaxial ellipsoid model of Vesta with surface albedo structure to its lightcurves, we first examined the lightcurves obtained closest in the sky to our observations, which were made when the asteroid was at Ecliptic coordinates (86;-5). The lightcurve obtained in 1954 by Binnendijk (83;-4) is shown in Taylor (1973), and the one obtained ten days after our observations at (84;-5) is given in McCheyne et al. (1985). The latter lightcurve was used primarily to investigate color variations of Vesta, and is further discussed in Sec. V. Using our pole and the lightcurve data given in Taylor et al. (1985) we have derived a slightly different sidereal period of 0.2225887 (± 0.0000001) day, compared to their 0.2225889 (± 0.0000002) day, or to Magnusson's 0.22258849 (± 0.00000005) day. Projecting the 1954 lightcurve forward with our pole and the average between Taylor's and our sidereal period for the same data set of 0.2225888 days resulted in the observed minimum occurring some 98° in rotational phase earlier than the one we would have predicted to have occurred during our observations at rotational phase 180° in Figs. 1 and 2. Thus the observed lightcurve minimum appears to have occurred when the maximum cross-sectional area (as seen by speckle interferometry) was viewed by the Earth. (For Taylor's or Magnusson's pole and period, the minimum would have occurred 91° or 122° earlier, respectively, in the projection of the lightcurve.)

The next step, then, was to produce a theoretical lightcurve with the effects of the spots taken into account. Initially we simply identified a few features visible particularly in the first four images, since the second four seemed to show less structure. Arbitrarily, we created circular spots of radius 14° , corresponding to the

radius of the effective resolution limit, centered at the locations of the features A-F, assigning dark regions albedos of 0 (equivalent to the limiting case of completely dark shadows), relative to the surrounding material of albedo 1, and bright regions relative albedos of 2. Since the features hardly appeared as circles it was anticipated that the theoretical lightcurves for the triaxial ellipsoid with spots would not match the observed ones without extensive modification and distortion of the spots. Furthermore, it seemed unlikely that even a remotely reasonable match could be obtained, since the basic triaxial ellipsoid shape found through the power spectrum analysis would yield two maxima and two minima per 5hr period, contrary to every lightcurve obtained.

Nevertheless, we proceeded to construct a theoretical lightcurve for the 1954 geometry, with the spots modulating the normal triaxial ellipsoid lightcurve. To our surprise, only a change of the relative albedo from 2 to 1.2 assigned to the spot at feature A resulted in a near perfect match in amplitude, rotational phase, and shape between our predicted lightcurve projected to 1954 and the observed one. Fig. 9 shows the observed lightcurve (plusses), the predicted lightcurve without spots (small dashed sinusoidal line), the predicted lightcurve with the effect of the spots included (solid line), and the products $\pi\alpha\beta$ (open circles) obtained from the measurements shown in Fig. 1, and shown here to depict the rotational phases of our measurements. These open circles show large scatter because of the effect of the spots on the power spectra of the assumed featureless ellipse, but notice that they scatter about the dashed line of the triaxial ellipsoid rather than the observed or calculated lightcurve.

An additional bright spot is required to match the lightcurve over longitudes that were not visible during our observations. This inferred feature G is placed at longitude 10° , latitude -50° , and also is given a radius of 14° and a relative albedo of 2. If this spot were not included in the analysis, the resulting lightcurve would be that shown in Fig. 9 as the longer dashed line departing from the solid line between 270° and 80° .

Not only does our model match the 1954 lightcurve, but it also produces equally good matches for every other low solar phase angle ($\leq 10^\circ$) lightcurve. Departures of up to 0.02 mag occur for lightcurves obtained at phase angles greater than about 10° , indicating a slight lightcurve amplitude and shape dependency on solar phase

angle, in the sense of increasing amplitude with phase.

As stated above, inspection of the images does not lead to the impression of circular spots. Indeed, the model of circular spots and relative albedos is only a simplification of what appears to be a complicated pattern of dark and bright areas. Because of the enhanced bright central region on all the images, and because the accurate apparent integrated magnitude of each image is unknown it is not possible to obtain absolute albedos for given regions. And neither is it possible to appeal to lightcurves for further information about the actual brightnesses of the features. For instance, doubling the area of the dark spots (by increasing their radii from 14 to 20°) and increasing their relative albedos from 0.0 to 0.5 results in exactly the same lightcurves to within the width of the lines in Fig. 9. However, some of the dark spots appear to be as dark as the sky (regions outside the asteroid) on some frames. Taylor et al. (1986) have determined that two 0.13 relative albedo spots on the asteroid Herculina can explain its lightcurve of up to nearly 0.2 mag amplitude; Vesta appears to have areas as dark if not darker.

V. Discussion and Summary

In the TRIAD file the polarimetrically determined diameter of 530km is closer than the radiometrically determined 579km to a mean diameter $(\alpha\beta)^{1/2}$ from speckle interferometry of 515 to 532km , corresponding to minimum and maximum projected area at a sub-Earth latitude of 30° . Since the obliquity between Vesta's orbital and rotational pole is 30° , the maximum excursion of the sub-Earth point from Vesta's equator is about 30° . Viewed from directly above its equator, Vesta's apparent mean diameter would vary between 498 and 522km .

The early reconstruction of Vesta by Worden et al. (1977; Worden 1979) from observations made on February 3, 1977, with the Kitt peak 4m telescope are remarkably consistent with the results obtained here. According to our pole, their observations were made when the Earth was at a sub-latitude of $+18^\circ$, and thus we can predict a variation in the ratio of major to minor axes of 1.11 to 1.24 , and a variation of position angle of the long axis of $\pm 7^\circ$ about a mean of 24° from the east-west direction. They obtained a major to minor axes ratio of 1.19 ± 0.02 and a position angle of $16 \pm 4^\circ$ relative to east-west. They determined a mean diameter of $550 \pm 23\text{km}$ for the date, whereas we predict between 506 and 526km . From ob-

NO-A189 295

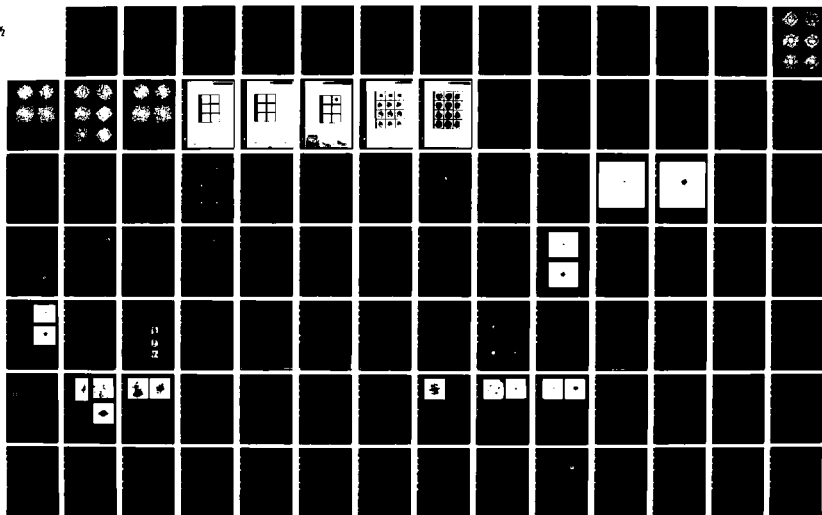
INVESTIGATIONS OF HIGH RESOLUTION IMAGING THROUGH THE
EARTH'S ATMOSPHERE (U) STEWARD OBSERVATORY TUCSON ARIZ
E K HEGE 15 MAR 87 AFGL-TR-87-0097 F19628-84-K-0035

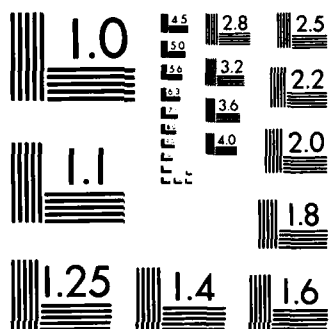
3/4

UNCLASSIFIED

F/G 20/6

NL





MICROCOPY RESOLUTION TEST CHART
NATIONAL BUREAU OF STANDARDS-1963-A

servations on December 1, 1976, they found a mean diameter of 513 ± 51 km, where we predict between 512 and 530 km for the sub-Earth latitude of 27° on that date.

With the mass of Vesta from Schubart and Matson (1979), we have calculated its density to be 3.62 ± 0.35 gm cm $^{-3}$, in good agreement with their best estimate of 3.3 ± 1.5 . The limiting factor on the accuracy of the density arises from the uncertainty in the mass. Using a V_0 of 3.46 from the TRIAD file we also calculate that the mean albedo at maximum light is $p_v = 0.261 \pm 0.005$, where the uncertainty applies to the range in the mean diameter at maximum light of 532 to 522 km, corresponding to sub-Earth latitudes between 0 and 30° .

Vesta is one of the few asteroids for which evidence exists for polarization variation with rotation (Degewij and Zellner 1978; Degewij et al. 1979; Gradie et al. 1978; Taylor et al. 1985). In fact, polarization measurements fully support the five over the ten hour period. As the polarization workers have noted, the minimum in the polarization occurs at minimum light, which from the model of this paper corresponds to the portion of the lightcurve dominated by dark albedo features. This is consistent with the fact that dark material (and asteroids) shows more negative polarization than brighter material.

Gehrels (1967) and Blanco and Catalano (1979) have shown that Vesta is also slightly bluer near minimum light (by 0.02 and 0.05, respectively, in U-V). However, McCheyne et al. (1985) find the opposite phenomenon, that is, Vesta appears bluer near maximum by 0.05 in B-V, 0.07 in B-K, and 0.06 in J-K. Extrapolating our Fig. 9 by ten days to Fig. 2 of McCheyne et al. we find that our zero rotational phase corresponds coincidentally to their zero rotational phase at 0^h UT on November 27, 1983. McCheyne et al. were unable to explain the discrepancies in color variation with rotation. One possibility that they suggested, that their observations refer to different maximum, is not allowed with the 5hr period. Gehrels obtained his results when the sub-latitude of the Earth was $+25^\circ$, the Blanco and Catalano observations were made at -6° , and McCheyne et al. at $+15^\circ$. Thus the discordant results cannot be attributed to the latitude of the sub-Earth point, since McCheyne et al. observed between the other two. However, since McCheyne et al. did not actually measure the U band flux, perhaps, as they found, the dark material is in fact redder than the average surface at longer wavelengths, but is relatively brighter in U as Gehrels and Blanco and Catalano observed.

Vesta has generally been considered as certainly differentiated and perhaps the parent body of eucrites. The composition of its mottled basaltic surface has been discussed by many, e.g. Gaffey and McCord (1979), Degewij et al. (1979), Gaffey (1983a,1983b), and McChayne et al. (1985). The map offered by Gaffey (1983b) and further elaborated upon by McChayne et al. (1985), consists of two constituents, two brighter and redder regions (or with the 5hr period, one region) composed of diogenite superimposed on the underlying darker eucrite. However, from our results it appears that at least three albedo components may be necessary to explain our maps, with extensive dark areas so dominating one hemisphere that a minimum is observed in the visible lightcurve when the maximum cross-sectional area is viewed. Vesta appears to be so much more Moon-like than a featureless triaxial ellipsoid that further high resolution imaging is very appealing and exciting.

References

- Blanco, L., and S. Catalano (1979). UVB photometry of Vesta. *Icarus* **40**, 359-363.
- Degewij, J., and B. Zellner (1978). Asteroid surface variegation. *Lunar Sci.* **9**, 235-237.
- Degewij, J., E. F. Tedesco, and B. Zellner (1979). Albedo and color contrasts on asteroid surfaces. *Icarus* **40**, 364-374.
- Drummond, J. D., W. J. Cocke, E. K. Hege, P. A. Strittmatter, and J. V. Lambert (1985a). Speckle interferometry of asteroids. I. 433 Eros. *Icarus* **61**, 132-151.
- Drummond, J. D., E. K. Hege, W. J. Cocke, J. D. Freeman, J. C. Christou, and R. P. Binzel (1985b). Speckle interferometry of asteroids. II. 532 Herculina. *Icarus* **61**, 232-240.
- Drummond, J. D. and E. K. Hege (1986). Speckle interferometry of asteroids. III. 511 Davida and its photometry. *Icarus* **67**, 251-263.
- Fienup, J. (1978). Reconstruction of an object from the modulus of its Fourier transform. *Opt. Lett.* **3**, 27-31.
- Gaffey, M. J. (1983a). Observational determination of asteroidal surface heterogeneity: Implications of (4) Vesta and (8) Flora for the meteorites. *B.A.A.S.* **15**, 826.
- Gaffey, M. J. (1983b). First 'map' of Vesta. *Sky and Tel.* **66**, 502.
- Gaffey, M. J. and T. B. McCord (1979). Mineralogical and petrological characterizations of asteroid surface materials. In *Asteroids* (T. Gehrels, Ed.) 688-723, University of Arizona Press, Tucson.
- Gehrels, T. (1967). Minor planets. I. The rotation of Vesta. *Astron. J.* **72**, 929-938.
- Gradie, J., E. Tedesco, and B. Zellner (1978). Rotational variants in the optical polarization and reflection spectrum of Vesta. *B.A.A.S.* **10**, 595.

Hardy, J.W., J.E. Lefebvre, and C.L. Koliopoulos (1977). Real-time atmospheric compensation. *J. Opt. Soc. Am.* **67**, 360-369.

Knox, K.T. (1976) Image retrieval from astronomical speckle patterns. *J. Opt. Soc. Am.* **66**, 1236-1239.

Knox, K.T. and B.J. Thompson (1974). Recovery of images from atmospherically degraded short-exposure photographs. *Astrophys. J.* **193**, L45-L48.

Magnusson, P. (1986). Distribution of spin axes and senses of rotation for large main belt asteroids. *Icarus* **68**, 1-39.

McAlister, H.A. and W.I. Hartkopf (1984). Catalog of interferometric measurements of binary stars. *CHARA Contr.* **1**, 1-74.

McCheyne, R.S., N. Eaton, and A.J. Meadows (1985). Visible and near-infrared lightcurves of eight asteroids. *Icarus* **61**, 443-460.

Nisenson, P. and C. Papaliolios (1983). Effects of photon noise on speckle image reconstruction with the Knox-Thompson algorithm. *Opt. Comm.* **47**, 91-96.

Nisenson, P., R.V. Stachnik, M. Karovska, and R. Noyes (1985). A new optical source associated with T Tauri. *Astrophys. J.* **297**, L17-L20.

Papaliolios, C., P. Nisenson, and S. Ebstein (1985). Speckle imaging with the PAPA detector. *Appl. Opt.* **24**, 287-292.

Schubart, J. and D.L. Matson (1979). Masses and densities of asteroids. In *Asteroids* (T. Gehrels, Ed.) 84-97. University of Arizona Press, Tucson.

Taylor, R.C. (1973). Minor planets. XIV. Asteroid (4) Vesta. *Astron. J.* **78**, 1131-1139.

Taylor, R.C., S. Tapia, E.F. Tedesco (1985). The rotational period and pole of asteroid 4 Vesta. *Icarus* **62**, 298-304.

Worden, S.P., M.K. Stein, G.D. Schmidt, J.R.P. Angel (1977). The angular diameter of Vesta from speckle interferometry. *Icarus* **32**, 450-457.

Worden, S.P. (1979). Interferometric determinations of asteroid diameters. In *Asteroids* (T. Gehrels, Ed.) 119-131. University of Arizona Press, Tucson.

Acknowledgments

We thank C. Papaliolios, P. Nisenson, and S. Ebstein for offering the use of their PAPA detector for this project, and for their expert assistance during and after the observations. This work is supported through NASA grant NAGW-867.

Table I
Aspect Data for
Speckle Observations

Date	R.A.	Dec.	λ	β
Nov. 16,17 1983	5 ^h 45 ^m	+18°	86°	-5°
Solar Phase Angle 12.3°	Distance from Earth 1.690 AU		Distance from Sun 2.572 AU	

Table II

Triaxial Solution

$$2a = 584 \pm 16km$$

$$2b = 531 \pm 11km$$

$$2c = 467 \pm 12km$$

$$\psi_0 = -38^\circ \pm 7^\circ$$

$$\theta = +16^\circ \pm 9^\circ$$

$$\rho_1 = 137^\circ \pm 1^\circ$$

$$\rho_2 = 317^\circ \pm 1^\circ$$

Pole₁

$$R.A. = 21^h00^m; Dec. = +41^\circ$$

$$\lambda = 336^\circ; \beta = +55^\circ$$

Radius of error circle around poles : 4 °

Pole₂

$$R.A. = 11^h52^m; Dec. = -56^\circ$$

$$\lambda = 209^\circ; \beta = -50^\circ$$

Normalized correlation matrix

	2a	2b	2c	ψ_0	θ	ρ
2a	-					
2b	-0.49	-				
2c	0.47	-0.55	-			
ψ_0	0.03	-0.21	0.18	-		
θ	-0.69	0.74	-0.81	-0.19	-	
ρ	0.03	-0.13	0.24	0.04	-0.23	-

Figure Captions

Fig. 1. Measured major (*) and minor (o) axes of Vesta, the model's (from Table II) major diameters for the projected asteroid and for the terminator (solid lines), and the model's minor diameters (dashed lines) for the projected asteroid and for the terminator plotted against rotational phase. Minimum cross-sectional area (minimum light) occurs at 0 and 180°. Rotational phase 0° corresponds to 7.674 UT, Nov. 16, 1983, and rotational phase 360° is 13.016 UT. The first and third points (with tick marks) are folded back from Nov. 17 using a period of 5hr and 20.5min.

Fig. 2. Same as Fig. 1, but for the position angle (γ) of the major axis relative to the position angle at maximum elongation (and light).

Fig. 3a - 3j. Deconvolved power spectra of the ten observations of Vesta shown with contour wraps at intervals of 2% of the peak power. Note in particular the artifacts along the horizontal and vertical axes.

Fig. 4a - 4j. Same as Fig. 3 but corrected for detector artifacts and seeing mismatches.

Fig. 5. Three different reconstructed images of the first Vesta observation (using 200 Fienup iterations in each case). In this figure, and in Figs. 6 and 7, true celestial North is up and East is to the left.

5a: The power spectrum of Vesta with detector artifacts, but corrected for seeing mismatches by recapping with the average power spectrum.

5b: The power spectrum corrected for detector artifacts, and corrected for seeing mismatches using the iterative method described in the text.

5c: The power spectrum corrected for detector artifacts, and corrected for seeing mismatches by recapping with the average power spectrum. This method was the one adopted for all observations.

Fig. 6. Four different reconstructed images of Vesta after 0, 50, 100, and 200 Fienup iterations (6a - 6d, respectively). Notice that the image of Vesta becomes more realistically circular after using Fienup iterations to correct possible initial

phase errors.

Fig. 7. Power spectra, Knox-Thompson phases, and reconstructed images of the double star SAO093840 (left column, headed by the characteristic power spectrum fringe pattern of a double star) and the first Vesta observation (right column). The power spectra are shown with contour wraps at 2% of the peak power, and the phases are shown with contour wraps of 2π .

Fig. 8. Reconstructed images of Vesta on Nov. 16, 1983. The top row shows the actual images; the middle row shows lines of longitude and latitude at 30° intervals, the sub-Earth point (plus at center), and the sub-Sun point (off-center dot) superimposed on the images, where the individual pixels have been smoothed; the third row shows the same as the second row, but superimposed on contours at 15% intervals, and, in addition, have features A-F circled right to left, (see text). True North is 36° to the right (West) of the vertical, which is the direction of astero-centric North.

Fig. 9. Model lightcurves of Vesta. Shown is the 1954 lightcurve (—) obtained closest to the position of the asteroid when we observed. The short dashed line is the lightcurve for our model without albedo features, the solid line includes the six features identified in Fig. 8 as well as the inferred spot not visible during our observations. The longer dashed line departing from the solid line is the predicted lightcurve without the inferred feature located on the other side of the asteroid during our observations. Open circles are the products $\pi\alpha\beta$ taken from Fig. 1 plotted at the rotational phases of our observations projected back to 1954 with the sidereal period and pole from our analysis.

4 VESTA

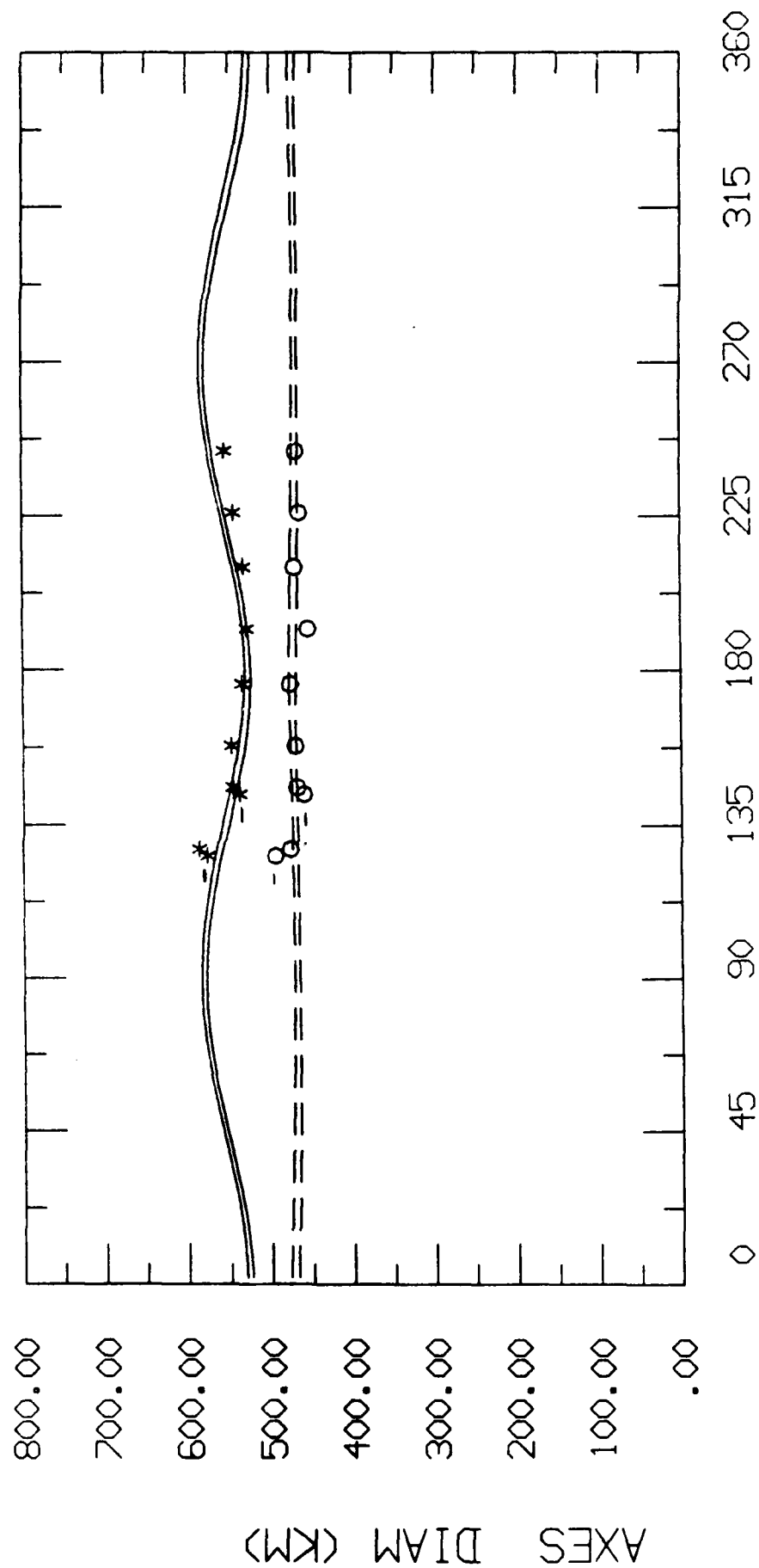
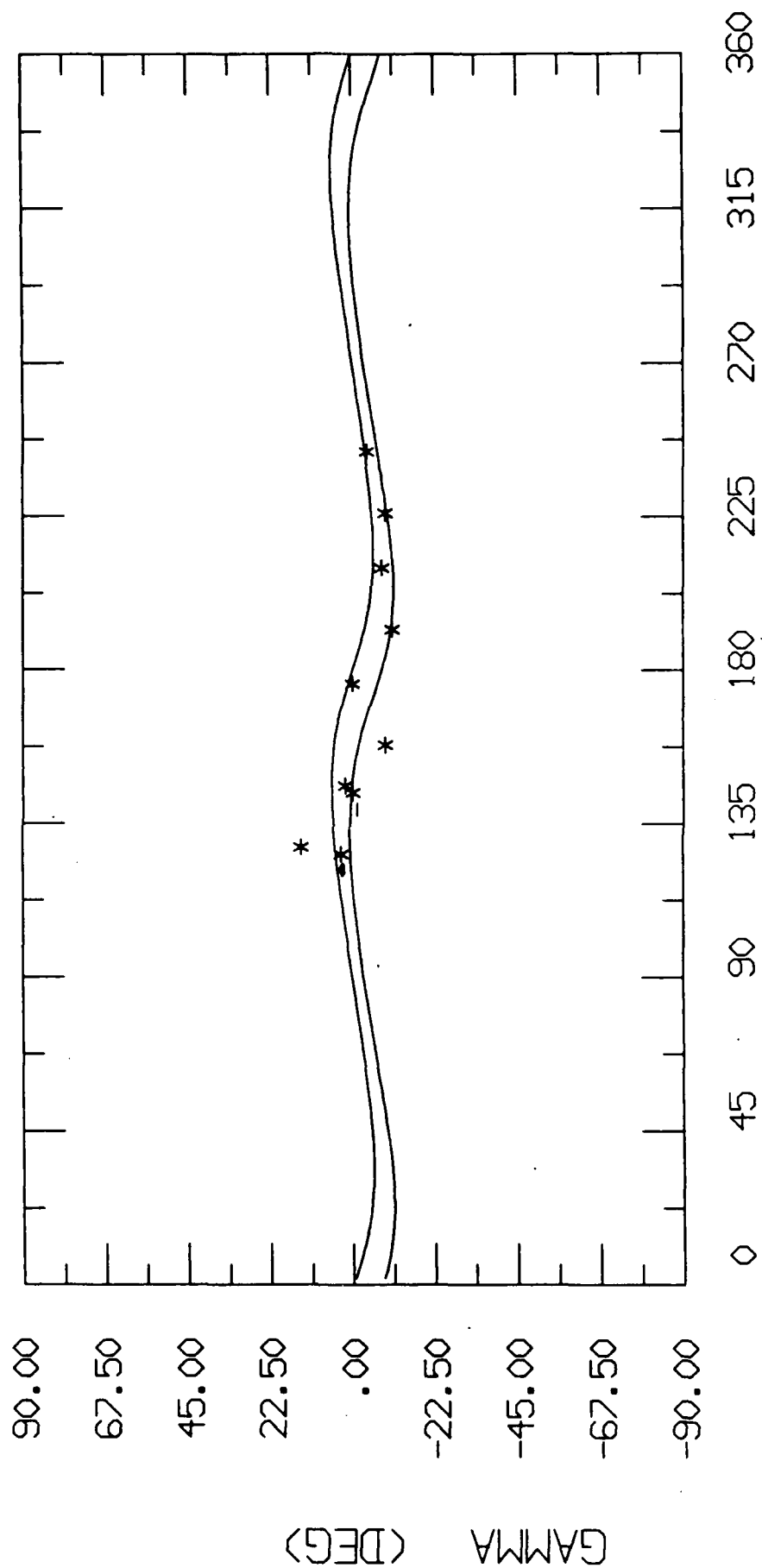


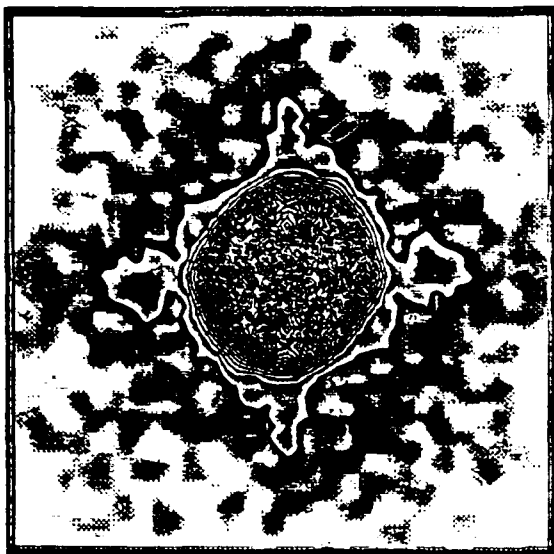
FIGURE 1

4 VESTA

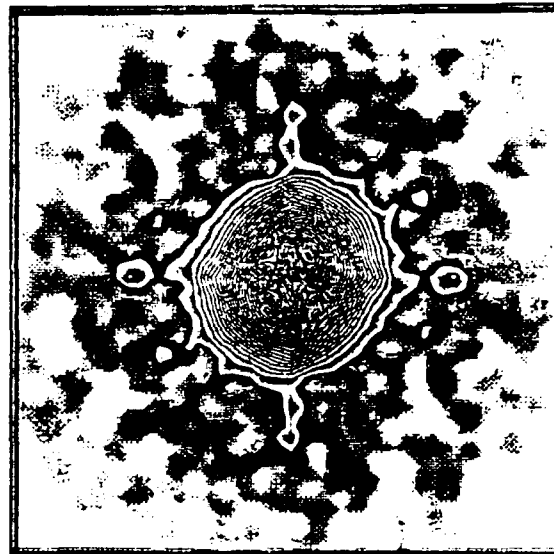


ROTATIONAL PHASE

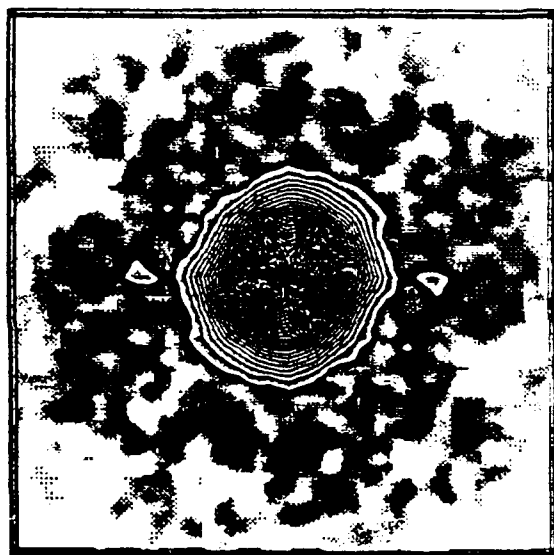
FIGURE 2



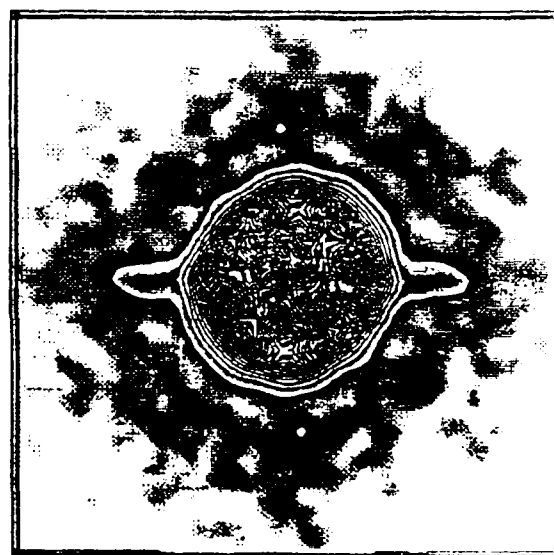
a



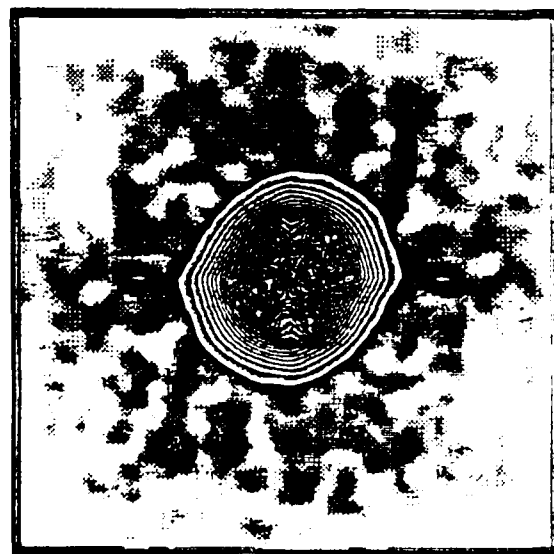
b



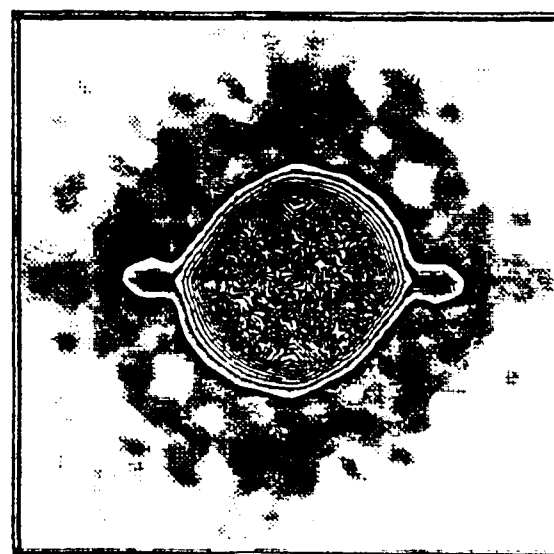
c



d

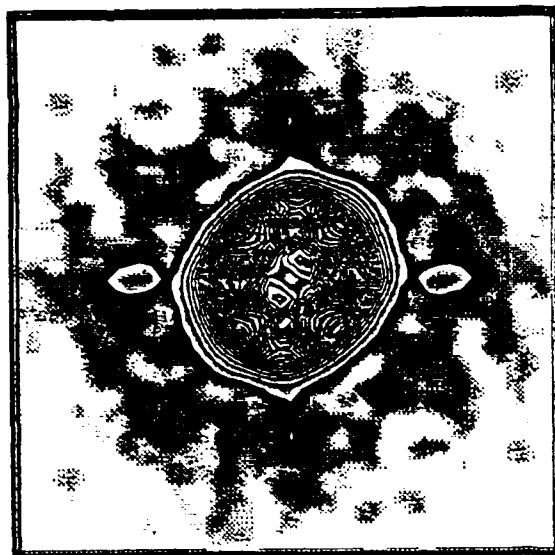


e

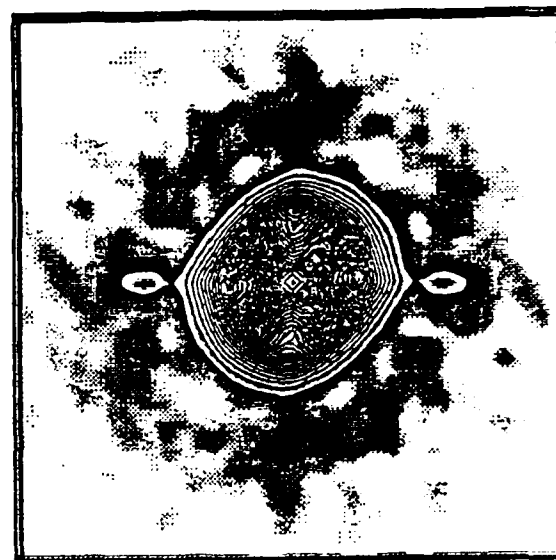


f

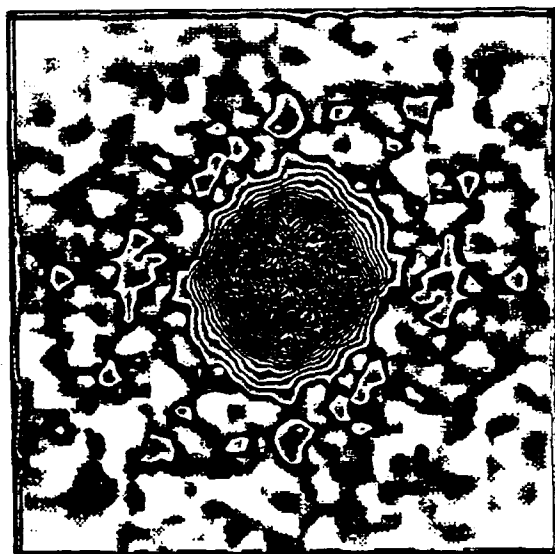
FIGURE 3



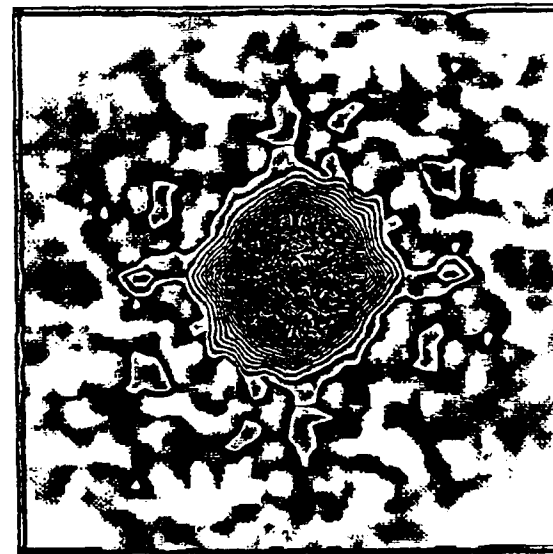
g



h

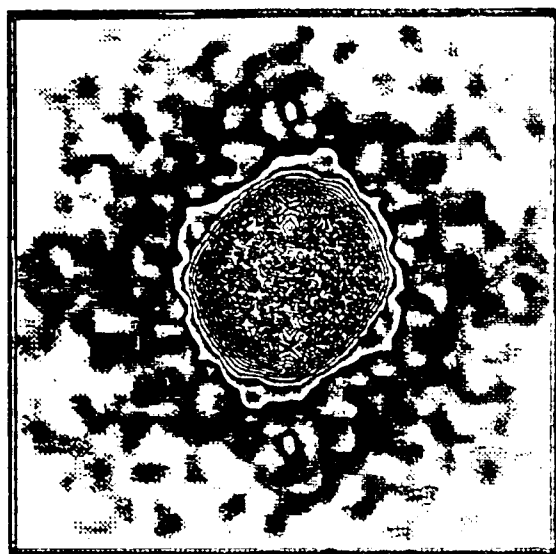


i

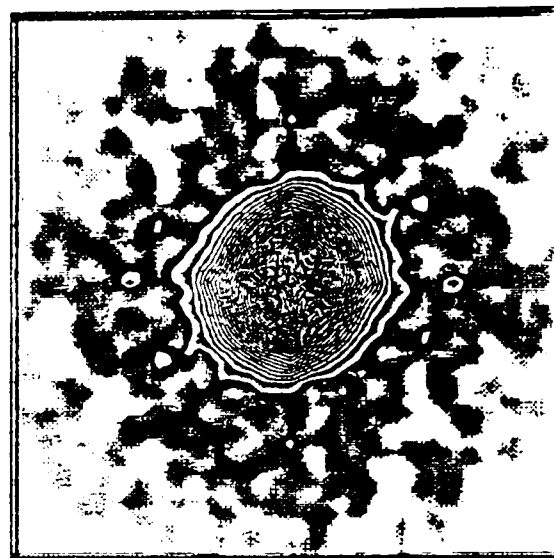


j

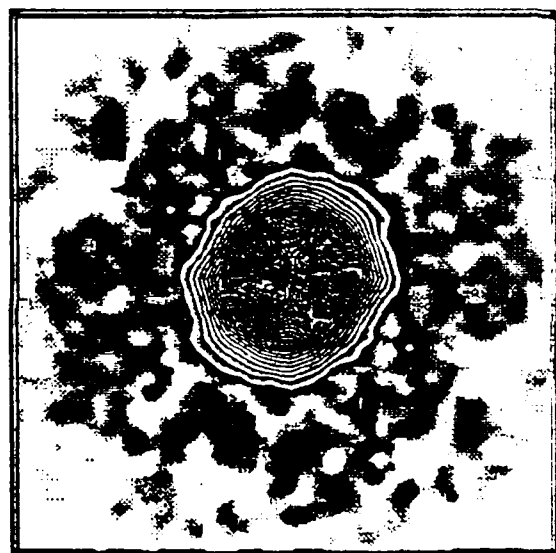
FIGURE 3 (Cont)



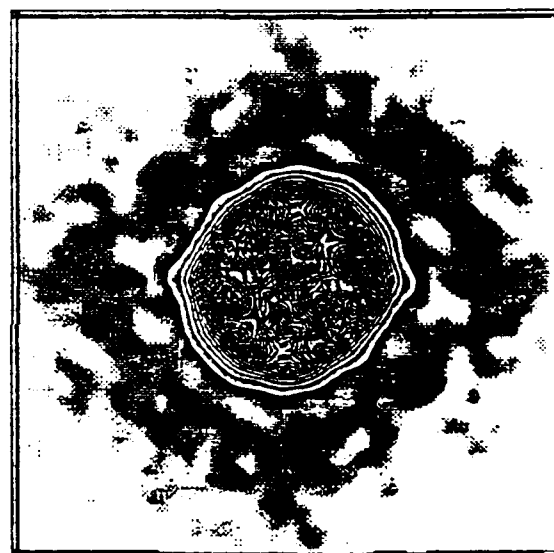
a



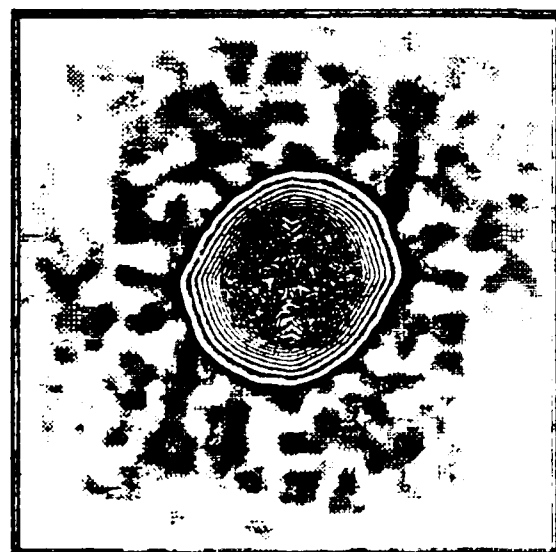
b



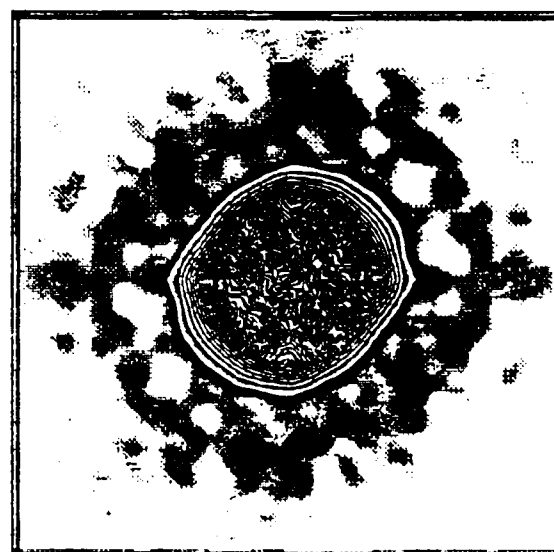
c



d



e

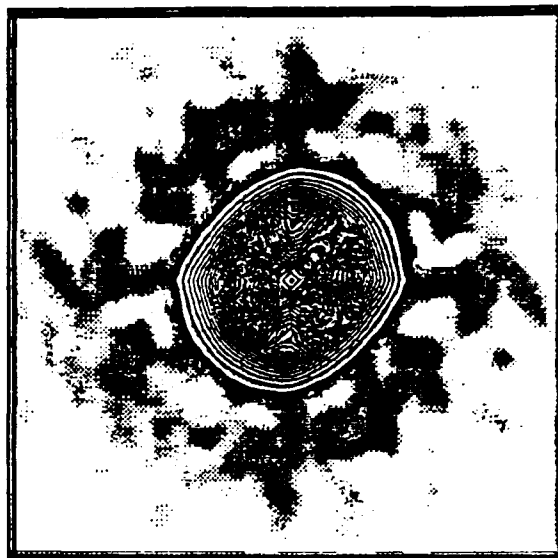


f

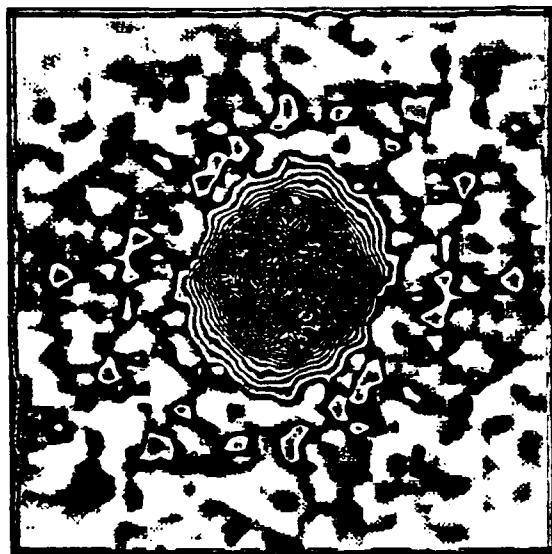
FIGURE 4



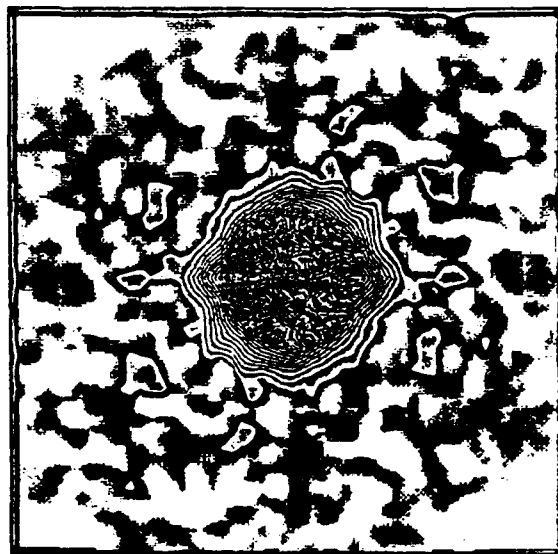
g



h



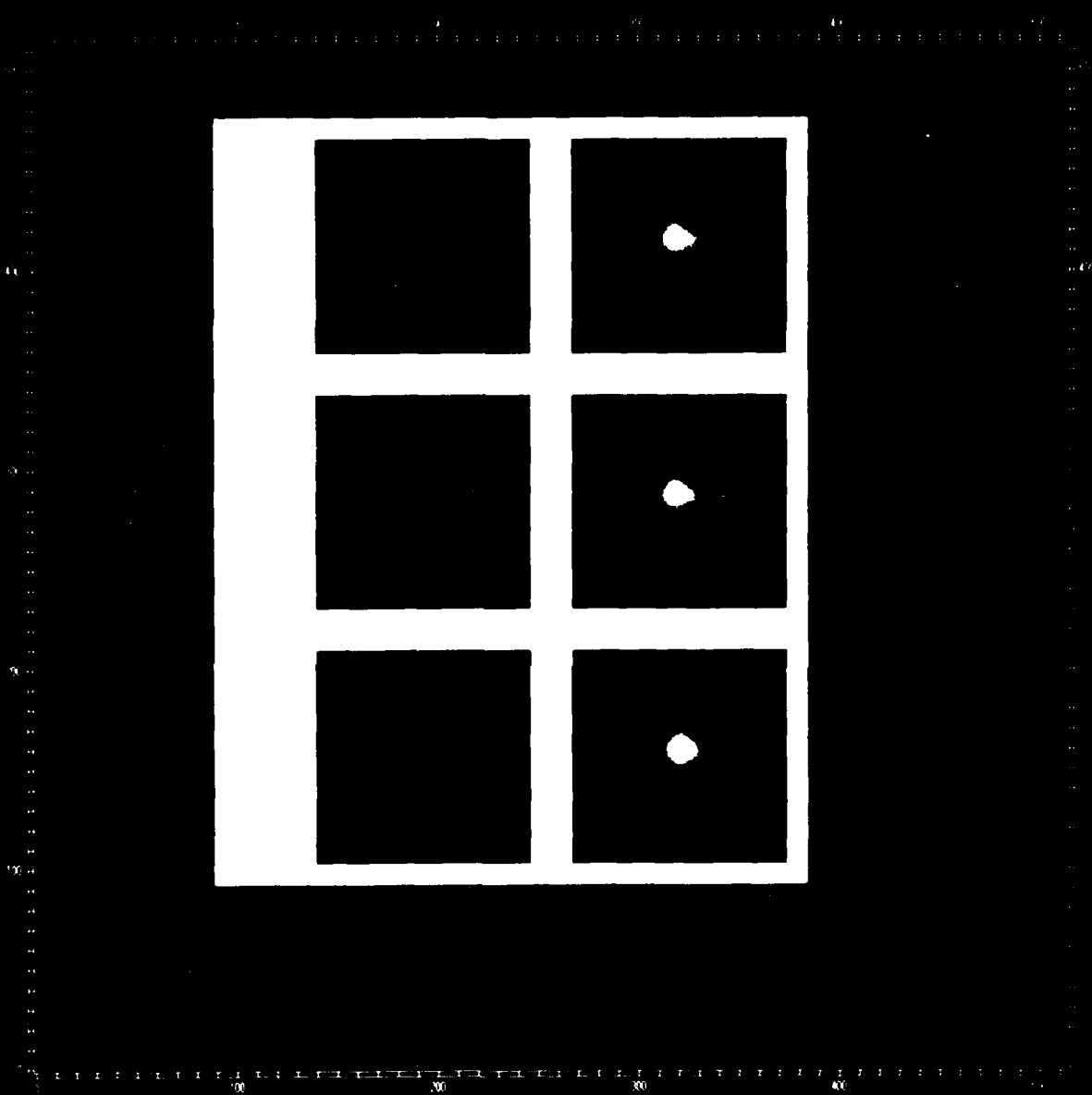
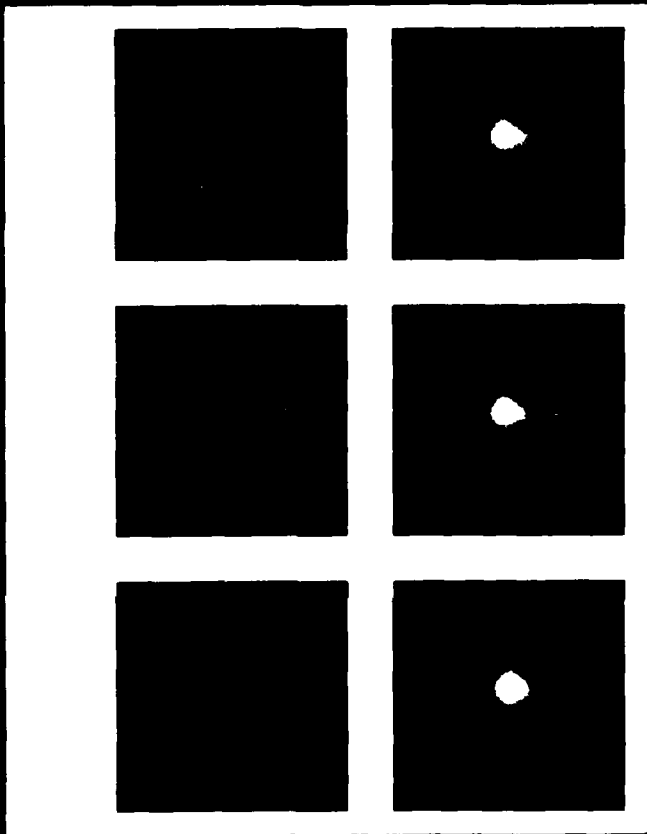
i



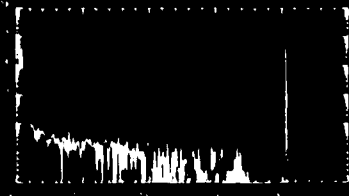
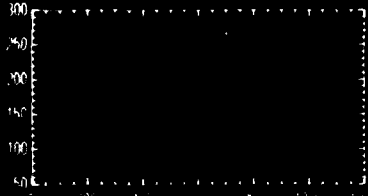
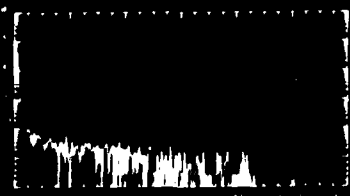
j

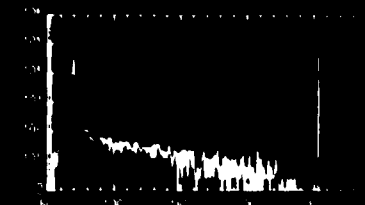
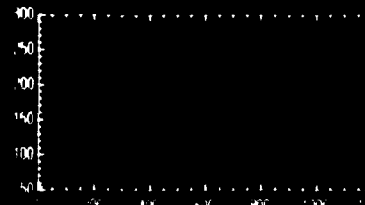
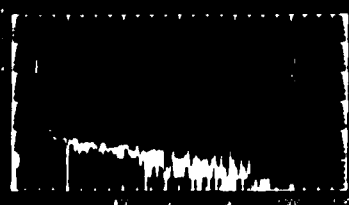
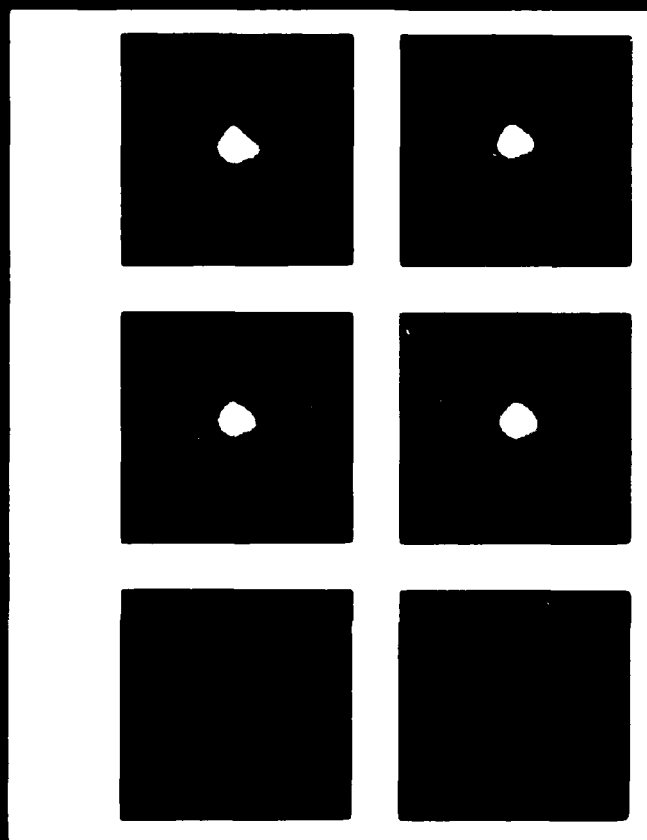
FIGURE 4 (Cont)

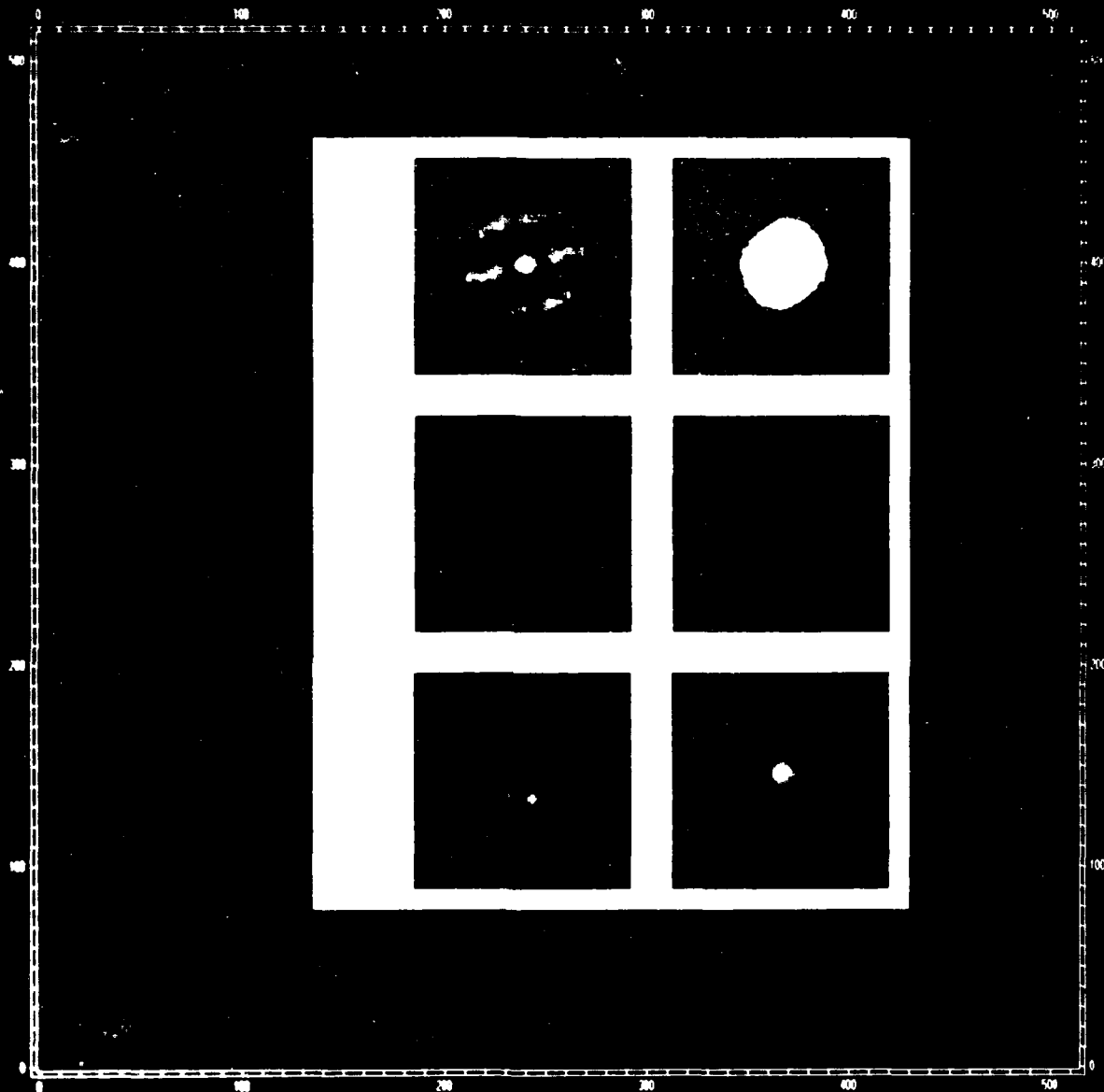
[Redacted]



National
Optical
Astronomy
Observatories

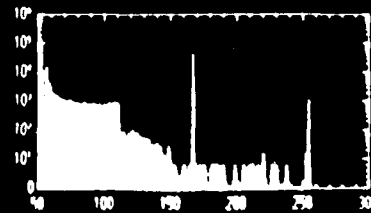
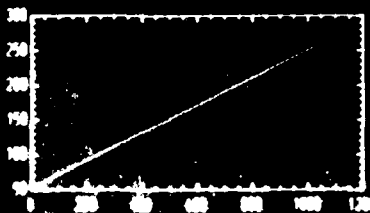






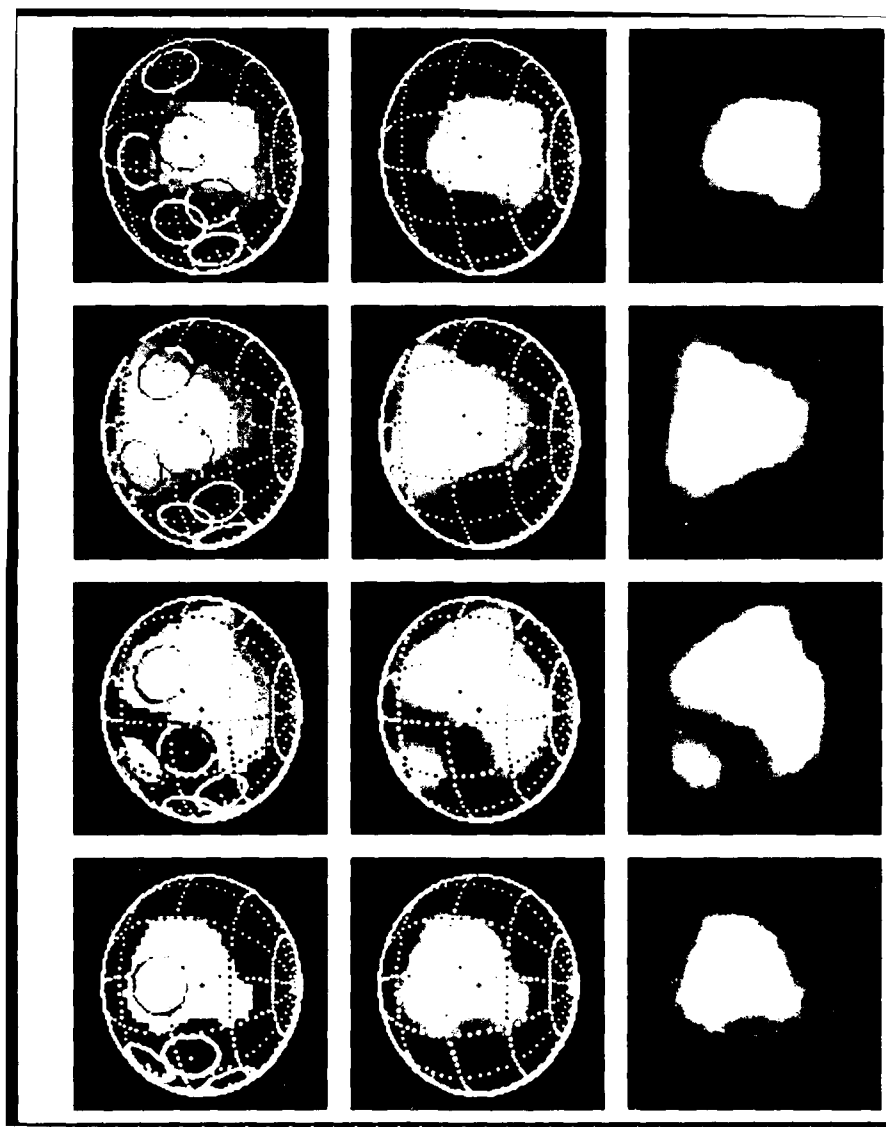
vesta083.1.snap.jpg

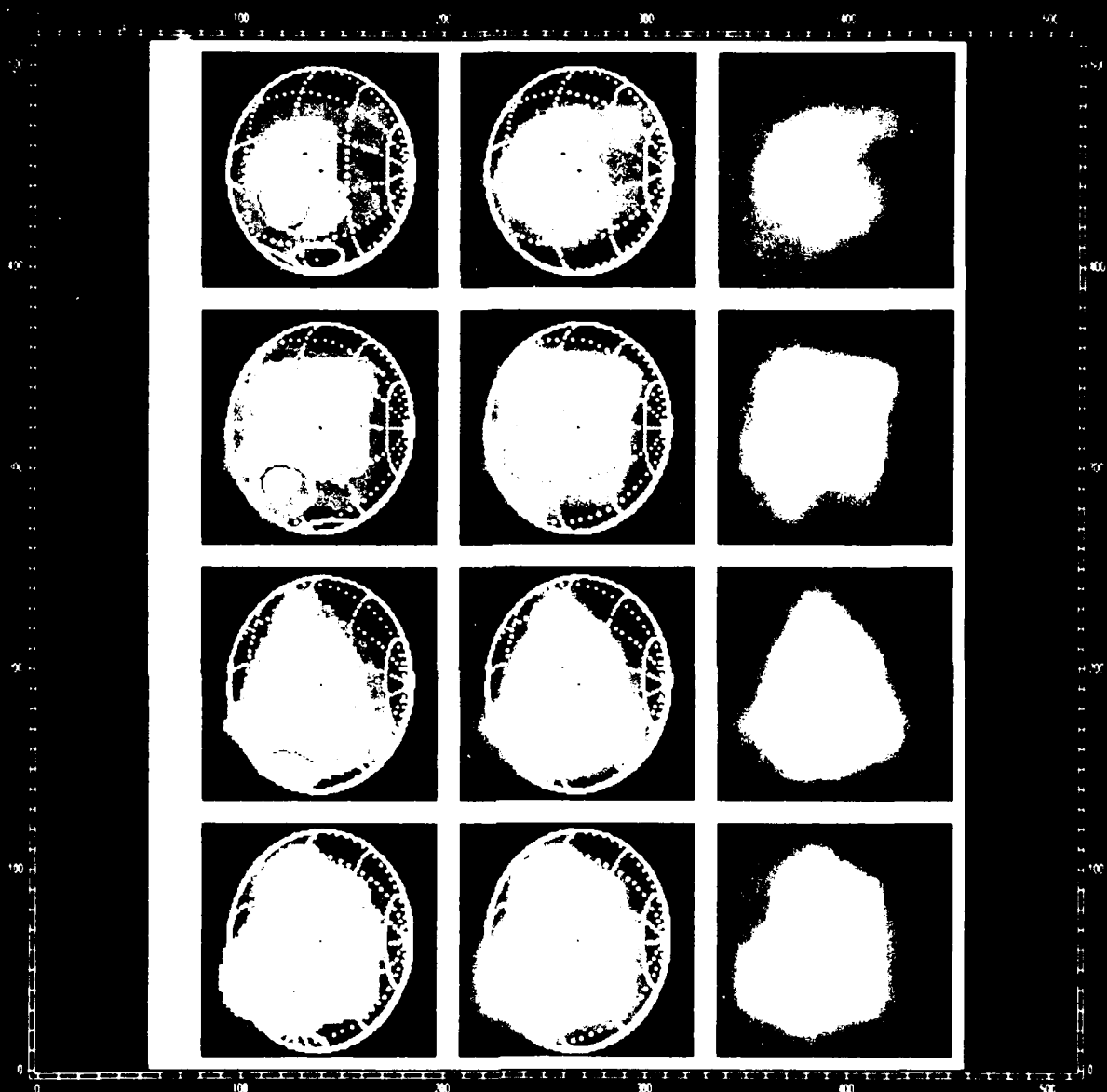
ncols=512 rows=512 zmin=8.00 zmax=1020.00 xc=256.50 yc=256.50 x_rep=4.00 y_rep=4.00



IRAO/IRAF V2.3 V9.0 draco Thu 17:27:25 11-Sep 86

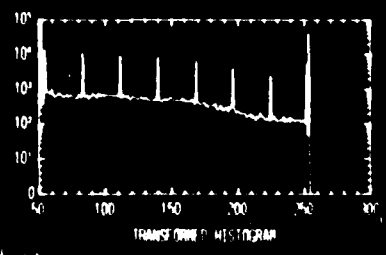
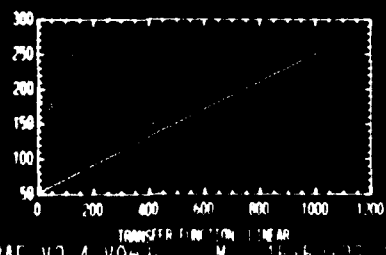
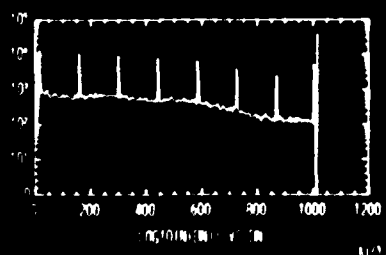
6167-017





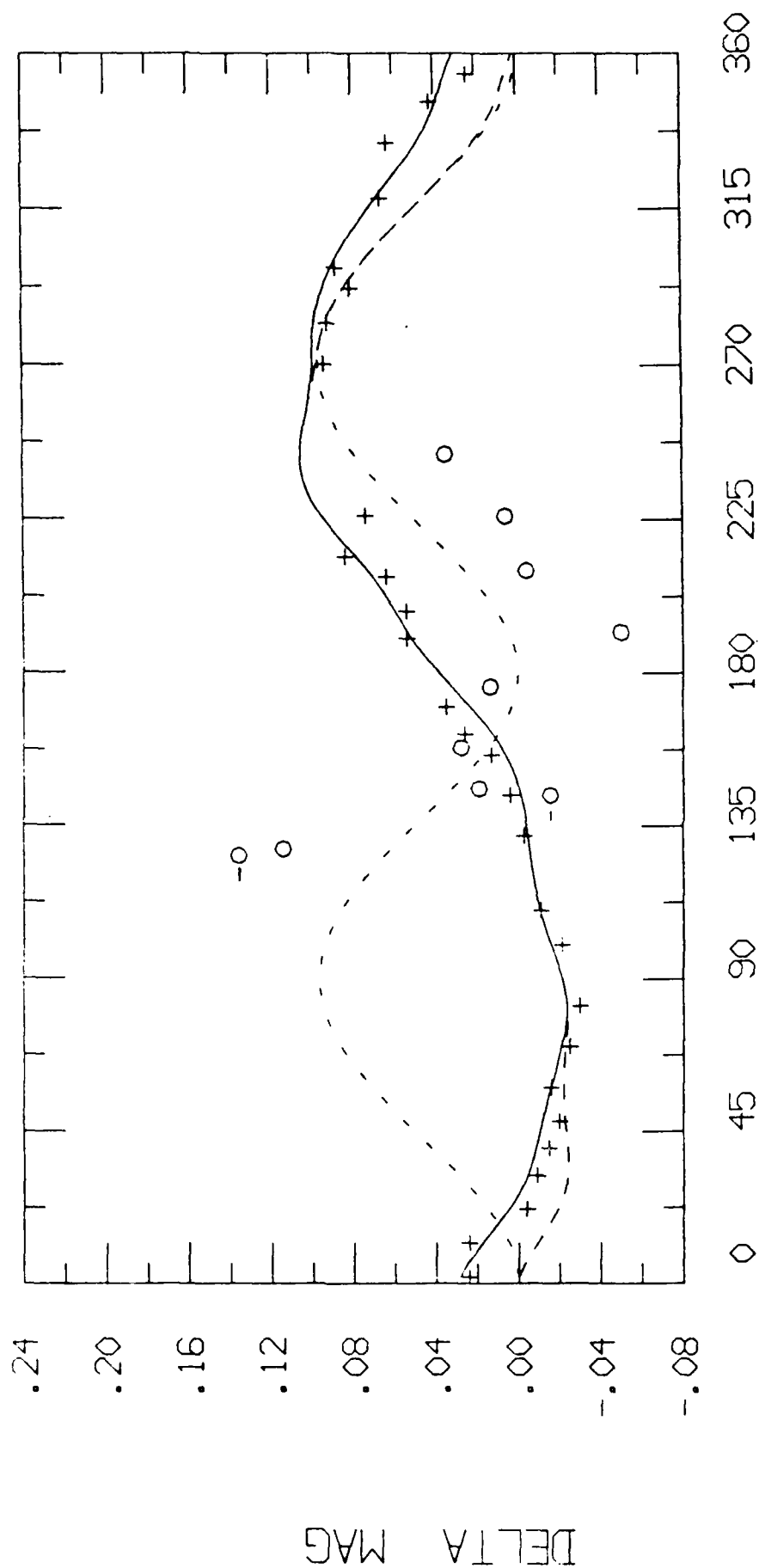
National
Optical
Astronomy
Observatories

v2.snap.imh:
ncols=512 nrow=512 zmin=0.00 zmax=1016.00 xc=256.50 yc=256.50 xrep 4.00 yrep 4.00



NRAO/IRAF V2.4 VQ=1.1 M=15.0/12.0 0.1

4 VESTA



ROTATIONAL PHASE

FIGURE 9

Statistical Analysis of the Weighted Shift and Add Image Reconstruction Technique

J.D.Freeman, E.Ribak, J.C.Christou^{**}, E.K.Hege⁺

Steward Observatory, University of Arizona, Tucson, Az 85721

Abstract

The Weighted Shift-and-Add algorithm (WSA) is an image reconstruction technique whereby diffraction limited images of astronomical objects are obtained from speckle interferometric data.

This paper attempts to put the understanding of WSA on a firm mathematical basis by a statistical analysis of the algorithm. The approach follows that of the Hunt, Fright, and Bates study carried out for the Simple Shift-and-Add algorithm. The expected WSA profile is found to be linearly dependent on the square modulus complex coherence function of a speckle pattern. The last section of this paper contains a discussion of how the statistical analysis compares to the results obtained with our new Weighted Shift-and-Add procedures using cross-correlation (WSA/XC) and deconvolution (WSA/WD).

Introduction

WSA is an extension of the Shift-and-Add image reconstruction technique (SAA) first proposed by Bates and Cady¹ and by Lynds, Worden and Harvey². SAA relocates the maximum intensity pixel in a specklegram to the frame center after which the frame is co-added to other shifted specklegrams to obtain the SAA image. This paper discusses a statistical model for both the weighted deconvolution (WSA/WD) and the cross-correlation (WSA/XC) variants of WSA as presented in Christou et al.³ WSA/XC correlates each specklegram with a set of delta functions representing the position and intensity of each point determined to be a local maximum. The WSA/WD result is obtained by deconvolving the WSA/XC result by the average power spectrum of the impulse distribution corresponding to the local maximum positions.

Our WSA statistical analysis is an extension of the analysis of the Simple Shift-and-Add algorithm undertaken by Hunt, Fright and Bates⁴. They found the expected SAA intensity profile to be

$$S(x) = 2\langle I \rangle + R_S(x) (I_m - \langle I \rangle) / \langle I \rangle^2 - I_m \quad (1)$$

where $\langle I \rangle$ is the average intensity of the specklegram and where I_m is the maximum intensity found in the frame. $R_S(x)$ is a real function of the complex coherence of the speckles and is independent of individual speckles under the assumption that the speckle process remains constant with time. $R_S(x)$ is related to the complex coherence function $u_A(x)$ by the expression⁵

$$R_S(x) = \langle I \rangle^2 [1 + |u_A(x)|^2] \quad (2)$$

where

$$0 \leq |u_A(x)| \leq 1$$

If eq. (2) is substituted into eq. (1) the result is

$$S(x) = (I - \langle I \rangle) |u_A(x)|^2 + \langle I \rangle \quad (3)$$

Since $|u_A(x)|^2$ is the only spatially variant term in eq. (3), any understanding of the results of the SAA analysis (and hence the WSA analysis, as will be shown) is based on a knowledge of the structure of the complex coherence function $u_A(x)$.

* Observations reported here were obtained at Kitt Peak National Observatory^{††}

** Visiting Astronomer from the Department of Astronomy, New Mexico State University, Las Cruces, NM 88003.

+ Visiting Astronomer, Kitt Peak National Observatory^{††}.

†† Kitt Peak National Observatory is a division of the National Optical Astronomy Observatories, operated by the Association of Universities for Research in Astronomy, Inc., under contract to the National Science Foundation.

Goodman⁵ uses the complex coherence function extensively. One expression that he derives is the conditional probability density

$$p(I_2|I_1) = \frac{\exp \left[-\frac{|u_A|^2}{\langle I \rangle (1 - |u_A|^2)} I_1 + I_2 \right]}{\langle I \rangle (1 - |u_A|^2)} I_0 \left(\frac{2\sqrt{I_1 I_2} |u_A|}{\langle I \rangle (1 - |u_A|^2)} \right) \quad (4)$$

where $I_0(x)$ is the modified Bessel function of the first kind, zeroth order and where I_1 and I_2 are two intensities separated by a distance x in a speckle pattern. Through the use of this probability density we are able to obtain estimates of the complex coherence function.

Observations

Using astronomical speckle interferometric data of the unresolved star Gamma Orionis taken at the KPNO 3.8m telescope at wavelength 650 nm, it is easy to build up histograms which are equivalent to plots of eq.(4) at constant radii. Assuming that the speckle intensity distribution can be approximated by a normal distribution, only those portions of the specklegram which are bounded by the radius corresponding to the FWHM of the mean seeing disk are used. For example, to determine the probability curve at a radius equal to one, the intensity of each pixel is divided into the value of the intensity of the immediately adjoining pixels. This quotient is then multiplied by one hundred and the appropriate location in the probability histogram is incremented. Approximately 100 frames are used in computing these curves. The frames are centered so that the same region of the speckle distribution is used each time. An estimate for $|u_A(x)|^2$ is then determined by finding that value which minimizes the summed squared difference between the model curve and the data. This procedure is repeated for each radius up to five pixels. The results of these measurements are seen in Table 1. The probability curves and the best model fits are seen in Figs. 1(a)-(d). The same curves calculated again using 2000 frames of data produce identical results. This shows that increasing the number of specklegrams used to compute the probability curves does not increase the signal to noise ratio for the data set digitized with our system.

Table 1. Comparison of Measurements

PIXEL	$ u_A(x) ^2$	WSA/WD	THEORETICAL AIRY DISK
1	.899	.892	.892
2	.612	.590	.624
3	.280	.304	.322
4	.250	.096	.101
5	~0	.017	.007

The obvious disagreement between the model and the calculated curves, seen in Figs. 1(a)-(d), is due largely to quantization effects of 8-bit digitization. This causes the data to look like it is composed of a large number of spikes. Especially prominent are the spikes located at 50, 100, 150, and 200. As an example, the spike at the division ratio 100 is caused by the very large number of pixels of intensity 1 divided by other pixels of intensity 1. Notice that one of these artifacts is centered at zero. This is a particularly limiting departure from the model as conditional probability curves of low $|u_A(x)|^2$ are distinguished from each other almost solely by the nature of the model at these low intensity ratios.

Applications to Weighted Shift-and-Add

As previously mentioned, WSA/XC differs from SAA in that WSA/XC weights and shifts on a number of points in the specklegram, ideally all of the set of local maxima $\{I_m\}$. If we were to assume that WSA/XC shifts on pixels of all intensities, that is to say if the intensity distribution of speckle maxima obeys the distribution

$$P(I_m) = (1/\langle I_m \rangle) \exp(-I_m/\langle I \rangle) \quad (5)$$

where $0 < I_m < \infty$ and where $\langle I \rangle$ is the average value of the specklegram, then the resulting WSA/XC profile $W(x)$ would equal:

$$W(x) = E_m [S(x)] \quad (6)$$

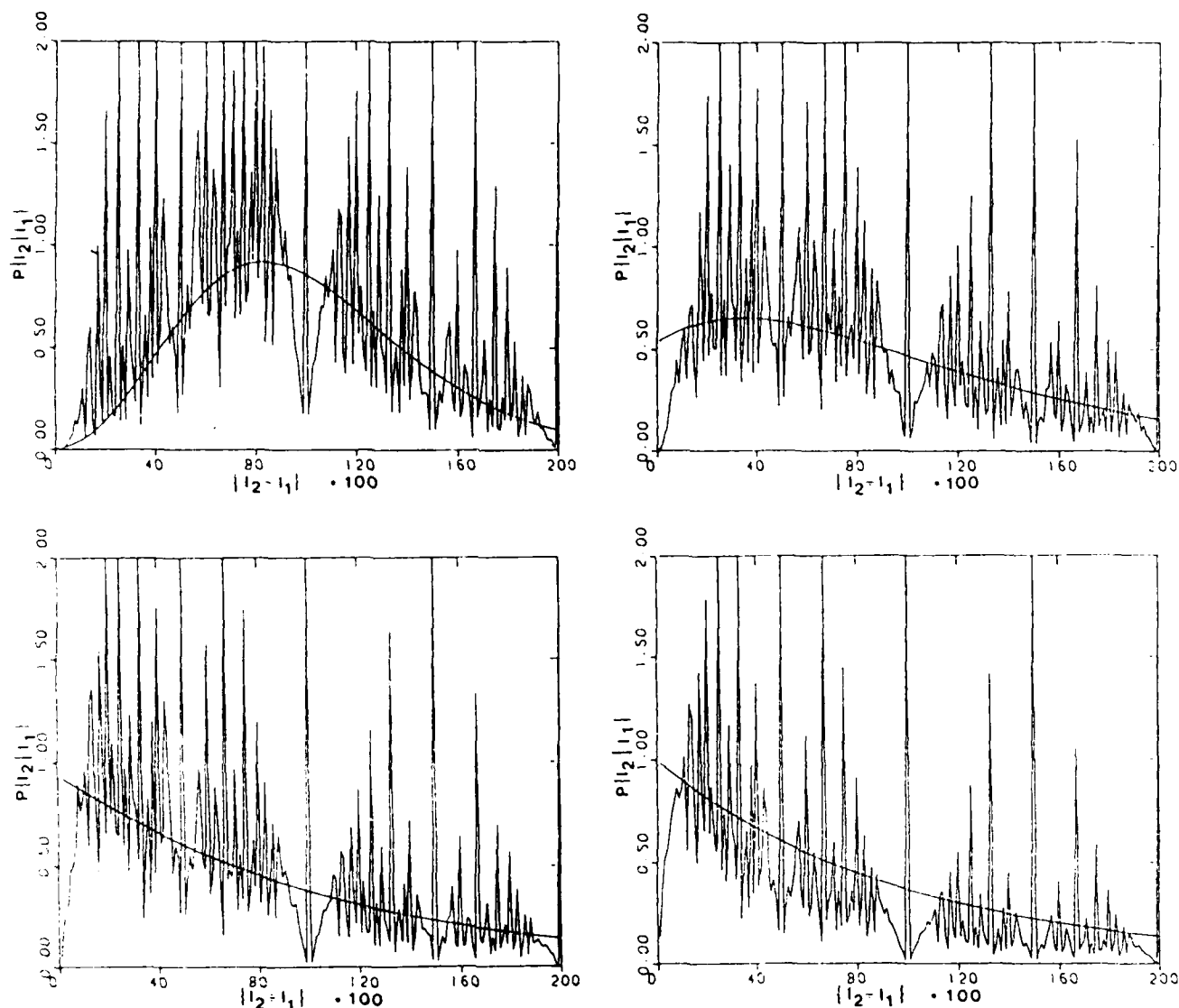


Figure 1: Conditional probability curves for (a) radius = 1, (b) radius = 2, (c) radius = 3 & (d) radius = 4 pixels.

where E_m denotes the expectation value taken over the random variable I_m and where $S(x)$ is given by eq. (3). Performing the expectation and summing over the specklegram data set yields

$$W(x) = \langle I \rangle^2 (|u_A(x)|^2 + 1) \quad (7)$$

Since $|u_A(0)| = 1$, we would expect the WSA/XC profile to look like some function with amplitude $\langle I \rangle^2$ superimposed on a constant background of value $\langle I \rangle^2$. In practice, however, the pixels that are used to develop the cross-correlation array are determined by a local maximum selection technique. Thus the probability distribution $P(\gamma)$ governing the experimentally detected speckle maxima is an empirically determined curve. In addition, suppose that the mean value $\langle \gamma \rangle$ of these maxima can be computed. Furthermore $\langle \gamma \rangle$ is greater than $\langle I \rangle$ because of the threshold for maximum detection. Then, we find that the WSA/XC profile equals

$$W'(x) = E_\gamma [S(x)] \quad (8)$$

where E_γ denotes the expectation value over the actually detected speckle maxima using the distribution $P(\gamma)$. Performing the expectation yields

$$W'(x) = (\langle \gamma^2 \rangle - \langle \gamma \rangle \langle I \rangle) |u_A(x)|^2 + \langle \gamma \rangle \langle I \rangle \quad (9)$$

which can be normalized to give

$$W(x) = |u_A(x)|^2 + \langle \gamma \rangle \langle I \rangle / (\langle \gamma^2 \rangle - \langle \gamma \rangle \langle I \rangle) \quad (10)$$

If $\langle I \rangle$, $\langle \gamma \rangle$ and $\langle \gamma^2 \rangle$ are computed frame by frame for the Gamma Orionis data set used to compute the conditional probability curves, the prediction for the WSA intensity profile is

$$|u_A(x)|^2 + .49$$

If the same data set is reduced using WSA/XC the result is

$$|u_A(x)|^2 + .44$$

which compares very well. The outcome of this WSA/XC reduction is seen in Fig. 2. In computing that result use was made of the fact that the seeing bias can be approximated by a normal curve plus a constant background. Since every point correlates perfectly with itself, $|u_A(x)|^2$ is identically equal to unity at the origin. If we assume that the estimation of the normal background is the main source of error in this calculation then further computation should allow a prediction of the signal to noise limit for a WSA reduction.

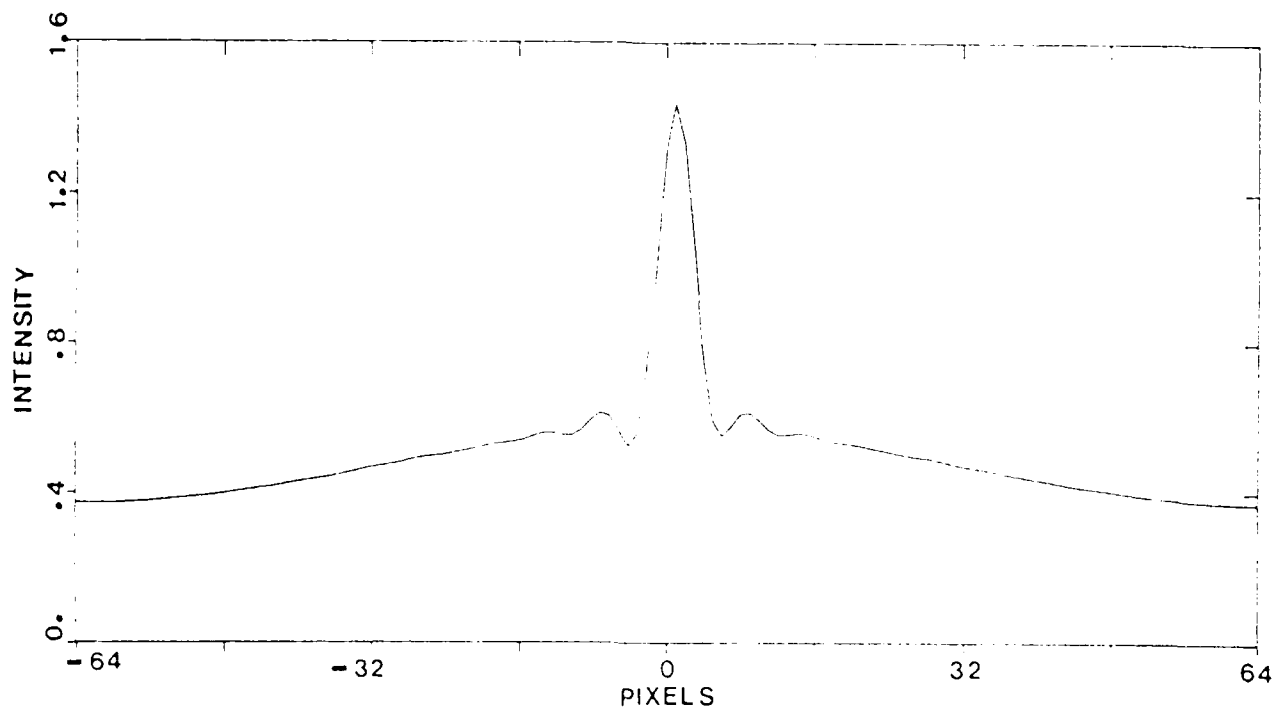


Figure 2: Cross section of WSA/XC image of Gamma Orionis. (1 pixel = 7.22 mas).

The weighted deconvolution WSA/WD is the method of choice as compared to WSA/XC in that it suppresses the seeing produced background almost to the noise level of the system³. Table 1 compares the computed values of $|u_A(x)|^2$ and the theoretical Airy disk with the results of the same Gamma Orionis data set reduced using WSA/WD. Fig. 3 plots the data presented in Table 1. Notice that $|u_A(x)|^2$ falls off in a very similar manner to both the other curves. This leads us to the conclusion that $|u_A(x)|^2$ is very similar in structure to the theoretical Airy disk (if indeed there is any difference). Specifically, these results indicate that the statistical model above appears to make accurate predictions about the behavior of the WSA process. The predictions about the structure of the complex coherence apply for both WSA/XC and WSA/WD.

Discussion

The entire preceding discussion makes no reference to the concept of "speckles". The term speckle is casually used to describe a distorted, diffraction limited image found in a specklegram. The number of speckles, usually computed as proportional to $(D/r_0)^2$,

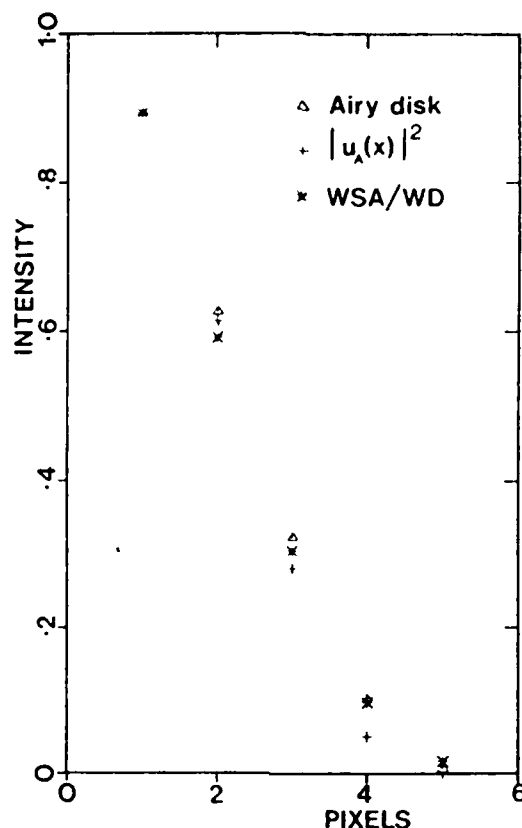


Figure 3: Comparison of measurements with theoretical Airy profile.

is always assumed to be much less than the number of pixels in a specklegram and each speckle is also assumed to have an identifiable maximum. If such isolated speckles exist, then the intensities in the area in the specklegram associated with a speckle should be qualitatively different from those for any arbitrary point in the field. Those assumptions suggest that a good way to identify the location of the speckles in a frame should be to find all the local maxima in a specklegram. The curves described in this paper can be recomputed excluding all the local maxima. Contrary to these assumptions, inspection of the second set of curves reveals no substantial change from the probability curves computed with the full frame. In fact, all differences between the two can be attributed solely to the fact that a maxima defines a pixel which is greater in intensity than all surrounding pixels, and therefore statistically carries more information.

This leads us to the conclusion that in a statistical sense, speckles exist continuously through a specklegram. For the case of the point source this would require that an Airy disk be centered at each point in the specklegram. Furthermore, it confirms that local maxima represent nothing more than pixels with good statistics. Due to exponential photon statistics in a single specklegram, statistical fluctuation at a particular maximum so dominates the local area that in effect an isolated speckle (a diffraction limited image) may be said to exist.

References

1. Bates, R.H.T. & F.W.Cady, 'Towards True Imaging by Wideband Speckle Interferometry', *Opt. Commun.*, 32, 368, 1980.
2. Lynds, C.R., S.P.Worden & J.W. Harvey, 'Digital Image Reconstruction Applied to Alpha Orionis', *Astrophys.J.*, 207, 174, 1976.
3. Christou, J.C., E.K.Hege, J.D.Freeman & E.Ribak, 'Images From Astronomical Speckle Data: Weighted Shift-and-Add Analysis', *Proc. SPIE*, 556-36, 1985.
4. Hunt, B.R., W.R. Fright, R.H.T. Bates, 'Analysis of the Shift-and-Add Method for Imaging', *J. Opt. Soc. Am.*, 73, No.4, pp. 456-465, 1983.
5. Goodman, J.W., 'Statistical Properties of Laser Speckle Patterns', in Laser Speckle and Related Phenomena, ed. J.C.Dainty, Springer-Verlag 1984.

TWO-DIMENSIONAL IMAGES OF ALPHA ORIONIS¹

J. C. HEBDEN, J. C. CHRISTOU,² A. Y. S. CHENG, E. K. HEGER,³ AND P. A. STRITTMATTER¹

Steward Observatory, University of Arizona, Tucson

J. M. BECKERS³

NOAO, Tucson

AND

H. P. MURPHY

NRAO, Socorro, New Mexico

Received 1985 November 1; accepted 1986 April 7

ABSTRACT

Between 1981 February and 1983 December a series of speckle interferometric observations were made of the M-type supergiant α Orionis in an attempt to produce two-dimensional images of the star at the H α line. The telescopes employed include the Steward Observatory 2.3 m and NOAO 4 m telescopes at Kitt Peak and the fully phased six-mirror Multiple Mirror Telescope. Two types of data reduction techniques were used: (1) shift-and-add methods applied to conventional speckle interferometric observations, and (2) differential speckle interferometry. Data analysis included the application of the CLEAN algorithm to calibrate the images produced by the shift-and-add technique with data reduced similarly for a point source. The images produced are encouragingly consistent in suggesting asymmetric atmospheric structure; possible evolution of that structure over the three-year period of observations is noted.

Subject headings: interferometry — stars: individual

1. INTRODUCTION

The low surface gravity and absence of strong magnetic field lines cause the surrounding envelopes of red supergiant and giant stars to be very extended and relatively cool. This makes them visible in the light of the hydrogen Balmer lines (e.g., H α λ 6563) and the singly ionized calcium lines (e.g., Ca II λ 8582). Occultation measurements by White, Kreidl and Goldberg (1982) and preliminary speckle observations (Goldberg *et al.* 1982) have presented evidence for spatially extended H α emission surrounding M-type supergiants. Asymmetry discovered in the cores of several strong resonance lines in M stars (Adams and MacCormack 1935) suggests that these giant stars are surrounded by huge circumstellar shells moving away from the central star at velocities on the order of 5 km s⁻¹. Furthermore, it has been shown (Deutsch 1956) that such shells are responsible for considerable mass loss.

The most thoroughly studied of all red giant stars has been α Ori, an M2 Iab late-type supergiant. Like most red giant and supergiant stars, α Ori is an irregular variable and displays a high mass loss rate, typically calculated as about $\sim 10^{-6} M_{\odot}$ yr⁻¹. Numerous observations have also identified variability in both the visual brightness and radial velocity of the supergiant star on time scales of a few weeks or months. The mean amplitudes are about half a magnitude and 6 km s⁻¹ respectively. For a review see Goldberg (1984). The long-term variability roughly satisfies the phase relation for a pulsating star,

i.e., maximum brightness coinciding with minimum radius (Sanford 1933), though Guinan (1984) observes that the short-term light and radial velocity variations are usually uncoupled. In addition, Hayes (1984) has produced results showing variation in the polarization of α Ori on time scales of months. Possible temporal irregularity and spatial inhomogeneity are in accord with the suggestion of Schwarzschild (1975) that the surfaces of supergiants may be irregular due to the presence of very large convective cells.

Since 1920, when Michelson and Pease (1921) first determined the angular diameter of α Ori, the star has become one of the most frequently observed objects using high-resolution interferometric techniques. The angular diameter measurements which have been obtained, as summarized by White (1980), show a wide scatter of values. However, a circumstellar envelope of outflowing material may have influenced those measures in a way dependent on the bandpass and the epoch of observation (Cheng *et al.* 1986). Purely interferometric methods (visibility measures) would be highly biased by such effects. Thus there is urgent need for real images to sort out these spatial effects.

It was not until 1976 that the first attempt at image reconstruction of this star (or indeed of any other star other than our own Sun) was published, by Lynds, Worden, and Harvey (1976, hereafter LWH). The breakthrough in ground-based high-resolution methods which led to this and subsequent results came when Labeyrie (1970) proposed the technique of stellar speckle interferometry (SI). This technique enables diffraction-limited resolution to be obtained from large optical telescopes, despite the effects of atmospheric turbulence, by utilizing single short-exposure narrow-bandwidth images (specklegrams). Since Labeyrie's original work, many extensions have been made to the theory and application of SI and, in particular, to the recovery of diffraction-limited images. One such image reconstruction technique which is relevant to the

¹ Data from the Multiple Mirror Telescope, a joint facility of the University of Arizona and the Smithsonian Institution; the 4 m Mayall reflector at Kitt Peak National Observatory, a division of National Optical Astronomy Observatories, which is operated by Associated Universities for Research in Astronomy, Inc., under contract to the National Science Foundation, and the Steward Observatory 2.3 m reflector.

² Also Department of Astronomy, New Mexico State University, Las Cruces.

³ Visiting Astronomer, Kitt Peak National Observatory.

work described here is known as shift-and-add (SAA). This is an extension by Bates and Cady (1980) of the method used by LWH and refined by Welter and Worden (1980), which produced that first stellar map. SAA is discussed in more detail in § III. Another recent modification of SI is a technique called differential speckle interferometry (DSI), as proposed by Beckers (1982). DSI uses two simultaneously acquired narrow-band images (see § IV).

Diffraction-limited imaging of the resolved disk and extended atmosphere of α Ori and other giant stars may become an invaluable aid to the understanding of stellar mass loss processes and to the study of stellar evolution. In addition, as Hartmann (1982) suggests, the combination of high-resolution images with radio measurements should yield a much clearer picture of electron densities and temperatures in the inner regions of the stellar wind.

In this paper we present the results obtained from a series of SI observations of α Ori made over a three-year period. The resolved disk and H α envelope of the star have been imaged using a variety of techniques. We note asymmetric features with a consistent position angle in each image, and the results suggest that the structure may have changed visually during the period between observations.

II. OBSERVATIONS

Between 1981 February and 1983 December, α Ori was observed on four separate occasions with the purpose of obtaining information on the structure of the star's disk and extended envelope at the H α wave band. Two basic SI techniques were employed: conventional SI, and DSI. The implementation of each method is discussed separately below.

a) Conventional Speckle Interferometry

Observations of α Ori were made at the NOAO 4 m telescope (pupil masked to 3.8 m) on 1981 February 2/3 and also on the Steward 2.3 m telescope at Kitt Peak on 1982 November 5/6 using the Steward Observatory intensified video speckle camera, as described by Hege *et al.* (1982). The instrumental and observational parameters for both runs were essentially the same. H α (26563.3 Å) and red continuum (26500/20 Å) bandpass filters were employed to observe the supergiant as well as point source calibration stars ϵ and γ Ori. We note that a recently detected secondary component of γ Ori (Papaliolios, Nisenson, and Ebstein 1985) is outside our field of view. Video specklegrams were recorded for ~ 15 minute intervals for α Ori, interspersed with 5 minute observations of the calibration stars. The specklegrams were recorded with 15 ms exposures at the rate of 7.5 Hz, equivalent to every fourth video frame. Excluding light from three of every four frames enables the image intensifier afterglow to decay sufficiently between exposures so that unevenness in the background signal can be removed by on-line subtraction of consecutive frames. The 15 ms exposure time is sufficiently short to effectively freeze the atmospheric turbulence so that specklegrams retain information at frequencies up to the diffraction limit of the telescope. Postobservational data processing begins with digitization of the specklegrams 8 bits deep in a 128×128 pixel array by a Grinnell digital television system. The digitized data is stored on nine-track tapes using the Steward Observatory Point 4 minicomputer system. Preliminary results of our one-dimensional analysis of these data, which produced a stellar radius of 42.1 mas with limb-darkening dependent on observing bandpass, have been presented in Cheng *et al.* (1986).

b) Differential Speckle Interferometry

DSI observations of α Ori were made using the Steward 2.3 m telescope on 1982 March 5/7 and on the fully phased six-mirror Multiple Mirror Telescope (MMT, see Hege *et al.* 1985) on 1983 December 16/17. This new technique utilizes the differential speckle camera (Beckers, Hege, and Murphy 1983), which enables an object to be observed at two wave bands simultaneously. This is achieved by passing the light from the star through a solid Fabry-Perot etalon, which has a different narrow passband at two orthogonal polarizations, and then shifting one polarized image with respect to the other using a Wollaston prism. In this way two specklegrams are produced, separated by ~ 7.38 mm in the image intensifier focal plane. Adjustment of the etalon temperature shifts the bandpasses for the two polarizations. The bandpass separation and full width at half-maximum at peak transmission are dependent on the choice of mica spacer in the etalon. The 1982 March observations were obtained at seven different wavelength positions centred around the H α line (H $\alpha \pm 1.5$ Å, H $\alpha \pm 1$ Å, H $\alpha \pm 0.5$ Å, H α), and simultaneously in the nearby continuum ~ 4 Å away. The bandwidth of the H α filter was 0.45 Å. The 1983 December MMT observations produced specklegrams at H α (bandwidth 1.2 Å) and continuum ~ 6 Å away. Once again, γ Ori was used as a point source calibration star. Data were obtained for the supergiant at two distinct sky position angles separated by $\sim 80^\circ$. Identification of image features which rotate correspondingly is a very strong validation of the technique. Video specklegram pairs were recorded in an identical manner to that described for conventional speckle observations. Each video frame was digitized as two 128×128 pixel arrays and stored consecutively on nine-track magnetic tape.

III. CLEAN SHIFT-AND-ADD IMAGES

The principal concept behind the imaging technique used by LWH is that each individual bright speckle in a specklegram may be considered as a photon-noise-limited representation of a randomly distorted but nearly diffraction-limited image of the star. Thus LWH realized that they might be able to form a useful image of a resolvable astronomical object by superposing the brighter speckles obtained from a series of specklegrams, thus averaging the random distortions and building an average which approximates the true image as more and more data are added. This was, as mentioned earlier, later developed into the technique known as shift-and-add by Bates and Cady (1980). This idea of stacking all the speckles from a large number of frames was applied to the H α data of α and ϵ Ori obtained on the 2.3 m telescope in 1982 November. In practice the stacking-up procedure consisted of cross-correlating the specklegram with an array containing a series of delta functions whose position and amplitude correspond to the position and peak height of the speckles. This process produces an image which is situated on a broad background. This background is subtracted to a high degree by comparison to a suitable Gaussian function. Figures 1a and 1b show the results for 1000 specklegram frames of α and ϵ Ori respectively. The general elongation in the vertical direction is due to the pixels having a smaller scale in the north-south direction than in the east-west direction. The ϵ Ori image, as well as the α Ori image to a much lesser degree, contains an artifact due to nonlinear effects of the video system. As the television camera scans across very bright speckles, nonlinearities in the Sony video cassette recorder cause the effective intensity of the scan to

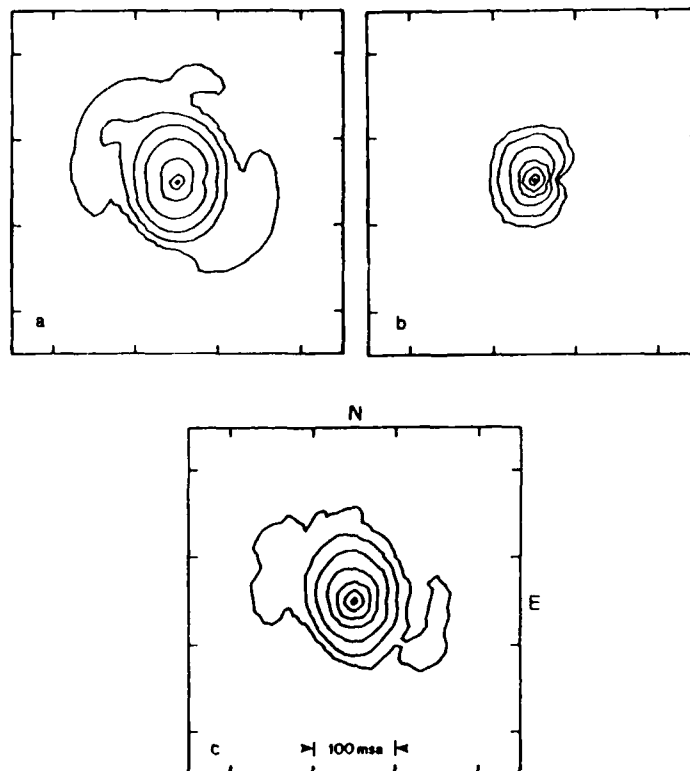


FIG. 1.—Shift-and-add images ($\lambda 6563$ 3 Å filter, 2.3 in telescope; resolution 50 mas) of (a) α Ori and (b) ϵ Ori; (c) the CLEANed image of α Ori

"undershoot," as illustrated in Figure 2. Thus the images appear compressed on one side, in the scan line direction adjacent to the part of the image at which the speckles are brightest (i.e., the center). The brighter, more pointlike, ϵ Ori speckles cause more severe "undershoot" to occur.

In order to produce an image of α Ori free from the effects of the telescope point-spread function (PSF) and from spurious systematic effects like those described above, attempts were made to deconvolve the image with the ϵ Ori image using the CLEAN algorithm. The CLEAN procedure (Högbom 1974) has been successfully applied in the past to radio interferomet-

ric data in order to remove structural features due to the synthesized interferometer beam.

Conventionally, the preprocessed image is referred to as the "dirty map," and the image with which the deconvolution is performed as the "dirty beam." CLEAN is an iterative process which locates the point of greatest intensity in the dirty map and subtracts at this location the dirty beam whose peak intensity is $G\%$ of the current peak in the dirty map. This process is repeated on the residual after subtraction. The quality of the final "CLEANed map" is dependent on both the value of the loop gain G and the number of iterations. In this way a set of delta functions of varying intensities are generated such that the dirty map can be considered as a weighted sum of dirty beams plus the final residual. The number of iterations is selected so that either the intensity in the final residual is equal to the expected noise level or that only a certain number of delta functions have negative intensities. The CLEANed map is then obtained by convolving the array of delta functions with an estimate of the "CLEAN beam," commonly obtained by fitting a Gaussian to the central component of the dirty beam.

Thus the CLEAN algorithm was applied to α Ori using Figure 1a as the dirty map and Figure 1b as the dirty beam. The CLEANing was performed by using 50 iterations and a loop gain of 70%. The CLEANed image of α Ori is shown in Figure 1c. Since, as mentioned above, the undershoot effect does not occur equally in the α and ϵ Ori data (more severe for brighter ϵ Ori speckles), the CLEAN procedure is likely to overcompensate a little. However, the undershoot effect apparent in Figure 1a does appear to have been eliminated to a high degree in Figure 1c. The outer 2" contour shows significant elongation in the northwest-southeast direction at a position angle of $\sim 120^\circ$ (mod 180°). However, the inner contours

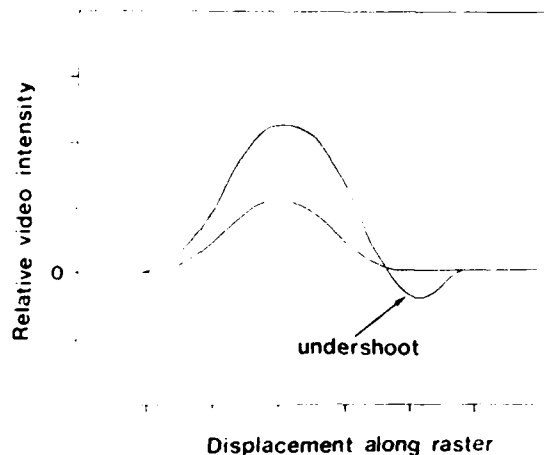


FIG. 2.—Illustration of video scan "undershoot" produced by excessively bright speckles. This is the source of "notch" downraster of peaks in Figs. 1a and 1b.

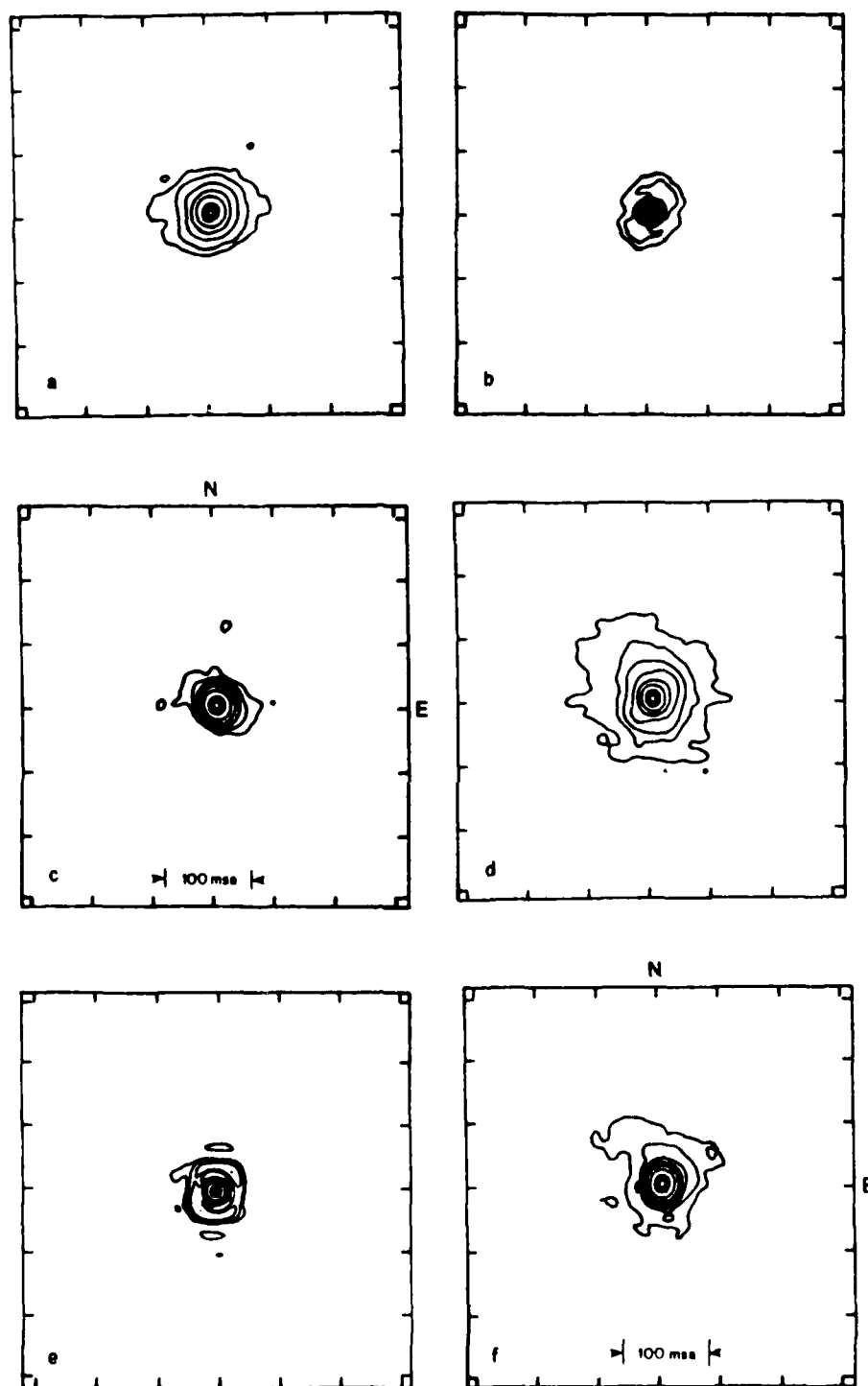


FIG. 3. Weighted shift-and-add images (3.8 m pupil of NOAO/KPNO Mayall telescope; resolution 33 mas) of (a) z Ori and (b) γ Ori at 6563 Å, and (d) z Ori and (e) γ Ori at 6500 Å (20 Å). (c) and (f) CLEANed z Ori images at 6563 Å and 6500 Å respectively.

exhibit an elongation at a position angle of $169^\circ \pmod{180^\circ}$. The 2 σ contour extends over a diameter of ~ 150 mas.

A recent modification of the SAA technique has been implemented which enables speckles to be co-added without producing the Gaussian-like background. Weighted shift-and-add (WSA), as described by Christou *et al.* (1985*a, b*), produces an array of impulses in an identical manner to that described above and then deconvolves each specklegram by its corresponding impulse array. Performing a complex deconvolution, a quotient in Fourier space, normally introduces spurious effects associated with the presence of small numbers in the denominator. WSA avoids this by weighting each complex quotient by the power spectrum of the impulse array and summing over a large number of frames. This technique was applied to the $\lambda 6500$ 20 Å and $\lambda 6563$ 3 Å observations of α and γ Ori obtained using the NOAO 4 telescope in 1981 February. Figures 3*a* and 3*b* show the WSA reconstructed images for 1500 specklegrams of α and γ Ori at H α wavelengths, and Figures 3*d* and 3*e* show similar images for 1500 specklegrams of the same stars using a $\lambda 6500$ 20 Å bandpass filter.

Using the γ Ori images as the dirty beams, the images of α Ori were CLEANed as described above. Fifty iterations were performed using a loop gain of 70%. The results of this cleaning process are shown in Figures 3*c* ($\lambda 6563$) and 3*f* ($\lambda 6500$). Once again the CLEANed H α image exhibits significant northwest-southeast elongation. The outermost contour yields a position angle of $\sim 117^\circ \pmod{180^\circ}$, whereas the inner contours suggest an elongation at $\sim 160^\circ \pmod{180^\circ}$. However the CLEANed $\lambda 6500$ image of α Ori shows practically no such elongation above the level of the noise.

IV. DIFFERENTIAL SPECKLE IMAGING

DSI involves recording two speckle images simultaneously. By observing an astronomical object at two distinct but nearby wavelengths, image information relating to the differences in the object as results from the difference in wavelength (e.g., stellar emission or absorption lines, Doppler shifts, Zeeman effects) can be derived. One inherent benefit of DSI is that information at very narrow (e.g., emission, absorption line) wave bands can be derived at a far greater signal-to-noise ratio (S/N) than that achievable using single-image (conventional) SI alone. Petrov, Roddier, and Aime (1985) show that the overall S/N for DSI is equal to the geometric mean of the two component specklegram S/Ns. Thus it is beneficial to use a reference specklegram as bright as possible. Unfortunately, at the moment we are constrained to the use of a single detector, so the line reference brightness ratio cannot become too large without sacrificing single photon detection in the line specklegram. A unique unambiguous image of an object at either wavelength can only be derived using the DSI techniques described here if the object intensity distribution at the other wavelength is known; this is a comparative technique.

The 42 mas diameter disk of α Ori is practically unresolved at continuum wavelengths on a 2.3 m telescope. Thus, assuming the DSI reference specklegrams obtained in 1982 March to be those of a nearly unresolved source, the image of the star at H α was reconstructed using the method known as speckle holography (Bates, Gough, and Napier 1973). Each H α specklegram was cross-correlated with its corresponding reference specklegram, and the cross-correlations were co-added. Cross-correlation produces a peak situated on a broad Gaussian-like seeing background. Assuming the continuum image to be unresolved, each of these peaks represents an

image of α Ori at the H α wave band superposed on the cross-correlated seeing in the two bandpasses. Isolation of these images was achieved by subtracting a least-squares fit Gaussian model of the seeing background. Figure 4 shows the images of α Ori obtained at the H α wave band and also in the near (± 0.5 Å) and far (± 1.5 Å) wings of the line. In accord with the other H α images of α Ori described so far, the line center image exhibits a very significant elongation in the northwest-southeast direction, particularly at the higher contour levels, with a position angle of $\sim 118^\circ \pmod{180^\circ}$. The images generated from observations in the wings of the line show very little evidence of such elongation above the level of the noise. Radial averaged profiles of these images, as shown in Figure 5, suggest that there is significant intensity out to a radius of ~ 400 mas. This simple method of Gaussian-model subtraction of the seeing background will inevitably produce a small positive spurious residual at the center of the image. A theory by Kolmogorov (see Fried 1976) predicts that the atmospheric transfer function (ATF) can be represented by an exponential 5/3 power law, i.e., nearly, but not quite, Gaussian. The seeing disk (long-exposure image) is the Fourier transform of the ATF. Figure 6 shows a Fourier-transformed 5/3 power function to which a Gaussian has been fitted using a least-squares routine. Also shown is the difference between the two curves. Since the background component produced by this DSI technique is in effect the cross-correlation of two of these Gaussian-like functions, we can expect there to be a positive central residual when subtraction of a best-fit Gaussian is performed. Thus all the images shown in Figure 4 are artificially broadened. Nevertheless, since this systematic effect is common to all the images, a qualitative comparison of the images is still valid. The relative form of the radial profiles is discussed in § V.

The fully phased six-mirror MMI has the effective aperture of a 6.86 m telescope masked by a hexagonal aperture plate (Hege *et al.* 1985). At the H α wave band, this corresponds to a diffraction limit of ~ 20 mas. Thus α Ori is quite easily resolved by the MMI. Whereas reference specklegrams obtained in the continuum with the MMI are now resolved and cannot be used to deconvolve the corresponding line specklegrams so as to produce an actual image, performing such a deconvolution still enables information relating to the physical differences at the different wavelengths to be derived.

The data reduction procedure implemented for the 1983 December MMI observations consisted of performing frame-by-frame complex deconvolutions of the H α specklegrams by their simultaneously acquired counterparts. In a similar manner to that described for WSA in § III, each complex quotient is weighted by the reference power spectrum and summed over a large number of frames. Since the result obtained is dependent on the appearance of the object at both bandpasses (H α and continuum), it is known as a "differential image."

Figure 7 (Plate 8) shows a differential image of the point source γ Ori. About 1000 frames of data were used. The result is essentially equivalent to the inverse Fourier transform of a cylindrical (top hat) function with radius equal to the frequency cutoff of the telescope (D/λ), consistent with the assumption that γ Ori is unresolved at both wavebands. The differential image is therefore a function of the form $J_1(x)/x$, whose half-power width is expected to be about $\sim 0.61 \cdot D$ radians, or ~ 12 mas for the 6.86 m aperture of the MMI at the H α wave band. The image scale in Figure 7 is equal to ~ 5 mas/pixel, and hence the half-power width is 3 pixels across, well with the expected result. The rather nonuniform bright-

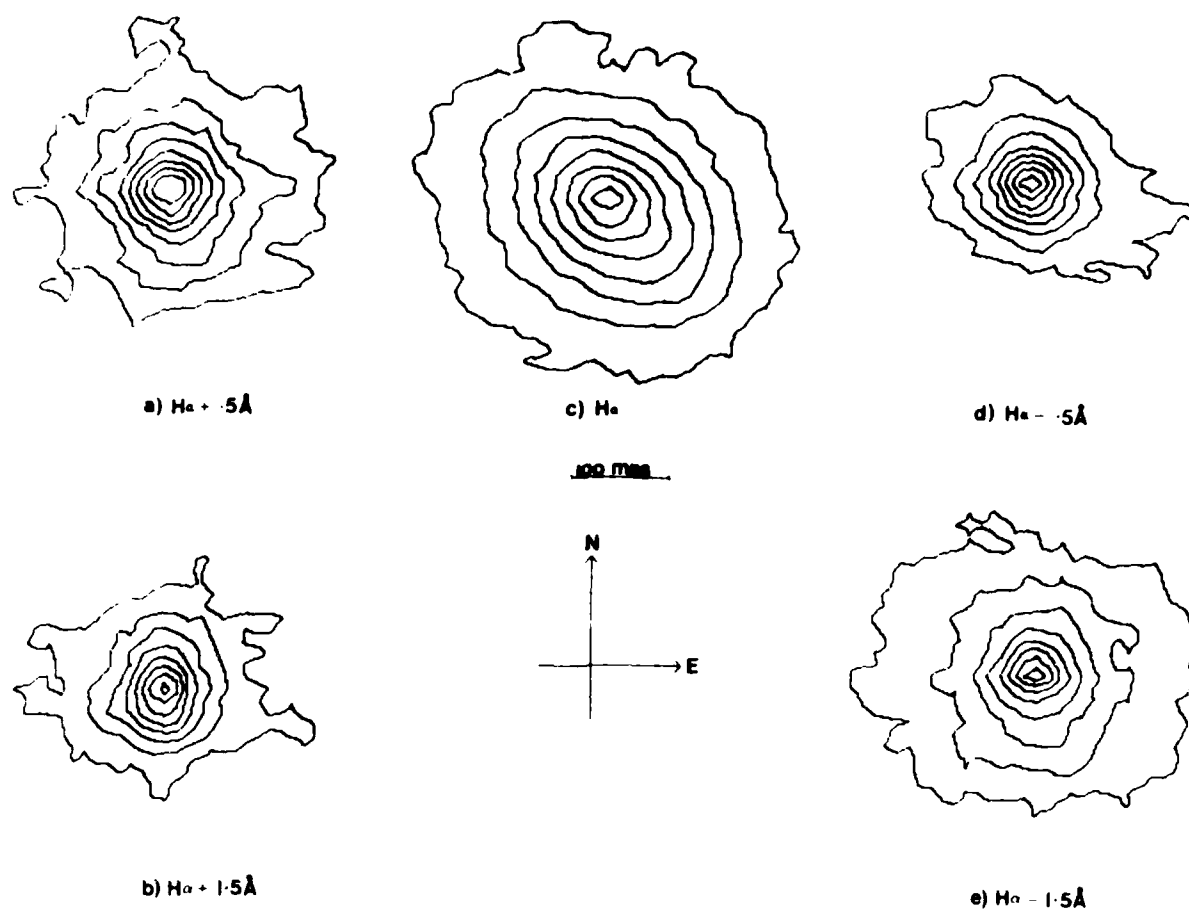


FIG. 4. DSI cross-correlation images of α Ori obtained at the center and $\pm 1.5\text{\AA}$, $\pm 0.5\text{\AA}$ wings of the $H\alpha$ line (2.3 m telescope, resolution 60 mas).

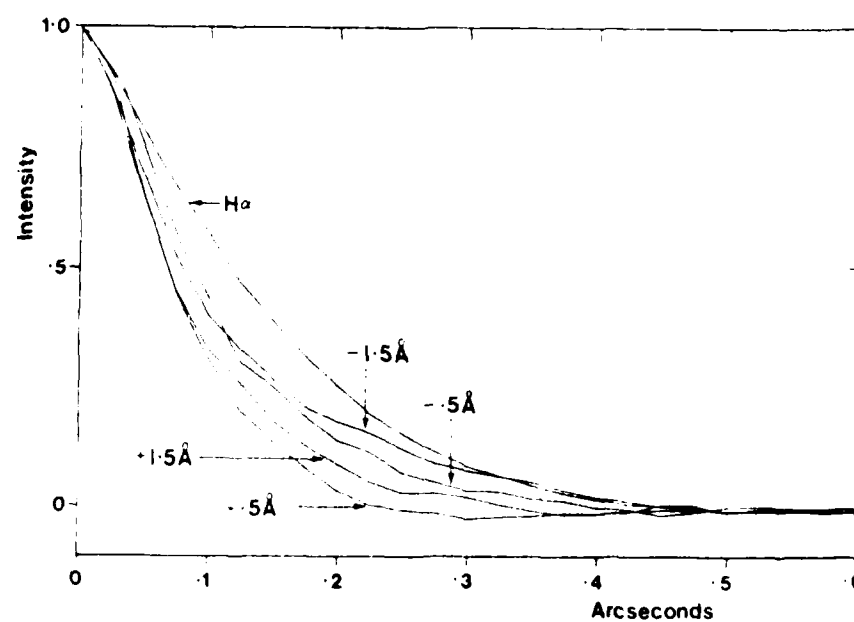


FIG. 5. Radial averaged profiles of the images (shown in Fig. 4) of α Ori obtained at the center and $\pm 1.5\text{\AA}$, $\pm 0.5\text{\AA}$ wings of the $H\alpha$ line.

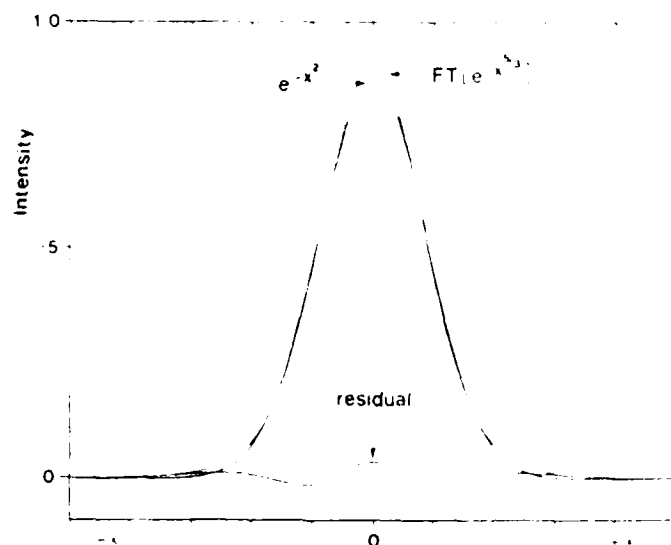


FIG. 6. Fourier-transformed S3 power exponential function and a best-fit Gaussian.

ness of the first secondary maxima suggests that there was probably less than perfect optical coherence between the six constituent mirrors of the MMI. Incidentally, a WSA image produced from the same data set (Christou *et al.* 1986a) shows this same nonuniformity. A region of a second ring is also apparent.

Figure 8 (Plate 9) shows a differential image of α Ori obtained from an identical number of frames. The overall S/N looks poorer, even though the supergiant is brighter in the bandpass used, because the object is resolved (more photons per speckle but considerably larger speckles). Further differential images of α Ori were generated using ~ 7000 frames of data for each sky position angle. Though radial average measurements confirmed the existence of structure over a diameter of at least 150 mas, very little evidence of the expected 80° image rotation was observed, due to the relatively poor S/N. A detailed analysis of the reduction technique revealed that the weighted deconvolution quotient contains a form of inherent Wiener-type filter which suppresses the signal at high spatial frequencies (see Hebden, Hege, and Beckers 1986). This inherent filtering effect is avoided by removing a noise bias term from the co-added power spectra which weight the deconvolution quotient. However, the power spectrum plus noise term is already multiplied by the Fourier transform modulus of the detector photon PSF. By assuming this response to be Gaussian, as experiments described by Hege *et al.* (1982) have indicated, removal of the noise bias was achieved by subtraction of a Gaussian model which was fitted to the data at spatial frequencies greater than the telescope cutoff.

Figures 9a and 9b show the differential images of α Ori at the two sky position angles after removal of the noise bias terms. About 7000 frames were used for each image. At large radii there still appears to be no evidence of asymmetrical structure which is not still noise-dominated. There are several possible reasons for this. First, the MMI sky rotator was not employed (due to technical difficulties), and consequently the image was permitted to rotate by $\sim 9^\circ$ during integration for each of the two observations, blurring the image at large radii. Second, imperfect coherence between the six mirrors may be responsible for the systematic fringes apparent in the images.

Finally, the absence of any gross northwest-southeast elongation evident in the conventional SI results may imply that the structure is visible in the nearby continuum, as well as in the H α wave band. However, at small (< 30 mas), high S/N, radii there is considerable evidence that an elongated asymmetric feature in the image having a position angle of $\sim 20^\circ$ is observed to rotate exactly as predicted. Figure 9c shows the differential image of β Ori for comparison. The elongation in this image, which is also apparent in Figure 7, is probably due to the imperfect coherence of the MMI in this initial attempt, as mentioned earlier.

V. DISCUSSION

The very first image reconstruction of α Ori by LWH exhibited only marginal evidence of surface structure detected above the noise level. Further data reduction using the LWH technique and image enhancement (Worden, Lynds, and Harvey 1976; Wilkerson and Worden 1977; Welter and Worden 1980) consistently demonstrated asymmetry in the image of α Ori at a variety of wavebands, though no quantitative measurements were produced. Digital restoration techniques applied to LWH > 5000 data by McDonnell and Bates (1976) also confirmed a departure from circular symmetry in the disk features of α Ori.

Observations of the supergiant were made by Roddier and Roddier (1983) in 1980 November. Their study of fringe visibility at $\lambda 5348.90$ Å suggested an elongation at 22° (mod 180°) at large spatial frequencies (small radii) and a northwest-southeast elongation at small spatial frequencies (large radii). Subsequent reconstruction of an image of the star (Roddier and Roddier 1985) from their map of fringe visibilities suggests the presence of a partial shell structure around the star at a distance of ~ 2.5 stellar radii. Preliminary results obtained from SI observations by Goldberg *et al.* (1982) also indicate the presence of elongated structure in the northwest-southeast direction. Measurements obtained in the H α wave band suggested a position angle of $\sim 157^\circ$ (mod 180°) for 1980 November and $\sim 176^\circ$ (mod 180°) for 1981 February. Similar observations were made in 1981 February by Hege *et al.* (1982) in the red continuum ($\lambda 6500.20$ Å). A significant elongation

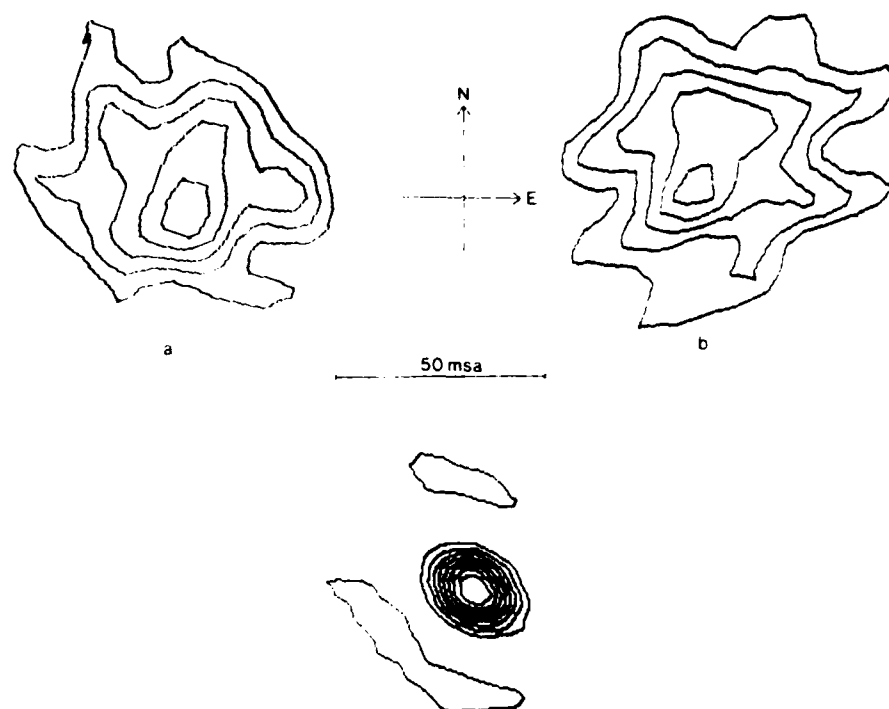


FIG. 9. Differential image of α Ori recorded at two sky position angles after removal of the inherent filtering effects. The differential image of γ Ori (PS1) is shown for comparison (contours are at 12% intervals).

was noted at a position angle of 28° (mod 180°). The same asymmetry was observed when these observations were used to reconstruct an image using the Fienup (1978) phase retrieval method.

Table 1 summarizes the recent measurements of asymmetrical features in the image of α Ori. There is overwhelming evidence for the existence of an elongated "cloud" of H α emission around α Ori, up to 3 times the estimated continuum diameter in length, in a northwest-southeast direction. Our results would suggest a position angle of $118 \pm 5^\circ$ with no apparent rotation of the feature relative to the sky over the 3 yr period. However, we tentatively suggest that the extension may have increased in the northwest direction while being reduced in the southeast direction. It is feasible, at least, that such variability would be produced by a cloud (possibly annular) rotating perpendicularly to the line of sight in a northwest-southeast oriented plane. The fact that there is generally less evidence of asymmetry in the continuum would suggest that

the cloud was predominantly gaseous rather than dust. One also might expect a dominant and temporally invariant (on the time scale of months at least) polarization angle if such a nearby, optically thin, asymmetric dust cloud were present.

Jones (1928) derived a period of 5.781 yr for the mean radial velocity variation of the photosphere of α Ori. Comparatively recent observations by Goldberg (1979) confirm this result to within 0.5%. This periodicity might be associated with a stellar rotation period of that duration, which corresponds to a surface (tangential) velocity of $\sim 20 \text{ km s}^{-1}$, or of the rotation period of an object orbiting the star. The possible rotation of extended features that we might have detected would imply a period of the order of the 6 yr variability.

The radially averaged profiles of the DSI images shown in Figure 5 show that the stellar envelope appears significantly broader at the center than in the wings of the H α line. However, the envelope is both larger and better visible in the blue wing than in the red wing. This is probably due to

TABLE 1
RECENT MEASURED ASYMMETRIES IN THE IMAGE OF ALPHA ORIONIS

Epoch	Wavelength (Å)	Position Angle (mod 180°)	Approximate Scale (mas)	Reference
1980 Nov 24	6563.3	157	< 300	Goldberg <i>et al.</i> 1982
1980 Nov 25-30	5348.90	22	< 50	Roddier and Roddier 1983
1981 Feb 2-3	6563.3	176	< 300	Goldberg <i>et al.</i> 1982
1981 Feb 2-3	6563.3	117	> 80	This work
1981 Feb 2-3	6563.3	160	< 80	This work
1981 Feb 2-3	6500.20	28	< 100	Hege <i>et al.</i> 1982
1982 Mar 5-7	6563.45	118	< 400	This work
1982 Nov 5-6	6563.3	120	> 100	This work
1982 Nov 5-6	6563.3	169	< 100	This work
1983 Dec 16-17	6563.12	20	< 30	This work

the expansion of an optically thick envelope with a velocity on the order of 20 km s^{-1} , which obscures the stellar disk only in the blue wing. In the red wing the much smaller stellar disk speckles dominate the specklegram data.

Three of the four observations reported here produced images which exhibited evidence for an additional asymmetrical position angle at radii comparable with the estimated continuum disk size (42 mas), where the S/N is highest. The measured position angles are 160° (mod 180° , 1981 February), 169° (mod 180° , 1982 November), and 20° (1983 December). It is not yet evident that these results could be consistent with a rotation period of 6 yr. Perhaps more likely is that each feature represents small-scale structure on the surface of the star that exists only on the time scale of months. Goldberg *et al.* (1982) attributed the presence of asymmetry in 1980 November and 1981 February to the existence of a "hot spot" on the surface of the star. This same feature would not be inconsistent with our 1981 February WSA result described in § III.

Hayes (1980) has suggested that the observed changes in polarization are consistent with the growth of a surface feature followed by changes in its orientation. Goldberg *et al.* (1982) find that their observations lend general support to this suggestion. In a comprehensive review of linear polarization variation of ϵ Ori between 1979 and 1983, Hayes (1984) concludes that large-scale convective cells fulfil the necessary requirement for production of the observed incessant polarization activity. He further suggests that ordered polarization changes, a manifestation of the waxing and waning of the cells, implies that only a few cells would be present at any one time. Such a model has also been hypothesized by Schwarzschild (1975). Incidentally, it is very improbable that the polarization variation occurs through scattering of light from matter around the star, since the observed short-term variation in polarization angle requires rotation of radial velocities inconsistent with current estimates. Unfortunately, there appears to be little correlation between our observed asymmetry position angles and the polarization angles as measured by Hayes (1984). Similarly, the changes in the intensity of polarized light appears unassociated with the occurrence or otherwise of central asymmetrical features.

Finally, it has recently been suggested by Karovska *et al.* (1986) that ϵ Ori may indeed have distinct optical companions. From high-resolution optical interferometric observations made in 1982 February and 1983 November, they suggested the presence of two sources. Their separations and position angles were (40 mas, 325°) and (500 mas, 85°) in 1982 February and (60 mas, 273°) and (510 mas, 278°) in 1983 November. The magnitude differences with respect to the primary, measured at 6563 Å (H α) and 6568 Å (red continuum) using our mica Fabry-Pérot filter, were derived as being 3.0 and 3.4 for the close and 4.3 and 4.6 for the distant source. Many other supergiants are known to be binary, and Parsons (1983) argues that

there exists a high probability of giant stars evolving as binary companions. In addition, it has been proposed that the observed polarization variation is produced by scattering off an extended dust shell from the companion which orbits inside it. It is unlikely we would have been able to detect the more distant companion, since it would have been barely within our field of view. So far we have been unable to provide any definite evidence which requires the existence of the close companion, and there is apparently no correlation between the reported position angle of either companion and that of our observed asymmetrical structure around the star. Incidentally, differential images would not reveal any companions, since that star exhibited significant spectral differences in and out of the emission line.

ACKNOWLEDGMENTS

The results of this study are being summarized in a paper. The presence of a large-scale asymmetric clonization on the ϵ Ori envelope has been verified by the results of several programs implemented ST techniques. It extends over a radius of 40 mas, and corresponds to a position angle of 160° (mod 180°). This position angle appears effectively constant over the entire period of observation, though extension in the northwest direction may have increased at the expense of the southeast extension. Smaller-scale asymmetries have also been identified within the diameter of the stellar disk. Two of these features appears to be consistent with random fluctuations of surface structure on the time scale of months. No correlation has been established between their bearing and position angle and their polarization variations over the same period.

An accurate determination of the continuous high-resolution temporal variation in the radial velocity, magnitude, and polarization of ϵ Ori and optical features on the surface and in the extended envelope of the star will require further extensive study using these high-resolution optical imaging techniques. Ultimately, such study of ϵ Ori and other rapid mass-loss objects will enable stellar evolution to be better understood (since giant stars which shed sufficient mass will avoid ending their existence in the form of supernovae) and may provide valuable information on the important question of "missing mass" in the universe. ST is now producing *real-time interferometric images*, and we are confident that a wide variety of speckle imaging methods will continue to provide valuable astronomical data with steadily increasing quantity.

This work has been supported in part by the National Science Foundation grants AST-8113702, AST-8307076, and AST-8412206 and by the U.S. Air Force AFOSR-82-0020. We wish to thank Andrew Eckart for the application of the CLEAN algorithm in the Fourier transformation of the speckle images.

REFERENCES

- Adams, W. S., and MacGraw, E. 1975, *Ap J*, **81**, 119.
 Bates, R. H. T., and Coffey, E. M. 1980, *Optics Comm.*, **32**, 368.
 Bates, R. H. T., Gough, P. T., and Napier, P. J. 1973, *Nature*, **22**, 316.
 Bickers, J. M. 1982, *Optics Lett.*, **29**, 361.
 Bickers, J. M., Hege, E. K., and Murphy, H. P. 1983, in *Interferometry in Astronomy*, L. and A. Boksenberg and D. Crawford (SPIE Proc. Vol. **445**), p. 167.
 Cheng, A. Y. S., Hege, E. K., Hubbar, E. N., Goldberg, E. S., and P. A. Crockett, W. F. 1986, *Ap J*, **309**, 737.
 Christou, J. C., Hege, E. K., Freeman, L., and Robak, E. 1986, *J. Opt. Soc. Am.*, **3**, 204.
 Crockett, W. F., Crockett, E. H., and Hege, E. K. 1985, *Ap J*, **291**, 103.
 Denehy, A. E. 1984, *Ap J*, **123**, 133.
 Eddington, R. 1959, *Ap J*, **130**, 33.
 Fied, D. E. 1983, *Optics Lett.*, **56**, 10.
 Goldberg, E. S., and Hege, E. K. 1981, *Ap J*, **20**, 10.
 Goldberg, E. S., and Hege, E. K. 1982, *Ap J*, **96**, 10.
 Goldberg, E. S., Hege, E. K., Hubbar, E. N., and Freeman, L. 1985, *Ap J*, **298**, 340.
 Karovska, M., and Hege, E. K. 1986, *Ap J*, **302**, 103.

- Guman, E. F. 1984, in *Lecture Notes in Physics*, vol. 193, *Cool Stars, Stellar Systems and the Sun*, ed. S. L. Baliunas and L. Hartmann (Berlin: Springer-Verlag), p. 336.
- Hartmann, L. 1982, *Highlights Astr.*, **6**, 549.
- Hayes, D. P. 1980, *Ap J (Letters)*, **241**, L165.
- 1984, *Ap J Suppl.*, **55**, 179.
- Hebden, J. C., Hege, E. K., and Beckers, J. M. 1986, *Opt. Eng.*, in press.
- Hege, E. K., Beckers, J. M., Strittmatter, P. A., and McCarthy, D. W. 1985, *Appl Optics*, **24**, 2565.
- Hege, E. K., Hubbard, F. N., Strittmatter, P. A., and Cocke, W. J. 1982, *Optica Acta*, **29**, 701.
- Hogbom, J. A. 1974, *Astr. Ap. Suppl.*, **15**, 417.
- Jones, H. Spencer 1928, *M.N.R.A.S.*, **88**, 660.
- Karovska, M., Nisenson, P., Noyes, R., and Roddier, F. 1986, *Ap J.*, **308**, 260.
- Labeyrie, A. 1970, *Astr. Ap.*, **6**, 85.
- Lynds, C. R., Worden, S. P., and Harvey, J. W. 1976, *Ap J.*, **207**, 1174 (LWH).
- McDonnell, M. J., and Bates, R. H. T. 1976, *Ap J.*, **208**, 443.
- Michelson, A. A., and Pease, F. G. 1921, *Ap J.*, **53**, 249.
- Papaliolos, C., Nisenson, P., and Epstein, S. 1985, *Appl Optics*, **24**, 287.
- Parsons, S. B. 1981, *Ap J.*, **247**, 560.
- Petrov, P., Roddier, F., and Aime, C. 1985, *J. Opt. Soc. Am.*, submitted.
- Roddier, C., and Roddier, F. 1983, *Ap J (Letters)*, **270**, L23.
- Roddier, F., and Roddier, C. 1985, *Ap J (Letters)*, **295**, L21.
- Sanford, R. F. 1933, *Ap J.*, **77**, 110.
- Schwarzschild, M. 1975, *Ap J.*, **195**, 137.
- Welter, G. L., and Worden, S. P. 1980, *Ap J.*, **242**, 673.
- White, N. M. 1980, *Ap J.*, **242**, 646.
- White, N. M., Kreidl, T. J., and Goldberg, I. 1982, *Ap J.*, **254**, 670.
- Wilkerson, M. S., and Worden, S. P. 1977, *Ap J.*, **82**, 642.
- Worden, S. P., Lynds, C. R., and Harvey, J. W. 1976, *J. Opt. Soc. Am.*, **66**, 1243.

J. M. BECKERS: National Optical Astronomical Observatories, 950 N. Cherry Avenue, Tucson, AZ 85726

A. Y. S. CHENG, J. C. CHRISTOU, J. C. HEBDEN, E. K. HEGE, and P. A. STRITTMATTER: Steward Observatory, University of Arizona, Tucson, AZ 85721

H. P. MURPHY: National Radio Astronomical Observatories, Socorro, NM 87801

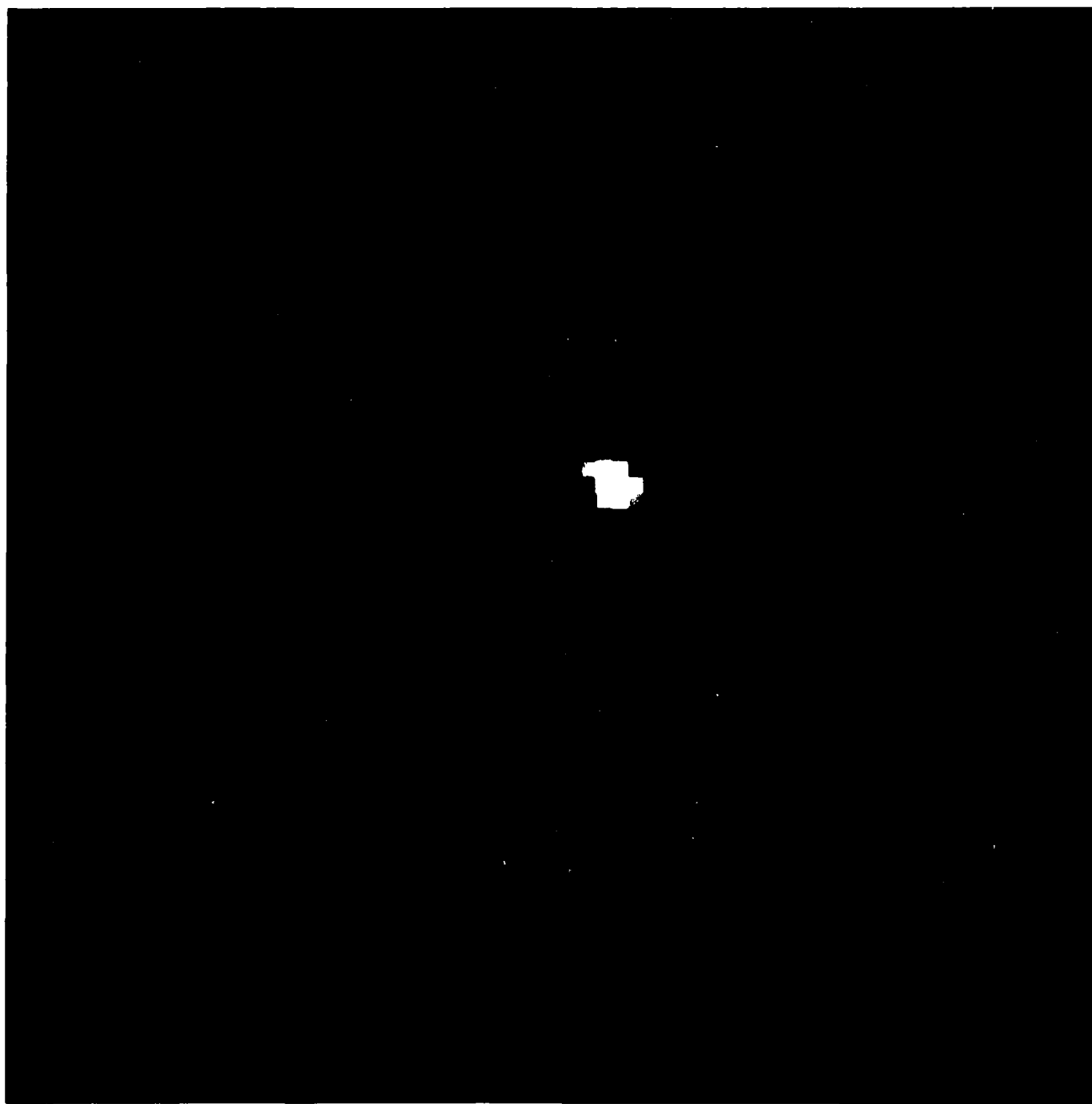


FIG. 7. Differential image of ϵ Ori obtained with the MMT (raw data image at 5 mas pixel⁻¹, resolution 20 mas).
HERDES *et al.* (see page 749)

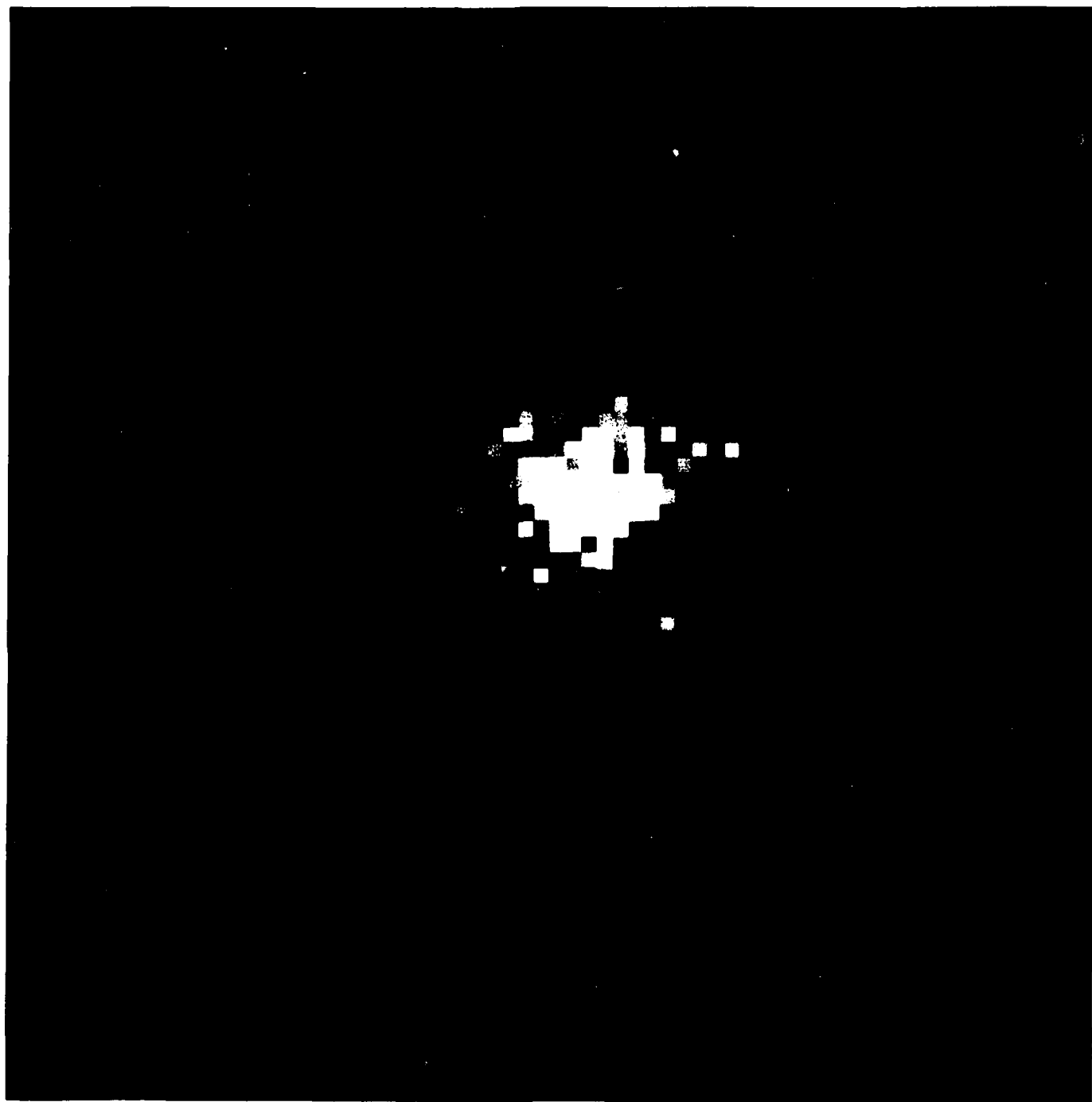


FIG. 8. Differential image of z Ori obtained with the MMT. (Raw data image at 5 mas pixel^{-1} . The resolution is that of the PSF shown in Fig. 5.)
HERBES *et al.* (see page 751)

THE H α CHROMOSPHERE OF ALPHA ORIONIS¹

JEREMY C. HEBDEN, ANDREAS ECKART, AND E. KEITH HUGH

Steward Observatory, University of Arizona

Received 1986 March 5; accepted 1987 January 1

ABSTRACT

Images have been obtained of the H α chromospheric envelope of α Ori at the diffraction limited resolution of the cophased Multiple Mirror Telescope. A phaseless image reconstruction was applied to speckle interferometric data obtained at continuum wavelengths, and the result was used to produce images of the highly extended H α region from results achieved using the differential imaging technique. Two such images are presented which were obtained from observations made almost 2 yr apart. Significant, and highly isotropic emission out to several stellar radii is exhibited. A very large optical depth in H α is indicated. A simple mathematical expression for the radially averaged profile of the images is derived empirically.

Subject headings: interferometry — stars: chromospheres — stars: individual

1. INTRODUCTION

The M supergiants are very luminous and are among the largest stars by volume. Their low surface gravity causes them to have highly extended atmospheres, and they are known to possess expanding envelopes of gas and dust which extend to distances of many stellar radii. The most intensively studied of all such stars has been α Orionis, an M2 Iab late-type supergiant. In addition to a wide variety of observations, several recent attempts have been made to model its extended atmosphere. A very common conclusion resulting from comparison with such models is that the actual nature of the star's atmosphere is a great deal more complicated than exemplified by the models. The theoretical study of α Ori has been further complicated by the recent discovery of two faint companion stars (Karoovska, Nisenson, and Noyes 1986), one of which is believed to orbit within a few stellar radii. However, a much clearer understanding of the observed anomalous behavior of the supergiant should result as a consequence of this discovery.

One major obstacle to a better understanding of supergiant atmospheres is that the heights and thicknesses of their chromospheres close to the star, in the region where the outward flow of matter is accelerated, has been relatively unknown. There exist both theoretical (Hartmann and Avrett 1984) and observational (Goldberg *et al.* 1982; Hebden *et al.* 1986) reasons for supposing that supergiant chromospheres may extend to several stellar radii above the photospheres. Absorption lines such as H α and Ca II 8542 provide a valuable diagnostic, since they are expected to be formed in such regions. Part of the α Ori visible spectrum containing the H α line was kindly provided for us by Dr. F. Chaffee and his staff at the Multiple Mirror Telescope (MMT). The spectrum, shown in Figure 1, was obtained using the MMT echelle spectrograph on 1986 January 15. The wavelength axis has been adjusted to accommodate the radial velocity of the star. The very strong H α line (the observed equivalent width is $\sim 1.1 \pm 0.1$ Å) is centered on 6563.4 Å. Such strong absorption suggests the existence of a chromosphere with significant optical depth in that line. Gray and Mullan (1985) suggest that an H α absorption line will be formed whenever the optical thickness in H α is

sufficiently large ($\tau > 20$), regardless of the specific distribution of electron density and temperature in the chromosphere of cool stars.

High spatial resolution measurements of α Ori have been made frequently ever since interferometric and speckle imaging techniques were first employed. The first actual two-dimensional image of the star was published by Lynds, Worden, and Harvey (1976). Further data reduction using their imaging technique (Worden, Lynds, and Harvey 1976; Wilkerson and Worden 1977; Welter and Worden 1980; McDonnell and Bates 1976) consistently demonstrated asymmetry in the image of α Ori at a number of wavelengths. Roddier and Roddier (1985) obtained an image which exhibited a partial shell-like structure, suggesting the existence of dust condensation close to the stellar disk. Recent images of α Ori obtained at Steward Observatory have been described by Hebden *et al.* (1986). An elongated region of H α emission was observed, which exhibited no apparent rotation relative to the sky over a 3 yr period. Until these most recent results, most speckle interferometric image reconstructions have been restricted to wide-band observations (20 Å or larger). This is due to the uncertainty of the previous imaging techniques at low photon fluxes in combination with the unavailability of appropriate narrow-band filters.

A one-dimensional analysis of speckle interferometric data obtained at several wavelengths by Cheng *et al.* (1986) produced an angular diameter of α Ori of 42.1 ± 1.1 mas, with a limb-darkening parameter highly dependent on observing bandpass. This value is consistent with many other estimates of the photospheric diameter of the supergiant (as summarized by White 1980). The diffraction-limited angular resolution of 2.3 m and 4 m class telescopes at, say, 6500 Å is 58 mas and 34 mas respectively. Thus the photospheric disk of α Ori is barely resolvable at best. However, the corresponding resolution of the fully phased MMT is only 20 mas, less than half the estimated disk diameter. In this paper we present images of the H α chromospheric envelope of α Ori obtained at this resolution, the highest currently available for imaging at optical wavelengths.

2. OBSERVATIONS

Differential speckle interferometry (DSI; Beckers 1982) observations of α Ori were made using the fully phased MMT

¹ Observations reported here were obtained at the Multiple Mirror Telescope Observatory, a joint facility of the Smithsonian Institution and the University of Arizona.

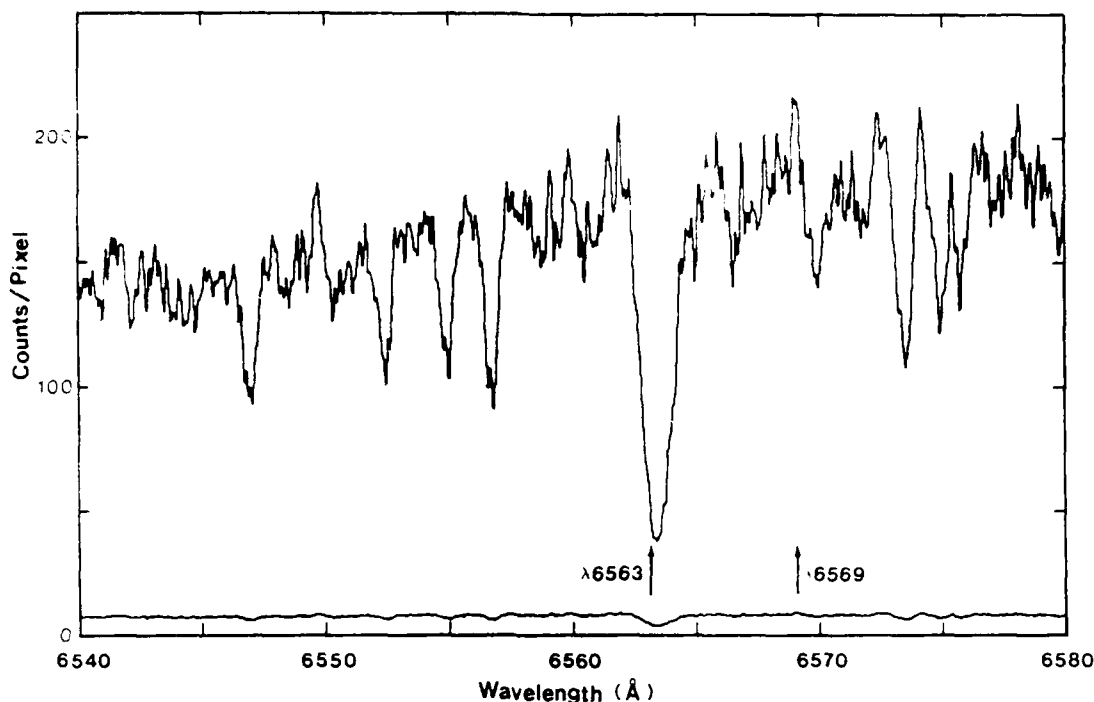


FIG. 1. Region of spectrum of α Ori containing H α absorption line. Positions of our two filters (1.2 Å bandwidth), in and out of the line, indicated. Lower curve estimated 1 σ noise contained in the spectrum.

on 1983 December 16/17, and again on 1985 November 2/4. Cophasing of the telescope, which is now a routine and relatively simple operation, is described by Hege *et al.* (1985) and Hebden, Hege, and Beckers (1986a). The DSI technique utilizes the differential speckle camera (Beckers, Hege, and Murphy 1983), which enabled the supergiant to be observed in the H α line (6563 Å, 1.2 Å effective bandwidth) and simultaneously in the nearby "continuum" (6569 Å, also 1.2 Å effective bandwidth). This is achieved by passing the light from the star through a solid Fabry-Perot etalon², which has a different narrow passband at two orthogonal polarizations, and then shifting one polarized image with respect to the other with a Wollaston prism. The polarization dependence was eliminated by the inclusion of a rotating quarter-wave plate which alternated the polarization state of the two images. In this way both images were observed in both polarization states equally. The temperature-controlled mica etalon was adjusted to accommodate the radial velocity of the star. Thus two speckle images (specklegrams) are produced which are recorded on video tape. The specklegram pairs (a few tens of thousands altogether) are later digitized eight bits deep into two 128 \times 128 pixel arrays. A more detailed description of the observing procedure is given by Hebden *et al.* (1986).

Both the observing wavelengths are indicated on the spectrum shown in Figure 1. For convenience, hereafter the 6569 Å bandpass is referred to as the "continuum" bandpass, although this is obviously not strictly true.

For calibration and technique verification purposes, several observations were made of the unresolved sources γ and ϵ Ori. Incidentally, the recently discovered secondary component of γ Ori (Papaliolis, Nisenson, and Ebstein 1985) is outside our field of view. Some of these point-source observations were also

made using a single wide (100 Å) bandpass filter for both the DSI observing channels. We recently reported (Hebden, Hege, and Beckers 1986a) that the MMT cophased configuration is currently stable over a period of at least 10 minutes with a standard error in optical path length of better than 12 μ m. This is insignificant compared to the 3.5 mm coherence length of our 6563 Å, 1.2 Å filter, and still quite smaller than the 30 μ m coherence length of a 5500 Å/100 Å filter. Thus such wide-bandwidth observations were feasible.

Shortly before the 1985 November observing run, one of the six constituent mirrors of the MMT was replaced with a spare while the original was realuminized. Unfortunately, the focal length of the short-term replacement had not been specified sufficiently accurately, and it was not possible to cophase it with any of the other five mirrors. Hebden, Hege, and Beckers (1986a) discuss the consequences of using the MMT in a five-mirror configuration and show that the effect on the overall resolution is small.

III. IMAGING METHODS

DSI produces diffraction-limited images which contain information about the object at two distinct but nearby wavelengths. The theory and reduction method has been discussed in much detail by Hebden, Hege, and Beckers (1986b). The technique involves deconvolving one specklegram (e.g., at H α) by another simultaneously acquired specklegram (e.g., in the nearby continuum). The result is called a differential image. Differential images of α Ori were obtained using 21,600 and 15,400 specklegram pairs from the 1983 and 1985 observing runs respectively. In addition, differential images were obtained of γ Ori, from H α :continuum data, and also from data recorded using a single 5500 Å/100 Å filter for both channels.

In order to obtain conventional images, i.e., images at the

² DayStar Filters, Pomona, CA

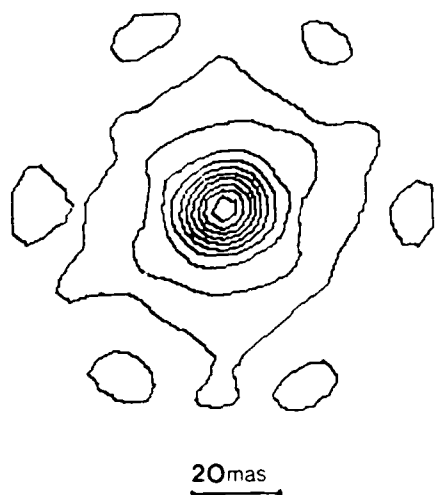


FIG. 2. Image of the point source γ Ori obtained at 5500 Å 100 Å using the MMT.

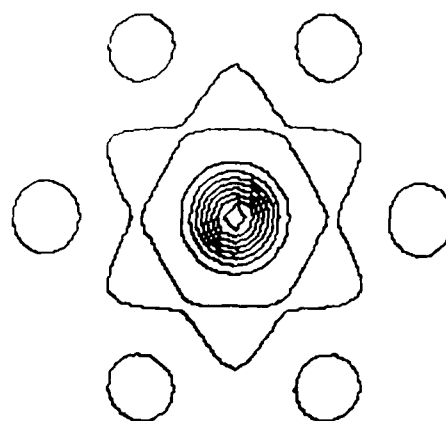


FIG. 3. Theoretical PSF of the MMT in its coherent six-mirror configuration.

H α bandpass alone, it is necessary to convolve the differential images with an image of the star in the continuum. Initially it was considered that perhaps an estimate of the continuum (6569 Å 1.2 Å) distribution of the supergiant could be obtained from a suitable wide-band observation (e.g., 6500 Å 100 Å) using a variation of the shift-and-add technique (Christou *et al.* 1986) which is particularly applicable to bright, wide-band observations. However, both one-dimensional (Cheng *et al.* 1986) and two-dimensional (Christou 1985) analyses of α Ori have shown that it is unrealistic to consider the star as having a typical continuum distribution. Due to blanketing of the visible spectrum by chromospheric lines, such as those of TiO (as evident in the spectrum shown in Fig. 1), the appearance of the star is likely to be bandwidth-dependent. Therefore, the distribution at 6569 Å should be obtained directly from the DSI data set itself.

The Fienup (1978) phaseless reconstruction method was used to produce images of α Ori at 6569 Å. The seeing effects were removed from the average debiased power spectrum of α Ori (6569 Å) by dividing it by a corresponding average debiased power spectrum of the unresolved source γ Ori. This invoked the reasonable assumption that the average seeing conditions throughout both observations were identical. An image is then obtained iteratively from the corrected α Ori amplitudes by assuming that there is a unique set of phases (except for a 180° rotational ambiguity) corresponding to the Fourier modulus of a real and positive image, and by assuming that the technique will converge to that set.

IV. TECHNIQUE VERIFICATION

We check the validity of a given method by testing whether it yields the correct result for a point source, which may be obtained analytically. In the case of the cophased MMT, which has a splendidly complex point-spread function (PSF), this exercise is particularly interesting.

Figure 2 shows an image of γ Ori, obtained using a single 5500 Å 100 Å filter, and Figure 3 shows the computed form of the PSF of the MMT in its six-mirror configuration. The agreement is excellent. An equally favorable comparison for the five-mirror configuration is given by Hebdén, Hege, and Beckers (1986a). Figure 4 shows another image of γ Ori

obtained using data recorded in the H α and nearby continuum (both bandpasses in which γ Ori is equally unresolvable). Although the result is noisier for the same number (1000) of specklegram pairs, there is nevertheless still excellent agreement with the analytical distribution. These results not only confirm the reliability of the imaging technique but demonstrate the effectiveness of the MMT as a coherent optical interferometer.

V. THE CONTINUUM IMAGES OF α ORIONIS

As mentioned above, images of α Ori at 6569 Å were obtained for both of our observations using the Fienup reconstruction method. These images are shown in Figures 5 and 6. The algorithm used was the error-reduction (Gerchberg-Saxton) algorithm, as described by Fienup (1982). The technique converged to these solutions within 200 iterations irrespective of our initial estimate of the complex phases. A small, broad seeing residual was apparent in the 1985 November image, due to an imperfect seeing calibration. This was removed by subtracting a Gaussian fit at radii at which the

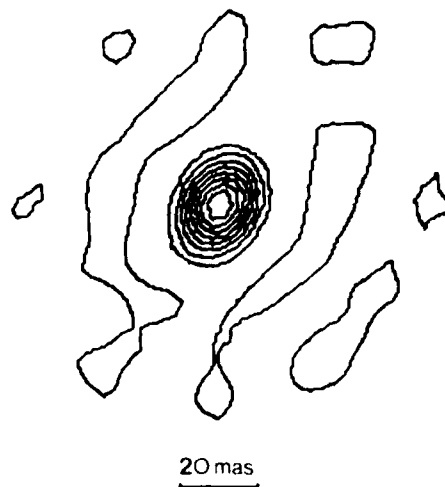


FIG. 4. Image of the point source γ Ori obtained in the H α line.

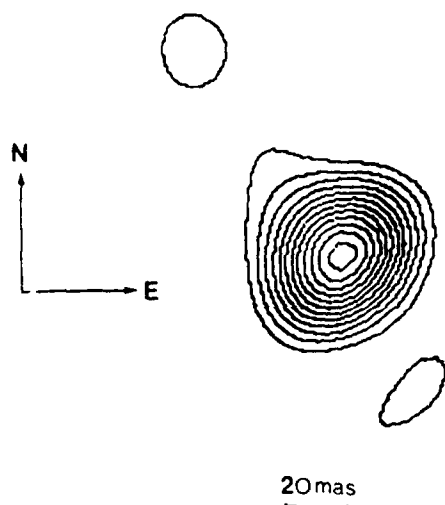


FIG. 5.—Fienup image reconstruction of the continuum (6569 Å) distribution of α Ori (1983 December).

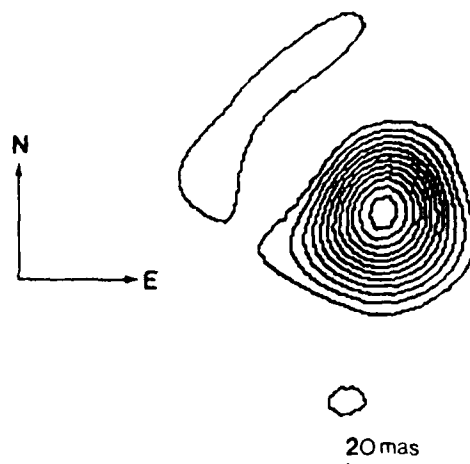


FIG. 6.—Fienup image reconstruction of the continuum (6569 Å) distribution of α Ori (1985 November).

1983 December image exhibits insignificant intensity (>40 mas). The image contours shown in Figures 5 and 6 are plotted at intervals of 8%. The asymmetrical features apparent outside the central disk of the star are most likely either systematic artifacts, due to the complex MMT PSF, or produced by second-order seeing calibration errors. Karovska, Nisenson, and Noyes (1986) suggest that the nearby companion is ~ 3.4 mag fainter than the supergiant at this wavelength. This corresponds to $\sim 4.4\%$ of the peak intensity of our images and thus is beneath the noise of the images. Incidentally, we hope to increase the effective signal-to-noise ratio of our continuum images in the future by employing matched-filter shift-and-add imaging techniques (Ribak, Hege, and Christou 1985), which are currently being developed for this purpose.

Despite the existence of low-power asymmetrical features, the radially averaged profiles of the two images are virtually

identical. Before using these results to produce images of the supergiant in the H α line, we checked whether the results were indeed sensible by comparing the radially averaged profiles with various models. Each model consisted of the MMT PSF (i.e., an image obtained for a point source) convolved with a limb-darkened disk defined by the expression

$$I(R) = (1 - L) + L \cos(\pi R / 2R_*), \quad (1)$$

where R_* is the radius of the disk and L is the degree of limb-darkening. Figure 7 shows one such comparison, where the disk radius is 20 mas. It is evident from Figure 7 that, for a given radius, the degree of limb-darkening may be specified very precisely. A best-fit of $L = 0.6 \pm 0.1$ for $R_* = 20$ mas is found. However, as discussed in Cheng *et al.* (1986), it is not possible to uniquely define both radius and limb-darkening simultaneously from a single measurement, even at this

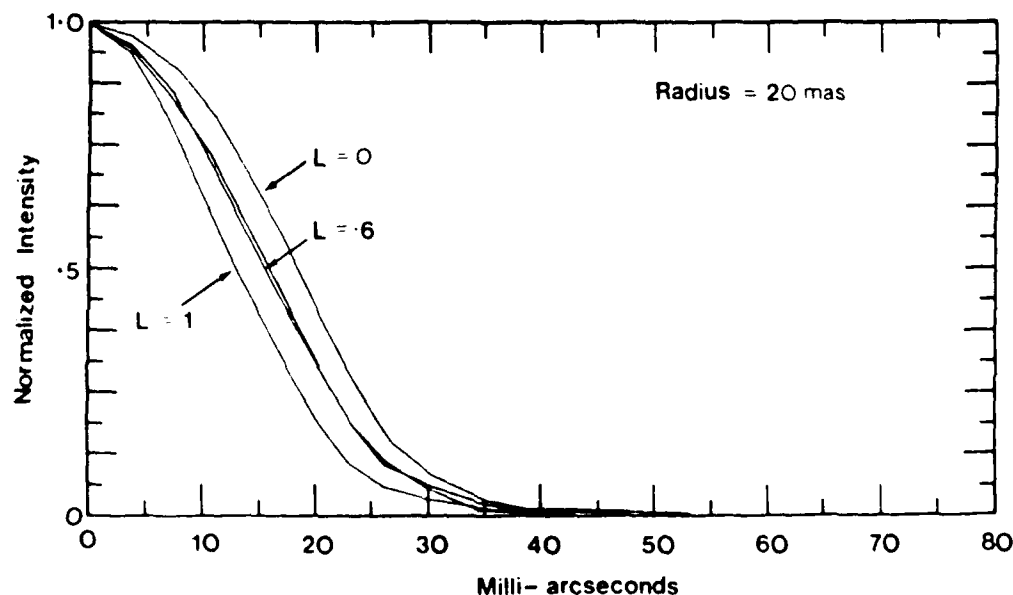


FIG. 7.—Radially averaged profile of the 1985 November continuum (6569 Å) image of α Ori compared to limb-darkened disk models.

TABLE 1
PARAMETERS OBTAINED BY FITTING
MODELS TO CONTINUUM
16569 Å IMAGES

Radius (mas)	Limb-Darkening (± 0.1)
17	0.0
18	0.2
19	0.4
20	0.6
21	0.8
22	0.9
23	1.0

resolution. Table 1 lists the equally excellent fits that were obtained over a range in stellar radius of $R_* = 17$ mas ($L = 0$) to $R_* = 23$ mas ($L = 1$). Cheng *et al.* (1986) have attempted to uniquely specify the radius of the photosphere of α Ori by assuming that it is wavelength-independent. The value of 21 mas they obtain is well within our range of possible radii. Tsuji (1978) also obtains a similar radius from a theoretical analysis of the supergiant's atmosphere. We have adopted a radius of 21 mas in the discussions which follow.

VI. THE H α IMAGES OF α ORIONIS

Images of α Ori in the H α line were obtained by convolving the differential image for each observation with the corresponding Fienup reconstruction continuum image. The latter reconstruction method has an inherent 180° rotational ambiguity. Thus convolutions were performed for each rotation of the continuum image. The final H α images selected, shown in Figures 8 and 9, were those containing the lowest amount of residual negativity. The contours are plotted at intervals of $\sim 5\%$. These results correspond to the orientations of the continuum images as shown in Figures 5 and 6. Because of the very large extent of the differential images of the supergiant, the images obtained in the H α line alone proved to be highly

insensitive to the orientation of, or even the presence of, the low-power asymmetrical features in the continuum images. Such insensitivity is desirable, since these features represent the only possibly significant source of phase error ambiguity or error due to poor seeing calibration. The DSI technique appears to be completely calibrated for seeing, as demonstrated by the results for point sources described in § IV. Since the differential images contain no 180° ambiguity and are insensitive to the continuum image orientation, the H α images are also unambiguous.

VII. DISCUSSION

Several striking and important characteristics are immediately apparent from the H α images of α Ori shown in Figures 8 and 9, and from their radially averaged profiles shown in Figure 10. First, the envelope of emission is very large. Significant intensity (greater than 1% of peak intensity) is evident out to a radius of ~ 95 mas, or $4.5 R_*$. The estimated signal-to-noise ratio in this region is $\sim 0.5\%$. Second, there is no apparent deviation from radial symmetry for either image out to a radius of ~ 50 mas. At larger radii, however, they both exhibit a small degree of asymmetry, corresponding to position angles of about 275° and 280°. This is reasonably consistent with the $118^\circ \pm 180^\circ$ elongation in the H α emission previously reported by Hebdén *et al.* (1986). Third, in neither image is a distinct photospheric component evident. Indeed, this was also apparent from the differential images of the supergiant before convolution with the continuum image, since there could exist no possible continuum distribution which could introduce an anomalously dominant central component.

Weymann (1962) and Goldberg (1979) note that radial velocities measured in the cores and wings of the H α line show no evidence of the variation observed in photospheric lines. Thus they conclude that the chromosphere is physically detached from the photosphere. A blue-shift in the absorption core supports the view that H α is formed in an expanding wind (see Fig. 1). A lunar occultation of the M2 Iab supergiant 119 Tau

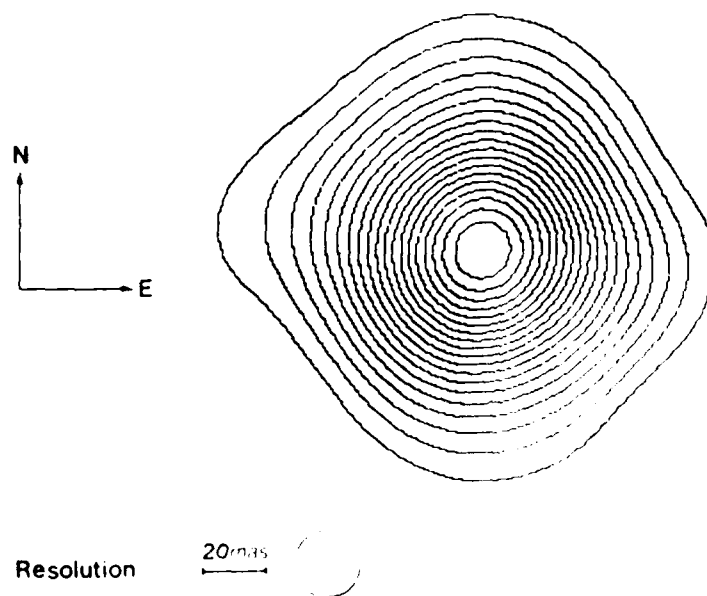
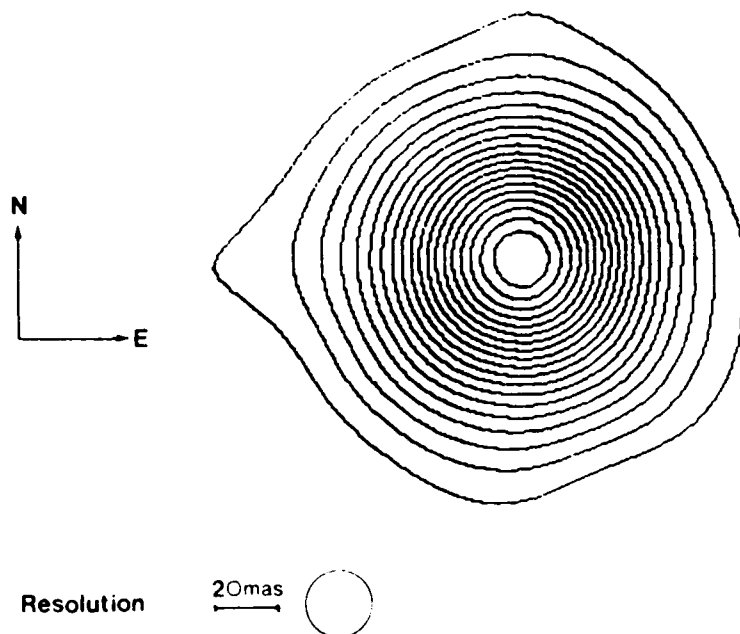


FIG. 8. Image of the H α envelope of α Ori obtained from observations made in 1983 December. Circle, 20 mas theoretical resolution of the MMT at H α .

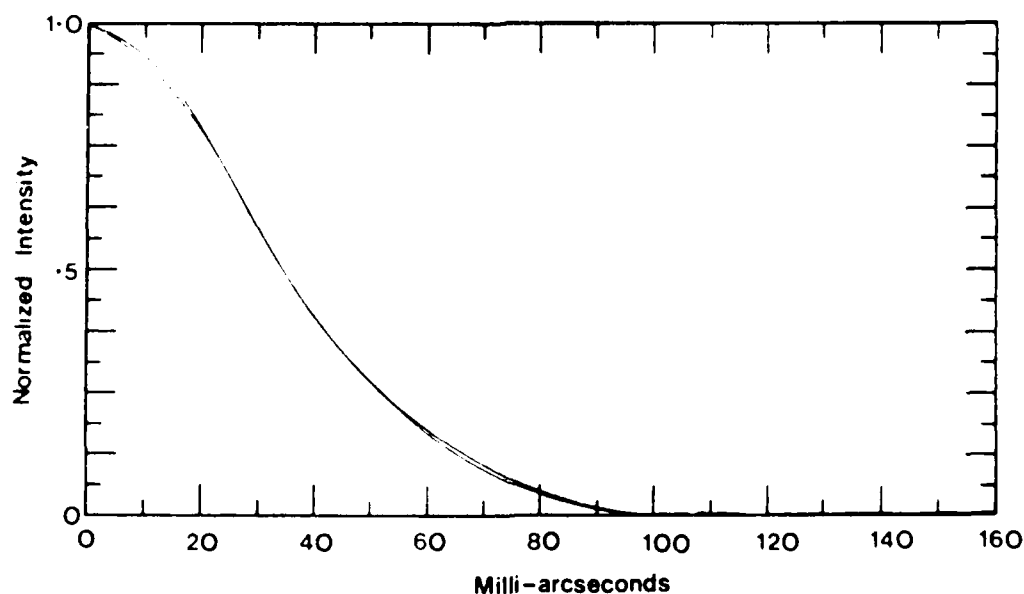
FIG. 9 Image of the H α envelope of α Ori obtained from observations made in 1985 November

(White, Kreidl, and Goldberg 1982) showed that the star's diameter in H α light was at least twice that observed in the continuum. However, the radial brightness distribution showed qualitative agreement with a model for an *optically thin* envelope. Such a model predicts an abrupt increase in intensity by a factor of 2 at the stellar limb. Patently, the radially averaged profiles shown in Figure 10 do not exhibit this characteristic.

Strong evidence for an extended chromosphere around α Ori has been obtained from radio observations. Altenhoff, Oster, and Wendker (1979) suggest that radiation at less than 20 GHz is that of a photosphere:chromosphere transition region extending $2-3 R_{\odot}$. Newell and Hjellming (1982) have con-

cluded that radio emission between 1 and 100 GHz is consistent with a warm chromosphere-like region extending from 1 to $4 R_{\odot}$. Both these estimates appear to conform to the approximate dimensions of the H α emission region we have observed.

In order to explain the observed behavior of cool winds of low-gravity stars, Hartmann and MacGregor (1980) investigated the possibility of such winds being driven by Alfvén waves. This was developed further by Hartmann and Avrett (1984) into preliminary models for the extended chromosphere of α Ori. They examined, in particular, the region within $\sim 5 R_{\odot}$ where the wind flow is being accelerated. The model they produce is consistent with the free-free emission in the radio spectrum region and also predicts a significant extension

FIG. 10 Radially averaged profiles of the H α images of α Ori

in the light of H α with a very large optical depth in that line. The authors kindly provided us with sufficient data so that we could compute a model H α surface brightness corresponding to our 1.2 Å bandwidth filter. The result we obtained was convolved with a suitable MMT PSF (since our images contain this also) and is shown compared to radial profiles of our H α images in Figure 11. The general shape of the observed emission is not represented well by the model, which appears to predict a greater central (photospheric) component. However, the radii at which both model and data fall to an intensity of $\sim 1\%$ of maximum coincide almost exactly ($4.5 R_\odot$).

Hartmann and Avrett conclude that the atmosphere of α Ori is "quasi-static" rather than rapidly expanding. They suggest that observed, nearly symmetric line profiles may be explained in terms of a "fountain" model, whereby only a fraction of ejected mass is accelerated to escape velocity. Draine (1981) has suggested that dust formation would be possible around α Ori at distances as close as $1.8 R_\odot$. A fountain model would, of course, produce higher gas densities, making dust formation more likely. However, most observational evidence (McCarthy, Low, and Howell 1977; Sutton *et al.* 1977; Bloemhof, Townes, and Vanderwyck 1984) suggests that most of the infrared emission at $10 \mu\text{m}$ does not originate close to the star. Our results show no evidence of inhomogeneity in surface brightness or obscuration which might be attributable to dust present within a few stellar radii.

Failure of the image profiles to conform to specific astrophysical models induced us to investigate their degree of correlation, empirically, with simple mathematical functions. A plot of the log of the intensity versus the log of the radius demonstrated that the images certainly do not conform to a simple power law. Then we investigated the agreement between the radial profiles and a function of the form

$$I(R) = I_0 a^{-1} (R/R_\odot)^n, \quad (2)$$

where a , σ , n , and I_0 are constants and R_\odot is the photospheric radius of the star. Such a distribution produces, when log

$[-\log(I/I_0)]$ is plotted against $\log(R/R_\odot)$, a straight line whose slope is equal to n , i.e.,

$$n = \frac{\log[-\log(I/I_0)]}{\log(R/R_\odot)} \quad (3)$$

Figure 12 shows such a plot produced from the radially averaged profile of the sum of the two H α images. There is an excellent linear relation over the range from $R = 0.3 R_\odot$ to $R = 4 R_\odot$. A value of $n = 1.933 \pm 0.008$ is obtained from a least-squares fit to the slope of the curve within this range. Thus the H α emission around α Ori has a strikingly Gaussian ($n = 2$) appearance. From the slope of a second plot of $\log(I/I_0)$ against $(R/R_\odot)^{1.933}$, we obtained a value of $\sigma = 2.038 \pm 0.012 R_\odot$ ($42.8 \pm 0.3 \text{ mas}$) for $a = e$. In other words, the intensity falls to a fraction $1/e$ of maximum at a radius of $\sim 2 R_\odot$, or $1 R_\odot$ from the surface of the star. Since the H α images still contain the MMT PSF, this value represents a very slight ($\sim 2\%$) overestimate of the actual physical distribution.

At the moment we are not able to qualify, in astrophysical terms, the perhaps surprising agreement of the radial distribution of our images with a function of the form given in equation (2). However, we are very confident indeed that this distribution does reflect the true nature of the H α chromosphere and is not a consequence of the imaging process.

An elongation in a northwest-southeast direction was shown to be dominant in all the H α images of α Ori reported by Hebdén *et al.* (1986). A slight northwest elongation is also evident in the very high resolution results we have presented here. Honeycutt *et al.* (1980) detected a K I $\lambda 7699$ gas shell surrounding the supergiant which extends to at least $50''$. They also noted that the northwest quadrant exhibited more intense K I emission, confirming the earlier observations of Bernat and Lambert (1976). They propose that this might be due to either an asymmetrical mass ejection or an asymmetrical stellar surface intensity. Honeycutt *et al.* (1980) estimate that the shell they observe was ejected ~ 4500 yr ago, and therefore it seems

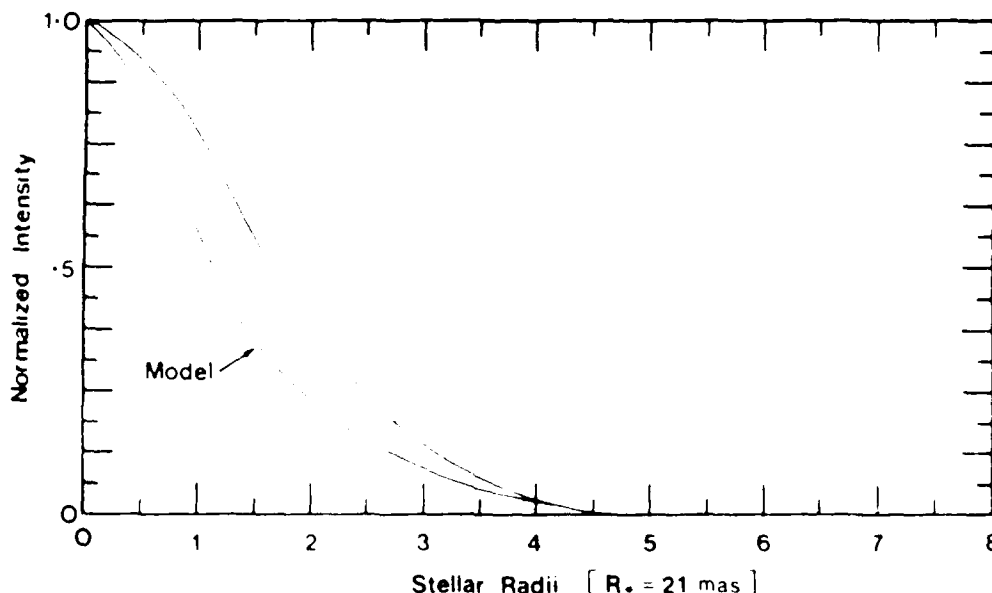


Fig. 11. Radially averaged profile in an H α image of α Ori compared to a model surface brightness distribution calculated by Hartmann and Avrett (1984).

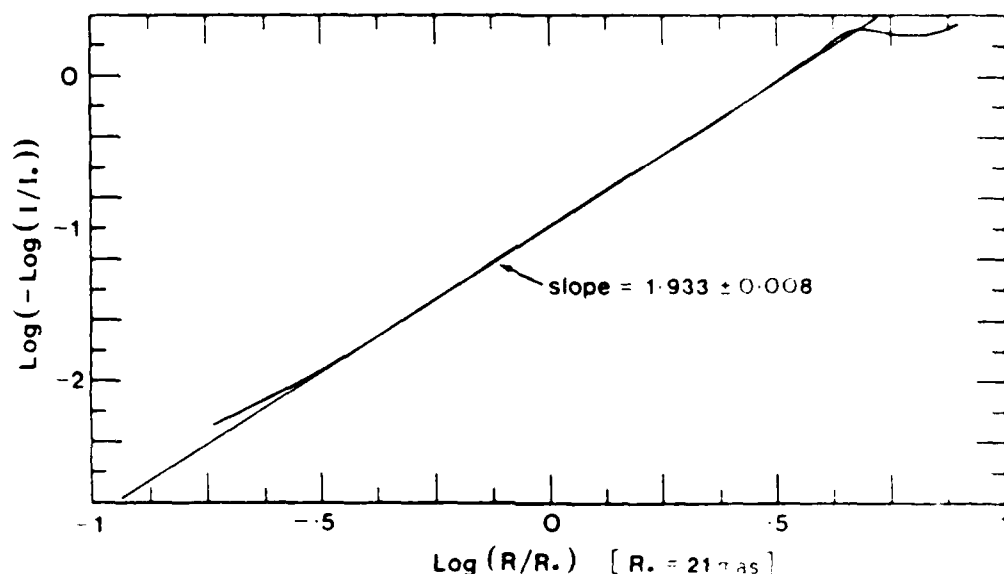


FIG. 12. Determination of the constant power n , as given in eq. (2), according to the linear relation expressed in eq. (3). A straight line is shown, produced from a least-squares fit between radii corresponding to $R = 0.3 R_0$ and $R = 4 R_0$.

unlikely that the same phenomenon would be responsible for producing the observed chromospheric elongation.

Finally, we should consider the possible influence of the recently discovered companion stars on the extended chromosphere of α Ori. Karovska, Nisenson, and Noyes (1986) have adopted a preliminary value of 50 mas for the semimajor axis of the closer star, implying that it is indeed buried well inside the H α envelope. The periastron of the orbit which has been proposed lies in the northeast quadrant, which appears to eliminate the possibility that the elongation we observe is that produced directly by the orbit of the nearest companion, perhaps in the form of a corotating shell of dust or gas. The distant companion was located at a position angle of 278 ± 5 and a distance of 510 ± 10 mas. No orbit has yet been established for it, and thus it is not yet feasible to attempt to connect the presence of the outer companion with asymmetry observed in the H α chromosphere.

VIII. CONCLUSIONS AND FUTURE WORK

The H α emission surrounding the supergiant star α Ori has significant intensity out to a radius of ~ 95 mas, or $4.5 R_0$. The optical depth at this wavelength is evidently very large. An asymmetry in the distribution is apparent in two observations made nearly 2 yr apart and has a similar position angle to that observed in past images of the star in the H α line. The radial extent of the H α emission appears to be in accordance with past optical and radio observations and agrees qualitatively with a model chromosphere derived by Hartmann and Avrett

(1984). The radially averaged intensity of the H α images of the supergiant exhibits a remarkable agreement with a Gaussian-like distribution.

Further H α DSI observations were made of α Ori in 1986 January, during which we obtained over 70,000 specklegram pairs. Reduction of this data is currently under way, and it is expected that it should yield an image of sufficient signal-to-noise ratio to enable us to investigate the intensity of the envelope out to less than 0.1% of the peak value ($6-7 R_0$). Further observations of the supergiant are planned at the Ca II $\lambda 8542$ line. A comparison of the relative intensities and extensions of the chromosphere at the two different emission lines will enable estimates to be made of the temperature structure and densities within a few stellar radii of the photosphere. Finally, we shall shortly be extending our investigations to the atmospheres of two other supergiants: α Scorpii and α Herculis.

We wish to thank Dr. L. Hartmann and Dr. E. H. Avrett for their assistance in enabling us to compare our data with their theoretical model. We are also very grateful to Dr. F. Chaffee, Dr. C. Foltz, and T. Fleming for providing the spectrum of α Ori. We also wish to acknowledge the contribution of R. Watkins for many hours of data digitization. This work has been supported in part by the National Science Foundation (grants AST-8113212, AST-8312976, and AST-8412206) and by the Air Force (contract F19628-84-K-0035).

REFERENCES

- Allenhoff, W. J., Oster, L., and Wendker, H. J. 1979, *Astr. J.*, **73**, L21.
 Beckers, J. M., Hege, E. K., and Murphy, H. P. 1983, *SPB Proc.*, **445**, 462.
 Bernat, A. P., and Lambert, D. L. 1976, *Ap. J.*, **210**, 395.
 Bloemhof, E. E., Townes, C. H., and Vanderwyck, A. H. B. 1984, *Ap. J. Letters*, **276**, L21.
 Cheng, A. Y. S., Hege, E. K., Hubbard, E. N., Goldberg, L., Strittmatter, P. A., and Cooke, W. J. 1986, *Ap. J.*, **309**, 737.
 Christou, J. C. 1985, Ph.D. thesis, New Mexico State University.
 Christou, J. C., Hege, E. K., Freeman, J., and Ribak, E. 1986, *J. Opt. Soc. Am.*, **4**, 3, 204.
 Cram, L. E., and Mullan, D. J. 1985, *Ap. J.*, **294**, 626.
 Draine, B. 1981, in *Physical Processes in Red Giants*, ed. I. Iben and A. Renzini (Dordrecht: Reidel).
 Fienup, J. R. 1978, *Opt. Letters*, **3**, 27.
 ———, 1982, *Appl. Optics*, **21**, 2758.

- Goldberg, L. 1979, *Quart. J. R. A. S.*, **20**, 361.
 Goldberg, L., Hege, E. K., Hubbard, E. N., Strittmatter, P. A., and Cocke, W. J. 1982, *Smithsonian Ap. Obs. Spec. Rept.*, **392**, 131.
 Hartmann, L., and Avrett, E. H. 1984, *Ap. J.*, **284**, 238.
 Hartmann, L., and MacGregor, K. B. 1980, *Ap. J.*, **242**, 260.
 Hebdén, J. C., Christou, J. C., Cheng, A. Y. S., Hege, E. K., Strittmatter, P. A., Beckers, J. M., and Murphy, H. P. 1986, *Ap. J.*, **309**, 745.
 Hebdén, J. C., Hege, E. K., and Beckers, J. M. 1986a, *SPIE Proc.* **628**, in press.
 ——— 1986b, *Opt. Eng.*, **25**, 712.
 Hege, E. K., Beckers, J. M., Strittmatter, P. A., and McCarthy, D. W. 1985, *Appl. Optics*, **24**, 2565.
 Honeycutt, R. K., Bernat, A. P., Kephart, J. E., Gow, C. E., Sandford, M. T., and Lambert D. L. 1980, *Ap. J.*, **239**, 565.
 Karovska, M., Nisenson, P., and Noyes, R. 1986, *Ap. J.*, **308**, 260.
 Lynds, C. R., Worden, S. P., and Harvey, J. W. 1976, *Ap. J.*, **207**, 174.
 McCarthy, D. W., Low, F. J., and Howell, R. 1977, *Ap. J. (Letters)*, **214**, L85.
 McDonnell, M. J., and Bates, R. H. T. 1976, *Ap. J.*, **208**, 443.
 Newell, R. T., and Hjellming, R. M. 1982, *Ap. J. (Letters)*, **263**, L85.
 Papaliolios, C., Nisenson, P., and Ebbstein, S. 1985, *Appl. Optics*, **24**, 287.
 Ribak, E., Hege, E. K., and Christou, J. C. 1985, *SPIE Proc.* **556**, 196.
 Roddier, F., and Roddier, C. 1985, *Ap. J. (Letters)*, **295**, L21.
 Sutton, E. C., Storey, J. W. V., Betz, A. L., Townes, C. H., and Spears, D. I. 1977, *Ap. J. (Letters)*, **217**, L97.
 Tsuji, T. 1978, *Pub. Astr. Soc. Japan*, **30**, 435.
 Welter, G. L., and Worden, S. P. 1980, *Ap. J.*, **242**, 673.
 Weymann, R. 1962, *Ap. J.*, **136**, 844.
 White, N. M. 1980, *Ap. J.*, **242**, 646.
 White, N. M., Kreidl, T. J., and Goldberg, L. 1982, *Ap. J.*, **254**, 670.
 Wilkerson, M. S., and Worden, S. P. 1975, *A. J.*, **82**, 642.
 Worden, S. P., Lynds, C. R., and Harvey, J. W. 1976, *J. Opt. Soc. Am.* **66**, 1243.

ANDREAS ECKART, JEREMY C. HEBDEN, and E. KEITH HEGE: Steward Observatory, University of Arizona, Tucson, AZ 85721

Differential speckle imaging with the
Cophased Multiple Mirror Telescope

J.C. Hebden, E.K. Hege

Steward Observatory, University of Arizona, Tucson, Az 85721

and J.M. Beckers

NOAO, 950 N. Cherry Ave., Tucson, Az 85726.

Abstract

A new technique known as Differential Speckle Interferometry has been applied to data obtained using the fully-phased six-mirror aperture of the Multiple Mirror Telescope. By observing stellar objects at two distinct wavebands simultaneously, differences in the object resulting from the different wavelengths can be derived. Observations were made of the supergiant star Alpha Orionis in order to investigate the Hydrogen-alpha emission from the surrounding envelope. The data reduction process consists of a frame-by-frame weighted deconvolution procedure. This process involves an inherent Wiener-type filtering which must be removed in order to preserve high spatial frequency information. Results for Alpha Orionis and for the unresolved source Gamma Orionis are presented.

Introduction

Differential Speckle Interferometry¹ (DSI) is a technique in which simultaneous speckle images (specklegrams) obtained in two nearby wavelengths are compared in order to derive image information relating to the difference in the appearance of the object resulting from the differences in the observing wavelength. For example such differences might be produced by Doppler shifts, stellar emission or absorption lines, and Zeeman effects. The technique utilizes the Differential Speckle Camera² which incorporates a solid Fabry-Perot etalon which has different narrow passbands (0.4Å - 1.6Å) at two orthogonal polarizations. One polarized image is shifted with respect to the other using a Wollaston prism. Adjustment of the etalon temperature shifts the bandpasses for the two polarizations. The bandpass separation (0.2Å - 8.0Å) and full-width-at-half-maximum at peak transmission are dependent on the choice of mica spacer in the etalon. A half-wave plate is employed to chop between the two polarization states in each of the two resulting observing channels, thus enabling the removal of object polarization dependency on the data.

In December 1983 the Multiple Mirror Telescope (MMT) was used in its fully-coherent six-mirror configuration to obtain DSI observations of the M-type supergiant Alpha Orionis and the unresolvable source Gamma Orionis. The obtainable resolution was thus equivalent to that of a 6.66 meter aperture. The stars were each observed at the Hydrogen-alpha waveband (6563Å, bandpass 1.2Å) and simultaneously in the nearby continuum about 6Å away. The altazimuth MMT mount permitted DSI observations of the supergiant at two distinct sky position angles, separated by about 80 degrees. This effective rotation of the detector system enables a very strong validation of the technique by indicating that any significant features seen in the resulting analysis are associated with the object rather than produced as artifacts of the methodology. Video specklegram pairs were recorded with 15ms exposures at the rate of 7.5 Hz, equivalent to every fourth video frame. Excluding light from three out of every four frames enables the image intensifier afterglow to decay significantly between exposures so that unevenness in the background signal can be removed by on-line subtraction of consecutive frames. The 15ms exposure time is sufficiently short to effectively freeze the atmospheric turbulence so that specklegrams retain frequencies up to the diffraction limit of the telescope. Post-observational data processing begins with digitization of the specklegrams 8 bits deep in a 128 x 128 pixel array by a Grinnell digital television system. The digitized data is stored on 9-track tapes using the Steward Observatory Point 4 minicomputer system.

The innovative utilization of two simultaneously acquired specklegrams allows information relating to the atmospheric behaviour to be extracted from the brighter, high signal-to-noise ratio (SNR) reference (i.e. continuum) specklegrams in order to remove such effects frame-by-frame from the corresponding line (in this case H-alpha) specklegrams. Thus astronomical information can be derived with a far higher SNR than that typically obtainable using single image (conventional) speckle interferometry. Petrov et al.³ show that the overall SNR for DSI is equal to the geometric mean of the

* The MMT is a joint facility of the University of Arizona and the Smithsonian Institution.

two component specklegram SNRs. Though it is desirable to implement a reference specklegram as bright as possible, at the moment we are constrained to the use of a single detector so the line/reference intensity ratio may not be too large without sacrificing single photon detection in the line specklegram. Note that a unique unambiguous image of an object at either wavelength can only be derived using the DSI technique described here if the object intensity distribution at the other wavelength is known: i.e. this is a comparative technique.

Data reduction method

At the H-alpha waveband the 6.86 meter effective aperture of the cophased MMT corresponds to a diffraction limit of about 20 milli-arcseconds (mas). Thus Alpha Orionis, which most measurements show to have a continuum diameter of about 50mas, is quite easily resolved by the MMT. Whereas reference specklegrams obtained in the continuum with the MMT can not be used to deconvolve the corresponding line specklegrams so as to produce an actual image, performing such a deconvolution can still enable information relating to the physical differences at the different wavelengths to be derived.

The adopted data reduction procedure consists of performing frame-by-frame complex deconvolutions of the H-alpha specklegrams by their simultaneously acquired counterparts. Performing a complex deconvolution, a quotient in Fourier space, normally introduces spurious effects associated with the presence of small numbers in the denominator. In order to avoid this, each complex quotient is weighted by the reference power spectrum and summed over a large number of frames. The resulting "Differential Image" of an object in the line emission with respect to its appearance in the nearby continuum may be represented by the expression

$$FT^{-1} \frac{\sum_N \frac{h(u,v)}{c(u,v)} \cdot |c(u,v)|^2}{\sum_N |c(u,v)|^2} \quad (1)$$

where N = the ensemble of DSI specklegram pairs,
 $h(u,v)$ = Fourier transform of the "line" specklegram,
 and $c(u,v)$ = Fourier transform of the "continuum" specklegram.

Since $|c(u,v)|^2 = c^*(u,v) \cdot c(u,v)$, where $*$ denotes the complex conjugate, this expression may be rewritten as

$$FT^{-1} \frac{\sum_N h(u,v) \cdot c^*(u,v)}{\sum_N |c(u,v)|^2} \quad (2)$$

Thus the reduction process involves calculating the summed cross-spectra between the two specklegrams and the summed power spectra in the continuum. In theory, the true object intensity distribution in the line is derived by convolving the differential image with a pre-determined object intensity distribution at the reference wavelength.

Initial results

Figure 1 shows a differential image of the point source Gamma Orionis obtained using 1000 specklegram pairs. Since it may be assumed that the star is unresolved at both the H-alpha and nearby continuum wavebands, equation 2 becomes equivalent to unity within the limits that the spatial frequencies u and v are defined. Thus the differential image of Gamma Orionis is essentially the (inverse) Fourier transform of a cylindrical (top-hat) function with radius equal to the frequency cut-off of the telescope. The result is therefore a Jinc function ($J_1(r)/r$) whose half-power width is expected to be about $0.61\lambda/D$ radians, or about 12mas for the 6.86 meter aperture of the MMT at the H-alpha waveband. It is interesting to note that this appears to suggest that the effective resolution of a differential image is twice that of a conventional image. However, analysis shows that the resolution power (i.e. the ability to distinguish two close objects) is not actually enhanced. The image scale in figure 1 is equal to about 5.2mas per pixel and hence the half-power width (about 3 pixels) agrees well with the expected result. The non-uniformity of the first secondary maxima suggests that there was probably less than perfect optical coherence between the six constituent mirrors of the MMT. A region of a second ring is also apparent.

Figure 2 shows a differential image of Alpha Orionis obtained for another 1000 frames of data. The overall SNR looks poorer, even though the supergiant star is brighter in

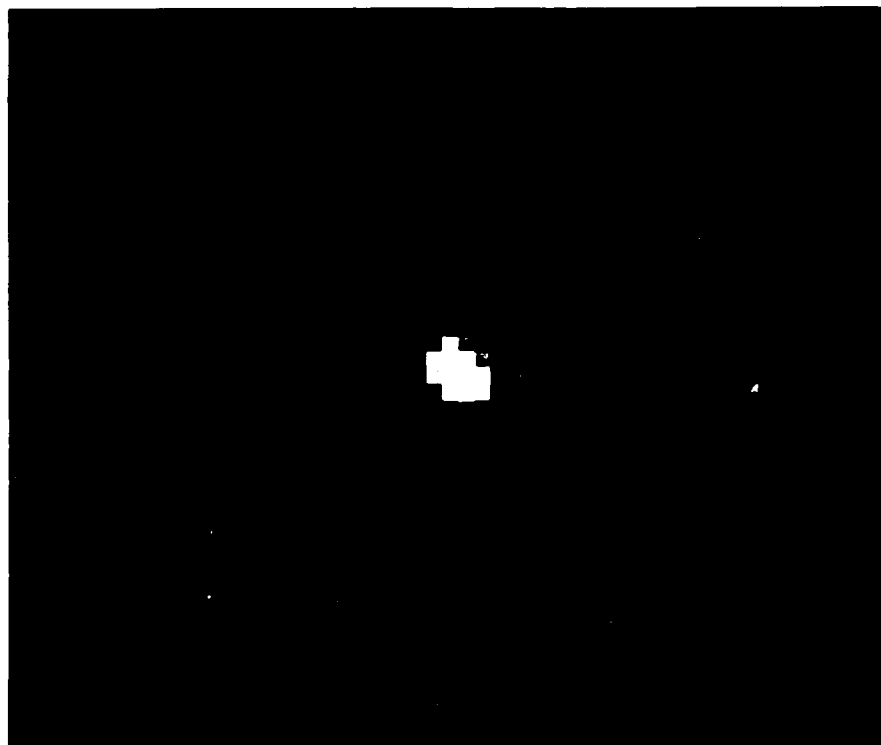


Figure 1. A small, bright, cross-shaped object in the center of a dark field.

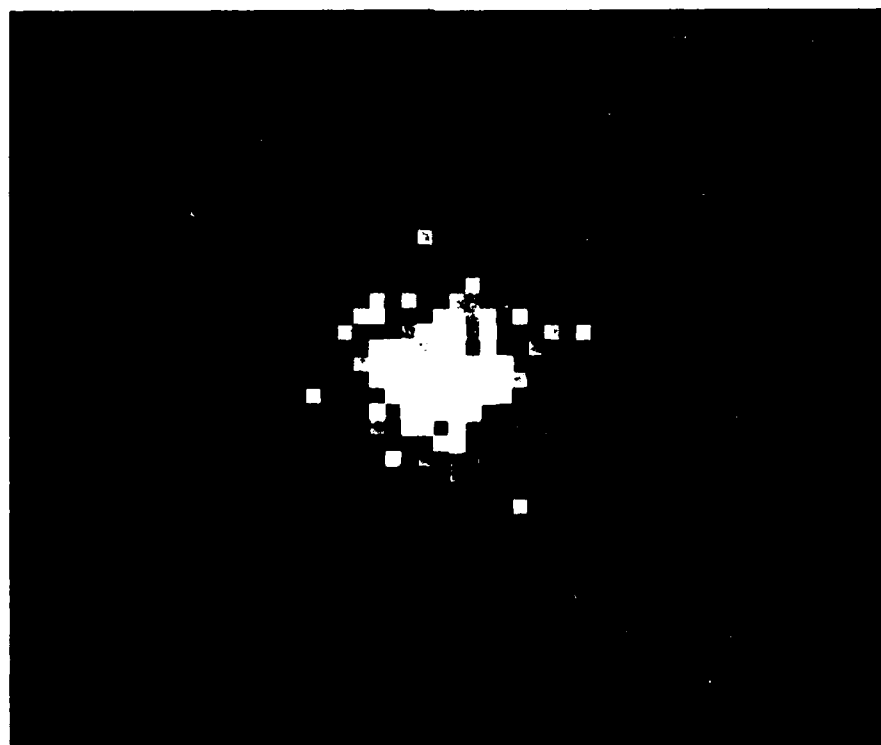


Figure 2. A large, bright, cross-shaped object in the center of a dark field.

the bandpass used, because the object is resolved (more photons per speckle but distributed in considerably larger speckles). Further differential images of Alpha Orionis were generated using about 7000 frames of data for each sky position angle. Though radial average measurements confirmed the existence of structure over a diameter of at least 150mas, very little evidence of the expected 80 degree image rotation was observed in these raw results.

These images do have additional significance in that they are the first images ever obtained at the full resolution of the MMT. They also demonstrate the successful implementation of the MMT as an imaging optical interferometer.

Understanding differential images

It is important to appreciate that a differential image is not an image in the conventional sense. For instance, consider the case where a source has a far more complex structure in the line emission than in the reference waveband (such as might be expected for Alpha Orionis at H-alpha with respect to the nearby continuum). Since convolution of the differential image with the pre-determined reference object distribution yields the true line intensity distribution, the differential image must contain negativities for the high frequency information to be introduced.

We also know that an expression for the differential image must contain a Jinc function term to which it is reduced when the line and reference object intensity distributions are equivalent to delta functions (i.e. a point source). This suggests the relationship

$$D(x,y) * O_c(x,y) = O_h(x,y) * J(x,y) \quad (3)$$

where $D(x,y)$ = differential image,
 $O_c(x,y)$ = object intensity distribution in the continuum,
 $O_h(x,y)$ = object intensity distribution in the line,
 $J(x,y)$ = a Jinc function (see above text),
 and where * denotes convolution.

A detailed analysis of the reduction technique has revealed that the weighted deconvolution quotient in equation 2 contains a form of inherent Wiener-type filter which suppresses the signal at high spatial frequencies. It can be shown that the power-spectra in the denominator contain a noise-bias term constant for all frequencies whereas the cross-spectra in the numerator are bias free. In addition, both summations contain a multiplicative term which is equal to the Fourier transform of the detector single photon point spread function. Thus equation 2 can be rewritten as

$$FT[D(x,y)] = \frac{\sum_N XS.g(u,v)}{\sum_N [PS + \bar{n}].g(u,v)} = \frac{\sum_N XS}{\sum_N [PS + \bar{n}]} \quad (4)$$

where XS and PS are the noise-bias free spectra,
 $g(u,v)$ = the detector function,
 and \bar{n} = the mean number of photon events per frame.

Equation 4 can then be separated into a "noise-bias free" differential image and a "filter" term as shown below.

$$FT[D(x,y)] = \frac{\sum_N XS}{\sum_N PS} \cdot w_c(u,v) \quad (5)$$

$$w_c(u,v) = \frac{\sum_N PS}{\sum_N PS + \sum_N \bar{n}} \quad (6)$$

$w_c(u,v)$ is of the form of a Wiener-type filter such that signals at high spatial frequency below the diffraction limit are suppressed as the (frequency independent) noise term becomes significant compared to the power-spectrum signal.

In order to prevent this inherent filtering effect, the bias must be removed from the recorded power-spectra in the denominator of equation 4. To achieve this it was assumed that the multiplicative detector response term was equivalent to a Gaussian. Hence

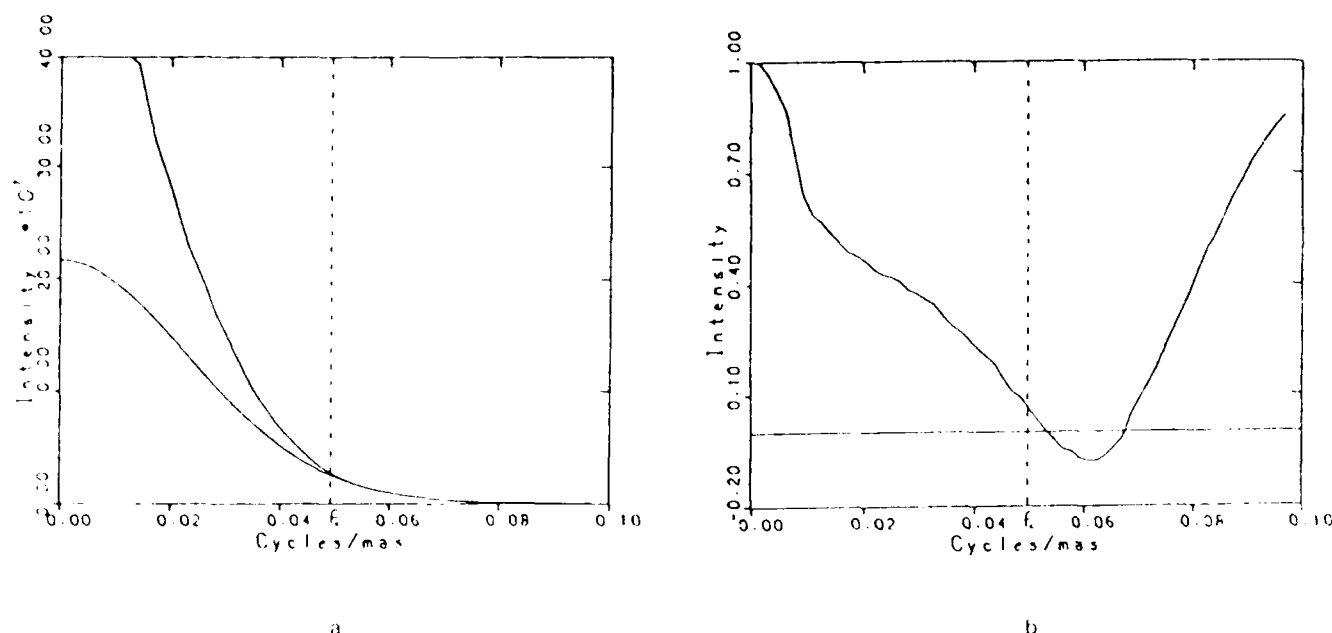


Figure 3. The debiasing process as applied to the Alpha Orionis data.

debiasing involved subtraction of a Gaussian model fitted to the data at spatial frequencies greater than the telescope cut-off frequency.

Figure 3 illustrates the debiasing process as performed for the Alpha Orionis data. Figure 3a shows the radially averaged profiles of the co-added continuum power-spectra and a Gaussian fitted above the cut-off frequency f_c . The filter $w_c(u,v)$ is obtained by dividing their difference (i.e. the debiased power spectra) by the original power spectra (from equation 6) and is shown in figure 3b. The spurious large signal at high ($f > f_c$) frequencies is produced by small number division. Note that the form of the filter is what we might expect from a resolved object (producing a central broad spike of low spatial frequencies) which also contains unresolved features on or around the stellar disk (signal exists out to the telescope cut-off). The bias-free differential image is then obtained by dividing the cross-spectra by the debiased power-spectra. This quotient also contains spurious signal due to small number division at large frequencies and therefore it is multiplied by a cosine-bell apodizing function (radius equal to f_c) before inverse Fourier transformation.

In conclusion, for real detectors and finite photon statistics equation 3 should be re-expressed as follows.

$$D(x,y) * O_c(x,y) = O_h(x,y) * J(x,y) * W_c(x,y) \quad (7)$$

where $W_c(x,y)$ is the Fourier transform of the filter $w_c(u,v)$.

Further results

Figures 4a and 4b show the differential images of Alpha Orionis at the two sky position angles after removal of the noise bias terms. About 7000 specklegram pairs were used for each image. At large radii there appears to be no evidence of asymmetrical structure which is not still noise dominated. There are several possible reasons for this. Firstly, the MMT sky-rotator was not employed due to technical difficulties and consequently the stars were permitted to rotate by about 9 degrees during each of the two integrations, blurring the image at large radii. Secondly, imperfect coherence between the six mirrors may be responsible for the systematic fringes apparent in these images. However, at small ($< 30\text{mas}$) radii, where the results have high SNR, there is considerable evidence that an elongated asymmetric feature in the image is observed,

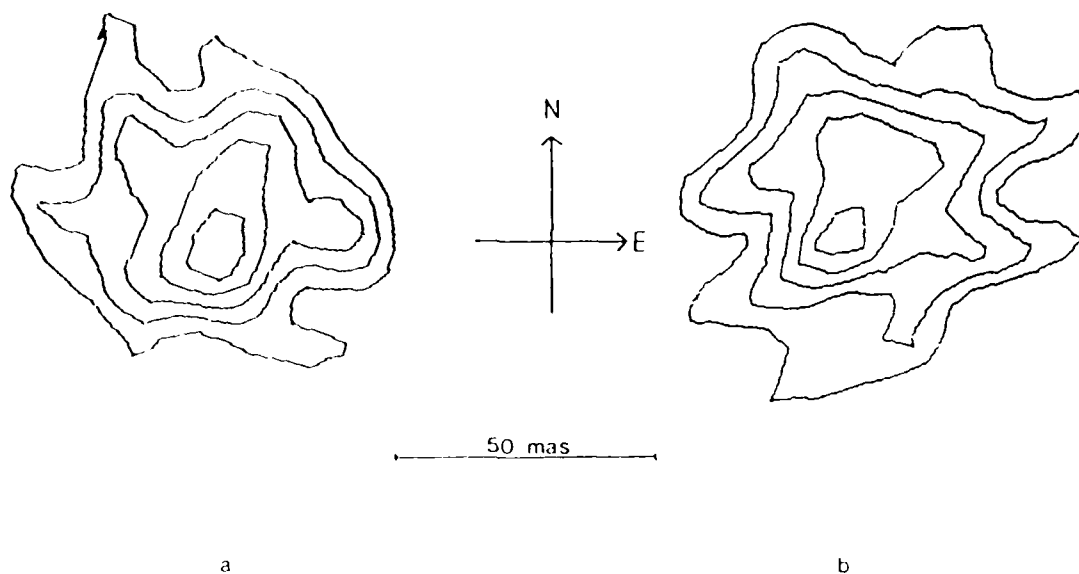


Figure 4. Differential images of Alpha Orionis at two sky position angles after removal of the noise bias terms.

rotated exactly as predicted.

Discussion

In order to significantly reduce the vast amount of computer time required to perform the DSI reduction process it was initially decided to extract the central 64×64 pixels from each of the 128×128 digitized data frames. All the results described above were achieved using this smaller data window. The SNR of the images produced so far can be much improved by i) utilising the full 128×128 data frames, and ii) reducing the 20,000 or so data frames from the Alpha Orionis observation that have yet to be analysed. Furthermore we hope that additional, better quality, MMT data can be obtained in the near future, at H-alpha and other wavebands such as the singly ionized calcium lines (e.g. 8542Å).

Eventually we wish to implement a dual-detector system. By having a separate detector for each of the line and reference specklegrams, there need be no restriction on the relative intensity, thus enabling a much greater SNR as explained earlier.

Several other imaging techniques have been applied to observations of Alpha Orionis in an attempt to study the resolved disk of the supergiant and its extended atmosphere⁴. These have all shown overwhelming evidence for the existence of aysmmetrical structure surrounding the star in H-alpha light and, as the relatively low SNR results presented here have shown, for the presence of inhomogenities within the stellar disk.

Acknowledgments

The work described here has been supported in part by the National Science Foundation (grants AST-8113212, AST-8201092).

References

1. Beckers, J.M., Opt. Acta, 29, 4, 1982
2. Beckers, J.M., Hege, E.K. and Murphy, H.P., Proc. SPIE, vol. 445, Instr. in. Astron., p462, 1983
3. Petrov, P., Roddier, F. and Aime, C., Submitted to J. Opt. Soc. Am. A
4. Hedden, J.C., Christou, J.C., Cheng, A.Y.S., Hege, E.K., Strittmatter, P.A. and Beckers, J.M., Submitted to Astrophys. J.

Differential speckle imaging with the cophased Multiple Mirror Telescope

J. C. Hebden
E. K. Hege

Steward Observatory
University of Arizona
Tucson, Arizona 85721

Jacques M. Beckers

National Optical Astronomy Observatories
950 N. Cherry Ave.
Tucson, Arizona 85726

Abstract. Differential speckle interferometry has been applied to data obtained using the fully phased six-mirror aperture of the Multiple Mirror Telescope. Wavelength-dependent differences in the appearance of a stellar object are derived from simultaneous observations at two distinct wavebands. The supergiant star Alpha Orionis was observed this way to investigate its appearance in hydrogen-alpha emission. Data reduction consists of a frame-by-frame weighted deconvolution. An inherent Wiener-type filtering must be removed in order to preserve high spatial frequency information. Results for Alpha Orionis are compared to similar results for the unresolved source Gamma Orionis.

Subject terms: speckle; differential speckle interferometry; astronomy; Multiple Mirror Telescope; phased array optical imaging.

Optical Engineering 25(6): 712-715 (June 1986)

CONTENTS

1. Introduction
2. Data reduction method
3. Initial results
4. Understanding differential images
5. Further results
6. Discussion
7. Acknowledgments
8. References

1. INTRODUCTION

Differential speckle interferometry (DSI) is a technique invented by Beckers¹ in which two speckle images (specklegrams), obtained simultaneously in two wavelengths, are compared to derive information about the difference in the appearance of the object due to differences in the observing wavelengths. The differential speckle camera² uses a mica Fabry-Perot etalon (Dobrowolski filter³) to transmit two narrow bandpasses simultaneously at two orthogonal polarizations. Control of the etalon temperature sets the bandpasses for the filter. The bandpass separation (6 Å) and the full-width-at-half-maximum at peak transmission (1.2 Å) at each bandpass are set by the thickness of the mica etalon. The polarized specklegrams are separated using a Wollaston prism. A half-wave plate is employed to alternate the two polarization states in the two observing channels, thus enabling unpolarized observations. The two resulting specklegrams are imaged simultaneously onto the photocathode of a single four-stage electrostatic image intensifier that is lens-coupled to a plumbicon TV camera.

In December 1983 the Multiple Mirror Telescope (MMT) was used in its fully coherent six-mirror configuration⁴ to obtain DSI observations of the M-type supergiant Alpha Orionis and the unresolvable source Gamma Orionis. The

maximum obtainable resolution was thus equivalent to that of a 6.86 m aperture. The filter was set to observe each star at the hydrogen-alpha ($H\alpha$) waveband (6563 Å, bandpass 1.2 Å) and simultaneously in the nearby continuum about 6 Å away. The altazimuth MMT mount permitted DSI observations of the supergiant to be made at two distinct sky position angles separated by about 80°. Video specklegram pairs were recorded at the rate of 7.5 Hz, equivalent to every fourth video frame (30 Hz interlaced). Excluding the light from three out of every four frames enables the image intensifier afterglow to decay significantly between exposures so that the nonuniform background signal can be removed by on-line subtraction of consecutive frames. The 17 ms exposure time (single video field time) is sufficiently short to effectively freeze the atmospheric turbulence so that specklegrams retain frequencies up to the diffraction limit of the telescope. The videotaped dual specklegrams are digitized 8 bits deep in a $2 \times 128 \times 128$ pixel array by a Grinnell Systems digital television system.

The innovative utilization of two simultaneously acquired specklegrams allows the atmospheric information to be extracted from the brighter, high signal-to-noise ratio reference (continuum) specklegrams in order to remove the atmospheric distortions frame by frame from the corresponding line ($H\alpha$) specklegrams. Thus, astronomical information can be derived with a far higher SNR than is typically obtainable using single-image (conventional) speckle interferometry. Petrov et al.⁵ show that the overall SNR for DSI is equal to the geometric mean of the two component specklegram SNRs. A unique unambiguous image of an object at either wavelength can be derived from DSI results only if the object intensity distribution at the other wavelength is known. This is a *comparative* technique yielding information relating to the physical *differences* in the images at the different wavelengths.

2. DATA REDUCTION METHOD

The data reduction procedure consists of frame-by-frame complex deconvolution of the $H\alpha$ specklegrams by their simultaneously acquired counterparts. Complex deconvolution, a quotient in Fourier space, normally introduces spurious effects associated with the presence of small numbers (or

Invited Paper ST 105 received Oct. 22, 1985; revised manuscript received Jan. 7, 1986; accepted for publication March 14, 1986; received by Managing Editor March 21, 1986. This paper is a revision of Paper 556-41 which was presented at the SPIE International Conference on Speckle, Aug. 20-23, 1985, San Diego, Calif. The paper presented there appears (unrefereed) in SPIE Proceedings Vol. 556.

© 1986 Society of Photo-Optical Instrumentation Engineers.

zeros) in the denominator. To avoid this, each complex quotient is weighted by the reference power spectrum and summed over a large number of frames. The "differential image" of the object in the line emission with respect to its appearance in the nearby continuum is represented by the expression

$$FI = \frac{\sum \frac{h(u,v)}{c(u,v)} |c(u,v)|^2}{\sum |c(u,v)|^2} \quad (1)$$

where N is the ensemble of DSI specklegram pairs, $h(u,v)$ is the Fourier transform of the "line" specklegram, and $c(u,v)$ is the Fourier transform of the "continuum" specklegram.

Since the reference power spectrum (weights) $|c(u,v)|^2 = c^*(u,v)c(u,v)$, where $*$ denotes the complex conjugate, this expression may be rewritten as

$$FI = \frac{\sum h(u,v)c^*(u,v)}{\sum |c(u,v)|^2} \quad (2)$$

Thus, the reduction process involves calculating the summed cross spectra between the two specklegrams and the summed power spectra in the continuum. Since power spectra contain a noise bias that is nonzero at all spatial frequencies, the denominator is never zero. In theory, the true object intensity distribution in the line is derived by convolving the differential image with a predetermined object intensity distribution at the reference wavelength.

3. INITIAL RESULTS

At the $H\alpha$ waveband the 6.86 m effective aperture of the cophased MMT corresponds to a DSI diffraction limit of about 12 milliarcsec. Thus, Alpha Orionis, which most measurements show to have an effective continuum diameter of about 50 milliarcsec, is quite easily resolved by the MMT.

Figure 1 shows a differential image of the point source Gamma Orionis obtained using 1000 specklegram pairs. Since it may be assumed that the star is unresolved at both the $H\alpha$ and nearby continuum wavebands, Eq. (2) becomes equivalent to unity within the limits that the spatial frequencies u and v are defined (i.e., up to the diffraction limit). Thus, the differential image of Gamma Orionis is essentially the (inverse) Fourier transform of a cylindrical (top-hat) function with radius equal to the frequency cutoff of the telescope. The result is therefore a Jinc function $[J_1(r)/r]$ whose half-power width is expected to be about $0.61 \lambda/D$ radians, or about 12 milliarcsec for the 6.86 m aperture of the MMT at the $H\alpha$ waveband. This appears to suggest that the effective resolution of a differential image is twice that (20 milliarcsec) of a conventional image. However, analysis shows that the resolution power (the ability to distinguish two close objects) is not actually enhanced. The image scale in Fig. 1 is equal to about 5.2 milliarcsec per pixel, and hence the half-power width (about 3 pixels) agrees well with the expected result. The nonuniformity of the first secondary maximum suggests that there was probably less than perfect optical coherence between the six constituent mirrors of the MMT. A region of a

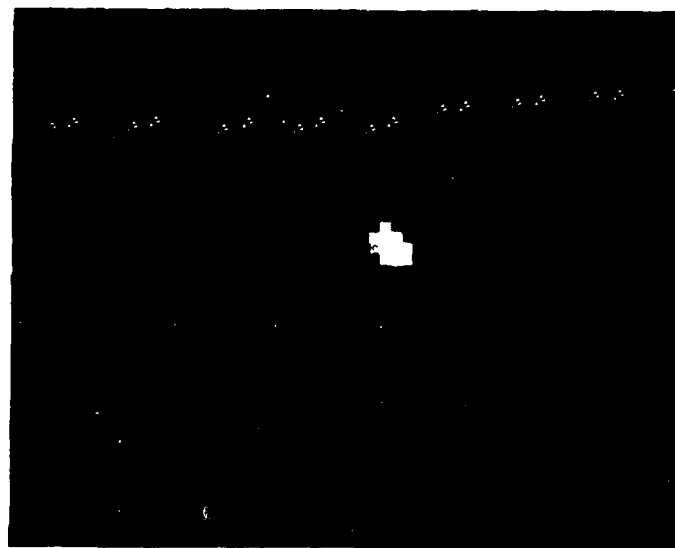


Fig. 1. Differential image of Gamma Orionis.

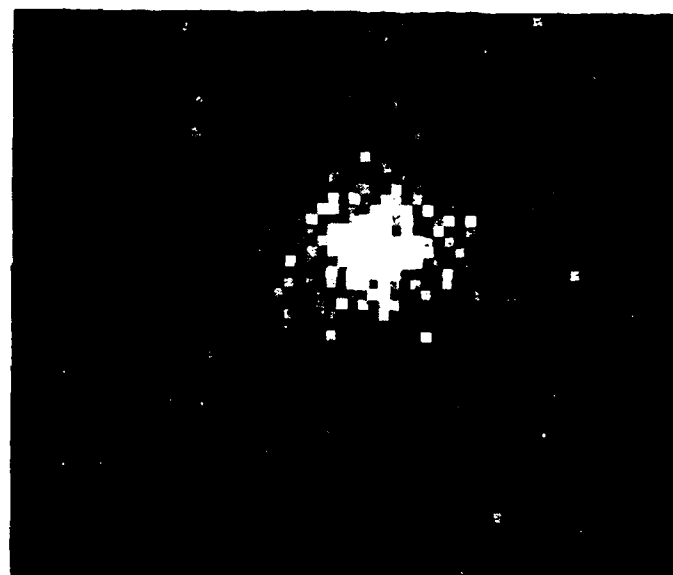


Fig. 2. Differential image of Alpha Orionis.

second ring is also apparent.

Figure 2 shows a differential image of Alpha Orionis obtained using 1000 frames of data. The overall SNR looks poorer, even though the exposure time is longer than in the bandpass used, because the object is extended (more photons per speckle but distributed at considerably larger speckles). Further differential images of Alpha Orionis were generated using about 3000 frames of data for each sky position angle. Though radial averages, emphasizing the existence of structure over a diameter of at least 10 pixels, show very little evidence of the expected symmetric distribution, was observed in these raw results.

These images are the first images generated out of the full resolution of the MMT. They are also the first successful implementation of the MMT as an interferometric interferometer.¹

4. UNDERSTANDING DIFFERENTIAL IMAGES

A differential image is not an image in the conventional sense. Consider the case in which the source has a far more complex structure in the line emission than in the reference waveband. This is expected for the extended atmosphere of Alpha Orionis seen in H α with respect to the stellar disk seen in the nearby continuum. An image of the structure seen in the line emission could be recovered by convolving the differential line emission image by a (predetermined) reference continuum image. Negativities contained in the differential image preserve high frequency information in such a convolution.

An expression for the differential image must contain a Jinc function term to which it is reduced when the line and reference object intensity distributions are equivalent to delta functions (i.e., a point source). This suggests the relationship

$$D(x,y) * O_c(x,y) = O_h(x,y) * J(x,y), \quad (3)$$

where $D(x,y)$ is the differential image, $O_c(x,y)$ is the object intensity distribution in the continuum, $O_h(x,y)$ is the object intensity distribution in the line, $J(x,y)$ is a Jinc function (see text above), and $*$ denotes convolution.

A detailed analysis of the reduction technique has revealed that the weighted deconvolution quotient in Eq. (2) contains a form of inherent Wiener-type filter that suppresses the signal at high spatial frequencies. The power spectra in the denominator contain a noise bias term whereas the cross spectra in the numerator are bias free. In addition, both summations contain a multiplicative term that is equal to the Fourier transform of the detector single photon point spread function (the detector function). Thus, Eq. (2) can be rewritten as

$$FT[D(x,y)] = \frac{\sum_N XSg(u,v)}{\sum_N (PS + \bar{n})g(u,v)} = \frac{\sum_N XS}{\sum_N (PS + \bar{n})}, \quad (4)$$

where XS and PS are the noise-bias-free spectra, $g(u,v)$ is the detector function, and \bar{n} is the mean number of photon events per frame. Equation (4) can then be separated into a "noise-bias-free" differential image and a "filter" term:

$$FT[D(x,y)] = \frac{\sum_N XS}{\sum_N PS} w_c(u,v), \quad (5)$$

where

$$w_c(u,v) = \frac{\sum_N PS}{\sum_N PS + \sum_N \bar{n}}. \quad (6)$$

The $w_c(u,v)$ is of the form of a Wiener-type filter such that signals at high spatial frequency below the diffraction limit are suppressed as the (frequency-independent) noise term becomes significant compared to the power-spectrum signal.

To prevent this inherent filtering effect, the bias must be removed from the summed power spectra in the denominator of Eq. (4). To achieve this, it was assumed that the detector

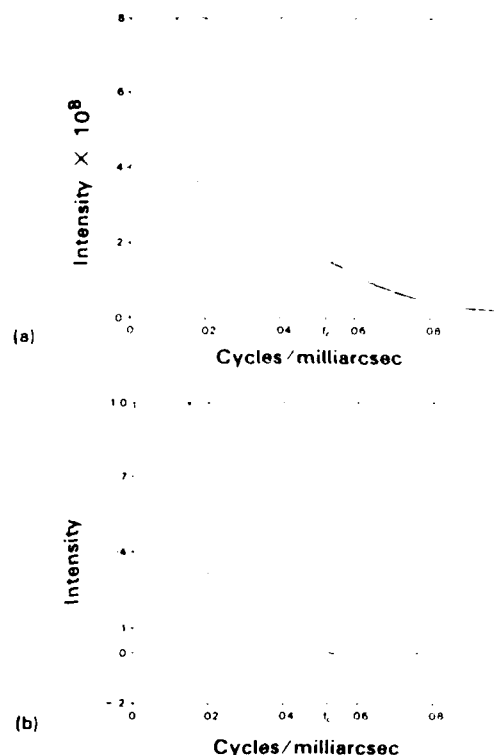


Fig. 3. Debiasing process as applied to the Alpha Orionis data. (a) Power spectrum and best-fit Gaussian. (b) Estimated Wiener-type filter.

function was equivalent to a Gaussian. Hence, debiasing involved subtraction of a Gaussian model fitted to the data at spatial frequencies greater than the telescope cutoff frequency.⁶

Figure 3 illustrates the debiasing process as performed for the Alpha Orionis data. Figure 3(a) shows the radially averaged profiles of the summed continuum power spectra and a Gaussian fitted above the cutoff frequency f_c . The filter $w_c(u,v)$ is obtained by dividing their difference (i.e., the debiased power spectra) by the original power spectra [from Eq. (6)] and is shown in Fig. 3(b). The spurious large but meaningless signal at high ($f > f_c$) frequencies is an inevitable consequence of division by small numbers. Note that the form of the filter is what we might expect from a resolved object (producing a central broad spike of low spatial frequencies) that also contains unresolved features on or around the stellar disk (signal exists out to the telescope cutoff). The bias-free differential image is then obtained by dividing the cross spectra by the debiased power spectra. This quotient also contains spurious signal due to small number division at large frequencies, and therefore it is multiplied by a cosine-bell apodizing function (radius equal to f_c) before inverse Fourier transformation.

In conclusion, for real detectors and finite photon statistics Eq. (3) should be reexpressed as

$$D(x,y) * O_c(x,y) = O_h(x,y) * J(x,y) * W_c(x,y), \quad (7)$$

where $W_c(x,y)$ is the Fourier transform of the filter $w_c(u,v)$.

5. FURTHER RESULTS

Figures 4(a) and 4(b) show the differential images of Alpha

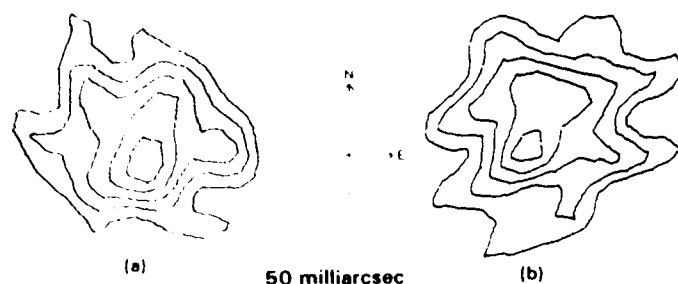


Fig. 4. Differential images of Alpha Orionis at two sky position angles after removal of the noise bias terms.

Orionis at the two sky position angles after removal of the noise bias terms. At large radii there appears to be no evidence of asymmetrical structure that is not still noise dominated. There are several possible reasons for this. First, no compensation was made for sky rotation, and consequently the stars rotated by about 9° during each of the two integrations, blurring the image at large radii. Second, imperfect coherence between the six MMT mirrors may be responsible for the systematic fringes apparent in these images. However, at small (< 30 milliarcsec) radii, where the results have highest SNR, there is some evidence that an elongated asymmetric feature in the image is observed, rotated exactly as predicted. The effective rotation of the entire telescope plus detector system enables a very strong validation of the technique if any significant features seen in the resulting analysis are associated with the object rather than produced as artifacts of the methodology.

6. DISCUSSION

In order to significantly reduce the vast amount of computer time required to perform the DSI reduction process, it was initially decided to extract the central 64×64 pixels from each of the 128×128 digitized data frames. All of the results described above were achieved using this smaller data window. The SNR of the images can be much improved by (a) utilizing the full 128×128 data frames and (b) reducing the 20,000 or so data frames from the Alpha Orionis observation that have yet to be analyzed. Furthermore, we hope that additional, better quality MMT data can be obtained in the near future at $H\alpha$ and other wavebands such as the singly ionized calcium lines (e.g., 8542 \AA).

Eventually, we wish to implement a dual-detector system. By having a separate detector for each of the line and reference specklegrams, there need be no restriction on their relative intensity, thus enabling a much greater SNR (e.g., by increasing the continuum image bandpass).

Several other imaging techniques have been applied to observations of Alpha Orionis in an attempt to study the resolved disk of the supergiant and its extended atmosphere.⁷ These have all shown overwhelming evidence for the existence of asymmetrical structure surrounding the star in $H\alpha$ light. The relatively low SNR results presented here suggest the presence also of inhomogeneities within the stellar disk.

7. ACKNOWLEDGMENTS

The MMT is a joint facility of the University of Arizona and the Smithsonian Institution. The work described here has been supported in part by the National Science Foundation (grants AST-8113212 and AST-8201092).

8. REFERENCES

1. J. M. Beckers, "Differential speckle interferometry," *Opt. Acta* 29, 4 (1982).
2. J. M. Beckers, E. K. Hege, and H. P. Murphy, "The differential speckle interferometer," in *Instrumentation in Astronomy*, D. Crawford, ed., Proc. SPIE 445, 462 (1983).
3. J. A. Dobrowolski, "Mica interference filters with transmission bands of very narrow half-width," *J. Opt. Soc. Am.* 49, 794 (1959).
4. E. K. Hege, J. M. Beckers, P. A. Strittmatter, and D. W. McCarthy, "The Multiple Mirror Telescope as a phased array telescope," *Appl. Opt.* 24, 2565 (1985).
5. P. Petrov, F. Roddier, and C. Aime, "The signal-to-noise ratio in differential speckle interferometry," *J. Opt. Soc. Am. A* (submitted).
6. E. K. Hege, E. N. Hubbard, P. A. Strittmatter, and W. J. Cocke, "The Steward Observatory speckle interferometry system," *Opt. Acta* 29, 701 (1982).
7. J. C. Hebden, J. C. Christou, A. Y. S. Cheng, E. K. Hege, P. A. Strittmatter, and J. M. Beckers, "Two-dimensional images of Alpha Orionis," *Astrophys. J.* (submitted).



Jeremy C. Hebden was born in London, England, in 1959. He received the B.Sc. degree in physics from Imperial College of Science and Technology (London) in 1981 and the Ph.D. degree from the same institution in 1984. His graduate work involved the application of a real-time digital correlator to astronomical speckle interferometry. He is currently a postdoctoral research associate at Steward Observatory, where his research interests involve the study of supergiant stars and their extended chromospheres using speckle interferometric imaging techniques and the full resolution capacity of the Multiple Mirror Telescope.



E. Keith Hege, Ph.D. physics, 1965, Rensselaer Polytechnic Institute, has been coordinating the efforts of the Steward Observatory Speckle Interferometry group since 1978. His research interests include the development of instrumentation and techniques for diffraction-limited image reconstruction using large astronomical telescopes. The results of these efforts have been applied to observations of various asteroids, the Pluto/Charon system, red supergiants, galactic nuclei, and gravitationally lensed quasar systems.



J. M. Beckers studied physics and astronomy at the University of Utrecht in The Netherlands. He received his Ph.D. there in 1964. From 1959 to 1962, he was a Research Fellow at CSIRO in Sydney, Australia. From 1962 to 1979, he pursued solar research at the Sacramento Peak Observatory in New Mexico. He was Director of the Multiple Mirror Telescope Observatory from 1979 to 1984. Since then, he directs the Advanced Development Program at the National Optical Astronomy Observatories.

Use of the Coherent MMT for Diffraction Limited Imaging

J.C.Hebden, F.K.Hege
Steward Observatory, University of Arizona, Tucson, Az 85721

and J.M.Beckers
NOAO, 950 N. Cherry Ave., Tucson, Az 85726

Abstract

All six MMT telescopes can now be optically cophased simultaneously over a wide field of view yielding coherent coverage of the complete Fourier transform plane corresponding to that of a pupil-masked telescope of 6.86m aperture. Open-loop phasing control compensates for flexure-induced path-length changes due to variable gravitational loading as a function of elevation. The system has been used to produce diffraction limited images and differential images of Alpha Orionis using narrow-band (1.2Å) filters centered both on Hydrogen-alpha and on a similar bandpass out of the absorption line. Corresponding wide (100Å) and narrow-band images of Gamma and Epsilon Orionis show the expected result for unresolved sources at the diffraction limited resolution of the fully-phased MMT.

Introduction

Although designed primarily as a large light-collecting telescope, recent experiments have shown that the Multiple Mirror Telescope (MMT) may be conveniently operated in a phased array configuration¹. Whereas the six constituent mirrors have an effective collecting area equivalent to that of a single mirror of diameter 4.45m, they can be used to achieve a resolution equal to that obtainable with a single 6.86m mirror. Cophasing of the six beams, as discussed briefly in the following section, is achieved using a wedge prism assembly. Since cophasing experiments were first attempted with the MMT it was observed that phasing of the telescope was highly dependent on the sky elevation and, to a much lesser degree, on the temperature of the MMT structure. Recent experiments, which have included compensation for the elevation dependency, have shown that we are now able to achieve a fully-phased mode quickly and efficiently. The telescope is stable in this configuration for sufficiently long periods of time, even at relatively large observing bandpasses, such that astronomical images at the full six-mirror diffraction limit may be obtained.

Cophasing the MMT

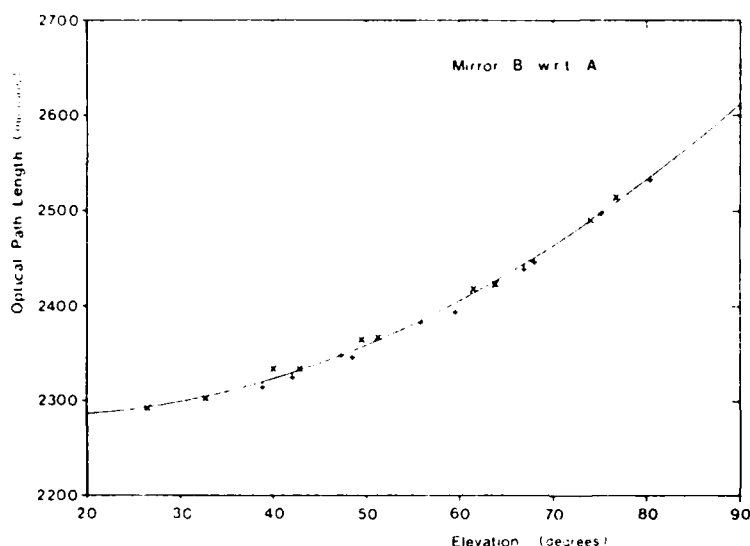
A full description of the various cophasing modes of the MMT, at infrared, submillimeter and optical wavelengths, is given by Hege et al¹. For the speckle interferometric experiments described here cophasing was achieved by adjusting pairs of glass wedges inserted in each of the six beams at positions located between the tertiary mirrors and the beam combiner which directs them to their common focal point. By translating one of the two complementary wedges with respect to the other the effective path length incurred by the beam arriving at the focal point may be adjusted. In practice, five of the beams are cophased with respect to the sixth, conventionally chosen to be that corresponding to mirror A (the six mirrors are labelled A through F). Each cophased pair of mirrors produces a series of fringes in the focal plane. The cophase condition is detected by visual examination of the video specklegrams produced by the intensified video speckle camera², i.e. we look for the appearance of fringes. The contrast of the fringes decreases with increasing bandwidth but a large bandwidth (typically 600Å) is nevertheless required in order to produce few enough fringes such that the center of their distribution may be positioned precisely on the center of the observed specklegram. The prisms are stepped in intervals corresponding to a path length change of 0.18 microns which, as the table shown below indicates, is significantly smaller than the coherence lengths of the optical filters we have implemented both for observation and cophasing purposes.

Filter	Coherence length
6563Å/1.2Å	3589 microns
8500Å/100Å	73 microns
5200Å/100Å	27 microns
6000Å/600Å	6 microns (cophasing only)

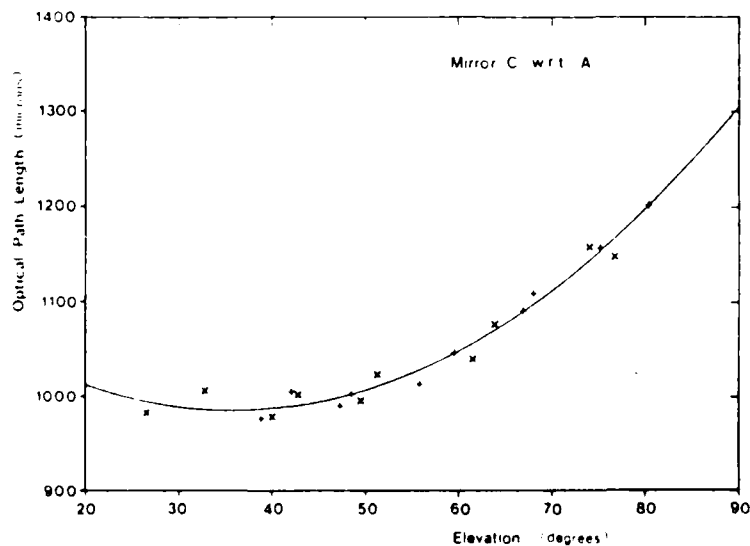
Table 1. Optical filters and their coherence lengths

The effect of telescope tilt on the cophase condition is automatically compensated for by assuming a quadratic fit between the prism-pair position and the elevation angle. The quadratic parameters are obtained experimentally at the start of each observing run and thereafter are used to enable the MMT computer to make suitable adjustments to the prisms during the observation of a given object. The calibration consists of observing a number of stars, say six, at various elevations between about 30 and 80 degrees, and obtaining the prism-pair settings (in 0.18 micron step units) at which fringes were observed to cross the video specklegram. The same stars are observed several times as they move over the sky so that a wide range of elevation angle is sampled sufficiently finely. The stars are observed in order of decreasing or increasing elevation, repeatedly up and down, thus any hysteresis involved can be evaluated.

Figure 1 (a-e) shows the change in optical path length as a function of elevation obtained for the mirror pairs A-B, A-C, A-D, A-E and A-F. The observations were made on 24th January 1986. Two different symbols have been used in order to indicate measurements taken during increasing (+) or decreasing (x) elevation. Also shown are the best-fit least-squares quadratic curves. The standard error calculated between the data points and the best-fit curves is given in Table 2.

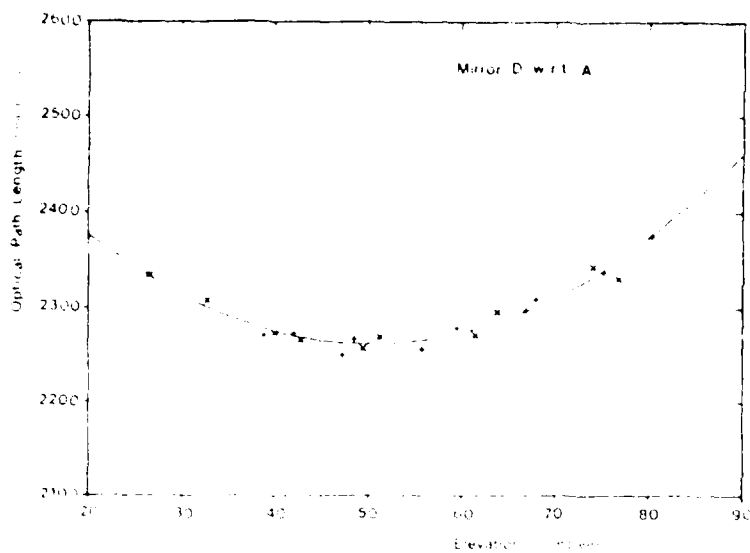


a) Mirrors A and B

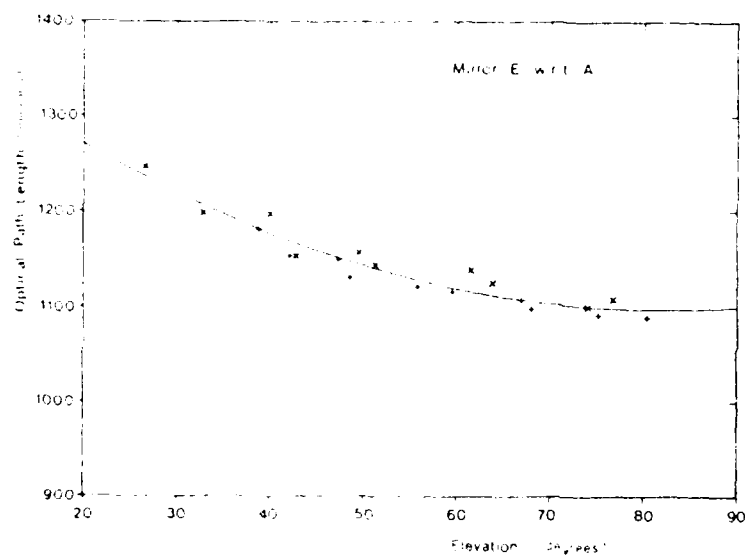


b) Mirrors A and C

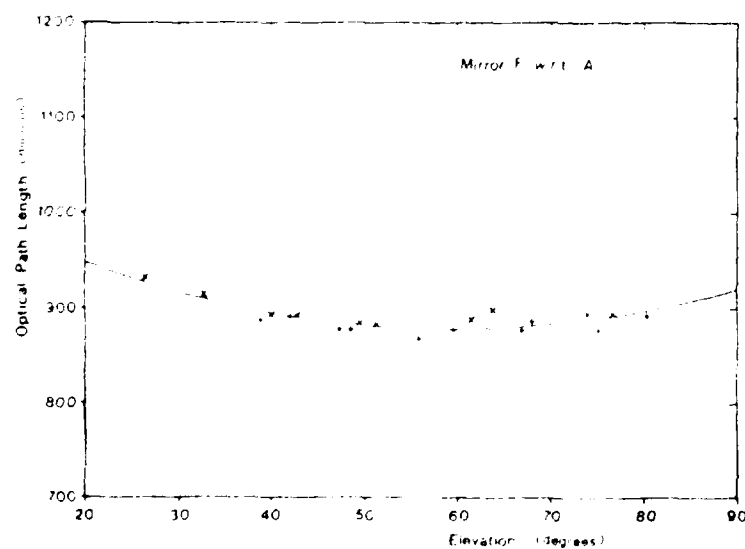
Figure 1 (a and b). Change in optical path length as a function of elevation.



c) Mirrors A and D



d) Mirrors A and E



e) Mirrors A and F

Figure 1 (c,d, and e). Change in optical path length as a function of elevation.

Mirror pair	Standard error
A - B	4.96 microns
A - C	12.6 microns
A - D	7.88 microns
A - E	7.43 microns
A - F	11.2 microns

Table 2. Standard error between cophasing condition evaluations and a best-fit least-squares quadratic curve.

It is evident from Tables 1 and 2 that whereas the error involved in using a single quadratic function in order to predict the required adjustment in phasing condition during change in elevation angle would be significant for observations using a very wide bandwidth filter, the error involved for observations made using our narrow hydrogen-alpha (6563Å) emission line filter is negligible. The small amount of hysteresis apparent in some of the data shown in figure 1 will therefore not inhibit adequate phase compensation for our applications.

Though this experiment was repeated at the beginning of each of our four nights of observation 24th - 27th January, we found that the curves we obtained on the very first night were more than adequate for observations on all subsequent nights. We noted that not only was the compensation sufficient to allow observation at a 100Å bandpass of a given object for ten or so minutes without significant loss of coherence (i.e. loss of fringes), but also it permitted us to jump between two objects of reasonably distant elevation (20 degrees, say) without loss of coherence at similar bandpasses. Typically the curves vary significantly between different observing runs, particularly if the telescope has been reconfigured in the intervening time (i.e. exchange of primary mirrors).

The seeing during our most recent observing run at the MMT in January 1986 was typically around 1.5 arcseconds throughout. During such conditions we have found that cophasing of the telescope, which is as yet only possible by visual inspection, is a reasonably fast and reliable process. However it has been our experience in the past that the seeing can be so poor that cophasing is quite impossible. Such conditions occurred in June 1985 when we found that the atmospheric correlation time was very much shorter than our shortest frame exposure time.

Shortly before our observing run in November 1985 one of the six constituent mirrors of the MMT was replaced with a spare while the original was re-aluminized. Unfortunately the focal length of the replacement had not been specified sufficiently accurately and we were unable to cophase it with any of the other five mirrors within the limits set by the wedge prisms in their original configuration. The point-source results obtained from these observations demonstrate a significantly different distribution to that obtained for six mirrors, as shown in a later section. The spare mirror was itself replaced by the original before the run in January 1986 and we experienced no further problems.

Observations

The results presented here have been obtained as part of an ongoing investigation of the resolved disks and extended atmospheres of giant and supergiant stars at the full diffraction-limited resolution of the MMT. In particular, considerable study is being made of the appearance of the M-type supergiant Alpha Orionis and its surrounding envelope in the hydrogen-alpha line. Throughout these investigations we have found it very useful, mainly for diagnostic purposes, to intersperse our supergiant observations with similarly acquired data for unresolvable sources. Gamma and Epsilon Orionis have frequently been observed in conjunction with Alpha Orionis for example. It is these "point source" results we particularly wish to present here, and to show that they are indeed diffraction limited in that they conform to theoretical predictions for the coherent MMT configuration:

Cophased MMT observations of Alpha Orionis were first made in December 1983. The preliminary results were presented³ at the SPIE "International conference on speckle" in August 1985 following a long period of technique validation. Further observations were made in November 1985 and January 1986, and more shall be attempted shortly in February 1986. We have deliberately chosen such short periods between our most recent observations in order to study the temporal evolution of the supergiant. Several past observations have indicated the presence of temporally variant (on the timescale of months) small-scale structure (at the diffraction limited resolution of the MMT) within the stellar disk⁴.

Both Differential Speckle Interferometry (DSI) and Weighted Shift-and-Add (WSA)

reduction techniques were used to produce the results described here. The former method, invented by Hedden², involves obtaining simultaneous specklegrams at two nearby wavelengths. Thus image information relating to the difference in the appearance of the object resulting from the differences in the observing wavelength can be derived. A detailed description of the implementation of DSI to observations such as those described here is given by Hedden et al.³. To summarise, the reduction process involves combining specklegrams obtained in the H-alpha line with simultaneously acquired specklegrams obtained in the continuum about 6Å away. Assuming identical atmospheric statistics we achieve a result known as a "differential image" which conforms to a conventional image when convolved with an image obtained in the continuum alone. This method is particularly useful if we can assume that the structure of the object in the line is significantly more extended, or if the structure in the nearby continuum is known reasonably accurately.

Weighted Shift-and-Add (WSA), as discussed in great detail by Christou et al.^{6,7} and Lind⁸, produces images in the conventional sense essentially by adding together all the speckles present in a specklegram. This method assumes each speckle is a low signal-to-noise estimate of the diffraction-limited object distribution and is particularly applicable to bright (large bandwidth) data. Images obtained using WSA may then of course be used to produce images in the H-alpha line by convolving with the DSI images as described above.

Results

Figure 2 shows the differential image of the unresolvable star Gamma Orionis obtained from 100 H-alpha-continuum specklegram pairs recorded in December 1983. It can be shown (see Hedden et al.³) that the differential image of a point source is equivalent to the inverse Fourier transform of a uniformly weighted spatial frequency domain bounded by the frequency cut-off of the multiple aperture telescope. Hence it is not equivalent to the actual image in the conventional sense which is defined as the power spectrum (Fourier modulus squared) of the telescope pupil. If the MMT pupil were assumed to be equivalent to that of a single 6.86m diameter mirror then the differential image of Gamma Orionis would be the transform of a cylindrical (top-hat) function with a radius equal to the frequency cut-off of the telescope. The result would therefore be a sinc function $J_1(r)/r$ whose half-power width is about 0.61 λ/D radians, or about 12 milli-arcseconds if arc (mas) for the 6.86 meter aperture at the H-alpha waveband. Figure 2 shows that the central half-power width agrees well with this approximate model of the MMT aperture.

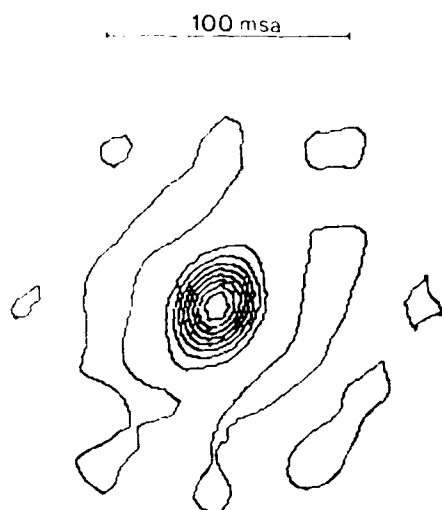


Figure 2. A differential image of Gamma Orionis (6563Å); December 1983.

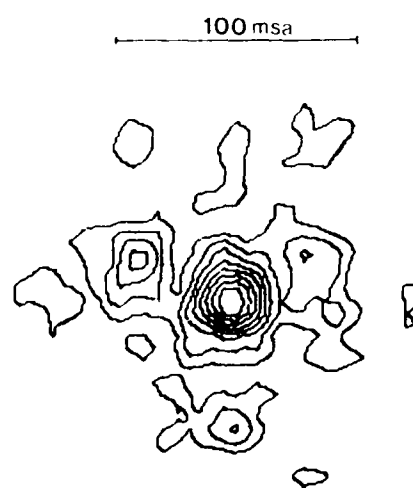


Figure 3. A differential image of Epsilon Orionis (6563Å); November 1985.

Figure 3 shows the differential image of another point source, Epsilon Orionis, obtained using another 1000 H-alpha/continuum specklegram pairs in November 1985. The signal-to-noise is significantly worse mainly due to the much poorer seeing conditions experienced during the latter observations. Specklegram pairs have also been obtained at large bandwidths in order to study the precise form of the point source differential image. For such experiments each of the two simultaneously acquired specklegrams are recorded at exactly the same wavelength. Figure 4 shows such an image achieved using 1200 specklegram pairs obtained at $5200\text{\AA}/100\text{\AA}$ in November 1985. Note that the decrease in wavelength has resulted in the expected corresponding decrease in image size. In fact this result represents the highest resolution image of this kind ever achieved at optical wavelengths.

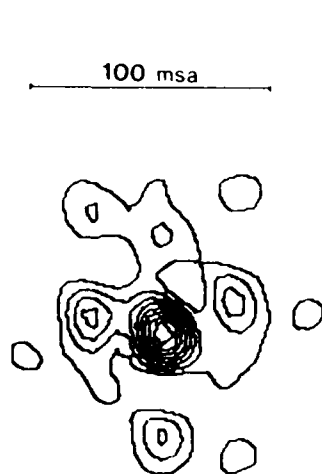


Figure 4. A differential image of Gamma Orionis (5200\AA); November 1985.

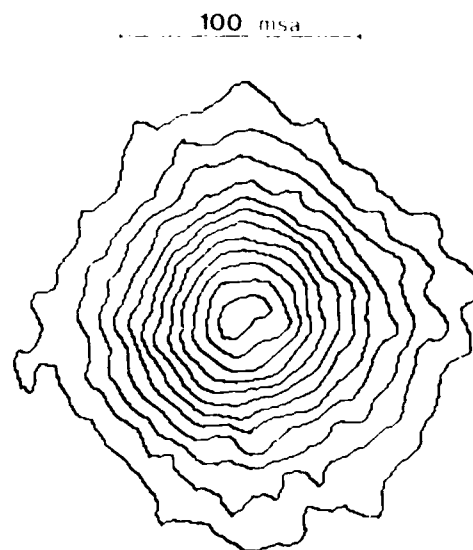


Figure 5. A differential image of Alpha Orionis (6563\AA); November 1985.



Figure 6. A WSA image of Gamma Orionis (6563\AA); December 1983.



Figure 7. A WSA image of Gamma Orionis (6563\AA); November 1985.

Figure 6 shows a differential image of the supergiant star Alpha Orionis obtained using about 1100 H-alpha continuum specklegram pairs in November 1981. Our knowledge of the astrophysics of cool stars tells us that supergiants such as Alpha Orionis are likely to have a large extended shell surrounding the central star that is visible in the light of H-alpha. Recently the photospheric (continuum) diameter has been estimated by Chen et al.⁷ to be 421 mas. Therefore the differential image of Alpha Orionis shown in figure 6 demonstrates the existence of excess intensity in H-alpha well beyond the expected photospheric radius. As mentioned earlier, a conventional image of the star at H-alpha may be obtained by convolving the differential image with a conventional image obtained in the nearby continuum. Before this can be done, however, the high-frequency spatial effects inherent in the L-I technique, as reported earlier,³ must be removed. This is currently in progress. The presence of an elongated feature within the central photospheric disk region of the image is in accordance with previous images of this star.^{8,9}

Figure 7 shows a WSA image of Gamma Orionis obtained using about 1100 H-alpha specklegram pairs in December 1981. Unlike those described above, this is an actual image in the visible continuum, and therefore represents an estimate of the point spread function of the MMT. In the WSA image of the same star obtained from the November 1981 specklegram pairs shown in figure 7, only 118 frames of the 1200 H-alpha bandpass data were used, and thus the result is an estimate of the MMT PSF in the H-alpha continuum.

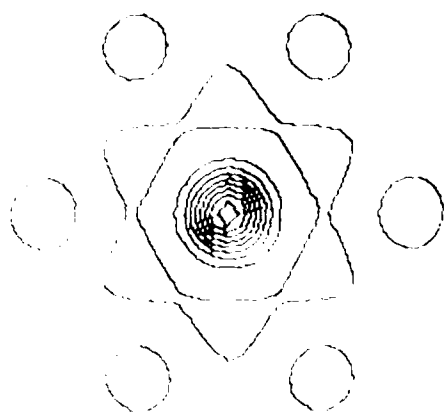


Figure 6. Theoretical MMT point spread function for six mirrors.

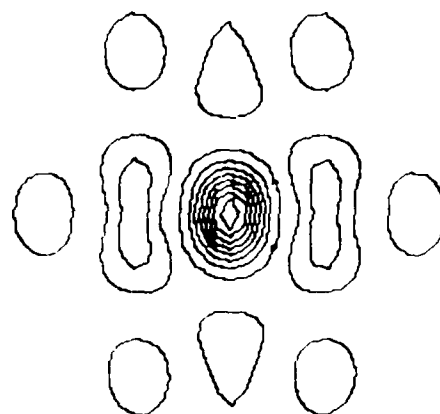


Figure 7. Theoretical MMT point spread function for five mirrors.

Discussion

In order to verify the appearance of our point source results, model intensity distributions were calculated. Figures 8 and 9 show the computed form of MMT PSFs for the six and five mirror configurations respectively. It was explained earlier that the theoretical distribution of a point source ISI image is not mathematically equivalent to that of the telescope I/F. However experiments show that the overall form of their distributions are very similar. Thus we are able to compare, qualitatively, figures 8 and 9 with the differential and conventional imaging results for the unresolvable stars.

Figures 6 and 7, the H-alpha and WSA point-source images for the six mirror configuration, demonstrate reasonably good agreement with the theoretical model shown in figure 8. The WSA result for the five mirror MMT, figure 7, shows a strong resemblance to that expected for in figure 9, although the central peak appears strangely elongated in a direction incommensurate with the model. However, unlike for the other results presented here, there was virtually no compensation made during the reduction process for the image distortion produced by the image intensifier/TV camera system. The

five mirror ISI results shown in figures 3 and 4 also compare favorably with figure 2. However, the apparent absence of one of the outer six lobes in both of these results does not correlate with the five-mirror MMT PSF. A closer examination of the results has shown that these "missing" lobes have very low power, barely detectable within the background noise of the images. However, since the two images correlate so much better with each other in this respect than they do with the theoretical model, we conclude that the combined ISI of the telescope/camera system is not exactly that expected from a non-aberrated five mirror MMT configuration. Although the WPA image does not exhibit this asymmetry, this may be due to the fact that a WPA point source image can often resemble the autocorrelated PSF, particularly in the case of poor photon statistics. Whether these effects are indeed due to optical aberrations, or in fact are produced systematically by the ISI imaging technique, is currently under investigation.

Conclusions

The results presented here further demonstrate the power of the MMT as a coherent optical interferometer, and our experiments show that the telescope may now be routinely operated in this configuration efficiently and reliably. Comparison of images of stars unresolved at the diffraction limit of the MMT with theoretical image intensity distributions shows that the results are indeed diffraction limited and nearly aberration free. The supergiant star Alpha Orionis exhibits H-alpha emission extending well beyond the expected photospheric radius of the star as well as structure within the stellar disk.

Acknowledgments

The authors would like to thank the MMT technical support staff for their enthusiastic assistance, and Dr. Julian Christou for his valuable comments. The work described here has been supported in part by the National Science Foundation (grants AST-8114212, AST-7710920) and by the Air Force (contract number F49620-84-F-0035).

References

1. Hege, E.K., Beckers, J.M., Strittmatter, P.A. and McCarthy, D.W., *Applied Optics*, **24**, 2585, 1985.
2. Beckers, J.M., Hege, E.K. and Murphy, H.P., *Proc.SPIE*, vol.445, *Instr. in Astron.*, p462, 1983.
3. Hebden, J.C., Hege, E.K. and Beckers, J.M., *Proc.SPIE*, vol.596, *International conference on Speckle*, p284, 1985.
4. Hebden, J.C., Christou, J.C., Cheng, A.Y.S., Hege, E.K., Strittmatter, P.A., Beckers, J.M. and Murphy, H.P., *Astrophys.J.* (submitted)
5. Beckers, J.M., *Optica Acta*, **29**, 4, 1982.
6. Christou, J.C., Hege, E.K., Freeman, J. and Ribak, E., *J.Opt.Soc.Am.A*, vol.3, 1986.
7. Christou, J.C., Ribak, E., Hege, E.K. and Freeman, J., *Opt.Inq.* (In press)
8. Cheng, A.Y.S., Hege, E.K., Hubbard, E.N., Goldberg, L., Strittmatter, P.A. and Cocke, W.J., *Astrophys.J.* (submitted)
9. Ribak, E., *J.Opt.Soc.Am.* (submitted)
10. Goldberg, L., Hege, E.K., Hubbard, E.N., Strittmatter, P.A. and Cocke, W.J., *SAO Special Reports*, **392**, 131, 1982.

IMAGES OF THE ENVELOPE OF ALPHA ORIONIS

Jeremy C. Hebden, E. Keith Hege, and Andreas Eckart
Steward Observatory
University of Arizona
Tucson
AZ 85721, USA

ABSTRACT. Two images have been obtained, from observations made almost two years apart, of the H-alpha chromospheric envelope of Alpha Orionis at the diffraction limited resolution of the co-phased Multiple Mirror Telescope. Significant emission out to a distance of several stellar radii above the photosphere is observed.

1. INTRODUCTION

Several recent attempts have been made to design theoretical models for the extended atmosphere of the M type supergiant Alpha Orionis. However, the heights and thicknesses of the chromosphere within a few stellar radii of the star, in the region where the outward flow of matter is accelerated, has been relatively unknown. The H-alpha absorption line provides a valuable diagnostic since it is expected to be formed in this region. Using a narrow (1.2Å) H-alpha filter, and the fully-phased six-mirror Multiple Mirror Telescope (MMT)¹, images were obtained of the H-alpha chromosphere of Alpha Orionis at the greatest resolution available for imaging at optical wavelengths.

2. OBSERVATIONS AND DATA REDUCTION

Differential Speckle Interferometry (DSI) observations were made using the fully-phased MMT (Hege et al. 1985) on 1983 December 16/17, and again on 1985 November 2/4. The observational and data reduction procedures are discussed in detail by Hebden et al. (1986) and Hebden, Hege, and Beckers (1986). In order to extract images of the supergiant in the H-alpha line, the DSI imaging technique requires a reconstruction of the star's image in an adjacent continuum bandpass. A well defined photospheric radius, R_* , was found of 17 milli-arcseconds (mas) to 23 mas, dependent on the limb-darkening assumed.

¹ The Multiple Mirror Telescope Observatory is a joint facility of the Smithsonian Institution and the University of Arizona.

3. IMAGES OF THE H-ALPHA ENVELOPE

The images of the H-alpha envelope of Alpha Orionis for the 1983 December and 1985 November observations are shown in figure 1. The contours are plotted at intervals of approximately five percent.

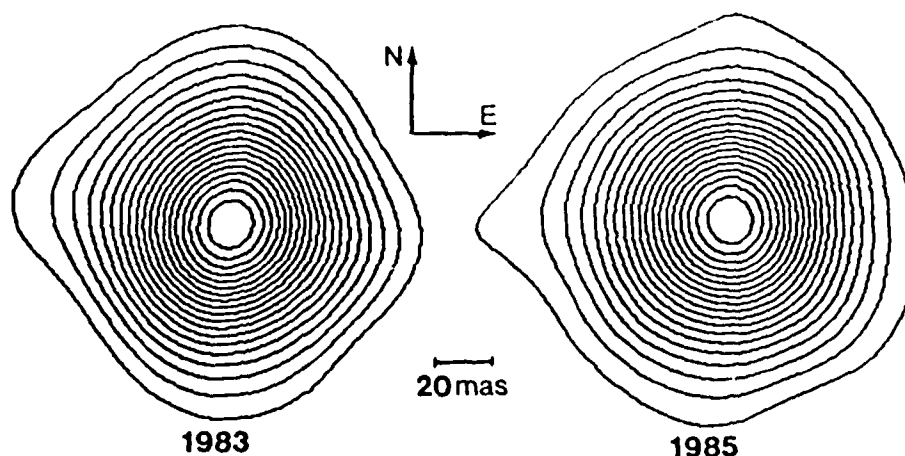


Figure 1. Images of the H-alpha envelope of Alpha Orionis

An intensity greater than one percent of maximum is detectable out to a radius of about 95 mas, or 4.5 stellar radii. Both images exhibit a small degree of asymmetry, corresponding to a position angle of about 280° . The absence of a distinct photospheric limb suggests that the optical depth in H-alpha is probably very large. The radial profiles of the images exhibit a remarkable agreement with a Gaussian-like distribution, with intensity falling to I_0/e at $2R_*$ and $I_0/10$ at $3R_*$. The size of the observed H-alpha envelope of Alpha Orionis appears to conform to estimates of the chromospheric radius obtained from radio observations (Altenhoff, Oster, and Wendker 1979; Newell and Hjellming 1982), and to the theoretical model of Hartmann and Avrett (1984). A quantitative comparison of our results and this theoretical model is described by Hebden, Eckart, and Hege (1987).

This work has been supported in part by the NSF (grant AST-8412206).

4. REFERENCES

- Altenhoff, W. J., Oster, L., and Wendker, H. J. 1979, *Astron.Astrophys.*, **73**, L21.
Hartmann, L., and Avrett, E. H. 1984, *Ap.J.*, **284**, 238.
Hebden, J. C., et al. 1986, *Ap.J.*, **309**, In press.
Hebden, J. C., Eckart, A., and Hege, E. K. 1987, *Ap.J.*, 312, In press.
Hebden, J. C., Hege, E. K., and Beckers, J. M. 1986, *Opt.Eng.*, **25**, 712.
Hege, E. K., Beckers, J. M., Strittmatter, P. A., and McCarthy, D. W. 1985, *Appl.Opt.*, **24**, 2565.
Newell, R. T., and Hjellming, R. M. 1982, *Ap.J.*, **263**, L85.

Reprinted from *Applied Optics*, Vol. 24, page 2565, August 15, 1985
Copyright © 1985 by the Optical Society of America and reprinted by permission of the copyright owner.

Multiple mirror telescope as a phased array telescope

E. Keith Hege, J. M. Beckers, P. A. Strittmatter, and D. W. McCarthy

By adjusting the optical path lengths of its individual beams, it is possible to make the multiple mirror telescope (MMT) into a phased array with a 6.86-m base line. A coherent phased focus can be achieved with tilted focal planes if the tilt angle is chosen so that the internal phase differences exactly compensate the external phase differences. This amounts to a slight change in configuration so that the beams are brought together at $f = 8.39$ rather than the originally designed $f = 9$. We summarize experiments which have used the MMT subapertures as a phased array and as a coherent phased telescope and present a simple analysis of the tilted focal plane geometry for coherent observation. The phased operation of the MMT is important not only for obtaining high angular resolution but also for obtaining the higher detection sensitivity which results from the better discrimination against the sky emission background for IR diffraction-limited images. Full aperture (six-beam) diffraction-limited results for the unresolved source Gamma Orionis, the well-known close binary Capella, and the resolved red supergiant Betelgeuse (including a diffraction-limited differential speckle image of the latter) are presented as preliminary demonstration of the potential capabilities of this configuration.

I. Introduction

We first summarize the experiments which have used the multiple mirror telescope (MMT) subapertures as a phased array in the optical, IR, and submillimeter spectrum regions. Those experiments exploit the unique, very high angular resolution of the MMT, equivalent to that of a conventional telescope 6.86 m in diameter. Although not discussed here, operation of the MMT as a phased array is not only important for obtaining high angular resolution but also for obtaining the high-detection sensitivity which results from better discrimination against the sky emission background for IR diffraction-limited images. We then describe work done at optical frequencies in converting the MMT into a phased telescope.

II. Multiple Mirror Telescope as Interferometer

The MMT was constructed primarily as a large light-collecting telescope for astronomical research on faint objects in the optical and IR spectrum regions. Experiments in the past few years have demonstrated the potential for using the MMT for high angular res-

olution research. Whereas its equivalent collecting diameter (= diameter of a single telescope having the same collecting area) equals 4.45 m, the MMT has a resolution diameter (= diameter of a single telescope having the same angular resolution) of 6.86 m. This higher angular resolution can, of course, only be achieved if the telescopes are cophased and if the earth's atmospheric effects are overcome, e.g., by speckle interferometric techniques.

Figure 1 shows a cross section of the MMT aperture and response in the Fourier plane or (u,v) plane, (image power spectrum plane) when used as a phased array. The (u,v)-plane response covers all angular frequencies up to the cutoff frequency set by the resolution diameter of the MMT. Many of the frequencies also are covered more than once because the MMT array is highly redundant.

Figure 2 shows a cross section of a subset of two (or three) MMT apertures. With this subset one covers only a fraction of the (u,v) plane, leaving large gaps. The Fig. 2 configuration is commonly called an interferometer. Other optical interferometers exist with a two-mirror configuration^{1,2} with base lines up to 40 m. Those configurations have a very thin (u,v)-plane coverage, but because of their large base line they are able to measure a single very high spatial frequency image parameter (e.g., the diameter of a stellar disk with an assumed, usually uniform, intensity distribution). By changing the base line and projection on the sky, one can improve the situation until a full image is synthesized, as is the case, for example, with the very large array at radio wavelengths. The MMT configuration

J. M. Beckers is with National Optical Astronomy Observatories, Tucson, Arizona 85726. The other authors are with University of Arizona, Steward Observatory, Tucson, Arizona 85724.

Received 14 March 1985.

0001-3748/85/0005-2565\$01.00/0.

© 1985 Optical Society of America.

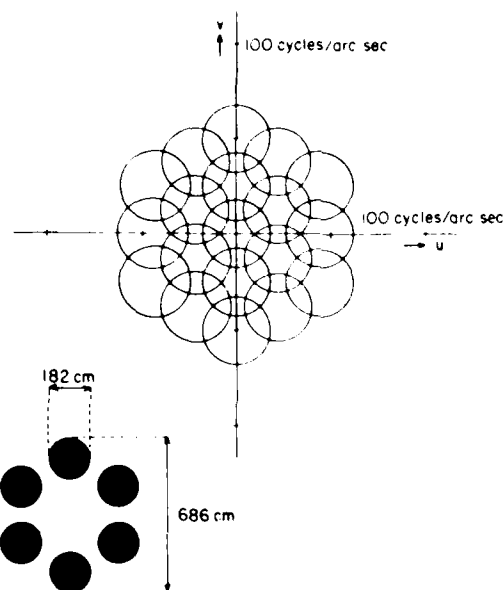


Fig. 1. Lower left: cross section of the MMT entrance aperture (vertical in figure is vertical on the sky). Central figure: coverage in the Fourier transform plane, or (u,v) plane, at a 500-nm wavelength if the six telescopes are phased.

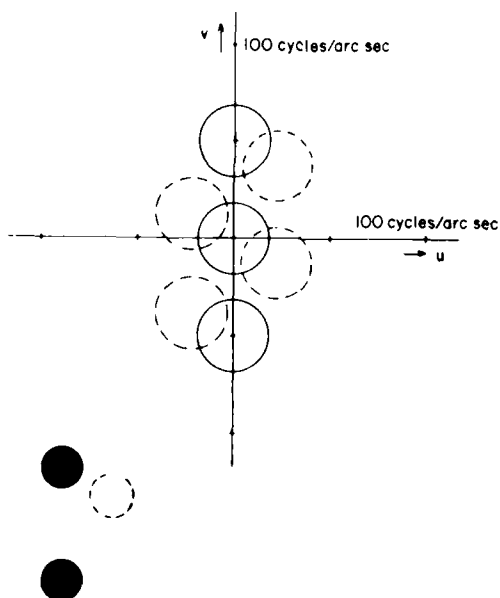


Fig. 2. As Fig. 1 but when only using two (or three) beams.

with three mirrors, also shown in Fig. 2, can be used that way either by using different triads of telescopes or by having its projection rotate across the sky, which is possible because of the altazimuth mount. In contrast to the interferometer mode shown in Fig. 2, we will refer to a device with a (u,v) plane as shown in Fig. 1 as a phased telescope. We report here experiments using the MMT as an interferometer (Fig. 2) and as a phased telescope (Fig. 1).

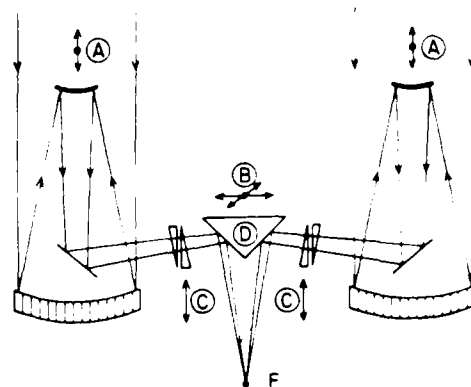


Fig. 3. Ways of adjusting path lengths of individual beams. A, by longitudinal translation of the secondary hyperbolic mirrors. This may defocus the image by an intolerable amount; B, by sideways translation of beam combiner in two orthogonal directions. This allows phasing only for up to three telescopes; C, by inserting in each beam two complementary wedges and translating one with respect to the other; D, by separating the six reflecting surfaces of the beam combiner and translating/tilting them. Drawing is not to scale.

III. Cophasing the MMT

The MMT has been used at optical (0.4–0.8- μm), IR (5- μm), and submillimeter (870- μm) wavelength regions as an interferometer or phased telescope. In Fig. 3 we show schematically how the relative path lengths are adjusted in the various experiments.

For submillimeter experiments the phasing is accomplished by longitudinal translation (i.e., focusing) of the MMT secondary mirrors (mode A). Since the Rayleigh focal range for the prime focus, $4\lambda f^2$ (primary), equals 25 mm at $\lambda = 870 \mu\text{m}$, the change in focusing for the ± 2 -mm secondary mirror adjustment needed for cophasing is insignificant so that the phase sensing is readily accomplished by peaking up the central intensity of an image of a point source. Ulich *et al.*³ showed the measured and calculated intensity distribution of Saturn to be in good agreement. More recently, Schulz *et al.*⁴ carried out further successful measurements with angular resolution of 25 of arc at 870 μm , which are expected to yield important new scientific results. This resolution compares favorably with the best resolution obtained with any single-dish radio telescope at any wavelength.

For infrared experiments the telescope path lengths are adjusted by translation of the beam combiner (mode B). This was done only for two telescopes⁵ so that the MMT worked as a two-element interferometer causing fringes across the stellar image when inphase. The cophased condition was sensed by detection of the white light fringe by eye in the optical region. This coincides with the phased condition in the IR as well because of the all-reflecting system. (The wedges used for mode C are normally not used for IR work.)

In the optical experiments the path lengths have been adjusted by focusing of the secondaries (mode A), translation of the beam combiner (mode B), and relative adjustment of pairs of glass wedges (mode C). Beckers



Fig. 4. Pupil shearing interferometer pupil fringes. A rotational shear has superimposed adjacent MMT subpupils. The actual fringe contrast (and coverage in the overlap region) is much greater than suggested in this vidicon image, which, because of video lag effects, is an integration for longer than the fringe correlation time set by the atmosphere.

*et al.*⁶ used the Roddier rotation shearing interferometer⁷ to obtain interference between two adjacent telescope pupils. Fringes, seen in low contrast due to inappropriate video recording, cross the overlapping pupils segment shown in Fig. 4. The secondary focusing motions could be used for phasing in this experiment as well since the interference occurs in the pupil plane and is thus quite insensitive to out-of-focus effects (the present cophasing systems not being available at that time). Detection of the cophase condition was done visually directly and by monitoring the TV image (Fig. 4).

For conventional speckle interferometry in the image plane, the telescope path lengths are adjusted (mode C) by adjusting pairs of wedges in each of the six beams. Figure 5 shows a speckle image (specklegram) so obtained with two telescopes showing the superposition of the two single telescope speckle images and the interference fringes resulting from the cophasing. Figure 6 shows the corresponding (u,v) plane result after coadding the power spectra of 300 frames such as Fig. 5. Figures 7 and 8 show, respectively, the fringes (speckles now) and (u,v) response for all six beams.

The cophase condition is detected by visual examination of the video specklegrams, there being at present no instrumentation for on line fringe sensing. We just watch the real time video display produced by the intensified video speckle camera.⁷ When cophasing the entire telescope, we adjust five of the six path lengths



Fig. 5. Specklegram of a point source obtained with an opposite pair of phased beams. The nearly vertical interference fringes are 27 msec of arc apart (650 nm wavelength).

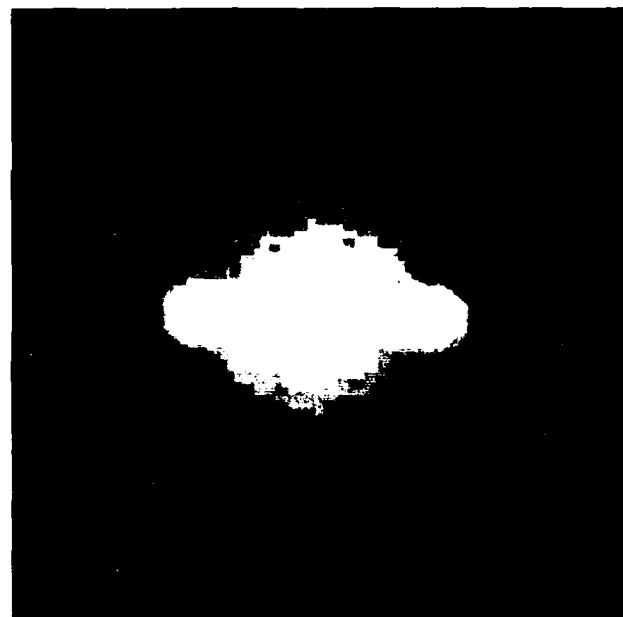


Fig. 6. Image power spectrum of 300 specklegrams of a point source using two phased telescopes as shown in Fig. 5. The interferometer frequencies are shown clearly as the autocorrelation of the two mirror pupil. The high frequency background is the detector colored noise bias.

relative to a sixth chosen as a reference. In order not to confuse the eye, the five telescopes are compared one at a time to the sixth so that only simple fringe patterns such as Fig. 5 need be inspected. Then all six beams are combined to produce the full aperture MMT specklegrams such as seen in Fig. 7.



Fig. 7. Multiple mirror telescope specklegram produced when all seeing conditions are used. An interferometer fringes are seen superimposed on the speckles where eight single mirror speckles from a 10 cm telescope is superimposed.

The co-phased condition can be sensed visually with a precision of $\pm 2 \mu\text{m}$ by centering the white light fringe of the star image. In the future we plan to design and construct an electronic fringe sensor, possibly based on a digital TV system and using the fast Fourier transform algorithm. We have demonstrated a procedure for measuring the contrast and position of interferometric fringes produced by two phased mirrors of the MMT. The goal of this experiment was to give a preliminary indication of whether an automatic mirror phasing system using one of the MMT point 4 computers would be feasible. We conclude that a given pair of mirrors can be co-phased in ~ 10 sec to a precision of better than $\pm 2 \mu\text{m}$ at stars up to eighth magnitude given a modest hardware FFT device.

For a proof of principle demonstration of an instrument fringe sensing system capable of detecting the magnitude and sense of telescope phasing errors, the fringe system was set up so that the two telescope fringes were essentially parallel to the video raster lines. Using a frame grabber, integrator and 8-bit analog-to-digital

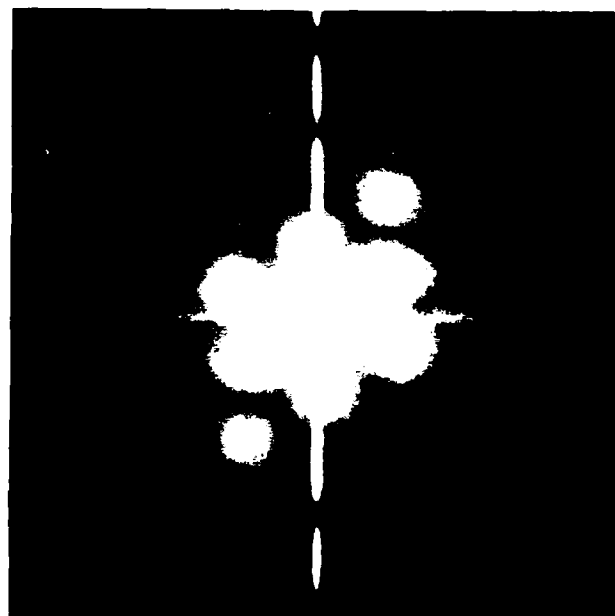


Fig. 8. Image power spectrum of 500 speckle runs of a point source. This is observed in a 10 nm bandpass centered at 630 nm in a 10 cm beam, as shown in Fig. 7. This is a measure of the net response of the MMT (including atmospheric effects) to a point source specklegram, speckling, and other artifacts. The horizontal and vertical artifacts were induced by a faulty camera window, caused speckling in the image plane, and a computer data transfer error window.

converter combination, a digitized amplitude was extracted from a sample position along each raster line. In that way a 1-D intensity profile across the fringe pattern was sampled.

When the two mirror interferometer is correctly co-phased, the fringes should be centered relative to the superimposed seeing distributions. To determine whether our algorithm could detect fringe position, we purposely positioned the fringes at both the top and bottom relative to the seeing distribution as well as at the center by slightly adjusting the path length.

We sampled data integrated in a strip of width corresponding to the single telescope speckle size across 128 video lines (see Fig. 10). The sample was also movable, we could sample the seeing distribution at the top, center, or bottom of the raster. For each relative fringe

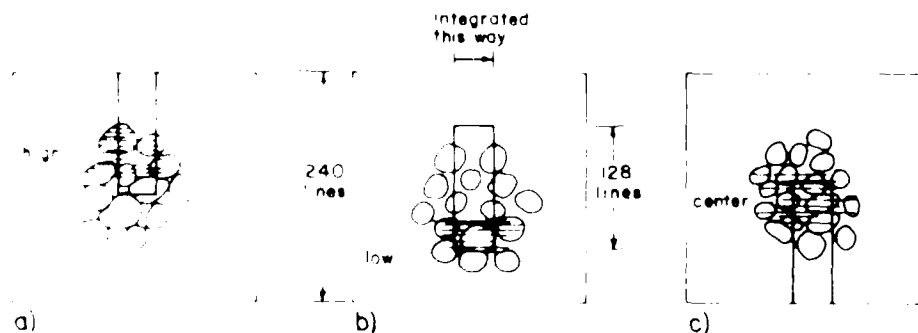


Fig. 9. Fringe sensing system. (a) Fringe position. (b) Low signal level. (c) Center signal level.

position, the sample was integrated over the width of the seeing distribution. The sample was also movable, we could sample the seeing distribution at the top, center, or bottom of the raster. For each relative fringe

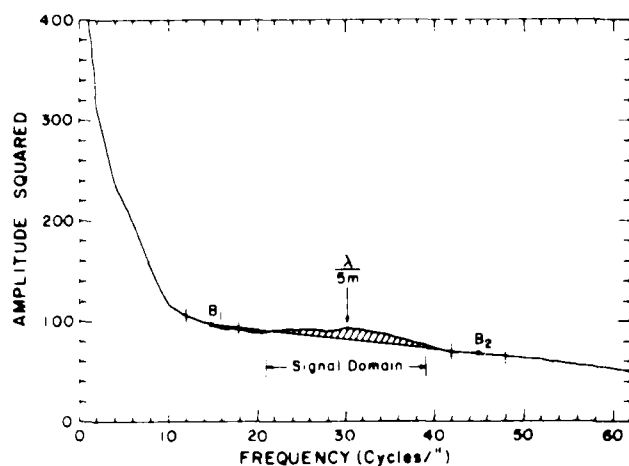


Fig. 10. One dimensional square Fourier modulus for an unresolved star using an opposite MMT mirror pair. The line segment and shaded area define the integrated signal calculated by our fringe contrast detection algorithm.

position, we sampled at the three raster positions. The experiment used the Fourier transformed results to compare fringe contrast statistics for data sampled at the top and bottom 128 lines of the video raster (the center sample being redundant). A typical power spectrum profile is shown in Fig. 10.

Letting F be the measured fringe contrast for a given fringe sample, we define an error signal E as $E = F$ (sample at bottom) $- F$ (sample at top) for a given fringe position. This gives an estimate of how well centered the fringes were over the length of the observation (see Table I). The fringe error (sixth column) is a visual estimate (± 5 fringes) of how far on average the fringes were off-center from the raster, i.e., the distance in number of fringes from the center of the image to the region of maximum fringe contrast. The path error column (visual estimates of the number of fringes by which the maximum contrast has been shifted) provides the path difference calibration of the phasing error. Thus, for observation A, in which the fringes were centered with respect to the seeing distribution, the +10 in the fringe error column indicates that the sample was taken at a position estimated to be ten fringe widths above the center of the seeing distribution. The fringe system could be cut-off center in the sample window due to either poor centering of the image or phasing errors which offset the fringes on the seeing distribution. Visual estimates of the magnitude of the offset could be made in either case. Four different average path length differences were investigated.

The data indicate that our algorithm could in fact detect when the fringes were off-center with respect to the sampling positions. For observation A, the algorithm found $E = -1.9$ indicating a stronger signal at the top than at the bottom. The sign of E tells the sense in which to make the correction. For observation B, in which the fringe error was twenty fringes low, $E = 2.1$, indicating a stronger signal at the bottom. The C and D observations showed similar results. We point out that statistics for the D observation (the dimmer star) are similar to those for the brighter star. Although at first surprising, this indicates that the statistics are dominated by atmospheric effects (seeing) and image motion (largely induced by telescope motion in this experiment) and not by photon statistics for such objects ($m_i < 4$). It is our experience with other measurements⁸ that this is true for objects to $\sim m = 6$ (if seeing is ~ 1 sec of arc). For fainter objects, the photon statistics begin to dominate. In these measurements the quantity F (sample position) is a measure of the mean number of correlated photons detected per scan at fringe frequencies, and our ratio is normalized by an arbitrary (but constant) factor.

Our contrast-detecting algorithm uses a linear approximation for the noise bias determined at frequencies immediately above and below the expected fringe frequency (see Fig. 10). The 5-m opposite mirror fringe spacing is 4.3 lines/fringe at 750 nm so that the 5-m base line is at $128/4.3 = 30$ in the 128-point transform. The algorithm then finds the average intensity at those frequencies and determines a line based on those averages. The line is, therefore, a linear estimator of the noise bias. The algorithm then integrates between the line and signal. A fringe contrast ratio is calculated (= integrated signal divided by the average value of the noise bias). Note that negative contrast ratios are possible because the line may actually be an overestimate of the noise bias; if a very small signal is present, our contrast may come out negative because the signal is sitting below this arbitrary line. The relative value (difference) is nevertheless valid.

All the data analysis was carried out on a Z-80 with a Forth floating-point FFT. Fringe contrast data for each fringe sample (a single pair of mirrors - 600 samples) took a whopping 15 min to compute. But the important point is that only 10 sec (= 600 fields/60 fields/sec) of data were used for each pair. For full phasing of all six mirrors, five base lines \times 2 sample pairs (at top and bottom) \times 600 FFTs/sample pair imply that a minimum of 6000 FFTs (or equivalent calculations) will have to be executed within 10 sec for

Table I. Fringe Contrast Sensing Experiments

Obs	Star	Error sig. $E(B) - E(T)$	Std. error	SNR	Fringe error	Path error (μ m)	Sensitivity (μ m)
A	α Oph	-1.9	1.0	1.9	+10	7.5	4
B	α Oph	2.1	0.7	3.0	-20	15	7
C	γ Her	1.2	1.1	1.1	+10	7.5	6
D	γ Her	0.7	1.2	0.6	<5	<4	<6

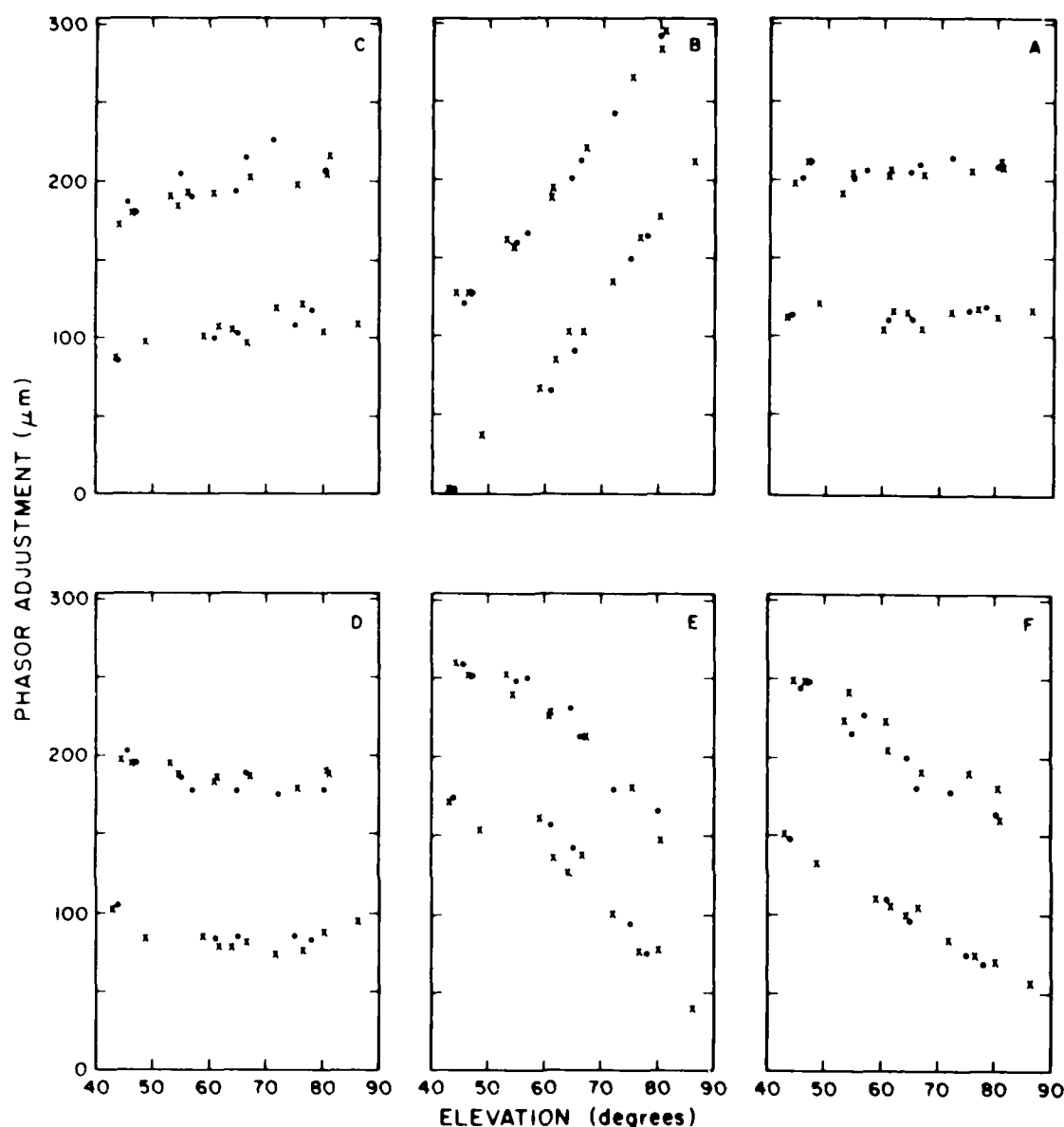


Fig. 11 Change of path length for all six telescopes as a function of elevation while repeatedly moving up and down.

phasing of all six telescopes. These numbers are only good to a visual magnitude of ~ 6 . For objects fainter than that, photon statistics dominate the signal, and phasing time increases with magnitude, requiring 100 sec for $m = 8.5$ (which is 0.1 times as bright as a sixth magnitude).

These figures show that a modest real-time processor which can reduce contrast computation times to < 63 μ sec (video line time), together with longer effective integration times, yielding better statistics, would improve the sensitivity to better than the ± 6 μ m or so of this proof of principle demonstration. This experiment was inadequate to allow a prediction of the ultimate cophasing precision one might attain in this way.

IV. Interferometer Stability

Visual observations of a star image using the TV monitor and a large optical filter bandwidth ($\lambda/\Delta\lambda \sim$

5–10) easily allow fringe detection for stars up to magnitudes $V \sim 4$. With an electronic detector and algorithms such as just described we may gain several magnitudes, but the fact remains that it will be possible to cophase the MMT telescopes only on relatively bright stars. We presently conservatively assume that we will be limited to $V \sim 8-9$ stars. To observe faint objects we, therefore, plan (1) to go to a nearby bright star, (2) to cophase the telescope on this star, (3) to go to the object to be studied, correcting for flexure effects, (4) to correct continuously the path lengths for flexure and thermal changes, and (5) to return to the bright star after some time Δt to check and improve cophasing. For reasonable use of the MMT as a phased telescope, it is necessary that Δt is long compared with the time needed to cophase the telescopes and that the corrections for path lengths for a 5° offset can be well modeled.

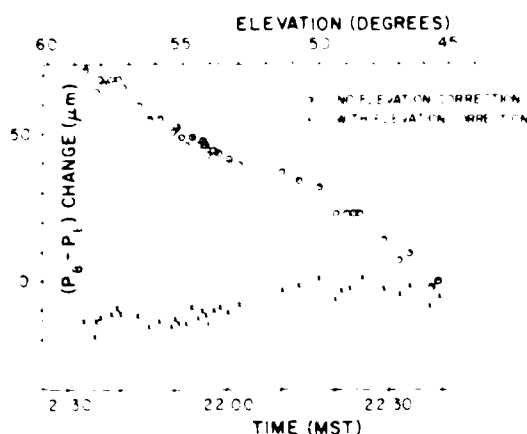


Fig. 12 Change of path length between telescopes *B* and *E* as a function of time while tracking a star in the western hemisphere: \circ , raw data; \times , the same data after correction for the elevation change shown in Fig. 11. The remaining variation of the crosses is mostly due to changes in the mount (OSS) thermal structure.

Figure 11 shows the result of an experiment in which the path length change between the two extreme vertical telescopes in the MMT was measured as a function of elevation change while moving the MMT both up and down. The change is very repeatable, and there is little hysteresis so that apparently the path length change can be modeled to a precision of $\sim 10 \mu\text{m}$. Much of the remaining variation is due to thermal changes in the optics support structure (OSS).

Figure 12 shows the path length change for an hour long sequence of observations for a star in the western hemisphere. Most of the change, shown in Fig. 11, is due to the systematic elevation change. The remaining path length change is, for a large part, due to thermal changes in the telescope which can also be modeled. It appears from Fig. 12 that even without further mechanical improvement, and with a simple open-loop model for the elevation change of path length, we can control the path length to $5 \mu\text{m}$ over ~ 30 min. Further tests are planned in the future which will include a network of thermal sensors placed across the OSS. We measured a path length change due to thermal variations of $\sim 65 \mu\text{m}/^\circ\text{C}$, the linear regression shown in Fig. 13, indicating that it will be necessary to monitor the OSS temperature to better than 0.1°C .

The six pairs of path length compensating prisms (mode C, Fig. 3) are controlled by an Aerotech system including stepping motor drives and precision stages with computer controllable absolute or incremental positioning. Since the controller is compatible with existing (spare) MMT telescope coalignment control interfaces, it was an extremely straightforward process to implement an open loop control for this cophasing system. We determine for each of the five relative paths a change of path length curve such as that shown for telescopes *B* and *E* in Fig. 11. We fit a quadratic equation to each of these five curves and let the computer adjust the paths correspondingly for changes in elevation. This system is now implemented, and the preliminary results using it indicate that the corrections

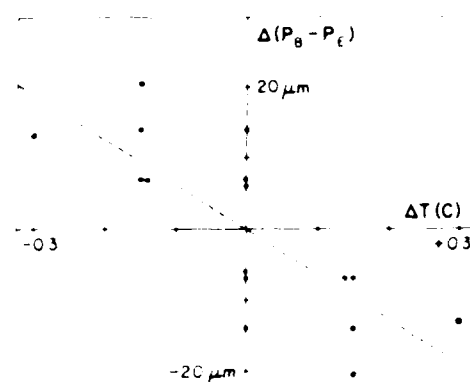


Fig. 13 Path length difference between telescopes *B* and *E* as a function of temperature difference. The dashed line corresponds to $65 \mu\text{m}/^\circ\text{C}$.

implied by \times in Fig. 12 can indeed be achieved for all five relative path lengths. We have not yet added thermal compensation to this system, but plans to do so are under way.

V. Instrumental Isoplanicity and Coherence Considerations

The telescope cophasing system just described allows us to bring the six principal rays together cophased in the MMT quasi-Cassegrain focus *F*. This does not imply that (1) the rays stay cophased when looking at a star off the axis of the telescope (so that the image is translated off the telescope axis), and (2) rays coming from other points of the telescope pupils are cophased with their principal rays.

We have analyzed the MMT optics⁹ to show that the first condition (1) is met by making the angular converging ray geometry, approaching the focus, *F*, match the linear aperture geometry of the telescope. Since the maximum edge-to-edge distance of the six 1.82-m diam MMT mirrors equals 6.86 m (Fig. 1), and since the individual telescope beams converge in *F* at $f/31.6$, that means that the overall f ratio of the MMT should be $f/8.39$ ($8.39 = 31.6 \times 1.82/6.86$). With this f ratio, the white light fringe crossing the superimposed images of an unresolved star stays centered on that image as the telescope is pointed slightly away from the star (i.e., as the image is moved off-axis). The small change in the f ratio from the original $f/9$ configuration of the MMT is presently accomplished by a small [1.5-cm (0.6-in.)] raising of the tertiary mirrors and a small adjustment in the tilt (0.1°) of these mirrors.

The second condition (2) also analyzed by Beckers *et al.*⁹ is automatically fulfilled in the focal plane of a single perfect telescope. The focal planes of the six beams are, however, tilted with respect to one another so that the average focal plane of the MMT (the plane at right angles to the overall telescope axis) deviates from the individual focal planes by 2.5° . As long as the distance between the planes is less than the Rayleigh focal range ($\pm 2\lambda$) or ± 4 mm at 500 nm and ± 10 mm at 5 μm , the

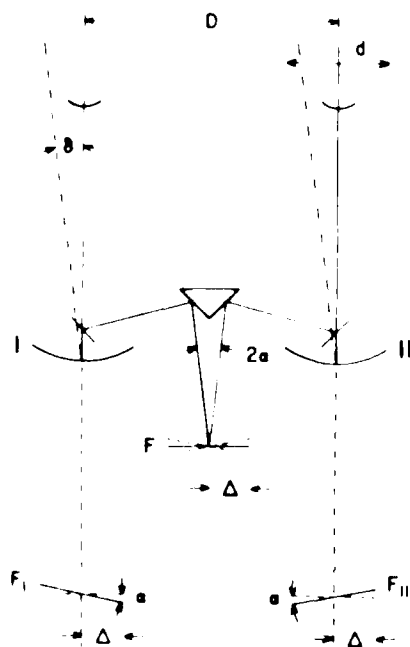


Fig. 14. Schematic of optical paths in MMT for two telescopes I and II. D , geometrical separation of centers of telescopes; d , geometrical diameter of single telescope; 2α , angles which principal rays make in the final image; δ , angle of the off-axis star to telescope axis; Δ , distance of off-axis star image to center of image plane.

phase difference between the central and edge rays of the pupil equals less than a quarterwave. This corresponds to a diameter of the instrumental isoplanatic field of view of 164 sec of arc at 500 nm and, in IR, 1640 sec of arc at 5 μ m. Over the so-called atmospheric isoplanatic patch at 500 nm (~ 4 sec of arc), the maximum phase difference is $\lambda/160$, much less than the differences introduced by the atmosphere and by other telescope imperfections, so that the focal plane tilts have a negligible effect on cophasing. If desired, however, these tilts can be removed by, for example, the scheme described by McCarthy *et al.*¹¹ In practice this is not necessary. By proper choice of the focal plane tilt angle, the internal off-axis phase difference induced by the tilted focal planes can be made to compensate exactly the phase difference of the off-axis plane wave incident across the telescope pupil(s).

Figure 14 summarizes the analysis of the off-axis condition (1). The condition which has to be met is that the path difference in the central rays for an off-axis star outside the telescope (δD) equals the path difference between the rays converging to the common plane F inside the telescope. The focal planes of each of the telescopes are shown as dashed lines in Fig. 14, whereas the image plane is shown as a full drawn line. The path difference for the off-axis star inside the telescope is, therefore, $2\alpha\Delta$. If the effective focal length of the telescopes equals F , then $\Delta = \delta F$ and $2\alpha = D/F$. The beam convergence θ ratio of each telescope is $\beta \text{ rad} = d/f = 1/31.6$ so that condition (1) is met by making $2\alpha/\beta = D/d$. This means that the angular convergent ray

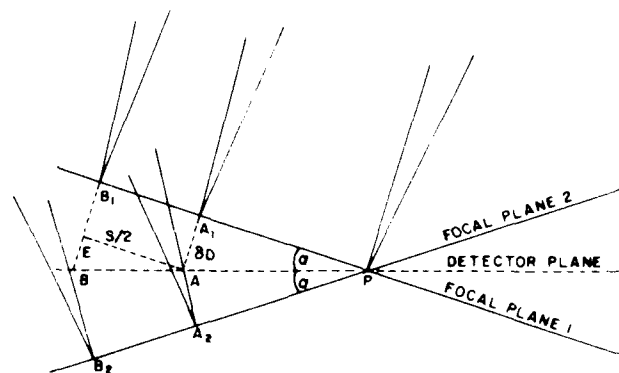


Fig. 15. Tilted focal planes of two single telescopes shown with reference to the detector focal plane, which is the mean focal plane for all telescopes. P is at the focus of the principal ray for an on-axis image. A and B are focal points at the center and edge, respectively, in a seeing-limited off-axis image.

geometry in the image plane must be mapped into the linear aperture geometry.

The same condition has to preserve not only the overall geometry of the MMT aperture but also the point-to-point geometry as well. We have analyzed the detailed effects of the tilted focal planes on the non-principal rays. Condition (2) is met exactly for the principal rays for both on-axis and off-axis objects. We can show that condition (2) is also met with sufficient precision for nonprincipal rays by referring to Fig. 15.

Figure 15 shows an off-axis focal-plane analysis of a seeing-limited image, S = seeing diameter. A is the principal ray at the center of the seeing distribution, and B is a ray at the edge, $BA = S/2$. Subscripts 1 and 2 denote rays from two telescopes converging in their respective focal planes. Clearly the cophasing condition (1) will assure that the path lengths for all wavelengths are equal at P . (The white-light fringe is centered.) The off-axis principal rays A_1 and A_2 which superimpose in the detector focal plane at A , are properly phase compensated (white-light fringe also centered) if the geometric condition (2) is satisfied. It remains only to investigate the effects due to the phase errors for the nonprincipal rays within the seeing distribution. The path length error at the edge of the seeing disk is $\Delta p = 2\alpha = S\alpha$, but $2\alpha = 5m/F$ and $S = F/2 \times 10^5$ for 1 sec of arc seeing. Thus $\Delta p = 12 \text{ nm}$.

Note that, just as the internal path difference at A_1 compared with P is matched by the external path difference, this path difference is also compensated by the external path difference. The only effect is the difference in phase for the light of different wavelengths transmitted in a finite bandpass traversing this distance. This coherence condition sets an upper bound (seeing dependent) on the observing bandpass. Let us require that, for negligible loss of contrast, this phase error be $< 1/10$. The condition $(\Delta p/\lambda_1) - (\Delta p/\lambda_2) < 1/10$ implies that $\Delta\lambda < \sqrt{120} \mu\text{m} = 2.1 \text{ nm}$ at 500 nm. There is also a phase error associated with seeing in the individual 1.83 m mirrors. For a 1.8 m mirror $n_s \sim (S/2)(t/F)$, where $t = 1/22\lambda$ is the (individual) telescope diffraction limit. Evaluating this at 500 nm yields

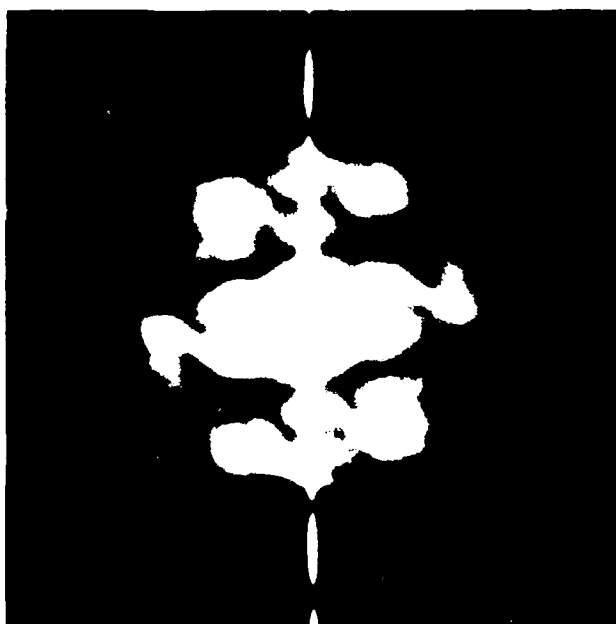


Fig. 16. Capella. Image power spectrum obtained from speckle fringes using the full 6.86-m MMT aperture in a 10-nm bandpass centered at 750 nm (compare with Fig. 8).

$n_p = 7.4$ cycles. This reduces the maximum permissible bandpass for the interferometer system to $\Delta\lambda < 1.6$ nm.

For a perfect $f = 39$ telescope of 6.86-m aperture in 1 sec of arc seeing, the path error at the edge of the seeing disk at 500 nm is $n_p \approx 28$. If again we insist that, after n_p cycles, the phase error is $< 1/10$, we find for 500 nm that $\Delta\lambda < 1.8$ nm. Comparing these bandpasses, the ratio of 1.8/1.6 implies they are the same to within 15%, i.e., to the precision of these approximations. Thus there is no significant degradation in the performance of this MMT configuration due to tilted focal-plane effects.

VI. Polarization Effects

An additional requirement for optical interference is that the polarization characteristic of the light passing through the six telescopes is not affected (or is affected in the same way). Calculations have shown¹⁷ that the resulting elliptical polarization for aluminum surfaces is only significant for optical and near-IR wavelengths $< 2 \mu\text{m}$. For optical wavelengths, linear retardation occurring on the off-axis reflections of the tertiary mirror and beam combiner will decrease somewhat the fringe contrast between nonopposite telescopes.

In the final coherent configuration the full contrast may be restored by insertion of retardation compensating optics. However, we emphasize that image power spectra do in fact contain energy at all frequencies expected, as can be seen by comparing an actual observed MTF (Fig. 8) with its predicted basis (Fig. 1). Our experience has shown that, in any case, independent calibration of the combined telescope plus atmosphere response function, by repeated observations of

Table II. Speckle Interferometry of Capella

	Observed	Predicted ¹²
Separation	40.5 ± 2.1 mas	40.1 mas
Position Angle	$327^\circ.3 \pm 5^\circ.0$	$321^\circ.2$
Relative Intensity	0.3 ± 0.2 mag	0.25 mag ⁹

⁹ K. O. Wright, "The Secondary Component in the Spectrum of Capella," *Astrophys. J.* 119, 471 (1954).

an unresolvable source, are required for conventional speckle interferometry.⁸ Differential speckle interferometry¹¹ is self-calibrating in any case.

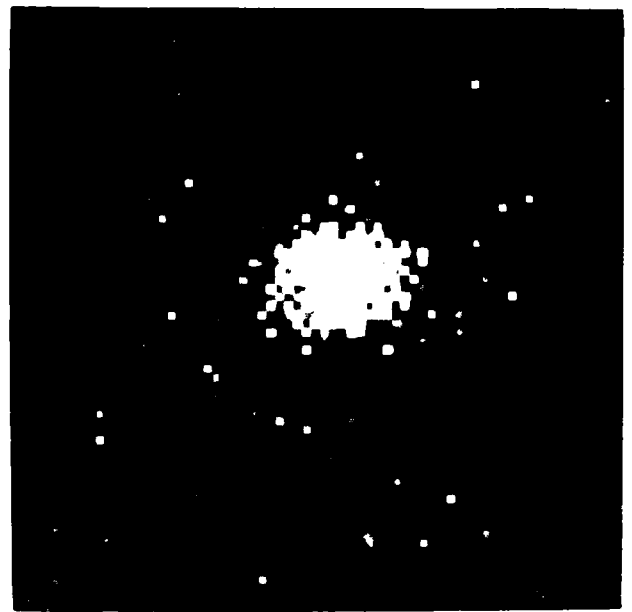
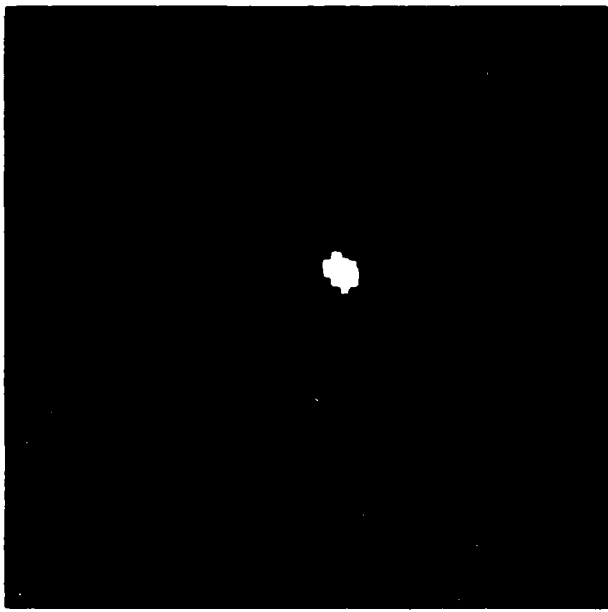
No detailed analysis of the relative amplitudes at particular frequencies in the (u,v) plane has yet been carried out. The particular example shown here (Fig. 8) results from data taken without even the closed-loop corrections operating, so it may be expected that amplitudes representative of imperfect cophasing may predominate over other effects seen in this preliminary measurement, presented here as only a qualitative proof of principle of these interferometer concepts.

VII. Six-Beam Optical Measurements

Further qualitative evidence of the validity of this interferometer configuration is shown in Fig. 16 where the binary nature of Capella is seen as visibility minima cross the 6.86-m image power spectrum, also obtained without benefit of the open-loop cophasing corrections described above. From this 10-nm bandpass measurement at 750 nm we infer a separation of components of ≈ 1.5 times the diffraction limit—the second visibility minimum occurs just as the power spectrum cutoff frequency. Table II shows the observed positional parameters together with those accurately known from the well-determined¹² orbital parameters.

In the Labeyrie^{13,14} method of speckle interferometry the relative intensity value is obtained by calibrating the image power spectrum (shown for Capella in Fig. 16) by dividing it by the image power spectrum for an unresolved object (shown for β Tau in Fig. 8), both corrected for noise bias. If the speckle MTFs for both of these measures were identical (including seeing effects), this would have produced the square of the 2-D visibility for this binary object. The 2-D result is shown in Fig. 17. The nonuniform appearance of the fringes represents the effects of errors in the point-source MTF calibration in this very preliminary result.

For a binary star, the intensity distribution $I(u)$ across the fringes is $I(u) = (I_1 + I_2) + 2\sqrt{I_1 I_2} \cos(2\pi pu)$ with fringe visibility V given by $V = 2\sqrt{I_1 I_2} / (I_1 + I_2)$. The cross-fringe intensity function was obtained by rotating the fringe pattern shown in Fig. 17 so that the fringe minima were parallel to the raster columns and then summing columns over the central 32 rows in the (u,v) plane. This effectively averaged the data along the fringes. A least-squares fit, $A + \cos(2\pi pu) + B$, to that averaged data gives $V = A/B$, which can be solved for the intensity ratio $\alpha = I_2/I_1$, reported as a magnitude difference in Table II. The model fit, together with the averaged intensity distribution, is shown in Fig. 18. Systematic departures from the expected cosine curve



THE END

for providing the γ Ori image shown in Fig. 19 and J. Hebben for the differential images of γ Ori and α Ori shown in Figs. 20 and 21. We also appreciate the willing and able assistance of the Multiple Mirror Telescope Observatory support group in the various reconfigurations of the telescope and the special instrument setups required for these experiments.

The MMT is a joint facility of the University of Arizona and the Smithsonian Institution.

References

1. A. Labeyrie, "Interferometric Analysis of the Images of the θ Aurigae Emission Nebula," *Opt. Acta*, **29**, 101 (1982).
2. J. M. Beckers, "The Multiple Mirror Telescope Speckle Interferometer," *NZ J. Astron.*, **22**, 137 (1989).
3. J. M. Beckers, J. L. Latta, N. E. Evans, J. P. Eggenstein, and G. K. Hoge, "The Multiple Mirror Telescope Phase Array," *Proc. Soc. Photo-Opt. Instrum. Eng.*, **332**, 1 (1983).
4. A. Strittmatter, "Properties of Stellar Interfer Spectroscopy with the Multiple Mirror Telescope," MMT Observer's Report, May 1984. Multiple Mirror Telescope Observatory, Tucson, 1984.
5. D. W. McCarthy, P. A. Strittmatter, E. K. Hoge, and E. J. Low, "MMT Interferometric Phase Array Interferometer and Phase Array," *Proc. Soc. Photo-Opt. Instrum. Eng.*, **332**, 1 (1983).
6. J. M. Beckers, E. K. Hoge, and P. A. Strittmatter, "Multiple Rotational Spectra of θ Aurigae from the MMT Observer's Report, May 1984. Multiple Mirror Telescope Observatory, Tucson, 1984.
7. J. M. Beckers, E. K. Hoge, and P. A. Strittmatter, "Astronomical Shearing Interferometer for the Multiple Mirror Telescope," *J. Opt. Soc. Am.*, **96**, 11 (1979).
8. E. K. Hoge, E. N. Hubbard, P. A. Strittmatter, and W. J. Cocke, "The Steward Observatory Speckle Interferometry System," *Opt. Acta*, **29**, 101 (1982).
9. J. M. Beckers, E. K. Hoge, and P. A. Strittmatter, "Optical Interferometry with the MMT," *Proc. Soc. Photo-Opt. Instrum. Eng.*, **144**, 85 (1983).
10. D. W. McCarthy, "MMT Polarization Properties," MMT Observer's Report, May 1984. Multiple Mirror Telescope Observatory, Tucson, 1984.
11. J. M. Beckers, "Differential Speckle Interferometry," *Opt. Acta*, **29**, 101 (1982).
12. H. A. McAlister, "The Apparent Orbit of Capella," *Astron. J.*, **86**, 74 (1981).
13. A. Labeyrie, "Attainment of Diffraction Limited Resolution in Large Telescopes by Fourier Analysing Speckle Patterns," *Astron. Astrophys.*, **6**, 8 (1970).
14. A. Labeyrie, "Stellar Interferometry Methods," *Ann. Rev. Astron. Astrophys.*, **16**, 1 (1978).
15. C. R. Lynde, S. F. Wampler, and J. W. Harvey, "Digital Image Reconstruction Applied to Alpha Orionis," *Astrophys. J.*, **207**, 174 (1976).
16. J. C. Christou, E. K. Hoge, J. Freeman, and P. Strittmatter, "Speckle Image Reconstruction: Weighted, Shift and Add Analysis," *Bull. Am. Astron. Soc.*, **16**, 88 (1984).
17. A. R. Menzel, M. P. Menzel, and N. J. Woot, "Multiple Aperture Telescope Diffraction Image," in *Astronomical Instrumentation Engineering*, ed. by R. K. Standaert and J. C. Wyant, Eds., Academic, New York, 1985, p. 149.
18. J. R. P. Angel, "Averaging of Ground-Based Telescopes for Optical and IR Astronomy," *Astron. J.*, **95**, 67 (1988).
19. J. M. Beckers, E. K. Hoge, and H. C. Margolis, "The Differential Speckle Interferometer," *Proc. Soc. Photo-Opt. Instrum. Eng.*, **145**, 10 (1983).

REAL-TIME SIGNAL PROCESSING REQUIREMENTS FOR DIFFRACTION LIMITED OPTICAL IMAGING

E. Keith Hege^{1,2} and Julian C. Christou
Steward Observatory
University of Arizona

Abstract

Diffraction limited optical images can now be produced using large ground-based astronomical telescopes. This is quite new, with convincing validation being achieved only in the past year. The computational requirements necessary to implement this capability for routine observations already challenge the capacity of present superminicomputers. Extension to larger telescopes will require supercomputer support from the beginning.

Introduction

In the present context the term "optical" is used for wavelengths shorter than those for which conventional radio techniques are applicable. The short wavelength optical limit is that at which the atmospheric correlation time becomes so short that the phase calibration problem becomes intractable. At present the limit is unknown, but appears to be about 400 nm where the correlation time t is 1 to 10 milliseconds.

Although the promise of astronomical studies with diffraction limited detail came in Labeyrie's 1970 proposal for speckle interferometry, the reality of validated diffraction limited astronomical images is a recent achievement. The optical image reconstruction problem is primarily a phase calibration problem. The original Labeyrie method yields visibility functions (amplitudes), but all phase information is lost. In tackling the phase problem, three approaches have evolved: i) blind phase reconstruction (Fienup 1978,9 and Bates and Fright 1983) constrained by amplitudes alone, ii) phase retention (Knox and Thompson 1974, the original shift-and-add methods of Lynds, Worden and Harvey 1976 and of Bates et al. 1980, Walker 1981 a phase encoding exponential filter, Bates 1985 zero-and-add, and Aitken et al. 1985 phase gradient) in which phase information is retained at each processing step, iii) shearing interferometry in which phases are measured directly (Roddier and Roddier 1983) and iv) phase self-calibration methods in which seeing effects are removed without reference to a point-source calibration (Lohmann et al. 1983 speckle masking triple correlation method, and Christou et al. 1986a weighted shift-and-add).

¹Visiting Astronomer at Kitt Peak National Observatory, operated by National Optical Astronomy Observatories under contract to National Science Foundation.

²The Multiple Mirror Telescope, also used for some observations reported here, is a joint facility of the University of Arizona and the Smithsonian Institution.

The principal efforts have been at Harvard (Papaliolios et al. 1985 and Nisenson et al. 1985) with the Knox-Thompson algorithm, at Erlangen (Weigelt et al. 1985) using the triple correlation technique they call speckle masking, at Nice (Rodier and Rodier 1983) with shearing interferometry and at Arizona (Hege et al. 1985b) with weighted shift-and-add and a promising matched filtered extension of that non linear deconvolution method (Ribak 1986).

Phase reconstruction from amplitudes alone is not unique, even though Bruck and Sodin (1979) have shown the ambiguity problem to be less severe in 2-D than in 1-D. Because of lack of convincing theory of why it should work and because there has been no quantitative analysis of its robustness to measurement noise, Greenaway (1985) notwithstanding, the phase-blind approach has not found favor.

Perhaps the best known phase retention algorithm is that of Knox and Thompson. It is certainly among the best understood theoretically. However, experience has shown the method to be very sensitive to detector systematics - particularly to photon noise bias (Nisenson et al. 1983 and Papaliolios et al. 1985) and especially so if the photon PSF is not a delta-function (our experience).

Among the most promising approaches are those which are self calibrating. Both the Knox-Thompson and the original shift-and-add methods require calibration by independent observations of point source references. This presents another problem since the seeing statistics, due to the high variability of optical seeing, may make the calibration data a poor match to the object data (Christou et al. 1985a). Therefore the recent promise of the triple-correlation method and the matched-filtered, weighted-shift-and-add method is very attractive. Unfortunately, this self-calibration does not come easy; it requires an increase in computation of up to an order of magnitude or more. The triple correlation, for example, increases the 2-D image problem into a 4-D computational problem.

Computational Implications of Recent Results

There are several objects with physically significant resolvable structure (other than binary stars) at the limited resolutions achieved with 3 to 5 μ class filled (conventional) optical apertures. Specifically, there is enough to be useful for validation of optical image reconstruction and self-calibration methodology as well as enough astrophysics to whet one's appetite for the larger optical apertures planned for the near future.

The advent of high-quantum efficiency, low-distortion, photon-counting imaging detectors (e.g. Papaliolios et al. 1985) proved to be crucial to the implementation of Knox-Thompson methods. On the other hand, experience with shift-and-add methods indicates that such methods are less sensitive to detector artifacts (Christou et al 1985b). In either case, considerable post-processing is required to produce the best possible data- and telescope-limited images.

Knox-Thompson results are characterized by non-physical negativities and other amplitude non-linearities which can be suppressed by Fienup

iteration using a well-calibrated visibility function. Recently techniques for controlling the effects of variable seeing between object and point source data have been developed (Christou *et al.* 1985a). Greenaway (1985) has shown that, given sufficient phase information, the Fienup method converges to the physical solution, even in otherwise analytically ambiguous 2-D cases.

Some of our recent results obtained using shift-and-add methods and MEAN with KPNO 4m telescope data are shown in figures 1 through 4.

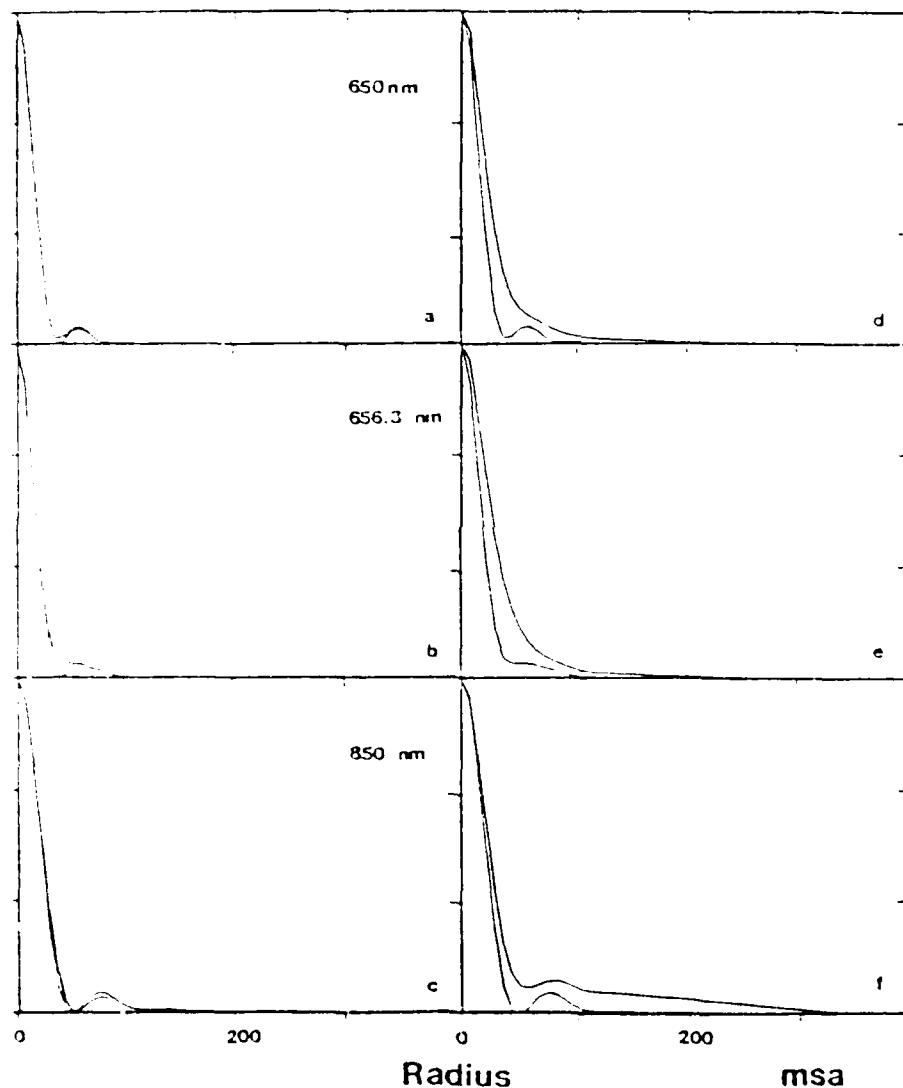


Figure 1. Azimuthally averaged radial profiles observed for Gamma Orionis are compared with the computed 3.8m Airy pattern in (a)-(c) and with similar observations of the resolved star Alpha Orionis in (d)-(f) for three wavelengths.

Figure 2 shows the expected statistical improvement proportional to square-root of number of photons observed (until limited by known detector systematics).

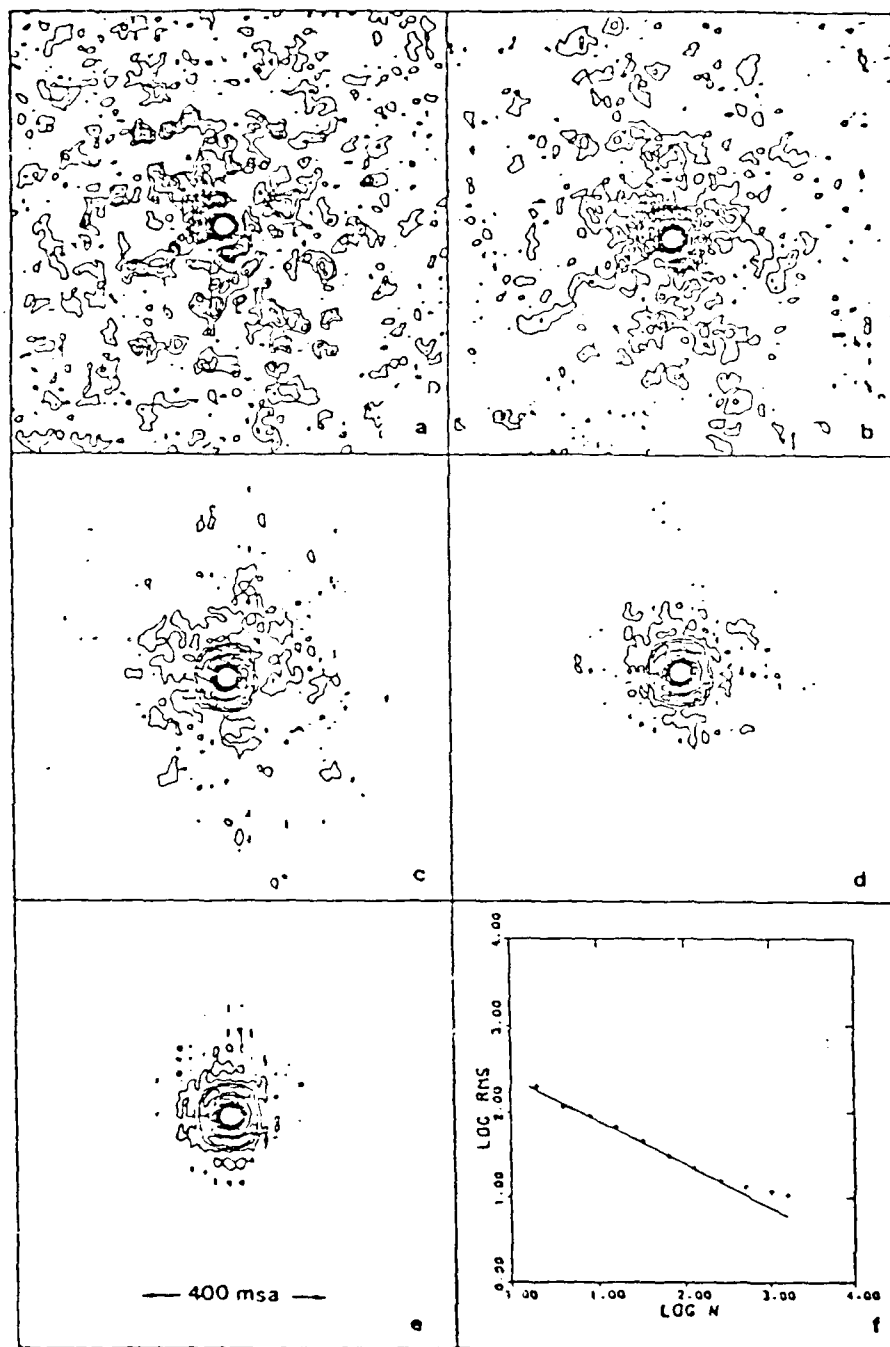


Figure 2 shows the expected statistical improvement proportional to square-root of number of photons observed (until limited by known detector systematics). The solid line is a power law of -0.5 .

Shift-and-add results contain the telescope point spread function. Point source observations are required to calibrate the observing beam. In this case, CLEAN or Maximum Entropy, as used in radio imaging, produce good results.

The good seeing calibration (sky background is flat) and diffraction limited PSF (Airy responses are seen in both figs. 1 and 2. Figure 3 shows qualitative agreement of the H-alpha and CaII (8542) radial image profile with that predicted by Hartmann and Avrett (1984) assuming a flux of Alfvén waves sufficient to drive an outflow of 10^{-6} solar mass per year and using electron densities from radio measurements. We see significant deviations at about 3-4 stellar radii which could be evidence of increased outflow of matter at an earlier epoch. This may relate to variations in visibility profiles which Roddier *et al.* (1986) have shown to relate to fluctuations in photometric intensity and which can be interpreted as signifying a variability in mass outflow.

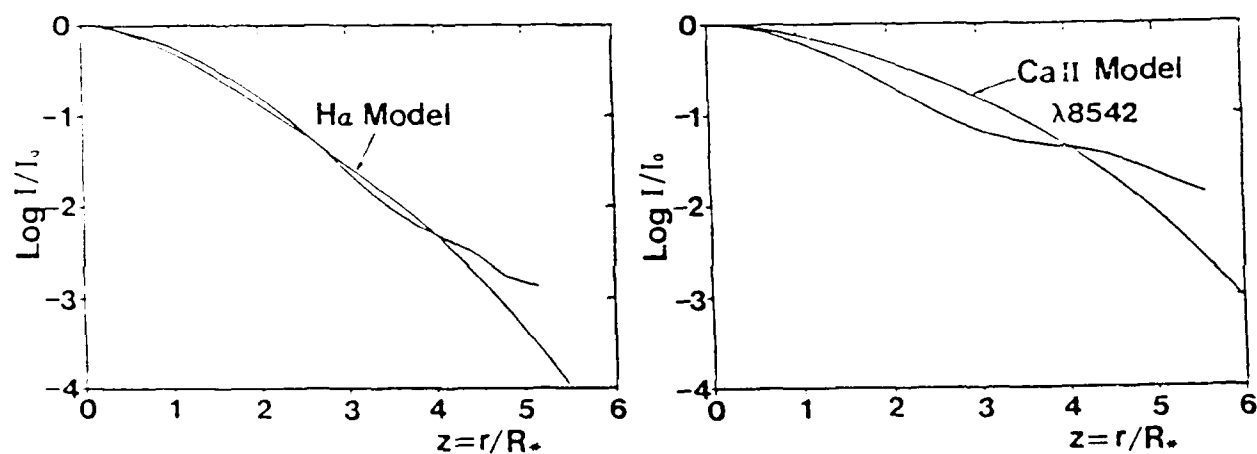


Figure 3. Observed radial profiles of Alpha Orionis compared to models computed by Hartmann and Avrett (convolved to resolution of observation).

Observations at all bandpasses showed evidence for excess emission at about $2R_*$ (i.e. at $\sim 42\text{mas}$) which agrees with the $0''.08$ dia. 2cm VLA images reported by Hjellming (1985). Figure 4 shows the residuals of our image data when limb-darkened stellar disk images (Cheng *et al.* 1986) are subtracted. In all cases excess activity is seen at about $2R_*$.

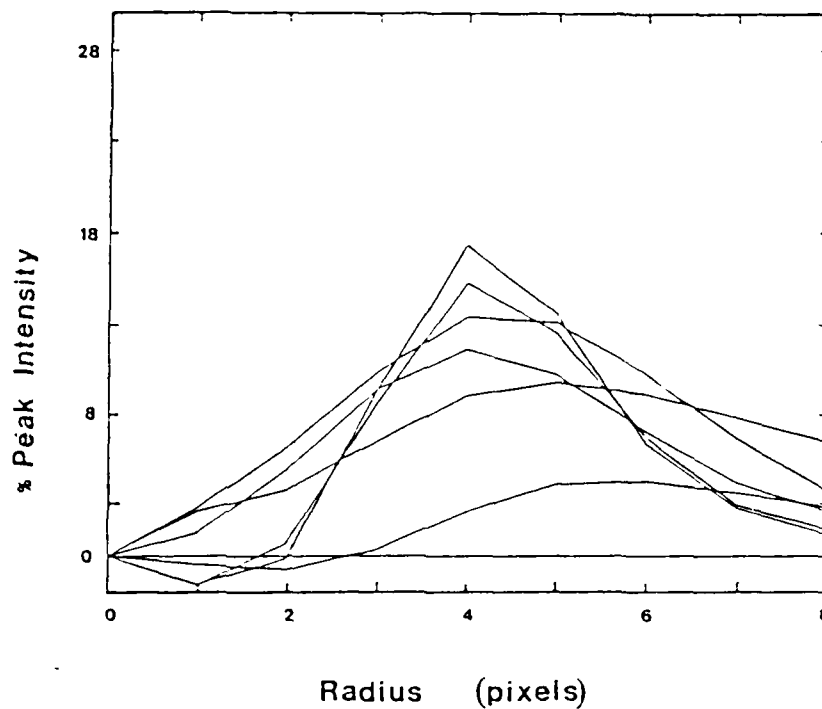


Figure 4. Residuals to limb-darkened Alpha Orionis disk profiles.

What are the figures?

Optical image reconstruction is, as it is for radio, Fourier transform intensive. Unlike radio, however, present optical interferometry integrates the correlated optical signal (specklegram) in an image plane detector. The bandwidth driver in the optical case is the short $O(10^{-2})$ s atmospheric correlation time t . The number of specklegrams required is the total integration time T , typically $O(10^3)$ s, divided by the correlation time t : $N = T/t = O(10^5)$. At minimum, the seeing distribution must be Nyquist sampled at the optical diffraction limit. This sets the maximum detector pixel scale d . At maximum the field of view P extends to the isoplanatic limit. For this argument, both are order of magnitude 1 arc-second (minimum). At 400 nm for a 5m class telescope, the number of pixels per specklegram $n = (P / d)^2 = (1 / .01)^2 = 10^4$. Each specklegram must be Fourier transformed $\#ft$ times. For calibration of detector response and other preprocessing there are $\#fp$ additional floating point operations to be performed. An estimate of the total number of operations to be performed can be given as

$$\#Ops = N \{ \#ft n \log(n) + \#fp n \}.$$

For this estimate, which is intended as only an order of magnitude estimate, neglect the additive term and assume $\#ft = O(1)$.

$$\#Ops = O\{N n \log(n)\}$$

$$\#Ops = O(10^5 \ 10^4 \ \log 10^4) = O(10^{10})$$

Since this is for a real-time integration of 10^3 s, the real-time processing bandwidth implied is $O(10)$ MHz just for the primary reductions.

Postprocessing using e.g. the Fienup method involves $O(10^3)$ iterations each with 2 Fourier transforms. This is a modest overhead, about 1%, by comparison. Other postprocessing methods require order of magnitude equivalent computation. For optical interferometric imaging, the processing overburden is in the primary amplitude and phase integrations.

This is already a significant demand on our Data General MV10000 superminicomputer. Typically, the primary processing expands $O(30)X$ over telescope aperture time. Thus, we can reduce completely only $O(3)$ nights/year of data, assuming dedicated use of that machine. We do not have dedicated use: we share the system with $O(100)$ users!

Self-calibration implies orders of magnitude more computation. The triple correlation

$$\{i(x) i(x + s)\} * i(x),$$

which Weigelt (1977) calls "speckle masking", is a Fourier transform (correlation) on the 2-D space x for every shift s which spans the same 2-D space as x , a 4-D problem. In recent publications, Weigelt et al. (1983), Lohmann et al. (1983), Bartlett et al. (1984) and Wirnitzer (1985) have refined and validated this imaging technique. This method requires the computation of the bi-spectrum (Fourier transform of triple correlation) for each specklegram. The bi-spectrum is

$$B(p,q) = I(p) I(q) I(-p-q)$$

where $I(f)$ is the Fourier transform of the specklegram $i(x)$ at spatial frequency f . Redundant information (symmetries) in the bi-spectrum for the one dimensional case (Bartlett et al.) requires that only $r^2/16$ floating point operations (multiplicative) are required for each specklegram (r = no. of elements in the 1-D array). Expanding this to two dimensional arrays, this then implies $O(r^2/16)^2$ "flops" will be required for each specklegram, assuming similar symmetries. Note that $r^2 = n = (P/d)^2$ and that this does not allow for oversampling of the diffraction limit (as is usual for good detector/aperture calibration). A reasonable estimate is

$$\#Ops = O(n/16)^2 \log(n) \text{ per frame}$$

which implies

$$\#Ops = 10^5 \cdot 10^6 \log 10^4 = O(10^{12}),$$

or $O(1)$ GHz Ops for real-time realization, which clearly approaches supercomputer capabilities.

The matched-filtered weighted shift-and-add does not make such great computational demands. It is an iterative procedure which may take $O(10)$ iterations to converge so that the existing modest problem is $O(100)$ MHz, computed as above.

These have been very conservative estimates. We have recently begun to use the cophased Multiple Mirror Telescope (MMT) for diffraction limited imaging (Hege et al 1985a). A more realistic calculation at MMT resolution ($d = .005$ arcsec) over the isoplanatic (patch $P = 2$ arcsec) requires $n = 0(10^5)$ pixels, another order of magnitude increase. This easily gets us to 100MHz to keep up with aperture integration time, considering only conventional approaches. Self-calibration techniques require another factor of 10 to 100, or more, depending upon method.

Differential Speckle Imaging (Beckers 1982, Hebdén et al. 1985) is a self-calibrating technique in which specklegrams obtained simultaneously in a single detector field are compared to reveal image differences. A significant elongation within the diameter of the stellar disk as well as evidence for H-alpha emissions extending to ~ 100 msa is seen in fig. 5.

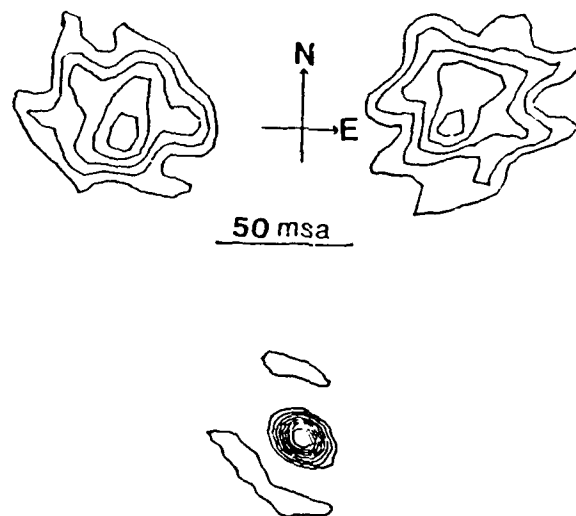


Figure 5. Differential images of Alpha Orionis obtained at two different parallactic angles compared to similar result for unresolved (PSF = 15 msa) Gamma Orionis.

Our results (figs. 1-4) were presented to demonstrate the state of the art of red supergiant imaging using optical imaging and (fig. 5) optical aperture synthesis interferometric techniques.

Where are we headed? The Keck telescope, at 12 m, requires $d = .003$ arcsec pixels, for Nyquist diffraction limited sampling, which pushes n near to 10^6 . The NNTT, at 22 m, pushes n well over 10^6 , clearly taking the problem to the (multi)GHz domain where supercomputers are required.

Conclusions

The bottom line: Whether conventional techniques with post-processing, or the newer self-calibrating techniques (especially triple correlation) are used, the computational overburden in removing the seeing nuisance is enormous. We emphasize nuisance and the difference between nuisance and limitation. This is important in decisions about what we attempt to do from the ground (transcending nuisance) and what can only be done from space (transcending physical limitation). Although the computational overburden is enormous, evidence suggests that with supercomputers we can compute away a considerable amount of atmospheric nuisance at a cost far less than that of the launching and operation of a space effort.

We already have ground based images (e.g. fig. 5) which exceed the resolution of space telescope by a factor of 2.5 (6 in number of resolution elements). If Space Telescope identifies higher resolution problems which can be done from the ground, then they should be done from the ground. But at millisecond of arc resolution, a supercomputer will be required as part of such a cost effective ground-based imaging system.

References

- Aitken, G.J.M., R.Houtmar, R.Johnson and J.-M. Pochet (1985) Appl. Opt. 24, 2926.
- Bartlett, H., A.W.Lohmann and B.Wirnitizer (1984) Appl. Opt. 23, 3121.
- Bates, R.H.T. and F.M.Cady (1980) Opt. Commun. 32, 365.
- " and W.R.Fright (1983) J. Opt. Soc. Am. 73, 358.
- " , A.M.Sinton and R.A.Minard (1985) Proc SPIE 556 37.
- Beckers, J.M. (1982) Opt. Acta 29, 361.
- Bruck, Y.M., and L.G.Sodin (1979) Opt. Commun. 30, 304.
- Cheng, A.Y.S., E.K.Hege, E.N.Hubbard, L.Goldberg, P.A.Strittmatter and W.J.Cocke (1986) Astrophys. J. (Submitted).
- Christou, J.C., A.Cheng, K.Hege and C.Roddier (1985a) Astron. J. (In press).
- " , E.K.Hege, J.D.Freeman and E.Ribak (1985b) Proc SPIE 556-36.
- " , E.K.Hege, J.D.Freeman and E.Ribak (1986a) J. Opt. Soc. Am. A 3 (In press).
- " , E.Ribak, E.K.Hege and J.D.Freeman (1986b) Opt. Engng. (In press).
- Fienup, J.,R. (1978) Optics Lett. 3, 27.
- " (1979) Opt. Engng. 18, 529.
- Greenaway, A. (1985) Cambridge Workshop on Imaging Interferometry in Space.
- Hartmann, L. and E.H.Avrett (1984) Astrophys. J. 284, 238.
- Hebden, J., K.Hege and J. Beckers (1985) Proc. SPIE 556, 284.
- Hege, E.K., J.M.Beckers, D.W.McCarthy and P.A.Strittmatter (1985a) Appl. Opt. 24, 2565.
- " , J.C.Hebden and J.C.Christou (1985b) Proc. Fourth Cambridge Workshop on Cool Stars, Stellar Systems, and the Sun (In press).
- Hjellming, R. (1985) Private communication.
- Knox, K.,T. and B.J.Thompson (1974) Astrophys. J. 193, L45.
- Lohmann, A.W., G.Weigelt and B.Wirnitizer (1983) Appl. Opt. 22, 4028.
- Lynds, C.R., S.P.Worden and J.W.Harvey (1976) Astrophys. J. 207, 174.
- Nisenson, P. and C.Papaliolios (1983) Opt. Commun. 47, 91.
- " , R.Statchnik, M.Karovska and R.Noyes (1985) Astrophys. J. (Lett) 297, L17.
- Papaliolios, C., P.Nisenson and S.Ebstein (1985) Appl. Opt. 24, 287.
- Roddier, F. and C. Roddier (1983) Astrophys. J. (Letters) 270, L23.
- " , C.Roddier, R.Petrov, F.Martin, G.Ricord and C.Aime (1986) Astrophys. J. (Submitted).
- Walker, J.G. (1981) Optica Acta 28, 1017.
- Weigelt, G. (1977) Opt. Commun. 21, 55.
- " , G.Baier, J.Ebersberger, F.Fleischmann, K.-H.Hofmann and R.Ladebeck (1985) Proc. SPIE 556-34.
- Wirnitizer, B. (1985) J. Opt. Soc. Am. A 2, 14.

HIGH-SPEED DIGITAL SIGNAL PROCESSING FOR SPECKLE INTERFEROMETRY

✓ E. K. Hege, W. J. Cocke, P. A. Strittmatter, S. P. Worden

Steward Observatory
Tucson, AZ 85721

William C. Booth

Signal Processing Systems
Waltham, MA 02154Abstract

Speckle Interferometry has now been shown capable of yielding diffraction limited information on objects as faint as visual magnitude 16. Research in progress at Steward Observatory is aimed at improving (a) the resolution, (by using the Multiple Mirror Telescope with its 6.9 meter baseline), (b) the accuracy of the derived results (by implementing better recording devices and reduction algorithms), and (c) the efficiency and speed with which the information can be provided (by means of high-speed digital signal-processing hardware).

The instrumentation proposed here will improve spatial resolution at visible wavelengths to approximately 15 milliarc-seconds (75×10^{-9} radians, the best possible for any existing telescope), reduce detector induced image distortion to less than 1% and increase the throughput to essentially real-time complex Fourier transform amplitude and phase integrations at the telescope.

Introduction

Speckle interferometry¹⁻³ is a post-detection image processing technique for producing diffraction limited images using large astronomical telescopes in the presence of Earth's turbulent atmosphere which otherwise limits the imaging resolution.

Since 1978 the basic design of the Steward Observatory digital video speckle camera has evolved, as reported in a series of publications⁴⁻⁷, to comprise three basic subsystems: a) video digitization of an intensified, magnified focal-plane image; b) Fourier transform (or vector autocorrelation) signal processing; and c) image analysis to produce the final interpreted results of speckle interferometry. Experience gained with these systems has shown the need for further refinements of these basic elements. a) Improved detectors are required to provide better spatial resolution and geometric fidelity as well as better linearity and dynamic range; b) real-time signal processing is required to permit the primary data compression to be accomplished at the telescope while the observations are in progress; and c) image processing systems (in addition to general-purpose computational capabilities) are required to efficiently reduce the speckle interferometric results. This basic speckle interferometry system design is shown schematically in Figure 1.

The present realization of this camera⁶, consisting of first generation electrostatic inverters (4 stages of Varo 8605), a plumbicon camera and a Grinnell digital video memory system for video digitization and general-purpose minicomputers of very limited capabilities (Data General Nova class) for both the signal processing and the image processing functions, has been applied successfully to observations of asteroids⁸, the Pluto-Charon system⁹ and the 15^m 7 QSO PG115+080¹⁰ as well as to observations of bright supergiants¹¹⁻¹³ and binary stars¹⁴⁻¹⁵. These observations and results have revealed both the capabilities and the limitations of this system. Among the demonstrated capabilities are included a) observations of structure as faint as $m_v=18$ in an $m_v=16$ system¹⁰, b) observations of structure at the diffraction limit of the Multiple Mirror Telescope^{13,16}, c) astrometric observations^{8-10,14-15} and d) mapping of faint envelopes around bright supergiants¹².

Among the limitations of this system, the most severe are a) detector limitations including large geometric distortions, limited linearity and low dynamic range; b) extremely limited signal processing throughput in which the primary signal processing time ranges up to 100 times that required for the observations at the telescope; and c) no special purpose array processing capability for image analysis. We anticipate upgrading of observatory computational capabilities to include array-processing image analysis.

* The Multiple Mirror Telescope is a joint facility of the University of Arizona and the Smithsonian Institution.

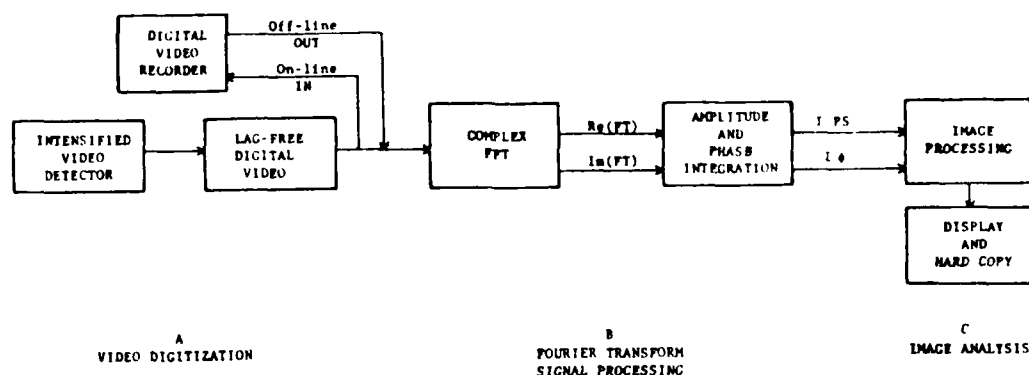


Figure 1. The Digital Speckle Interferometry System.

It is the purpose of this paper to propose instrumentation, specifically detectors and real-time Fourier signal processors, to alleviate limitations of present detectors and signal processors, in order to a) exploit the 75 nanoradian (15×10^{-3} arc seconds) full resolution of the Multiple Mirror Telescope¹ over a distortion-free field at least 10 microradians (2 arc seconds) square, and b) provide the required primary signal processing, with at least 256-pixel resolution in each direction, in real time at the telescope.

Detector Requirements

Experience with our present intensified plumbicon video system⁶, together with evidence from other workers¹⁸, establishes rather strong criteria for detector performance. In order to have single-photon detection, detector-lag elimination⁵ is required to remove frame-to-frame correlation. This can be accomplished by frame-subtraction⁶ for analogue detection or video-raster event-localization schemes⁷, as shown in Figure 2. Event-localization using newly developed time-tagging detector readout schemes^{19,20} are intrinsically lag-free. For bright-object work, these readout systems must be highly linear and have a large dynamic range (at least 8-bits deep for analogue intensities) or very fast (10^6 events/sec for photon-counting schemes). For astrometric work, or for multiple specklegram differential work¹², very low geometrical distortion (less than one pixel in a 512×512 primary raster) is required.

Proximity focused electrostatic image intensifiers²¹, configured in a system with sufficient gain for good photo-electron pulse discrimination, as represented schematically in Figure 3, provide greatly improved geometrical fidelity and geometrical stability compared to either electrostatic inverters or magnetic focused devices. High quantum efficiency ($>20\%$) and low dark current ($<10 \text{ e.cm}^{-2}.\text{sec}^{-1}$ at -30°C) are required in order to obtain useful specklegrams of $m_v=15$ or fainter objects, although these levels of dark-emission are difficult to achieve for proximity focused devices with good red response. Also, very fast (1 microsecond) output phosphors are required if event detection at $10^6/\text{sec}$ is to be achieved.

The geometrical fidelity and stability and the linearity and dynamic range of the system cannot be better than that of the image intensifier readout system. This immediately rules out electron-gun video systems in the changing environments of an instrument mounted on an astronomical telescope. Solid-state (CCD or Photodiode) cameras²², as well as the event localizing schemes noted above, appear to meet the requirement that the performance of the primary detector (the first stage image intensifier photocathode) not be degraded.

Although the majority of speckle interferometry to date has used exposures of 20-50 milliseconds (we typically use 33ms as defined by the 30Hz video framing rate), we have experienced atmospheric conditions on many occasions when speckle interferometry could not be effectively accomplished with exposures greater than 1 to 10ms. In this case rapid shuttering with frame-subtraction (with subsequent loss of duty-cycle in a standard video raster scheme), or time tagging schemes (with subsequent increase in specklegram rate) are required. The time-tagging, photoelectron-localization schemes of Timothy *et al.* and Papaliolios *et al.* appear very attractive as means of introducing variable (and therefore

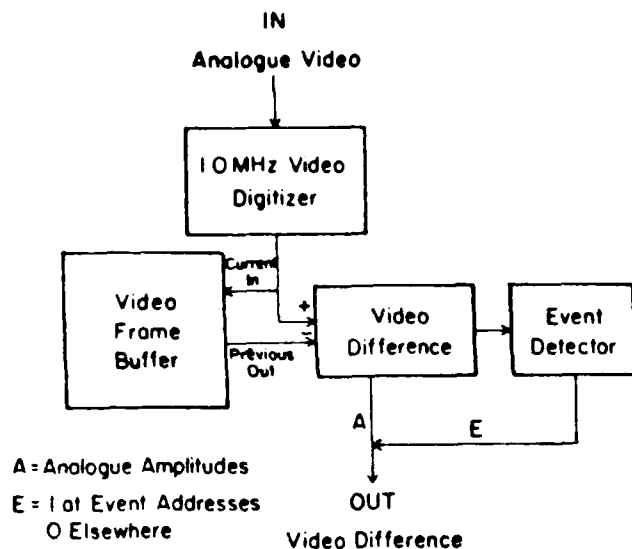


Figure 2. Lag-free Digital Video.

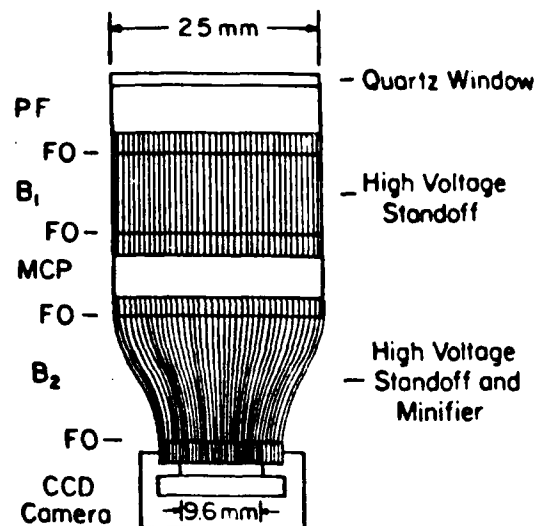


Figure 3. A low-distortion, high-gain multi-stage image intensifier. a CCD camera can provide standard video readout, or a time-tagging event detector readout may be used. PF = proximity focus image intensifier. FO = fiber optics. MCP = micro-channel plate image intensifier.

optimizable) frame rates. However, particularly for short correlation times, this places even greater demands upon subsequent signal processor bandwidths. It may be desirable to have both time-tagging and conventional video detectors.

Our experience with analogue video data-logging has also revealed severe limitations, both in dynamic range and bandwidth of U-matic 3/4inch video cassette recorders. This same experience has, however, proven the value of archiving the primary data domain, which should be preserved even as on-line data-reduction capabilities are implemented. Archived data can subsequently be reduced by different algorithms to extract different information (or to correct prior procedural or parametric errors) if it is preserved in its original form.

Since certain aspects of the data reduction process are applied to nearly all data sets (complex FFT, co-addition of power spectra or autocorrelation functions, co-addition of image phases or phase differences, co-addition of centroided frames), we considered the possibility of moving one step away from the primary video domain, namely logging the (possibly "super-resolved") complex FFT for each video frame on standard digital magtape. A simple calculation quickly revealed that conventional 9-track digital techniques are quite inadequate. The compressed format of time-tagged event addresses is the best contender for a high-fidelity primary data archive, especially for fainter objects where recording only non-zero pixels is a considerable advantage. Although quite expensive, digital video recording techniques can maintain the speeds required if full-format recording of amplitudes for bright objects is required.

Speckle Data Processing Algorithms

All Speckle Interferometry proceeds from the accumulation of co-added power spectra (or equivalently for photoelectron limited observations, co-added autocorrelation functions). Since this processing loses all image phase information, it is also desirable to include some image phase integration method as well. No single method has yet proven superior to any other, so we wish to specify a system with sufficient flexibility to accommodate several possible image phase retrieval (as contrasted to image phase "reconstruction") methods^{12,23-28}.

The differential method¹² requires co-addition of the complex deconvolution of two specklegrams obtained simultaneously in two different wavelengths. Cocke's²⁴ phase unwrapping method requires super-resolution (i.e. increased size of input raster) and neighborhood processing to recover missing multiples of 2π (Figure 4.).

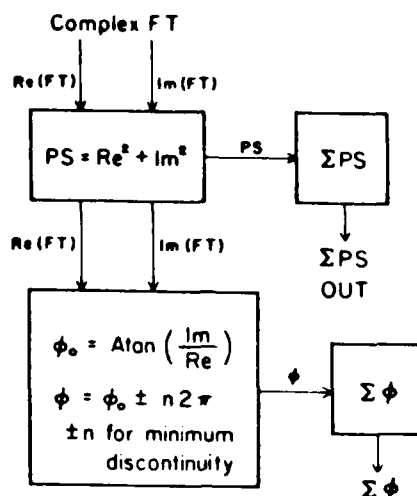


Figure 4. The Phase-unwrapping method.

The shift-and-add²⁸ methods (derivative of that used originally by Lynds, Worden, and Harvey²⁵) require neighborhood processing to extract a sampling function which is cross-correlated with the original specklegrams to produce image estimates which are co-added. A variant²⁶ of the LWH method extracts a weighted sampling function by which the specklegrams are deconvolved frame-by-frame to produce seeing-corrected image estimates (a la the differential method) which are co-added.

Nisenson, et al.²⁷ have proposed a scheme based upon the accumulation of four arrays, each of which is derived from the complex Fourier transform and summed over the ensemble of specklegrams, which can be the basis for an integration yielding the Fourier phases. We propose in this paper a hardware realization of that procedure.

Given $FT(i(x,y)) = I(u,v) = A(u,v)e^{if(u,v)}$, the four arrays which are to be accumulated are:

- | | |
|--|----------------------------------|
| (1) $\langle I(u,v) \rangle$ | Equivalent to the Long Exposure. |
| (2) $\langle I(u,v) ^2 \rangle$ | The usual Power Spectrum. |
| (3) $\langle I^*(u,v)I(u + \Delta u, v) \rangle$ | An X-phase array. |
| (4) $\langle I^*(u,v)I(u, v + \Delta v) \rangle$ | A Y-phase array. |

Nisenson, et al. show that (3) and (4) effectively yield phase differences which can be integrated to yield the desired transform phases for a Knox-Thompson style two-dimensional image reconstruction. In a subsequent paper²⁹, Nisenson et al. have shown that this method can also be corrected for the effects of photon noise bias. Hence it is our method of choice for both bright objects as well as faint objects for which the photon noise bias becomes dominant.

In practice, we have found that ordinary computational methods are prohibitively slow for even the usual power spectrum processing and that ordinary array processors of the AP-120B class would not provide the through-put to implement the above four-array algorithm on a sufficiently fine grid to sample the diffraction limit of the MMT in a real-time integration at 60Hz (or even 30Hz). We require the accumulation of the four arrays noted above for 8-bit video data digitized on a 256 x 256 raster for every 16.7ms (60Hz) video field in order to utilize the full duty cycle of the observation for faint objects. In searching for a technology capable of this task, we found that the special-purpose signal-processing hardware optimized for radar and sonar signal processing appears to satisfy our requirements. Hence we propose a Signal Processing Systems SPS-1000 based system.

Real-time Video Fourier Transform Signal Processing

The configuration of the proposed SPS-1000 signal processing subsystem for digital speckle interferometry is illustrated in figures 5 and 6. The system is shown in minimum, and maximum configurations. The minimum system provides a modest but acceptable level of performance at a minimum cost. The maximum system can be incrementally expanded to improve

throughput until an optimum configuration is reached. The maximum configuration uses a different basic processor and therefore would involve a more extensive modification if a smaller configuration is built first. However, since all models of the SPS-1000 use the same byte sliced building block modules, the smaller processor can be converted, at the factory, to the larger one. Thus the proposed system provides a systematic means whereby the performance of the digital speckle interferometry system can be increased over a period of time.

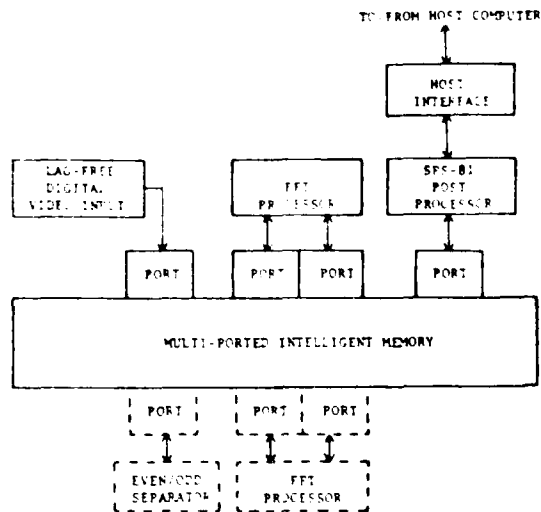


Figure 5. Minimum system.

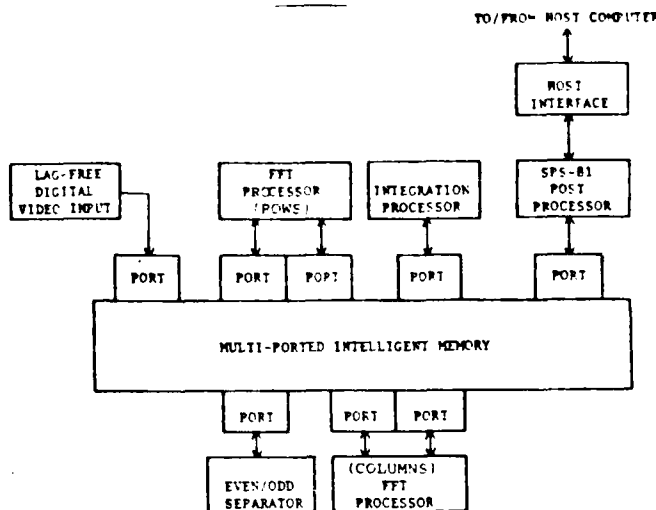


Figure 6. Maximum system.

As mentioned previously, the use of a conventional programmable processor such as a general purpose computer and/or an array processor is precluded by the high computational rates required by the algorithms used. At the same time, it is desired that the system be programmable to some reasonable level to permit modification of the techniques used. This desire, coupled with the high cost and schedule risk associated with development of a special purpose hard-wired processor, motivated the selection of the SPS-1000 for the signal processor.

The SPS-1000 is a memory centered multi-processor system which was developed to facilitate implementation of high speed real-time signal processing systems such as radar and sonar. It uses a multi-ported intelligent memory to provide attachment points for a variety of processors each optimized for a specific part of the overall signal processing task. These processors may be general purpose computers, array processors, micro-processors, hard-wired modules, etc. For applications which involve Fourier Transforms, the manufacturer offers an imbedded Fast Fourier Transform (FFT) processor which attaches to two of the ports of the memory. A general purpose programmable signal processor (the SPS-81) with throughput comparable to that of a high speed array processor is also offered as an imbedded processor.

The use of intelligent memory as the system integration medium, coupled with a manufacturer supported block diagram compiler, permits the system to operate under program control by application oriented high level language statements.

For the minimum system we selected a small SPS-1000 processor designated the SPS-1016-15. This system includes an imbedded FFT processor which will perform continuous FFTs of up to 1024 complex points at sample rates up to 1.9 megahertz. FFTs larger than 1024 points are accomplished at one half that rate. Two dimensional FFTs are accommodated by using the same pipeline for both the row and column FFTs. The throughput of the system can be doubled by adding a second FFT processor so that the row and column FFTs are accomplished concurrently. The SPS-1000 can be prewired to accept the second FFT processor as a plug-in option to facilitate future expansion.

For the maximum system we selected a faster version of the SPS-1000 designated the SPS-1016-45 with an additional FFT processor. This system can perform continuous two-dimensional FFTs on complex data input at over 6 megahertz.

Both the minimum and maximum systems use an SPS-81 imbedded processor as a post FFT processor. In the case of the minimum system, the SPS-81 can perform the integration of the transformed data as well as the post integration processing. For the maximum system, the SPS-81 is not fast enough to do the integration. Therefore, for this version a specialized

imbedded processor will be used to accomplish the integrations and the SPS-81 will be required to perform only the post integration processing.

Both the minimum and maximum systems are programmable, so that a variety of application software packages can be developed to provide tradeoffs between various performance parameters. For example, Table I indicates the tradeoff between frame size and frame rate for each of the two configurations discussed in this paper.

Table I System Performance Tradeoffs

Frame Size (pixels)	Minimum System		Maximum System	
	Frame Rate (Hz)	Pixel Rate (MHz)	Frame Rate (Hz)	Pixel Rate (MHz)
128 x 128	70	1.15	270	4.42
256 x 256	18	1.17	84	5.51
512 x 512	4.6	1.21	23	6.03

The frame rates and corresponding pixel rates indicated in the table are the maximums which can be accommodated by the system. Since the system is data driven, the data can be input at any rate up to the maximum for the particular frame size used with no change to the software. The maximum frame rates given above for the minimum system can be approximately doubled by adding the second FFT processor which is indicated by broken lines in Figure 5. The performance numbers for the maximum system already include the second FFT processor. All of the above numbers presume maximum utilization of the capability of the hardware. Prudence dictates, however, that some 5% to 10% reduction of these numbers be applied to allow a performance margin as in all programmable digital processors.

The reader will note that the input data to the system are real whereas the FFT operation is inherently a complex number algorithm and the outputs from the FFT are complex. Although several algorithms exist for performing real to complex FFTs, the FFT processor of the SPS-1000 does only complex to complex FFTs. For the minimum system, the input data will be made complex by inputting zeros in the imaginary parts of the complex input words. This makes for some inefficiency in the first (row) FFT operation but is in keeping with the concept of a minimum system. The result of a complex FFT on real input data is a conjugate symmetric array, one half of which is the desired result. Therefore, one half of these results can be ignored in doing the column FFTs and no further inefficiency results. Thus, the processing of an $N \times N$ input array results in an $N/2 \times N$ intermediate array and a similar output array.

For the maximum system, advantage is taken of an option offered by the manufacturer of the SPS-1000 to efficiently perform real to complex FFTs. This option, called an even-odd separator unscrambles the results obtained by performing an FFT on a pseudo-complex input array which is obtained by packing successive even and odd input samples as the real and imaginary parts of complex words. This technique reduces the input rate and the size of the row FFTs by half and results in increased system performance. The even-odd separator can also be included in the minimum system to provide a further performance improvement over and above that which can be achieved by a second FFT processor.

The implementation of the signal processing functions for the minimum and maximum systems are illustrated by Figures 7 and 8. The two implementations are identical except for the packing on input and the even-odd separate between the row and column FFTs. In the minimum system the four integrations will be performed by the SPS-81 processor whereas in the maximum system these will be done by a specialized processor attached to a separate port. In both cases the image reconstruction will be done by the SPS-81 processor.

The entire signal processor is attached to a host computer which provides the application program files and the downloading function. The host computer can be connected directly to a port or can interface to the system through the SPS-81 processor. We have chosen the latter since the SPS-81 requires a host interface in any case and thus one port can be saved.

Since the basic concept for this system is an intelligent, multi-ported memory system, considerable flexibility in implementation of and variants to the basic speckle processing algorithm are possible. We have discussed only the requirements for Knox-Thompson based image reconstruction in order to limit the scope of this discussion. However, the flexibility of the system is adequate to allow implementation of other image retrieval methods such as the complex deconvolution of differential speckle imaging or the neighbor-

hood processing required by phase-following approaches. By employing more integration buffers and simple first-moment calculations one could implement "r₀-monitoring"³⁰ as proposed by Mariotti *et al.* to improve the precision of seeing calibrations, for example.

We believe this type of system provides an optimal compromise between hard-wired signal processors (the ultimate in speed) and conventional, floating-point processors (the ultimate in algorithmic flexibility).

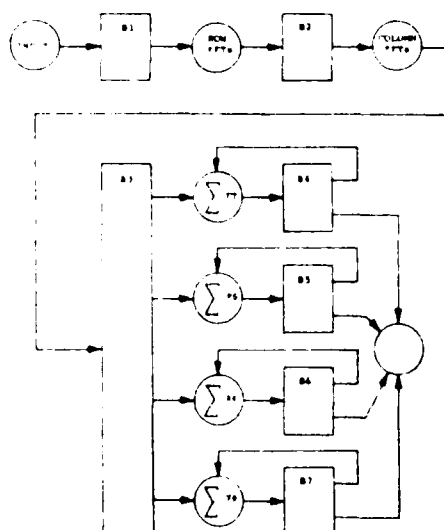


Figure 7. Minimum processing.

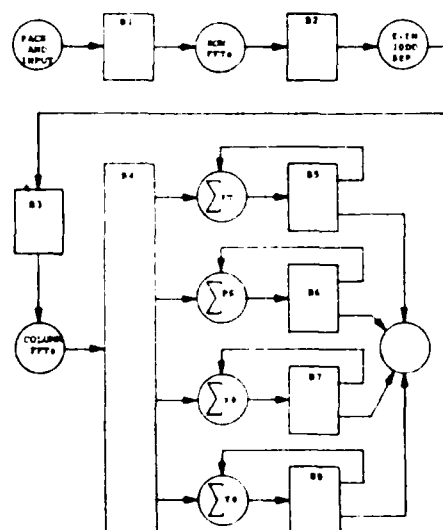


Figure 8. Maximum processing.

Conclusions

Present detector limitations appear to be surmountable by implementation of currently available proximity-focused image intensifiers suitably coupled to solid-state video readout devices. The data-processing requirements, which now make speckle image reconstruction computationally impractical, can be met by implementation of currently available signal-processing technology. The raw data sets from which true image reconstruction can be achieved can be accumulated in real-time (image power spectra and image phase arrays) at the telescope just as optical spectra (in raw form) are presently integrated in real-time while the observation progresses. No serious implementation of diffraction limited astronomical optical image reconstruction can settle for less.

Acknowledgements

We thank P. Nisenson and C. Papaliolios for several useful discussions about signal processing and R. Cromwell for the basic outline for the proximity focused image intensifier system.

References

1. Labeyrie, A. "Attainment of Diffraction-Limited Resolution in Large Telescopes by Fourier Analysing Speckle Patterns in Large Telescopes", *Astron. and Astrophys.*, **65**, 1972.
2. Labeyrie, A. "Stellar Interferometry Methods", *Ann. Rev. Astron. and Astrophys.*, **16**, 1978.
3. Worden, S. P. "Astronomical Image Reconstruction", *Proc. SPIE*, **1977**.
4. Hubbard, G., E.K. Hege, M. Reed, P.A. Strittmatter, and J. B. Stetson, "The University of Wisconsin Observatory Speckle Camera", *Astron. J.*, **1437**, 1979.
5. Hege, E.K., E.N. Hubbard and P.A. Strittmatter, "The University of Wisconsin Television System for Astronomical Speckle Interferometry", *Proc. SPIE*, **1979**.
6. Hege, E.K., E.N. Hubbard, and P.A. Strittmatter, "The University of Wisconsin Observatory Speckle Interferometry System", *Proc. SPIE*, **1979**.
7. Macklin, R. R., E.K. Hege, and P.A. Strittmatter, "The University of Wisconsin Event-detecting Video System", *Proc. SPIE*, **1979**.

NO-A189 295

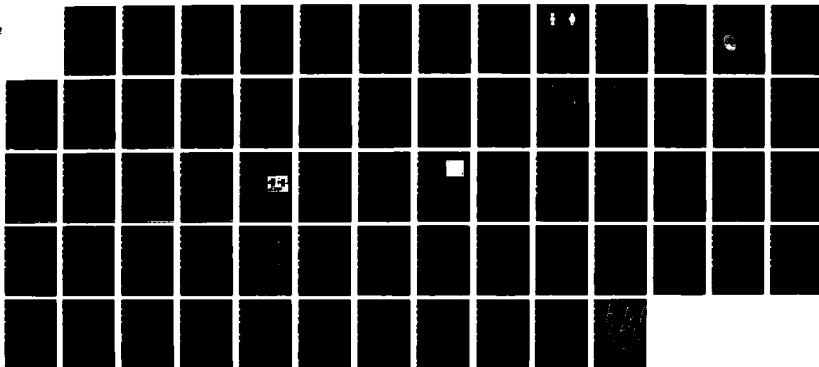
INVESTIGATIONS OF HIGH RESOLUTION IMAGING THROUGH THE
EARTH'S ATMOSPHERE (U) STEWARD OBSERVATORY TUCSON ARIZ
E K HEGE 15 MAR 87 AFGL-TR-87-0097 F19628-84-K-0035

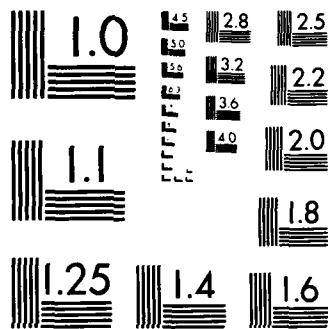
4/4

UNCLASSIFIED

F/G 20/6

NL





MICROCOPY RESOLUTION TEST CHART
NATIONAL BUREAU OF STANDARDS-1963-A

8. Drummond, J.D., W.J. Cocke, E.K. Hege, and P.A. Strittmatter, "Speckle Interferometry of Asteroids. 433 Eros" Submitted to Icarus, 1983.
9. Hege, E.K., E.N. Hubbard, J.D. Drummond, P.A. Strittmatter, S.P. Worden, and T. Lauer, "Speckle Interferometric Observations of Pluto and Charon" Icarus 50, 72, 1982.
10. Hege, E.K., E.N. Hubbard, P.A. Strittmatter, and S.P. Worden, "Speckle Interferometric Observations of the Triple QSO PG1115+08" Astrophys. J. (Letters) 248, L1, 1981.
11. Goldberg, L., E.K. Hege, E.N. Hubbard, P.A. Strittmatter, and W.J. Cocke, "Speckle Interferometry of a Ori: Preliminary Results" SAO Special Reports 392, 131, 1982.
12. Beckers, J.M., E.K. Hege, and H.P. Murphy, "The Differential Speckle Interferometer" SPIE Proceedings 445, 1983.
13. Beckers, J.M., E.K. Hege, and P.A. Strittmatter, "Optical Interferometry with the MMT" SPIE Proceedings 444, 1983.
14. Cocke, W.J., E.K. Hege, E.N. Hubbard, P.A. Strittmatter, and S.P. Worden, "An Image Reconstruction for Capella" Lowell Observatory Reports, In press, 1983.
15. Hege, E.K., E.N. Hubbard, W.J. Cocke, P.A. Strittmatter, S.P. Worden, and R.R. Radick, "Recovery of Intensity Information from Speckle Data" Lowell Observatory Reports, In Press, 1983.
16. McCarthy, D.W., P.A. Strittmatter, E.K. Hege, and F.J. Low, "MMT as an Optical-Infrared Interferometer and Phased Array" SPIE Proceedings 332, 57, 1982.
17. Beckers, J.M., E.K. Hege, F.J. Low, D.W. McCarthy, and P.A. Strittmatter, "The use of the Multiple Mirror Telescope as a Phased Array" SPIE Proceedings 440, 1983.
18. Nisenson, P., J. Apt, R. Goody, and C. Papaliolios, "Speckle Imaging for Planetary research" Icarus 53, 465, 1983.
19. Timothy, J. G., C.L. Joseph, and S.C. Wolff, "High resolution spectroscopy with the multi-anode microchannel array detector systems" SPIE Proceedings 331, 301, 1982.
20. Papaliolios, C., and L. Mertz, "New Two-dimensional Photon Camera" SPIE Proceedings 331, 1982.
21. Cromwell, R.H., H.W. Funk, K. Frank, P.A. Strittmatter, R.G. Allen, E.K. Hege, and H. Kuhr "A Proximity Focused Image Intensifier for Astronomy" Eighth Symposium on Photo-electronic Image Devices, London, 1983.
22. McAlister, H.A., W.G. Robinson, and S.L. Marcus "Development of a Dual Micro-channel Plate Intensified CCD Speckle Camera" SPIE Proceedings 331, 113, 1982.
23. Knox, K.T. and B.J. Thompson "Recovery of Images from Atmospherically Degraded Short-exposure Photographs" Astrophys. J. 193, L45, 1974.
24. Cocke, W.J. "Computer Simulation Comparisons of Speckle Image Reconstruction Techniques" SPIE Proceedings 231, 99, 1980.
25. Lynds, C.R. S.P. Worden and J.W. Harvey "Digital Image Reconstruction Applied to Alpha Orionis" Astrophys. J. 207, 174, 1976.
26. Christou, J. and J. Freeman (Private communication) are currently developing and evaluating a self-calibrating deconvolution variant of the original Lynds-Worden-Harvey method.
27. Nisenson, P. and R. Stachnik, C. Papaliolios, and P. Horowitz, "Data Recording and Processing for Speckle Image Reconstruction" SPIE Proceedings 243, 88, 1980.
28. Bates, R.H.T., and F.M. Cady "Towards True Imaging by Wideband Speckle Interferometry" Opt. Commun. 32, 365, 1980.
29. Nisenson, P., and C. Papaliolios "Effects of Photon Noise on Speckle Image Reconstruction with the Knox-Thompson Algorithm" Opt. Commun., In Press, 1983.
30. Mariotti, J.M., A. Chelli, R. Foy, P. Lena, F. Sibille, and G. Tchountonov "Infrared Speckle Imaging: Improvement of the Method; Results on Miras and Protostars" Astron. Astrophys. 120, 237, 1983.

DIFFRACTION LIMITED IMAGE OF A GEOSYNCHRONOUS OBJECT USING THE MULTIPLE MIRROR TELESCOPE AND FIENUP PHASE RECONSTRUCTION

E. Veith Hege and Andreas Eckart*
University of Arizona, Steward Observatory, Tucson, Arizona 85721

Submitted to Applied Optics

Abstract

The geosynchronous communications satellite FLTSATCOM1 has been resolved at the diffraction limit of the Multiple Mirror Telescope* (MMT). At 550nm the resolution corresponds to a beam size of approximately three meters at the object. Image amplitudes were obtained using speckle interferometry and image phases were reconstructed using Fienup's method. Four 10 minute segments of video data were recorded with a 10nm bandpass centered at 550nm. The image intensifier system was operated at full gain so that individual photoelectron events could easily be localized in the video raster. The telescope was cophased using a bright star, as described in ref. 1, before each observation of the satellite. Video data from the bright star was recorded before and after each recording of the satellite. This allowed us to verify that the telescope cophasing had not changed significantly during the satellite observation. Open-loop predictions⁶ were used to keep the telescope cophased as it was offset from the reference star to the satellite position.

Observation

FLTSATCOM1 was observed at elevation 50°, azimuth 160°, range 37800 km from Mt. Hopkins on 4 November 1985 between 0210 and 0315 UT. The observations were made using the coherently cophased MMT. Data was recorded using the Steward Observatory intensified video speckle camera². Four 10 minute segments of video data were recorded with a 10nm bandpass centered at 550nm. The image intensifier system was operated at full gain so that individual photoelectron events could easily be localized in the video raster. The telescope was cophased using a bright star, as described in ref. 1, before each observation of the satellite. Video data from the bright star was recorded before and after each recording of the satellite. This allowed us to verify that the telescope cophasing had not changed significantly during the satellite observation. Open-loop predictions⁶ were used to keep the telescope cophased as it was offset from the reference star to the satellite position.

Using the technique described in ref. 4, lists of the coordinates of photoelectron events detected in the 1/60 sec video fields were obtained. In this way the satellite specklegrams are represented as:

$$i_k(x,y) = \sum_{i=1}^{m_k} \delta(x-x_i, y-y_i),$$

where m_k is the number of events detected in the k-th specklegram defined as the set of event coordinates $\{x_i, y_i\}_k$, $i=1,2,\dots,m_k$. Let $(x,y)=r$, then

*Max-Planck Institute für Extraterrestrische Physik
D-8046 Garching bei München, WEST GERMANY.

*The Multiple Mirror Telescope is a joint facility of the University of Arizona and the Smithsonian Institution.

$$i_k(x,y) = \sum_{i=1}^{m_k} \delta(x-x_i, y-y_i) = i_k(r).$$

Using the definition of the autocorrelation function

$$a(r) = \int_{|r'|=0}^{\infty} i(r+r') i(r') dr',$$

we can derive the corresponding photon event list result

$$\begin{aligned} a(r) &= \int_{|r'|=0}^{\infty} \sum_{i=1}^{m_k} \delta(r-r_i+r') \sum_{j=1}^{m_k} \delta(r'-r_j) dr' \\ &= \sum_{i,j=1}^{m_k} \delta(r-r_{ij}). \end{aligned}$$

This is just the two-dimensional histogram of all occurrences of $r = \Delta_{ij}$, the vector differences $\Delta_{ij} = r_i - r_j$ in the list $\{r_i\}_k$. The iterated autocorrelation function $ACF(r)$ is then the sum of the autocorrelations of the N individual specklegrams.

$$ACF(r) = \sum_{k=1}^N \sum_{i,j=1}^{m_k} \delta(r-\Delta_{ij}).$$

If the input lists are defined in a raster $\theta \leq x_i, y_i < L_{x,y}$ then ACF is defined in the space $(-L_{x,y}, L_{x,y}) \leq x,y < (L_{x,y}-1)$.

There are two problems with this "discrete event" autocorrelation function⁷. There is a noise bias "spike" at $ACF(0,0) = \sum_{k=1}^N m_k$ = total number of events detected. There is a noise bias "deficit" at $ACF(L_{x,y}, L_{x,y})$ because the event localization technique requires at least one pixel to define a minimum between adjacent maxima: two events in adjacent pixels cannot be resolved. By oversampling the telescope diffraction limit by 2 x Nyquist sampling frequency, we can reconstruct the high-frequency ACF structure by use of a model which interpolates the $ACF(0,0)$ and $ACF(L_{x,y}, L_{x,y})$ values from fits at larger distances. We call this "recapping" and the procedure is described in ref. 7.

Seeing Compensation

The recapped ACF is corrected for detector point spread function dependent noise bias effects. It still contains atmospheric seeing effects. In this experiment, we used models to correct the ACF for seeing effects. This is a heuristic approach. Atmospheric perturbations will occur at all image frequencies; however, an object of finite extent will

have a low-spatial frequency cut-off corresponding to the size of the object. For an object which is small compared to the seeing, the autocorrelation function of the atmospherically perturbed image will show a broad component due mainly to the seeing, upon which is superimposed the diffracton limited autocorrelation function of the object.

Assuming that the atmosphere can be described by a random Gaussian process, one can understand this approximation. Note that the speckle transfer function is a sum of two spatial frequencies, f , dependent components. The principal component is the seeing-limited transfer function $S(f)$. To this is added a small fraction, dependent upon seeing, r_0 , and the aperture diameter, D , of the diffraction limited transfer function, $D(f)$.

$$P(f) = S(f) + k \frac{r_0^2}{D^2} D(f).$$

The speckle power spectrum is then given by the product of the object power spectrum and this speckle transfer function.

$$PS = |O(f)|^2 P(f) = |O(f)|^2 S(f) + k \frac{r_0^2}{D^2} |O(f)|^2 D(f).$$

For the case of an object small compared to the seeing, $|O(f)|^2$ is a slowly varying function of f compared to $S(f)$ which rapidly approaches zero at a seeing cut off frequency much less than the first zero of the object power spectrum. Thus, to good approximation in this case,

$$PS = S'(f) + k \frac{r_0^2}{D^2} |O(f)|^2 D(f),$$

where $S'(f) = |O(f)|^2 S(f) \approx \text{const} \cdot S(f)$, i.e. the seeing distribution is only negligibly altered from that of a point source. In autocorrelation space, this approximation is

$$ACF = FT^{-1}(PS) \approx ACF'_{\text{seeing}} + k \frac{r_0^2}{D^2} ACF_{\text{diffraction limited image}},$$

where $ACF'_{\text{seeing}} = \text{const} \cdot (ACF_{\text{seeing}} * ACF_{\text{object}})$ is thereby characterized by a function which is slowly varying, compared with $ACF_{\text{diffraction limited image}}$. We model it as a linear combination of Gaussian functions fit at sizes greater than the size of the ACF_{dli} which is easily seen as a break in the ACF for small, sharp-edged objects. For soft-edged or large objects it will be more difficult. Thus, to within some scaling factor, proportional to $(r_0/D)^2$, the seeing calibrated diffraction limited image autocorrelation function is given by the difference

$$k \left(\frac{r_0}{D} \right)^2 ACF_{\text{dli}} = ACF - \text{Model}(ACF(r; r_0 > r_{\text{break}})).$$

The azimuthally averaged raw profile of one of the 20 minute integrations of the autocorrelation function so obtained from the FUTSATCOM1 observations, is shown in Figure 1. Similarly the seeing-model calibrated ACF is shown in Figure 2. The four 10 minute observations were combined as two 20 minute integrations to allow for consistency checks.

Finup Image Reconstruction

In order to obtain an image of the satellite we decided to use an iterative method similar to the Finup error-reduction algorithm. This type of algorithm allows us to retrieve object phases, with a 180 degree ambiguity, from the Fourier amplitudes only. We obtained the Fourier amplitudes as the square root of the Fourier transform of the seeing model calibrated and noise bias corrected ACF_{dli} .

To use an iterative Finup algorithm one needs an initial phase estimate. Our initial estimate was obtained from the phases of an image containing a random set of ten delta functions of unity amplitude. We used some of the information obtained from the autocorrelation analysis and placed the delta functions in a circular area, of the approximate size of the object, located in the center of the image frame.

In each Finup iteration, Figure 3, the following procedure was applied: The measured Fourier amplitudes were combined with the current phase estimate and Fourier transformed to give a current image of the object. All negative image amplitudes were set to zero, and, in addition, the image was set to zero at all locations outside a circular area of approximately four times the diameter of the object, giving a mild finite-support constraint. From the resulting image we extracted the new phase estimate for the next iteration.

Following that procedure for a few hundred iterations, no further significant change in the current images was observed. The final images, Figure 4, were low-pass filtered using the 3×3 filter represented by the matrix

$$\begin{array}{ccc} 0 & 1 & 0 \\ 1 & 1 & 1 \\ 0 & 1 & 0 \end{array}$$

The weighting factors used to calculate the value of the pixel at the central filter position takes into account the values of neighboring pixels as well. We applied the filter twice using $i = 2$ and $n = 2$.

Two different random initial phase estimates were tried with the two partial data sets and led to comparable final images which are shown in Figure 4. The narrow, central features at the lowest image contours, which appear horizontally but with opposite phase in both reconstructions and vertically in the second reconstruction, are associated with video camera/VCR/digitizer raster noise.

Analysis of Results

To aid in understanding what to expect is the result of this imaging experiment, we created a model object with morphological similarity to the FLTSATCOM1 target. We assumed different reflectivities for the major components illuminated face on, and blurred the result to the same resolution and pixel scale as for our measurement. That image, Figure 5 (negative), at the resolution of the camera pixels, shows a 3:1 brightness ratio between a circular central object and extended rectangular panels. A bright unresolvable external feature offset from the central object is included. Figure 5 also shows the same computer generated object at the resolution of our measurement, presented as halftoned contour plots. Corresponding features can be seen in the reconstructed images shown in Figure 4.

Quantitative measures of the object's overall shape, size, and orientation can be obtained from models fit to its seeing calibrated autocorrelation function (ACF). With the phase restored image these parameters can be directly inferred from the image contours, for example the contour at which the signal is twice the RMS noise in the background. In the ACF fitting method, our experience [1,12] has shown that high spatial frequency surface structure biases the models. This causes the models to underestimate the size of the object: only upper bounds of an object's size can be obtained. Image contours, however, are associated with the true outlines and surface brightness of the object, subject to spatial resolution and measurement noise (see Fig. 6).

The ACF model fits uniform disk (no surface structure) elliptical object profiles to the data. That severely oversimplified model is useful for estimating length, width and orientation of the sky-projected object. The result, for our averaged FLTSATCOM1 data sets, yields least squares estimates of the minimum elliptical image ACF support (see Fig. 2).

Major Axis: > 11.4 m
Minor Axis: > 5.7 m

Position Angle: 3.5 degrees

The position angle is with respect to the elevation great circle defined by the telescope, FLTSATCOM1 and Zenith. The ACF model is particularly sensitive to such position angle measures (Ref. 10).

Our estimate of the image size is taken from the 2 sigma contours of the images shown in Figure 4. The estimate of precision corresponds to the mean contour spacing at the 2 sigma contour. The computed beam size at the object, $(\lambda/D) \times$ Range, is 3.0 m. We define the Signal-to-Noise Ratio = $\text{SNR} = \text{Brightest Feature} / \text{Background Noise}$. This measurement gives quite convincing precision, judged from the degree of reproducibility of the contours compared to the telescope's diffraction limited beam size plotted at the same scale. The reduction of the first two 10 min data segments compares favorably with the reduction of the last two 10 min segments.

Major Axis: 13.0 ± 2.3 m
Minor Axis: 7.4 ± 2.3 m
SNR: 6

We made no attempt to calibrate image amplitudes or to obtain quantitative estimates of the relative albedos of the identifiable components of our images. There is qualitative evidence i) that the central component is brighter than the extended features, ii) for asymmetry corresponding to the unresolvable component offset from the main object, iii) that, due to the solar phase angle, there appear to be strong brightness variations across the central object, and iv) that the extended components do not reflect equally. Figure 6 compares our first image contour plot to a schematic representation of FLTSATCOM1.

FLTSATCOM1, launched 9 February 1978, has a 4.8 m diameter parabolic antenna amid two solar arrays extending 13.2 m tip-to-tip and a laterally offset spiral antenna mast [3] and is rotationally stabilized. The orientation is indicated schematically in Figure 6. The images in Figures 4 and 6 have a 180° ambiguity since Flenu's phase reconstruction method can yield a solution rotated by 180° as easily as the unrotated solution.

Conclusion

We have demonstrated a multiple aperture geosynchronous imaging capability by using the Multiple Mirror Telescope to obtain a diffraction limited image of the communications satellite FLTSATCOM1 from which its size and orientation was measured. Evidence of the object's structure is seen in images presented as contour plots. After 20 minutes integration, the precision of the measures is 75% of the size of the diffraction limited beam projected at geosynchronous range.

Acknowledgements

This work could not have been accomplished without the assistance of the Multiple Mirror Telescope Observatory's support staff and telescope operators, as well as the Steward Observatory Technical Division, in achieving the cophased collimated operation of the MMT in tracking a non-sidereal object. This work received support from the National Science Foundation (AST-8312976 and AST-8412206), from the Air Force Geophysics Laboratory (F19628-84-K-0035) and from NASA (Contract NAGW-2241). We thank Dr. Eric Jensen and the Aerospace Corporation for assistance in obtaining telescope coordinates for FLTSATCOM1. A.E. thanks Steward Observatory for its hospitality and the University of Arizona and the Alexander von Humboldt Stiftung for post doctoral research support.

References

1. E. K. Hege, J. M. Beckers, P. A. Strittmatter and D. W. McCarthy, "The Multiple Mirror Telescope as a Phased Array Telescope," Appl. Opt. **24**, 2565, 1985.
2. E. K. Hege, E. N. Hubbard, P. A. Strittmatter and W. J. Coker, "The Steward Observatory Speckle Interferometer System," Optica Acta **29**, 701, 1982.
3. E. K. Hege, F. H. Cromwell and N. J. Woolf, "Quantum Noise Limited Readout of Spectrographic Data Using Image Intensifiers and a Reticon Photodiode Array," Adv. Electron. Electron Phys. **52**, 397, 1979.
4. R. H. Macklin, E. K. Hege and P. A. Strittmatter, "A Real-time Photoelectron Event-detecting Video System," Proc. SPIE **359**, 135, 1982.
5. J. C. Hebdon, E. K. Hege and J. M. Beckers, "Use of the Coherent MMT for Diffraction Limited Imaging," Proc. SPIE **628**, 42, 1986.
6. C. C. Jones and J. M. Monrothery, "Co-phasing and Co-aligning the Multiple Mirror Telescope," Proc. SPIE **748**, paper 04, 1987.
7. E. K. Hege, A. Eckart and J. C. Christou, "The Noise Bias Problem in Optical Speckle Imaging: Experience with a Real Detector," Proc. SPIE **627**, 772, 1986.
8. J. C. Dainty, "Stellar Speckle Interferometry," In Laser Speckle and Related Phenomena, Topics in Applied Physics. Vol 9, ed. J. C. Dainty, Second ed., p225, Springer-Verlag, 1984.
9. J. R. Fienup, "Reconstruction of an Object from the Modulus of its Fourier Transform," Optics Lett. **3**, 27, 1978.
10. J. D. Drummond, W. J. Coker, E. K. Hege, P. A. Strittmatter and J. Lambert, "Speckle Interferometry of Asteroids. I. 433 Eros," Icarus **61**, 132, 1985.
11. J. D. Drummond, W. J. Coker, J. D. Freeman, J. C. Christou and R. P. Binzel, "Speckle Interferometry of Asteroids. II. 532 Herculina," Icarus **61**, 232, 1985.
12. J. D. Drummond and E. K. Hege, "Speckle Interferometry of Asteroids. III. 511 Davida," Icarus **67**, 251, 1986.
13. TRW Space Log **17**, 11, 1979 and **18**, 1, 1980.

Figure Captions

- Figure 1. Raw Autocorrelation Function (Averaged radial profile). The dotted line at $r \leq 2$ pixels is the result of the recapping correction of noise bias. The "break", indicating the extent of the diffraction limited component, is marked, and the gaussian seeing model is shown as the dotted line. Other indicated features, related to our photon detection PSF, are also discussed in the text. 1 Pixel = $24''$ radian = $0.87''$ m.
- Figure 2. Recapped, Seeing Calibrated Autocorrelation Function. A linear combination of two elliptical Gaussians, fit at $r > 15$ pixels was subtracted from the recapped ACF shown in Figure 1. The dotted curve is the averaged radial profile of the uniform disk autocorrelation function model fit to the data. The telescope diffraction limit = $80''$ radian = 3.4 pixels.
- Figure 3. Flow Chart for the Fienup Algorithm Used.
- Figure 4. Reconstructed Images of FLT SATCOM1. a) First half of data. b) Second half of data. c) Contour plots superimposed. Contours are at 1,2,...,6 times the rms noise in the image plane exterior to the resolved object outline. Fienup reconstructions are ambiguous by 180° rotation. The second image was rotated 180° to give best contour matching compared to the first image.
- Figure 5. Resolution Degraded Image Model. a) A pixel resolution limited computer generated negative image. b) Resolution degraded contour plot of image 5a. (Not intended to be a realistic model for FLT SATCOM1)
- Figure 6. Schematic outline of FLT SATCOM1 compared to our first reconstructed MMT image. The circle gives the diffraction-limited MMT beam size (= 3 m at geosynchronous range).

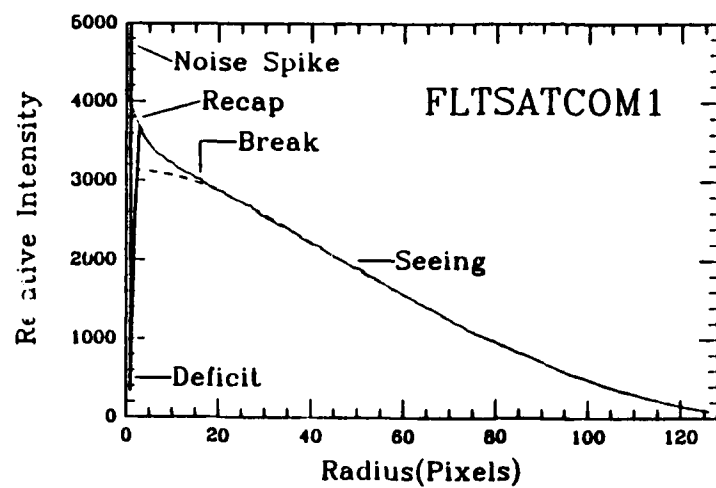


FIGURE 1

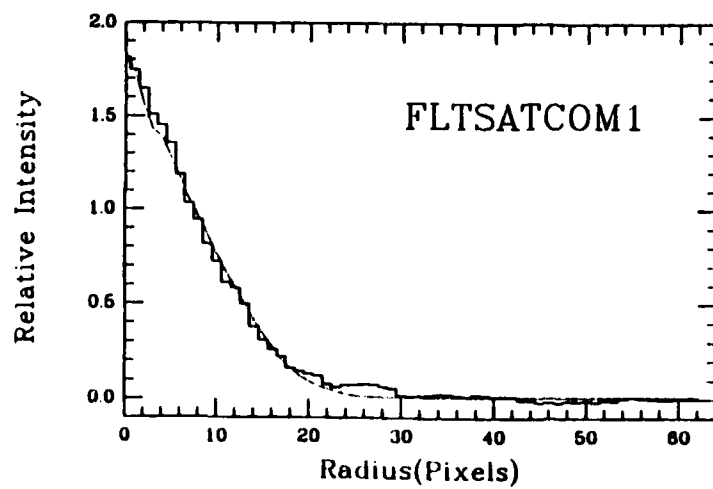
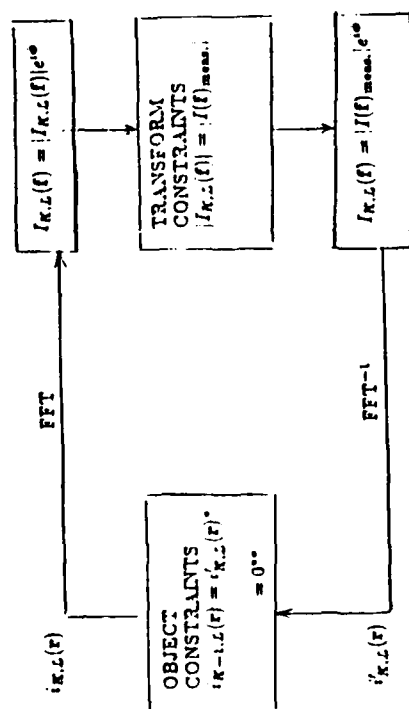


FIGURE 2



** For negative values and for positive values outside the image plane filter
* else

FIGURE 3

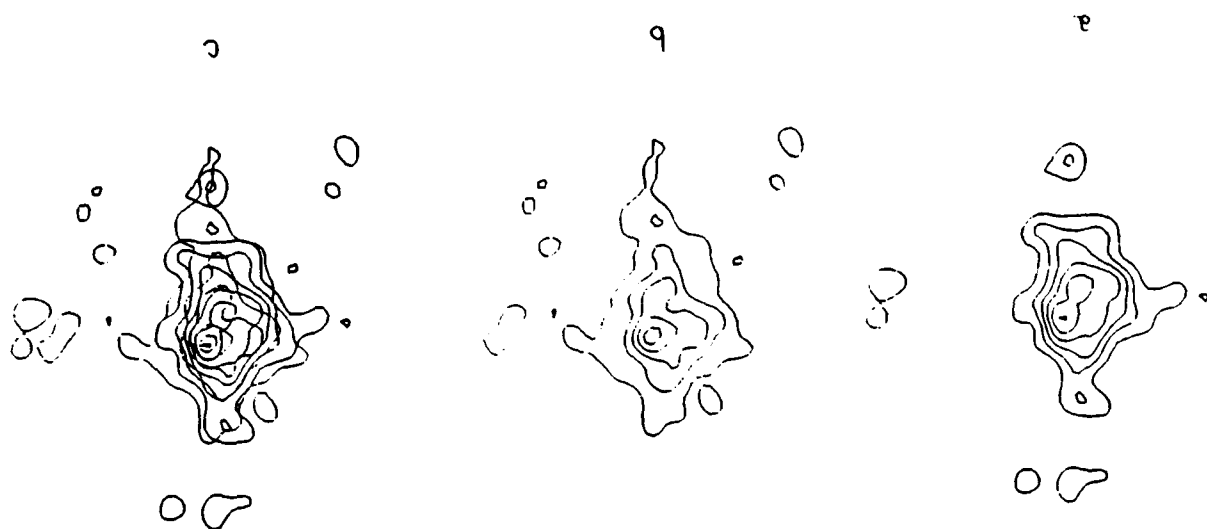
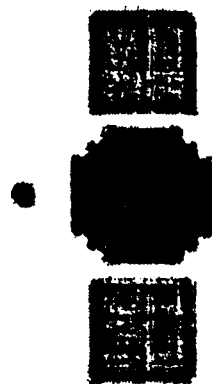
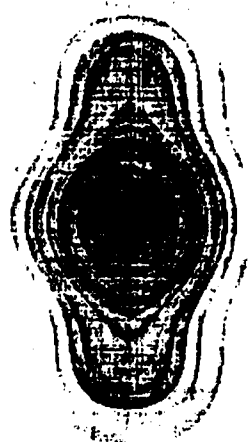


FIGURE 4



a



b

FIGURE 5

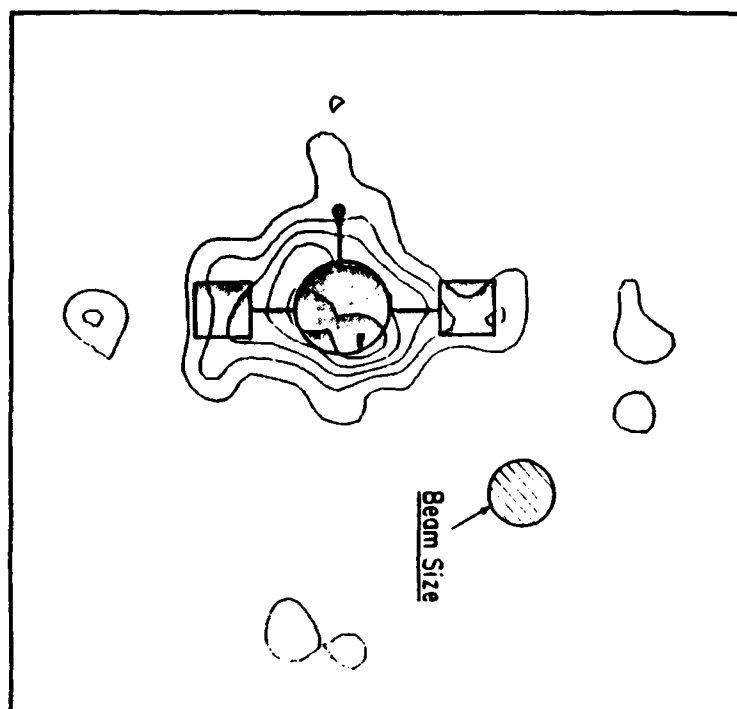


FIGURE 6

THE NOISE BIAS PROBLEM IN OPTICAL SPECKLE IMAGING Experience with a Real Detector

E. K. Hege, A. Eckart and J. C. Christou

Steward Observatory, University of Arizona
Tucson, AZ 85721

Abstract

We have obtained diffraction limited images for bright objects using various large astronomical telescopes, including the MMT, but the results have not been convincing for fainter objects. All speckle interferometric techniques utilizing image power spectrum or autocorrelation methods to obtain calibrated image amplitudes are subject to noise bias induced by the Poisson statistics of photon detection. This noise bias, independent of image frequency for ideal detectors with delta-function like point spread functions, must be removed to obtain calibrated image amplitudes. The noise bias characteristic of our intensified TV detector, both as a raster event localizer (faint object mode) and as a conventional image amplitude detector (bright object mode), is not only image frequency dependent but signal rate and signal distribution dependent as well. This precludes signal independent calibration of the characteristic bias functions and sets limits on object faintness for successful image recovery. Implications for detector development are noted.

Background

Typical previous theoretical studies¹⁻⁵ of the statistics of diffraction limited optical interferometry (astronomical speckle interferometry⁶) were mainly concerned with the limits of detection of unresolved sources and the detectability of extended objects.

This work reports experience with the limits of calibration using a video raster detector⁷ in both analog mode (for bright objects) and event detecting mode (for faint objects). We have encountered calibration limitations in applying corrections for photon noise bias and corrections for atmospheric seeing effects. In both cases the limiting factors have been identified with systematic, but data dependent, detector effects. These limitations have prevented satisfactory image reconstructions using the Knox-Thompson algorithm⁸. Fortunately differential speckle imaging⁹ is less sensitive to these effects.

In discussing the statistical limits of detectability using the Knox-Thompson method, Nisenson and Papaliolios⁵ explicitly noted that the noise bias is "colored", i.e. image frequency dependent. For the discrete photon case $i(x) = \sum \delta(x - x_k) * \phi(x)$, i.e. the photon detection point spread function (PSF) $\phi(x)$ is detected at the event addresses $\{x_k\}$. The Fourier transform of this image is $I(u) = \Phi(u) \cdot \sum \exp(-ju \cdot x_k)$. In Knox-Thompson image reconstruction, averaged cross-spectrum-like quantities are measured: $P_M(u; \Delta u) = \langle I^*(u) \cdot I(u + \Delta u) \rangle$. For $\Delta u = 0$ this is the conventional image power spectrum.

The measured cross spectra $P_M(u; \Delta u)$ contain an additive noise term due to photon shot noise (Poisson statistics)¹⁰.

$$P_M(u; \Delta u) = B(u; \Delta u) + P_{DS}(u; \Delta u) \quad (1)$$

where $B(u; \Delta u)$ is the noise bias and is of the form

$$B(u; \Delta u) = N \frac{| \Phi(u) |^2}{\Phi(0)} G(\Delta u) \quad (2)$$

$P_{DS}(u; \Delta u)$ is the desired bias free quantity, which is still filtered by the detector PSF and aperture optical transfer function (OTF) and which contains seeing effects.

$$P_{DS}(u; \Delta u) = N^2 \langle \exp(ju \cdot x_k) \exp[-j(u + \Delta u) \cdot x_l] \rangle \quad (3)$$

For $\Delta u = 0$, $P_{DS}(u; 0)$ is the conventional astronomical speckle transfer function⁴ (STF). Rewriting $i(x) = o(x) * p(x)$ and $I(u) = O(u) \cdot P(u)$, $STF = P_{DS}(u; \Delta u)_{\Delta u=0} = \langle |P(u)|^2 \rangle$.

Table I and figure 1 show the effects of noise bias on the STF for sources of various brightness using a large optical aperture. The STF contains a seeing limited term $G(\Delta u)$ and an aperture (diffraction) limited term $A(u)$ scaled according to seeing and aperture

size⁴. $STF = G(0) + [r_0/D]^2 A(u)$ where r_0 is the Fried parameter and D is the telescope aperture. For a magnitude 0 star observed with a 4.5m effective light gathering area and a 5% detection efficiency using a 20nm observing bandpass, 3×10^7 photons/frame (at 60Hz) will be detected. Both table I and figure 1 are computed for $r_0 = 20$ cm (good seeing at the MMT) and $D = 6.86$ m (the effective MMT interferometric diameter) giving $[r_0/D]^2 = 8.5 \times 10^{-4}$, i.e. the diffraction limited MMT contribution $A(u)$ is about .1% of the power in the seeing distribution $G(u)$ at $u = 0$.

Table I. Aperture-limited Signal vs Noise Bias

m_v	N /frame	Bias/STF /min	S/N /min	S/N /10 min	S/N /hr
0	3×10^7	4.3×10^{-9}	2×10^5		
2.5	3×10^6	4.3×10^{-8}	2×10^4		
5.0	3×10^5	4.3×10^{-7}	2000		
7.5	3×10^4	4.3×10^{-6}	200	630	
10.0	3000	4.3×10^{-5}	20	63	
12.5	300	4.3×10^{-4}	2	6.3	120
15.0	30	4.3×10^{-3}	.2	.63	12
17.5	3	4.3×10^{-2}	.02	.06	1.2

For our video raster photon detector in which photons are detected as a "splotch" of pixels, where the signal exceeds some threshold set to discriminate against low-level electronic noise, $\phi(x)$ equals $\phi(x)$, signal rate, signal distribution). The PSF is rate dependent because of photon "pile up" problems (overlapping responses are detected as a single larger response) and AGC-induced variable "black-level" responses detected against a fixed threshold. The PSF is distribution dependent because detector pincushion causes the shape of $\phi(x)$ to vary over the detector field of view. $\Phi(u)$ is approximately Gaussian because the image intensifier output response $\phi(x)$ is Gaussian, but the video recording process distorts this response in a non-linear way for the larger pulses¹¹ in the intensifier output pulse-height distribution. We find, nevertheless, that a Gaussian shape is a good model of $\Phi(u)$, and we use such a model throughout this paper. The curves of figure 1 are for $m_v = 2.5, 5, 7.5, 10$, and 12.5.

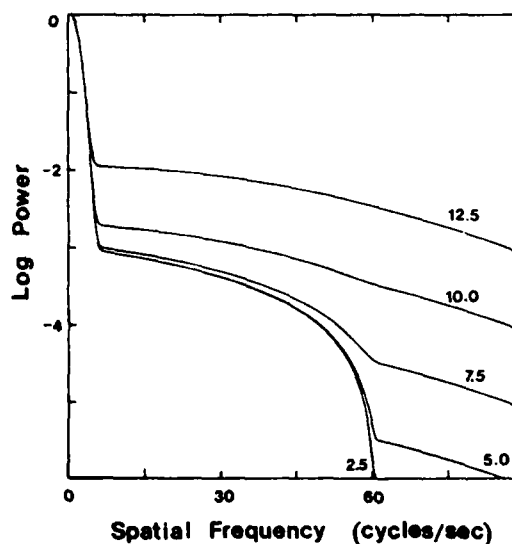


Figure 1. STF with Gaussian-colored noise bias.

Seeing Calibrations

Since the detector color term $D(u) = \langle |\Phi(u)|^2 \rangle$ is contained in both terms of (1), the power spectrum case of (1) can be rewritten $P_M(u) = D(u) \{N + |O(u)|^2 \langle |P(u)|^2 \rangle\}$ or $|O(u)|^2 \langle |P(u)|^2 \rangle = \{P_M(u) / D(u)\} - N$. The seeing calibration is then accomplished by an observation of a point source under similar seeing conditions, particularly so that the time average $\langle |P(u)|^2 \rangle$ is the same for both resolved object and seeing calibrator.

$$|O(u)|^2 = \frac{\{P_{M_0}(u) / D(u) - N_0\}}{\{P_{M_*}(u) / D(u) - N_*\}} \quad (4)$$

In practice, the debiased quantities required for the numerator and denominator of (4) are produced by dividing the measured power spectra by a model of $D(u)$ obtained by fitting the data $P_M(u)$ at $|u| > f_c$, the diffraction cut-off frequency. We always oversample so that f_c occurs at less than the Nyquist frequency in order to accomplish this modelling. Figure 2 shows a typical result of such a fit: the model always fits the power above f_c to within about 1% rms. Regardless of the signal statistics, this 1% discrepancy seems to be a systematic limit of the PSF model. For bright objects, this is no limitation; for faint objects it is disastrous.

The model can be applied in either the power spectrum domain as done in figure 2 or as a "recapping" in the autocorrelation function domain as done in figure 3.

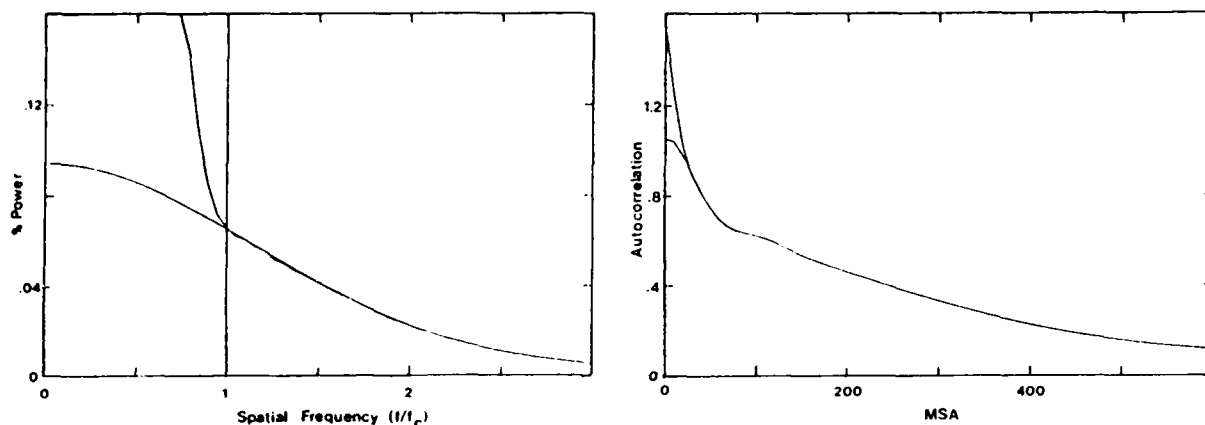


Figure 2. Left: Noise bias model fit to Gamma Orionis power spectrum data at $|u| > f_c$. Right: Corresponding autocorrelation function (ACF) with noise bias manifest as central spike.

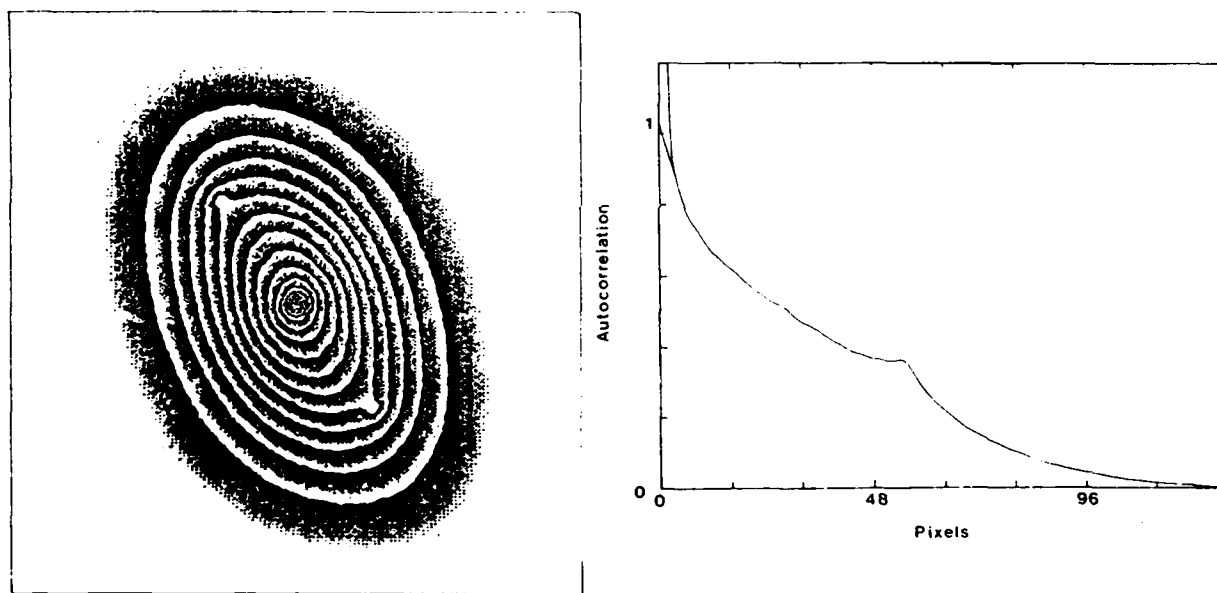


Figure 3. Noise bias correction by recapping of ACF. ADS 2630. Left: Raw ACF. Right: Cut through secondary side-lobe showing clipping of bias spike.

Figure 4 shows the results of the seeing calibration process (4) for a fainter binary ($m_v = 11$) and a point source calibrator of similar magnitude. The quotient (4) is nonsense at $|u| > f_c$, so an aperture restoring filter must be applied (usually with $f_0 < f_c$) to suppress these spurious high frequency results.

Figure 5 shows the filtered, seeing-corrected result shown in figure 4 inverse Fourier transformed back to the autocorrelation function domain. This 4m telescope result yields a S/N consistent with that implied by Table I, and is typical of the results we have achieved in our asteroid interferometry program¹². Integration time of 90 seconds was used for both object and reference star. The first Airy ring of the central response is seen above the noise. Noise bias errors may enhance the apparent magnitude difference of binary star components.

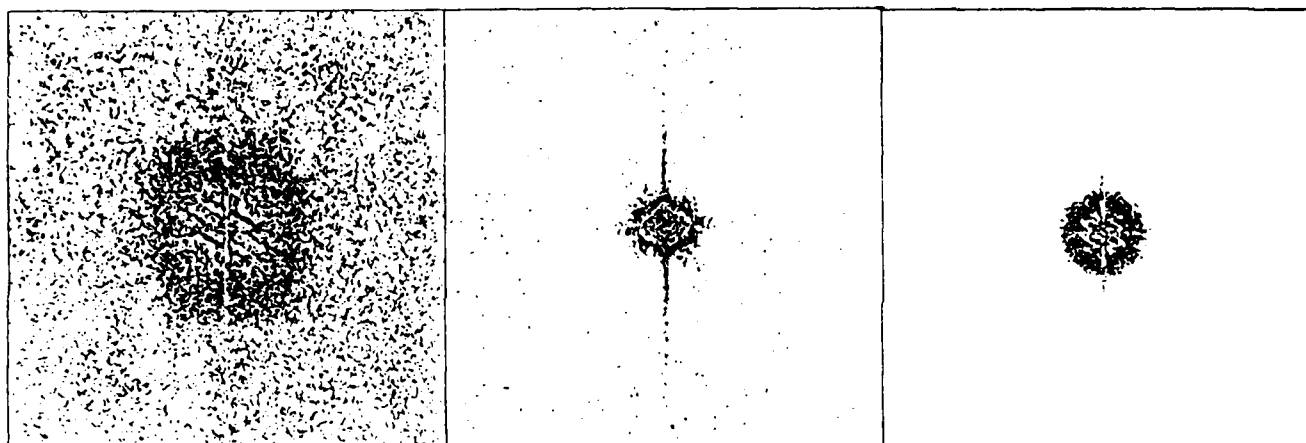


Figure 4. Seeing Calibration. Left: Debiased power spectrum of $m_v = 11$ binary. Middle: Debiased power spectrum of point source. Right: Filtered quotient.

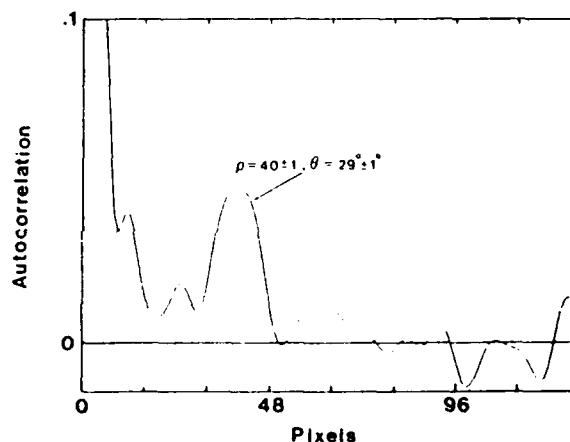
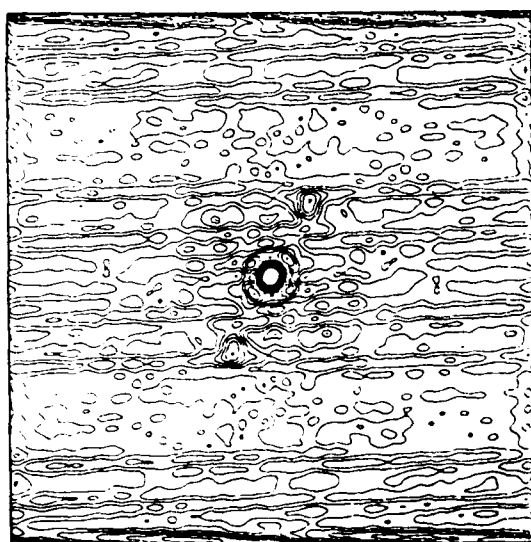


Figure 5. Calibrated ACF for $m_v = 11$ field star with $m_v = 13.8$ component. Left: Contours at 1% of peak intensity plotted up to 50% of peak intensity. Right: Expanded ordinate plot of cut through secondary lobe. (Image scale = 10mas/pixel.)

Although we have published interferometry for fainter objects¹³⁻¹⁴, we have not succeeded in achieving quantitatively reliable amplitude calibrations for objects fainter than about 10th magnitude. Figure 6 shows power spectra resulting from 90 second observations of the nucleus of NGC 1068 and of a calibration star of similar magnitude. The noise in the observation makes fitting of the Gaussian noise bias model quite uncertain. The short integrations, chopping back-and-forth between object and reference, are required to assure that seeing variations are sampled equivalently for both observations. We have discussed elsewhere¹⁵ the effects of variable seeing on (4).

The averaged radial profiles of these measures have higher signal-to-noise ratio than implied by these single-line (-column) cuts. Figure 7 compares the averaged radial profiles of the results of applying the seeing calibration (4) to such data sets (after debiasing with such models). The galaxy power spectrum was calibrated using the average of a pair of reference star data sets (observed before and after) and the point source power spectrum was calibrated by using the other reference star. Many pairs of short integrations are required for a reasonable two-dimensional determination of a faint object power spectrum.

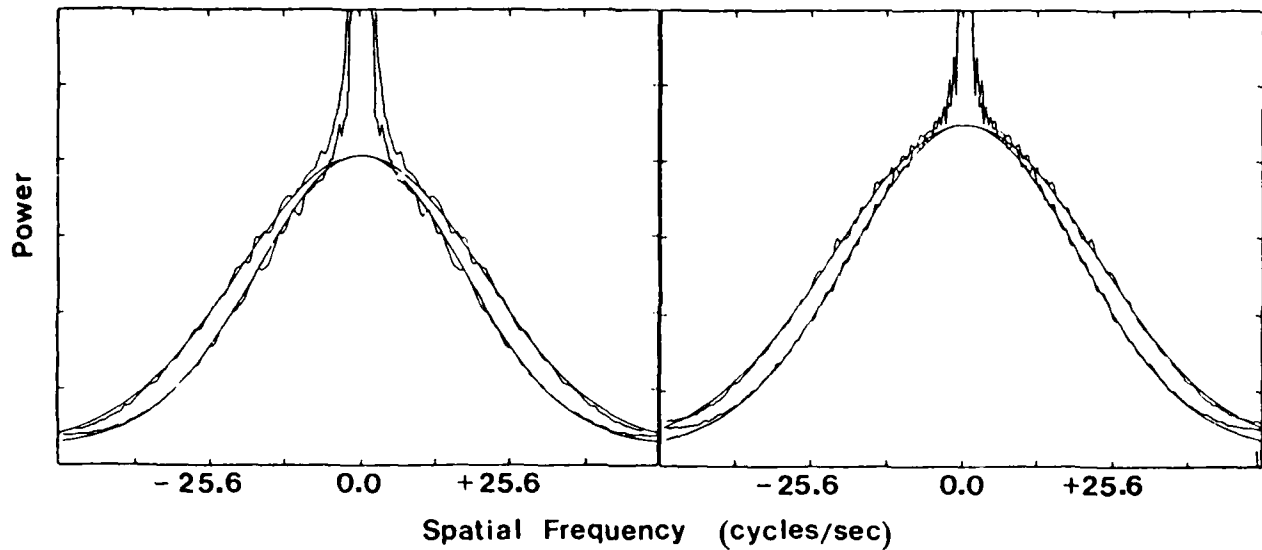


Figure 6. Orthogonal cuts through observed power spectra (90 sec integrations) for Left: NGC 1068 and Right: A field star of similar brightness. The smooth curves are corresponding noise bias models.

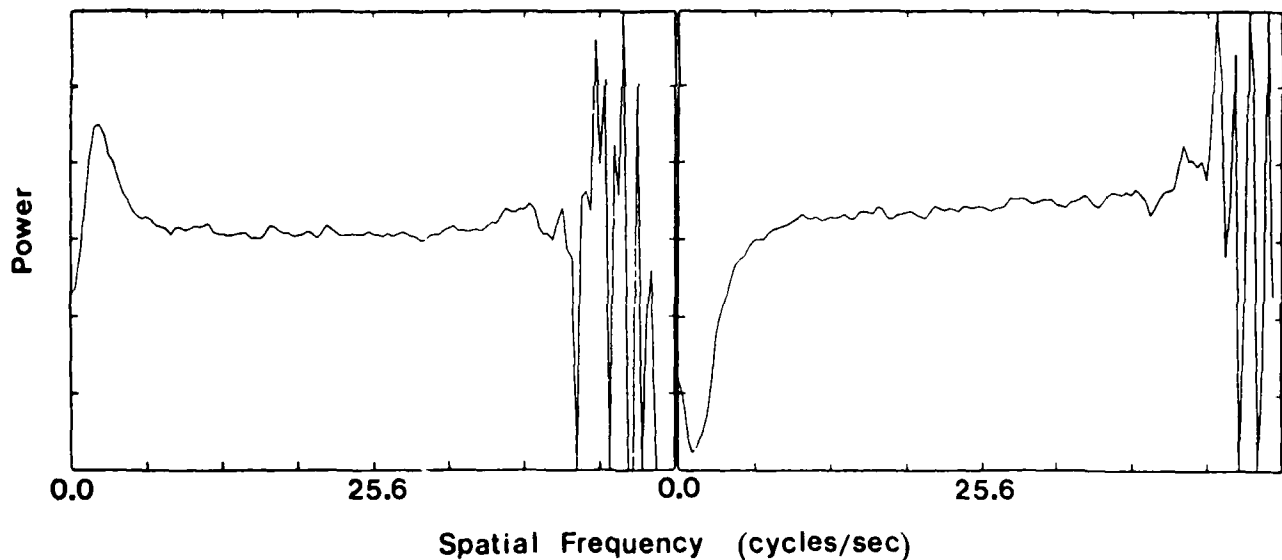


Figure 7. Radial (azimuthal) average of calibrated power spectra for reference star (Left) and NGC 1068 (Right).

Two problems are strongly apparent in the reductions of figure 7. The reference star should reduce to a constant value (unresolved) up to the telescope cut-off frequency f_c . The large inflection at low frequencies shows that the seeing over the two 90 second observing intervals compared in the two observations yielding this quotient were quite different, as discussed in Christou et al.¹⁵. There is also an upward trend, becoming much larger near f_c . Both effects are strongly exaggerated in the galaxy observation. It is a principal purpose of this paper to explain the source of this second calibration problem.

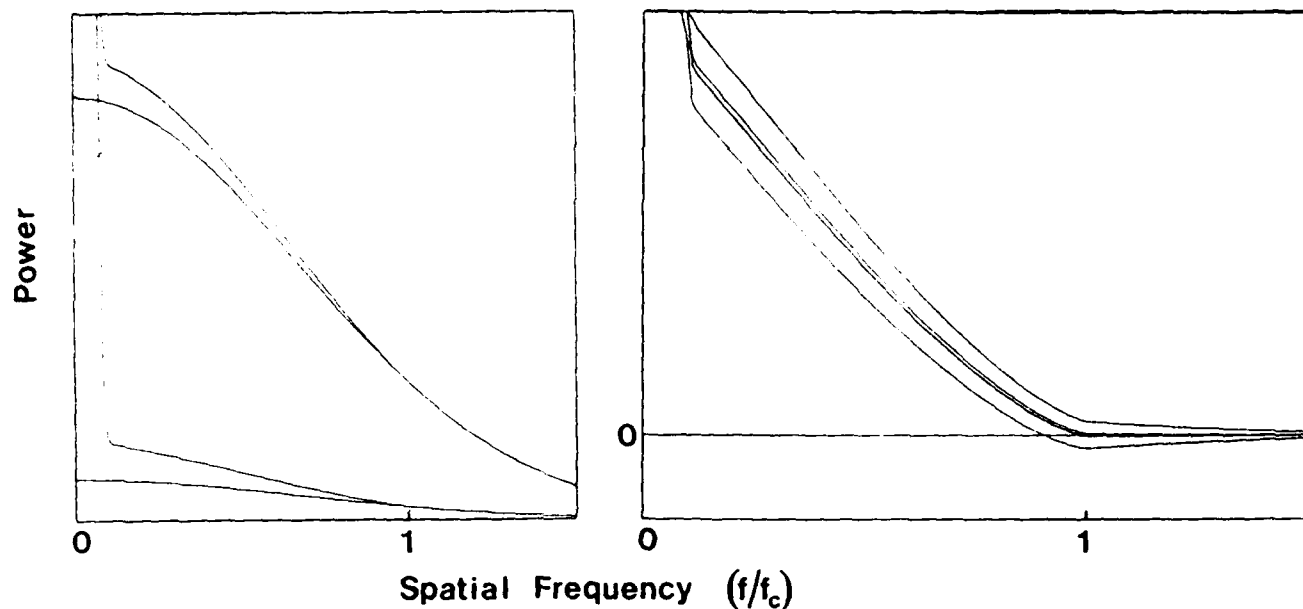


Figure 8. Effect of errors in noise bias determination. Left: Curves for 10th (lower) and 12.5th magnitude (upper) cases from figure 1 replotted on a linear scale. Right: $\pm 1\%$ errors in bias corrections applied to the same data, 10th (inner pair) and 12.5th magnitude (outer pair) -- ordinate expanded 10x.

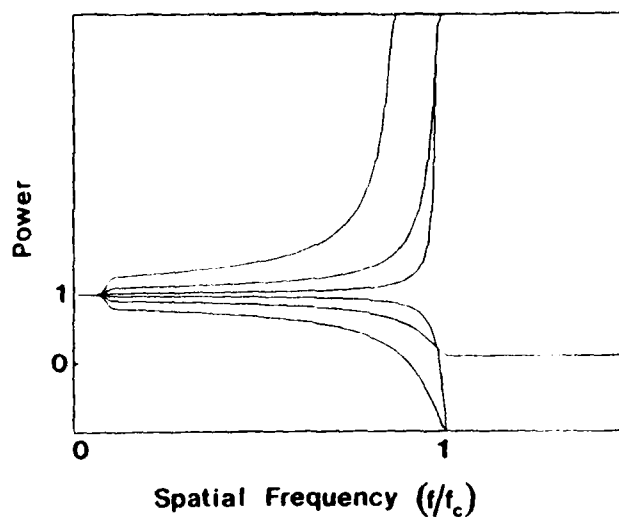


Figure 9. Calibration (4) with 1% errors in debiased estimates when observations of two 10th (inner pair), two 12.5 (outer pair) and a 10th and 12.5th magnitude (intermediate pair) objects are used. (Data as shown in figure 8, right.) Error free debias would yield a constant power = 1.0 from $f = 0$ to $f = f_c$.

Noise Bias Calibrations

It has proven to be impossible to achieve a stable photon detection PSF with our present Plumbicon video camera/Sony video cassette recorder data acquisition⁷. The differences between successive measures of the PSF are greater than the typical 1% residuals in Gaussian models fit to those measures. Therefore, we have adopted the self-calibration scheme noted in the discussion above in which the noise bias model is fit to the data of the observation itself at frequencies greater than the aperture cut-off frequency. Figures 8 and 9 show the effect of this 1% limitation in our ability to determine the exact shape and amplitude of the noise bias. We compare simulations based on two of the theoretical cases shown in figure 1: for 10th and 12.5th magnitude respectively.

The 1% error in bias determination induces 1% errors in the debiased 10th magnitude result since the power in the noise bias is the same order of magnitude as the $(r/4D)^2$ attenuated diffraction-limited component. However, it induces a 10% error in the 12.5th magnitude case where the power in the noise bias is a magnitude larger than the diffraction limited component. When these errors are propagated through the quotient (4) their effects become more drastic, especially approaching the diffraction limit where they may become infinite!

In our asteroid work¹⁴, we have the goal of detecting and measuring albedo markings which may induce 10% power spectrum modulations. Thus better than 1% calibration of the noise bias is required if the seeing calibrated power spectrum data is to be trusted at frequencies greater than 80% of f_c for these typically 10th magnitude objects. At 12.5th magnitude a 1% error in determination of the noise bias can induce factor of two variations at 70% of f_c which is totally unacceptable.

Failure of Knox-Thompson Method

We discussed effects of noise bias calibrations on power spectra, i.e. image amplitudes. The effect on the cross spectral quantities needed for the determination of the Knox-Thompson image phase differences is just as severe (c.f. 1 and 2). For our rate-dependent and distribution dependent PSF the problem is even worse. If $\Phi(u)$ ($u; r, d$) is signal rate and signal distribution dependent as noted above, the determination of the complex noise bias $B(u; \Delta u) \Delta u$ will depend upon the quality of our determination of $\Phi(u; r, d)$ within the diffraction limit.

If the noise bias fit does not match the actual shape of the biases at low frequencies, or if the low frequencies of the cross-spectra are distorted by non-centrosymmetric flat-field distortions -- which appear as convolutions in the cross spectra -- then systematic errors are induced in the calculated phase differences. A further problem in applying the Knox-Thompson method arises since most of the artifacts induced by the video raster detector are located along the u and v axes (see figure 4 in Fourier space). Therefore an integration of the phase differences along these axes will lead to contaminated phases.

Further, we cannot "flat-field" photon-detected images where all detected photons are weighted equally. The Harvard group (Papaliolios and Nisenson¹⁵) do apply flat-field corrections by using floating point Fourier transform techniques, even in the faint object limit, in which case photons can be weighted by a floating-point number, depending upon where in the detector field of view they arrive. (The flat-field correction is multiplicative in image space, and therefore must be removed frame by frame before FT processing.)

We suspect these complications explain our failure to achieve reasonable results for faint objects with the Knox-Thompson method using data from our present video raster detector.

It is reassuring to note that Differential Speckle Imaging¹⁷ (DSI) is not subject to such noise bias calibration limitations. In fact this is a case in which the noise bias acts in a beneficial filtering way. The differential image (DI) is given by the inverse Fourier transform of an inverse filtered cross spectrum.

$$DI = FT^{-1} \{ (XS_{12} / PSF) \} \quad (5)$$

Since the cross spectrum is obtained from statistically independent image data (two simultaneous but discrete specklegrams), it is a bias-free estimator. The inverse filter used is the (biased) power spectrum of one of the input specklegrams, and the non-zero bias for all frequencies assures the existence of the inverse filtered quotient. In fact, the inverse filter, with its noise bias, has the nature of a Wiener filter¹⁷.

Conclusion

Extremely stable photon-counting detectors are required for this work. The nature of our conclusion is not dependent upon the spatial frequency dependency of the noise bias; it is equally applicable to perfect delta-function detectors if, for example, they are subject to multiple detection of the same event¹⁸, in which case the DC noise bias is no longer strictly equal to N (= the number of events counted). One percent errors in the determination of a DC level have quite similar effects on quotients. It is particularly encouraging that several of the photon-counting approaches reported at this conference may prove to yield very stable and calibratable PSF's. The success of diffraction limited interferometric imaging at the faint object limit is crucially dependent upon this technology.

It is not clear whether flat fielding requirements will preclude the use of an "all photons are detected equally" image space (autocorrelation, cross-correlation) implementation of the Knox Thompson integration as proposed in our companion paper¹⁹. The last word on detector development is not yet in.

References

1. Miller, M.G., "Noise Considerations in Speckle Interferometry," *J. Opt. Soc. Am.* **67**, 1176-1181, 1977.
2. Burnett, M.E., and G. Parry, "Photon Noise Limitations on the Recovery of Stellar Images by Speckle Interferometry," *Opt. Commun.* **21**, 60-62, 1977.
3. Walker, J.G., "Signal to Noise Ratio in Speckle Interferometry in the Photon Counting Autocorrelation Mode at Low Light Levels," *Opt. Commun.* **29**, 273-278, 1979.
4. Walker, J.G., "Statistical Accuracy in Speckle Interferometry at Low Light Levels," *Optica Acta* **28**, 885-905, 1981.
5. Dainty, J.C., "Stellar Speckle Interferometry", in *Laser Speckle and Related Phenomena*, ed. J.C. Dainty, pp254-320, Springer-Verlag, 1984.
6. Nisenson, P., and C. Papaliolios, "Effects of Photon Noise on Speckle Image Reconstruction with the Knox Thompson Algorithm," *Opt. Commun.* **47**, 91-96, 1983.
7. Labeyrie, A., "Attainment of Diffraction-Limited Resolution in Large Astronomical Telescopes by Fourier Analyzing Speckle Patterns of Star Images," *Astron. Astrophys.* **6**, 85-87, 1970.
8. Hege, E.K., E.N. Hubbard and P.A. Strittmatter, "An Intensified Event-detecting Television System for Astronomical Speckle Interferometry," *Proc. SPIE* **264**, 29-33, 1980.
9. Hege, E.K., E.N. Hubbard, P.A. Strittmatter and W.J. Cocke, "The Steward Observatory Speckle Interferometry System," *Optica Acta* **29**, 701-715, 1982.
10. Knox, K.T., and B.J. Thompson, "Recovery of Images from Atmospherically Degraded Short exposure Photographs," *Astrophys. J.* **193**, L45-L48, 1974.
11. Beckers, J.M., "Differential Speckle Interferometry," *Optica Acta* **29**, 361-362, 1982.
12. Goodman, J.W., and J.F. Belsher, "Fundamental Limitations in Linear Invariant Restoration of Atmospherically Degraded Images," *Proc. SPIE* **75**, 141, 1976.
13. Cromwell, R.H., P.A. Strittmatter, R.G. Allen, E.K. Hege, K.-H. Marien, H. Kühr, H.W. Funk and K. Frank, "A Proximity Focussed Image Intensifier for Astronomy," *Adv. Electron. and Electron Phys.* **64A**, 77-92, 1982.
14. Drummond, J.D., W.J. Cocke, E.K. Hege and P.A. Strittmatter, "Speckle Interferometry of Asteroids I. 433 Eros," *Icarus* **61**, 132-151, 1985.
15. Drummond, J.D., E.K. Hege, W.J. Cocke, J.D. Freeman, J.C. Christou and R.P. Binzel, "Speckle Interferometry of Asteroids II. 532 Herculina," *Icarus* **61**, 232-240, 1985.
16. Hege, E.K., E.N. Hubbard, P.A. Strittmatter and S.P. Worden, "Speckle Interferometric Observations of the Triple QSO PG1115+08," *Astrophys. J. Lett.* **248**, L1-L3, 1981.
17. Hege, E.K., E.N. Hubbard, J.D. Drummond, P.A. Strittmatter, S.P. Worden, and T. Lauer, "Speckle Interferometric Observations of Pluto and Charon," *Icarus* **50**, 72-81, 1982.
18. Christou, J.C., A.S.Y. Cheng and E.K. Hege, "Seeing Calibration of Optical Astronomical Speckle Interferometric Data," *Astron. J.* **90**, 2644-2656, 1985.
19. Papaliolios, C., P. Nisenson and S. Ebstein, "Speckle Imaging with the PAPA Camera," *Appl. Opt.* **24**, 287-292, 1985.
20. Hebdon, J.C., E.K. Hege and J.M. Beckers, "Differential Imaging with the Cophased Multiple Mirror Telescope," *Proc. SPIE* **556**, 284-289, 1985. Also to be published in *Opt. Engng.* (1986).
21. Ebstein, S. (Private communications, 1985, 1986).
22. Hege, E.K. and P. R. Vokac, "Real time Amplitude and Phase Integrations for Diffraction Limited Imaging. Discrete Photon Case," *Proc. SPIE* (This conference), 1986.

THE H-ALPHA ENVELOPE OF ALPHA ORI

E. K. Hege, J. C. Hebden and J. C. Christou
Steward Observatory
Tucson, AZ 85721 USA

We use weighted shift-and-add with deconvolution (WSA/WD) to produce well-calibrated images of Alpha Orionis using data from the KPNO¹ 4m and the Steward 2.3m telescopes. Differential speckle interferometry (DSI) images have also been produced with data from the 2.3m and the Multiple Mirror Telescope² (MMT). We find evidence for a Northwest-to-Southeast elongated circumstellar envelope, extending to >4 stellar radii, around a limb-darkened 42 millisecond of arc (mas) stellar disk. Azimuthally averaged radial intensity profiles are in qualitative agreement with those predicted by Hartmann and Avrett, although significant quantitative differences suggesting non-uniform outflow are seen. MMT diffraction limited images of Alpha Orionis, observed in a narrow band centered on H-alpha, show measurable, resolved surface structure within the stellar disk. Our images do not show clear evidence for secondary companions.

Observations of Alpha Orionis and calibrating observations of Gamma Orionis were made using conventional speckle interferometry (Hege *et al.* 1982) at the KPNO 4m Mayall reflector on 2 and 3 February 1981, and with the Steward Observatory 2.3m telescope on 6 November 1982. On 6 March 1982 Alpha Orionis was observed with the 2.3m telescope using DSI (Beckers 1982) with a very narrowband filter (0.045nm) which was scanned in 0.05nm steps across the H-alpha spectral profile. On 17 December the line-centered DSI observations were repeated (with 0.12nm filter) using the fully cophased MMT (Hege *et al.* 1985).

WSA/WD (Christou *et al.* 1986) has been shown to produce diffraction limited point spread functions (PSF's) for both the 2.3m and 4m telescopes as well as for the MMT (Hege *et al.* 1985). The PSF's are in good quantitative agreement with the theoretically computed Airy patterns. The signal-to-noise improves as the square root of the number of frames processed, and a dynamic range of $>250:1$ is realized (Christou *et al.* 1985). This dynamic range is presently limited by a well-understood digitizer artifact. The results are self-calibrated for seeing and are insensitive to variable seeing conditions.

The telescope plus instrument PSF, obtained from the point source calibration, can be used to produce diffraction limited images of the extended source by using the radio astronomers' CLEAN algorithm (Högbom 1974). This eliminates effects of side responses (Airy rings) due to the PSF.

In DSI two specklegrams are acquired simultaneously in two different wavelength bands. By adjusting the filter so that one bandpass spans a chromospheric emission line and another spans only a region of the continuum (about 0.6nm away), the specklegram pair will

¹Kitt Peak National Observatory is operated by the National Optical Astronomy Observatories under contract to the National Science Foundation.

²The MMT is a joint facility of the University of Arizona and the Smithsonian Institution.

reveal differences between the chromospheric and continuum images (Beckers *et al.* 1983). The cross-correlation of the point-source-like (at the resolution of the 2.3m telescope) continuum specklegram with the resolvable (in the H-alpha line) specklegram produces a map of the resolved object (Hebden *et al.* 1986).

The cleaned images of Alpha Orionis obtained from the February 1981 data are consistent with a limb-darkened 42 (mas) stellar disk (Cheng *et al.* 1986) surrounded by elongated circumstellar emissions. In H-alpha, the elongation is at a position angle of 117° - 297° . This chromospheric elongation was again suggested by the lower resolution measure of the November 1982 data. The strongest evidence for the elongation is from the self-calibrating DSI result of March 1982 which confirmed the existence of the Northwest-to-Southeast extension seen in both the 4m and the lower resolution 2.3m images. In all three of these results, the extension appears at approximately the same 120° - 300° position angle with a suggestion that the intensity was stronger in the NW quadrant in the later measures (Hebden *et al.* 1986). Smaller scale asymmetries were also noted, but the evolution of those features appears to be consistent with fluctuations of surface structure. No evidence of correlation with polarization variations over the same period was noted.

Azimuthally averaged radial image profiles are shown for the March 1981 data in H-alpha 656.3nm (Figure 1) and CaII 854.2nm (Figure 2). Narrow-band (0.3nm) filters were used for both observations. The radial profiles predicted by Hartmann and Avrett (1984), convolved to the same spatial resolution as the data, are shown superimposed for comparison. The Hartmann and Avrett profiles assume a flux of Alfvén waves sufficient to drive an outflow of 10^{-6} solar mass per year and used electron density data obtained from radio measurements. There is qualitative agreement with the predictions, but quantitative differences are noted, particularly for CaII where the model over-predicts at small radii and under-predicts at larger radii. The expanding shell model is the closest fit to the data. There is an inflection in our data, seen in both profiles, at about 3-4 stellar radii. This could be evidence of increased outflow of matter at an earlier epoch. This may relate to variations in visibility profiles which Roddier (1985) has shown to relate to fluctuations in photometric intensity and which can be interpreted as signifying a variability in mass outflow (Goldberg 1984).

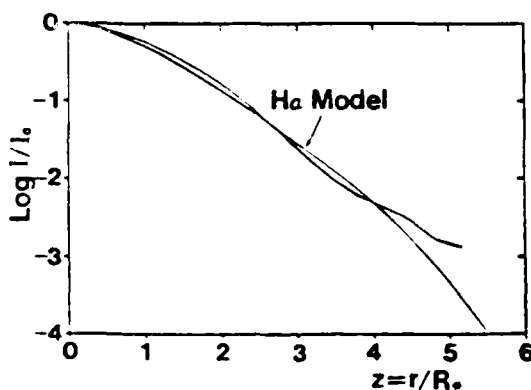


Figure 1

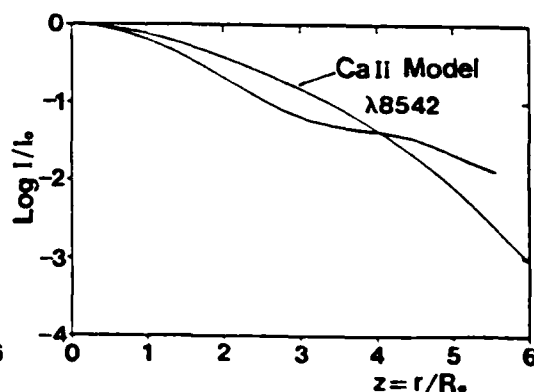


Figure 2

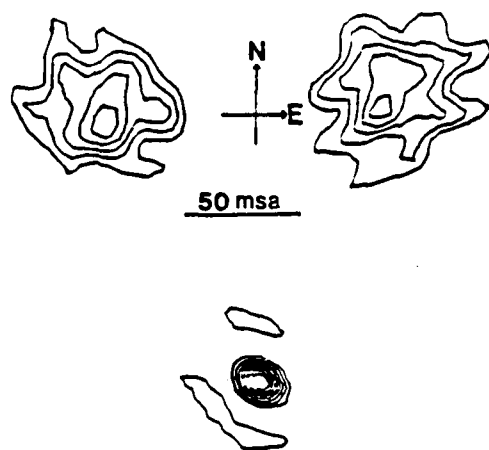


Figure 3

Preliminary evidence of chromospheric (H-alpha) structure within the stellar disk is seen in Figure 3. This pair of DSI images obtained with the MMT, together with the unresolved DSI PSF observed for Gamma Orionis, taken at different camera-telescope parallactic angles is printed in the same orientation. They show evidence for an unresolved bright spot and for a resolved extension within the disk in this differential observation.

We have limb-darkening measures and radial intensity profiles for Alpha Orionis (Christou 1985) observed at the diffraction limit of the KPNO 4m

telescope (pupil masked to 3.8m). Differential images with the resolution implied by the full 6.86m resolution of the MMT suggest surface structure seen at 2.5 times the resolution possible with a diffraction limited Space Telescope at the same wavelength. Structure in both the averaged image profile and on the stellar disk appears to evolve in time. This emphasizes the need for synoptic image studies, coordinated with conventional photometric, polarimetric and spectroscopic studies in optical, IR, and radio wavelengths, to obtain a qualitative advance in the detailed understanding of this rapidly evolving star.

This work was supported in part by NSF (AST-8201092 and AST-8312976) and by the Air Force (AFOSR 82-0020 and AFGL-F19628-82-K-0025).

- Beckers, J.M. (1982) *Optica Acta* 29, 361.
 " , E.K.Hege and H.P.Murphy (1983) *Proc SPIE* 445, 462.
 Cheng, A.Y.S., E.K.Hege, E.N.Hubbard, P.A.Strittmatter, W.J.Cocke and L.Goldberg (1986) *Astrophys. J.* (submitted).
 Christou, J.C. (1985) Ph.D. dissertation, New Mexico State University.
 " , E.K.Hege, J.D.Freeman and E.Ribak (1985) *Proc. SPIE* 556-36.
 " , E.K.Hege, J.D.Freeman and E.Ribak (1986) *J. Opt. Soc. Am. A* (in pres).
 Goldberg, L. (1984) *Publ. Astro. Soc. Pacific* 96, 366.
 Hartmann, L. and E.H.Avrett (1984) *Astrophys. J.* 284, 238.
 Hebdén, J.C., J.C.Christou, A.Y.S.Cheng, E.K.Hege, P.A.Strittmatter, J.M.Beckers and H.P.Murphy (1986) *Astrophys. J.* (submitted).
 Hege, E.K., E.N.Hubbard, P.A.Strittmatter and W.J.Cocke (1982) *Optica Acta* 29, 701.
 " , J.M.Beckers, P.A.Strittmatter and D.W.McCarthy (1982) *Appl. Opt.* 24, 2565.
 Högbom, J.A (1974) *Astron. Astrophys. Supp.* 15, 417.
 Roddier, F. (1985) Reported at this conference.

Phased Array Imaging with the Multiple Mirror Telescope

E. Keith Hege
Donald W. McCarthy, Jr.
Jeremy C. Hebden
Julian C. Christou*
Steward Observatory
University Of Arizona
Tucson AZ 85721

Introduction

The 6.86m Multiple Mirror Telescope (MMT) has been operated as a co-phased optical array since 1983 [1]. We have used it to obtain seeing calibrated diffraction-limited images of the point source γ Orionis and the resolved red supergiant α Orionis. The point source images validate the imaging performance of the system as a function of wavelength (4100 – 8500 Å) and of coherence length (6 μ m to 3.6mm). We have measured a stable point spread function (PSF) with an FWHM of 75 nanoradians or 15 milli-arcseconds (mas) which matches the theoretical prediction. Images of α Orionis have been obtained both in the chromospheric H_α emission and in the adjacent line-blanketed "continuum" with $\lambda^2/\Delta\lambda = 3.6$ mm. In addition, we have also obtained images of a geosynchronous communications satellite in a broader bandpass ($\lambda = 5500$ Å with $\lambda^2/\Delta\lambda = 30\mu$ m). The resolution of both of these images is consistent with the observed PSF's.

Pathlength Correction

The MMT consists of six 1.8m telescopes comounted in a hexagonal array. However, the MMT Optics Support Structure (OSS) flexes allowing up to 500 μ m of differential variations in the optical pathlengths as a function of elevation. We have found that these elevation dependent variations can be compensated by means of open-loop co-phasing. Figure 1 shows how the beams from a pair of the telescopes combine and

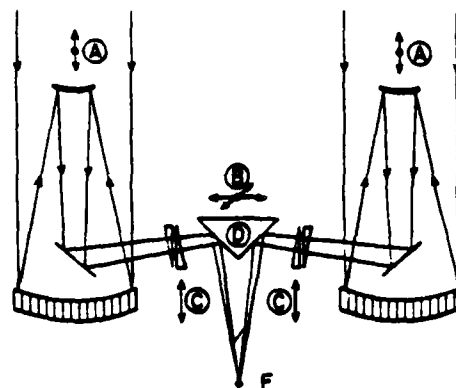


Figure 1: Pathlength correction geometries between two mirrors.

the four different ways the pathlengths may be adjusted. These are: A - translation of the secondaries effectively adjusting the focus, B - two-dimensional translation of the beam combiner, C - the use of complimentary wedges, and D - the separation of the beam combiner into six independent facets which can be translated independently. We currently use optical wedge prisms, C, although an automatic pathlength compensation D, which can be applied in the infrared, is in preparation.

In order to compensate the elevation dependent pathlength changes we use an empirical determination of the changes vs. elevation angle. This is done by observing a number of stars at various elevations between 25° and 85° and obtaining the wedge prism positions (with a 0.18 μ m resolution) when interference fringes are produced. A quadratic fit through these points is then used to model the variations. The MMT coalignment computer calculates the expected positions of the prisms at the instantaneous elevation angle during the observation.

*Currently at the Advanced Development Program, National Optical Astronomy Observatories, operated by the Association of Universities for Research in Astronomy Inc., under contract with the National Science Foundation.

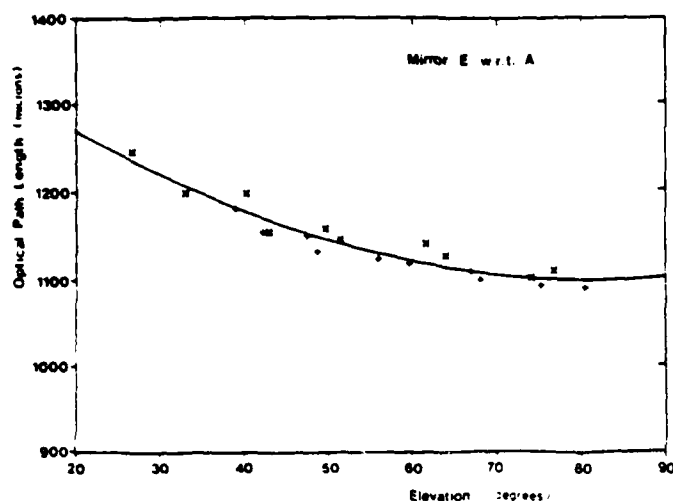


Figure 2: Phasing curve for mirror pair A-E showing pathlength change as a function of elevation angle.

Apart from absolute pathlength changes caused by temperature induced focus changes, these curves are very stable during an observing run of several nights. Figure 2 shows a typical phasing curve for mirror E with respect to mirror A. A worst case of pathlength variation of $\sim 300 \mu\text{m}$ has been measured for a 60° change of elevation. From three years experience the hysteresis effects appear to be $\leq 10 \mu\text{m}$ and from these measurements we find that the OSS is a very stable and calibratable platform.

Recent measurements taken in October 1986 during 4 hours of conditions with stable temperature show that the pathlengths were successfully predicted to an accuracy of $\sim 10 \mu\text{m}$. This is consistent with the accuracy of the measured calibration and the amount of focus change expected from the measured temperature variations of $\leq 0.1^\circ\text{C}$. Further improvement seems possible but requires more accurate methods of focussing the individual telescopes and of correcting the temperature variations in the OSS members. We have recently undertaken a program to monitor the absolute temperatures and temperature gradients throughout the OSS in an effort to improve the accuracy of our open-loop corrections. This program involves the installation of 10 temperature sensors on the OSS as well as surveillance of the OSS by a thermographic infrared camera throughout the night.

The role of the temperature-induced changes in the vertical positions of the secondary mirrors is especially critical since the structural members, which

support the secondaries, are relatively long steel tubes whose lengths vary causing a pathlength change at the rate of $65 \mu\text{m}/^\circ\text{C}$. Thus it is important to minimize the temperature gradients across the OSS so that the foci of all the telescopes will change identically, and the MMT will remain in phase. Experience to date indicates that the OSS becomes remarkably uniform in temperature ($\leq 0.1^\circ\text{C}$) approximately two to three hours after exposure to the sky. A wind can accelerate this effect. This performance is the result of the low emissivity aluminum coating surrounding the individual structural members and their small thermal inertias.

PSF Measurements

To confirm the ability of the co-phasing to yield true diffraction-limited performance we applied the weighted shift-and-add imaging technique [2,3] to specklegrams of the γ Orionis at a number of band-passes. Two of these results are shown in Figure 3 representing the extreme range of our intensified video speckle camera [4]. These PSF's, at $4100\text{\AA}/100\text{\AA}$ and $8500\text{\AA}/100\text{\AA}$, show the expected diffraction-limited beam size. However the detailed low level symmetrical structure of the PSF, seen in previous results[4], is lost in the measurement noise at the detector's extreme wavelength range. These PSF's demonstrate the ability of both the imaging algorithm and the cophasing to operate over 4400\AA range of wavelength. Figure 4 also shows an image of γ Orionis using a technique known as differential speckle interferometry (DSI) [5], discussed below, along with the corresponding analytic PSF.

Images of α Orionis

We have obtained diffraction-limited images of the H_α envelope of α Orionis using the co-phased beams and the DSI technique. This technique records co-temporal specklegrams (short exposure images less than the atmospheric correlation time) of the object in the H_α line (6563\AA) and the nearby line blanketed "continuum" (6569\AA), each with a bandwidth of 1.2\AA . The H_α specklegrams are deconvolved by the continuum specklegrams to remove the atmospheric perturbations and produce a differential image. When this differential image is convolved with an estimate of the star's appearance in the continuum

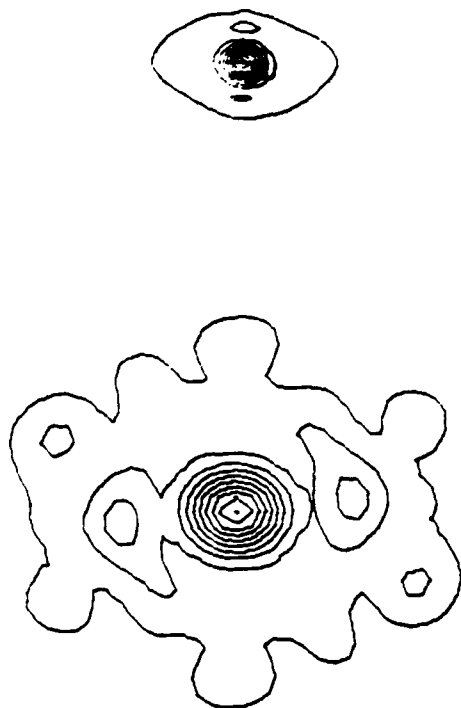


Figure 3: Measured PSF's of the co-phased MMT at 4100Å (top) and 8500Å (bottom).

an image of the star in H_α is produced. Continuum images were produced by using the Fienup phaseless image reconstruction technique [6].

Figure 5 shows the continuum image of α Orionis compared to the restored H_α image. The azimuthally averaged radial profiles of this and a second continuum image are consistent with a radius of $R_* = 21$ mas, with limb-darkening 0.6 in accordance with other estimates [7,8] and the theoretical work of Tsuji [9]. The low level features in the continuum image are most likely either systematic artifacts, due to the complex MMT PSF, or produced by second-order seeing calibration errors. The H_α image clearly shows the extended chromosphere which appears to be consistent in size over ~ 2 years between this and the second observation. This is further illustrated in Figure 6 which shows the average of the two azimuthally averaged radial profiles of the H_α images. Comparison of this profile to a model, developed by Hartmann & Avrett[10], indicates that the chromosphere is more extended than their model suggests. Wider bandpass observations (2.8Å) obtained at the KPNO 4m support this [8]. A more thorough discus-

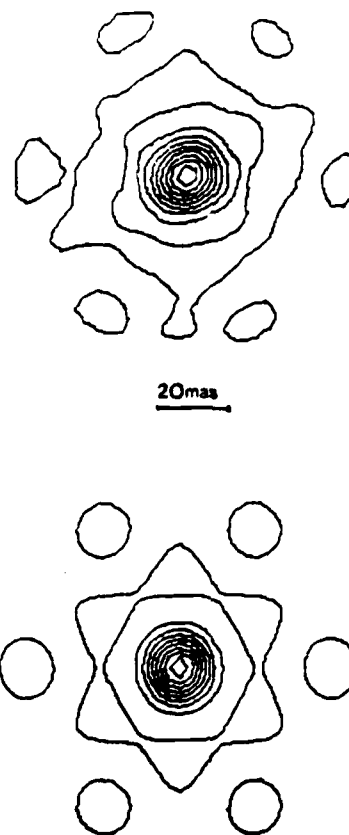


Figure 4: DSI point spread functions. Top - experiment, bottom - theory.

sion of these results is given by Hebden *et al.* [11].

Images of A Satellite

The geosynchronous communications satellite FLT-SATCOM was observed in two twenty minute data segments using the co-phased MMT at 5500Å/100Å on 4 November 1985. Images of the satellite were obtained using the Fienup technique. Figure 7 shows a contour plot of one of these images with the contour levels at 1, 2, ..., 6 times the RMS background noise. An approximate representation of the outline of the object is shown for comparison. The second twenty minute data segment result is comparable to the first. At this distance the beam size (FWHM) is ~ 3 meters. The object's size was estimated to give a major axis of $13.0 (\pm 2.3)$ m and a minor axis of $7.4 (\pm 2.3)$ m with a precision of 75% of the beam size. Despite the noise in the reconstructed image (RMS background = 1/6 peak) the asymmetries of the object are clearly seen.

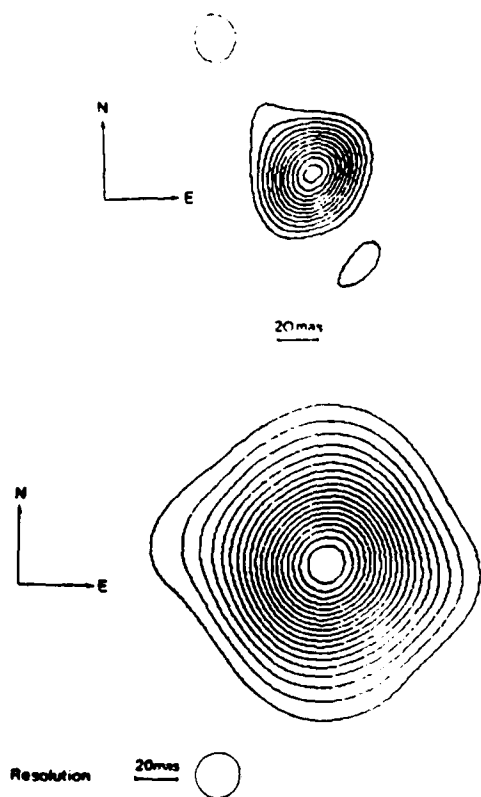


Figure 5: Images of α Orionis. Top - continuum (6569Å), bottom - H_α (6563Å).

Acknowledgements

This work was supported in part by Air Force contract F19628-84-K-0035 and NSF grants AST-8312976, AST-8418188 and AST-8519506.

References

- [1] Hege, E.K., Beckers, J.M., Strittmatter, P.A., & McCarthy, D.W., *Applied Opt.*, **24**, 2565, (1985).

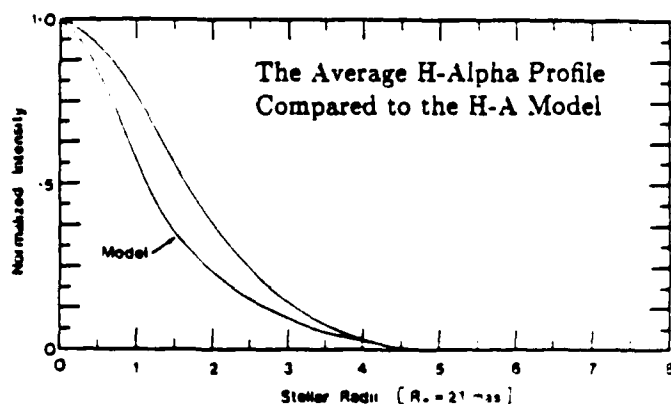


Figure 6: Comparison of H_α radial profile of α Orionis to the Hartmann - Avrett model.

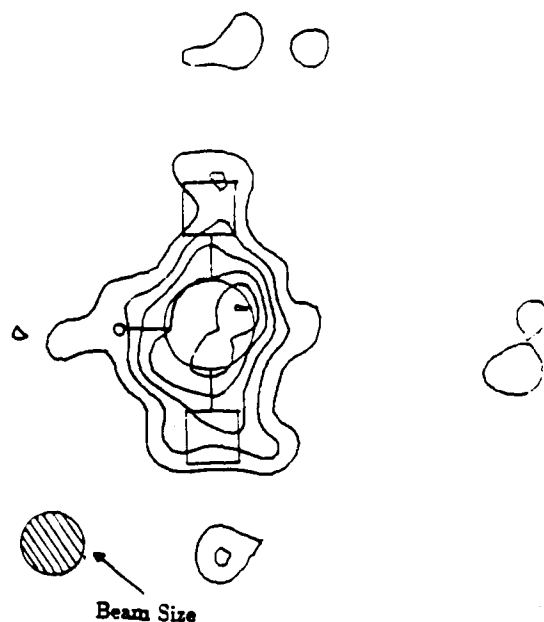


Figure 7: Reconstructed image of FLTSATCOM compared to the object's outline.

- [2] Christou, J.C., Hege, E.K., Freeman, J.D., & Ribak, E., *J. Opt. Soc. Am.*, **A3**, 204-209, (1986).
- [3] Christou, J.C., Ribak, E., Hege, E.K., & Freeman, J.D., *Opt. Eng.*, **25**, 724-730, (1986).
- [4] Hege, E.K., Hubbard, E.N., Strittmatter, P.A., & Cocke, W.J., *Opt. Acta*, **29**, 701, (1982).
- [5] Beckers, J.M., *Opt. Acta*, **29**, 361, (1982).
- [6] Fienup, J.R., *Opt. Lett.*, **3**, 27, (1978).
- [7] Cheng, A.Y.S., Hege, E.K., Hubbard, E.N., Goldberg, L., Strittmatter, P.A., & Cocke, W.J., *Astrophys. J.*, **309**, 737, (1986).
- [8] Christou, J.C., Hebden, J.C., & Hege, E.K., *in preparation*.
- [9] Tsuji, T., *Pub. Astron. Soc. Jap.*, **30**, 435, (1978).
- [10] Hartmann, L., & Avrett, E.H., *Astrophys. J.*, **284**, 238, (1984).
- [11] Hebden, J.C., Eckart, A., & Hege, E.K., *Astrophys. J.*, *in press*, (1987).

REAL-TIME AMPLITUDE AND PHASE INTEGRATION FOR DIFFRACTION LIMITED IMAGING Discrete Photon Case

E. Keith Hege
Steward Observatory, University of Arizona
Tucson, AZ 85721

Peter R. Vokac
Digital Television Imagery
Tucson, AZ 85741

Abstract

Both video raster detectors and newly developed 2-D photoelectron event locators are now employed to collect data at large astronomical telescopes for diffraction limited optical imaging by a number of speckle interferometric techniques. The Knox-Thompson algorithm is among the best understood of these techniques. The image amplitude and phase integrations required for its implementation can be accomplished directly in event-coordinate space (in the extreme photon-limited case) more efficiently than in the more conventional Fourier transform space. We describe hardware to accomplish the integrations required for Knox-Thompson image reconstruction in real-time at the telescope, thus alleviating the principal data processing bottleneck in the present applications of diffraction limited astronomical imaging. Parallel digital recording of the photon coordinate lists permits subsequent off-line re-analysis of the data by other methods if desired. The basic system consists of hardware to localize discrete photoelectron responses in a CCD TV raster and for accumulation of the complex autocorrelogram. A generalization of the system can integrate triple correlations.

Introduction

Nisenson and Papaliolios¹ discussed the discrete photon realization of the Knox-Thompson² image reconstruction method and the Poisson noise limits applicable in the faint object limit. Three products of the form

$$P(\Delta u) = \langle I^*(u) \cdot I(u + \Delta u) \rangle \quad (1)$$

must be averaged. $\Delta u = \Delta u_f + \Delta u_v$ is a frequency shift in the image Fourier transform plane. The three products correspond to i) $\Delta u = 0$ (power spectrum), ii) $\Delta u = \Delta u_f$ (u-shifted cross spectrum), and iii) $\Delta u = \Delta u_v$ (v-shifted cross spectrum). In the discrete photon case, these products are noise biased estimators (Photon detection Poisson statistics).

$$P(u) = \langle |D(u; u)|^2 \rangle [N + N^2 \langle \exp[ju \cdot x_k] \exp[-j(u + \Delta u) \cdot x_1] \rangle] \quad (2)$$

where $\{x_k\}$, $\{x_1\}$ are the set of photon addresses for the nth specklegram containing, on the average, N photons. When N is small it is more efficient to compute in image (coordinate) space than in transform (coordinate⁻¹ = frequency) space. The discrete Fourier transform (DFT) of the products (2) are autocorrelations (histograms of the differences $\{x_k - x_1\}$) weighted by the factor $\exp[-ju \cdot x_1]$. In the usual case, $|u| = 1 \text{ pixel}^{-1} = 2\pi/L$ if L is the size of the DFT. The weighting factor can be expressed as $\exp(-ju \cdot x_1) = \cos(2\pi x_1/L) + j \cdot \sin(2\pi x_1/L)$. Thus there are three coordinate space histograms to be computed:

$$q(x; s) = N \sum_{k,1} \exp(j2\pi s \cdot x_1/L) \cdot \delta(x_k - x_1 - x) \quad (3)$$

where

$s = 0$ is the autocorrelation function
 $s = i$ is the x-shifted cross correlation
 $s = j$ is the y-shifted cross correlation.

System Requirements

The objective is to produce a real-time realization of (3) suitable for photon-noise limited observations (faint object case) using conventional video technology and conventional digital technology. The Digital Television Imagery DTI-10 vector autocorrelator³, presently used by McAlister⁴, is the conceptual starting point.

We require an optimized photon event localizing detector with high quantum efficiency, low geometric distortion, lag-free response and a stable PSF. For high

quantum efficiency, a high-gain, low-noise image intensifier with a good pulse-height distribution feeding a stable, low-noise video detector is required. In order to preserve time resolution (commensurate with the atmospheric correlation time), events must be localized to one video frame. Address localization is required to avoid multiple detection of events so that the number of events counted is accurately equal to the number of actual photons detected. A very stable PSF is required as argued in a companion paper⁵. This places very strong constraints on the photon event detection technology, requiring negligible geometric distortions in the image intensifier and low read-out noise and high stability in the video camera.

Proposed System

The system proposed will feature:

1. Proxitronic image intensifier system⁶
2. CCD TV - Pulnix (Sony)
3. Anti-aliasing filter
4. No AGC; D.C. coupled video
5. 8-bits A/D conversion at 2x pixel rate
6. Digital filter: 2x back to 1x pixel rate
7. Full-frame subtract - for event localization
8. Digital video processor - for real-time integrations
9. Event-list data logging for off-line (re)processing

A five-stage proximity-focus image intensifier is required to assure quantum-limited single-photon detection capability. Proximity-focus technology is required for low geometric distortion and for the good pulse-height distribution required for high quantum-efficiency event detection. The development of such a detector has been described by Cromwell *et al.* elsewhere⁶.

The digital video system is shown in block outline in figures 1 and 2.

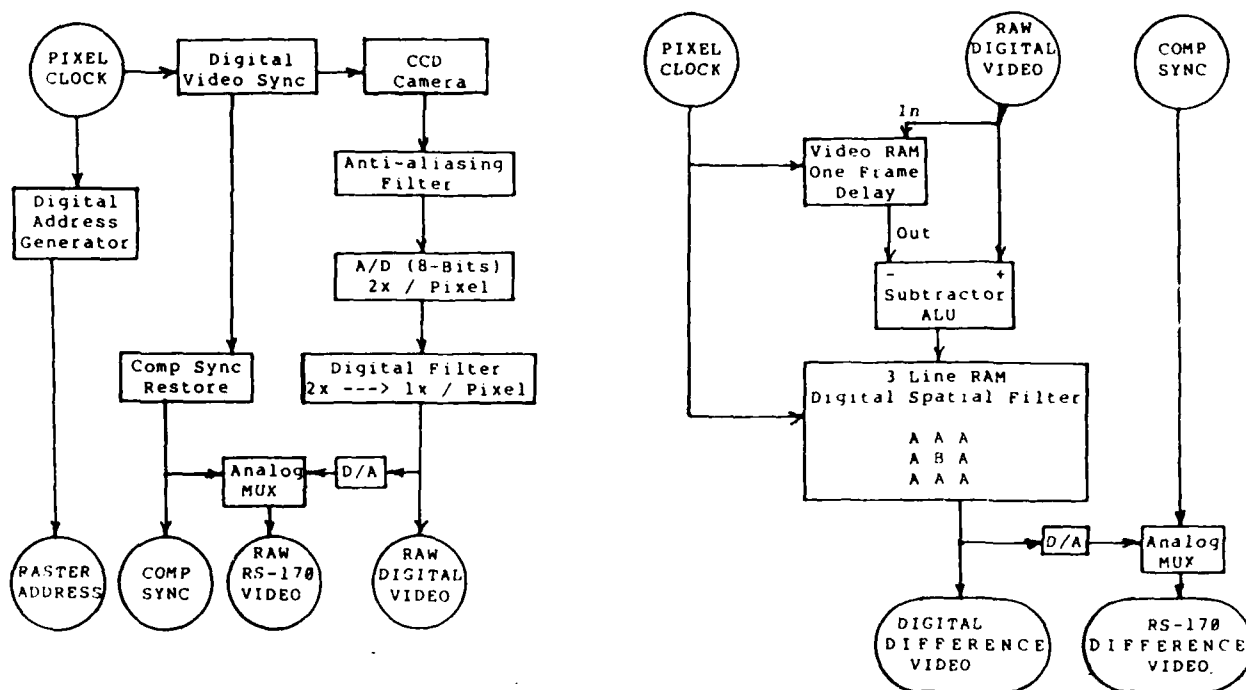


Figure 1. The CCD TV/Digital Video event detector is shown as three subsystems. Left: Raw digital video. Right: Full-frame video difference.

A CCD TV is required for good geometric fidelity and stability. The system must be operated synchronously to assure one-video-output-pixel to one-physical-CCD-pixel correspondence. A synchronous system with an anti-aliasing filter (including correlated double sampling) and which rigorously preserves the DC levels at the input of the Analog-to-Digital (A/D) converter as well as digital output filtering is essential for low-noise operation and PSF stability. The digital video sync, derived from the CCD

camera driver, consisting of H, V and Pixel Clock, is used to generate the digital video addresses required for fully synchronous operation of the entire digital video processing system. Synchronous operation is required to maximize processor throughput as well as to maintain rigorous correspondence of the digital video pixels to their physical origins in the camera.

Full-frame subtraction is necessary to force video black level to digital zero. It is also necessary, in a video system reading output responses with non-negligible rise times and long decay times, to inhibit multiple detection of photon events so that the very accurate noise bias estimates required⁷ may be determined. In order to assure localization of events in the proper video raster, further comparator logic is required to detect the events in only the raster in which their maximum response occurs. This is necessary to preserve the temporal correlation of the specklegrams.

The primary digital video unit, figure 1 left, is a stand-alone unit located at the camera head to assure video fidelity. The raw digital video is coupled to the full-frame digital video difference unit, figure 1 right, using dual differential transmitters. The video difference unit, as are all of the following digital video processors, is to be supported on a VMEbus MC68000 hosted microprocessor system.

The full-frame subtract is accomplished by video multiplexing of two video frame buffers. The digital memories required for the double-buffered full-frame subtract can be very economically realized using contemporary video-raster optimized dynamic RAM. The cost of this memory is no longer a significant limiting factor in the design of such a system.

A two-dimensional spatial filter at the video difference output can be programmed by the host to be either high-pass, neutral or low-pass. For the event localization application being proposed here, high-pass filtering will enhance the small-area photoelectron peaks. This will aid in discriminating partially overlapping peaks. For other applications in which the analog video amplitudes are required, low-pass filtering can smooth the individual photoelectron responses commensurate with the resolution of the imaging system.

Monitors both for the raw digital video camera output and for the filtered video difference output are driven by analog multiplexors which produce RS-170 video output with composite sync restored from the system H and V and analog video from D/A synchronized by the Pixel Clock.

The event localization algorithm is a 3x3 realization of the 5x5 event localization technique developed at Kitt Peak as the primary event-detector for the photon-centroiding camera also described in this conference⁷. The pixel-under-test (PUT) lags

the current pixel (CP) from the camera. The 3x3 matrix ALU is fed the appropriate 9 pixels from a three-line RAM. An event is detected at the PUT for which the central pixel response exceeds the eight nearest neighbor responses in the 3x3 detection matrix which is scanned through the video raster so that the position of CP is maintained. The event is further validated by requiring that it only be detected in the frame for which its response is maximum. The full-frame comparator is required because the threshold-qualified decision on maximum cannot be made until one frame after that in which the peak occurred when the decay is detected by a digital comparator. The Events List output is the digital X,Y address of PUT and the previous frame number (time).

Such a detection process has a unique non-delta-function-like signature (PSF). Although the event is detected uniquely on only one pixel, two events can never be detected on adjacent pixels -- a minimum must be detected to define two adjacent maxima. We have simulated this event detection scheme in our present video raster system. The events are localized to one pixel along the raster lines with

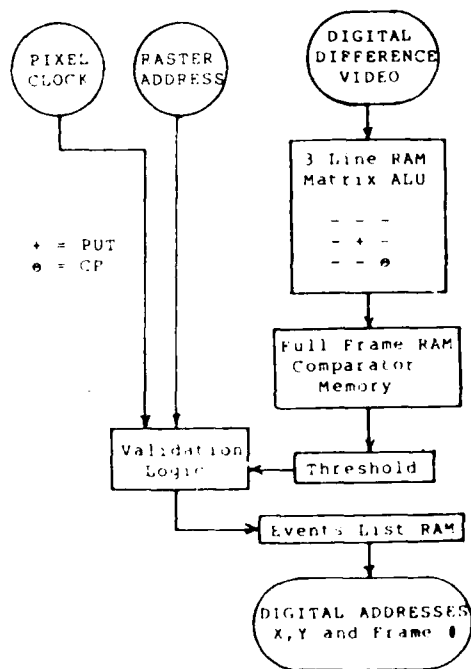


Figure 1. Event detection logic.

hardware⁸ (a digital comparator) and the multiply detected events are localized to a single line in software during subsequent data reductions. The characteristic signature of the PSF for detection of events which produce responses on more than one pixel in a video raster is strongly evident in both the autocorrelation function (ACF) and the power spectrum (PS) as shown in figure 3. In the ACF, no signal is detected at $|r| = 1$ since for detection of adjacent maxima there must be an intermediate minimum at least one pixel broad. This produces the corresponding cosine-like dip in the PS.

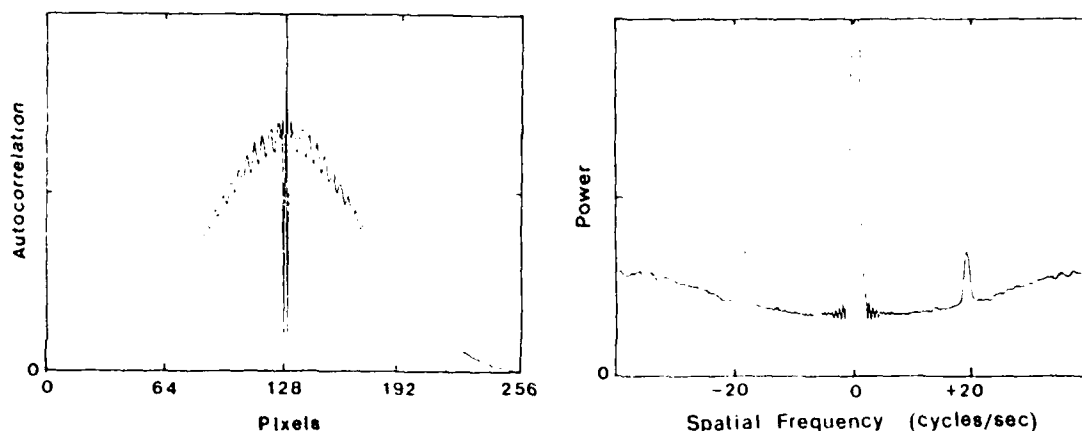


Figure 3. Left: Autocorrelation function with noise bias (spike at 128) and PSF (dips at 127 and 129) signature. Right: Corresponding power spectrum for pixel-unique raster event detector. Data from double-slit calibrator in pupil.

Experiments with this software simulation have shown that the detailed shape of this noise bias function (figure 3.) is also signal rate dependent⁵ (Probably due to rate-dependent errors in resolving the "adjacent photon" problem). It remains to be determined if this is a limiting factor in the effectiveness of such a system in the faint object case for which this system is expected to be most effective.

RS-170 analog video to drive monitors is useful to assure valid performance of the video pre-processors. The extra memory required for an event buffer/video scan converter is a small increment to the total cost of the system.

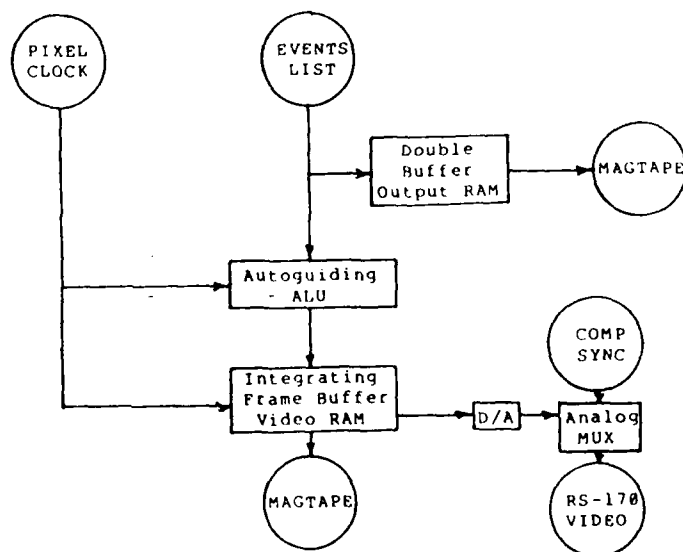


Figure 4. Data archiving subsystem.

The addition of autoguiding to the integrating frame buffer accumulating the output event data can also be of use in seeing compensation⁹⁻¹¹. Double-buffered data-logging (with frame sequence identification) assures loss-free capture of the unprocessed specklegrams. Nine track magtape at 1600bpi can accommodate the data rates of P20 phosphor image intensifiers read out by 60Hz video raster event detectors. This data-archiving subsystem is outlined in figure 4. It can be controlled by the microprocessor required as host for speckle camera and digital video processor control.

The digital processor must accumulate quantities from which image phase information as well as image amplitude information can be recovered. It should be a parallel processor in which the additional tasks are accomplished at no further cost in execution time. Fully synchronous operation of a static RAM memory system with pipelined computations is required.

The algorithm to be accomplished is shown schematically in figure 5. The control logic is identical to that required for accumulation of the conventional vector (event address differences) autocorrelation histogram^{3,4}. The new computational elements are the four sin/cos calculations and the four new 2-D result accumulations. The sin/cos calculations can proceed in parallel, pipelined to follow immediately the outer loop data fetch. Since all of the new cross correlation (XCOR) accumulations occur at fixed address offsets from the autocorrelation accumulation (figure 6) all of the address offset calculations can occur in parallel so that in the next cycle all of the read/add/write data accumulations can occur in parallel.

The expected performance of this system can be predicted using the performance of the existing DTI-10 as a benchmark. The input array size is 256x256 pixels sampled over a square 3x3 aspect ratio centered in the 4x3 standard video raster. The X-Y address of each detected pixel is entered into a 4K RAM list. The DTI-10 calculation array is a subset of the full 512 horizontal by 256 vertical ACF field of a 256x256 input field. The present DTI-10 accumulates ACF's 128x64x16bits deep: we propose enlarging this to 256x128x24bits. This array can be placed anywhere in the full 512x256 ACF field. ACF display is enhanced by a reflection circuit that gives it the full symmetry and appearance of a 512x512 field.

The DTI-10 was implemented using static RAM's in a fully synchronous system operating at 100ns/cycle. At that rate real time can be maintained at 60Hz video field rate when less than 640 events/frame are detected. This is a rather good match to the rate at which events can be detected as discrete responses in a 60Hz video raster. Obviously, it is inadequate to keep up with the higher event rates possible with other digital camera techniques^{12,13}.

Conclusions

Given the present availability of 2Kx8 (8Kx8 anticipated soon) 35ns SRAM, it appears reasonable to expect 50ns operation, in which case the maximum throughput is increased to about 900 events/frame or about 5×10^4 /sec which will be adequate to keep up with real-time data rates for objects $m_v = 10$ or fainter with telescopes as large as the MMT. This includes most of the interesting objects for which long integrations, and therefore expensive off-line reductions, are required. For brighter objects, analog video amplitudes requiring full-frame FFT processing are more appropriate.

With our reservations about the performance of the Knox-Thompson method (our companion paper⁵), we note that the Knox-Thompson integration proposed here is a subset of the integrations required for the more rigorous triple correlation reductions proposed by Lohmann, Weigelt and Wirnitzer¹⁴. In that method the four-dimensional expression (3) expands by allowing s to span the same space as x . In that case n^2 complex integrations (x_i, y_j) are required rather than the two (i, j) required for Knox-Thompson processing. We have noted elsewhere¹⁵ that the amplitude of the complex correlation falls off on the scale of the object being imaged. Thus triple correlation methods spanning a space small compared to n^2 , but significantly larger than two, might prove to be an optimal approach for compact objects (e.g. asteroids, bright stars, etc.) or for extended objects with bright, compact components (e.g. active galactic nuclei). The system proposed here can easily be expanded to this larger problem: all it costs is memory.

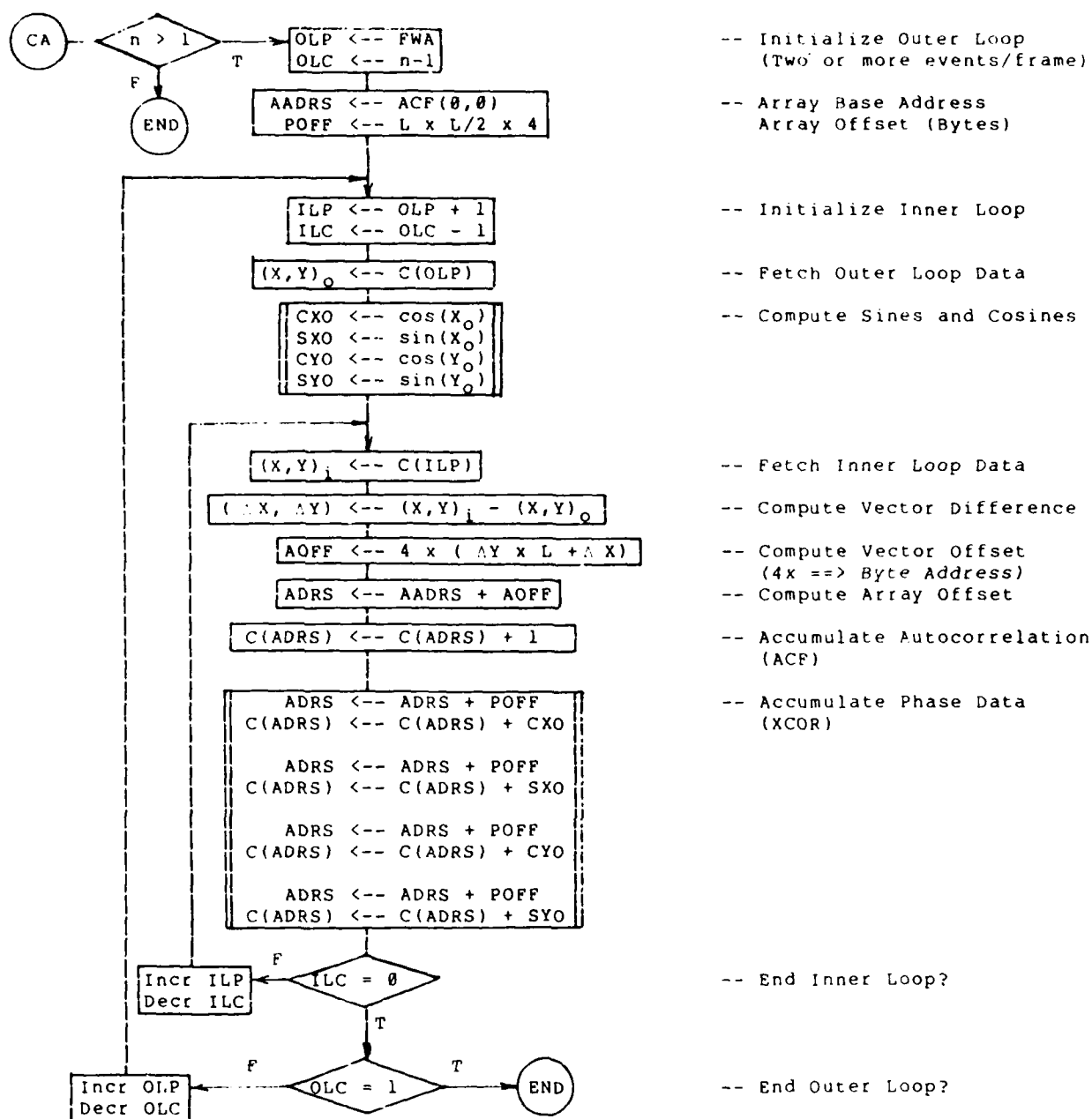


Figure 5. Outline of Discrete Photon Knox-Thompson Integration (Complex Autocorrelogram, CA). The parallel (concurrent) operations in the double-lined boxes are the new additions to the basic existing DTI-10 vector autocorrelogram integrator⁴. L is the array size (=256), n is the number of events detected, FWA is the address of the input list, and ACF(0,0) is the address of the integrator memory, figure 6.

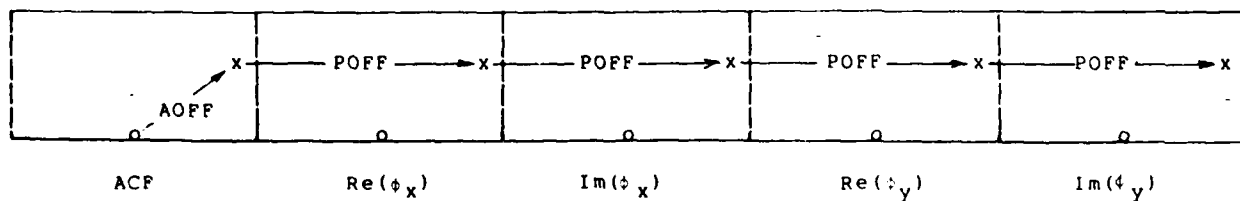


Figure 6. Parallel ACF, XCOR (= Complex Autocorrelogram) accumulations at x with constant offset $ox = AOFF$ in each array. $\phi_x = q(x,1)$ and $\phi_y = q(x,j)$.

References

1. Nisenson, P. and C. Papaliolios, "Effects of Photon Noise on Speckle Image Reconstruction with the Knox-Thompson Algorithm," Opt. Commun. **47**, 91-96, 1983.
2. Knox, K.T., and B.J. Thompson, "Recovery of Images from Atmospherically Degraded Short-exposure Photographs," Astrophys. J. **193**, L45-L48, 1974.
3. Vokac, P.R., "An On-line Digital Autocorrelator for Speckle Interferometry," Proc. SPIE **119**, 223-321, 1977.
4. Hartkopf, W.I., H.A. McAlister and D.J. Hutter, "Reduction and Analysis Techniques Developed for the GSU IDDC Speckle Camera," Bul. Am. Astron. Soc. **17**, 551 1985.
5. Hege, E.K., A. Eckart and J.C. Christou, "The Noise Bias Problem in Optical Speckle Imaging: Experience with a Real Detector," Proc SPIE **627** (This conference) 1986.
6. Cromwell, R.H., P.A. Strittmatter, R.G. Allen, E.K. Hege, K.-H. Marien, H. Köhr, H.W. Funk and K. Frank, "A Proximity Focussed Image Intensifier for Astronomy," Adv. Electron. and Electron Phys. **64A**, 77-92, 1982.
7. Reed, R., S.E. Bulau, W.F. Ball, E.A. Bell and W.G. Robinson, Jr., "2D Photon Counting System for Spectroscopic Applications at Kitt Peak National Observatory," Proc. SPIE **627** (This conference) 1986.
8. Macklin, R.H., E.K. Hege and P.A. Strittmatter, "A Real-time Photoelectron Event-detecting Video System," Proc. SPIE **359**, 135-138, 1982.
9. Hege, E.K., E.N. Hubbard and P.A. Strittmatter, "An Intensified Event-detecting Television System for Astronomical Speckle Interferometry," Proc. SPIE **264**, 29-33, 1980.
10. Christou, J.C., A.S.Y. Cheng, E.K. Hege and C. Roddier, "Seeing Calibration of Optical Astronomical Speckle Interferometric Data," Astron. J. **90**, 2644-2656, 1985.
11. Morgan, R.L., C. Standley and H.A. Vine, "Speckle Interferometry at Imperial College," Proc. SPIE **627** (This conference) 1986.
12. Gonsiorowski, T., "New Product for Photon-limited Imaging," ibid
13. Timothy, J.G., and J.S. Morgan, "Imaging by Time-tagging Photons with the Multianode Microchannel Array Detector System," ibid.
14. Lohmann, A., G. Weigelt and B. Wirtz, "Speckle Masking in Astronomy - Triple Correlation Theory and Applications," Appl. Opt. **22**, 4028-4073, 1983.
15. Freeman, J., E. Ribak, J. Christou and K. Hege, "Statistical Analysis of the Weighted Shift-and-Add Image Reconstruction Technique," Proc. SPIE **556**, 279-283, 1985.

Co-Phasing and Co-Aligning the Multiple Mirror Telescope

C. C. Janes and J. W. Montgomery

Multiple Mirror Telescope Observatory,
Smithsonian Institution / University of Arizona
Tucson, Arizona 85721-0465

Abstract

The Multiple Mirror Telescope is an array of six 1.8 m diameter folded Cassegrain telescopes used to achieve the collecting area equivalent to that of a telescope with a single 4.5 m primary mirror. For most applications, the six images are co-aligned in such a way that overlapping images appear to result from a single telescope. Another application requires that the wavefronts from all six telescopes be co-phased within 1 micron, concurrent with co-alignment. This paper describes the successful operation of the co-alignment and co-phasing capabilities, the control system and devices used in the applications, and test results to date.

General description

The Multiple Mirror Telescope (MMT) (Figure 1) uses six separate 1.8 m telescopes whose light is brought to a common focal point to achieve the effective optical light collection aperture of a single 4.5 m primary mirror, making the MMT, at this writing, the third largest optical telescope in the world. A co-alignment system, called the Telescope Coalignment System (TCS), permits precise measurement of image positions from each of the six telescopes and repositioning of the images as required. A second alignment system, called the Telescope Phasing System (TPS), co-phases the six separate wavefronts to the limits imposed by the atmosphere and the diffraction limit of the telescope. TCS and TPS are described in previous SPIE proceedings^{1,2,3} but both are summarized here for convenience.

Tertiary mirrors, one mounted above each primary mirror, relay images from each of the six telescopes to a beam combiner at the center of the telescope cluster (Figure 2), which is called the optics support structure (OSS). The beam combiner has six reflecting facets, each one of which relays a separate telescope beam to the focal plane 136.42 m below the beam combiner. A tilted reflective surface at the focal plane, typically the aperture plate on a spectrograph, reflects the overlaying fields from all six telescopes to a package containing the object acquisition cameras, called the "top box."

The overlaying fields are reimaged at an acquisition TV camera in the top box. Composite video from the camera is fed to a video digitizer, in this case a Grinnell GMP270. The Grinnell feeds digitized video to a computer system on demand in small regions. Generally, six data regions are requested, one for each image.

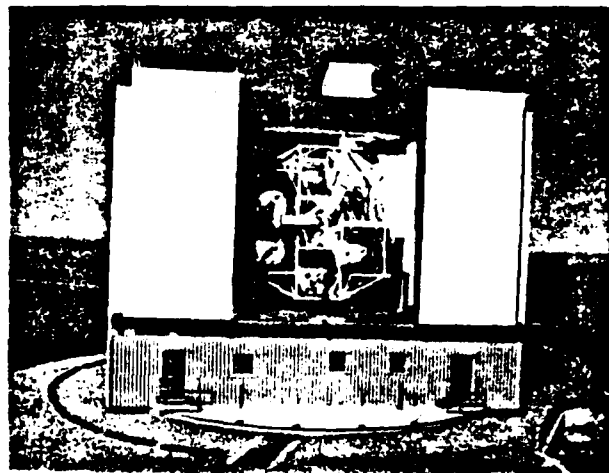


Figure 1. The Multiple Mirror Telescope is situated on 8600' Mt. Hopkins south of Tucson, Arizona, in a 55' high rotating building.

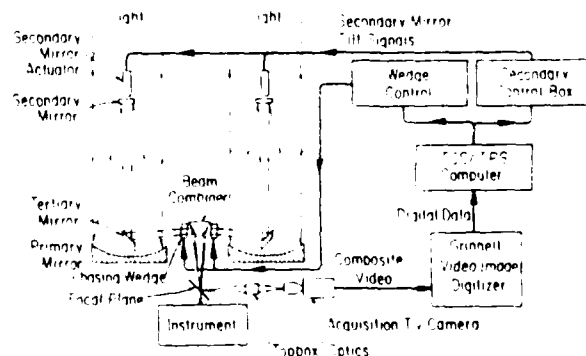


Figure 2. A cross section of the MMT Telescope Co-alignment System and Telescope Co-phasing System.

JANES

The TCS computer routine determines the image positions from the digitized video using a centroiding algorithm. Armed with the known positions, the TCS computer can change the image positions at the focal plane by commanding secondary mirror tilts in either of two orthogonal axes. The primary mirror, tertiary mirror, beam combiner, and focal plane are all stationary surfaces; active control of image position is accomplished solely by tilting the corresponding secondary mirror surface. The motion is accomplished using stepping motors driving a micrometer through a 110:1 gear reducer; resolution of the motion is 0.06 arcsecond per stepping motor step. Co-alignment, once established, is maintained automatically under computer control.

Co-phasing is accomplished by changing the path length of each telescope with a pair of glass wedges inserted in the optical path immediately in front of each beam combiner facet. A stepping motor translates one wedge with respect to the other to change the primary to focal plane path length of that telescope in 0.18 micron increments. An intensified video speckle camera mounted in the differential speckle interferometer instrument produces video specklegrams which are visually inspected for interference fringes between telescope pairs⁴. Since the fringes indicate that the telescope pair is co-phased, the wedges are manually commanded to move until the fringes appear. The fringes can then be maintained under either manual or computer control.

Passive co-alignment

Tracking errors, that is, unexpected movement of an object on the focal plane, at the MMT are quite small (0.1 to 0.2 arcseconds RMS at tracking velocities under 1 arcminute per second), and pointing errors all across the sky rarely exceed an arcsecond. The dominant error in tracking an object is the difference in mechanical flexure between the six telescopes. Flexure of the entire OSS is corrected by pointing coefficients. To correct for differential flexure, coefficients of a quadratic equation are determined from empirical measurements made on three stars. The equations, one for each axis of each telescope, are used while tracking to predict the secondary mirror tilts required to correct for flexure.

Ideally, flexure corrections applied to the individual telescopes will cause the seeing disk of an object composed of the overlaying fields to be no larger than the seeing disk of the same object on a single telescope. The seeing disk is the apparent diameter of an object caused by diffusion of the light through the atmosphere. In practice, atmospheric turbulence causes variations in the seeing disks and image motions between telescopes. The nonuniformity of the seeing phenomena plus small errors in the predicted corrections renders passive co-alignment unusable for imagery, that is, taking pictures of overlaying star fields using long integrations. However, passive co-alignment is adequate for spectroscopy where the bulk of the light from each image must only pass through an aperture nominally one arcsecond in diameter.

Co-alignment is a misnomer for much of the MMT operation because it implies the images always exactly overlay. To overcome the large focal plane scale (3.58 arcsecond/mm) produced by the f/32 1.8 meter telescopes, much of the spectroscopy is done with the individual focal plane images partially separated so that the six images pass through separate lenses at the focal plane. The lenses redirect each telescope beam down a common optical axis and another lens reconverts the beam, which began as an unfilled f/9 beam, to a filled f/32 one.⁵ The corrections imposed by co-alignment minimize the amount of hand guiding required to keep each image on its respective lens.

Successful co-alignment using predicted differential flexure corrections depends on structure stiffness in the presence of a 90° variation in gravitational loading. The flexures must repeat well and present minimal hysteresis. Figure 3 shows that the flexure in elevation may be as much as 20 arcseconds as the OSS moves from zenith to horizon. In addition, the telescopes at the side of the cluster (A, F, C, and D) diverge outward as much as 20 arcseconds over the same range. The curves repeat and maintain their characteristic shapes over a long period of time. The difference in amplitude between curves of data taken in July and November is thought to be caused by differences in temperature. Experience has shown that the "flexure coefficients" must be updated seasonally and after major optical adjustments. The tracking errors that occur with co-alignment imposed are illustrated in Figure 4.

Automatically guided co-alignment

The top box and TCS may be used to automatically guide the six telescopes. For spectroscopy in which each telescope image is sent through a separate aperture, as described above, TCS is used to measure the spilled-over light in four quadrants around the six instrument apertures and send the necessary corrections to the appropriate secondary mirror, thereby forcing the object to remain centered on the aperture. Where only one aperture is

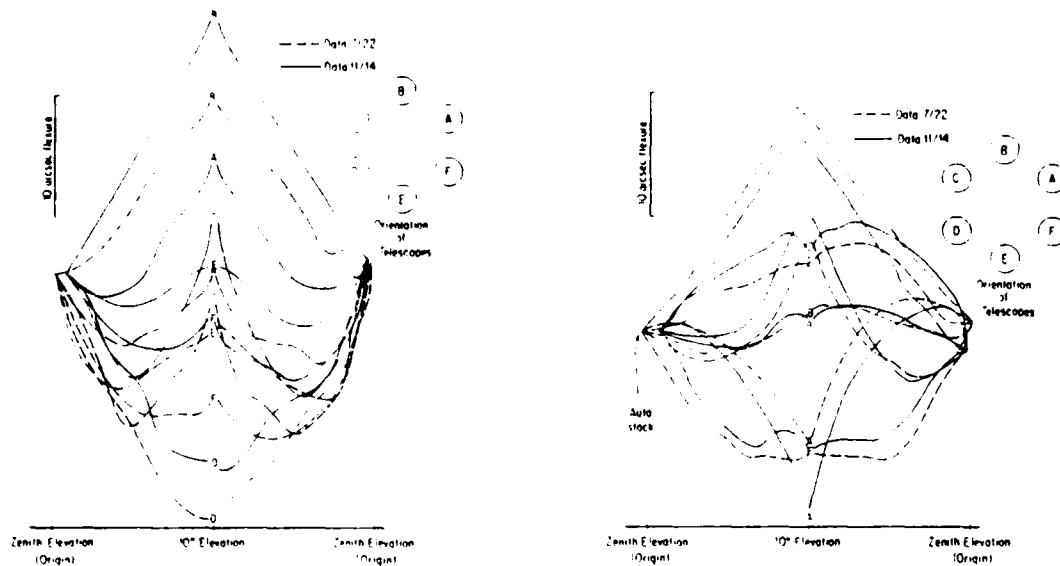


Figure 3. Differential flexure of telescopes measured from near zenith to 10° elevation and return, by measuring pointing errors of stars at different elevations with pointing corrections applied but not differential flexure corrections. Figure on left shows the flexure in elevation as a function of OSS elevation, while the figure on the right shows the flexure in azimuth as a function of OSS elevation.

used or where multiple apertures are too close together at the telescope focal plane to resolve the spilled-over light from the individual telescopes, an array of six wedge prisms may be inserted at the pupil plane in the top box causing images which are superimposed in the telescope focal plane to be clearly separated in the transferred top box focal plane. The pie-shaped wedges form a circular array with one wedge used for each telescope. "Spilled-over light" automatic co-alignment has been used routinely since January 1986.

Because of the stringent co-alignment tolerance required to achieve seeing limited imagery at the MMT, it is not practical to carry out such co-alignment manually and automatic co-alignment is required. Typically, the motion of an image offset from the one of scientific interest is measured, and corrections are applied to the secondaries accordingly. For this operation, an image in the field is selected for guiding. The wedge prisms are inserted to separate the individual telescope images in the TCS acquisition camera focal plane, and TCS is used to calculate the individual centroids of the separated images. Commands to the secondary mirrors are issued to force the centroids to remain at an initial starting point. To obtain the scale required for measuring the centroid, a lens in the top box acquisition optical path produces a field of 20 arcseconds for the acquisition camera, yielding a scale of six pixels per arcsecond. To permit selection of the 90 arcsecond segment from anywhere in the MMT 4 arcminute field, a pair of achromatic wedge prisms (AWP's), located at the pupil plane in the top box, rotate with respect to each other, thereby steering the portion of the optical beam desired to the camera. Imagery presumes the fields for all six telescopes are confocal across the full diameter of the field. Offset automatic guiding was successfully used in June 1986 and is available for routine use.⁶

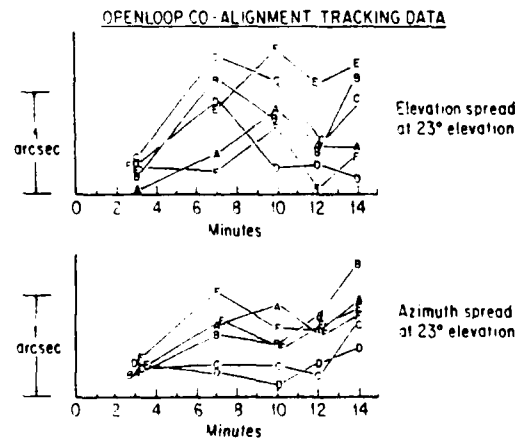


Figure 4. Relative movement of telescope images measured after a "stacking" operation with predicted corrections for flexure applied.

Figure 5 shows the results of automatic guiding during a 20 minute integration with a CCD camera. The images are round and their measured diameters are no larger than that expected from a single telescope, indicating that the fields remained co-aligned during the entire integration.

Automatic guiding corrects for tracking errors and mount pointing as well as flexure; however, the tracking and pointing errors are small as explained earlier. All corrections are sent, therefore, to the secondary mirrors alone rather than a combination of mount drives and secondaries. The 600 arcsecond tilt range of the secondary mirrors is sufficient to permit correction of the flexure errors currently being encountered. Some translation of the secondaries occurs with the tilt corrections so that collimation errors begin to appear beyond a tilt diameter of about 200 arcseconds. Corrections for flexure are well within this range.

The rate for corrections is theoretically limited to 30 Hz by the frame rate of the composite video from the acquisition TV; however, the phosphor on the intensifier stage of the acquisition camera has a slower time constant. Even slower is the TCS computer which permits corrections no faster than 3 Hz with current coding. In practice, the limit is the brightness of the guide star or spilled-over light. Usually an integration of a second or two is required for each measurement so that corrections are issued only at a 1 or 0.5 Hz rate. Fortunately, tracking errors faster than 0.5 Hz are of low amplitude and the relatively slow correction rate is much faster than flexure changes. Corrections for image motion as a result of variation in seeing conditions, or "image shrinking," is expected to require a correction rate of 10 Hz or faster. Assuming the TCS computer and code were updated to permit centroid calculations at this rate, the object being measured would have to be brighter than 15 - 16 magnitude for the acquisition camera currently in use to develop sufficient contrast for measurement.

Tilting the secondaries moves the images at the focal plane but has negligible effect on the pupil positions at the top box pupil plane. Movement of the focal plane caused by flexure of the instrument, conversely, has negligible effect on the image positions at the acquisition camera focal plane but has a dramatic effect on the positioning of the pupils as they overlay the wedge prism array mentioned earlier. The instrument must be carefully aligned and focal plane flexure minimized when the wedge prisms are in use; otherwise, the pupils will vignette or spill over on a neighboring prism and compromise automatic guiding.⁸

Field rotation inherent in an altitude-azimuth mount is compensated for by the co-rotation of the instrument, AWP's, and wedge prism array proportional to the parallactic angle. The optical components in the top box are controlled precisely with stepping motors and torque motors via the TCS computer. The rotations must have a sufficient dynamic range to track the rotating field over a velocity range of 0-90 arcminutes per second. The instrument rotator should have a resolution of motion such that an image at the edge of the field on the focal plane may be tracked to an accuracy equal to the tracking accuracy of the telescope, in this case 0.1 arcsecond peak.

Automatically guided co-alignment is currently not possible without the top box. However, when only predicted flexure corrections are required, the top box is not necessary. The MMT infrared photometer, for example, is used without the top box so that the beam combiner can be included in the instrument dewar and cooled to reduce its emissivity.

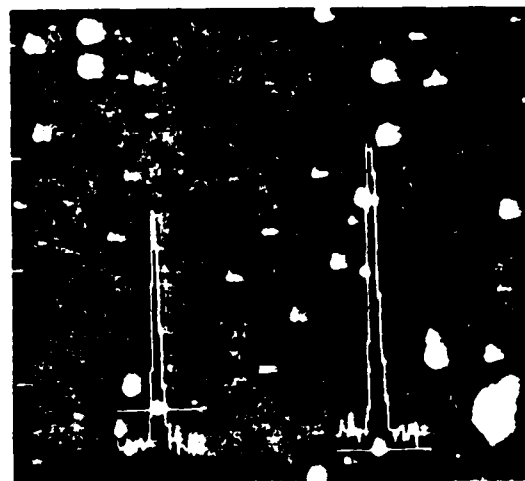


Figure 5. A star field image formed from a 20 minute integration of 6 overlaying auto-guided images. The curves are star intensity profiles traced along the lines intersecting two of the stars. The full wave half maximum of the curves was measured to be 1.2 arcseconds, equal to the atmospheric seeing at the time. The image was taken with a CCD camera by Dr. Rudy Schild of the Smithsonian Astrophysical Observatory.

Concurrent co-phasing and co-alignment

The MMT offers the largest baseline in the world for optical interferometry on a telescope of its size, i.e., the complete Fourier transform plane of a pupil-masked telescope with a 6.86 m aperture. With speckle interferometry, it is theoretically possible to achieve a λ/D resolution of 12 milli-arcseconds at 4100 Å wavelength, the full 6-mirror diffraction limit; image resolutions have been achieved to date of 20 milli-arcseconds at 6560 Å wavelength (Figure 6)⁹. E.K. Hege et. al. have observed point spread functions, i.e. unresolved stellar images, as sharp as the predicted theoretical limit, at 4100 Å ($\lambda/D = 12$ milli-arcseconds).¹⁰

Overlapping fields are coherently phased when the respective path lengths are equal to or less than the coherence length imposed by the observing bandpass filters. The phasing produces interference fringes which are clearly visible on the video output of a TV camera looking at a highly magnified image. To establish co-phasing, the phasing wedge prisms mentioned earlier are moved by manual command to position the fringe distribution precisely over the center of the specklegram as determined from visual inspection. A wide bandwidth filter (600 Å) is used to establish co-phasing because its shorter coherence length produces fewer fringes in the field of view, which simplifies the centering operation. The coherence length for the wide band filter is only 6 microns so that, once co-phased, a narrow-band filter is used to increase the coherence length. The coherence length for a 1.2 Å filter centered at 6536 Å is 3560 microns; in this narrow band extreme the telescope co-phasing is nearly insensitive to elevation-induced path length variations.

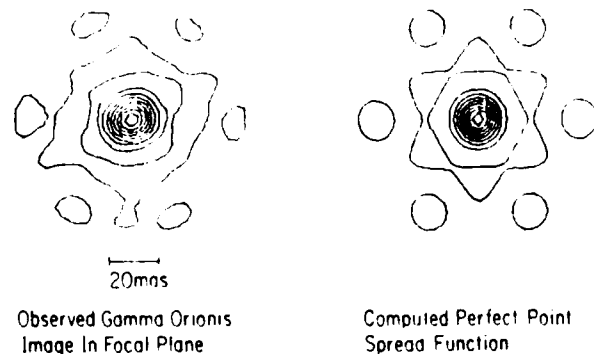


Figure 6. A comparison of images computed from observed data and images computed from a perfect model showing the close correlation of the results and the image resolution possible with the speckle interferometry technique.

The curves that relate path length changes to the elevation of the OSS are measured empirically much as are the flexure curves for co-alignment. The curves are sufficient to predict phase corrections for 10 to 30 minutes of tracking before manual corrections must be imposed. The corrections have a range of 200 microns; the standard error between measured co-phased conditions and the best-fit least-squares quadratic curve is 5.6 to 13 microns, depending on mirror pair. The path length changes as a function of secondary focus and tilt as well as of wedge prism motion. For example, a one arcsecond tilt of a secondary mirror introduces a path length change of 15 microns. The Telescope Phasing System software is being revised to calculate and impose the guiding and phasing corrections concurrently.

The correction curves maintain their characteristic shapes throughout an observing run, though their shape can change between observing runs. The latter changes are thought to result from manual adjustments that are occasionally required to the telescope optics or from temperature changes. Temperature changes introduce a bias in the correction curves; a recent test showed that a change of 1.8°C caused an average change in path length of 220 microns, in agreement with that expected as a result of the thermal expansion of the OSS. We are currently installing a temperature sensor array which will permit the correction curves to be adjusted as a function of temperature changes on the OSS. Measurements with a 10 micron thermographic camera show a remarkable homogeneity of temperature across the bottom of the OSS. Such temperature uniformity will simplify the task of applying corrections as the result of temperature changes.¹¹ The overall thermal stability and uniformity of the structure are in part the result of an aluminum foil OSS covering¹² and is key to the success of TCS and TPS.

The MMT is currently building an articulated beam combiner which will permit path length correction over a wider spectral range than that permitted by the wedge prisms. The facets will have a dynamic throw of 750 microns and a step increment of 0.18 micron. Interferometry over a wavelength range of 0.4 to 20 microns will be possible with the new beam combiner and new instrumentation currently being planned.

Automatically guiding the six images for co-alignment while applying path length predicted corrections is currently in operation. K. Hege of Steward Observatory has proposed an acquisition camera and video processing equipment that would develop path length correction information automatically as well, by measuring variations in the signal power at

the white light fringe frequency as calculated from a fast Fourier transform performed on the fringe information measured between telescope pairs.

Summary

Successful phased operation of multiple telescope structures requires the simultaneous co-alignment of each telescope and the maintenance of co-phased wavefronts from each telescope. Altitude-azimuth mounts introduce additional complexities associated with field and pupil rotation. The combination demands a level of hardware and software sophistication rarely encountered on optical telescopes. Stiff, repeatable structural design is key to the routine use of image co-alignment at the MMT and the successful use of co-phasing for optical interferometry. Although the current OSS may be replaced by one holding a single 6.5 m telescope when such a mirror becomes available, the studies at the MMT should prove useful to future large multiple mirror telescopes planned by the University of Arizona and the National Optical Astronomy Observatories. The co-phasing and co-alignment systems can then be utilized in a re-deployment of the 1.8 m mirrors now used in the array to achieve optical resolutions corresponding to baselines as long as 50 m, where $\lambda/D = 2$ milli-arcseconds at 0.4 micron!

Acknowledgments

The Multiple Mirror Telescope Observatory is jointly funded by the Smithsonian Astrophysical Observatory and the the University of Arizona. This work was partially funded by NSF grants AST 8201902 and AST 8418188. Drs. Jacques Beckers, Frederic H. Chaffee, Jr., E. Keith Hege, Don W. McCarthy, and Bobby Ulich along with other scientists, both past and present at the Smithsonian Astrophysical Observatory and the University of Arizona, developed the concepts of TCS and TFS and provided the leadership to implement them, while the capable and dedicated staff at the MMTO brought the ideas to fruition.

References

1. Beckers, J., Poland, C., Ulich B., Angel, R., Low, F., Wyatt, W. "MMT Telescope Coalignment System", International Conference on Advanced Technology Optical Telescopes, ed. by G. Burbidge and L. Barr, SPIE, March 1982.
2. Montgomery, J. and Janes, C. "Acquisition, Image Stacking, and Autoguiding with the MMT", Advanced Technology Optical Telescopes III, ed. by L. Barr, SPIE, March 1986.
3. Hege, K., Hebden, J., Beckers, J. "Use of the Coherent MMT for Diffraction Limited Imaging," *ibid.*
4. Hege, K., Beckers, J. M., Strittmatter, P. A., McCarthy, D. W. "Multiple Mirror Telescope as a Phased Array Telescope," Applied Optics, 24, 2565 - 2576 (1985).
5. Chaffee, F.H., Jr. and Latham, D.W. "An Image Stacker for High Resolution Spectroscopy on the Multiple Mirror Telescope," (1982), Pub. Astr. Soc. Pacific, 94, 386.
6. Janes, C. and Montgomery, J. "Offset Autoguiding with the SAO-CCD", MMTO Technical Memorandum 86-1, MMTO, June 17, 1986.
7. Schild, R. Center for Astrophysics private correspondence, September 10, 1986.
8. Blanco, D., Janes, C., Vaughn, L., Williams, J. "Alignment Requirements for Autoguiding," MMTO Technical Memorandum 85-6, MMTO, June 28, 1985.
9. Hebden, J. C., Eckart, A., and Hege, E. K. "The H-Alpha Chromosphere of Alpha Orionis," Astrophysical Journal, (January) 1987.
10. Hege, E. K., McCarthy, D. W., Hebden, J. C., and Christou, J. C. "Phased Array Imaging with the Multiple Mirror Telescope," OSA Technical Digest, October 1986, page 87.
11. McCarthy, D. and Hege, E. K. "MMT Observer's Report: Nights of 15-17 October 1986," November 24, 1986.
12. Beckers, J. M. and Williams, J. T. "Seeing Experiments with the MMT," International Conference on Advanced Technology Optical Telescopes, ed. by G. Burbidge and L. Barr, SPIE, March 1982.

A real-time photoelectron event-detecting video system

R. H. Macklin, E. K. Hege and P. A. Strittmatter

Steward Observatory, Tucson, AZ 85721

Abstract

We describe a system for localization of photoelectron events utilizing an intensified Plumbicon camera and a Grinnell video digitizer. The Grinnell digitizer, arithmetic unit and memory are used to produce a real-time video difference between current pixel value and previous pixel value thereby suppressing multiple detection of the same event. A master clock provides synchronization with the camera in operation at 60 Hz in 240 lines/field, repeat field mode. Our event-localization scheme provides double-buffered line-address and event-amplitude for up to 32 events along a 512 pixel video line. A software algorithm allows localization of multiple detections of the same event, and provides a unique address interpolated with 1/2 line resolution by the host minicomputer in a 480 x 512 format.

Introduction

For high resolution imaging of astronomical objects through the Earth's atmosphere it is necessary to sample images in the telescope focal plane at the diffraction limit of the telescope with integration times sufficiently short to freeze the atmospheric turbulence. Most interesting objects are so faint that only a gentle rain of photons is collected, even with the largest telescopes. The atmospheric correlation time is so short that only a few detector pixels will collect even one photon during the short exposure at the required image scale. The object is to record the coordinates of the pixels which detect photons.

Since even the best direct integrating video detectors have a readout noise of a few electrons per pixel, an image intensifier system is used to make the signal due to a single photoelectron event unambiguously detectable by a standard video camera. Our present detector consists of four stages of electrostatic inverters transfer-lens coupled to a Plumbicon camera, and produces video events of 0.4 volts average peak amplitude for corresponding photoelectron events¹.

Other astronomical applications, e.g. high-resolution spectroscopy, also require unique-pixel detection of photoelectron responses. Therefore, we have developed a real-time video-raster event-detection system. The purpose of this paper is to describe our system for localizing the coordinates of video events in 240 line, 60 Hz, non-interlaced video fields on a 480 line by 512 pixels/line grid.

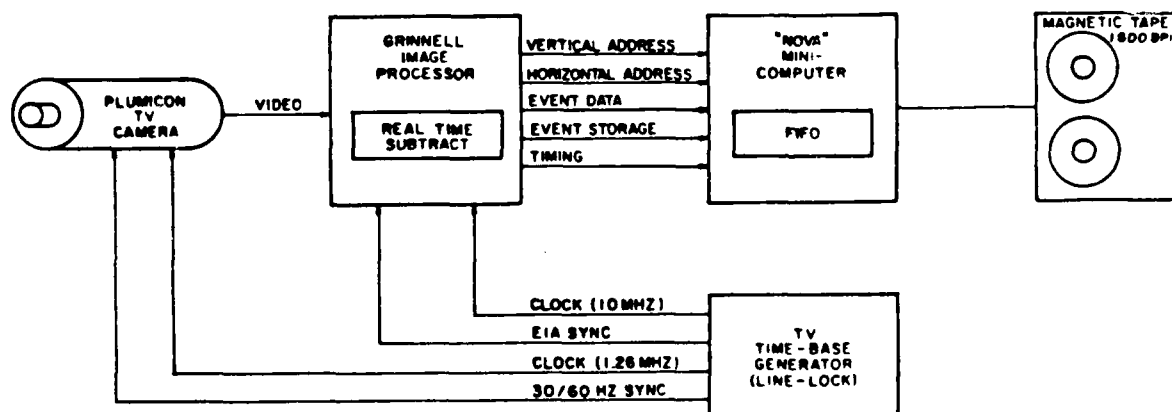


Figure 1. The basic data path.

The digital television system

The components of our digital system are 1) a Grinnell Systems 8-bit video digitizer and memory, 2) a Steward Observatory specified video subtractor provided by Grinnell, 3) real-time digital peak-detection hardware, 4) a FIFO-buffered burst-transfer DMA-channel interface to the host computer, and 5) cross-line centroiding logic.

The basic data path is shown in Figure 1. In the Grinnell system, the RS-170 video is applied to the input of a TRW-1007 flash converter which produces an 8-bit Analogue-to-Digital conversion at 10 MHz. The system is totally synchronous from the TV camera to the computer interface. Camera synchronization is provided by a 10.080 MHz crystal-controlled oscillator phase-locked to the 60 Hz line at 168,000:1.

The video subtractor option allows this 8-bit video to be stored in the frame memory as the previous sample for the same pixel is retrieved and then forms the 8-bit video difference: current value minus previous value. This video difference is then analyzed by our circuitry to localize all peaks which exceed a predetermined threshold amplitude.

The video difference is hardware constrained to be positive or zero; negative differences are suppressed. Thus only new information in the current field is detected. This eliminates any lag effects due to the detector. Figure 2 shows a typical example of the digital video input stream.

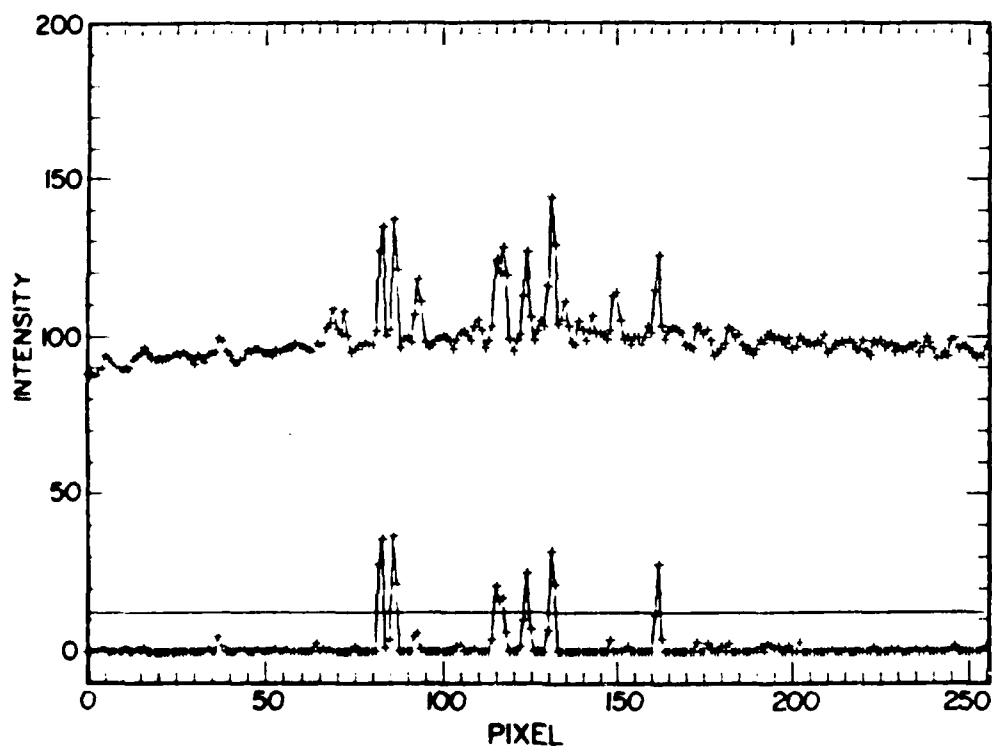


Figure 2. Digital video difference. The upper trace (shown arbitrarily displaced) is a single line of the digitized input video stream. The lower trace is the digital video difference output for the same line resulting when the previous frame is subtracted. The traces are arbitrarily shown with 256 point/line by plotting only even numbered pixels. The point spread function of these photoelectron events is 4.4 pixels FWHM (2.2 points as plotted here) after convolution with the response functions of the image intensifier, relay lens, camera, video tape recorder, time base corrector and video digitizer. This is equivalent to 13 μ m FWHM at the photocathode. The localization of such events with ± 1 pixel precision improves the effective resolution of the system by somewhat more than a factor of 4 to 30 μ m FWHM at the photocathode. Our system resolves the response 114 through 118 as two events at 115 and 117.

Real-time digital peak-detection

The video difference is stored in an 8-bit parallel, single-cell shift-register. The inputs and outputs of this shift-register are applied to an 8-bit comparator. As the difference data is being shifted past the comparator at 10 MHz, the logic tests for the shift-register input to be less than the shift-register output. When this occurs an event-detection strobe is generated. In order to discriminate between low-level noise peaks and large-amplitude signal peaks, the comparator is enabled or disabled by a second 8-bit comparator comparing the difference amplitude to an 8-bit threshold value. The qualified event-detection strobe is then passed to the computer interface.

Centroiding logic for 10 MHz events

The centroiding logic, shown schematically in Figure 3, contains a horizontal address/vertical address multiplexor, The 64 by 16-bit 10 MHz FIFO buffer, horizontal and vertical qualification registers, and data channel (DMA) control logic are all in the computer interface.

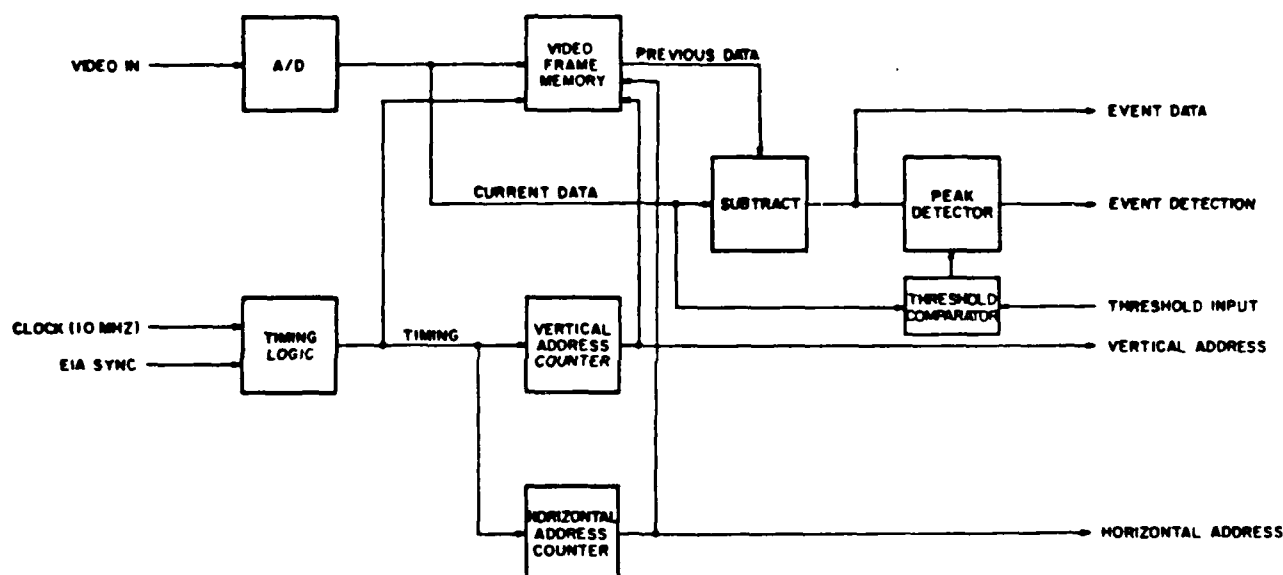


Figure 3. The centroiding logic.

Data is stored in the computer through the data channel. There are $1 + n$ words for each video line within the vertical qualification window, $0 \leq n \leq 32$. The number n is the number of horizontal events detected along the line. The upper bound 32 is set somewhat arbitrarily by the data channel rate of the Nova* class host computer used in our application. The entry of a video line-number is tagged by $MSB = 1$. Horizontal event entries, tagged by $MSB = 0$, contain both the horizontal address and the 5 most significant event amplitude bits. The present system produces 9-bit (1 in 512) horizontal addresses, however, our design anticipates eventual implementation of 10-bit (1 in 1024) horizontal addresses ($\pm 15 \mu m$ at the photocathode).

The interface uses a 64 by 16-bit FIFO to allow the computer to accept burst transfers at up to 6 times the rate that the data channel can accept them. For a 10 MHz video-sample rate, the maximum peak detection rate is 5 MHz (200 ns peak separation). The data channel rate is only 800 KHz (1.2 μs per word). The 64 word FIFO provides a 2-line buffer with input at 5 MHz and output at 800 KHz.

*Nova, a registered trademark of the Data General Corporation, is used in a generic context here.

When the vertical address equals the bottom of the vertical qualification window, an interrupt is generated to inform the event-logging program that the current frame of data is complete.

Data-logging

Presently cross-line centroiding (1 in 489) is produced by a software algorithm in the host computer. Thus photoelectron addresses are localized to the unique pixel events on a 489 x 512 grid which recognizes cross-line events with -1, 0, or +1 pixel horizontal displacements. The maximum data-logging rate of 60,000 Hz is set by the 75 ips 1600 bpi mag-tape system. This is compatible with the 32^2 event/frame saturation of the interface.

Conclusion

Although we are aware of faster schemes for localizing the addresses of photoelectron events^{2,3} we find that this solution has the particular merit of utilizing off-the-shelf digital video technology and current microcomputer capabilities.

Acknowledgement

This project received support from the Air Force Geophysics Laboratory through contract No. F19628-82-K-0025.

References

1. Hege, E. K., Hubbard, E. N. and Strittmatter, P. A., "An intensified event-detecting television system for astronomical speckle interferometry," Proc. SPIE, Vol. 264, p. 29-31. 1980.
2. Papaliolios, C. and Mertz, L., "New Two-Dimensional Imaging Photon Camera," Proc. SPIE, Vol. 331-23. 1982.
3. Timothy, J. G., Joseph, C. L. and Woolf, S. C., "High-Resolution Spectroscopy with the Multi-anode Microchannel Array," Proc. SPIE, Vol. 331-31. 1982.

Reprinted from *Journal of the Optical Society of America A*, Vol. 3, page 2069, December 1986
Copyright © 1986 by the Optical Society of America and reprinted by permission of the copyright owner.

Astronomical imaging by filtered weighted-shift-and-add technique

Erez Ribak

Jet Propulsion Laboratory-NASA, Mail Stop 169-314, California Institute of Technology, 4800 Oak Grove Drive,
Pasadena, California 91109

Received January 23, 1986; accepted July 28, 1986

The weighted-shift-and-add speckle imaging technique is analyzed using simple assumptions. The end product is shown to be a convolution of the object with a typical point-spread function (psf) that is similar in shape to the telescope psf and depends marginally on the speckle psf. A filter can be applied to each data frame before locating the maxima, either to identify the speckle locations (matched filter) or to estimate the instantaneous atmospheric psf (Wiener filter). Preliminary results show the power of the technique when applied to photon-limited data and to extended objects.

1. INTRODUCTION

Recent efforts in the field of stellar speckle interferometry¹⁻⁴ have been directed toward achieving true images of the observed objects. A great deal has been done to reconstruct the Fourier phases of these objects in order to obtain the true image. Approaches known as the shift-and-add techniques try to retain the phases as they appear in the original specklegram.

Bates and Cady¹ realized that at least one Fourier-plane phase is easy to find: that corresponding to the strongest intensity in the specklegram frame. If the displacement of this point is known, then the frame can be shifted to place this maximum at its center. Adding many such shifted frames will yield the average intensity around the brightest spots in all the specklegrams. This is known as the shift-and-add (SAA) technique. Lynds, Worden, and Harvey⁵ (LWH) locate not just the absolute maximum in each frame but also the brightest local maxima (after some initial smoothing). A set of weighted delta functions is created, corresponding to the coordinates and intensities of these maxima. A cross correlation of this set with the original frame shifts the brightest local maxima to the center, producing a result similar to the SAA technique, though with higher efficiency.

The seeing-calibrated weighted-shift-and-add¹ (WSA) is a natural continuation of these two methods. Similar to the LWH method, it finds all the local maxima. A set of delta functions is created, multiplied (or weighted) by the intensities of the corresponding maxima to create a set of impulses. Each frame is correlated in the Fourier plane with its set of impulses, and the correlations are averaged. Finally, the average cross spectrum is deconvolved by the average power spectrum of the impulses in order to reduce the atmospheric-seeing effects on the final result.

All realizations of the SAA technique have one problem in common: they rely strongly on finding local maxima and on the assumption that these are equivalent to speckle locations. Shot noise, atmospheric effects, and object morphology can all invalidate this assumption.

Because of the effect of photon statistics, the number of maxima can be much larger than the number of speckles. If the intensity of the object is low, there are some speckles that will contain only one photon, with no structure information in them. If the object has a wide maximum, then both Poisson noise and atmospheric phase fluctuations might distort its image and create spurious local maxima. Finally, the object could be multiple peaked, which can be mistaken as multiple speckled, with the final result resembling an autocorrelation instead of an image. Bates¹ calls this "ghosting."

As a remedy, we use a filter that smooths out each speckle and at the same time defines its location. The best filter should be close to the mean speckle itself: a matched filter. Since the mean speckle is initially unknown, a crude guess is used to locate filtered speckle maxima. These are then used to produce a better mean-speckle estimate by SAA. The procedure is iterated until the mean speckle converges.

We find that the iterative speckle estimate is not the optimum matched filter. The most suitable filter must suppress the variable background created by coalescing speckles in a large speckle cloud as well as smooth the single-photon-event noise. Thus we combine the mean speckle with a bandpass filter into a Wiener filter. Local speckle maxima are thus enhanced, whereas single photons are discriminated against by using a comparison low-pass-filtered frame. The combined process, speckle identification and WSA, can be carried out in the image plane or in the Fourier plane. We have experimented in both domains.

2. MATHEMATICAL FORMULATION OF WEIGHTED SHIFT-AND-ADD

We first summarize the WSA formalism of Christou *et al.*¹ Let us write the k th quasi instantaneous image $i_k(\mathbf{x})$ as the Poisson realization of the convolution of the object $o(\mathbf{x})$ with the instantaneous speckle point-spread function $s_k(\mathbf{x})$. For ease of understanding, we choose to define the Poisson noise as the difference between the realization and the convolution, i.e.,

$$n_i(\mathbf{x}) = i_i(\mathbf{x}) - [o(\mathbf{x}) + s_i(\mathbf{x})]. \quad (1)$$

When detecting this image, we must assume a detector point-spread function $d(\mathbf{x})$, which is not necessarily point-like; specifically, single photons create typical splotches when they are recorded. We revise the definition of the image to be

$$i_i(\mathbf{x}) = d(\mathbf{x}) * [o(\mathbf{x}) + s_i(\mathbf{x}) + n_i(\mathbf{x})]. \quad (2)$$

We create an impulse frame from $i_i(\mathbf{x})$ by substituting delta functions for local maxima only. We assume that each is weighted by the corresponding maximum. This nonlinear process can be viewed as a crude estimate $a_i(\mathbf{x})$ of the instantaneous speckle point-spread function $s_i(\mathbf{x})$ because the grainy appearance of the speckle pattern can be attributed chiefly to the atmosphere. At the same time, this estimate also has a portion that can be attributed to maxima in the noise $n_i(\mathbf{x})$. This algorithm, which singles out maxima only, assumes that the object $o(\mathbf{x})$ has a single, sharp peak. The following sections will deal with the problems of extended objects and how to minimize their influence on the speckle estimate.

The next step is to apply a Fourier transform to the specklegram and the impulse frame. Denoting all quantities in the Fourier plane in upper-case letters and using nondimensional units $\mathbf{u} = \mathbf{f}/\lambda$, we have

$$I_i(\mathbf{u}) = D(\mathbf{u})[O(\mathbf{u})S_i(\mathbf{u}) + N_i(\mathbf{u})] \quad (3)$$

for the image transform and $A_i(\mathbf{u})$ for the transform of the impulse frame $a_i(\mathbf{x})$. Now we calculate the cross spectrum of these two quantities:

$$C_i(\mathbf{u}) = D(\mathbf{u})[O(\mathbf{u})S_i(\mathbf{u}) + N_i(\mathbf{u})]A_i^*(\mathbf{u}). \quad (4)$$

$$\begin{aligned} \langle C_i(\mathbf{u}) \rangle &= \left\langle \left(\iint d\mathbf{v} d\mathbf{v}' \mathcal{L}(\mathbf{v}) \mathcal{L}^*(\mathbf{v} + \mathbf{u}) P(\mathbf{v}) P^*(\mathbf{v} + \mathbf{u}) P^*(\mathbf{v}) P(\mathbf{v} + \mathbf{u}) \right) \right. \\ &\quad \left. S_i(\mathbf{u}) A_i^*(\mathbf{u}) \right\rangle \\ &= \frac{S^{-2}}{S^{-1}} \iint d\mathbf{u} M(\mathbf{u}, \mathbf{u}') H(\mathbf{u}, \mathbf{u}') \\ &= \frac{P_i(\mathbf{u})}{T(\mathbf{u})}, \end{aligned} \quad (10)$$

and create the impulse power spectrum

$$R_i(\mathbf{u}) = A_i(\mathbf{u}) A_i^*(\mathbf{u}) = |A_i(\mathbf{u})|^2. \quad (5)$$

The cross spectrum and the power spectrum are accumulated for a large number of frames, yielding averages $\langle C_i(\mathbf{u}) \rangle = C(\mathbf{u})$, $\langle R_i(\mathbf{u}) \rangle = P(\mathbf{u})$. To get the final WSA result, $T(\mathbf{u})$, we divide these two quantities:

$$W(\mathbf{u}) = \frac{C(\mathbf{u})}{R(\mathbf{u})} = \frac{D(\mathbf{u})[O(\mathbf{u})S(\mathbf{u})A^*(\mathbf{u}) + \langle N(\mathbf{u})A^*(\mathbf{u}) \rangle]}{|A(\mathbf{u})|^2}. \quad (6)$$

We now see the importance of having a good estimate of the atmosphere. If this is really the case, then $A(\mathbf{u})$ does not contain any terms that correlate with the photon noise, and the last term in the numerator can be considered negligible. Therefore,

$$W(\mathbf{u}) \approx D(\mathbf{u})[O(\mathbf{u})S(\mathbf{u})A^*(\mathbf{u})] / |A(\mathbf{u})|^2. \quad (7)$$

To find out more about the averages involved in Eqs. (6) and (7), let us write the speckle point-spread function (pst) as¹

$$s_i(\mathbf{x}) = \text{FT}\{P(\mathbf{u})/P(\mathbf{u})\}, \quad (8)$$

where $P(\mathbf{u})$ is the telescope aperture function and $\mathcal{L}(\mathbf{u})$ is the atmospheric transfer function. $\text{FT}\{\}$ stands for a Fourier transform. Let us assume that our estimate $a_i(\mathbf{x})$ is actually equal to the instantaneous pst $s_i(\mathbf{x})$ deconvolved by the telescope transfer function:

$$a_i(\mathbf{x}) = \text{FT}\{P(\mathbf{u})/P(\mathbf{u})\} / \text{FT}\{P(\mathbf{u})\}, \quad (9)$$

where $/$ denotes deconvolution (division in the Fourier space). This assumption would be exact in the case when the speckles can be represented simply as a double convolution of the object, the telescope pst, and a set of delta functions (which in turn represent the atmosphere). This description is adequate at high frequencies [see Eqs. (22) below]. Replacing each maximum by a delta function amounts to a crude deconvolution, similar to that of the CLEAN algorithm.¹ The numerator in expression (7) is the average cross spectrum of the Fourier transforms of Eqs. (8) and (9). Following the reviews and definitions of Roddier and Dainty,²

where $M(\mathbf{u}, \mathbf{u}')$ is the fourth-order moment of the atmospheric wave-front fluctuations, $P^*(\mathbf{u})$ is the speckle transfer function, $H(\mathbf{u}, \mathbf{u}')$ is the fourth-order correlation of the telescope, $T(\mathbf{u})$ is the second-order correlation of the telescope or the telescope transfer function; and S is the pupil area. Factoring the integral into a product of two integrals is possible since $M(\mathbf{u}, \mathbf{u}')$ is a function of the frequency difference $\mathbf{u} = \mathbf{v} - \mathbf{v}'$.

The denominator in expression (7) is the average power spectrum of the Fourier transform of Eq. (9)

$$\begin{aligned}
\langle |A(\mathbf{u})|^2 \rangle &= \left\langle \iint d\mathbf{v} d\mathbf{v}' \psi(\mathbf{v}) \psi^*(\mathbf{v} + \mathbf{u}) \psi^*(\mathbf{v}') \psi(\mathbf{v}' + \mathbf{u}) P(\mathbf{v}) P^*(\mathbf{v} + \mathbf{u}) P^*(\mathbf{v}') P(\mathbf{v}' + \mathbf{u}) \right\rangle \\
&= S^{-2} \iint d\mathbf{v} d\mathbf{v}' P(\mathbf{v}) P^*(\mathbf{v} + \mathbf{u}) P^*(\mathbf{v}') P(\mathbf{v}' + \mathbf{u}) \\
&= S^{-2} \int d\mathbf{u}' M(\mathbf{u}, \mathbf{u}') H(\mathbf{u}, \mathbf{u}') \\
&= S^{-2} \int d\mathbf{u}' H(\mathbf{u}, \mathbf{u}') \\
&= \frac{P_s(\mathbf{u})}{T^2(\mathbf{u})}.
\end{aligned} \tag{11}$$

Substituting Eqs. (10) and (11) into expression (7), we get

$$W(\mathbf{u}) \geq D(\mathbf{u}) O(\mathbf{u}) T(\mathbf{u}). \tag{12}$$

To evaluate this expression further, we follow previous work^{7,8} and assume that the k th frame is composed of a set of N_k photons at positions \mathbf{x}_n , each producing the detector psf $d(\mathbf{x})$:

$$i_k(\mathbf{x}) = d(\mathbf{x}) * \sum_{n=1}^{N_k} \delta(\mathbf{x} - \mathbf{x}_n). \tag{13}$$

The estimate of the speckle psf, $a_k(\mathbf{x})$, is composed of a different set of impulses, which we model to be the realization of a point process representing the atmosphere. Because of the digital form of our data, we consider every impulse to be the sum of all delta functions within the same pixel. Unfortunately, our estimate is contaminated by the Poisson process, which creates some spurious local maxima. Here we have L_k speckles and K_k contaminating photons:

$$a_k(\mathbf{x}) = \sum_{l=1}^{L_k} \delta(\mathbf{x} - \mathbf{x}_l) + \sum_{j=1}^{K_k} \delta(\mathbf{x} - \mathbf{x}_j). \tag{14}$$

In this way we model our data $i_k(\mathbf{x})$ as a Poisson process of rate $\lambda_k(\mathbf{x})$ proportional to the ideal image $o(\mathbf{x}) * s_k(\mathbf{x})$. Our estimate of the atmospheric speckles $a_k(\mathbf{x})$ is modeled as the sum of two processes. The first is an unknown point process with rate $\mu_k(\mathbf{x})$ proportional to the atmospheric psf (Fried's "short exposure"⁶). In the cases when the atmospheric turbulence is low, the object is extended, or the light level is low, the variance that is due to the photon noise can be comparably large. The Poisson process is then assumed to be independent of the atmospheric process.⁹ Thus it is written on the right-hand side of Eq. (14) as an additive term of rate $\lambda_k(\mathbf{x})$. Next we calculate the expectation value of the cross spectrum of the Fourier transforms of the data and the estimate [Eq. (4)] with respect to coordinates:

$$\begin{aligned}
\mathbf{E}_{n,l} [C_k(\mathbf{u})] &= D(\mathbf{u}) \left\{ \sum_{n=1}^{N_k} \sum_{l=1}^{L_k} \mathbf{E}_{n,l} [\exp - 2\pi i \mathbf{u} \cdot (\mathbf{x}_n - \mathbf{x}_l')] \right. \\
&\quad \left. + \sum_{n=1}^{N_k} \sum_{j=1}^{K_k} \mathbf{E}_{n,j} [\exp - 2\pi i \mathbf{u} \cdot (\mathbf{x}_n - \mathbf{x}_j)] \right\}.
\end{aligned} \tag{15}$$

The total number of elements in the first summation is $N_k L_k$, almost all of which are not unity, as they originate from different, independent processes (Poisson and atmo-

spheric). The number of elements in the second summation is $N_k K_k$, of which K_k are unity (when $\mathbf{x}_n = \mathbf{x}_j$). For the first summation the probability of an event's occurring at \mathbf{x}_n is $\lambda_k(\mathbf{x}_n) / \int \lambda_k(\mathbf{x}) d\mathbf{x}$, where the integral is over the frame. The probability of a speckle's occurring at \mathbf{x}_l is similarly $\mu_k(\mathbf{x}_l) / \int \mu_k(\mathbf{x}) d\mathbf{x}$. The joint probability of the two is their product, these being independent point processes, yielding an average cross term

$$\begin{aligned}
&\int \lambda_k(\mathbf{x}) \exp - 2\pi i \mathbf{u} \cdot \mathbf{x} d\mathbf{x} \int \mu_k(\mathbf{x}) \exp - 2\pi i \mathbf{u} \cdot \mathbf{x} d\mathbf{x} \\
&\quad \int \lambda_k(\mathbf{x}) d\mathbf{x} \int \mu_k(\mathbf{x}) d\mathbf{x} \\
&= \frac{\Lambda_k(\mathbf{u}) M_k^*(\mathbf{u})}{\Lambda_k(0) M_k^*(0)}.
\end{aligned} \tag{16}$$

where we assume that $\Lambda(\mathbf{u})$ and $M(\mathbf{u})$, the Fourier transforms of $\lambda(\mathbf{x})$ and $\mu(\mathbf{x})$, are Hermitian. The second summation yields a similar term. From Eqs. (15) and (16) we have

$$\begin{aligned}
\mathbf{E}_{n,l} [C_k(\mathbf{u})] &= D(\mathbf{u}) \left[K_k + (K_k N_k - K_k) \frac{|\Lambda_k(\mathbf{u})|^2}{|\Lambda_k(0)|^2} \right. \\
&\quad \left. + L_k N_k \frac{\Lambda_k(\mathbf{u}) M_k^*(\mathbf{u})}{\Lambda_k(0) M_k^*(0)} \right].
\end{aligned} \tag{17}$$

Now we average over the Poisson statistics of the photons and the atmospheric statistics of the speckles,

$$\begin{aligned}
\mathbf{E}_{n,l,N,L} [C_k(\mathbf{u})] &= D(\mathbf{u}) \left[K + (KN - K) \frac{|\Lambda(\mathbf{u})|^2}{|\Lambda(0)|^2} \right. \\
&\quad \left. + LN \frac{\Lambda(\mathbf{u}) M^*(\mathbf{u})}{\Lambda(0) M^*(0)} \right],
\end{aligned} \tag{18}$$

where L and N are the average numbers of speckles and photons per frame and K is the corresponding number of coincidences between the estimate and the photons. Similarly, we get for our estimate for the atmosphere $a_k(\mathbf{x})$ an average power spectrum

$$\begin{aligned}
\mathbf{E}_{n,l,N,L} [R_k(\mathbf{u})] &= L + L^{(2)} \frac{|M(\mathbf{u})|^2}{|M(0)|^2} + K + K^{(2)} \frac{|\Lambda(\mathbf{u})|^2}{|\Lambda(0)|^2} \\
&\quad + KL \frac{\Lambda(\mathbf{u}) M^*(\mathbf{u})}{\Lambda(0) M^*(0)},
\end{aligned} \tag{19}$$

where $L^{(2)} = \mathbf{E}[L_k(L_k - 1)]$ is the second factorial moment of

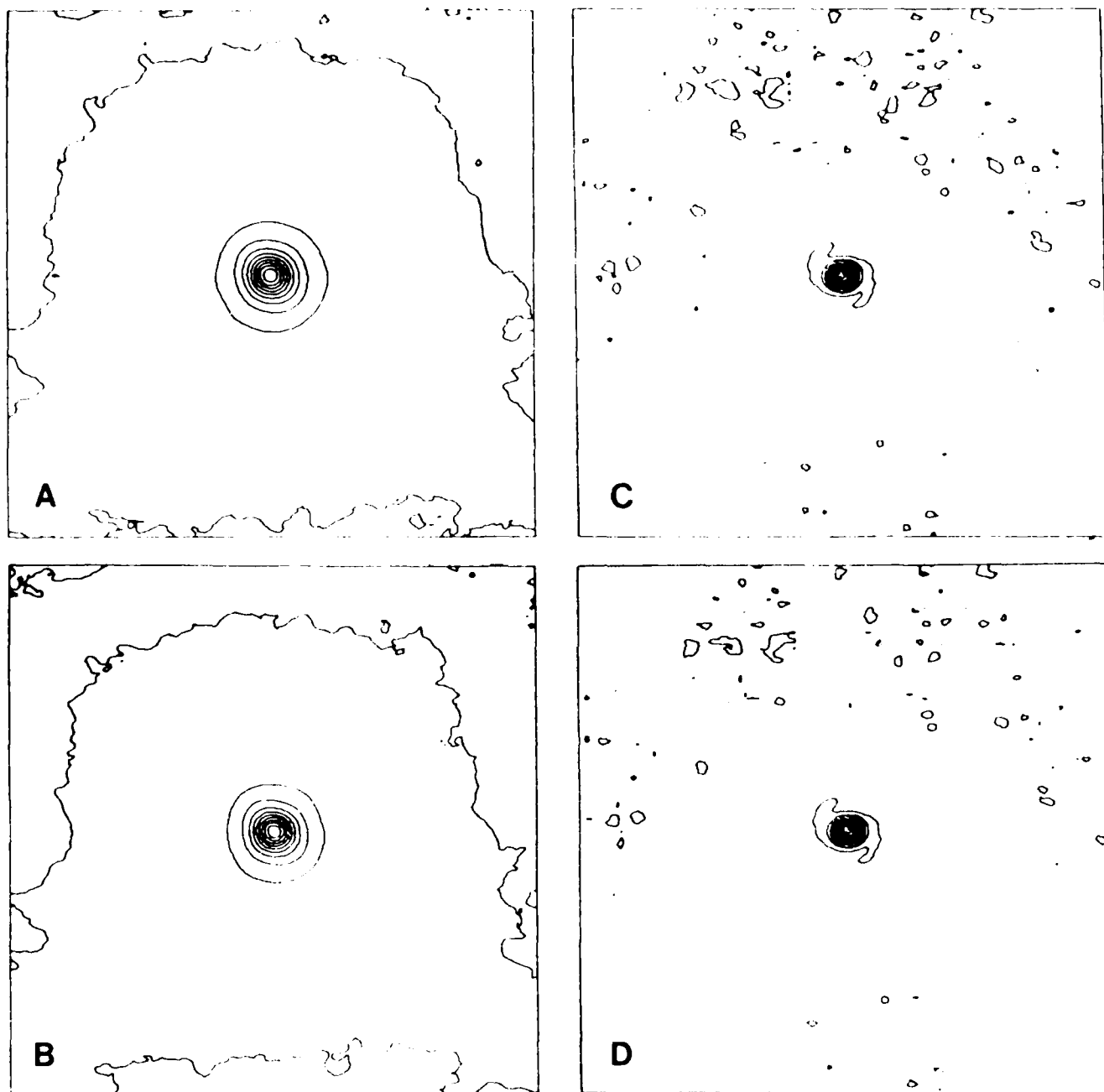


Fig. 1. A, B, *Alpha Orionis* and C, D, *Gamma Orionis* for two apodizations applied to the matched filter. A, C, 28 pixels FWHM; B, D, 12 pixels FWHM. Frame size is 128×128 . Observations were made with a 3.8-m telescope at 650 ± 1 nm. The image of *Gamma Orionis* is rate-scaled. The images of *Alpha Orionis* are different by 10% in size (50 frames for each image).

changes for coherence and aperture size accounted for.^{1,10} The drawback of this description is that it assumes stationarity of the speckles, true only in the middle of the speckle cloud. As mentioned earlier, we model the specklegram as a triple convolution of the object with the telescope (Fig. 2) and with a set of delta functions representing the atmosphere. In the different realizations of SAA, an effort is made to proceed in the reverse direction. An estimate of a subset of the (strongest) delta functions is produced; the original specklegram is deconvolved by it, and the result is averaged over many frames. From this average it is possible to remove the atmospheric seeing background (due to

the incompleteness of the subset of the estimator and the central photon spike (due to the Poisson statistics).

Despite the fact that it is possible to remove the seeing background and the photon spike from the final image, it is preferable to devise a matched filter that would give the right answer directly. Since some information is available about the power spectra of the Poisson noise and the seeing, we incorporate it into the matched filter while performing the iterative data reduction. In the Fourier plane, the main effect of the seeing background is in the very low frequencies (what is called the "long exposure"), whereas the Poisson noise exists at all frequencies. Thus the total noise power

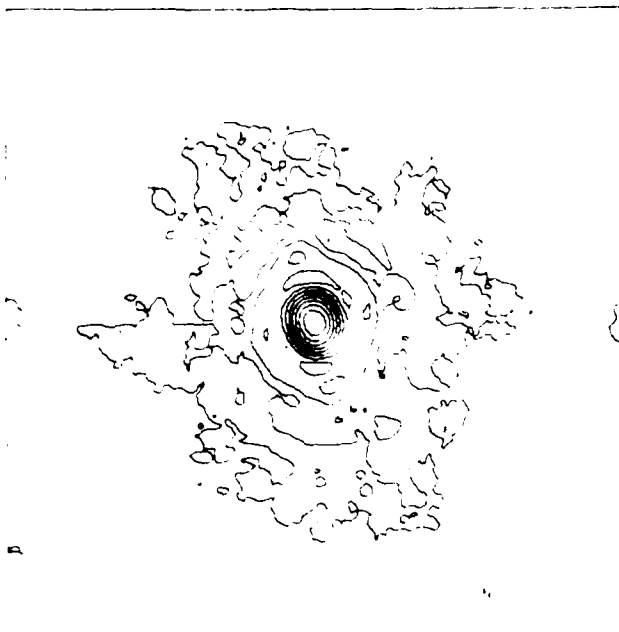


Fig. 2. An image of an unresolved star (Zeta Aquarii A) with the 2.28-m telescope at 750 ± 10 nm, showing the (aberrated) telescope-detector psf. Logarithmic intensity scale. Processed from 100 frames, about 100 photons each. All figures are with North down, East to the right.

spectrum [Eq. (24)] is accentuated at the very low frequencies and constant elsewhere. Dividing the object transform by this power spectrum is equivalent to multiplying it by its reciprocal, i.e., a bandpass filter.

The combination of a bandpass filter with the object produces an optimum matched filter, which is now applied to the specklegram. The bandpass filter, convolved with the object, partially solves both problems (3) and (4) discussed earlier. It smooths out single-photon events below the threshold level, so that they are not regarded as speckles. At the same time it sharpens the wide autocorrelations between the speckles and the object, and as a result the efficiency of detecting speckle maxima increases.

4. WIENER FILTER APPROACH

The other approach possible is not to locate the speckles (using the assumption that each one is a replica of the object) but to find the original distribution of the atmosphere, apply some nonlinear process (such as maximum finding) and, continue from there on as with the standard WSA. As mentioned in Section 3, this calls for a Wiener filter, since there is no prior knowledge of the atmospheric distribution and its shape is varying from one realization to the other. Our estimate is now achieved by applying a Wiener filter $F_w(u)$ to the current image transform:

$$\begin{aligned} A_s(u) &= F_w(u)I_s(u) \\ &= F_w(u)D(u)[O(u)S_s(u) + N(u)]. \end{aligned} \quad (26)$$

Actually, we also apply here the nonlinear process of maximum singling in the image plane described above. [If only linear processes were applied, we would get $F_w(u)$ as the end product]. We form the least squares difference ϵ between the speckle psf and the estimate

$$\epsilon = \left\langle \left| \int dx [s(x) - a(x)] \right|^2 \right\rangle = \left\langle \left| \int du [S(u) - A(u)] \right|^2 \right\rangle \quad (27)$$

using Parseval's theorem. Combining Eq. (26) with Eq. (27), and assuming that the cross spectrum of the atmosphere and the noise average out, we arrive at the required filter^{10,15}

$$F_w(u) = \frac{O(u)^* P_s(u)}{D(u)[|O(u)|^2 P_s(u) + P_n(u)]} \quad (28)$$

where $P_s(u)$ and $P_n(u)$ are the speckle and noise power spectra, respectively. We make use of the value of the average image power spectrum calculated elsewhere^{7,8}

$$P_i(u) = |D(u)|^2 [|O(u)|^2 P_s(u) + P_n(u)] \quad (29)$$

to get the final filter

$$F_w(u) = \frac{|D(u)O(u)|^2 P_s(u)}{P_i(u)} \quad (30)$$

This is much like the intuitive filter that was mentioned before in combination with the matched filter. It tells us that by using iterative estimates of the object, the image power spectrum, and the speckle power spectrum, we can generate a valid Wiener filter. The speckle power spectrum and the detector transfer function can be achieved before the calculation by observing a point source under similar atmospheric conditions with the same detector. If the atmospheric conditions are different, then the ratio of the reference speckle power spectrum $P_s(u)$ to the actual one will differ mainly in the $u = r_0/\lambda$ regime.¹⁶ At higher frequencies this ratio will tend toward the ratio of the numbers of speckles for the two cases. So unless the object has a great information content at low frequencies, it is safe to use a reference speckle power spectrum. If not, a theoretical estimate can be made from the image power spectrum, which is actually the matched-filter method discussed above.

5. APPLICATION AND RESULTS

The data processed were produced on the Kitt Peak National Observatory 3.8-m telescope and the Steward Observatory 2.3-m telescope. The detector used was the Steward Observatory speckle camera,¹⁷ with television frames digitized to a 128×128 format with 8-bit integers. Some of the data were photon limited (see Figs. 1-3).

The first reductions were done in image space, in an approach similar to the simple SAA. An estimate of the object, usually a Gaussian, was slid along and multiplied with the frame (image-plane correlation). At the same time a smoothing function (a wider Gaussian) was correlated with the frame. Every local maximum that was higher in the filtered frame than in the smoothed frame was counted as a speckle, and the corresponding part in the original specklegram was added to the running sum. With bright objects, where the photon noise is negligible, the result appeared after only one frame. The computational efficiency of this method was rather low, especially for larger objects, which demanded many multiplications. The advantage was that only one full frame resided in memory at any time.

The process was then repeated in the Fourier plane (Fig. 4). The cycle for each frame is as follows: (a) read frame in, (b) transform the frame, (c) multiply the frame transform

since the apodizing bell should be larger than the object extent (Fig. 1).

The main deficiencies of the current implementation of the matched/Wiener-filter method are the following: (1) complicated calculations requiring much computer time are necessary, (2) for extended objects, too few speckles are found, which lead to an extended seeing background,^{12,13} (3) for multiple-peak objects, great care must be taken when building the filter lest the filtered frame have more than one maximum per speckle and thus lose the advantage over simple SAA methods.

ACKNOWLEDGMENTS

I would like to thank J. C. Christou, E. K. Hege, F. Roddier, and J. D. Freeman for many thought-provoking conversations and for astronomical data. I would also like to acknowledge the support of the Weizmann Fund. Some of the observations reported here were obtained at Kitt Peak National Observatory, a division of the National Optical Astronomy Observatories, operated by the Association of Universities for Research in Astronomy, Inc., under contract with the National Science Foundation.

The author was formerly with the Steward Observatory, University of Arizona, Tucson, Arizona 85721.

REFERENCES

1. J. C. Christou, E. K. Hege, J. D. Freeman, and E. Ribak, "A self-calibrating shift-and-add technique for speckle imaging," *J. Opt. Soc. Am. A* **3**, 204-209 (1986); "Images from astronomical speckle data: weighted shift-and-add analysis," in *International Conference on Speckle*, H. Arsenault, ed., *Proc. Soc. Photo-Opt. Instrum. Eng.* **556**, 255-262 (1985).
2. G. P. Weigelt and B. Wirtzner, "Image reconstruction by the speckle masking method," *Opt. Lett.* **8**, 389-391 (1983).
3. R. H. T. Bates, "Astronomical speckle imaging," *Phys. Rep.* **90**, 203-297 (1982).
4. R. H. T. Bates and F. W. Cady, "Towards true imaging by wide-band speckle interferometry," *Opt. Commun.* **32**, 365-369 (1980).
5. C. R. Lynds, S. P. Worden, and J. W. Harvey, "Digital image reconstruction applied to *Alpha Orionis*," *Astrophys. J.* **207**, 174-179 (1976).
6. F. Roddier, "The effects of atmospheric turbulence in optical astronomy," in *Progress in Optics XIX*, E. Wolf, ed. (North-Holland, Amsterdam, 1981), pp. 281-376; J. C. Dainty, "Stellar speckle interferometry," in *Laser Speckle and Related Phenomena*, 2nd ed., J. C. Dainty, ed. (Springer-Verlag, Berlin, 1983).
7. J. W. Goodman and J. F. Belsher, "Photon limited images and their restoration," RADC-TR-76-50, March 1976; ARPA order #2646 (Rome Air Development Center, Griffiss AFB, N.Y.). "Fundamental limitations in linear invariant restoration of atmospherically degraded images," in *Seminar on Imaging through the Atmosphere*, J. C. Wyant, ed., *Proc. Soc. Photo-Opt. Instrum. Eng.* **75**, 141-154 (1976).
8. J. C. Dainty and A. H. Greenaway, "Estimation of spatial power spectra in speckle interferometry," *J. Opt. Soc. Am.* **69**, 786-790 (1979).
9. B. Saleh, *Photoelectron Statistics* (Springer-Verlag, Berlin, 1978), Sec. 5.2.9.
10. K. R. Castleman, *Digital Image Processing* (Prentice-Hall, Englewood Cliffs, N.J., 1979).
11. E. Ribak, E. K. Hege, and J. C. Christou, "Identification of speckles by matched filtering," *Bull. Am. Astron. Soc.* **16**, 885 (1984); "Use of matched filtering to identify speckle locations," in *International Conference on Speckle*, H. Arsenault, ed., *Proc. Soc. Photo-Opt. Instrum. Eng.* **556**, 196-201 (1985).
12. A. M. Sinton, R. A. Minard, and R. H. T. Bates, "Generalization of shift-and-add imaging," in *International Conference on Speckle*, H. Arsenault, ed., *Proc. Soc. Photo-Opt. Instrum. Eng.* **556**, 263-269 (1985).
13. B. R. Hunt, W. R. Fright, and R. H. T. Bates, "Analysis of the shift and add method for imaging through turbulent media," *J. Opt. Soc. Am.* **73**, 456-465 (1983).
14. J. D. Freeman, E. Ribak, J. C. Christou, and E. K. Hege, "Statistical analysis of the weighted shift-and-add image reconstruction technique," in *International Conference on Speckle*, H. Arsenault, ed., *Proc. Soc. Photo-Opt. Instrum. Eng.* **556**, 279-283 (1985).
15. B. R. Frieden, *Probability, Statistical Optics, and Data Testing* (Springer-Verlag, Berlin, 1983).
16. J. C. Christou, A. Y. S. Cheng, E. K. Hege, and C. Roddier, "Seeing calibration of optical astronomical speckle interferometric data," *Astron. J.* **90**, 2644-2651 (1985).
17. E. K. Hege, E. N. Hubbard, P. A. Strittmatter, and W. J. Cocke, "The Steward Observatory speckle interferometry system," *Opt. Acta* **29**, 701-715 (1982).

DETECTION OF THE LENSING GALAXY IN PG 1115+08¹

STUART B. SHAKLAN AND E. K. HEGE

Steward Observatory, University of Arizona

Received 1985 June 24; accepted 1985 October 1

ABSTRACT

We have fitted models to good-seeing (0.6") postguided observations of the triple quasar PG 1115+08 in blue and red light. The four components (A, A', B, and C) all have similar point spread functions in the blue fit. There are no significant blue residuals after subtraction of the model from the image. The fits to components A, A', and C in the red image are consistent, but that of the B component suggests that there is an excess red flux from an area between all four components. The residuals show that this flux has a peak magnitude of 19.8 ± 0.3 mag in the *R* band and a $I - R$ color of at least 2.7 ± 0.5 mag. The position of this flux excess is consistent with that of the lensing galaxy in models of gravitational imaging.

Subject headings: gravitation — quasars

1. INTRODUCTION

Of the five possible candidates for gravitational lenses, only one, PG 1115+08 (A, B, C), better known as the "triple QSO," has more than two components. Weymann *et al.* (1980) discovered the triple images. Hege *et al.* (1981) used the technique of speckle interferometry to show that A, the brightest component, was itself a double (which we designate A and A'), with components separated by 0.54". Others (Young *et al.* 1981, hereafter Young; Vandernest *et al.* 1983) have modeled the triple and also concluded that A consists of two overlapping components. Foy, Bonneau, and Blazit (1985, hereafter Foy) may have detected the expected fifth component. No one has yet detected the lensing galaxy.

The geometry of the triple QSO is most easily simulated by placing an elongated lensing mass distribution between components A, A', B, and C. The lensing is much more likely to be the result of a single galaxy rather than a cluster of galaxies (Young). Young put forth a possible image solution in which a massive spiral galaxy at $z = 0.8$ was situated between all three components, but closer to components B and A. However, they were unable to detect the galaxy at $m = 21.5$.

The present work attempts to fit heuristic models to our (Hege *et al.* 1980, hereafter Hege) observations of the triple QSO in blue and red light. Any lensing galaxy should be brighter in the red observation. A comparison of the red and blue models and their residuals should reveal whether there is excess red flux. Young has already reported that B is slightly redder than C, and we attempt to go a step further and show where the excess red flux originates.

II. DATA ANALYSIS

The triple QSO was observed on 1980 June 3 and 4 with one mirror of the MMT (Hege). The intensified Plumbicon television images were logged in 5 minute sections using a Sony half-inch reel-to-reel video tape recorder. The red passband was set by a Schott RG 715 filter and photocathode cutoff (7150-8500 Å). The blue band was defined by a Hoya B-390 filter and photocathode cutoff (4100-4800 Å). The video data were digitized at a scale of approximately 0.1 pixel.

¹ These observations were made with the Multiple Mirror Telescope, a joint facility of the University of Arizona and the Smithsonian Institution.

The present work improved upon Hege by using a more sophisticated rapid guider and better flat-fielder techniques. Hege integrated 1 s of video, determined the peak intensity within a 25×25 pixel ($2.5'' \times 2.5''$) window to the nearest pixel, then stacked the frames so that the peak was always at the center of the final field. The systematics in the background were approximated by subtracting the same blank field of video from each 1 s integration. There were two problems with this technique: (1) all shifting of the image was performed on 1 s integrations, although the data showed obvious movements on a 0.1 s time scale; (2) the background subtraction suffered from detector- and digitizer-induced effects which were not guided the same way, and therefore were not statistically representative. The flat-fielding was adequate for that analysis but had to be improved for the model fitting discussed below.

The present analysis reduced the effects of both these problems. Only 0.1 s of data was integrated before stacking, increasing the postguider bandwidth over Hege by a factor of 10. The rows were summed to find the *x*-axis peak, and the columns summed to find the *y*-axis peak, allowing use of all of the data in the 25×25 pixel window. This improved the guiding statistics, thereby allowing the shorter integrations. Orthogonal one-dimensional parabolae were fitted to the intensities of the pixel of the peak and ± 3 pixels from this. An example is shown in Figure 1. The peak location given by the the parabolae determined the pixel that would be shifted to the center of the stacked array.

Although more sophisticated and a better statistical representation of the rapid-guiding averaged flat field than in the previous work, the flat-fielding was still quite simple. The end-points of a linear baseline which was subtracted from each row and column were just the average of 4 pixels (0.4") at (for a column) the top and bottom of the array. The algorithm stepped through the array, fitting a line at a time. This process eliminated clock noise, seen as vertical "strips" about 1.6" apart, and a background slope (VTR artifact induced by automatic gain control) which was several percent of the peak value.

One of the biggest problems with that data set is that we have no definitive calibration of the x to y pixel scale; there being approximately a 13% stretch in the x direction, the precision of the reported positions is limited by this scale uncertainty. The absolute component separations reported in Hege

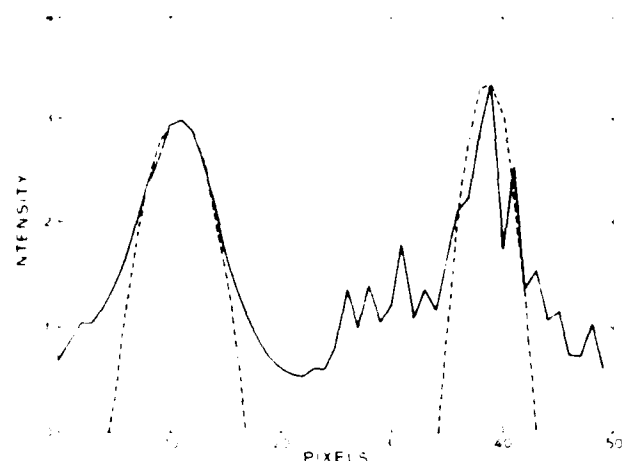


FIG. 1. Parabolic fits to an 0.1 s data integration. The left side is the summation of the rows; the right side of the columns. The column summation is much rougher due to the odd-even effect of television field interlacing. The choice of 43 pixels is a reasonable estimate of the seeing size.

and in Hege *et al.* (1981) are sufficiently imprecise to be consistent with the recent very accurate measure of the A-A' component separation observed by Foy.

Two elliptically concentric Gaussians (one primarily to fit the peak, the other to fit the wings) served as the basic point-spread function (PSF). The wing Gaussian had the same elliptical shape and rotation as the peak Gaussian. A simplex routine (Caceres and Caceres 1984) was used to fit the center (x and y), rotation angle (θ), peak amplitude (A), and semimajor axes (a and b) of the peak Gaussian, and the relative width and relative amplitude that scaled the two Gaussians. Table 1 lists the results of the fits for both the blue and red images.

The 32 parameters were allowed to fit freely and independently, except for the major and minor axes of the A and A' components, which were constrained to be the same. These results are characterized by a strong similarity of the shape-defining PSF parameters (the last five in each column), with the single outstanding (factor of 10) exception being the peak wing amplitude ratio for the red B component. The heuristic model revealed something. Further analysis is required to test its significance.

Taking advantage of the flexibility of the simplex routine, the procedure in fitting the images was to iterate components AA' and BC as follows. Initially the base level, relative amplitude and width, and position angle were fixed while fitting all four components simultaneously. From this, a rather good fit to A and A' was obtained (peak signal-to-noise ratio of 60 over the whole image). The fits to B and C were poor due to their weakness compared to A and A'. The fitted A and A' models were then subtracted from the image. Full eight-parameter models (all free to iterate) were next fitted to B and C. These models were subtracted from the original image. We iterated back and forth between AA' and BC in this manner until the fits had converged adequately.

III. RESULTS

The best-fit models and residuals (data minus model) are shown for blue and red images in Figures 2 and 3. They show the models to be in excellent agreement with the data for both the red and blue images. The largest discrepancy is on the right side of the AA' peak (inside the dashed line). This is due to a videotape recorder (VTR) nonlinearity which is understood but could not be simply modeled to eliminate it. The dashed region was not used in the model fitting because of this known effect.

The blue model is a better fit than the red. It is cleaner, more self-consistent, and because the signal was smaller, less subject to the VTR nonlinearity which is manifest in proportion to the degree of video saturation. The rms amplitude of the residuals is 6.4 mag below peak signal value (i.e., the center of the combined AA' peak). The largest residual lies on the 50% contour of the original data and is 4.8 mag below peak value. We emphasize that the blue models of A, A', B, and C all have approximately the same width and shape: the PSFs of each peak are consistent to within 10% when the parameters are allowed to vary independently.

To show that all four components in the blue image can be fitted satisfactorily by a single PSF, we created a model in which A, A', B, and C have the same PSF (Fig. 4). The widths, position angle, relative amplitude, and relative width that determine this PSF are the average values of the respective parameters in the fits to the four components. Table 2 lists the parameters that determine the model. The residuals after sub-

TABLE 1
PSF PARAMETERS FOR BEST-FIT MODELS

PARAMETER	COMPONENT							
	A		A'		B		C	
	Blue	Red	Blue	Red	Blue	Red	Blue	Red
x (pixels)	7.0 ± 0.9	4.7 ± 0.4	$38. \pm 0.9$	4.9 ± 0.6	1	1	$18. \pm 0.3$	1.5 ± 0.3
y (pixels)	-1.0 ± 0.2	-1.1 ± 0.1	1.9 ± 0.6	1.1 ± 0.2	6.9 ± 0.02	6.9 ± 0.02	18.3 ± 0.03	18.6 ± 0.03
θ (deg)	7.0 ± 0.3	2.1 ± 0.3	2.70 ± 0.2	2.1 ± 0.3	17.2 ± 0.04	15.7 ± 0.03	2.7 ± 0.02	3.0 ± 0.01
Semimajor axis ^a	6.3 ± 0.2	4.4 ± 0.2	6.3 ± 0.2	4.4 ± 0.2	6.1 ± 0.4	6.2 ± 0.1	6.2 ± 0.6	4.5 ± 0.3
Semiminor axis ^b	4.2 ± 0.1	3.7 ± 0.1	4.2 ± 0.1	3.7 ± 0.1	4.2 ± 0.1	4.7 ± 0.1	4.4 ± 0.5	3.9 ± 0.3
Rotation angle ^c	57 ± 1	76 ± 8	97 ± 1	84 ± 8	57 ± 1	80 ± 1	91 ± 1	79 ± 2
$\text{Amp}_{\text{peak}}/\text{Amp}_{\text{wing}}$ ^d	2.0 ± 0.6	2.2 ± 0.8	1.5 ± 0.3	1.5 ± 0.2	18 ± 0	16.5 ± 6.5	1.7 ± 0.4	3.0 ± 0.2
$\text{Wid}_{\text{peak}}/\text{Wid}_{\text{wing}}$ ^e	0.56 ± 0.02	0.54 ± 0.04	0.66 ± 0.02	0.57 ± 0.03	0.60 ± 0.07	0.52 ± 0.16	0.61 ± 0.2	0.52 ± 0.08

^a Ratio of peak amplitude to peak amplitude of B.

^b Pixels (x, y) defined as midpoint between A and A'.

^c Measured clockwise from horizontal.

^d Ratio of amplitude of peak Gaussian to amplitude of wing Gaussian.

^e Ratio of width of peak Gaussian to width of wing Gaussian.

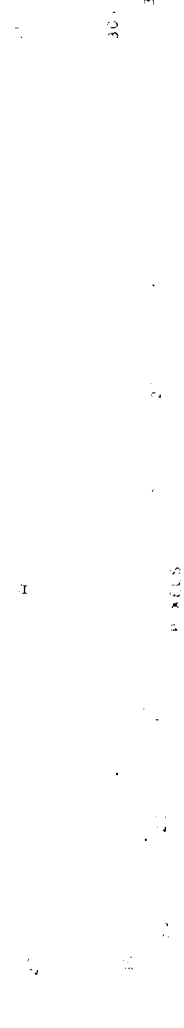
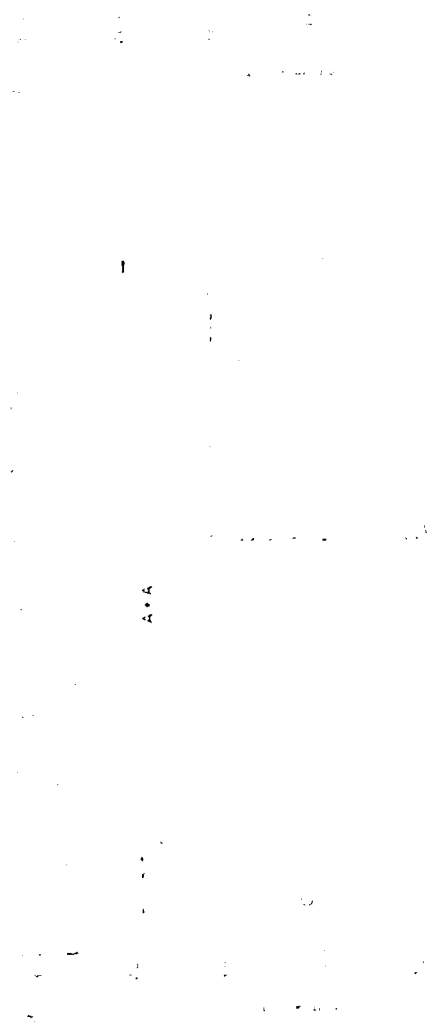


Fig. 1. Relationship between A+A and P.

100

100

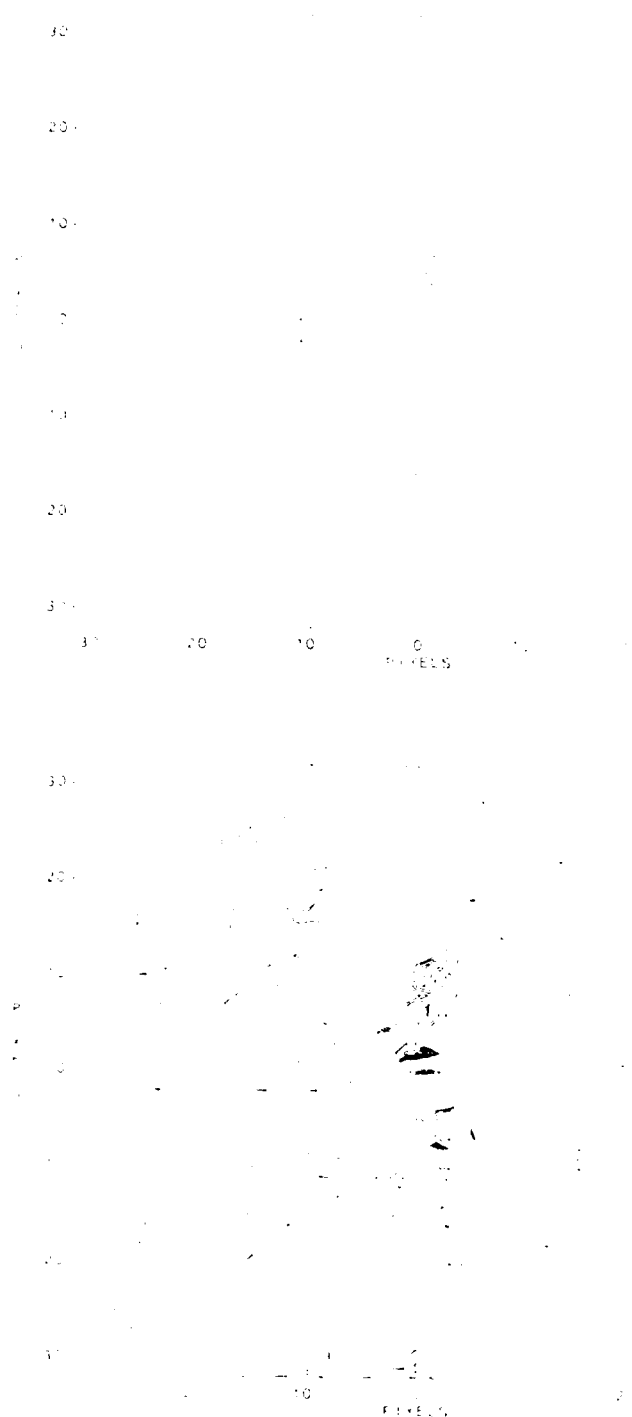


Fig. 4. VA peak, which VA, B, and C all have in common. Plot is as in Fig. 1. The results of the average noise in this case are plotted using the same method as in the case of the results in map 1. Fig. 5. The same as in Fig. 4, but the peaks are all of the same intensity as the combined VA peak. The rms noise in the results is 0.0001, which is the VA peak.

TABLE 1
PARAMETERS FOR S-NR (PSF, BLUE) MODEL
A, RED; A', BLUE; B, RED; C, BLUE; D, BLUE; E, BLUE

Parameter	Component			
	A	A'	B	C
Position	1.0	3.0	1.0	1.0
Width	1.0	1.0	1.0	1.0
Amplitude	1.0	1.0	1.0	1.0

B, S-NR (S-NR) PARAMETER

Parameter	Value
Semimajor axis	1.0
Semiminor axis	1.0
Rotation angle	0.0
Amplitude	1.0
Width	1.0

S-NR (S-NR) is a measure of the signal-to-noise ratio. It is defined as the ratio of the signal to the noise. The S-NR (S-NR) is a measure of the signal-to-noise ratio. It is defined as the ratio of the signal to the noise.

tracing this model from the blue image are comparable to the residuals of the best-fit model. The rms noise is 6.1 mag below peak signal value, and the largest residual is 4.2 mag below peak value.

In contrast, red component models for A, A', and C are consistent with the data in the region away from the nonlinear artifact, but B was found to be wider and more like a single Gaussian in character (the large value of peak to wing impolder). The largest red residual (labeled D in Fig. 2) lies at about the 6- σ contour, between all three components, and is 4.8 mag below the peak, 1.2 mag above the noise (3σ). This residual is more extended, rounder, and more Gaussian-like than any other residual in either the red or blue. On this basis alone, it is an interesting feature. Its significance will be discussed below.

An obvious difference between model fits to the red and blue images is the different relative amplitudes of A and A'. This is almost certainly due to distortion of the peak values by the VTR nonlinearities mentioned above: the more nearly saturated red image has more distortion on the down-raster side (higher pixel values) than the blue. This is a nonlinear effect, and it is difficult to say just how the cutoff will influence the image shapes and relative amplitudes. While the nonlinear region was avoided in the model fitting, the distortion of the peaks could not be avoided, and little physical significance can be placed on the relative amplitudes derived for A and A' in the red case. Nevertheless, the high degree of similarity of the A peak PSFs to those of all of the blue peaks (Table 1) is significant.

This gives us a high degree of confidence in the validity of our video detector recorder PSF and suggests that it is highly likely that all the image components are unresolved and therefore characterized by the same PSF, subject to the saturation-induced nonlinearity down-raster of the red image AA' peak. Image intensifier pinchion distortion is responsible for the 10% differences, which are significant, but small compared to the factor of 10 discrepancy in one of the shape characteristic parameters of the B component PSF.

The nonlinearity, being primarily a down-raster phenomenon, and only to second order a cross-line phenomenon (each

video scan being an independent measurement), it is likely that the greatest effect of the nonlinearity is the distortion of the amplitude of the southern (A) component which lies two pixels down-raster from A'. The effect of the saturation is to have clipped both components. The less saturated blue image appears to be nearly free of this saturation-induced artifact and exhibits an even larger amplitude difference than suggested earlier (Hege *et al.* 1981), with the southern (A) component brighter (opposite to the conclusion of Foy).

We have already noted that the most remarkable feature of Table 1 is in the anomalous fit to red component B. It is wider, more like a single Gaussian, and redder by 0.1 ± 0.1 mag than A, A', or C, consistent with Young. No down-raster distortions can shift a peak location perpendicular to the raster, significantly, in this free fit where the peak position is also a free parameter; the red peak is 1.8 ± 0.8 pixels closer to A and A' than in the blue model.

There are four possible reasons for this: blue obscuration of B, red obscuration of A, A', and C, an excess red flux from the B region, or underestimation of red wing of A. Figure 5 shows a vertical cut through B after subtraction of the computed A wing, which is also plotted. It shows that the A wing was actually an *overestimation*; part of image B appears to be "missing," implying that B is *even redder* than presented in Figure 3 and Table 1. Several different models for A were fitted and that shown in Figure 5 gave the smallest residuals over a region 20 pixels wide centered on the A peak. Yet there is no evidence that the A-component PSFs have excess width. This is a strong signature of a model with too few components.

Obscuration is not likely to be the cause of the anomalous red B fit. While obscuration can account for the redness, it cannot explain why all four components have the same PSF in the blue model, and why A, A', and C have similar PSFs in the red model. Due to atmospheric dispersion and the broad observing bandpasses used, the blue PSF is expected to be elongated in elevation, compared to the red PSF, in qualitative agreement with the differences seen in the fit (Table 1); the vertical elongation is about 40% greater for the blue PSF than for the red PSF.

A red excess near B could certainly explain why it appeared brighter, wider, and closer to AA' in the red model. Since red A,

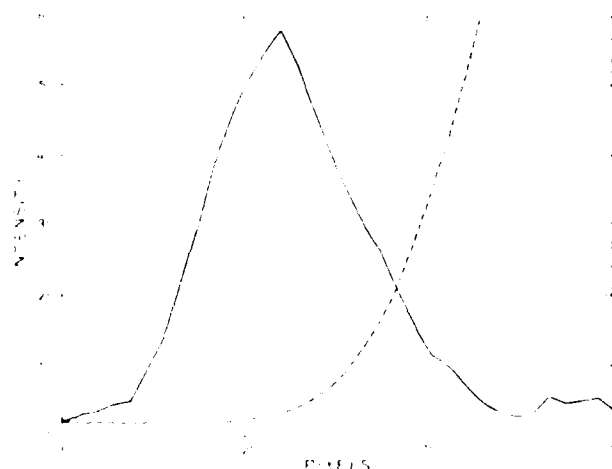


FIG. 5. A vertical cut through the peak of red image B. Also shown is the fit to the A wing which was subtracted from B, resulting in B'. The A model appears to be a slight overestimate.

flux variations, a knowledge of the redshift, mass, and general shape of the lensing galaxy should help to yield more stringent constraints on the Hubble parameter.

This paper would not have been possible without the use of the computer facilities of the National Radio Astronomy Observatory at Tucson, which is operated by Associated Uni-

versities, Inc., under contract with the NSF. Many thanks to C. Salter, R. Narayan, M. Rieke, T. Singer, J. Christou, J. Hebdem, and the Speckle Interferometry group at Steward Observatory for many helpful discussions. A. Cheng provided the simplex routines. This research was supported in part by the Air Force Office of Scientific Research grant AFOSR 82-0020.

REFERENCES

- Cacciari, M. S., and Cichonis, W. P. 1984, *Bull.*, Vol. 9, No. 5 (May), p. 340.
 Heger, E. K., Angel, J. R. P., Weymann, R. J., and Hubbard, E. N. 1980, *Nature*, **287**, 436 (Heger).
 Heger, E. K., Hubbard, E. N., Strittmatter, P. A., and Worden, S. P. 1981, *Ap. J. (Letters)*, **248**, L1.
 Falco, E. E., Gorenstein, M. V., and Shapiro, I. I. 1985, *Ap. J. (Letters)*, **289**, L1.
 Foy, R., Bonneau, D., and Blazit, A. 1985, *ibid.*, **149**, L13.
 Vandernest, C., Wierick, G., Leflage, A., Lechevre, G., Servan, B., and Micher, D. 1983, in *24th Lunar and Astrophysical Colloquium, Quasars and Gravitational Lenses* (Gee, Institut d'Astrophysique), p. 182.
 Weymann, R. J., Falco, E. E., Angel, J. R. P., Green, R. L., Ekers, J. W., Turnsheat, D. A., Linnartz, D. L., and Lyser, J. A. 1980, *Nature*, **285**, 641.
 Young, P., De Grijl, R. S., Gunn, J. E., Westphal, J. A., and Kristian, J. 1981, *Ap. J.*, **244**, 73 (Young).
 Young, P., Gunn, J. E., Kristian, J., Oke, J. B., and Westphal, J. A. 1980, *Ap. J.*, **241**, 80.

E. K. HEGE and S. B. SHAKRYAN: Steward Observatory, University of Arizona, Tucson, AZ 85721

Use of matched filtering to identify speckle locations.*

E. Ribak, E. F. Hege** and J. C. Christou†

Steward Observatory, University of Arizona
Tucson, Arizona 85721Abstract

In many cases the speckle maxima required for the our realization of the Shift-and-Add method¹ are not well defined. This is due mainly to Poisson noise, inherent in the detection process, which obliterates the shape of faint speckles. The problem is aggravated for extended objects with local peaks, such as binary stars. As a remedy, we use a filter that smoothes out each speckle and at the same time defines its location.

The best filter should be very close to the mean speckle itself: a matched filter. The initial guess for this filter is a bell function, slightly wider than the expected mean speckle. This initial guess is used to locate filtered speckle maxima which are then used to produce a better mean speckle estimate by shift-and-add. The procedure is iterated until the mean speckle converges.

We find that the iterative speckle estimate is not the optimum matched filter. The best suitable filter must suppress the variable background created by coalescing speckles in a large speckle cloud as well as smooth the single-photon event noise. Thus we combine the mean speckle with a band-pass filter into a matched filter. Local speckle maxima are thus enhanced, whereas single photons are discriminated against by using a comparison low-pass filtered frame, since they do not contain much power. The combined process, speckle identification and weighted-shift-and-add, can be carried out in the image plane or in the Fourier plane. We have experimented in both domains.

Shift-and-Add methods

Recent efforts in the field of stellar speckle interferometry^{2,3} are directed towards recovering true images of the observed objects. A great deal has been done to reconstruct the phases of these objects to combine with their power spectra in order to obtain the true image. Other approaches, known as the Shift-and-Add techniques, try to retain the information they appear in the original specklegram.

Lynds and Jay⁴ realized that at least one Fourier-plane phase is easy to find: that corresponding to the strongest intensity in the specklegram frame. If the displacement of this point is known, then the frame can be shifted to place this maximum at its center. Adding many such shifted frames will yield the average intensity around the brightest spots in all the specklegrams. This is known as the Shift-and-Add routine. Lynds, Warden and Harney⁵ (LWH) devised an approach that locates not just the absolute maximum in each frame, but also the brightest local maximum (after some initial smoothing). A set of equal-amplitude delta-functions is created, corresponding to the coordinates of these maxima. A cross-correlation of this set with the original frame shifts all the local maxima to the center, producing a similar result to the Shift-and-Add technique (though with higher efficiency).

The natural continuation to these two methods is the seeing calibrated Weighted Shift-and-Add⁶. Like the LWH method, all the local maxima are found, and a set of delta-functions is created according to their locations. Each one of these delta functions is multiplied (or weighted) by the intensity of the corresponding maximum. Each frame is correlated in the Fourier plane with its set of weighted delta functions and the correlations averaged. Finally the average cross-correlation is deconvolved by the average power spectrum of the delta functions in order to reduce the atmospheric seeing effects in the final result.

* Observations reported here were obtained at Kitt Peak National Observatory, a division of the National Optical Astronomy Observatories, operated by the Association of Universities for Research in Astronomy, Inc., under contract to the National Science Foundation.

** Visiting Astronomer, Kitt Peak National Observatory.

† Visiting Astronomer from the Dept. of Astronomy, New Mexico State University, Las Cruces, NM 88003.

All realizations of the Shift-and-Add technique have one problem in common: they rely strongly on finding local maxima and on the assumption that these are equivalent to speckle locations. Shot noise, atmospheric effects and object morphology can all invalidate this assumption.

Due to Poisson statistics, the number of maxima can be much larger than the number of speckles. If the intensity of the object is low, there are some speckles which will contain only one photon, with no structure information in it. If the object has a wide maximum, then both Poisson noise and atmospheric phase fluctuations might distort its image and create a spurious local maximum. Finally, the object could be multiple-peaked, which can be mistaken as many speckles, with the final result resembling an auto-correlation instead of an image.

Matched filter approach

The problem to address is how to locate speckles of approximately the same shape but of different intensity in a noisy background, even if this shape might not be single-peaked. If there is no knowledge of this shape, the answer is Wiener filtering; if there is full knowledge, matched filtering should be applied. Fortunately, in most cases prior information about the object is available, usually through conventional speckle interferometry which provides the object auto-correlation. This enables us to use matched filtering, which is more efficient than Wiener filtering⁶. The initial estimate provides a filter, which is applied to the speckle frame. A peak-finding algorithm detects all maxima above a threshold, and the corresponding speckles are shifted to the centre (by any of the Shift-and-Add methods described above). Averaging over a few frames, we have a better estimate for the object, which can be modified into a matched filter for the next frames. After a few such iterations most of the refinements to the estimate are in the finer details.

Suppose we have an image of our object $o(x,y)$ with an additive noise $n(x,y)$ whose power spectrum is $P_n(u,v)$. We denote quantities in the Fourier transform by capital letters, i.e. $FT\{o(x,y)\} = O(u,v)$. We now apply a filter to the noisy frame, and require that the S/N power ratio is maximal at the output of the filter. As a result we get for the filter⁶

$$F(u,v) = C \exp[-2\pi i(ux_0 + vy_0)] O^*(u,v) / P_n(u,v) \quad (1)$$

where C is an arbitrary constant. In the simple case of white noise, where $P_n(u,v) = N^2$, we can set $C = P_n$ and get, in reference to some arbitrary point (x_0, y_0) :

$$F(u,v) = O^*(u,v) \exp[-2\pi i(ux_0 + vy_0)] \quad (2)$$

Transforming back, the filter will be $o(x_0 - x, y_0 - y)$, which is the reversed object in respect to the point (x_0, y_0) .

Going through the assumptions leading to the above derivation, we find some departures from our case. The main ones are: (a) the exact shape of the object is not known; (b) speckle power is variable and can be below noise level; (c) white noise spectrum cannot describe properly the speckle and Poisson processes; (d) the low-pass filtering inherent in the application of the matched filter hinders detection of close speckles, especially for larger objects. None of these departures invalidates the process, and we describe what has been done in order to reduce their effect.

We have used our algorithm with different initial guesses, in order to test its sensitivity to the fact that the object shape is not really known. We found that for sufficient iterations and an initial guess not smaller than the object (whose size can be inferred from the power spectrum), the process always converged toward the same answer. Specifically, a Gaussian bell of the approximate size always seems to be a proper initial guess (fig. 1).

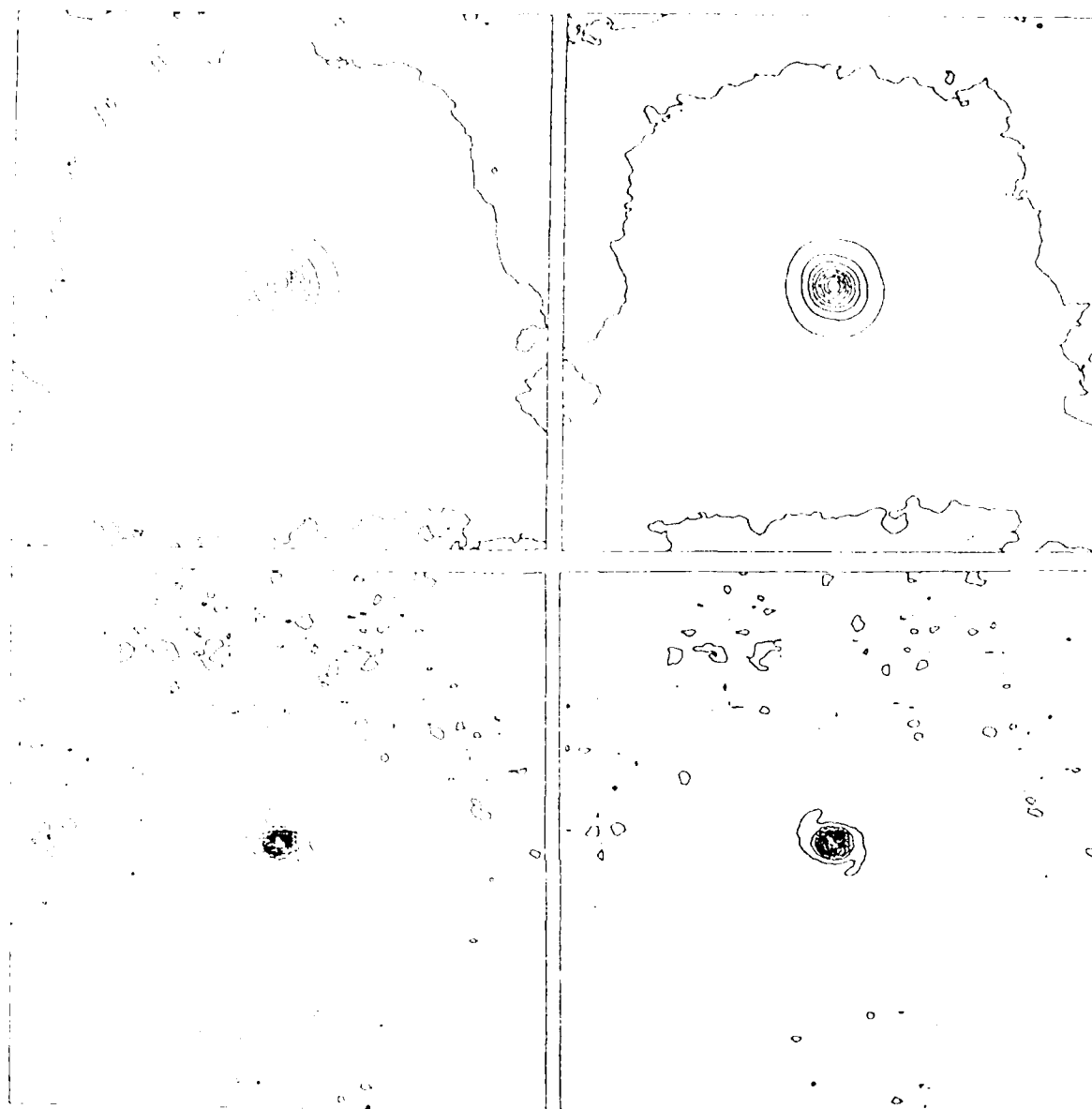


Figure 1. Alpha Orionis (top) and Gamma Orionis (bottom) for two apodizations applied to the matched filter (28 pixels FWHM, left, 52 pixels FWHM, right). Observations were made with a 3.8 m telescope at 650 ± 1 nm, and Gamma Orionis is unresolvable. The images of Alpha Orionis are different by 10% in size.

The problem of speckles of different power seems to be very easy to solve. When applying a matched filter the following step is to detect all the signals above the noise. To that end, a constant threshold is set just above the noise level. Since in the case of speckle frames the noisy background is higher in the center, we chose to utilize a variable threshold which depends on the intensity around the speckles. At the same time that the frame is passed through a matched filter, it is also passed through a smoothing filter. The highly smoothed version of the frame then serves as a threshold for the filtered frame, and only maxima above it are considered as speckles.

The two last problems regarding the statistics of the atmospheric distortions and the detection process seem to be more severe, especially because of the lack of a full theory. The models describing the speckle process usually work well in the pupil plane, whereas we are interested in a statistical description of speckles in the image plane. We are trying to combine a partial model for Shift-and-Add⁷ with our own measurements to produce a better model for the specklegram⁸. In essence, it seems possible to describe a speckle pattern as a triple convolution of the object with the telescope and with an infinite set of delta functions (fig. 2). The latter has a random distribution of both

locations and intensities governed by the atmosphere. During detection, shot noise is added to the speckle pattern, and the result is convolved with the detector transfer function. In the different realizations of Shift-and-Add an effort is made to proceed in the reverse direction. An estimate of a subset of the delta functions is produced, the original specklegram is deconvolved by it, and the result averaged over many frames.¹ From this average it is possible to remove the atmospheric seeing background (due to the incompleteness of the subset of delta functions) and the central photon spike (due to the Poisson statistics). Both are done using appropriate models. Another deconvolution by the telescope transfer function (reduced from an unresolvable star) is needed to obtain the original image.

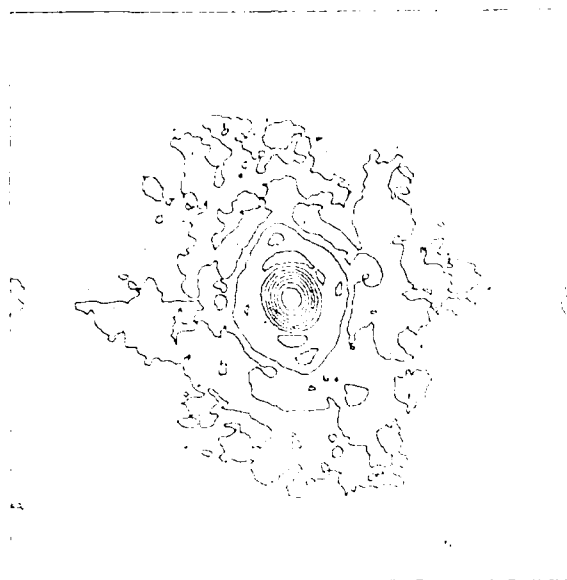


Figure 2. An image of an unresolvable star (Zeta Aquarii A) with the 2.28 m telescope at 750+10 nm, showing the (aberrated) telescope point spread function. Logarithmic intensity scale. All figures are with north down, east to the right.

Despite the fact that it is possible to remove the seeing background and photon spike from the final image, it is preferable to devise a matched filter that would directly give the right answer. Since some information is available about the power spectra of the Poisson noise and the seeing, we incorporate it into the matched filter while performing the iterative data reduction. In the Fourier plane, the main effect of the seeing background is in the very low frequencies, whereas the frequencies at which the Poisson noise is noticeable are high, usually beyond the telescope diffraction limit. Thus the total noise power spectrum (eq. 1) is more accentuated at the very low and very high frequencies. Dividing the object transform by this power spectrum is equivalent to multiplying it by its reciprocal, i.e. a band-pass filter.

The combination of a band-pass filter with the object produces an optimum matched filter which is now applied to the specklegram. Still, one can look at this as a triple convolution between the inverted object, the band-pass filter and the frame. The band-pass filter partially solves both problems (c) and (d) discussed earlier. It smooths out single-photon events below the threshold level, so that they are not regarded as speckles. At the same time it sharpens the wide auto-correlations between the speckles and the object, and as a result the efficiency of detecting speckle maxima increases.

Application and results

The first reductions were done in image space, in an approach similar to the simple Shift-and-Add. An estimate of the object, usually a Gaussian, was slid along and multiplied with the frame (image plane correlation). At the same time a smoothing function (a wider Gaussian) was correlated with the frame. Every local maximum that was higher in the filtered frame than in the smoothed frame was counted as a speckle, and the corresponding part in the original specklegram was added to the running sum. With very bright objects, where the photon noise is negligible, the result appeared after only one frame. The computational efficiency of this method was rather low, especially for larger objects which demanded many multiplications. The advantage was that only one full frame resided in memory at any time.

The availability of a larger computer (Data General MV1000) at Steward Observatory made it possible to work in the Fourier plane. The cycle for each frame is as follows: (a) read frame in; (b) transform the frame; (c) multiply the frame transform with the current matched filter estimate; (d) multiply the frame transform with the smoothing (low-pass) filter; (e) inverse-transform the filtered frame; (f) inverse-transform the smoothed frame; (g) locate all the peaks in the filtered frame above the smoothed one and create a frame with corresponding impulses in it; (h) transform the impulse frame; (i) multiply the frame transform of the impulse transform and add to running sum; (j) add impulses power spectrum to running sum. This process is very similar to the weighted Shift-and-Add process, which requires two Fourier transforms per frame. The matched filter process includes the extra steps c-f, which imply two more transforms per frame. It turns out that the time required per frame is about six seconds, compared to four with Weighted Shift-and-Add.

Once every 1000 - 10000 filtered speckles, depending on the nature of the data and the expected object shape, we update the matched filter estimate. This is done by (a) dividing the average frame-impulse cross-spectrum by the average impulse power spectrum to get the current speckle image; (b) inverse-transforming this average image; (c) apodizing the result to get rid of noise in the wings of the filter; (d) transforming the apodized image; (e) multiplying by the band-pass filter to give the optimum matched filter. The apodization is usually not necessary, except for the first iterations when the noise at the outskirts of the image can correlate with the specklegrams to produce false maxima. Also, for multiple-peaked objects which tend to have sidelobes, an apodization can deter positive feedback which leads to growth of these sidelobes (fig. 3). Care should be taken when applying apodization, since the apodizing bell should be larger than the object extent (fig. 1).

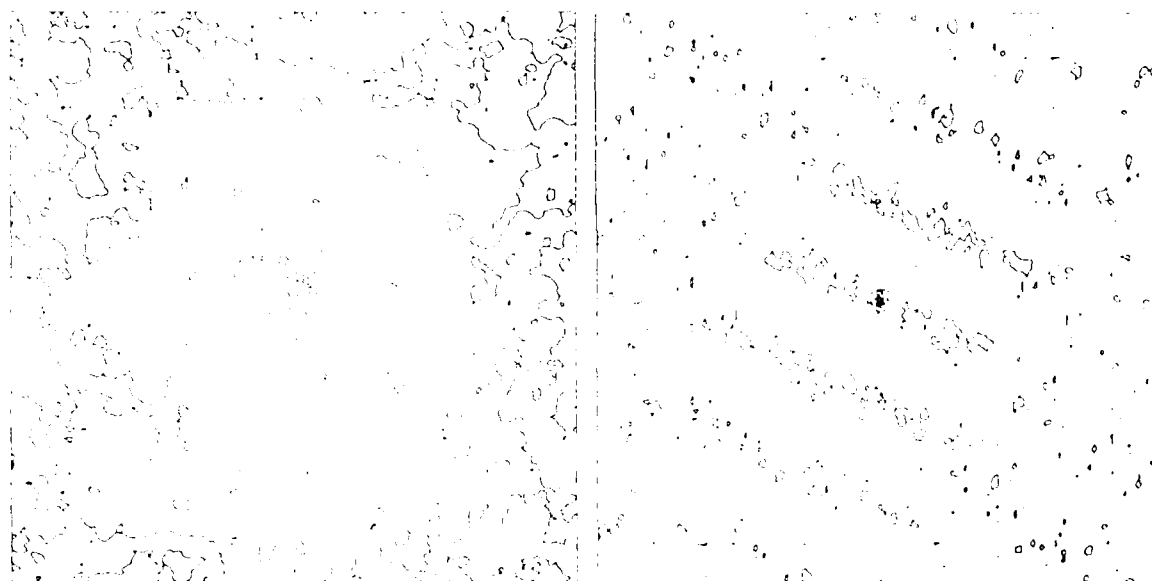


Figure 3. Left: The binary star Alpha Centauri (1.6 m telescope, 550+10 nm), with two sidelobes at the top and bottom, created by double-detections of single speckles. At right, the impulse frames power spectrum for the same data, showing residue fringes at the 0.5% level produced by this effect. No apodization was applied to the matched filter.

The main deficiencies of the current implementation of the matched filter method are: (a) complicated calculations requiring much computer time; (b) for extended objects, too few speckles are found, which lead to an extended background; (c) for multiple peak objects, great care must be taken when building the filter, lest the filtered frame will have more than one maximum per speckle, losing the advantage over other Shift-and-Add methods.

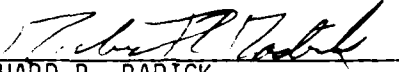
Acknowledgements

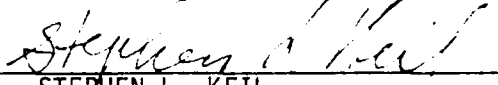
This work is supported in part by NSF (grants AST-8113212, AST-8201092). E. R. is a recipient of a Weizmann Fellowship.

References.

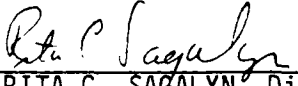
1. Christou, J. C., E. K. Hege, J. D. Freeman & E. Ribak, "Images From Astronomical Speckle Data: Weighted Shift-and-Add Analysis", Proc. SPIE 556-36, 1985.
2. Dainty, J. C., "Stellar Speckle Interferometry", Laser Speckle and Related Phenomena, J. C. Dainty, Ed., 2nd Ed., Springer-Verlag, 1983.
3. Bates, R. H. T., "Astronomical Speckle Imaging", Physics Reports **90**, 203, 1982.
4. Bates, R. H. T., & F. W. Cady, "Towards True Imaging by Wideband Speckle Interferometry", Opt. Commun. **32**, 368, 1980.
5. Lynds, C. R., S. P. Worden & J. W. Harvey, "Digital Image Reconstruction Applied to Alpha Orionis", Ap. J. **207**, 174, 1976.
6. Castleman, K. R., Digital Image Processing, Prentice-Hall, 1979.
7. Hunt, B. R., W. R. Fright & R. H. T. Bates, "Analysis of the Shift and Add Method for Imaging through Turbulent Media", J. Opt. Soc. Am. **73**, 456, 1983.
8. Freeman, J. D., E. Ribak, J. C. Christou & E. K. Hege, "Statistical Analysis of the Weighted Shift-and-Add Image Reconstruction Technique", Proc. SPIE, 556-40, 1985.

This technical report has been reviewed and is approved for publication.


RICHARD R. RADICK
Contract Manager


STEPHEN L. KEIL
Chief, Solar Research Branch

FOR THE COMMANDER


RITA C. SAGALYN, Director
Space Physics Division

This report has been reviewed by the ESD Public Affairs Office (PA) and is releasable to the National Technical Information Service (NTIS).

Qualified requestors may obtain additional copies from the Defense Technical Information Center. All others should apply to the National Technical Information Service.

If your address has changed, or if you wish to be removed from the mailing list, or if the addressee is no longer employed by your organization, please notify AFGL/DAA, Hanscom AFB, MA 01731. This will assist us in maintaining a current mailing list.

Do not return copies of this report unless contractual obligations or notices on a specific document requires that it be returned.

END

DATE

3-88

DTIC